

MEASUREMENT OF THE COSMIC $e^+ + e^-$ FLUX
FROM 0.5 GEV TO 1 TEV
WITH THE ALPHA MAGNETIC SPECTROMETER (AMS-02)
ON THE INTERNATIONAL SPACE STATION

Valerio Vagelli

Zur Erlangung des akademischen Grades eines
DOKTORS DER NATURWISSENSCHAFTEN
von der Fakultät für Physik der
Karlsruher Institut für Technologie (KIT)

genehmigte

DISSERTATION

von

M.Sc. Valerio Vagelli
aus Cecina, Italien

Tag der mündlichen Prüfung: 14. November 2014

Referent: Prof. Dr. W. de Boer
Institut für Experimentelle Kernphysik
Korreferent: Prof. Dr. U. Husemann
Institut für Experimentelle Kernphysik

Abstract

The measurement of positrons and electrons (e^\pm) in cosmic rays provides fundamental information about the origin and the propagation of cosmic rays in the Galaxy. The interest in the e^\pm measurements is enhanced by the possibility to observe indirect evidences of Dark Matter annihilation in the e^\pm spectral shapes and arrival directions. The most precise space experiment for the detection of cosmic rays is the Alpha Magnetic Spectrometer (AMS). AMS is a large acceptance cosmic ray detector which has been installed on the International Space Station in May 2011 to conduct an unique long-duration (~ 20 years) mission of fundamental physics research in space. In this thesis, the events collected by AMS in the first 30 months of data taking have been analyzed to measure the $(e^+ + e^-)$ energy spectrum. A total of 10.6 million events have been identified as e^\pm and have been used for the measurement of the $(e^+ + e^-)$ flux from 0.5 GeV to 1 TeV[1]. In this thesis the AMS detection capabilities, the e^\pm identification procedure, the $(e^+ + e^-)$ flux measurement, and the discussion of the result are presented.

I declare that I have developed and written the enclosed thesis completely by myself, and that I have not used sources or means without declaration in the text.

Karlsruhe, 27.10.2014

Valerio Vagelli

To my superheroes: my mom, my dad, my brother, my grandpas and grandmas.

Contents

Introduction	1
1 Cosmic ray physics and the search for Dark Matter	5
1.1 Charged cosmic rays	5
1.1.1 Origin of cosmic rays	7
1.1.2 Propagation of galactic cosmic rays	8
1.1.3 Propagation of cosmic rays in the heliosphere and in the magnetosphere	12
1.1.4 Detection of cosmic rays	14
1.2 Electrons and positrons in the cosmic radiation	19
1.2.1 Propagation of cosmic ray electrons and positrons	19
1.2.2 Measurements of the local electron and positron fluxes	20
1.2.3 Astrophysical interpretation of the cosmic electron and positron fluxes	22
1.3 Dark Matter	26
1.3.1 Evidence for Dark Matter at galactic and galaxy cluster scales	26
1.3.2 Evidence for Dark Matter at cosmological scales	28
1.3.3 Dark Matter candidates and the WIMP miracle	31
1.3.4 Experimental searches for Dark Matter	33
1.3.5 Indirect Dark Matter search in the cosmic electron and positron fluxes	41
1.3.6 Conclusions	44
2 The AMS-02 detector	47
2.1 Transition Radiation Detector TRD	48
2.2 Time Of Flight TOF	51
2.3 AntiCoincidence Counter ACC	52
2.4 Permanent Magnet PM	53
2.5 Silicon Tracker TRK	54
2.6 Ring Imaging Cherenkov RICH	56
2.7 Electromagnetic Calorimeter ECAL	58
2.8 Data Acquisition DAQ and Trigger	61
2.9 AMS operations	62
2.10 AMS physics	63
3 Introduction to the flux measurement	65
3.1 The flux measurement	65
3.2 Data sample	67
3.3 The Monte Carlo simulation spectral shape and normalization	69
3.4 Energy intervals for the flux measurement	70

4	Electron and positron identification with the AMS experiment	71
4.1	Sample definition	72
4.1.1	(a) Good data taking and attitude conditions	73
4.1.2	(b) Geometric selection and clean event reconstruction	73
4.1.3	(c) Charge-one particle	78
4.1.4	(d) Geomagnetic cutoff selection	81
4.1.5	Selection summary	83
4.2	ECAL and TRD and their role in the e^\pm identification	83
4.2.1	ECAL electron/proton separation	84
4.2.2	TRD electron/proton separation	92
4.3	Electron and positron signal extraction	97
4.3.1	TRD classifier templates	97
4.3.2	Signal yield extraction	100
4.4	Electron and positron identification uncertainties	105
4.4.1	Data driven estimation of signal identification systematic uncertainties	108
4.5	Summary	113
5	Normalization to the $(e^+ + e^-)$ flux on top of the detector	117
5.1	Exposure time	117
5.2	Trigger	118
5.3	AMS acceptance for e^\pm	121
5.3.1	Acceptance formulation	121
5.3.2	Acceptance calculation for the $(e^+ + e^-)$ flux measurement	122
5.4	Assessment of the acceptance systematic uncertainties	125
5.4.1	Comparison between data and MonteCarlo simulation	126
5.4.2	Acceptance corrections and systematic uncertainties	135
5.5	Summary	145
6	The $(e^+ + e^-)$ flux measurement	147
6.1	The ECAL energy measurement	147
6.1.1	ECAL resolution and absolute scale	148
6.1.2	Where to stick the data points	153
6.2	The measurement of the cosmic ray $(e^+ + e^-)$ flux from 0.5 GeV to 1 TeV	155
6.3	Phenomenological interpretation of the measurement	163
6.3.1	Model independent $(e^+ + e^-)$ flux spectral analysis	163
6.3.2	Model dependent parametrization of the e^- and e^+ fluxes	167
6.4	Summary	175
	Conclusions	179
	A Cosmic ray events collected by AMS	185
	B ECAL Longitudinal BDT	187
	C TRD template fit examples	193
	D Differential acceptances for the $e^+ + e^-$ flux measurement	201
	E Further aspects of the e^+ and e^- flux parametrization	205

Introduction

The physics of cosmic rays began in 1912, when Victor Hess measured for the first time an increase in the level of ionizing radiation in the atmosphere. The presence of energetic particles coming from outer space, the cosmic rays, was confirmed by many experimental observations in the later years. Cosmic rays represented the only source of energetic particles available to the physics community to explore the sub-nuclear scales before the accelerator technology took over in 1950s and provided a controlled source of energetic particles in the laboratory. The discovery of the positron in the cosmic radiation by Carl Anderson in 1932 represents, as example, the first experimental observation of antimatter. This observation confirmed the predictions theorized by Paul Dirac in 1928. Both scientists won Nobel prizes for their contributions to the community.

The physics of cosmic rays, or astroparticle physics, involves extreme energy and distance scales. This renders the astroparticle physics field challenging from the experimental and phenomenological sides. Only most recently, indeed, the origin of cosmic rays as particles produced by supernovae and accelerated in supernova remnant shocks has been confirmed by the experimental observations of the Fermi-LAT satellite experiment [2].

The accurate measurement of electrons (e^-) and positrons (e^+) in cosmic radiation represents one of the major topics addressed by astroparticle physics research in the latest decades.

The properties of the e^\pm cosmic component fully justify the experimental efforts. Electrons and positrons are the lightest charged cosmic rays. During their propagation in the Galaxy e^\pm suffer relevant energy losses due to their interactions with the interstellar medium and with the turbulent galactic magnetic fields. Cosmic ray hadrons, instead, suffer much smaller energy losses and they consequently travel longer distances. Electrons and positrons can therefore probe the origin and propagation of cosmic rays in the local interstellar medium in a complementary approach with respect to that of the more abundant hadronic cosmic ray component.

The measurements of cosmic e^- and e^+ point to a flaw in the current models of primary production and propagation of the cosmic rays. The standard e^\pm production and propagation model assumes that only e^- are produced in the standard cosmic ray accelerators and that e^+ are a secondary product of interactions of cosmic ray hadrons with the interstellar medium. However, this model is not sufficient to explain the observed spectral features. The abundance of the e^+ component is, in fact, much higher than what this standard model can allow. The excess of cosmic ray e^+ , reported in the measurement of the positron fraction $e^+/(e^+ + e^-)$ and of the e^+ flux, steadily increases as function of energy starting from ~ 10 GeV up to ~ 275 GeV. Above this energy, the level of excess of e^+ flattens out. This behavior is not expected by the standard cosmic ray model.

The e^\pm cosmic ray component represents a window to investigate in a complementary approach the open problems of the fundamental particle physics field. The Standard Model of particle physics, recently further confirmed by the observation of the Higgs Boson signature in the LHC proton-proton collisions [3, 4], does not explain all the experimental observations. One of the most intriguing open

problems in fundamental physics is the nature of Dark Matter. The race for the search of Dark Matter is engaged in collider experiments, in underground laboratories and in cosmic ray observations. The excess of the e^+ component observed in cosmic rays could be indeed explained in terms of a primary additional production of e^\pm from Dark Matter annihilation and other exotic models. Besides to the Dark Matter signature, purely astrophysical primary production and acceleration from nearby pulsars can also explain the features observed in the cosmic e^\pm fluxes. Accurate measurements of several observables of the e^\pm components in cosmic rays will serve to disentangle these hypotheses and to correspondingly constrain the allowed phenomenology in the Dark Matter searches.

The low abundance of the e^\pm component with respect to the dominant hadronic component in the cosmic radiation makes the experimental measurement of this components challenging. A large experimental effort has been undertaken in the last 20 years by balloon [5, 6, 7, 8, 9, 10, 11, 12, 13], space born [14, 15, 16, 17, 18, 19] and ground based [20, 21] detectors in order to study this low abundant cosmic ray component in an extended energy range. The highest experimental accuracy is achieved by space experiments, which measure the components of the cosmic radiation outside the screening effect of the Earth atmosphere. The typical measured quantities are the fluxes of e^- , e^+ , and the sum flux ($e^+ + e^-$), namely the measurement of the e^\pm flux disregarding the charge sign. The use of a spectrometer is mandatory for the measurement of the separate e^+ and e^- fluxes¹.

The latest and most accurate results for the e^\pm fluxes have been provided by the Alpha Magnetic Spectrometer (AMS) operating on the International Space Station (ISS). AMS is a high acceptance multi-purpose particle physics detector that has been installed on the ISS in May 2011 and that is collecting cosmic rays in the GeV to TeV energy range with no major interruption since the start of the data taking. The precise measurement of the cosmic e^\pm component represents one of the primary AMS targets, and AMS has been equipped with dedicated subdetectors to achieve this goal. AMS recently measured the e^- flux from 0.5 GeV to 700 GeV and the e^+ flux from 0.5 GeV to 500 GeV with a percent level accuracy and up to a maximum energy never achieved before. It also provided the most accurate measurement of the positron fraction up to 500 GeV.

The measurement of the ($e^+ + e^-$) flux represents the latest contribution by the AMS experiment to the understanding of the cosmic e^\pm spectral features. With respect to the separate e^- and e^+ fluxes, the ($e^+ + e^-$) flux measurement does not distinguish the charge sign of the detected e^\pm . This allows for less stringent requirements on the quality of the detected events during the data analysis which consequently enhance the e^\pm data sample. The ($e^+ + e^-$) measurement extends to higher energies with limited uncertainty and provides more precise information on the flux in the whole energy range with respect to the separate e^- and e^+ flux measurements.

In addition to the energy dependence of the positron fraction, prominent spectral features in the ($e^+ + e^-$) spectrum at ~ 500 GeV have been reported in recent measurements [7, 9]. However, such spectral features have not been observed by other experiments [18, 21].

The measurement of the ($e^+ + e^-$) flux with AMS is the main topic of this thesis; the details and results of this analysis (which has been published in [1]) will be presented. The ($e^+ + e^-$) flux has been measured from 0.5 GeV to 1 TeV using the first 30 months of data collected by AMS. The data corresponds to $\sim 41 \times 10^9$ cosmic rays among which $\sim 10.6 \times 10^6$ have been identified to be e^\pm and were consequently used for the ($e^+ + e^-$) flux measurement. The redundant e^\pm detection capabilities of AMS and the accuracy of the collected data allow for the measurement of the flux with an unprecedented precision. Therefore the result of the measurement adds new and distinct information to the experimental

¹Although the Fermi-LAT satellite experiment does not feature any spectrometer, it exploited the properties of the geomagnetic field to discriminate the charge sign of the detected e^\pm [19]. The energy reach and the accuracy of the measurement using such technique is however worse than standard spectrometric measurements.

scenario.

Chapter 1 provides an overview of the physics of charged cosmic rays. The origin and properties of cosmic rays, the experimental detection of cosmic rays and the phenomenology of the e^\pm cosmic ray component is discussed in detail. Subsequently, the Dark Matter paradigm is introduced together with the status of the experimental searches. The possibilities to explain the features observed in the e^\pm as an indirect signature of Dark Matter phenomenology or in terms of primary e^\pm astrophysical production are reviewed. The phenomenological and experimental prospects to address the explanation of the e^+ anomalous abundance in cosmic rays are finally discussed.

Chapter 2 reviews the AMS detector. AMS is fully introduced, including its subdetectors and their properties, capabilities and performances.

In Chapter 3 the basic concepts useful for the $(e^+ + e^-)$ flux measurements are introduced and discussed, including the definition of the detector acceptance and exposure time.

Chapter 4 covers the e^\pm detection and the proton background separation capabilities of AMS. In this chapter, first the event selection based on the information provided by the whole AMS detector is described. Subsequently the $(e^+ + e^-)$ signal identification procedure, based on a data driven approach which uses the combined information provided by the Electromagnetic Calorimeter (ECAL) and the Transition Radiation Detector (TRD) subdetectors is discussed. The systematic uncertainties introduced on the flux measurement by the $(e^+ + e^-)$ identification procedure are finally reviewed.

The number of $(e^+ + e^-)$ events has to be rescaled to represent the flux at the top of the detector. Chapter 5 reviews the calculation of the trigger efficiency, the detector exposure time and the detector acceptance that are used for the correction to the flux at top of the detector. Their relative uncertainties and their contribution to the measurement systematic uncertainty are also reviewed.

In Chapter 6 the ECAL energy resolution and the level to which the energy measurement absolute scale is known are discussed. The measurement of $(e^+ + e^-)$ flux from 0.5 GeV up to 1 TeV, using the results obtained in the previous chapters, is presented and it is contextualized into the previous experimental scenario. Finally, a selection of basic implications of this measurement on the phenomenology of the cosmic e^\pm component are presented and discussed.

Chapter 1

Cosmic ray physics and the search for Dark Matter

Cosmic ray (CR) physics began in the first decades of the twentieth century, when different experiments observed the presence of an ionizing radiation coming from the sky. From the 1930s to the early 1950s, the cosmic radiation provided a natural source of high energy particles, energetic enough to penetrate into the nucleus and to produce secondary particles. The use of energetic CRs as matter probe in those early years led to the discovery of positrons [22], muons [23], pions [24] and strange particles [25] which have been all first observed in the cosmic radiation. By 1950s, accelerator technology allowed to produce energetic particles in the laboratory, becoming the main source used in particle physics studies. Only a few decades ago, with the development of new experimental techniques and with the improvement of space and balloon flight technologies, a new interest on cosmic rays as fundamental particle physics probe has arisen, not only to answer to some fundamental questions on the Universe and cosmology, but also to test new theories beyond the Standard Model of particle physics.

In the next section, a review of the properties of the cosmic radiation will be presented, with particular emphasis on the charged components at energies below $\sim 10^{15}$ eV. The problems related to the origin of CRs and their propagation through the galactic, solar and geomagnetic environments will be discussed, together with the experimental techniques used for the detection at Earth.

Subsequently, the properties of the electron (e^-) and positron (e^+) component of the cosmic radiation will be discussed. The analysis of their spectral features which are not expected by the “cosmic ray standard model” and the explanation through astrophysical hypotheses will be covered in the same section.

The e^\pm component in the cosmic radiation could be, however, also used as a probe to measure indirectly the properties of Dark Matter particles. In the final section, the Dark Matter problem will be introduced. The proofs for the existence of Dark Matter at galactic, extragalactic and cosmological scales will be presented. The experimental Dark Matter detection status will be reviewed, with more details about the potential indirect detection of Dark Matter using measurements of cosmic rays and, in particular, of cosmic e^+ and e^- .

1.1 Charged cosmic rays

The cosmic radiation hitting the top of the atmosphere includes all stable charged particles and nuclei with lifetimes of the order of 10^6 years or longer. A wide range of energies, ranging from $\sim 10^8$ eV/nucleon to $\sim 10^{20}$ eV/nucleon have been observed.

The flux of particles per unit of energy, area, solid angle and time ($\Phi(E)$, measured in $\text{GeV}^{-1} \text{m}^{-2} \text{sr}^{-1} \text{s}^{-1}$) is shown in Figure 1.1 for a selection of CR species. The flux of all cosmic rays shows a steep power law energy dependence $\Phi(E) \propto E^{-\gamma}$ with the spectral index γ ranging between 2.7 and 3.0 depending on the energy range.

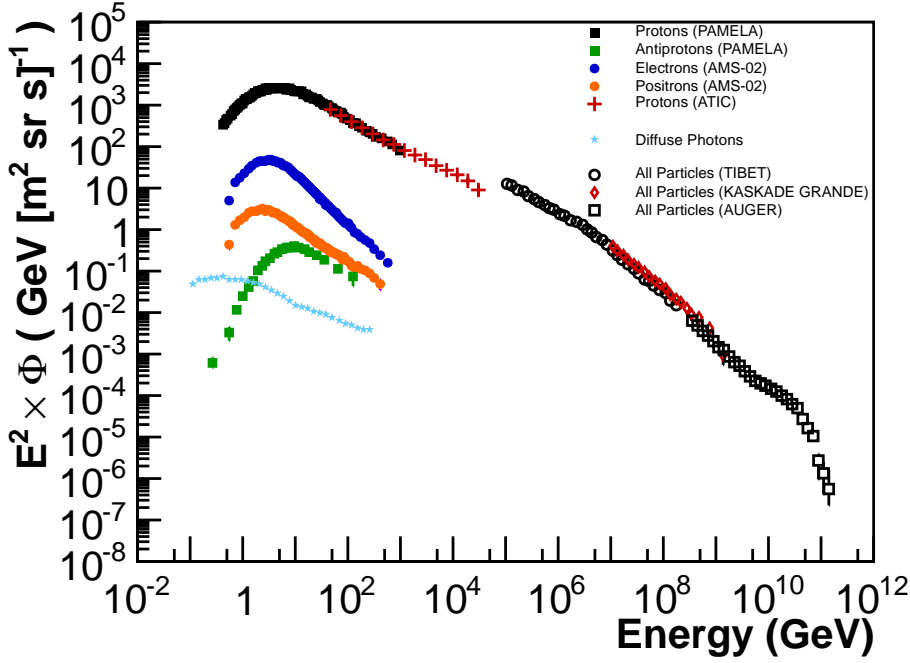


Figure 1.1: All-particle differential energy spectrum from 10^8 to 10^{20} eV multiplied by E^2 as measured by a selection of recent ground based, balloon and space experiments. Data collected from [26, 27]. Over this energy range, the total intensity decreases by nearly 30 orders of magnitude: the measurement of high energy cosmic rays is therefore very challenging. The all-particle spectrum is observed to be a power law with two features, the *knee* at $\sim 10^6$ GeV and the *ankle* at $\sim 10^9$ GeV, where the slope of the spectrum changes. Particles below the *knee* at 10^6 GeV have galactic origins. Above the knee the measured particles probably have extragalactic origins, and different cosmic ray acceleration mechanisms have to dominate at different energy scales in order to explain the change of slope. The presence of a cutoff energy at 10^{20} eV is also investigated by ground experiments to set constraints on the physics of extragalactic particle accelerators.

It is customary to define the particles accelerated in astrophysical sources as *primary* cosmic rays, and the particles produced by the interaction of primaries with the interstellar medium (ISM) as *secondary* cosmic rays.

The cosmic radiation is dominated by light nuclei. Below $\sim 10^6$ GeV, where most of the detected cosmic rays have galactic origins, the cosmic radiation is roughly composed of 99% protons and nuclei and 1% electrons. Among the hadrons, 90% are protons, 9% are He nuclei and the remaining $\sim 1\%$ are heavier nuclei. Besides the most abundant ordinary matter particles, a small fraction of antimatter particles, like e^+ and \bar{p} , and also γ rays, have been observed in the cosmic radiation.

For energies below 30 GeV/nucleon the local CR spectra show an attenuation due to interactions with the Solar Wind.

The energy density of CR in our Galaxy amounts to $\rho_{CR} \sim 1 \text{ eV/cm}^3$, the same order of magnitude compared with the energy density of magnetic fields and of the thermal interstellar gas. CRs are thus not negligible in the dynamics of our Galaxy.

Magnetic fields at different scales and in different environments affect the acceleration and propaga-

tion of CRs. The particle magnetic rigidity – or simply rigidity – defined as

$$R = \frac{p}{Ze} \quad (1.1)$$

measures the resistance of charged particles with momentum p and charge Ze to trajectory deviations in an external magnetic field. For a given magnetic field, the motions of different particles with the same rigidity are equally affected. As discussed in the next section, most of the CR propagation and acceleration mechanisms are expressed as function of their rigidity.

1.1.1 Origin of cosmic rays

The origin of CRs is one of the most debated fields in astrophysics. Nevertheless, the common idea is that the main source of galactic cosmic particles are supernova remnants (SNR). From the energetic point of view, SNRs can explain the energy density of CRs: assuming a supernova (SN) explosion every 50 years in our Galaxy and an average energy budget of 10^{51} erg/explosion, the total power released by these events turns out to be $\sim 5 \times 10^{41}$ erg/s. In order to explain the measured CR power in our Galaxy of $w_{CR} \sim 3 \times 10^{40}$ erg/s, a conversion factor for the SN energy to the CR energy in the range of 1% to 10% is needed, and it is well compatible with current SN models.

The galactic origin of CRs is further confirmed by the observed abundance of nuclei in CRs (see Figure 1.2). The correlation between most of the relative nuclear abundances in CRs and in the solar system suggests that this latter is representative of a typical CR source environment. On the other hand, the relative excess observed in the Be region ($Z=3$ to $Z=5$) and the sub-Fe region ($Z=22$ to $Z=25$) are signatures of secondary production of CRs due to interaction with the ISM.

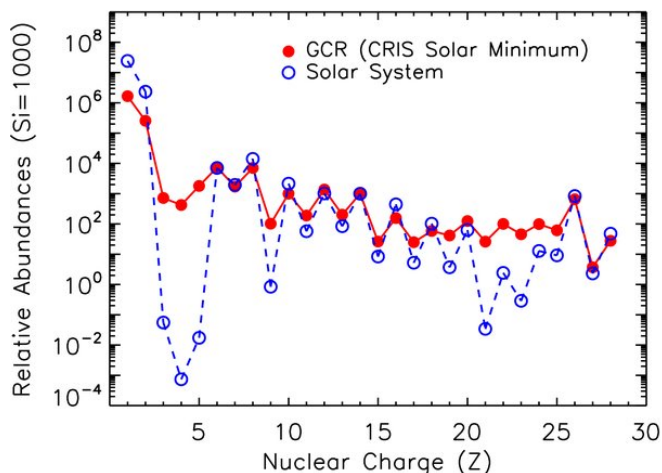


Figure 1.2: Cosmic ray abundances in the solar system (full red circles, measured by the CRIS experiment during solar cycle minimum) and solar system chemical abundances. Data are normalized to Si=1000 [28]. The similarities for most of the nuclear species confirm that CRs originate in an environment similar to the Solar System. The higher abundance in the Be and in the sub-Fe region is a signature of secondary CRs produced by the interactions of primary CRs with the ISM.

After CRs have been produced, they are accelerated and ejected into the ISM. The basic mechanism to accelerate CRs is the diffusive shock acceleration (DSA) mechanism, or first order Fermi acceleration¹. After the SN explosion, a shock wave propagates in the ISM. Charged particles can gain energy

¹The name refers to the energy gain per acceleration step, which is proportional to v/c , differently from what was originally proposed by Fermi (second order Fermi acceleration), proportional to $(v/c)^2$ [29]

interacting with the shock: this happens when the particle crosses the shock front and, after diffusing in the nearby turbulent magnetic field, returns to the shock itself. A particle can be accelerated to higher and higher energies after accumulating many interactions of this kind, with a probability decreasing at each shock front crossing. The result of this stochastic process is a spectrum $\Phi(E) \propto E^{-\gamma}$ (with $\gamma \sim 2.1 - 2.4$) independent of the properties of the shock wave and magnetic fields [30]. The spectral index at the source provided by this model agrees with the experimental observations, after propagation effects are taken into account (see Section 1.1.2). The hypothesis of SNR shocks as acceleration sites has been confirmed by the observation of MeV to TeV γ rays produced by the *in situ* interaction of accelerated particles with the medium ($p + \text{ISM} \rightarrow p + \pi^\pm + \pi^0$, $\pi^0 \rightarrow \gamma + \gamma$) from γ ray observatories like the FERMI satellite and the HESS ground detector [2, 31].

At energies $\sim 10^{15}$ eV the CR all-particle spectrum gets steeper (softens) with a spectral index change from $\gamma \sim 2.7$ to $\gamma \sim 3.1$, while at higher energies ($\sim 10^{18}$ eV) the spectrum hardens again². Those transitions are usually referred as, respectively, *knee* and *ankle*. The origin of these structures are still debated. The most widely accepted hypothesis is that the knee represents the maximum energy E_p^{max} to which protons can be accelerated by SNR through the DSA mechanism. Since the maximum acceleration energy is proportional to the particle charge Ze , the maximum energy for nuclei (E_Z^{max}) amounts to $E_Z^{\text{max}} = Z \times E_p^{\text{max}}$: the spectrum above the knee is a superimposition of the spectra of different nuclei species with different cutoffs. This scenario is confirmed by the experimental observation of a change of chemical composition around the knee [32]. In addition to this, at the same energy the propagation volume reaches the galactic magnetic field confinement and CRs are more likely to escape our Galaxy. The feature observed at the ankle is probably the consequence of the combination of both effects.

The commonly accepted explanation for the ankle in the CR spectrum is a change in CR sources. At this energy, the harder extragalactic component of CRs takes over and starts to dominate over the galactic component. CRs in the high energy range are usually also called Ultra High Energy Cosmic Rays (UHECR). The origin of UHECRs is not yet clear. Large scale shocks from extragalactic object, like Active Galactic Nuclei (AGN), are one of the candidate sources. The experimental detection of UHECR, as described in Section 1.1.4.3 is, however, very challenging and the properties of UHECR flux and composition are still uncertain.

In the highest energy region $E > 10^{19}$ eV, the flux is suppressed by the so called Greisen-Zatsepin-Kuzmin (GZK) mechanism [33]: CRs start to interact with Cosmic Microwave Background (CMB) photons through the Δ^+ resonance ($p + \gamma_{\text{CMB}} \rightarrow \Delta^+$) and their path length in the ISM steeply decreases. Cosmic rays are not expected to be observed above this limit without invoking exotic explanations, and the flux measured by ground experiments above 10^{19} eV shows a significant suppression as predicted by this model [34].

1.1.2 Propagation of galactic cosmic rays

After production and acceleration, the primary particles are injected into the ISM and start to propagate in this medium. The propagation is mainly dominated by the interaction with the medium and with magnetic turbulences. The common model used for the description of the CR propagation in the galactic

²In cosmic ray physics, the terms “hard” and “soft” indicate the spectral behavior of the flux. A “hardening” in the flux corresponds to an increase of the high energy component, while a “softening” corresponds to a decrease in the high energy component of the flux. For monotonously decreasing spectra, a “hard” flux has a lower value of the spectral index than a “soft” flux.

environment is based on diffusive propagation described by a Fokker-Planck type equation [35]

$$\frac{\partial \psi_i(\vec{r}, p, t)}{\partial t} = Q^{\text{tot}}(\vec{r}, p, t) + \vec{\nabla} \cdot (D_{xx} \vec{\nabla} \psi_i - \vec{V} \psi_i) + \frac{\partial}{\partial p} p^2 D_{pp} \frac{\partial}{\partial p} \frac{1}{p^2} \psi_i - \frac{\partial}{\partial p} [p \psi_i - \frac{p}{3} (\vec{\nabla} \cdot \vec{V}) \psi_i] - \Gamma \psi_i \quad (1.2)$$

where $\psi_i(\vec{r}, p, t)$ represents the density per momentum units p at spacetime coordinates (\vec{r}, t) for the i^{th} CR species.

The temporal, spatial and energetic evolution of the CR densities is ruled by several factors:

- **Sources:** the source term $Q^{\text{tot}}(\vec{r}, p, t)$ represents any possible production mechanism for primary particles. The spatial distribution of CR sources is assumed to be correlated with the density of known pulsars or SNRs. The energy injection spectrum of the source term is modeled as a power law spectrum $\frac{\partial}{\partial p} Q \propto p^{-\gamma}$.
- **Galactic magnetic field:** CRs propagate through the Galaxy under the influence of the interstellar magnetic fields, which tangle their trajectories. The bending of the charged particle direction in the magnetic field is determined by the particle rigidity R , defined in Equation 1.1. Different particles with the same rigidity are equally affected by the magnetic fields.

The galactic magnetic field can be decomposed in a regular component, which follows the distribution of the arms of the Galaxy, and a turbulent component in the form of perturbations of the regular field. The resonant scattering of charged CRs with these random small fluctuations $\delta(B) \ll B$ (with $B \sim 6 \mu\text{G}$ in our Galaxy [36]) leads to a diffusive motion. The diffusion coefficient amounts to $D_{xx} = 3 - 5 \times 10^{28} \text{ cm}^2/\text{s}$ at energies $\sim 1 \text{ GV/nucleon}$ and with a scaling law $D_{xx} \propto R^\alpha$ due to the turbulent nature of the perturbations. This mechanism is responsible for the isotropization of the charged CR fluxes and for the consequent loss of source directionality. In addition to the spatial diffusion, the interaction with the turbulent galactic fields induces a stochastic acceleration, also known as “re-acceleration” [37]. This process is modeled by a diffusion in momentum space with a coefficient $D_{pp} \propto |\vec{V}|^2/D_{xx}$, where the Alfvén velocity \vec{V} is the characteristic velocity of the fluctuation propagation in the magnetic field.

- **Convection:** During the propagation in our Galaxy, the galactic wind that moves from the bulk of the Galaxy to the Galaxy halo affects the motion of CRs [38]. The galactic winds are composed of a stream of charged particle moving out of the Galaxy bulk, with velocities that grow linearly with the distance from the galactic plane up to hundreds of km/s. The coupling to such a stream does not only induce a movement towards the external regions of the Galaxy, but it also induces adiabatic energy losses as the wind speed increases. The topology, the speed and the evolution of the galactic winds are highly constrained by measurements of secondary to primary CR ratios, like the boron to carbon ratio (B/C), and of the unstable isotope ratios, like the $^{10}\text{Be}/^9\text{Be}$ ratio [39](see Section 1.1.2.1)³.
- **Nuclear processes:** Unstable nuclei can decay into other nuclear products with a total lifetime Γ , thus decreasing their density by the factor $\Gamma \psi_i$ and increasing the product densities by a factor proportional to the decay probabilities.

³The results provided by the analysis of the primary to secondary ratios and of the isotope ratios in CRs show some tension with the measured galactic wind properties. Many different models have been proposed to solve the tension with the measured data, like a two-zone diffusion model, where convection happens only in the outer zone $|z| > 1 \text{ kpc}$ [40], up to models with anisotropic diffusion coefficients [41].

Spallation processes of CRs with the ISM also contribute to the evolution of the density⁴. Nuclear processes are responsible for the production of secondary species that are not accelerated in astrophysical sources.

- **Energy losses:** During the propagation in the ISM, CRs suffer energy losses due to interactions with the environment. Nuclei mainly lose energy by ionization. For the lightest CRs, e^+ and e^- , other processes dominate their energy losses: synchrotron energy losses from the interaction with the interstellar magnetic fields, and inverse Compton scattering from the interaction with the radiation field. Such processes drastically affect the propagation of CR e^\pm , as discussed in Section 1.2.

The solution of Equation 1.2 in the steady-state assumption $\frac{\partial \psi_i(\vec{r}, p, t)}{\partial t} = 0$ completely describes the Local Interstellar Spectrum (LIS) for each species before entering the solar system. The equation can be solved both semi-analytically or numerically using dedicated packages like USINE [42], GALPROP [43] or DRAGON [44].

1.1.2.1 Measured observables

The unknown parameters in Equation 1.2 – that characterize the model of CR propagation – are inferred by the solution of the equation with constraints from experimental data. Usually a *leaky box model* for particle propagation in the Galaxy is used, which defines the confinement volume properties and the border conditions before CRs can escape from our Galaxy after a typical escape time τ_{esc} . [45].

The ratios between secondary and primary nuclei, predominantly the B and C nuclei fluxes, are one of the most commonly used observables. With C being a product of stellar nucleosynthesis and B a secondary product of heavier nuclei spallation with the ISM, the B/C ratio provides information about the amount of matter encountered by CRs during their propagation through the Galaxy. The observable inferred from the secondary to primary ratio is the grammage $\bar{\xi}$, proportional to τ_{esc} and to the mean traversed matter density $\bar{\rho}$ during the propagation:

$$\bar{\xi} = \beta c \bar{\rho} \tau_{\text{esc}} \quad (1.3)$$

The typical value determined from data amounts to a traversed grammage of $\bar{\xi} \sim 5 \text{ g/cm}^2$. The rigidity dependence of the B/C ratio (and of all other secondary to primary ratios) can be also used to infer limits on the diffusive propagation. The rigidity gradient of the ratio is indeed proportional to the spectral index α of the diffusion spectrum $D \propto R^\alpha$. The current measurements constrain the diffusive index in a typical range of $0.3 < \alpha < 0.75$.

Another important observable are the ratios between unstable and stable isotopes. The ratio $^{10}\text{Be}/^9\text{Be}$ is the most widely used due to the relatively higher abundances of Be isotopes in the cosmic radiation with respect to other nuclear unstable species. The lifetime of ^{10}Be amounts to $\sim 1.4 \times 10^6$

⁴ The production probability of the species i from collisions of the species j with the interstellar hydrogen and helium gas, with densities respectively $n_H \sim 0.9 \text{ cm}^{-3}$ and $n_{He} \sim 0.1 \text{ cm}^{-3}$, can be expressed by:

$$\Gamma_{j \rightarrow i} = \beta_j c \int_0^{+\infty} n \sigma_{j \rightarrow i}(E, E') dE'$$

where $\sigma_{j \rightarrow i}$ is the spallation cross section from a nuclear species j to i on hydrogen or Helium targets. The total spallation source term q^{sp} can be written as:

$$q_i^{sp} = \sum_{k>i} \psi_k \Gamma_{k \rightarrow i}$$

years⁵, while ${}^9\text{Be}$ is a stable isotope. Their relative abundance can therefore be used to estimate the time spent by the cosmic particle from the source until their propagation to the solar system. The typical value inferred from the ${}^{10}\text{Be}/{}^9\text{Be}$ ratio amounts to $\tau_{\text{esc}} \sim 10^7$ years which, combined with the $\bar{\xi}$ measurement, can be used to constrain $\bar{\rho}$ and therefore the height of the diffusive galactic halo.

The measurements of B/C and ${}^{10}\text{Be}/{}^9\text{Be}$, shown in Figure 1.3, are used to constrain the basic parameters of the CR propagation. The precision of the ${}^{10}\text{Be}/{}^9\text{Be}$ measurements is however poor, and the typical constraints on the diffusive halo height allow values between 2 kpc and 16 kpc⁶. The analysis of other nuclear element fluxes, from protons up to iron nuclei, and measurements of e^- , e^+ and γ do not only improve the limits set on propagation parameters, but are also used to improve the knowledge on the details of the cosmic ray sources, like their abundances and acceleration mechanisms. Constraining all these parameters is important in order to have a reliable prediction for the less abundant secondary products, like e^+ , \bar{p} and \bar{D} , whose fluxes are a primary tool to probe the existence of exotic particle models and in the search for Dark Matter signatures (see Section 1.3).

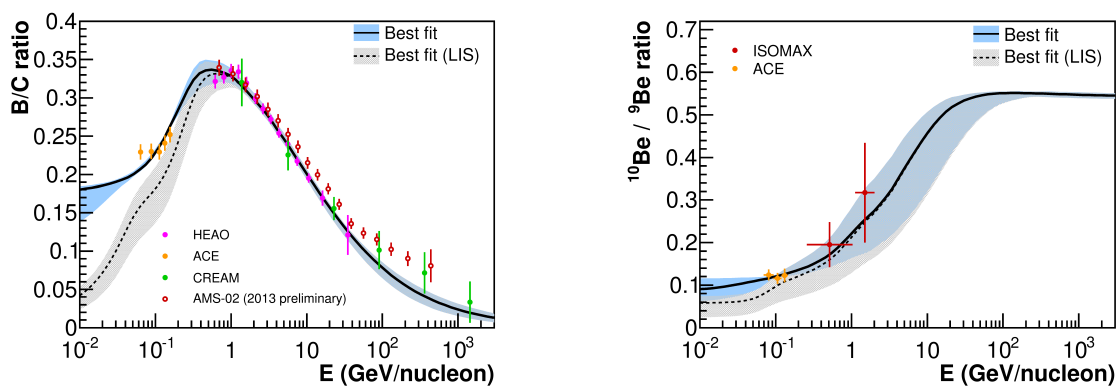


Figure 1.3: **Left:** Collection of measurements of the B/C ratio in cosmic rays [47]. The slope of the rigidity dependence of the B/C ratio is used to infer limits on the value of the spectral index for the diffusive propagation in the turbulent galactic magnetic fields. **Right:** Measurements of the ${}^{10}\text{Be}/{}^9\text{Be}$ ratio in cosmic rays [47]. The latest measurement comes from the ISOMAX balloon spectrometer, which took data in 1998 [48]. The ratio between unstable and stable isotopes provides information on the typical time spent by cosmic rays during the propagation in the Galaxy. Together with the secondary to primary CR ratio measurements, this constrains several propagation parameters, like the traversed density and the height of the diffusive halo. The bands represent the value of the observables predicted by the solution of the propagation equation (Equation 1.2). Different models have been tested, and the bands represent all the models within 1σ from the best model (here represented by the line). The validity of the models is constrained by hadronic observables like the p flux, the \bar{p}/p ratio, secondary to primary ratios, unstable nuclei ratios (the AMS data have not been used here to constrain the parameters). The improvement in the accuracy of the measurements (essential for the ${}^{10}\text{Be}/{}^9\text{Be}$ ratio) will help to further reduce the uncertainty on the model parameters.

⁵Another motivation why the ${}^{10}\text{Be}/{}^9\text{Be}$ is widely used is that the lifetime of ${}^{10}\text{Be}$ is of the same order of magnitude as the propagation time spent typically by GeV to TeV energy CR in our Galaxy. The sensitivity to the local galactic properties of the ${}^{10}\text{Be}/{}^9\text{Be}$ is therefore higher than for other unstable species.

⁶Additional independent constraints on the diffusive halo height can be further set by the analysis of the diffuse galactic e^- synchrotron emission [46].

1.1.3 Propagation of cosmic rays in the heliosphere and in the magnetosphere

Solar Wind is the common word used to refer to the outflow of \sim keV charged particles from the Sun's atmosphere. The Solar Wind is composed of a supersonic proton and electron magnetized plasma. The Solar Wind energy density dominates over the Sun magnetic field energy density. Therefore the Sun's magnetic field line are frozen with the plasma, which carries them until the so called *Termination Shock* region, where the wind becomes subsonic. The combination of the radial ejection of the wind from the solar atmosphere with the rotational movement of the Sun, tilted with respect to the magnetic dipole, leads to a spiral structure of the magnetic field lines [49]. The region up to which the Solar Wind extends until the ISM stops the flow of particles is referred to as *Heliosphere*: this boundary is well outside the Sun planetary system, at distances greater than 100 astronomical units (AU). The Voyager 1 probe, launched in 1977, took 36 years to finally exit the Heliosphere and enter the interstellar space in 2013.

The Solar Wind affects the flux of CRs that enters the Heliosphere. The 11 year solar activity cycle induces adiabatic time dependent effects. Stochastic perturbations can be induced by peaks of solar activity in the time scale of hours to days. The long term effect can be modeled in the so called *Force Field Approximation* model [50], which relates the LIS flux (Φ_{LIS}) to the solar modulated flux (Φ_{mod}) at a certain energy E by the following relation:

$$\Phi_{\text{mod}} = \frac{E^2 - m^2}{(E + Ze\phi)^2 - m^2} \Phi_{\text{LIS}}(E + Ze\phi) \quad (1.4)$$

where m and Ze are respectively the particle mass and charge, while ϕ is the effective solar modulation potential. The modulation potential describes the typical energy losses of CR particles in the Heliosphere, with typical values between \sim 300 MV and \sim 1500 MV at the solar minimum and maximum activity. The effect of the Solar Wind on the proton flux is shown in Figure 1.4.

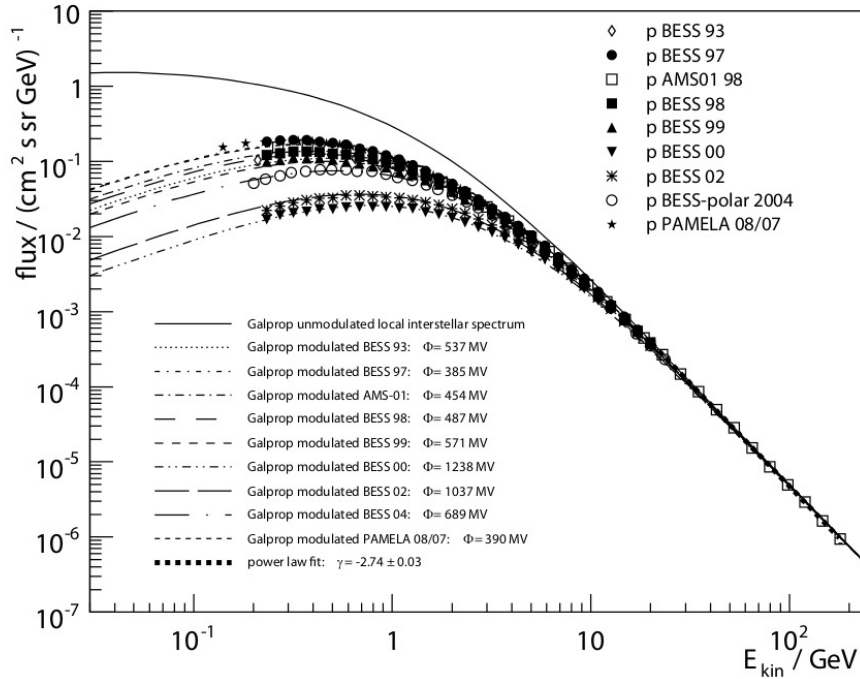


Figure 1.4: Proton spectra measured by the BESS, AMS-01 and PAMELA experiments (data taking years specified in the legend). Spectra lines are obtained in the force field approximation using the indicated modulation potentials applied to the assumed unmodulated LIS spectrum, also shown in the figure [51].

The effect of solar modulation can be refined by the introduction of a charge sign dependent effect. Gradient and curvature drifts due to the geometry of the solar magnetic field affect the motion of opposite sign particles differently [52]. Such effects have to be taken into account when comparing low energetic matter and antimatter fluxes in the heliosphere [53].

A precise and continuous measurement of CR fluxes across a complete solar cycle will provide an important tool to improve the understanding of CR propagation in the heliosphere. AMS (see Chapter 2) will, among other measurements, collect particle fluxes down to ~ 500 MeV for more than 20 years, accomplishing this task.

The last environment crossed by CRs before they reach the Earth's atmosphere is the *Magnetosphere*, namely the region in which the magnetic field of the Earth dominates the dynamics of CRs. The geomagnetic field, generated by the fluid nickel-iron motion in the Earth's outer core, can be approximated by a tilted dipole field with moment $M = 8 \cdot 10^{17}$ Tm², displaced by ~ 400 km from the center of the Earth and inclined by $\sim 11^\circ$ with respect to the Earth rotation axis [54]. Outside the magnetosphere, the dipole field is extremely distorted by the incoming Solar Wind, as shown in Figure 1.5.

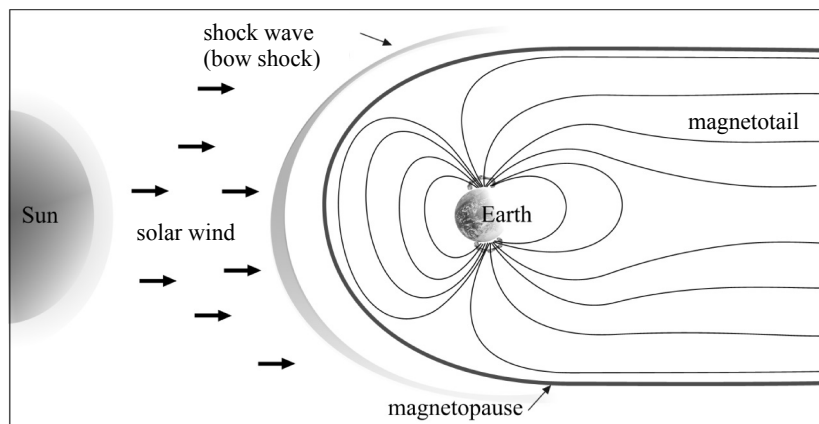


Figure 1.5: Schematic diagram showing the structure of the Earth's Magnetosphere. The Solar Wind impinging towards the Earth creates a shock wave and distorts the dipole geomagnetic field. The *Magnetopause* region sets the boundary where the Earth's magnetic field becomes dynamically dominant over the Solar Wind. It is sited at $\sim 11R_H$ from the closest point to the ground, where R_H is the Earth's radius length [55].

Due to the dipole configuration, the magnetic field on the ground surface (shown in Figure 1.5) is also distorted. A notable consequence is the appearance of the *South Atlantic Anomaly* (SAA). The SAA is the region where the Earth's inner Van Allen radiation belt is closest to the ground and the Earth's magnetic field reaches its lowest value [56]. In this region, the cosmic radiation flux is dominated by the low energetic particles confined by the magnetic field of the Van Allen radiation belt.

The geomagnetic field affect the low energy particle flux at the level of the Earth's surface. It also confines the motion of low energetic secondaries produced by interactions of primary CRs with the local environment. Depending on the particle rigidity, on the intensity of the geomagnetic field and the particle incoming direction, a galactic CR may be not be able to reach the detector. This screening effect is summarized by the rigidity cutoff R_c parameter: if the particle rigidity is below R_c , its trajectory cannot be extrapolated outside the Magnetosphere, and the particle has to be a trapped secondary, as it could not have reached the detector at Earth from outside the Magnetosphere. In the approximation of a

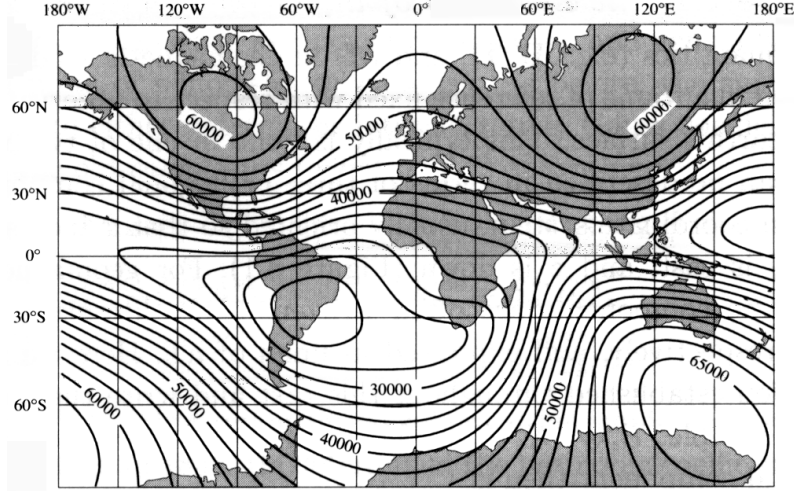


Figure 1.6: Total magnetic field isolines at the Earth's surface, measured in nT. The minimum region (South America) is caused by the Earth's inner Van Allen radiation belt configuration. It is usually referred to as South Atlantic Anomaly [57].

dipole field, R_c can be evaluated for any position in the so called Størmer approximation [58]:

$$R_c = \frac{M \cos^4 \lambda}{r^2 (1 \pm \sqrt{1 - \sin \epsilon \sin \xi \cos^3 \lambda})^2} \quad (1.5)$$

where M is the geomagnetic field dipole moment, λ is the latitude from the magnetic equator, ϵ is the zenith angle, ξ is the azimuthal angle to the north magnetic pole, r is the distance from the dipole center and the \pm sign refers to the sign of the particle charge. For a given point in space there is an aperture cone in which all galactic particle trajectories are allowed to reach that point, a cone in which galactic particle trajectories are completely forbidden and a *penumbra* region in which only a subset of all galactic trajectories is allowed (see Figure 1.7).

1.1.4 Detection of cosmic rays

Once the cosmic ray passed through the magnetosphere, it can be detected by dedicated experiments. Because of the high energy span covered by the CR spectrum (see Figure 1.1) and the steeply falling power law flux, very different experimental concepts have been developed in the last decades in order to fully explore the CR properties. The presence of the Earth's atmosphere prevents the detection of primary CRs at ground level. Experiments dedicated to the direct detection of primary CRs have to be operated above the atmosphere. The technological constraints limit the instrument acceptance to the detection of primary CRs up to the TeV range. In order to detect CRs above this energy, experiments have to be sited on the ground, where the effective sensitive area can be increased up to hundreds of km². The nature of the primary CR, which interacts with the atmosphere, is difficult to reconstruct from ground detectors. Such experiments are however able to detect cosmic rays up to 10²⁰ eV allowing to investigate the most powerful phenomena of the Universe.

In the following section, the most common experimental techniques used to measure charged CRs are reviewed, with particular emphasis on charged cosmic rays. Other experimental techniques, like the detection of neutrinos through ground telescopes or underground detectors, will not be covered here.

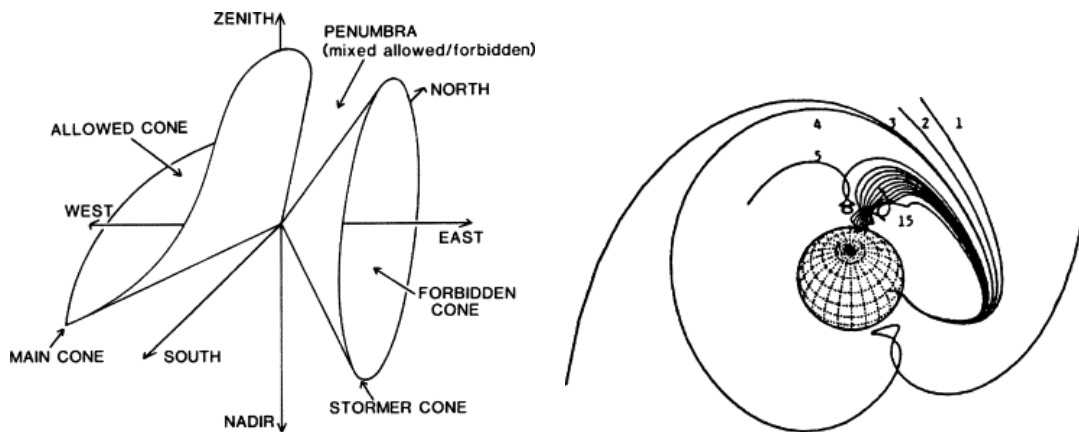


Figure 1.7: **Left:** Geometric visualization of the geomagnetic cutoff. “Allowed” and “forbidden” cones refer to galactic trajectories. The *penumbra* is a transient region where both galactic and local secondary trajectories are allowed. **Right:** Trajectory tracing in the geomagnetic field. Highest to lowest rigidities are labelled from 1 to 15. Trajectories from 1 to 4 can be traced back outside the geomagnetic field, thus they are associated with galactic particles. Other trajectories, if traced back, are trapped or they hit the Earth’s surface: such trajectories cannot originate from outside the Magnetosphere, and they can only be associated with secondary particles produced inside the Magnetosphere [58].

1.1.4.1 Space borne experiments

The absorption thickness of the Earth’s atmosphere, corresponding to an average of 25 radiation lengths (X_0), screens the ground from primary CRs, which interact before reaching the detector. Direct detection of electromagnetically interacting CRs is therefore carried in space. In order to identify the nature of the detected particles, space borne instruments exploit typical high energy physics detection techniques, like μm precision tracking using silicon detector technology or calorimetric energy measurements. Despite the detection concept is very similar to the modern accelerator experiments, the technological realization differs significantly. The requirements of a space borne experiment are in fact very challenging. Weight, dimension and power consumption constraints limit the size of the detector (thus their acceptance) to the $\sim 10\text{ m}^3$ range. The limited bandwidth for the data transfer (to ground), the extreme thermal environment and the transport from ground to space also shape critically the detector concept.

In a typical direct CR detection experiment, particles traversing the instrument are fully characterized via the simultaneous measurement of the energy E , mass M , charge Z and charge sign. In a minimalistic experiment, a calorimeter is used to measure the energy E , dE/dX detectors are used to measure Z and a time of flight system is used to trigger the data acquisition and to measure the velocity and hence the mass M . A magnet can be used to deflect the particle trajectory and infer the charge sign. Some experiments are also equipped with additional detectors dedicated to the identification of CR rare species, like transition radiation detectors or neutron detectors that improve the identification of e^\pm .

The measurement of CRs in space began in the 1970s with the measurement of nuclear isotopes in the energy range $\leq 1\text{ GeV}$ with the IMP satellites [60]. The field flourished in 2000s, when the FERMI-LAT satellite observatory [61] provided for the first time high precision γ rays direct measurements and the PAMELA satellite mission [62] (see Figure 1.8) provided the direct measurement of charged CRs up to the 100 GeV range. The state-of-the-art space borne experiment is the AMS-02 detector [63]. AMS is the first particle detector located on the International Space Station (ISS) where it has been collecting high precision data up to the TeV range since 2011. The AMS detector will be exhaustively described in Chapter 2.

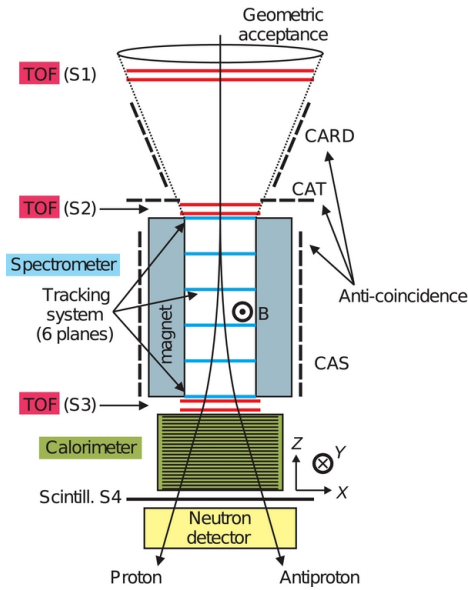


Figure 1.8: The PAMELA detector scheme represents the typical setup of direct CR detection experiments. The detector is composed of several subdetectors, each contributing with a different task to the particle detection and identification. Cosmic rays crossing the detector are triggered by the energy deposit in the time-of-flight scintillators and their velocity and charge are measured. The trajectory is curved inside the magnet, and the silicon tracker system reconstructs the curvature inferring the charge sign and the particle rigidity. The particle is finally stopped in the electromagnetic calorimeter, where its energy is measured. The anticoincidence system is used to reject cosmic rays crossing the detector out of its field of view. Figure taken from [59].

AMS successfully confirmed the possibility of operating a particle physics detector on the ISS, hence stimulating the development of the next (and “next-to-next”) generation experiments to be operated on space stations, like the JEM-EUSO observatory [64] or the DAMPE/HERD [65] instrument.

1.1.4.2 Balloon borne experiments

Balloon ascension experiments have been playing a major role in the CR field since the 1930s. They were in fact the only solution to directly explore the cosmic radiation before space borne technology was achieved. Balloon experiment concepts are very similar to space borne experiments, as they mount typical particle physics detectors that measure the properties of the primary CRs crossing the experiment.

In balloon experiments, the detector is usually sustained by stratospheric balloons. The flights commonly take place in the polar regions during local summer, when the atmospheric conditions allow the maximum duration of the flight. With the latest Ultra Long Duration Balloons (ULDB) technologies, 4 t payloads can be carried at altitudes above 40 km up to 6 weeks [66]⁷. Due to the constrained flight time, experiments are typically recovered on ground, updated and re-flown in the following convenient season.

Differently from space experiments, balloon detectors have less stringent technological constraints. Several different missions can be accomplished with much lower economic impact. Therefore, the detector setup is usually optimized for a dedicated purpose. Roughly, balloon experiments can be separated in spectrometric and calorimetric experiments. Spectrometers, like BESS [68], can measure the charge sign and are dedicated to antimatter and Dark Matter searches. Their acceptance is limited by the magnet size and their energy reach by the maximum spectrometer resolution. Calorimetric experiments can instead reach higher energy with improved accuracy. They cannot however distinguish between positive and negative particles. The maximum detected energy reached so far by balloon experiments is the TeV range for electromagnetic calorimeters, like the ATIC experiment [7], shown as example in Figure 1.9.

Hadronic calorimeter experiments, like CREAM [70] or TRACER [71], measure nuclei up to 10 TeV/nucleon probing the cosmic rays composition at the knee. Above this energy, with the current technology, no direct detection of cosmic rays is possible. The field of balloon experiments is in high

⁷At this altitude, the atmospheric depth crossed by incoming CRs amounts to $\sim 5 \text{ g/cm}^2$ depending on the particle’s incoming direction [67]

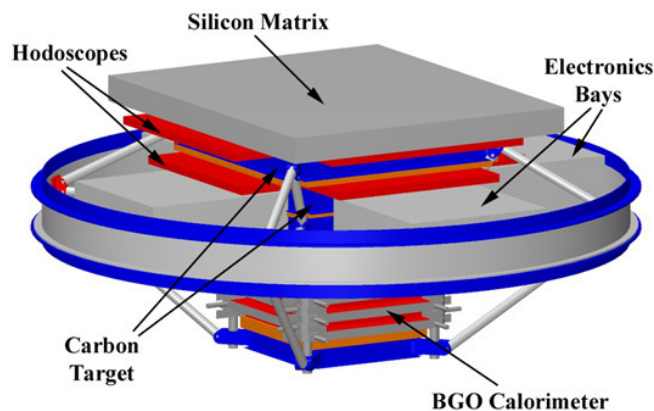


Figure 1.9: The ATIC balloon borne detector scheme. The core of the detector is the fully active calorimeter at the bottom, composed of 10 layers of Bismuth Germanate (BGO) scintillating crystals. The calorimeter has an acceptance of $\sim 0.4 \text{ m}^2\text{sr}$ and it can measure the energy of incoming cosmic rays from 50 GeV to the TeV range. Above the calorimeter a hodoscopic system of plastic scintillating strips, interleaved by inactive carbon layers to induce interactions, defines the instrument aperture and provides a redundant measurement of the particle charge and trajectory. On the top, the highly segmented silicon matrix detector provides the accurate measurement of the charge of the primary particle [69].

development, and new missions like the GAPS detector [72] for the search of \bar{D} in the cosmic rays or the SUPERTIGER experiment [73] for the measurement of heavy nuclei are being deployed and taking data.

1.1.4.3 Ground based experiments

The detection limits and the small acceptance of space and balloon borne experiments prevent the direct detection of CRs above $\sim 10^{15}$ eV. The flux of primary CRs from $\sim 10^{15}$ eV up to 10^{20} eV has been measured by experiments sited on the ground (sometimes addressed to as “indirect” CR detection experiments).

Charged primary CRs that enter the Earth’s atmosphere interact with the medium and produce secondary particles. The atmosphere acts similarly to a calorimeter, leading to the production of a particle shower. During the shower development, the chain of decays of short-lived hadrons produces different types of particles. At the end of the decay chain, apart from the hadronic components, γ and e^\pm constitute the so-called electromagnetic components; μ^\pm and ν constitute the penetrating component. All components travel approximately along the same direction of the primary particle, with different spreads around the axis depending on the component. On the ground, Extensive Air Shower (EAS) arrays measure the development of such showers in order to infer the properties of the primary particle.

Usually EAS arrays are constituted by a set of detectors spread over a large area ($\gg \text{km}^2$) to collect large enough datasets at high energy, where the natural flux is very low. Scintillator detectors, water Cherenkov tanks and muon detectors are used to measure the radiation at the EAS array altitude. The amount of muonic and electromagnetic components, the difference in the arrival time and the reconstruction of the shower front are used to infer the properties of the primary CR. In addition, Cherenkov light telescopes can be incorporated to measure the light emitted by the relativistic components to provide further information. Finally, the fluorescence light emitted from the de-excitation of nitrogen can be detected to measure the shower profile for primary energies above 10^{18} eV.

Indirect CR measurements are subject to high uncertainties, dominated by the limited knowledge of

the atmospheric parameters and of the high energy shower development. The properties of the primary CRs are indeed inferred through MC simulation of shower developments in the atmosphere (CORSIKA [74] being the most widely used package). Since this energy range is not accessible by modern accelerators, the uncertainties on the hadronic interactions of CRs with air nuclei represent another unavoidable limit of the indirect detection [75]. On the other hand, EAS array measurements are, together with ultra high energy neutrino detectors, the only possibility so far to investigate the physics of the most energetic phenomena of the Universe.

The last generation of EAS arrays combines measurements from different techniques in order to decrease the measurement uncertainties. The state of the art of such “hybrid” EAS detector is represented by the Pierre Auger Observatory, sited in Argentina in the southern hemisphere, and by the Telescope Array experiment [76], sited in USA in the northern hemisphere. Both observatories combine fluorescence and surface array detection techniques to enhance the single detector capabilities and to provide an accurate cross-check of systematic uncertainties of the two detection methods (see Figure 1.10 for a graphical representation of the hybrid measurement technique).

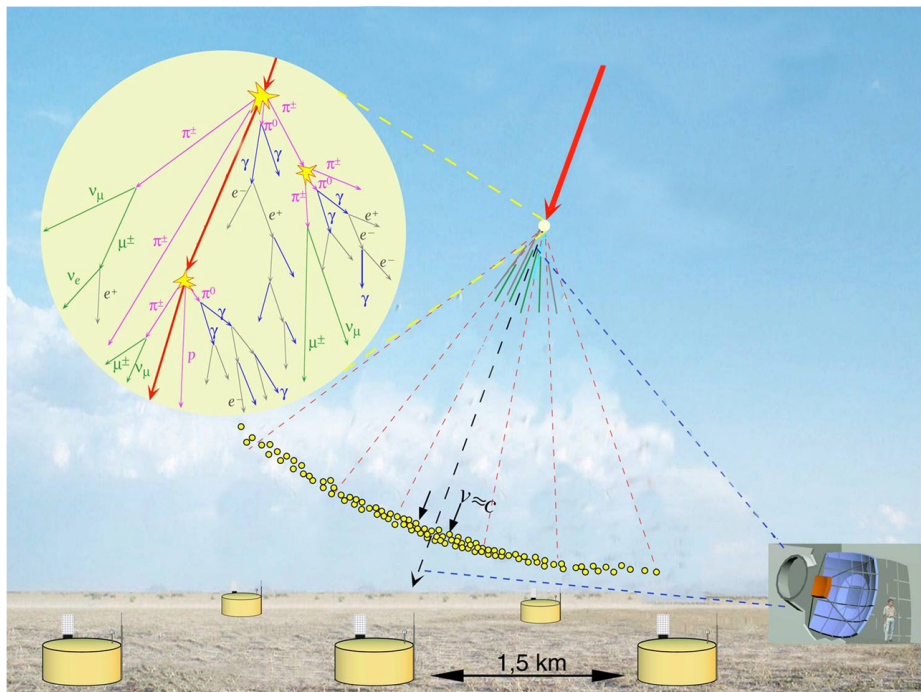


Figure 1.10: Pierre Auger “hybrid” EAS detection technique. The surface detector (SD) array consists of 1600 water Cherenkov detectors spaced by ~ 1.5 km on a grid covering a total area of 3000 km^2 . The SD tanks measure muons and the electromagnetic component of the shower produced by the interaction of the primary cosmic ray with the atmosphere. The 24 fluorescence detector (FD) units, operated only during favorable night, measure the photon intensity generated by the air shower. The presence of surface and fluorescence detectors allows the measurement of the development of the air shower with reduced systematics [77].

Ground array experimental results have had a big impact in the study of the astrophysical phenomena that could accelerate CRs to very high energy. The CR energy spectra [34], the mass composition [78] and the search for anisotropies in the high energy CR arrival direction [79] are examples of the typical observables measured by ground based experiment to unveil the origin and the properties of UHECRs.

1.2 Electrons and positrons in the cosmic radiation

Electrons and positrons represent only a minor contribution ($\sim 1\%$) to the total cosmic ray flux. A big experimental effort has been undertaken in the last decades to measure the e^\pm flux with high precision. The e^\pm channel in the cosmic radiation is, in fact, unique. The analysis of the amount of e^\pm in CRs is fundamental to understand the CR production, acceleration and galactic propagation mechanisms.

Differently from hadrons, e^\pm suffer much higher energy losses. For GeV energies and above, e^\pm detected at the Earth are produced within kpc distances. The analysis of the spectral shape, of the time dependence and of the preferred arrival direction of the CR e^\pm is useful to improve the knowledge of the local propagation environment. Moreover, in the standard cosmic ray scenario, e^- are abundantly produced by the standard SNR acceleration process described in Section 1.1.1, while e^+ are instead mainly produced by interactions of hadrons with the ISM⁸. This assumption alone is however not sufficient to completely describe the latest experimental results. In the next section, the physics of electrons and positrons in CRs, the experimental status and the tension with the standard CR propagation models are reviewed.

1.2.1 Propagation of cosmic ray electrons and positrons

Cosmic e^- are expected to be primaries produced in SNR like hadrons. Interactions of hadrons with the ISM are a source for both secondary e^+ and e^- . In the standard propagation scenario, e^+ are not abundantly produced in any astrophysical source.

The propagation of e^\pm in the ISM is different than that of hadrons. Energy losses are more severe for e^\pm due to their much lower mass. Two main mechanisms dominate the energy losses of energy for energetic e^\pm [81, 30]:

- **Synchrotron radiation:** relativistic e^\pm moving through the galactic magnetic fields emit synchrotron radiation. The power emission for a particle of mass m with velocity β and Lorentz factor γ , computed in Larmor's approximation, is:

$$\frac{dE}{dt} = \frac{4}{3}\sigma_T\beta^2\gamma^2\epsilon_B = b(E) = \propto m^{-4} \quad (1.6)$$

where $\sigma_T = 6.65 \times 10^{-25}$ cm² is the Thompson cross section and ϵ_B is the magnetic field energy density. The power emission is usually denoted as $b(E)$ in CR propagation theories and will be used in this form later in this section. Since $m_p/m_e \cong 2000$, the synchrotron emission for protons is highly suppressed.

A single particle emits radiation whose spectrum is peaked at the critical synchrotron frequency $\omega_s = \gamma^3\omega_c$ where ω_c is the cyclotron angular frequency. The emission of radiation for particles with a non-thermal power law spectrum with spectral index Γ between energies E_{\min} and E_{\max} is a power law spectrum itself with spectral index $s = \frac{\Gamma-1}{2}$ between $\omega_s(E_{\min})$ and $\omega_s(E_{\max})$ [30]. The analysis of synchrotron emission from astrophysical objects in the radio and microwave domain is indeed used to set indirect constraints on the physics of CR e^\pm in a wide energy range, from below 1 GeV to hundreds of GeV.

- **Inverse Compton (IC) scattering:** relativistic e^\pm can interact with low energy photons via inverse Compton scattering processes transmitting energy to the photon. The typical target for this process are photons of the Interstellar Radiation Field (ISRF) with different wavelengths. The

⁸ e^+ are also produced in SNRs but with a much smaller abundance (at the percent level) than e^- [80]. In the standard models this contribution is usually neglected.

ISRF mostly consists of photon from starlight, dust emission and CMB. The power emission is similar to that of synchrotron radiation losses, but it is proportional to the target ISRF photon energy density ϵ_γ :

$$\frac{dE}{dt} = \frac{4}{3}\sigma_T\beta^2\gamma^2\epsilon_\gamma = b(E) \quad (1.7)$$

IC accelerated photons are one of the most important component of the diffuse gamma ray emission from the Galaxy, and are used to trace the spatial distribution of the CR e^\pm and of the ISRF.

Above 1 GeV, the e^\pm density evolution is dominated by the mentioned energy losses (see Figure 1.11). High energy nucleons have longer propagation lengths after production than low energetic nucleon. For e^\pm , instead, the energy dependence of the IC and Synchrotron losses limits the travel distance for high energy e^\pm .

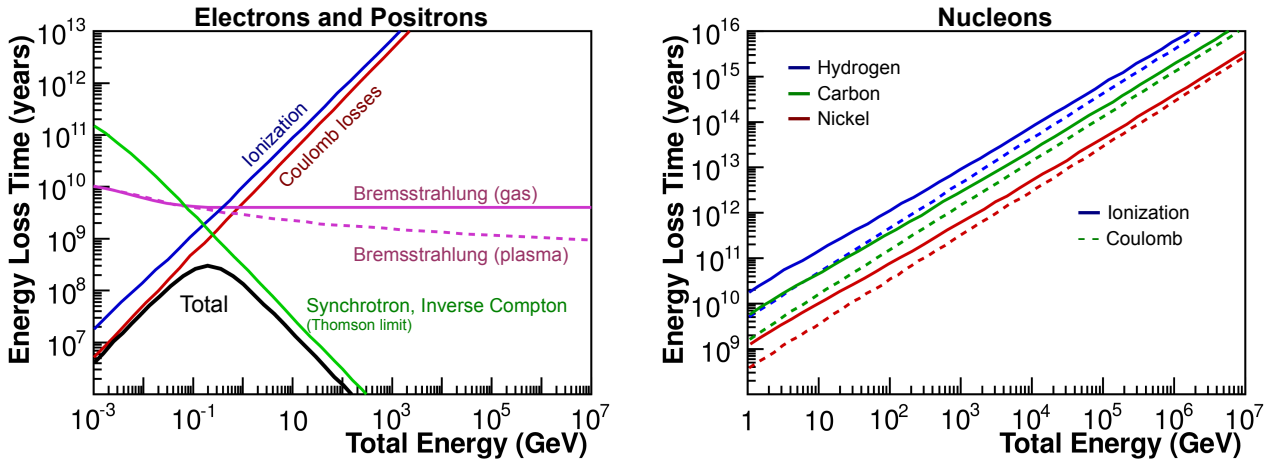


Figure 1.11: Energy loss processes for e^\pm (Left) and nuclei (Right) during the propagation in the ISM. The typical time spent to lose a relevant fraction of the particle energy is shown as function of the CR energy itself, for a set of ISM and propagation parameters typical for the galactic environment [82]. For e^\pm above 1 GeV, only IC scattering and synchrotron losses dominate their energetic evolution. Differently from nuclei, the mean average traversed path for e^\pm decreases as the energy increases.

The propagation Equation 1.2 can be adapted to e^\pm as follows:

$$\frac{\partial\psi_{e^\pm}(\vec{r}, E, t)}{\partial t} = Q^{\text{tot}}(\vec{r}, E, t) + D(E)\nabla^2\psi_{e^\pm} - \frac{\partial}{\partial E}[b(E)\psi_{e^\pm}(E)] \quad (1.8)$$

where the factor $b(E) = dE/dt$ is the total energy loss rate of e^\pm with energy E .

The solution of Equation 1.8 shows that the typical path length of e^\pm with energies above ~ 1 GeV is smaller than the galactic halo. Therefore, e^\pm CRs detected at the Earth above the GeV energies must have galactic origins. Moreover, differently from hadrons, the propagation volume they occupy drastically decreases with increasing energies. In the galactic environment, a 100 GeV e^- has to originate from a distance $d < 1$ kpc. At 10 TeV, the distance decreases to 200 pc. This is remarkable, as the measurement of high energy e^\pm could potentially improve the knowledge of the galactic neighborhood with important consequences on the phenomenological interpretation of the measurements of all the CR species.

1.2.2 Measurements of the local electron and positron fluxes

The current experimental status of the CR e^- and e^+ measurements is shown in Figure 1.12. The separate e^- and e^+ fluxes have been measured by balloon and space spectrometers. A magnetic field is

needed in order to infer the charge sign of the incoming particle⁹.

Ground, space and balloon experiments have also measured the flux of the ($e^+ + e^-$) CR component, namely the flux of e^\pm disregarding the charge sign.

Until 2011, the most precise results have been released by the H.E.S.S. ground telescopes, by the ATIC balloon experiment and by the PAMELA and Fermi-LAT satellite experiments. The deployment and the operations of the AMS spectrometer on board of the ISS have finally provided e^\pm data with unprecedented accuracy in the energy range [0.5 - 1000.0] GeV, with a huge impact on the understanding of the physics of the CR e^\pm component. The AMS experiment will be reviewed in detail in Chapter 2. The analysis of the AMS ($e^+ + e^-$) flux measurement ($\Phi_{e^++e^-}$), which is the result of this PhD thesis, will be presented and discussed in detail.

The e^- and e^+ fluxes are subject to solar modulation effects up to ~ 30 GeV. The comparison between measurements taken in different time periods and the analysis of the flux itself is therefore complicated by this additional factor. Above ~ 30 GeV the spectral shape is not influenced by the solar modulation within the current experimental accuracy.

The e^- spectrum, measured from 0.5 GeV to 700 GeV by AMS, does not show any feature above ~ 30 GeV. Above ~ 50 GeV, the e^- flux can be parametrized with 90% CL by a single power law ($\Phi(E) \propto E^{-\gamma}$) up to 700 GeV [26].

The e^+ flux, measured by AMS from 0.5 GeV to 500 GeV, can also be parametrized by a single power law spectrum with 90% CL starting from ~ 30 GeV up to 500 GeV within the current experimental accuracy. A detailed analysis of the local spectral shape shows that the e^+ flux hardens above ~ 35 GeV and then softens again above ~ 200 GeV [26]. The flux of e^- and e^+ are significantly different in their magnitude and in their energy dependence. This indicated that most of the e^+ CR have a different origin than e^- CR.

The different origin of e^- and e^+ is confirmed by the positron fraction (PF), the ratio of the e^+ flux over the total ($e^+ + e^-$) flux, measured by AMS from 0.5 GeV to 500 GeV [83]. The PF decreases rapidly from 0.5 GeV to ~ 8 GeV, consistent with the expectation of purely secondary e^+ production from interactions of other particles with the ISM. Above 8 GeV, the PF tends to steadily increase up to ~ 200 GeV and then it flattens out. The PF reaches its maximum value at $E = 275 \pm 32$ GeV. Above this energy, the PF no longer increases with energy. The spectral shapes of the e^- and e^+ fluxes confirm that the rise in the PF is given by an additional source of e^+ and not by a decrease in the e^- flux.

The ($e^+ + e^-$) flux, measured with higher accuracy than the separate e^\pm fluxes, has been measured by AMS from 0.5 GeV to 1 TeV. The ($e^+ + e^-$) flux can be parametrized by a single power law spectrum with 90% CL starting from ~ 30 GeV up to 1 TeV. The resulting spectral index amounts to $\gamma = -3.170 \pm 0.008$ (stat.+syst) ± 0.008 (energy) [1]. The AMS ($e^+ + e^-$) flux is softer than previous measurements, and does not confirm the feature in the spectrum first observed above 300 GeV by the PPB-BETS and by the ATIC experiments [7, 9]. The AMS $\Phi_{e^++e^-}$ measurement agrees at high energies with the data provided by the H.E.S.S. ground based experiment and by the Fermi-LAT satellite experiment within the systematics introduced by each detector energy scale uncertainties.

The actual experimental results cannot be explained by any diffusion model based on the standard hypotheses discussed so far. The assumption of a primary production of e^- in SNR accelerators and secondary e^- and e^+ production from interactions of hadrons with the ISM, well constrained by the accuracy of the proton and nuclei fluxes, is not compatible with the rise observed in the PF. In this standard scenario, the PF is in fact expected to continuously decrease as a function of energy due to the energy dependence of the e^\pm production cross section from nuclear spallation with the ISM. The rise of the PF at high energies and the constraints provided by the e^\pm flux measurements hint to the presence

⁹The Fermi-LAT satellite, although it is not equipped with a magnet, has been able to distinguish between positive and negative sign particles in peculiar locations of the geomagnetic field, where the field configuration prevents positive or negative particles to reach the detector [18].

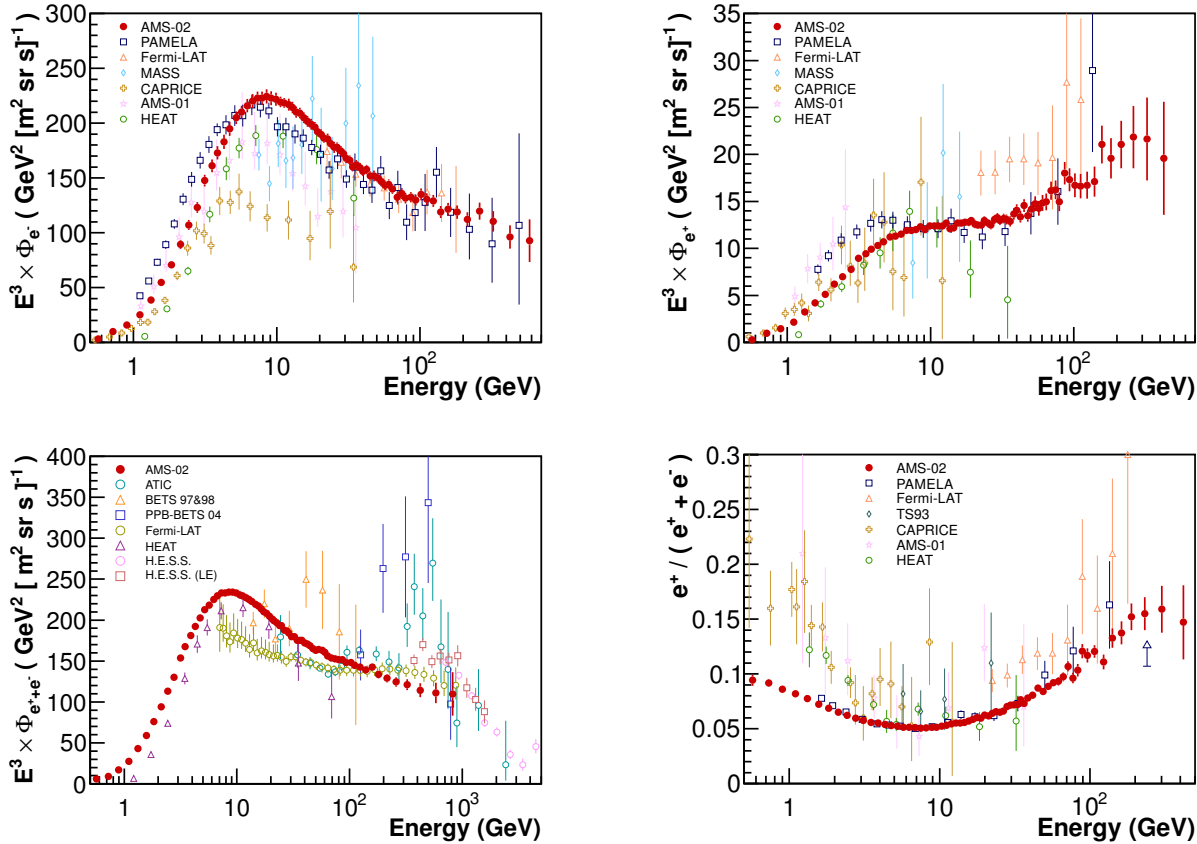


Figure 1.12: Experimental measurements of the e^- flux (**Top Left**), of the e^+ flux (**Top Right**), of the $(e^+ + e^-)$ flux (**Bottom Left**) and of the positron fraction, $e^+/(e^+ + e^-)$ (**Bottom Right**)^a. Cosmic e^\pm have been measured in the last 20 years by balloon [5, 6, 7, 8, 9, 10, 11, 12, 13], space [14, 15, 16, 17, 18, 19] and ground [20, 21] experiments. The latest measurements provided by the AMS experiment [83, 26, 1] increased the accuracy of the data and reached energy ranges never explored so far. The direct comparison of different experimental results below ~ 30 GeV has to further take into account of solar modulation effects due to the different solar activity in the data taking periods.

^aThe error bars do not include the systematic introduced by the uncertainty of the energy scale measurement. More details will be addressed in Chapter 6.

of an additional source of e^+ . In the following section, purely astrophysical hypotheses used to explain these features in the e^\pm fluxes are addressed.

1.2.3 Astrophysical interpretation of the cosmic electron and positron fluxes

The increasing contribution of e^+ to the total e^\pm CR flux cannot be accounted for by a purely secondary production from spallation of hadrons with the ISM. An additional unaccounted *primary* source of e^+ could, on the other hand, provide the necessary contribution to explain the rise in the PF.

A widely investigated possibility is the presence of nearby pulsar e^\pm sources. The term “pulsar” refers to isolated, rotating, magnetized neutron stars [84]. The first pulsar observation (PSR1919+21¹⁰) goes back to 1967, when Hewish and Bell recorded a series of regular radio pulses with 1.33 s period. The

¹⁰The british post-punk band Joy Division used an image of PSR1919+21 radio pulses on the cover of their debut album Unknown Pleasures [85].

pulses originate from beams of radio emission emitted along the magnetic axis of the pulsar – misaligned with the rotation axis itself – and they are associated with the passage of the beam across the line of sight of the observer. The radiation emission, extracted from the rotational energy of the neutron star which therefore slows down, is produced by the variation of the dipole moment. The mechanism is also known as *magnetic breaking*. Typical pulsars have rotational periods of the order of seconds, and lifetimes between 10^5 and 10^7 years. The immediate environment of the pulsar, the pulsar’s magnetosphere, is characterized by strong surface magnetic fields, in the range $10^6 - 10^9$ T. The Lorentz force just outside the star surface is strong enough to exceed the gravitational attraction and to remove particles from the star surface, resulting in electric current flows in the magnetosphere. Part of the magnetic field lines close to the star magnetic poles extends far from the nucleus of the neutron star, and particles can escape the environment and can be accelerated in the interstellar space. The emission of radiation in the strong electromagnetic field results in the consequent production of particle/antiparticle pairs, among which e^+ and e^- .

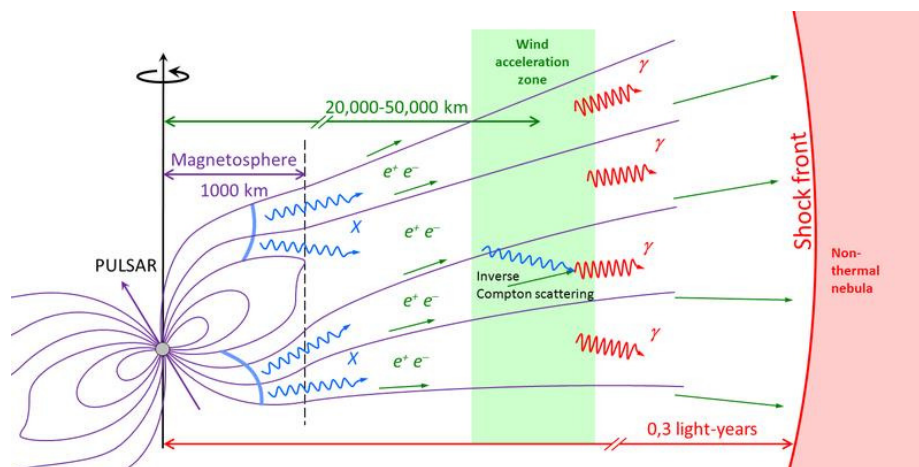


Figure 1.13: Schematic of a pulsar environment and e^\pm acceleration processes [86]. Particles are dragged off the pulsar surface by the strong magnetic field and flow in the magnetosphere following the magnetic lines. Interactions with the medium can produce e^\pm pairs. The pulsar wind nebula (PWN), a region of hot magnetized plasma between the ejecta and the back-propagating pulsar termination shock, accelerates the e^\pm pairs which are finally injected in the ISM.

Before the particles completely escape the pulsar environment, they are trapped in the Pulsar Wind Nebula (PWN), a region of hot magnetized plasma between the ejecta and the back-propagating pulsar termination shock. In the PWN, particles are further accelerated for typically $\sim 50 \times 10^3$ years and then injected in the ISM [87]. Figure 1.13 shows a scheme of a typical pulsar environment, together with the processes involved in the e^\pm acceleration in the different regions surrounding the neutron star. The process through which e^\pm are injected from the PWN into the ISM is not completely understood. However, the spectrum of e^\pm trapped inside the PWN can be inferred by observations of the emission of synchrotron radiation and IC scattering off protons. The PWN source term is usually parametrized as:

$$Q(\vec{r}, E) = Q(E) \delta(\vec{r}) \quad (1.9)$$

where the spectral shape of the source is assumed to follow a power law description with an exponential energy cutoff:

$$Q(E) = Q_0 E^{-\gamma_P} e^{-\frac{E}{E_{\text{cut}}}} \quad (1.10)$$

with γ_P being the injection index, E_{cut} being the e^\pm acceleration cutoff energy and Q_0 being the flux

normalization factor. These phenomenological parameters are loosely constrained by observation of the pulsar age, distance and energy releases [88] available in pulsar catalogs.

The pulsar e^\pm acceleration hypothesis is widely explored in the literature to explain the features in the e^\pm spectra. The separate e^- and e^+ fluxes, the $(e^+ + e^-)$ flux and the PF measurement are used to constrain the pulsar parameters. The same normalizations and the same spectral indices are usually assumed for e^- and e^+ accelerated in PWN. Different approaches to the data interpretation are usually tested: a homogeneous, galactic PWN component or one (or more) single nearby PWN contributions¹¹ are both used to explain the data. More exotic assumptions allow for nearby pulsar e^- production only or even a charge asymmetric e^\pm PWN injection, which is however not justified by the current data [89].

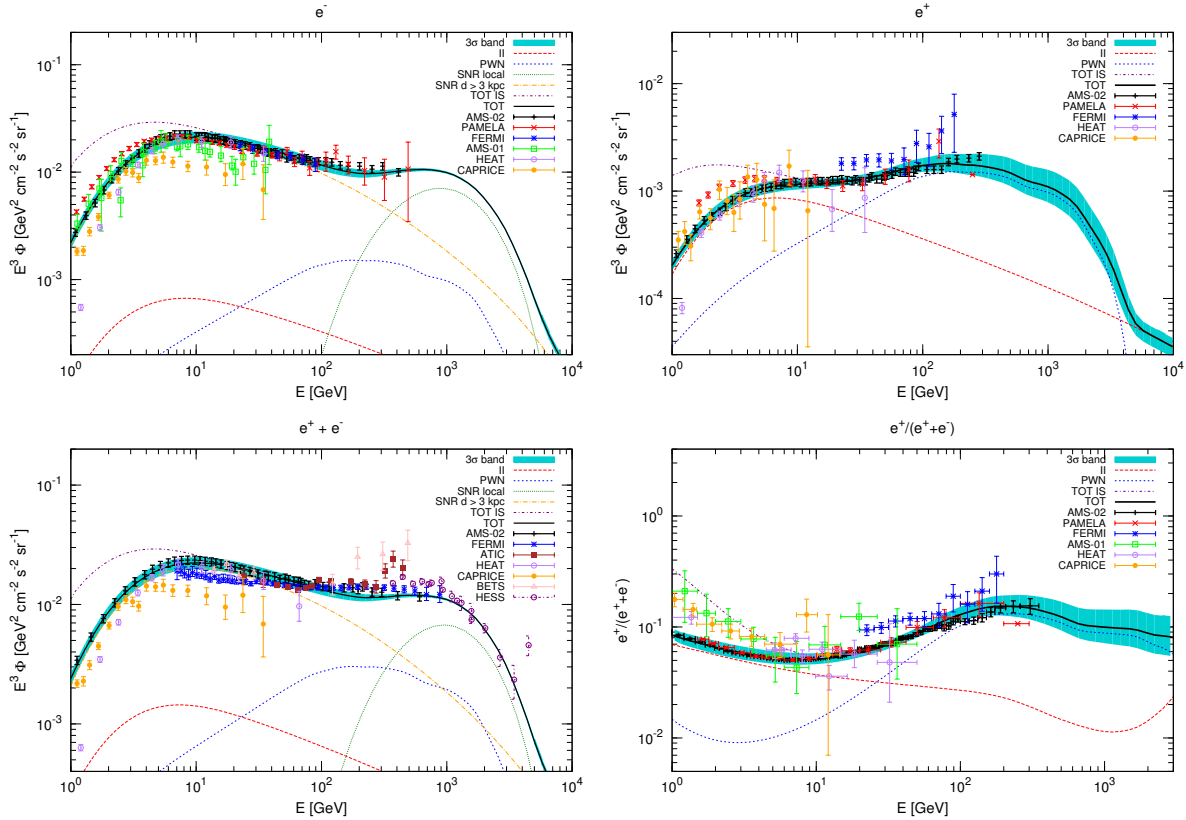


Figure 1.14: Simultaneous fit to the AMS data using a homogeneous SNR e^- contribution (here a local and far SNR contribution with different parameters are assumed) and a PWN e^\pm contribution. The plots represent the data of the e^- flux (**Top Left**), of the e^+ flux (**Top Right**), of the $(e^+ + e^-)$ flux (**Bottom Left**) and of the positron fraction (**Bottom Right**) together with the fit result. The result is taken from [90]. The dot-dashed yellow line represents the e^- flux from the far (> 3 kpc) SNR population, the dotted green line the e^- from the local SNRs, while the short dashed blue line describes the e^+ and e^- flux from the PWNs. The long dashed red line takes into account the secondary contribution to both e^- and e^+ flux from ISM spallation. The best fit model is represented by the solid black line with its 3σ uncertainty cyan band. The scenario described here is a typical result coming from the assumption of PWNs as additional primary e^\pm sources. While the e^- and the $(e^+ + e^-)$ flux is dominated by the SNR component, the e^+ flux and the positron fraction measurements cannot be explained by pure secondary ISM spallation. The extrapolation at high energies shows, in this PWN acceleration assumption, that the PF and the e^+ flux are expected to *slowly* decrease with increasing energy.

An example of a combined fit to the e^\pm data, assuming a PWN contribution from several pulsars, is

¹¹Monogem, Geminga and Vela are an example of the most widely used known pulsars.

shown in Figure 1.14. The scenario pictured in this interpretation is representative of the usual outcome of a PWN e^\pm source interpretation. The e^- flux is dominated by the SNR production component. The e^+ is dominated at low energies by the pure secondary ISM spallation production. Starting from ~ 20 GeV, the primary PWN production contribution starts to dominate the e^+ flux up to the highest energies, until the maximum acceleration energy is reached. The primary PWN component correctly describes the rise observed in the positron fraction, which would be otherwise expected to monotonously decrease. The extrapolation at high energies shows that, in this PWN acceleration assumption, the PF and the e^+ flux are expected to *slowly* decrease with increasing energy. The energy cutoff E_{cut} for a typical pulsar is expected to be, in fact, around 2 TeV. Already starting below the TeV scale, therefore, the weakest pulsars stop to contribute to the common e^\pm production. Different scenarios are also allowed by the current data. In particular, it has been shown that the contribution of strong, nearby pulsars could lead to a *sharp* break in the e^\pm PWN contribution, mimicking the signature expected from other primary e^\pm production mechanisms (like Dark Matter production, as explained in the next section). Figure 1.15 shows an example of this possibility.

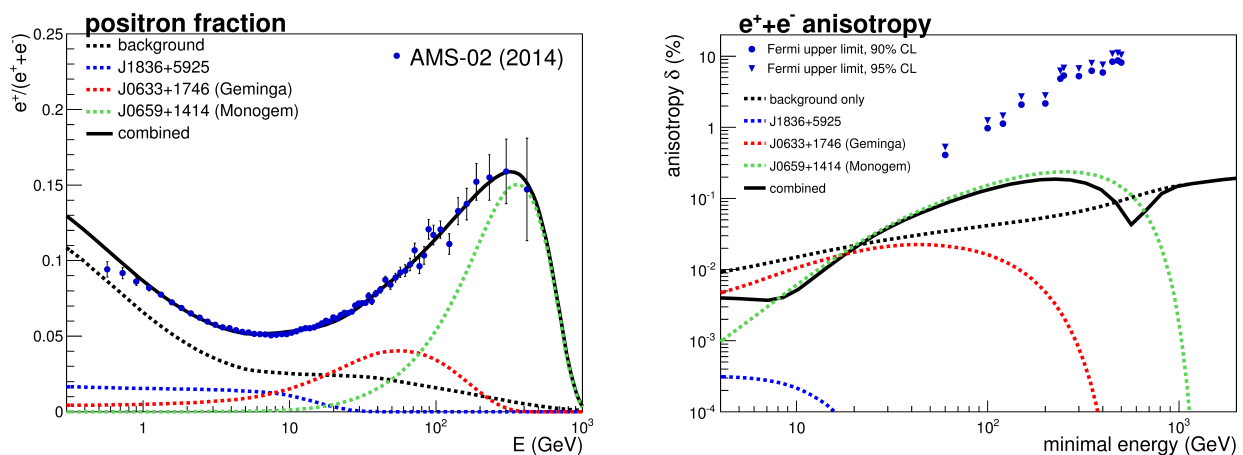


Figure 1.15: **Left:** Possible contribution from three nearby pulsars to the PF. The pulsar parameters are tuned within their measured property uncertainties to fit the data. The black dotted line represents the secondary e^+ contribution alone. The red, blue and green lines represent the PWN e^+ contributions. In this scenario the positron fraction is expected to sharply decrease above 500 GeV. **Right:** Expected dipole anisotropy for the $(e^+ + e^-)$ flux from the pulsar scenario described in the left-side figure. The pulsar contribution increases the anisotropy in the $(e^+ + e^-)$ incoming direction above the expected anisotropy contribution from the standard SNR spatial density (black dotted lines). The level of expected anisotropy depends on the pulsar scenario and on the propagation model that is assumed. In blue, the upper limits on the dipole anisotropy measured by the Fermi-LAT experiment are shown [91]. The improvement in the upper limits or even the detection of an anisotropy in the e^\pm incoming direction will be an useful tool to constrain the propagation models. As discussed in Section 1.3, it would also provide distinct information to unveil the nature of the primary additional production of e^\pm in CRs.

Finally, if a contribution from nearby PWNs is present, a preferred incoming direction for the flux of e^\pm measured at Earth is expected. This is quantified by the level of deviation of e^\pm arrival directions from an isotropic distribution, usually shortened as level of anisotropy. PWNs are e^\pm point-like sources and the detected flux of PWN e^\pm would therefore have a directional preference. The directionality is, however, diluted by the diffusive propagation in the turbulent galactic magnetic fields. The level of expected anisotropy is very low, typically below the percent level for 100 GeV e^+ . In addition to this, the anisotropy for the PWN e^\pm has to be identified among the more abundant and more isotropic standard SNR e^\pm component. The anisotropy level depends on the channel which is taken into account (e^+ , e^-

or ($e^+ + e^-$) flux), on the e^\pm energy and on the propagation model that is assumed. An example of expected anisotropy for a PWN e^\pm primary production model is shown on the right in Figure 1.15. So far, no experiment claimed the detection of any anisotropy in the e^\pm channels [91, 92, 83]. The upper limits on the e^\pm anisotropy constrain the allowed pulsar models and the diffusive transport propagation parameters. Additional astrophysical effects, like a peculiar local diffusion or the presence of non detected pulsars in the opposite direction of the expected anisotropy, can lower the level of anisotropy expected by the known pulsar contributions and reduce the sensitivity to exclude a larger ensemble of pulsar and propagation models.

As discussed so far in this section, the features in the e^\pm spectra can be explained in terms of astrophysical primary e^\pm production. Alternative mechanisms have also been theorized. The most attractive for the implications on the fundamental physics and cosmology is the hypothesis that the excess of e^+ in the cosmic radiation could be explained by decay or annihilation of primordial Dark Matter. Dark Matter is indeed a fundamental component of the Universe, but it has not yet been detected. The analysis of the e^\pm data could confirm this hypothesis and set strong constraints on the nature of Dark Matter. In the next section, the Dark Matter problem is introduced and the application to the cosmic e^\pm excess puzzle is discussed and compared to the astrophysical hypotheses.

1.3 Dark Matter

The search for Dark Matter (DM) represents one of the most dynamic physics topics in the last decades. Since the early 1930s a series of astronomical, cosmological and particle physics observations pointed to the existence of a “dark” component of the Universe which constitutes the highest contribution to its matter content. The term “dark” has historical origins, and refers to matter that does not couple to photons and that consequently does not emit substantial electromagnetic radiation. Although the existence of DM is well established by now through several evidences at all scales, DM has not been detected yet experimentally and its physical nature is still not clear. Nevertheless, the observed DM abundance points to new physics at the electroweak scale ($\text{GeV} \sim \text{TeV}$). In this section, an overview of the evidences for the existence of DM is discussed. Subsequently, the connection between DM, cosmology and the “WIMP miracle” is examined. Finally, a summary of DM experimental searches, with emphasis on the indirect search using cosmic rays, is presented.

1.3.1 Evidence for Dark Matter at galactic and galaxy cluster scales

Historically, the first evidence of DM in our Universe comes from its gravitational effect. Opik’s 1915 studies about dynamical matter density in the solar vicinity was the first study about matter that does not emit radiation and can thus be observed only by its gravitational effect. The current connotation of Dark Matter appeared in 1933 with Zwicky’s work on the dynamics of galaxies [93]. Measuring the velocity dispersion in the Coma cluster, Zwicky was the first scientist to apply the virial theorem to the cluster volume in order to infer the average mass of galaxies. The value he obtained was greater than what expected from the cluster luminosity, assuming it is composed of baryonic matter only. The hypothesis of Zwicky of the existence of a “dark” matter component was not taken seriously until the 70s.

In this period, the first confirmation of DM existence came from the measurement of galactic rotational curves, pioneered by Rubin and Ford [94] and confirmed by more recent surveys. Observations of gas clouds in galaxies show that the rotational velocity approaches a constant value as the distance from the galaxy center increases. If only the visible matter (i.e. stars and interstellar gas) contributes to the mass of the galaxy, then the rotational velocity at a distance r outside the luminous disk would

decrease proportional to $1/r$. Instead in most galaxies, as shown in Figure 1.16, the rotational velocity levels off for large values of r . The most common explanation, first accounted in [95], is the hypothesis that galaxies are surrounded by a diffuse halo of dark matter, with a radial profile¹² $\rho^{\text{DM}}(r) \propto r^{-2}$. The same analysis can be applied to the Milky Way to infer the local galactic DM density. Due to the peculiar position of the observer inside the galaxy itself, the local DM halo density is still uncertain to at least a factor of 2 ($\rho_{\text{loc}}^{\text{DM}} \sim 0.3 \pm 0.1 \text{ GeV}/\text{cm}^3$).

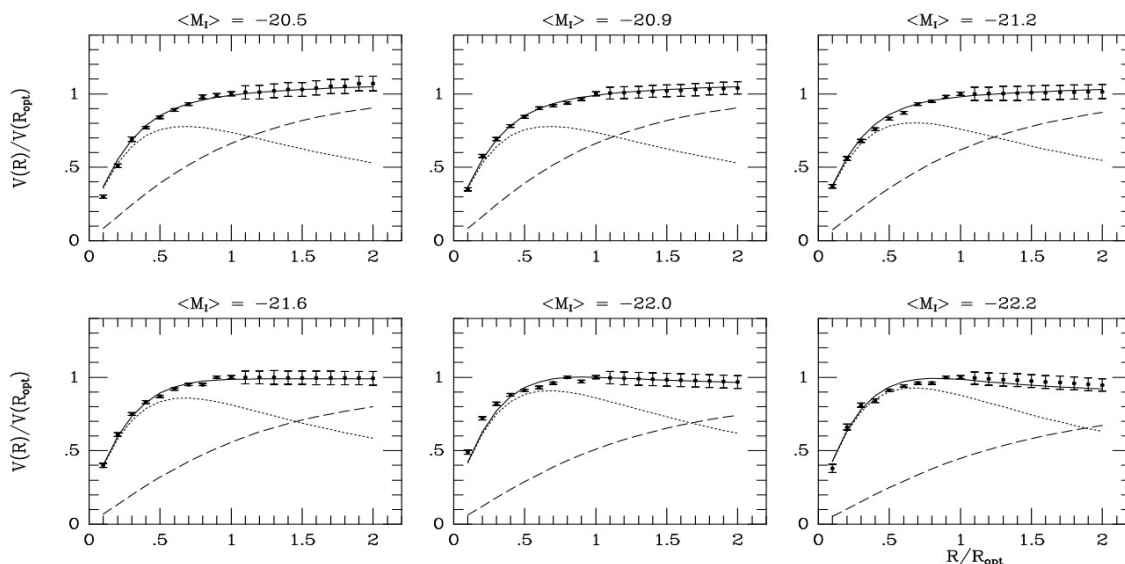


Figure 1.16: Rotational curves for a selected set of galaxies as function of the optical radius R_{opt} , defined as the radius containing 83% of the total integrated light [96]. The rotational curves are fitted with a superposition of the stellar and gaseous disk (dotted line) and the dark halo (dashed line). At small radii, the luminous component dominates, while at higher distances from the galactic center the DM contribution dominates and flattens out the velocity distribution.

Another independent proof of the existence of “dark” gravitationally interacting matter relies on observations of galaxy clusters through gravitational lensing. The gravitational lensing effect, proposed by Einstein in 1936 [97] and first observed in 1979 [98], allows to determine the gravitational mass distribution of a cluster by the analysis of travel paths of emitted light. According to the general relativity theory, light propagates along geodesics which deviate from straight lines when passing near intense gravitational fields. The distortion of the images of background objects due to the gravitational mass of a cluster can be used to infer the spatial distribution of the gravitation potential associated to the mass of the cluster and, therefore, to DM. This approach, which is completely independent from the DM dynamics, confirms the DM profile results obtained by other techniques and provides an independent support for the DM hypothesis.

An important direct proof of the existence of DM is provided by the observation of the so-called *Bullet Cluster* (see Figure 1.17). In this cluster merger, where two separated clusters collided, gravitational lensing measurements show that the center of total mass has an offset with respect to the center of the baryonic mass distribution. During the collision, stars and galaxies (observed in visible light) passed through each other with minor disturbances. The hot baryonic gas (observed in the X-ray band), which constitutes the dominant baryonic component of the system, instead slowed down due to electromagnetic interactions. Since the gravitational mass bulk nearly corresponds to the visible galaxy domain, the

¹²Most recent analyses use a more complicated profile description (a typical example is the *Einasto* profile parametrization $\rho_{\text{Ein}}^{\text{DM}} \propto \exp(-d_n[(r/r_s)^{1/n} - 1])$).

natural explanation is that this latter is composed of collisionless DM [99]. After this observation, other similar topology merging clusters have been observed, but with lower spatial resolution ¹³.

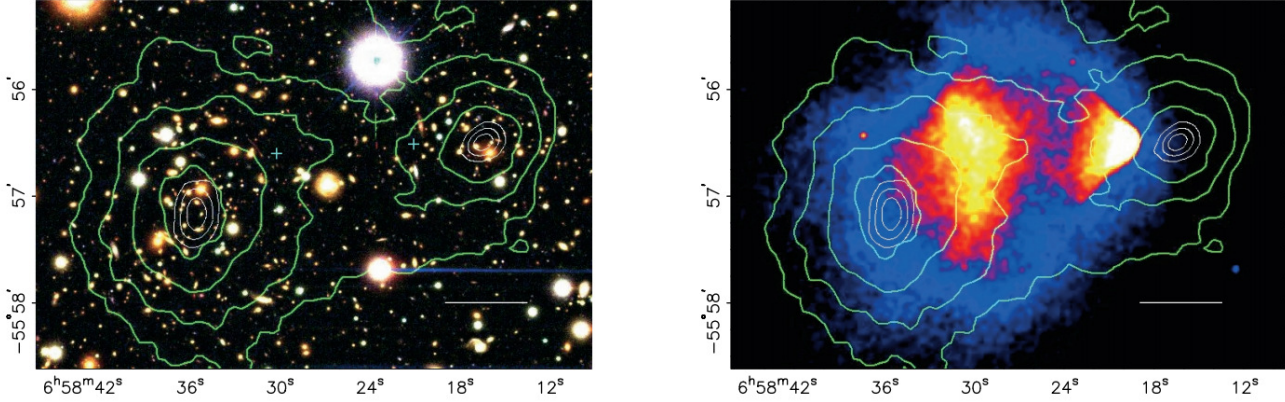


Figure 1.17: **Left:** Optical image of the *Bullet Cluster* (1E 0657-558). The white bar indicates 200 kpc scale. **Right:** X-ray map emission measured by Chandra experiment of the 1E 0657-558 merging cluster, roughly proportional to the square of the plasma density. Superimposed in green contour in both images are the isodensity curves from gravitational lensing measurement. The X-ray emitting baryonic matter is displaced from the galaxies and the collision-less DM (inferred through gravitational lensing).

1.3.2 Evidence for Dark Matter at cosmological scales

The existence of DM plays a primary and essential role within the Standard or Big Bang Cosmology theory. The Big Bang Cosmology is the theory which describes the evolution of the early Universe, starting from a fraction of a second up to now.

This theory (which is today validated by different observations like the Universe expansion, the presence of the cosmic radiation background CMB and the abundance of light elements) describes the evolution of the Universe dynamics – parametrized by the time dependent scale factor $a(t)$ – according to the Friedmann-Lemaître equations:

$$H^2(t) = \left(\frac{\dot{a}(t)}{a(t)} \right)^2 = \frac{8\pi G}{3} \rho - \frac{k}{a^2(t)} + \frac{\Lambda}{3} \quad (1.11)$$

and

$$\frac{\ddot{a}(t)}{a(t)} = -\frac{4\pi G}{3} (\rho + 3p) + \frac{\Lambda}{3} \quad (1.12)$$

where $G = 6.674 \times 10^{-11} \text{m}^3 \text{kg}^{-1} \text{s}^{-2}$ is the Newtonian gravitational constant, p and ρ are the pressure and energy density and $H(t)$ is the Hubble constant. The parameter k is the curvature parameter. For a flat Universe $k = 0$. For an open Universe $k < 0$. For a closed Universe $k > 0$. The parameter Λ is the Cosmological Constant, which can give a contribution associated with the vacuum energy in quantum

¹³It is worth to mention that part of the observational evidence for DM, based on the impact of their gravitational potential on the astrophysical environment, could be explained by theories which do not account for the existence of DM [100]. Such theories assume that the general relativity theory predictions fail at galactic and cosmological scales, being a smaller scale limit of more complex gravitational theories (Modified Newtonian Dynamics, MOND). MOND can provide a better description of the galactic rotational curves than the DM hypothesis does. However, it fails on the scale of galaxy clusters and cannot explain the segregation of bright and dark matter observed in the *Bullet Cluster*. Moreover, it cannot satisfactory explain the CMB anisotropies and the large structure formation, as the standard DM cosmology does (see Section 1.3.2). For these reasons, the DM hypothesis is still considered the most probable explanation for the observations.

field theory. This term, related to the so-called Dark Energy, constitutes one of the most fundamental field of research in astrophysics and cosmology today.

If a critical density ρ_c is defined such that $k = 0$ when $\Lambda = 0$ (a spatially flat Universe without Cosmological Constant):

$$\rho_c = \frac{3H^2}{8\pi G} \quad (1.13)$$

the dimensionless cosmological density parameters $\Omega_i = \rho_i/\rho_c$ are consequently defined as the energy density ρ_i relative to the critical density ρ_c for the contributions of matter (Ω_M), radiation (Ω_r), Cosmological Constant (Ω_Λ) and curvature (Ω_k). Using these definitions, Equation 1.11 becomes:

$$\sum_i \Omega_i = 1 \quad (1.14)$$

The cosmological model is confirmed by many representative observations:

- **Hubble constant direct measurement:** Using the period-luminosity relations for Cepheid variable stars, it is possible to obtain the distances of several galaxies. The Hubble Space Telescope Key Project [101] measured the recession velocities for type Ia Supernovae located in nearby galaxies (i.e. $z \ll 1$) and directly estimated $H_0 = 73.8 \pm 2.4$ km/(s Mpc). The most recent estimation of the Hubble constants comes from the PLANCK mission CMB data (see next point), $H_0 = 67.3^{+1.2}_{-1.1}$ km/(s Mpc) [102].
- **Supernovae Ia measurement:** The relation between the galaxy recession velocity in the expanding Universe and the redshift parameter z is expressed as:

$$d_L = \frac{1}{H_0} \left[z + \frac{z^2}{2}(1 - q_0) \right], \quad (1.15)$$

where d_L is the luminosity distance and $q_0 = 2\Omega_M - \Omega_\Lambda$ is the Universe deceleration parameter¹⁴. It is worth to point out that Ω_Λ is the only contribution to the Universe expansion acceleration, and the relative weight between the matter and the Λ energy contribution defines the sign of the Universe's acceleration. Using Equation 1.15 and the definition of d_L for a set of $z > 1$ Supernovae Ia stars, it is possible to determine a confidence interval for q_0 . With this technique, evidence for an accelerating Universe has already been found in 1998 [103]. Combined with CMB results, this confirms that a Cosmological Constant component in the energy density of the Universe exists, and it amounts to $\sim 70\%$ of its energy composition. This “negative pressure” term, which dominates the Universe acceleration, has been given the name of “Dark Energy” (DE).

- **CMB spectrum:** The Cosmic Microwave Background (CMB) is one of the observable relics of the Big Bang. Photons were generated in the early Universe and underwent the last scattering at the recombination time (when H atoms were formed from cosmological plasma, leading to a transparent Universe), corresponding nearly to $z \sim 1000$. The PLANCK satellite mission [104] confirmed that the CMB has a perfect blackbody spectrum at a temperature of $T_{\text{CMB}} = 2.726 \pm 0.001$ K as already measured by previous experiments like the WMAP satellite [105]. Moreover the CMB has been measured to be isotropic at the 10^{-5} level. With the CMB temperature fluctuations

¹⁴For nearby galaxies ($z \ll 1$) Equation 1.15 simplifies to the well known Hubble's law

$$v = H_0 d = cz$$

where v is the galaxy recession velocity with respect to the observer at distance d .

measured to be purely gaussian, all the information contained in the CMB map is carried by its power spectrum¹⁵. The power spectrum of the CMB is used to infer the cosmological physical information. Figure 1.18 shows the CMB power spectrum observed by PLANCK, which can be fitted assuming a cosmological model typically containing 6 to 7 parameters. In first approximation, the first peak constrains the Universe's curvature; the second constrains the baryon density content of the Universe; the third brings information about the matter density content. The best fit to CMB data from PLANCK results in a baryonic content of $\Omega_b h^2 = 0.02205 \pm 0.00028$ and a matter content of $\Omega_M h^2 = 0.315 \pm 0.017$ [106].

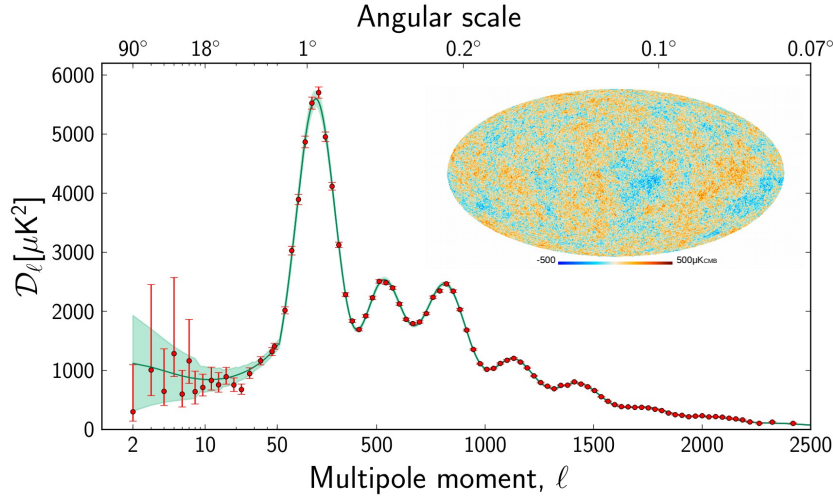


Figure 1.18: In the top right, the CMB map measured by the PLANCK experiment, after subtraction of the galactic emission and the Solar System dipole to the CMB “rest frame”, is shown. The map measured by the PLANCK experiment is isotropic at the 10^{-5} level. The CMB temperature angular power spectrum derived from the PLANCK measurements is shown by the red data points. The green line represents the best fit six-parameter cosmological model, with the shaded area associated uncertainty. The analysis of the CMB power spectrum is used to infer several cosmological parameters. Figure adapted from [107].

The results from previously discussed measurements, as well as other measurements like galaxy cluster patterns, visible baryonic densities and patterns and gravitational waves searches, confirm the Big Bang Cosmological Model as the best description of the data available today. Although the single CMB experiment PLANCK is able to set boundaries to most of the cosmological parameters [106], stronger conclusions can be extracted by the combination of complementary experimental results.

The experimental measurements constrain the spatial curvature of the Universe to be compatible with flatness ($\Omega_k \sim 0$) [106]. Most of the energy content of the Universe is dominated by the Cosmological

¹⁵The typical procedure to analyze the CMB relies on the expansion of the temperature anisotropies in spherical harmonics $Y_{lm}(\theta, \phi)$:

$$\frac{\delta T}{T}(\theta, \phi) = \sum_l \sum_{m=-l}^{+l} a_{lm} Y_{lm}(\theta, \phi) \quad (1.16)$$

and on the consequent analysis of the power spectrum of the variance C_l of the expansion coefficients a_{lm} :

$$C_l \equiv \langle |a_{lm}|^2 \rangle \equiv \frac{1}{2l+1} \sum_{m=-l}^{+l} |a_{lm}|^2 \quad (1.17)$$

Constant term Λ , with $\Omega_\Lambda \sim 68\%$. The remaining energy content is dominated by matter, $\Omega_M \sim 32\%$. The ordinary baryonic matter component is measured with high accuracy from CMB and large scales structure measurements: such measurements set $\Omega_b \sim 5\%$, a result that is independently confirmed by the Big Bang Nucleosynthesis predictions. The rest of the matter energy contribution is therefore attributed to the presence of Dark Matter, for a total of $\Omega_{DM} \sim 27\%$. Cosmological parameter measurements hence prove that we live in a nearly flat, expanding Universe whose energy content is dominated by Dark Energy and whose matter content is dominated by Dark Matter.

1.3.3 Dark Matter candidates and the WIMP miracle

The widely accepted hypothesis on the nature of DM is that DM is a Big Bang relic.

The primordial Universe can be described as a thermodynamic gas in equilibrium, with different particle species interacting with each other and *freezing out* (going out of equilibrium) at different times. When the interaction rate $\Gamma(t)$ of a particular kind of particle with the rest of the environment is well below the Universe expansion rate:

$$\Gamma(t) \ll H(t) \quad (1.18)$$

then that particular species decouples from the thermodynamic equilibrium and expands without interactions, like a free gas, with a distribution strictly connected with equilibrium.

The Boltzmann transport equation describes the density of decoupled particle species from the primordial soup. The relationship between the number density $n_\chi(t)$ of any species χ during the thermodynamical and chemical equilibrium with the particle gas and the Universe expansion is ruled by the following equation:

$$\frac{dn_\chi}{dt} + 3H(t)n(t) = \langle\sigma v\rangle(n^2(t) - n_{\text{eq}}^2(t)) \quad (1.19)$$

where $\langle\sigma v\rangle$ is the thermal average total cross section of the χ species with the environment. A complete treatment and derivation of Equation 1.19 can be found in [108]. The solution of this equation can be used to infer the relic density at the freeze out period $n_{\text{eq}}(t_{\text{fo}})$. Depending whether the species is relativistic or not when it decouples, the relic density evolves differently in time. The possibility of an ultra-relativistic particle to be a good DM candidate is ruled out by large-scale formation arguments and from stringent limits set by accelerator experiments [109]. Therefore, DM has to be a *cold* (not-relativistic at the freeze-out) relic of the Big Bang. Solving Equation 1.19 for this hypothesis, the properties of cold DM candidates are well constrained: the higher the annihilation rate $\langle\sigma v\rangle$ is, the smaller is the relic abundance of DM (see Figure 1.19).

To correctly account for the relic DM density observed today ($\Omega_{DM} \sim 27\%$), according to this scenario the most probable DM candidate has to be *massive* (mass in the range 100 GeV \sim TeV), with *weak scale interactions* and *stable* on cosmological time scales. The family of possible candidates is usually referred to as *Weakly Interacting Massive Particles* (WIMPs). Since there is no *a priori* connection between the Universe DM density and the Fermi constant, and since there are families of particle candidates with the right mass range theorized independently from cosmological inputs in several theoretical frameworks, this fact is usually titled “The WIMP miracle”.

1.3.3.1 Supersymmetry and the LSP

The Standard Model (SM) of particle physics describes the fundamental interactions between the elementary particles. The electromagnetic, weak and strong interactions between the twelve spin 1/2 fermions (six leptons and six quarks) are mediated by four spin 1 gauge bosons. The model is completed by the spin 0 Higgs boson field, introduced in the model to explain the mass of the fermions and bosons. The SM has been tested experimentally and found to be self-consistent and predictive for most of the

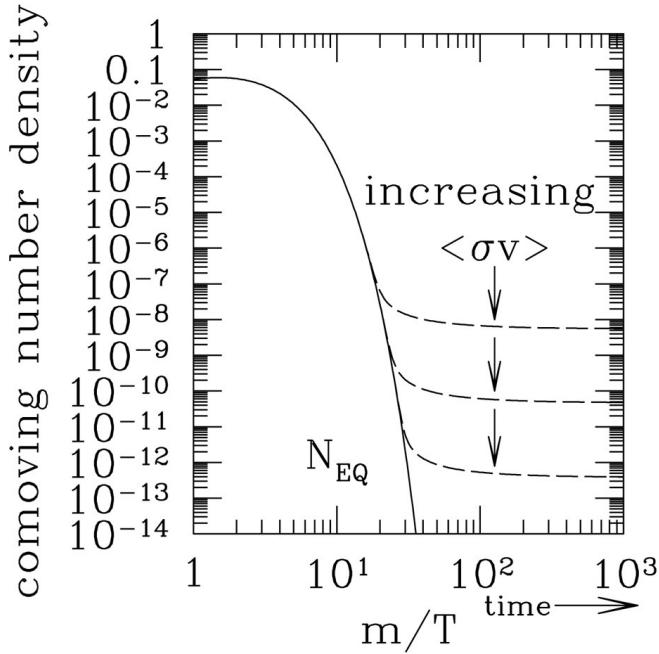


Figure 1.19: Evolution of the relic particle number density in a volume expanding with the Universe (comoving density) in the early Universe. During the equilibrium phase with other particle species, the relic particle comoving density decreases exponentially. After its decoupling, the density tends to a constant value. For cold DM, the higher the annihilation rate $\langle \sigma v \rangle$ is, the smaller is its relic abundance. In order to explain the current relic DM density, the candidate particle has to have an interaction cross section typical of weak scale interactions [110].

observed phenomena. However, it fails to incorporate gravitational interactions, to explain the mass of neutrinos and to explain other phenomenological observations. In addition to this, it does not provide any DM candidate among its constituents.

The most promising WIMP candidate, the *Lightest Supersymmetric Particle* (LSP), arises in the context of electroweak scale supersymmetric models (SUSY) [111].

From the phenomenological side, the term SUSY denotes a family of extensions (or generalization) of the Standard Model (SM), where for each elementary fermion a bosonic partner (or “superpartner”) with same quantum numbers but integers spin is associated, and viceversa. The symmetry between SM particles and their superpartners is usually denoted as R -parity. The additive quantum number R – which is assigned to be $R = +1$ for SM particles and $R = -1$ for their supersymmetric partners – is conserved in elementary interactions. If supersymmetry was, however, an exact symmetry, supersymmetric partners would have had the same mass as SM particles. Since such particles have not been experimentally detected at those scales, the symmetry has to be a spontaneously broken symmetry [112].

SUSY was first introduced during the early 1970s to solve the so-called “hierarchy problem” in the SM [111]. Among all other supersymmetric models, the Minimal Supersymmetric Standard Model (MSSM) is the minimal natural theoretical extension of the SM that can introduce supersymmetry. In the MSSM, the SM Higgs scalar sector is extended to a doublet h_d, h_u and the corresponding *higgsinos* superpartners \tilde{h}_d, \tilde{h}_u are added to the model. The natural completion of the model is achieved by adding the *sleptons* and *squarks* superpartners of the SM fermionic fields, the *gluinos* superpartners of the SM gluon field and the *gauginos* superpartners of the SM gauge fields. Such a model allows not only to solve the divergent radiative corrections to the Higgs field mass in the SM (“hierarchy problem”), but it also unifies the gauge couplings at high scales in favor of a possible Grand Unified Theory (GUT) of the SM gauge groups [113].

The conservation of the R -parity has fundamental consequences in the WIMP scenario framework. First of all, starting from SM ordinary states, supersymmetric particles can only be produced in pairs. Moreover, the LSP has to be stable. In order to completely meet the WIMP requirements explained already in Section 1.3.3, the LSP has also to be neutral and colorless.

In the context of the MSSM, the LSP is the lightest neutralino $\tilde{\chi}_1^0$. Neutralinos $\tilde{\chi}_{i=1,\dots,4}^0$ are the

mass eigenstates of the electroweak symmetry breaking mixing, which involves the neutral electroweak gauginos (\widetilde{B} and \widetilde{W}^0) and the neutral Higgsinos ($\widetilde{H}_{d,u}^0$). The properties of the neutralinos are determined by the parameters involved in the mixing matrix, which depend on the particular MSSM model investigated. It is possible, however, to explore a big number of self-consistent MSSM models predicting the existence of neutralinos with the right properties expected from a DM candidate. This leads the neutralinos in the SUSY framework to be the most studied WIMP candidate so far¹⁶.

1.3.4 Experimental searches for Dark Matter

The experimental search for DM is one of the physics fields that has most developed in the last years, due to the increase of interest of the community in the search for the nature of DM. Given the peculiarity of the topic, which interconnects several fields of fundamental physics and astrophysics, the experimental techniques are very diverse. The experimental challenge increases year after year in order to enhance the sensitivity of the searches, pushing the detection technologies for multiple applications to the edge.

In the following section, the main scenarios for DM search are reviewed. For definiteness, almost only the search for WIMPs, and in particular for the LSP (see Section 1.3.3.1), is covered. Different DM candidates do need slightly different detection techniques, up to completely different experimental approaches.

Given the expected nature of the DM candidates, the only feasible way to investigate their properties is to measure the effect of their interactions using SM particles, whose properties are already well known. Depending on the topology of the interaction, the experiments are usually distinguished into collider **production** experiments, **direct** search and **indirect** search experiments, as sketched into Figure 1.20. Despite the similarities at the level of fundamental physics, the detection techniques used in the three different searches are different. The detection of a positive signal in one of the channels alone could be not sufficient to conclusively identify the nature of DM. Only the combination of results from different approaches could solve the mystery of the DM nature.

The following sections present the most up to date experimental results and phenomenological interpretations. Due to the dynamics of the field, statements are subject to continuous updates and the experimental status shows conflicting experimental results. The conclusions drawn from experimental results have therefore to be taken with care and correctly weighted before drawing any strong physical conclusion.

1.3.4.1 Direct searches

DM direct detection techniques aim to detect the scattering of local WIMPs off nuclei using suitable detectors to observe the energy transferred by the nuclear recoil in the target [114]. The rate of expected scattering events $\frac{dR}{dQ}$ for a WIMP with mass M_χ as function of the energy transfer Q is given by:

$$\frac{dR}{dQ} \propto \beta(Q) \frac{\sigma_{\text{scat}} \rho_{\text{DM}}}{M_\chi} \int_{v > v_{\text{min}}} \frac{f(v, t)}{v} d^3v \quad (1.20)$$

where ρ_{DM} is the local DM density, σ_{scat} is the scattering cross section, $f(v, t)$ is the local time dependent DM velocity distribution function (in the rest frame of the experiment) and v_{min} is the minimum velocity to transfer the energy Q . The scattering cross section contains a spin dependent and spin independent

¹⁶It is important to remember, however, that other supersymmetric extensions of the SM predict alternative WIMP candidates. The spin 1/2 superpartner of the axion, the *axino*, and the 3/2 superpartner of the graviton, the gauge boson that mediates gravitational interactions, the *gravitino*, could in fact show a similar phenomenology as the LSP. This depends, however, on the SUSY model adopted and on the early Universe condition. Moreover, due to their lightness, they tend to belong to the more “exotic” warm (ultra relativistic at the freeze-out) DM framework.

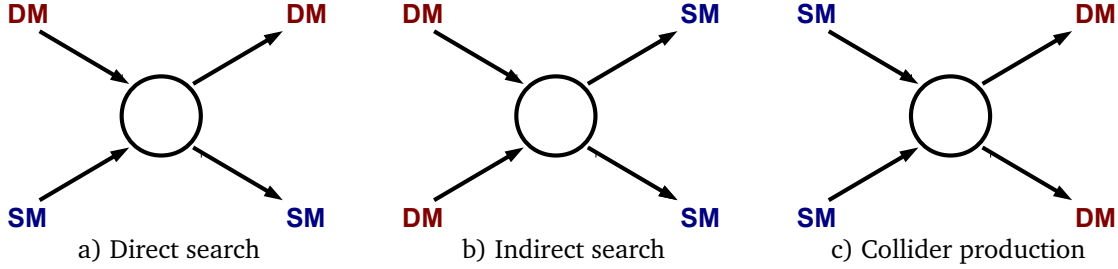


Figure 1.20: **a) Direct search:** a stable DM particle interacts with ordinary SM matter. The detectable effect of the interaction on the SM particle is used to infer the DM properties. A typical example is the scattering of WIMPs off nuclei. **b) Indirect search:** DM candidates can annihilate and produce detectable SM particles. The most sensitive channel is the production of high energetic rare components of the cosmic radiation. **c) Collider production:** SM particle (typically $p - p$, $p - \bar{p}$, $e^+ - e^-$) are accelerated, let collide and produce a pair of DM candidates. DM particles usually leave the detectors without being detected. Their presence in the collision products and their properties are thus inferred by the analysis of the SM particles produced during the same interaction.

interaction term. Targets with high nuclear number A are used to enhance the spin independent interaction. The factor $\beta(Q)$ represents the experimental correction to apply to the theoretical recoil spectrum. This typically includes Earth motion effects, nuclear form factors and scale factors to relate the theoretical nuclear scattering cross section to the observed experimental target scattering cross section [115]. Typically the value for the local DM density $\rho_{DM} \sim 0.3 \text{ GeV/cm}^3$ – much higher than the cosmological density due to the gravitational potential of our Galaxy – (see Section 1.3.1) is taken as reference. The value is mostly constrained by the analysis of the rotation curves of our Galaxy [116]. The local DM velocity profiles are usually inferred through numerical simulations of large scale structures [117]. The uncertainties on the local DM density and velocity distribution constitute one of the major limiting factors for these techniques. The measured scattering rate or the limit inferred by the observation of signal events compatible with background fluctuations only is used to set constraints on M_χ and σ_{scat} .

The typical recoil energy transfer Q expected from a WIMP off nuclei scattering amounts in the range $[5 \sim 100] \text{ keV}$. The detectors must therefore be sensitive to this energy range. Moreover, they have to be able to discriminate a possible signal from the background. Experiments are set in underground laboratories, in order to reduce at minimum the rate of incoming cosmic rays. The remaining background originates from natural radioactivity of the environment and any radio-impurities in the detector shielding or in the detector active volume itself. Finally, the detection techniques have to be able to discriminate between a WIMP recoil and suppress any other signal from neutron or electron recoil. Experimental efforts are made to lower the detection threshold to be sensitive to lighter WIMP signals and to increase the understanding of the background permeating the experimental setups.

Direct DM detection detectors mostly differ from each other on the techniques used to detect the recoil signal. The last generation of experiments typically combines two or more techniques to increase the energy resolution, the signal sensitivity and the background suppression. Among all the experiments, EDELWEISS [118], CDMS [119] and its follow up SuperCDMS[120] are good examples of the combination of heat and ionization readout, CRESST [121] of heat and scintillation readout, XENON [122] and LUX [123] of scintillation and ionization readout. The experimental detection techniques are many:

bolometers for phonon detection; semiconductors, scintillating crystals and bubble chambers to detect ionization; liquid noble gases used for pulse shape analysis of scintillating light. Different active materials are used to investigate a wide interaction modes of WIMPs. The search for an annual modulation in the detector response due to the time variation of the DM scattering rate induced by the motion of the Earth relative to the Sun, like in DAMA/LIBRA [124] or CoGeNT [125] experiments, is also a promising detection channel.

The direct DM experimental detection scenario is very dynamic and its interpretation is quite complicated. CDMS II Si [119] and DAMA/LIBRA [124] observed a WIMP signature not compatible with statistical background fluctuations in the detector, constraining the allowed values of M_χ and σ_{scat} for WIMP candidates. However, those allowed regions are highly disfavored by the exclusion limit set by other experiments which found no signal above the background, like EDELWEISS [118], XENON100 [122], CRESST-II [126] and LUX [123] (see Figure 1.21). Besides Ge detectors, SuperCDMS will also operate Si detectors at low and high voltages to investigate the region of interest claimed by CDMS II Si and to improve the Si results at lower WIMP masses.

A new generation of direct search experiments is already foreseen (as, for example, the EURECA [127], the XEXON1T [128] and the LZ (LUX-Zeplin) [129] projects). Taking advantage from the current experience and combining even more detection techniques in the same experiment, the sensitivity for the DM direct search will increase at least by an order of magnitude in the next 10 years. This will help to clarify the current tensions in the experimental result scenario and to eventually confirm the detection of DM. However, experiments sensitive to such low scattering cross sections would also be sensitive to the large flux of solar and atmospheric neutrinos, which will probably become the highest irreducible background for such experiments.

1.3.4.2 Collider searches (LHC)

DM particle pairs can be produced during high energy interactions in particle colliders. While early constraints have been already set by $e^+ - e^-$ collisions at LEP and $p - \bar{p}$ collisions at the Tevatron, the most stringent results have been recently produced using $p - p$ collisions at the Large Hadron Collider (LHC) [131]. The LHC at CERN is the largest accelerator ever built, able to reach the highest center-of-mass energy yield during collisions so far. The LHC interaction points are surrounded by four main experiments. Among them, ATLAS [132] and CMS [133] are two multi-purpose experiments developed to confirm the SM theory¹⁷ and to search for physics beyond the SM. In order to achieve the necessary performance to reach those tasks, such detectors have a forward-backward symmetric cylindrical geometry with a nearly “hermetic” 4π solid angle coverage. The design goals of the accelerating machine are to collide proton beams with a center-of-mass energy of 14 TeV at a luminosity of $10^{34} \text{ cm}^{-2}\text{s}^{-1}$. The machine was operated at 7 TeV and 8 TeV center-of-mass energy. This allowed the CMS and ATLAS experiments to collect, so far, a total integrated luminosity of 5 fb^{-1} (7 TeV) and 20 fb^{-1} (8 TeV) each.

Stable, chargeless and weakly interacting DM particles produced in pairs during $p - p$ collisions escape detection. A fundamental signature of possible DM pair production is therefore the detection of missing energy in the transverse direction (E_T^{miss}) in the collision event. The hermetic properties of such detectors are therefore critical for DM searches.

Several final states are investigated to search for DM at LHC. DM particle pair production can be assumed in a framework where their interactions with SM particles happens through a contact interaction (mediated by a heavy new particle). For this effective theory approach, the detected observables (like the p_T distributions) can be easily related to DM particle properties, like the scattering cross sections. The

¹⁷The typical signature expected from the Higgs boson particle has been observed in the data analyzed by the ATLAS and CMS collaboration. The results, published in 2012, finally completed the observation of all the particles predicted in the framework of the Standard Model [3, 4].

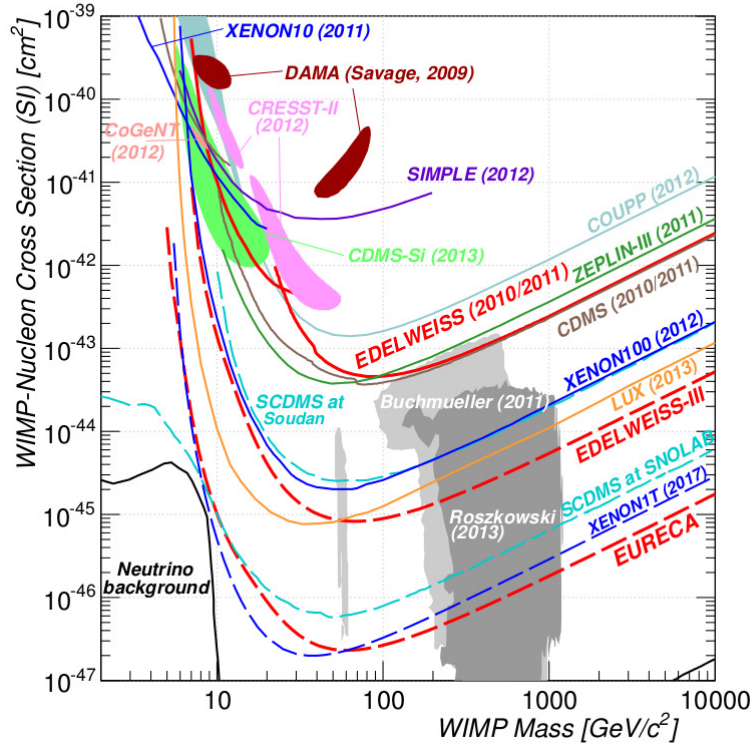


Figure 1.21: 90% confidence interval limit on the spin-independent WIMP-nucleon scattering cross section as function of the WIMP mass. The colored filled areas represent the allowed parameter region for experiments that measured a signal for which a WIMP signature is favored over background fluctuations in the detector. The continuous lines represent the exclusion limit for experiments whose result is compatible with background only signatures. The tension between the experimental results is clear. The dashed lines represent the projection for next generation experiments, whose sensitivity will increase at least by an order of magnitude in the whole WIMP mass region. The gray regions highlight the expected phase-space populated by a selection of theoretical models [130].

results from collider searches can be therefore consistently compared to results from direct and indirect search strategies. In such a framework, one of the most popular search channel is a final state involving one high p_T jet or a single photon, radiated by one initial state quark, and high E_T^{miss} . ATLAS and CMS detected no events above the background expectation in this channel and they set limits on the DM production cross sections [134, 135].

Another investigated channel is the DM production in the Higgs-portal DM mode. In this extension of the SM, the Higgs boson is the mediator between the SM particles and the Dark sector¹⁸. The most sensitive search looks for invisible decays of the Higgs boson in DM stable particles ($H \rightarrow \chi\chi$) in associated Higgs boson production with a Z boson. No evidence for signal has been found in any of the invisible Higgs boson decay searches by the ATLAS and CMS experiments [136, 137]. The limits on the Higgs invisible decay width can be reinterpreted in terms of constraints on the DM mass and on

¹⁸ The scenario in which the Higgs boson is the mediator between the SM and the DM sector could justify the limits on the nuclear interaction cross section set by direct DM search experiments (Figure 1.20 a). The limits are in fact many orders of magnitude smaller than the value of the DM annihilation cross section fixed by the relic density constraints (Figure 1.20 b). The small coupling of the Higgs boson to the light quarks of the proton can easily explain the difference in magnitude between the two cross sections.

the spin-independent DM-nucleon elastic cross section. Figure 1.22 shows the comparison of the limits inferred by this search with the direct search experimental results. This search provides stringent limits on low mass DM candidates up to half the Higgs boson mass.

Other DM search strategies assume a complete underlying theory and search for detected footprints from specific particles. Assuming a SUSY scenario, a typical example is a final state with significant E_T^{miss} and a high number of hadronic jets. This is a possible signature of the production of *squark* ($\tilde{q}\tilde{q}$) or *gluino* ($\tilde{g}\tilde{g}$) pairs which further decay in SM hadrons and $\tilde{\chi}_1^0$. Other searches look for final states with significant E_T^{miss} and a high lepton number, which can be the signature of supersymmetric Drell - Yan *slepton* ($\tilde{l}^+\tilde{l}^-$) production that decay to a final state neutralino through the chain $\tilde{q}\tilde{q} \rightarrow \tilde{l}^+\tilde{l}^- \rightarrow (\tilde{\chi}_1^0 l^+) + (\tilde{\chi}_1^0 l^-)$. In the search of SUSY particles through this and other channels the observations are so far consistent with the SM expectations [138, 139].

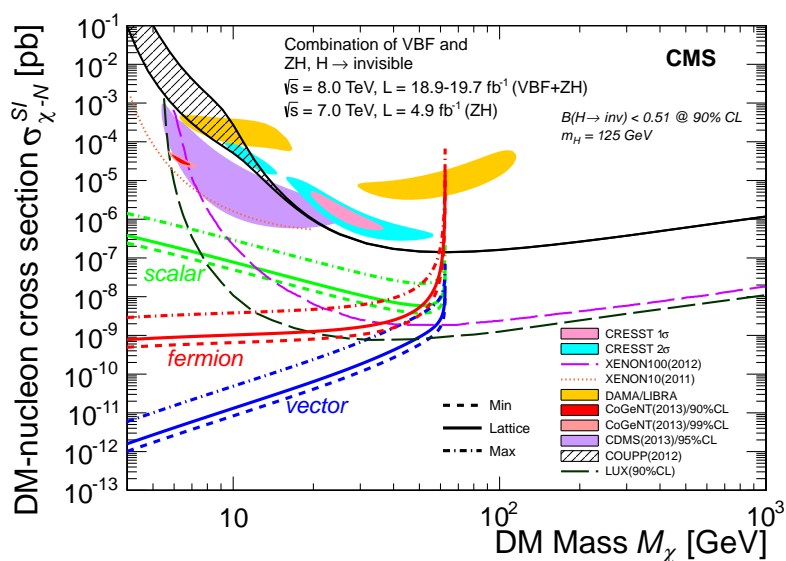


Figure 1.22: Upper limits for the spin independent DM-nucleon cross section as function of the DM candidate mass. The constraints are set by the analysis of invisible Higgs boson decays in Higgs boson production associated with a Z boson or in Vector Boson Fusion (VBF) processes by the CMS collaboration [136]. Similar results are obtained also by the ATLAS collaboration [137]. The limits on the invisible Higgs boson decay width have been reinterpreted in the context of a Higgs-portal model of DM interactions, in the assumptions of scalar, fermionic or vector DM. The solid line represent the value of the Higgs-nucleon coupling obtained from lattice calculations. The dashed lines represent the uncertainty introduced by the bounds on this parameter. The figure also shows the experimental results from direct DM search experiments. The Higgs-portal DM search is sensitive only to DM masses up to half the Higgs boson mass and provides complementary information at low energies, where the direct search experiment sensitivity decreases.

Although no signal of DM signature has been found in collider interactions, with all the channels compatible with just background expectations, the next run of the LHC in 2015 with a center of mass energy of 13 TeV could provide the expected conditions and data yield to finally observe the production of DM particles. If this will not be the case, the new data will, however, set more stringent constraints to the allowed DM theoretical models.

1.3.4.3 Indirect searches

DM signatures from WIMP-WIMP annihilation can be searched for through the observation of SM particle excesses in several observables of the cosmic radiation. WIMPs are expected to annihilate in

regions with large DM density and to consequently produce SM particle products. Of particular interest for indirect searches are γ -rays, neutrinos and rare CR antimatter particles like e^+ , \bar{p} and \bar{D} . These products are a minor component of cosmic rays because they are not produced abundantly during standard astrophysical processes like for protons, nuclei or electrons. Therefore, they are sensitive channels to search for indirect signatures of DM annihilation. Each of these channels exhibit different features related to its production mechanism and propagation. Indirect DM searches aim to detect the signatures of annihilation (or decay) of DM particles in the flux of the mentioned channels, in a region where the background from standard astrophysical processes does not dominate.

Gamma rays are the most studied channel for indirect DM searches: they can be produced with relatively high rates in DM annihilations and they carry directional information about the source. The expected differential flux of prompt γ rays¹⁹ from DM annihilation (or any neutral annihilation product) is given by the following formula [116]:

$$\frac{d\Phi_\gamma}{d\Omega dE} = \langle \sigma v \rangle \sum_f \frac{1}{4\pi M_\chi^2} b_f \mathcal{N}_\gamma^{(f)}(E) \int_{\text{l.o.s.}} \rho_\chi^2(r(s, \theta)) ds, \quad (1.21)$$

where $\langle \sigma v \rangle$ is the velocity-averaged WIMP annihilation cross section. The contribution is summed over all the possible production channels f with probability b_f and $\mathcal{N}_\gamma^{(f)}(E) = dN/dE$ is the differential spectrum of the photon products, per annihilation, in the channel f . The last integral is the integral along the line of sight (l.o.s.) of the squared DM density ρ_χ^2 which depends on the distance from the galactic center r . Since the flux of DM annihilation products is proportional to the square²⁰ of the DM density ρ_χ^2 , typical detector targets are regions with expected high concentration of DM. CR photons are a privileged channel for the indirect DM detection. Their unperturbed propagation through the ISM leads to distinctive spectral signatures and pointing capabilities [140]. In spectral searches, the energy spectrum of diffuse gamma rays is investigated for DM signatures. If DM annihilates directly in gamma pairs $\chi\chi \rightarrow \gamma\gamma$ ²¹ it produces monochromatic γ rays with a spectral feature well distinguishable from the astrophysical background (usually called “line”). Despite this channel is loop-suppressed and not dominant, the experimental sensitivity could be high enough for detection. The search for lines in the diffuse γ spectrum is therefore considered a smoking-gun for indirect evidence of DM annihilation. Recently, the claim of observation of a 130 GeV line in the Fermi-LAT galactic center γ spectrum [141] arose a wide interest in the community. The sensitivity of the signal, however, is decreasing as the analysis systematic uncertainties are more carefully investigated, disfavoring the interpretation of the line as a DM signature [142]. The search for lines in the γ spectrum remains however a priority channel, and next generation experiments – like the GAMMA-400 gamma ray satellite telescope [143] – will increase the sensitivity of the searches by several orders of magnitude.

Other recent studies confirmed a high significance excess in the diffuse γ spectrum from the inner few degrees around the Galactic Center, already spotted in the early Fermi-LAT data [144, 145]. The emission is usually explained in terms of ~ 30 GeV DM annihilating predominantly in $b\bar{b}$ pairs. Due to the strong and diverse astrophysical activity in the Galactic Center region, the analysis of the data has to cover many uncertainties and the conclusions are not straightforward. The result is indeed under deep investigation by the community. If it will be confirmed by further studies, this could be a strong

¹⁹The term “prompt” refers to γ rays produced directly during annihilation (or decay) of DM particles, to be distinguished from γ rays produced by e^\pm through synchrotron emission, bremsstrahlung or IC scattering processes.

²⁰In case of decaying DM hypothesis, whose possibility is addressed in Section 1.3.5, an equation similar to Equation 1.21 still holds. The main difference originates from the fact that the DM decay product flux is linearly, instead of quadratically, proportional to the DM density.

²¹DM annihilation in gamma rays is strongly suppressed because the fundamental process is allowed only via mediation by internal loops.

signature of $\sim 10 - 40$ GeV DM annihilation, where the low masses are allowed for DM annihilating preferentially into lepton pairs [146].

A graphical example extracted from the pioneering works that first hinted to the 130 GeV line and to the galactic center excess are shown in Figure 1.23

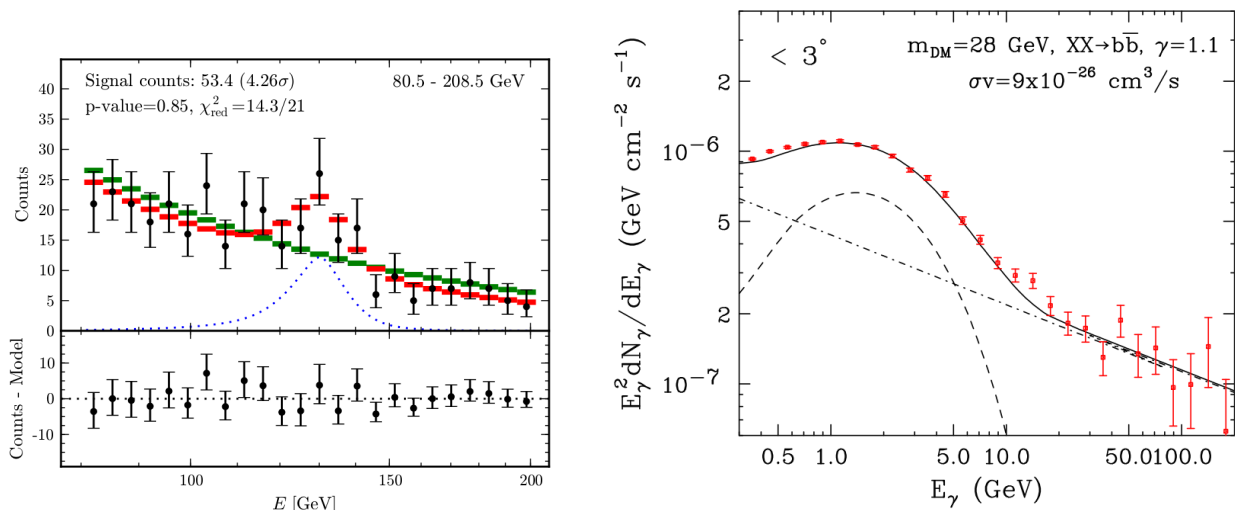


Figure 1.23: **Left:** γ ray spectrum measured by Fermi-LAT in a region with optimized signal sensitivity. The data points, in black, are fitted using a model with a ~ 130 GeV DM component (red) and without the DM contribution (green). The blue profile shows the contribution of the DM alone. In the bottom panel the residual distribution after subtraction of the model with DM contribution from the data is shown. More details are available in [141]. **Right:** γ ray spectrum measured by Fermi-LAT within 3° of the galactic center. The spectral shape is fit as a sum of diffuse emission (dashed-dotted line) and a contribution of a 28 GeV DM annihilation in $b\bar{b}$ (dashed line). The Figure is adapted from the pioneering work [144]. More updated details are addressed in [145].

The indirect search in the charge neutral cosmic ray channel is completed by searches on ground. The gamma ray H.E.S.S. telescope, as example, extends the Fermi-LAT satellite search at much higher energies but with lower sensitivity. No excess in the γ spectrum has been found by ground experiments in the search for DM annihilation lines so far [147].

The flux of neutrinos at Earth can also be used to search for indirect DM signatures in the cosmic radiation. The detection of high energy neutrinos from the Sun, as example, is considered a privileged channel for DM searches. Standard solar neutrinos are produced by nuclear fusion processes in the Sun with much lower energies, and there is no known astrophysical processes able to mimic the possible high energy neutrino DM signal. Limits has been set by the neutrino telescope IceCube that measured no significant excess beyond the background expectations both from neutrinos coming from DM annihilation in nearby galaxies [148] or from the center of the Sun [149].

Apart from γ rays and neutrinos, charged CRs may disclose evidence for indirect DM signatures. The data interpretation is, in this case, much more complicated due to the propagation through the galactic magnetic fields (as explained in Section 1.1) that drastically washes-out the DM spatial and spectral signature in the annihilation product fluxes. An useful property of the search for DM in the charged CRs is that, differently from the DM searches using γ s, the theoretical predictions do not depend drastically on the choice of the DM density distribution profile. All DM profiles used in indirect DM searches in the

γ channel are normalized at the local value $\rho_{\text{DM}} \sim 0.3 \text{ GeV}/\text{cm}^3$, and the extrapolation to the galactic center can differ by orders of magnitude for different profile hypotheses. For DM searches in charged CRs most of the observables, like high energy positrons, are much less affected by the choice of the profile parametrization since they have to be produced in the nearby environment [150].

The search for DM annihilation signatures in charged CRs has to face the observation that the latest \bar{p} data show no excess in the cosmic \bar{p} flux and in the more sensitive \bar{p}/p ratio compared to the predicted astrophysical background (see Figure 1.24). This sets strong constraints on the phenomenology of DM candidates [151]. For DM annihilating or decaying in hadronic channels, the constraints inferred from the \bar{p} data provide more compelling limits on the DM interpretation than from the γ ray measurements [152, 153]. The future measurement of the \bar{p} component from the AMS experiment will improve the limits by an order of magnitude if no DM signature will be discovered in this channel.

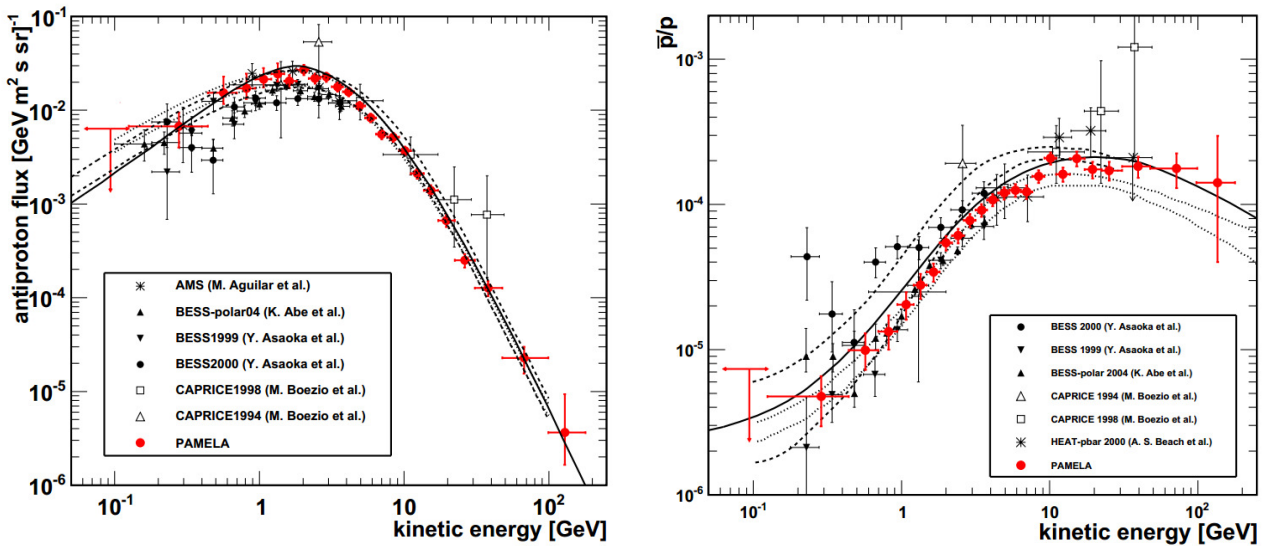


Figure 1.24: Collection of the latest measurements of the \bar{p} flux (**Left**) and its ratio to the proton component \bar{p}/p (**Right**). Several standard diffusion model expectations are superimposed to the data [154]. The \bar{p} measurements do not show any deviation from the predicted astrophysical background. This sets stringent constraints on DM annihilation models.

Among charged cosmic rays, antideuterons (\bar{D}) are a promising tool for the search of DM [155, 156]. \bar{D} can be produced during DM annihilation by the formation of a bound system of a \bar{p} and a \bar{n} . The production mechanism kinematics favors the energy region well below the GeV range, where the astrophysical \bar{D} background is expected to be not significant. Due to kinematic constraints, in fact, the astrophysical production of \bar{D} through the interaction of the ISM is allowed only for high energy protons, whose power-law flux is suppressed at high energies. On the other hand, the spectrum of \bar{n} and \bar{p} produced by the annihilation of relatively light DM particle ($< 100 \text{ GeV}$) peaks at low energies and it favors the production of low energetic \bar{D} . The production of \bar{D} by DM processes is however very suppressed, and no evidence of \bar{D} has been found in the cosmic radiation yet. Only one upper limit has been set by the BESS experiment [157]. The detection of low energy \bar{D} in the cosmic radiation would be a strong indirect proof of DM production, but it is experimentally very challenging. The AMS experiment will look for \bar{D} in the cosmic radiation using standard spectrometer techniques. The GAPS balloon instrument, instead, will employ a novel technique to capture \bar{D} inside the detector, form an exotic atom and detect it through the characteristic signature in the emitted X-ray and pion radiation [72].

In addition but similarly as the \bar{D} channel, the flux of heavier antinuclei like $\overline{{}^3\text{He}}$ produced from DM annihilation is expected to have an even more favorable ratio of DM production to astrophysical production at energies below ~ 5 GeV/n. The expected flux is however low and not compatible with the current experimental sensitivity of space experiments, like AMS, in the majority of scenarios [158, 159].

The most impressive hint for an indirect DM signature observed today in the charged channel is represented by the features in the cosmic e^\pm spectra. This will be discussed in the dedicated next section.

1.3.5 Indirect Dark Matter search in the cosmic electron and positron fluxes

As already discussed in Section 1.2, the current experimental measurements of the cosmic e^+ and e^- components are not compatible with the standard scenario of primary production of e^- in astrophysical sources and a purely secondary production of e^+ (and, in smaller yield, of e^-) from interactions of hadrons with the ISM. The e^+ flux and the positron fraction (PF) measurements, shown in Figure 1.12, hint to the presence of an additional component which dominates the e^+ flux starting at ~ 35 GeV. Although the PF rise can be explained in terms of primary production in unaccounted astrophysical sources, like PWNs, it may also contain signatures of DM activity in the Galaxy.

DM particle annihilation into pairs of SM particles – like lepton pairs as $\tau^+\tau^-$, quark pairs as $b\bar{b}$ or boson pairs like W^+W^- and so on – can produce a flux of energetic, lighter CRs – like e^+e^- pairs – by decaying or showering processes. The spectra of the e^\pm products depend on the primary SM particle from which they originate, and are modified by the propagation in the galactic environment. Typically the spectra are characterized by a sharp kinematic cutoff above the DM mass and decreasing tails at lower energies. A graphical example of the dependence of the PF spectral shape on the DM candidate mass and on the DM annihilation channel is shown in Figure 1.25.

The candidate DM must fulfill strong criteria to describe the measurements [150]:

- The DM candidate mass is constrained to be of the order of few TeVs to reproduce the features in the PF and in the e^\pm fluxes.
- The DM candidate has to be *leptophilic*: it must decay almost exclusively in leptonic channels. The strong limits imposed by the \bar{p} measurements constrain indeed the DM annihilation in hadronic channels.
- The DM annihilation cross section $\langle\sigma v\rangle$ has to be much larger than the thermal expectation value, of the order of $10^{-23}\text{cm}^3/\text{s}$ or more. A boost factor B to the thermal cross section of the order of $\sim 10^3$ and more is needed to produce enough e^\pm pairs from DM annihilation which could explain the abundant rise in the PF and the $(e^+ + e^-)$ and e^+ flux features (see Figure 1.26).

A number of possible explanations have been proposed to conceive the WIMP paradigm with the need of a boost factor B to the thermal annihilation cross section. The e^\pm yield from DM annihilation can be boosted with no fine tuning of the cross section itself by the presence of a local DM over-density in the galactic halo. Localized DM clumps are allowed by numerical simulations, but the achieved B factor is however not larger than ~ 10 [161]. Fundamental physics explanations invoke models in which the DM annihilates into SM particles X through an intermediate state ϕ as $\chi\chi \rightarrow \phi\phi \rightarrow 2X^+2X^-$, also known as eXciting Dark Matter XDM scenario [162]. If suitable conditions on the ϕ mass and resonance width are met, the boost factor B could reach values up to the target $\sim 10^3$. Another possibility is to exploit the Sommerfeld effect [163] in the Dark Matter sector. The annihilation cross section can be enhanced in presence of a long range interaction when the relative velocity between the annihilating particles is small. If the annihilation is mediated through a \sim GeV light new force carrier, strongly

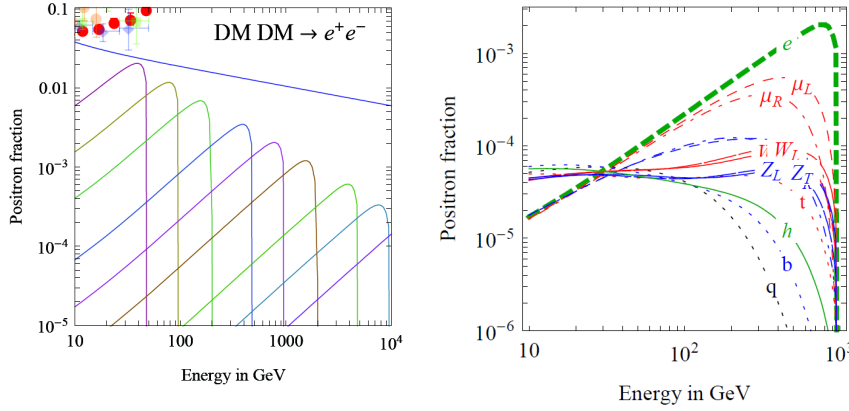


Figure 1.25: **Left:** Expected contribution to the positron fraction from DM annihilation into e^-e^+ pair as function of the DM mass. The PF measurement is shown for various experiments by the points in the top left corner, which are out of scale at higher energies with respect to the theoretical predictions. No boost factor to the e^\pm production has been applied here. The sharp cutoff at the DM mass is induced by the kinematic constraints of the interaction. The upper line shows the astrophysical background contribution. The positron fraction data cannot be explained by a plain DM contribution: an enhancement of the e^\pm yield from DM annihilation is needed as described in the text. **Right:** Comparison of the positron fraction contribution from 1 TeV mass DM annihilating in different channels. Annihilation in e^-e^+ pairs produce a sharp decrease at the DM mass with tails at low energies due to galactic propagation and energy loss effects. Annihilation in other leptons or in W,Z bosons also shows a cutoff at the DM mass. The hadronic or hh channels show a smooth spectrum with high contribution at very low masses instead. Figures are adapted from [160].

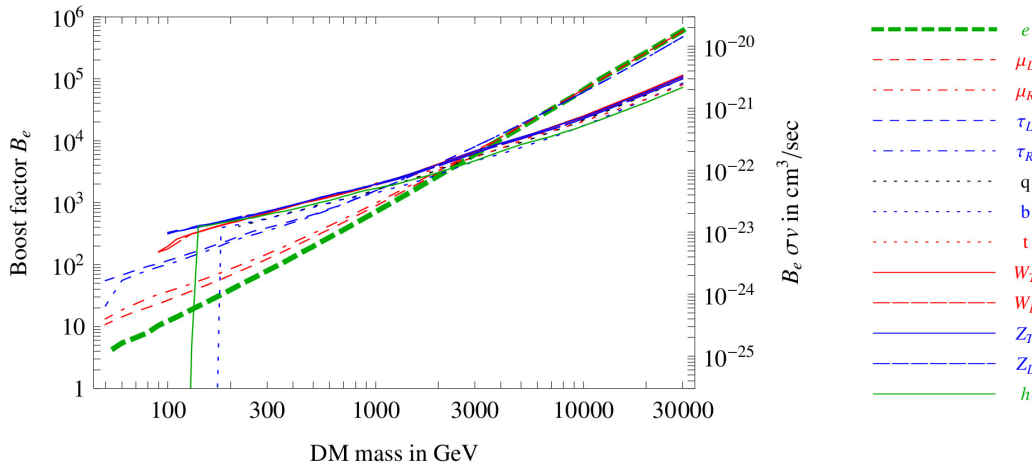


Figure 1.26: Value of the boost factor B applied to the DM annihilation cross section used to reproduce the e^+ abundance to explain the positron fraction rise [160]. For DM masses of \sim TeV energies, the required boost factor is of the order of $\sim 10^2 - 10^3$ for all the decay channels.

coupled with DM particles, the Sommerfeld effect could provide the necessary boost factor B to explain the data [164].

An example of a fit to the positron fraction in the XDM scenario is provided in Figure 1.27.

The outlined phenomenology severely limits in any case the possibility to adopt the traditional LSP *Neutralino*, whose properties have been described in Section 1.3.3.1, as DM candidate. The SUSY

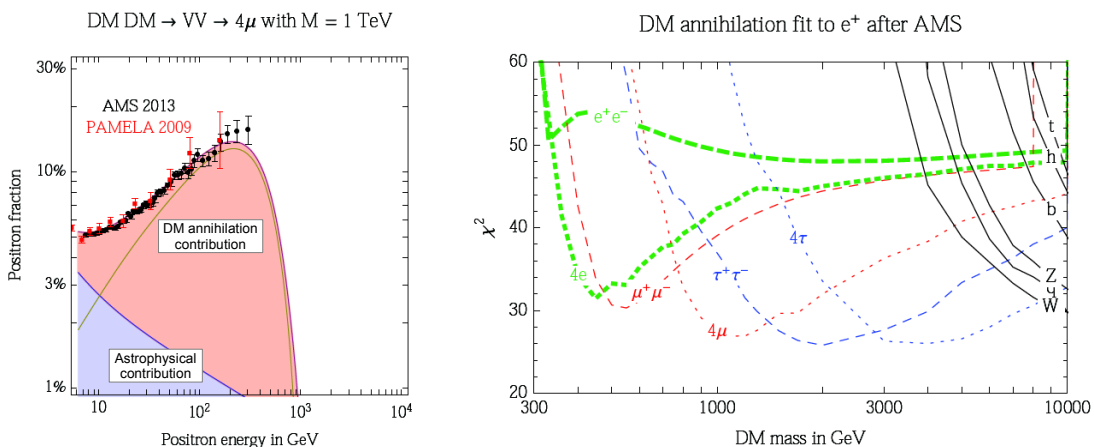


Figure 1.27: **Left:** PAMELA and AMS positron fraction data are fit as sum of the astrophysical background contribution (blue) and a DM contribution (green line). A XDM scenario in which the 1 TeV DM particles annihilate in an intermediate state VV to finally produce 4μ is assumed [165]. **Right:** χ^2 of the fit to the positron fraction as function of the DM mass and annihilation channel. The best fit, in this case, is given by 2 TeV DM annihilating in τ^\pm pairs (with a necessary boosting to the annihilation cross section) or by 1(4) TeV DM annihilating in $4\mu^\pm(\tau^\pm)$. In the last case, the boosting factor is provided by the annihilation into an intermediate, not SM, vector state VV .

Neutralino annihilation does not distinguish in fact between leptonic and hadronic annihilation channels. Moreover, its mass is expected to be smaller than the TeV scale and the annihilation in light final states is kinematically suppressed.

Alternative DM candidates can be provided by comprehensive and self-consistent theory frameworks. The Universal Extra Dimensions (UED) theory predicts the existence of a stable particle, the Lightest Kaluza-Klein Particle (LKP), which meets all the requirements to be a DM candidate. Other scenarios, grouped in the Minimal Dark Matter (MDM) models, try to add a minimal set of additional particles to the SM dedicated to explain selected measurements [116]. All such approaches require, however, a boost factor to the annihilation cross section. Most of the community efforts have been therefore lately dedicated to provide and justify physics processes that could enhance the cross section as explained before.

On the other hand, the e^\pm channel has been also studied to set stringent constraints on the low DM mass annihilation cross section. As shown in Figure 1.28, the absence of any spectral feature in the low and medium energies of the positron fraction has been used to derive limits on the DM annihilation cross section, which are much more stringent than the constraints provided by the indirect searches using γ measurements.

Recently, the independent possibility that DM consists of particles with large decay time ($> 10^{26}$ s) has been investigated [167]. Decaying DM hypotheses typically fit the data better than annihilating DM, if hadronic decay channels are suppressed. Moreover, since the e^\pm production from decaying DM is linearly proportional to the local density of DM and not quadratically proportional as for annihilating scenarios, tensions with constraints from other DM searches like gamma rays or neutrino are less stringent.

For all the DM scenarios used to explain the e^\pm spectral features no preferred arrival direction of e^+ and e^- at Earth is expected. Differently from primary e^\pm accelerated by PWNs, e^\pm produced by DM annihilation or decay do not originate from localized sources. The anisotropy in the arrival direction at Earth of primary e^\pm expected by the spatial gradient in the annihilating DM density is much smaller

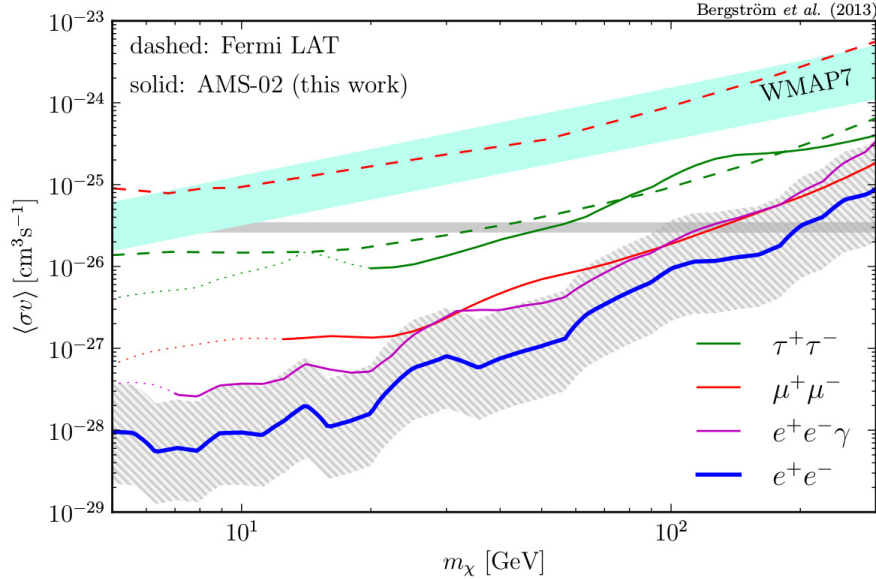


Figure 1.28: 95% CL upper limits on the DM annihilation cross section for various final states derived from the AMS positron fraction measurement under the hypothesis of no DM signature in the positron fraction spectral shape [166]. The gray horizontal band indicates the thermal annihilation cross section. The hatched band (shown for the e^+e^- channel only) represents the error induced by the propagation models and the local DM density uncertainties. The limits set with this method on DM models are stronger than those derived by the observations of the CMB and by γ ray measurements. Light DM candidates annihilating in light leptons with an annihilation cross section typical of a thermal WIMP are excluded by these observations.

than the anisotropy expected for standard e^\pm due to the spatial distribution of SNRs and of other standard astrophysical sources. The detection of an anisotropy in the arrival directions at Earth of e^+ and e^- would completely disfavor a dominating DM origin of such species, while it would still allow the explanation of the positron excess from primary production of e^\pm pairs in astrophysical sources [168]. No anisotropy has been detected in the e^\pm channels so far. The latest results on the upper limits of the anisotropy of cosmic e^\pm arrival direction in the ~ 100 GeV energy range (and below) set by the AMS [83] and Fermi-LAT [91] experiments are used to constrain the astrophysical primary production of e^\pm , but are not sensitive enough to detect the level of anisotropy expected by typical PWN production scenarios (shown in Figure 1.15). In the next years, the size of the dataset collected by the AMS experiment will provide more insights and possibly definitively rule out the possibility to explain the positron excess by a predominant DM production.

1.3.6 Conclusions

The cosmic ray physics scenario presented in this chapter is very intriguing. The analysis of the cosmic radiation discloses many possibilities to investigate astrophysics and fundamental physics processes at all scales. In particular, the puzzle introduced by the hints of DM signatures in the cosmic radiation has attracted a lot of interest in the last decades. Although it has not been directly detected yet, several gravitational indirect observations prove that Dark Matter does exist. Since the first hints of its existence, the experimental effort faced to improve the accuracy of the measurements dedicated to DM detection has been diverse and dynamical.

The analysis of the e^- and e^+ cosmic ray fluxes represents one of the most investigated channels in this field. The features spotted in the positron flux by early experiments and confirmed by the AMS

measurement lead to many discussions in the community. The excess in the positron fraction, if interpreted in terms of DM annihilation, could point to the existence of a TeV, leptophilic self-annihilating or decaying DM component. The annihilation cross section constrained by the measurement is orders of magnitude above the expected value for the standard thermal relic WIMP candidate, but several model extensions and dynamic mechanisms can allow the boost needed to justify the data.

On the other hand, the explanation of the rise in the positron flux as consequence of a primary astrophysical component, starting to dominate above ~ 30 GeV on top of the secondary e^+ contribution, seems favored by the data. Standard astrophysical models fit the data without any need to introduce new physics processes. If this hypothesis will be confirmed in future, the primary astrophysical e^+ production will be one of the most dominating background for the indirect search for DM in charged cosmic rays.

The increase of the accuracy in the e^\pm data will help to improve the sensitivity to distinguish between the two hypotheses. The AMS detector is the leading experiment in the field.

The evidence that would almost completely rule out the DM hypothesis as exclusive contribution to the excess would be the detection of an anisotropy in the arrival direction of the e^\pm fluxes above the expected level of background anisotropy. This would indicate a located source origin, totally incompatible with the diffuse DM annihilation or decay.

The analysis of the $(e^+ + e^-)$ flux up to 1 TeV with the AMS experiment, which is the result of this thesis, is presented. Differently from the separate flux analysis, the $(e^+ + e^-)$ flux measurement is characterized by lower systematic uncertainties and by larger data samples. This allows to achieve a higher energy range and to increase the measurement accuracy in the whole energy range.

The large amounts of cosmic rays already collected by the AMS experiment and the accuracy of its measurements allow to coherently measure for the first time the $(e^+ + e^-)$ flux in the whole energy range from 0.5 GeV to 1 TeV. This last energy corresponds to the maximum energy achieved so far by space spectrometer experiments and it overlaps with the minimum e^\pm energy measured from ground based detectors.

The increase of accuracy in the $(e^+ + e^-)$ measurement allows to definitively disprove the observation of an excess of e^\pm above 300 GeV claimed first by PPB-BETS and then by ATIC experiments. Moreover, no prominent features are observed in the $(e^+ + e^-)$ flux. This constrains the presence of additional propagation mechanisms or CR sources in the 100 GeV - 1 TeV energy range. Finally, as all the other high precision measurements of AMS, it effectively improves the limits on propagation parameters in the Galaxy and it therefore decreases the systematic uncertainties induced in the phenomenological analyses.

Chapter 2

The AMS-02 detector

The Alpha Magnetic Spectrometer (AMS) [169] is a cosmic ray detector which has been installed on the International Space Station (ISS) in May 2011 during the STS-134 NASA Endeavour Space Shuttle mission, where it will collect cosmic rays until the end of the ISS mission, currently set to 2024. AMS-02 is an improved version of the AMS-01 magnetic spectrometer, which flew on the Shuttle Discovery (STS-91 NASA mission) in June 1998¹.

AMS has been designed and assembled taking advantage from the experience gathered in high energy particle physics experiments. Its core is composed of a permanent magnet generating a field of about ~ 0.14 T within a cylindrically shaped volume (diameter and height $\cong 1$ m). Seven planes of silicon detectors inside this volume and two planes outside the field volume measure the coordinate of the points used to reconstruct the tracks of the charged particles. The magnetic spectrometer is able to measure rigidities from fractions of GV to few TV. Two segmented scintillator planes (TOF) are placed at both ends of the magnet. They measure the time of flight of the particle through the planes and provide part of the trigger of the experiment. An anti-coincidence scintillator system (ACC) provides the veto signal in the trigger for particles crossing the detector outside its field of view. The AMS detector particle identification capabilities are completed by three sub-detectors: the Ring Imaging Cherenkov (RICH) detector, below the magnet, for the measurement of the particle velocity and charge; the Transition Radiation Detector (TRD), placed on top, to identify e^\pm and the Electromagnetic Calorimeter (ECAL), at the bottom, for the accurate discrimination between leptons and hadrons and energy measurement.

The main goal of the AMS experiment is the search for antimatter of primordial origin. Since the probability of detection of $\overline{\text{He}}$ produced by spallation of primary CRs with the interstellar medium (ISM) is below the AMS detection sensitivity, the detection of anti-nuclei in the cosmic radiation would be a direct proof of the existence of antimatter domains in which anti-nuclei could be produced.

Another relevant goal for AMS concerns the indirect Dark Matter detection. Its large acceptance, long exposure time and excellent particle identification capabilities allow to measure the spectra of the cosmic radiation rare components (\bar{p} , \bar{D} , e^\pm , γ) with great accuracy over an energy range never explored before.

The large amount of data collected by AMS for all the charged CR species, including chemical species up to iron and isotopes up to carbon, will improve the knowledge of the galactic space environment and will help to solve several fundamental questions concerning CR propagation. The measurements of low energy CR fluxes during an entire 11 years solar cycle will help in the understanding of solar physics

¹In this work, the term AMS will be used to refer to the AMS-02 instrument.

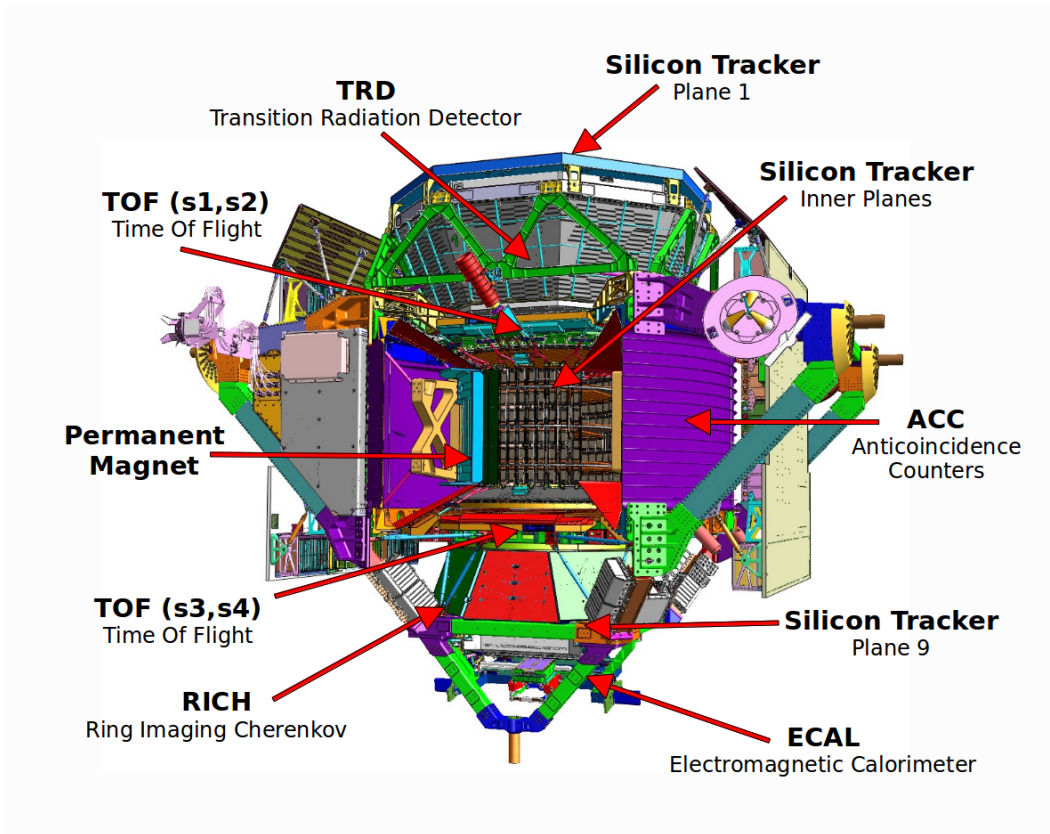


Figure 2.1: Cutaway view of AMS, with main subdetectors labelled [169].

and in the propagation of CRs in the Heliosphere environment.

The AMS detector also has γ -ray astronomy capabilities. AMS detects γ rays by the measurement of track pairs produced in a pair conversion ($\gamma \rightarrow e^+ e^-$) in the Tracker material, or by an electromagnetic shower initiated in the electromagnetic calorimeter (in this case the ECAL is used as a stand-alone detector).

The requirements for a space-borne high energy physics experiment are extremely challenging. Several constraints are imposed by the transport on the Space Shuttle and by the transfer and the permanence on the ISS, as the strict weight limit of 7 t, the very low power consumption (≤ 2 kW) and the limited data rate transfer to ground. In addition, the AMS experiment must work properly in space without any external operation for the whole mission and it has to withstand vibrations up to 150 dB during shuttle launch and temperature cyclic variations between -30 °C and $+50$ °C in space vacuum. Each sub-system and electronic component is produced in prototypes (engineering, qualification and flight models) tested in order to provide the expected physic performances and to meet the mandatory space safety requirements.

2.1 Transition Radiation Detector TRD

Particles traversing the interface between two different materials have a probability to emit Transition Radiation (TR) X-rays with probability proportional to their Lorentz gamma factor $\gamma = E/m$, where E is the energy and m the mass of the particle [170, 171, 172]. The detection of TR X-rays can therefore

in general be used to detect highly relativistic particles.

The AMS Transition Radiation Detector (TRD) [173, 174] is used to discriminate between e^\pm and protons up to the TeV energy range. The TRD, placed on top of the magnet case and under the first Tracker silicon plane, has an octagonal 80 cm height pyramidal structure, with diameters on the top and bottom layer measuring respectively 220 cm and 150 cm (see Figure 2.2).

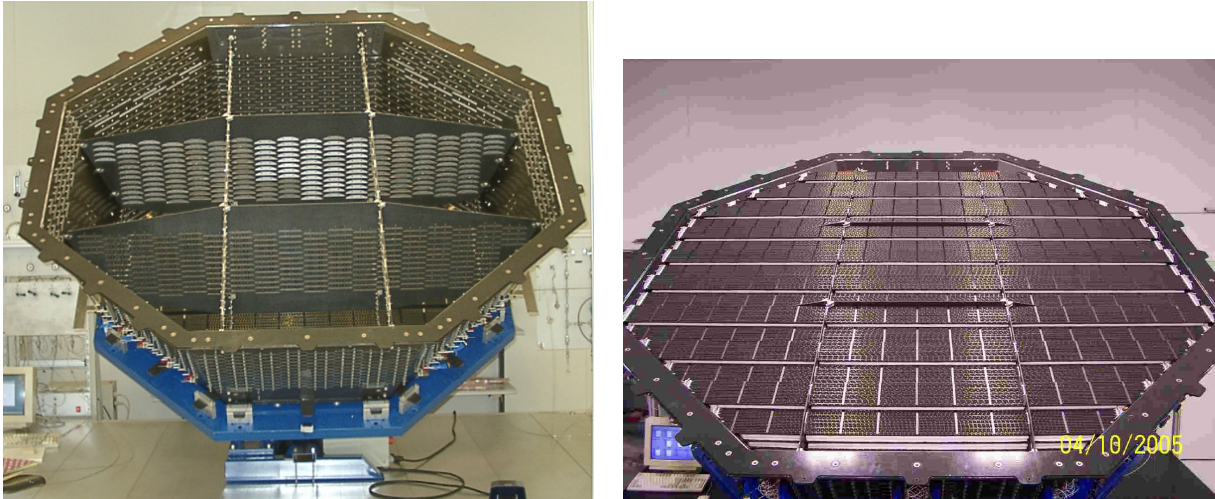


Figure 2.2: **Left:** TRD structure skeleton, made of aluminum honeycomb walls and carbon fiber skins and bulkheads. The octagonal pyramid shape has been chosen to optimize the TRD acceptance keeping the weight and size at a minimum. **Right:** TRD top layer, with modules installed.

The basic mechanical unit of the TRD is named module. Each module contains:

- **Radiator:** 22 mm thick polypropylene/polyethylene fiber fleece radiators, corresponding to a density of 0.06 g/cm^3 . A large number of interfaces increases the probability of TR X-rays production (up to 50% for 5 GeV electrons);
- **Proportional chamber:** 6 mm straw tubes filled with a Xe:CO₂ ($\sim 90\%:10\%$) gas mixture operating in full-avalanche mode ($\sim 1500\text{V}$). The wall of the straw tubes, made of $72 \mu\text{m}$ thick double-layered kapton-aluminum foil, works as cathode. A $30 \mu\text{m}$ thick fine gold plated wire in the center of the tube works as anode for the proportional chamber.

The TRD is made up of 328 modules (see Figure 2.3) arranged in 20 layers, for a total of 5248 straw tubes. The 12 central layers are oriented parallel to the AMS magnetic field axis, while the rest top and bottom layers are oriented perpendicular to it, providing 3D tracking capabilities to the detector.

Highly relativistic particles crossing the TRD may produce Transition radiation X-rays in the radiators. Such photons are efficiently absorbed and detected in the proportional chambers using Xe as absorber. The CO₂ works as quencher for charge multiplication. The combined measurement of the energy deposit in the 20 layers allows the TRD to discriminate e^\pm from hadrons up to 1 TV, making it a fundamental tool for e^\pm analyses. The electron/proton separation capabilities of the TRD are summarized in Figure 2.4.

The energy deposit in each tube is read out and digitalized by a 12-bit ADC converter. The dynamic range of the read out has been set to resolve the low energy deposits for ionizing protons and to consequently maximize the electron/proton separation. The measurement of the direct ionization from nuclei $dE/dx \propto Z^2$ is used to infer the charge of the crossing particle up to carbon ($Z = 6$). Above this

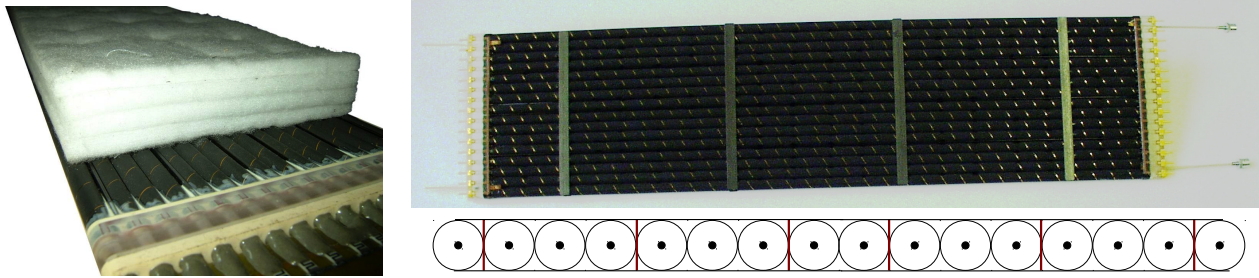


Figure 2.3: **Left:** TRD module prototype with polypropylene/polyethylene fiber fleece radiator layers on top. **Right:** 40 cm TRD space qualification module with 16 proportional chambers. Carbon fiber stiffeners are placed lengthwise every 10 cm and widthwise (see scheme below) to ensure straw stabilization [175].

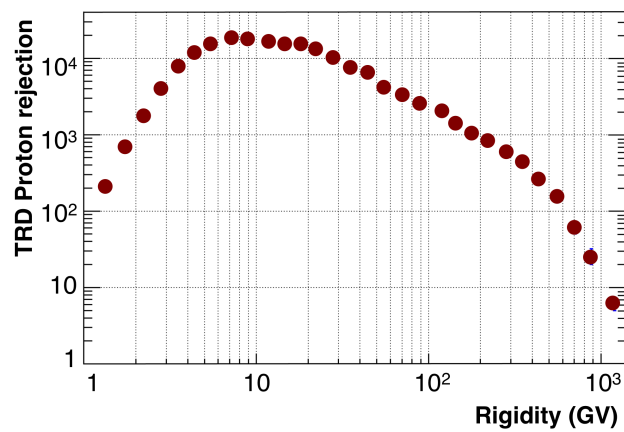


Figure 2.4: Electron/proton rejection measured with data collected by AMS. The e^\pm/p separation is achieved by combining the measurements of the energy deposit in the 20 layers of the TRD detector [176]. The efficiency of the selection on e^\pm is 90%. The proton rejection is well above 10^3 up to 200 GV. At ~ 400 GV, protons start to produce transition radiation and the TRD rejection capabilities drastically decrease.

charge, the ADC saturates. Nevertheless, techniques based on δ -rays detection can be used to extend the identification up to iron ($Z=26$) [177]. More details about TRD discrimination techniques will be covered in Section 4.2.2.

In the vacuum of space, gas continuously diffuses out of the straw tubes. Since CO_2 molecules are smaller than Xe molecules, they are the component leaking the most, with a total measured average leak rate of 4.5 mbar/day. In order to operate the detector at stable parameters, the TRD is coupled to a gas supplier system (see Figure 2.5).

At the time of the launch, the TRD gas system was equipped with 49 kg Xe and 5 kg CO_2 ². It is composed of the two supply boxes, a mixing vessel and a circulation box. This latter is responsible to transfer the freshly mixed gas to the gas network system with the help of a pump. The complete proportional chamber gas volume amounts to 230 L. The TRD modules are connected in series in groups of 8 to form a gas circuit. The gas is circulated in a total of 41 gas circuits.

After the first commissioning phase, monthly gas refills have been regularly performed since the start

²Such a gas supply will guarantee ~ 30 years lifetime, assuming steady operation in space.

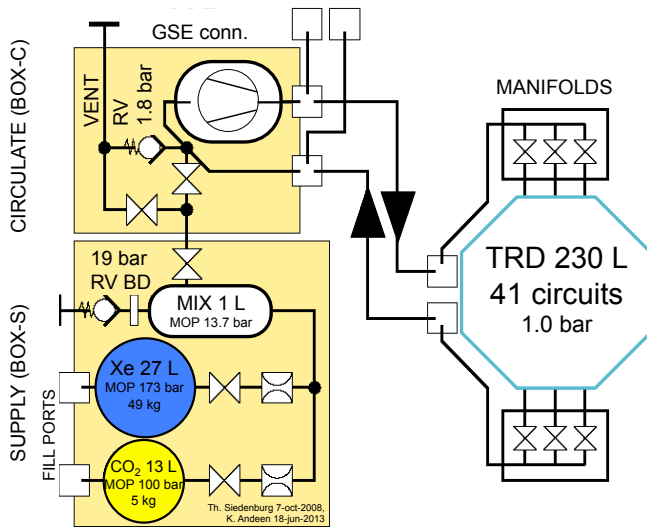


Figure 2.5: TRD gas system schematic. The gas in the supply boxes is first mixed (BOX-S). A pump (BOX-C) helps the circulation of the gas through 41 gas circuits, feeding the whole TRD detection volume. Each gas circuit is composed of eight straw tubes connected in series. Ten separate manifolds with a shut-off valve control a variable number of gas circuits. Single gas groups can be isolated in case of a gas leak in a tube [175].

of the data acquisition in order to maintain an optimal gas composition for the detector performances. Moreover, daily HV adjustment are applied to correct the straw tubes gas gain change due to the continuously changing gas composition [175].

2.2 Time Of Flight TOF

The AMS Time Of Flight (TOF) system [178, 179] consists of a total of four layers of scintillator counters, placed in pairs above (Upper-TOF) and below (Lower-TOF) the magnet. The TOF measures the particle velocity (βc), flight direction and charge, and it provides the main trigger to the whole experiment (see Section 2.8).

The four TOF layers are composed (from top to bottom) of 8, 8, 10, 8 paddles. The counters are made of 1 cm thick polyvinyl-toluene scintillators in two shapes: rectangular shape for the inner counters (width ~ 12 cm) and trapezoidal for the external counters (width 18 to 26 cm), all having a length between 117 and 134 cm. In each pair of layers, paddles are oriented respectively in both x and y directions, in order to provide a two-dimensional measurement with a 12×12 cm² resolution (see Figure 2.6). The scintillation light is collected from both sides of each counter using 2 or 3 photomultiplier tubes (PMT). In order to reduce the effect of the fringing magnetic field on the light collection efficiency, special PMTs operating at high voltage and with compact dynode structure (*fine-mesh* PMT) have been adopted. Also, the angle between the PMTs and the light guides with respect to the external magnetic field has been fixed in order to further reduce such effects. In total 144 PMTs collect the light from 34 TOF paddles.

The anode signal is read out from PMTs and compared to the three different thresholds: *Low Threshold* (LT, $\sim 20\%$ of a proton MIP signal), *High Threshold* (HT, $\sim 50\%$ of a proton MIP signal) and *Super-High Threshold* (SHT, $\sim 400\%$ of a proton MIP signal). HT and SHT signals are used by the Level-1 trigger logic (see Section 2.8) to trigger $Z \geq 1$ particles (“Single charge” trigger) and $Z > 1$ particles (“Normal-Slow ions” trigger). The LT TDC (Time to Digital Conversion) signal is used for timing measurement. The particle velocity $\beta = \Delta s/c\Delta t$ is measured using the time of flight Δt between Upper-Tof and Lower-Tof and the trajectory length Δs . The timing resolution of TOF is ~ 48 ps for C nuclei. The resulting TOF velocity resolution $\Delta\beta/\beta$ has been measured using data collected in space to be $\sim 4\%$ for $Z = 1$ particles and decreasing up to $\sim 1\%$ for $Z \geq 4$ (see Figure 2.7). This precise velocity measurement allows to distinguish downward-going particles from upward-going particle (fundamental

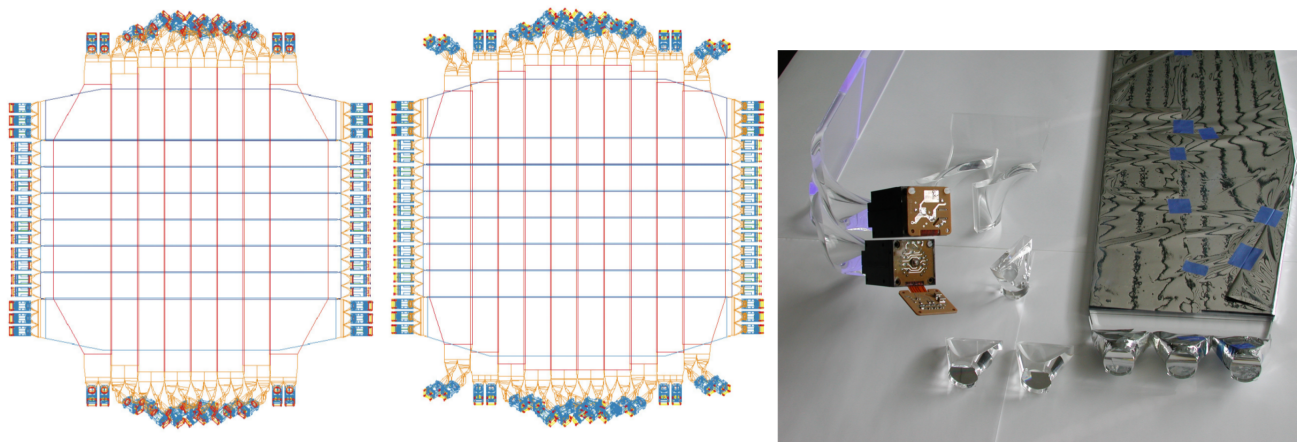


Figure 2.6: **Left:** AMS TOF planes configuration for Upper-TOF (left) and Lower-TOF (right). For each pair, paddles are arranged along opposite direction to ensure 2-dimensional measurements. In each layer, the paddles overlap by ~ 0.5 cm to increase the detector efficiency. **Right:** TOF scintillating counter, light guides and PMTs [180].

for anti matter searches) at a level better than 10^{-9} .

The anode ADC signal is used to measure the particle energy deposit ($dE/dx \propto Z^2$) and consequently to infer the particle charge Z . The anode is used to measure charges up to $Z = 4$. Above this charge, the anode starts to saturate and the dynamic range is increased using the PMT dynode signal to measure charges up to Zn ($Z = 30$).

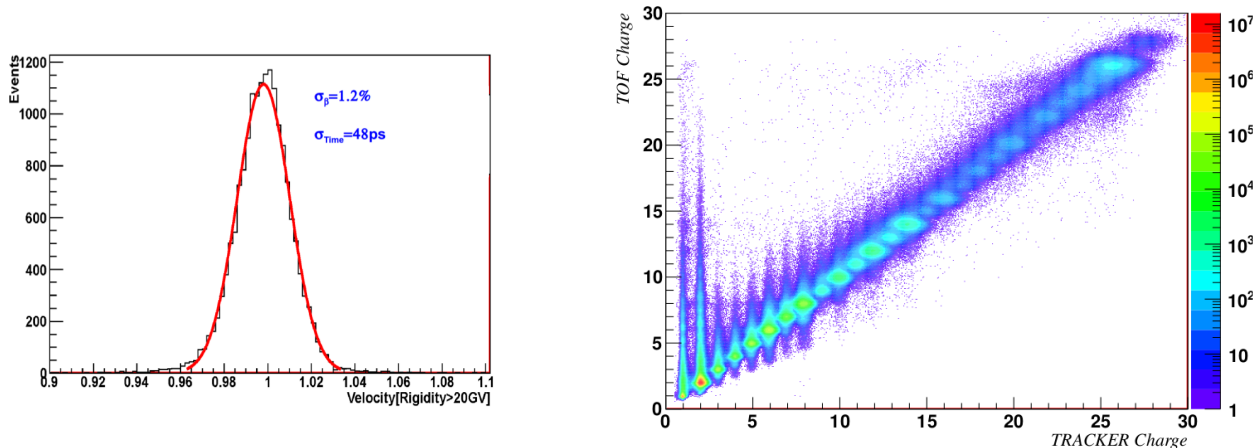


Figure 2.7: **Left:** AMS TOF velocity measurement resolution for carbon ($Z = 6$) [180]. **Right:** Distribution of TOF and Silicon Tracker charge estimators measured using cosmic particles up to Zn ($Z = 30$). The z scale represents the numbers of collected events. The redundancy of the AMS detector, here appreciable in the multiple measurement of the charge by two independent subdetectors, allows to reduce systematic uncertainties in the charge separation capabilities increasing the accuracy of the measurement to unprecedented level [181].

2.3 AntiCoincidence Counter ACC

The Anti-Coincidence Counter (ACC) [182, 183] is composed of 16 paddles with dimensions $220 \times 830 \times 8$ mm³ arranged on a cylinder surrounding the inner Tracker. The light coming from the scintillation panels

is collected in wavelength shifter fibers of 1 mm diameter and then routed through clear fibers up to the 16 PMTs (8 on the top and 8 on the bottom side) similar to the TOF ones. The high efficiency and high degree of homogeneity of the scintillating fibers will ensure a reliable and fast ACC veto trigger signal for high inclination particles that cross the detector outside its field of view. The signal from the ACC paddles is indeed used in the trigger logic (see Section 2.8). The veto efficiency is measured to be 100% at the level of 10^{-5} , in complete agreement with the design specifications.

2.4 Permanent Magnet PM

At the core of the AMS detector is the permanent magnet. Although AMS was initially designed to operate with a superconducting magnet with an expected lifetime of 3 years, the extension of the ISS mission duration up to 2024 made it necessary to replace the superconducting magnet with the AMS-01 prototype permanent magnet (see Figure 2.8) [184].

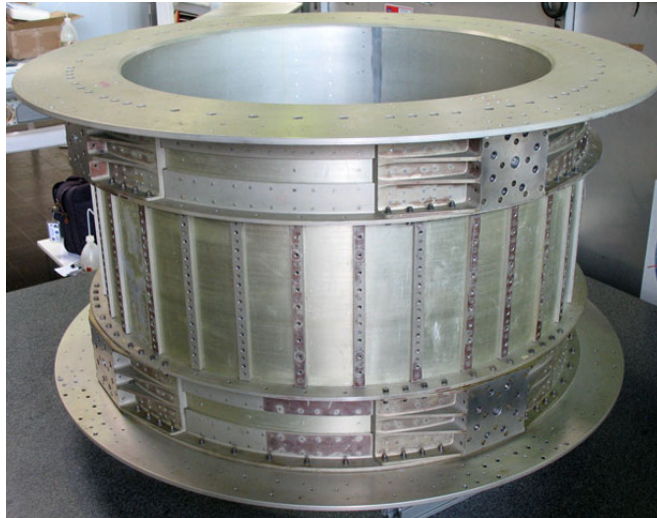


Figure 2.8: AMS permanent magnet, already employed for AMS-01 experiment on board of Space Shuttle Discovery [185].

The magnet is made of 6400 $5 \times 5 \times 2.5 \text{ cm}^3$ Nd-Fe-B blocks. Blocks are distributed in 100 circle shape layers, each formed by 64 blocks, and assembled in a toroidal structure 1 m height with inner and external radius respectively $r_i = 111.5 \text{ cm}$ and $r_e = 129.9 \text{ cm}$. This configuration builds up a $B = 0.149 \text{ T}$ dipole field within the magnetic walls. The external field has been designed to be less than 10^{-2} T in order to minimize interferences with electronic boards and detectors next to the magnet, but also to avoid mechanical torques on the ISS [186]. The resulting dipolar magnetic field is sketched in Figure 2.9.

The AMS coordinate reference frame is centered in the center of the magnet. The cylindrical symmetry of the magnetic lines defines the z axis, passing through the center of the magnet and pointing towards the top of the experiment. The x axis points along the magnetic lines. Finally, the y axis completes the right-handed Cartesian coordinate system. Using this definition, the curved motion of particles passing through the magnet is confined to the $x - y$ plane, also called *bending* plane.

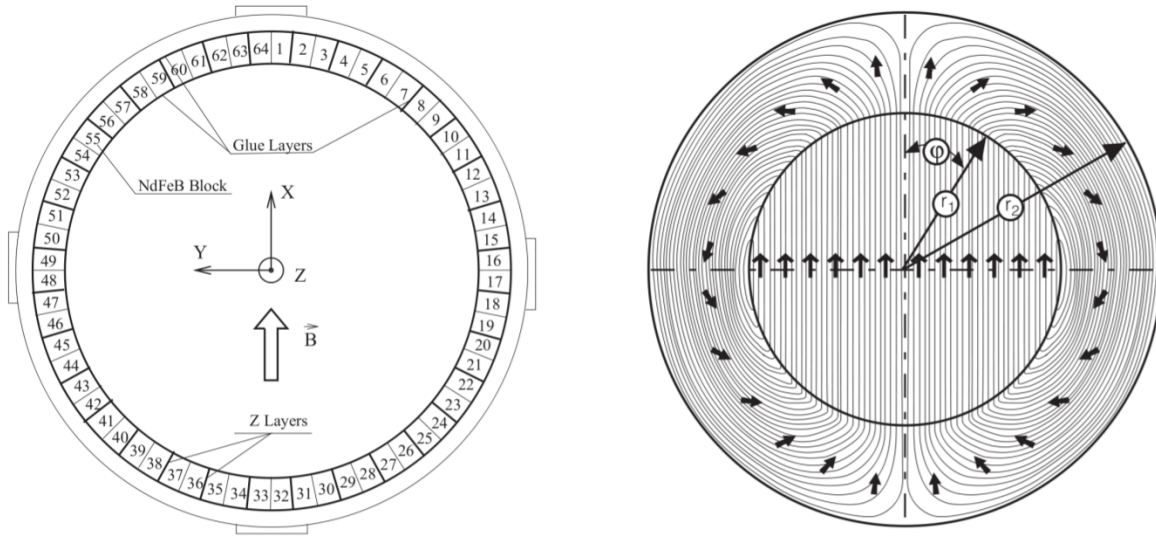


Figure 2.9: **Left:** AMS magnet configuration. 64 Nd-Fe-B blocks are distributed in the toroidal structure to provide an uniform dipole field in the magnet inner volume. Superimposed in the picture is the AMS coordinate reference frame. **Right:** Magnetization vector. Its flux is confined in the magnet volume, providing a negligible leaking field [187].

2.5 Silicon Tracker TRK

The Silicon Tracker (TRK) system [188, 189] is used in the AMS experiment to measure the trajectories of charged particles sampling their crossing positions at various z coordinates.

The basic element of the tracking system are $2264 \times 72 \times 41 \times 0.3 \text{ mm}^3$ silicon micro-strips sensors. On each face of the sensor, metallic strip implants run in perpendicular directions, providing a two-dimensional measurement for each sampling. The sensors are operated at 80 V reverse bias voltage. On the junction side (or p-side), p^+ strips are placed with a (readout) implantation pitch of (110) $25.5 \mu\text{m}$. On the opposite side, the ohmic or k-side, n^+ strips are placed with a (readout) implantation pitch of (208) $104 \mu\text{m}$, oriented in the perpendicular direction. The p-side is used to measure the crossing y coordinate, the k-side is used to measure the crossing x coordinate. The capacitive coupling between the strips and the analog readout allow to achieve a single point resolution of 10 (30) μm on the y (x) side for $Z = 1$ particles.

The readout component of the Silicon Tracker is called “ladder”. Each ladder consists of 7 to 15 wire-bonded silicon sensors. The energy deposit is read out, for each ladder, by 1024 readout channels: 640 on the p-side, 384 on the k-side. The readout electronics is placed directly on the front end board at the end of the ladder. The number of ladder composing the AMS tracking system is 192, for a total of $\sim 200,000$ readout channels and a total active area of 6.4 m^2 .

The ladders are arranged among 9 layers (see Figure 2.10). The top layer (Layer 1 or L1) is fixed on top of the TRD. The bottom layer (L9) is fixed between the RICH and the ECAL. L1 and L9 are usually addressed to as “external Tracker”, and are used to extend the lever of arm for the trajectory determination. The other 7 layers (L2 to L8) form instead the “inner Tracker”: L2 is located below the TOF, just above the magnet, while L3 to L8 are inside the magnet volume.

Due to the high number of readout channels, the Tracker front end electronics produces $\sim 200 \text{ W}$ of heat. In order to assure optimal performance of the detector and to keep the temperature away from the maximum limit of 30° , the heat has to be radiated to outer space. The Tracker Thermal Cooling

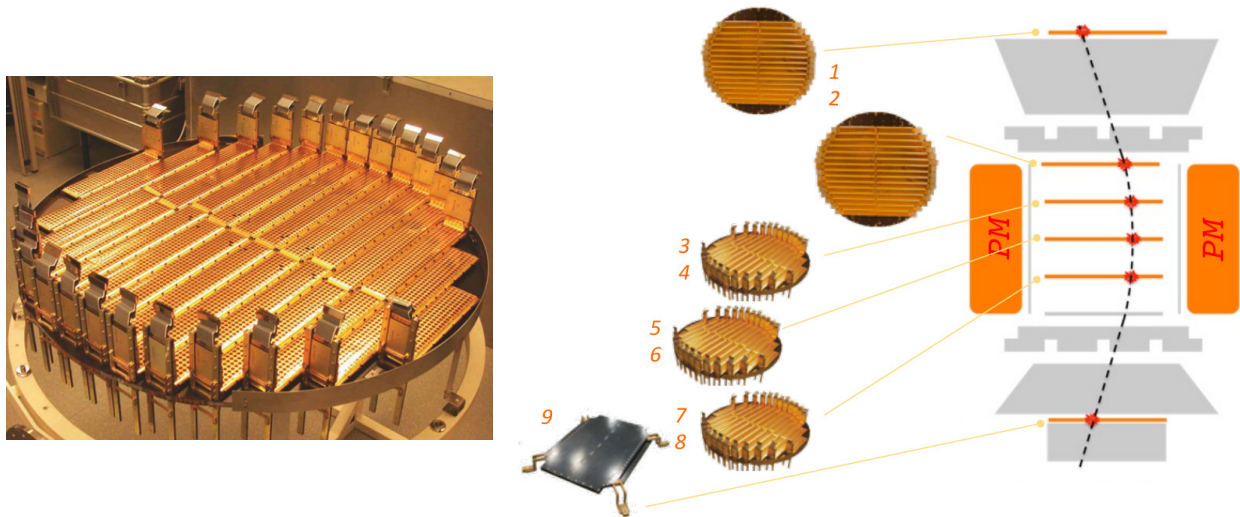


Figure 2.10: **Left:** One inner layer of the Silicon Tracker. Each layer is composed of several readout units (ladder). On the end of each ladder, the front-end electronics is installed in vertical. **Right:** Positions of the Silicon Tracker planes. L1 and L9 compose the so-called “external Tracker”, while L2 to L8 constitute the “inner Tracker” [190].

System (TTCS) [191] is a CO₂ two-phase-loop thermal cooling system which is used to keep the Tracker electronic and Tracker layer temperatures stable within 1 °C. The electronics is thermally connected to thermal bars which keep the temperature stable. Liquid CO₂ close to the boiling point is pumped through the bars, whose heat is absorbed by the CO₂ before and during the boiling phase. The boiling CO₂ exiting from the bars is in thermal contact with the incoming CO₂ to bring it as closest as possible to the boiling point: this makes the two-phase-loop more efficient than a single-phase loop. The outgoing boiling fluid radiates the heat to outer space through dedicated radiators. The whole TTCS system is completely double redundant to be operated safely in space.

The ionization loss in the sensors ($dE/dX \propto Z^2$) is used to estimate the charge Z of crossing particles, by the collection of the electron-hole pairs which migrates to opposite sides of the sensor. The dynamic range of the electronics allows to measure charges up to iron ($Z = 26$) and above (see Figure 2.11). The charge misidentification probability is estimated to be 10^{-4} for nuclei up to Oxygen ($Z = 8$) [192].

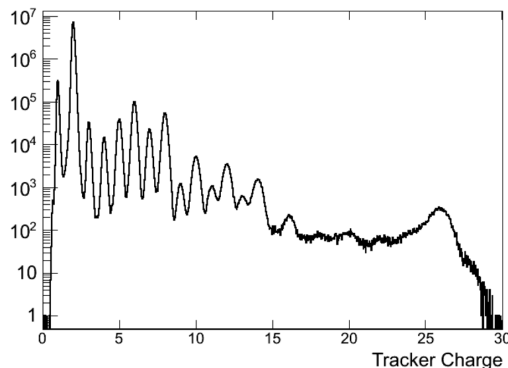


Figure 2.11: Charge distribution for cosmic nuclei measured by the Tracker. The misidentification probability from neighboring species is 10^{-6} for carbon ($Z = 6$) and 10^{-8} for oxygen ($Z = 8$). Nuclei can be distinguished up to iron ($Z = 26$), whose peak in the picture is well evident due to its natural abundance [192].

In order to maximize the Tracker resolution, it is necessary to know the position of each sensor to

few μm . Since the mechanical positioning measurement has an uncertainty of $\sim 100 \mu\text{m}$ (even higher than the single sensor intrinsic resolution), it is necessary to estimate alignment parameters to be applied during the offline track reconstruction algorithm. First, a *static alignment* of all the 2284 sensors is performed using cosmic protons to correct for the sensor shifts. Moreover, a *dynamical alignment* procedure is applied to the external layers: their supporting structures suffer in fact deformations and shifts due to the large temperature gradient which they are exposed to (up to $\pm 80^\circ\text{C}$ in a 2 month beta angle cycle³). Using cosmic protons to provide a time-dependent correction, the outer plane alignment is known with a precision $\sim 3 \mu\text{m}$ [193]. In parallel to the alignment procedure, the 7 inner planes movements are monitored by the Tracker Alignment System (TAS) [194], which consists of 5 laser beams produced by diodes installed on the L2 support structures.

The incoming particle rigidity is inferred by the measurement of the track curvature in the magnetic field. A fit to the measured crossing coordinates is applied to extract the trajectory parameters. The accuracy of the curvature measurement depends, among other parameters, on the distance between the uppermost and the bottommost crossing coordinate measurement. This distance is called “span”. The rigidity resolution of the Tracker – which grows linearly as function of the rigidity itself as $\sigma(R)/R \propto R$ – depends on the Tracker span (see Figure 2.12). In particular the Maximum Detectable Rigidity (MDR), at which the relative error on the curvature amounts to 100%, is $\sim 2 \text{ TeV}$ for protons and $\sim 3.2 \text{ TeV}$ for Helium nuclei in the maximum span configuration [190].

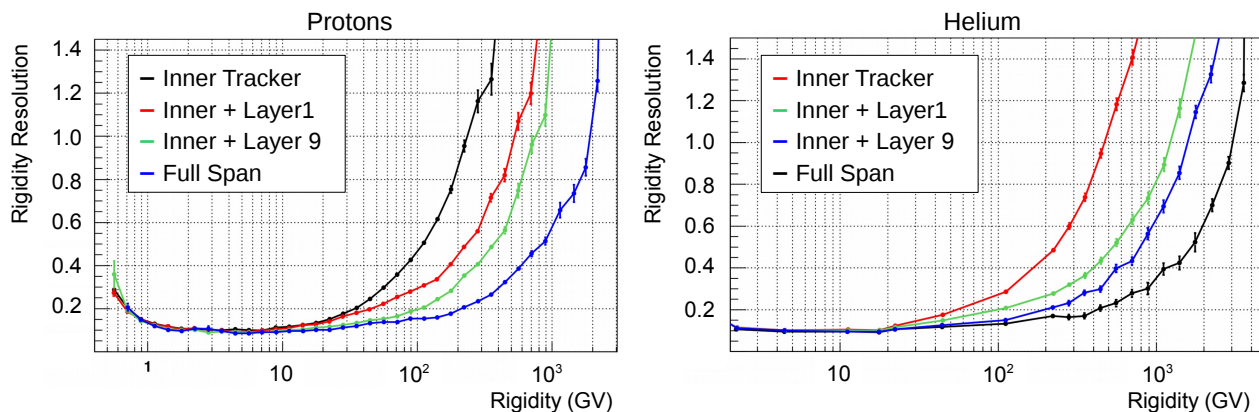


Figure 2.12: Rigidity measurement resolution for protons (**Left**) and Helium (**Right**) estimated from MC. Different colors identify different Tracker spans. The presence of the external layers used to increase the trajectory lever of arm allows to measure the rigidity of particles crossing the Tracker layers up to the TeV range [190].

2.6 Ring Imaging Cherenkov RICH

Cherenkov radiation is emitted by charged particles crossing a medium with velocity β greater than the phase velocity of the electromagnetic field in the material itself. The light is emitted in a cone, whose aperture angle θ_c is determined by the particle velocity β and by the refractive index of the material n :

$$\cos(\theta_c) = 1/n\beta \quad (2.1)$$

³The beta angle is defined as the angle between the ISS orbit plane and the vector to the sun. It defines the amount of radiation impinging on the AMS from the sun.

The number of photons N_γ produced per track length is instead used to infer to charge Z of the particle. The Rich Imaging Cherenkov (RICH) [195, 196] has been developed to detect such Cherenkov light in order to provide a precise velocity measurement complementary to the TOF and the charge measurement in the bottom part of the AMS detector. The measurements of the RICH are essential for the accurate estimation of the particle mass.

The RICH consists of a radiator plane, a conical mirror and a photon detection plane (see Figure 2.13). It is placed below the lower TOF plane.

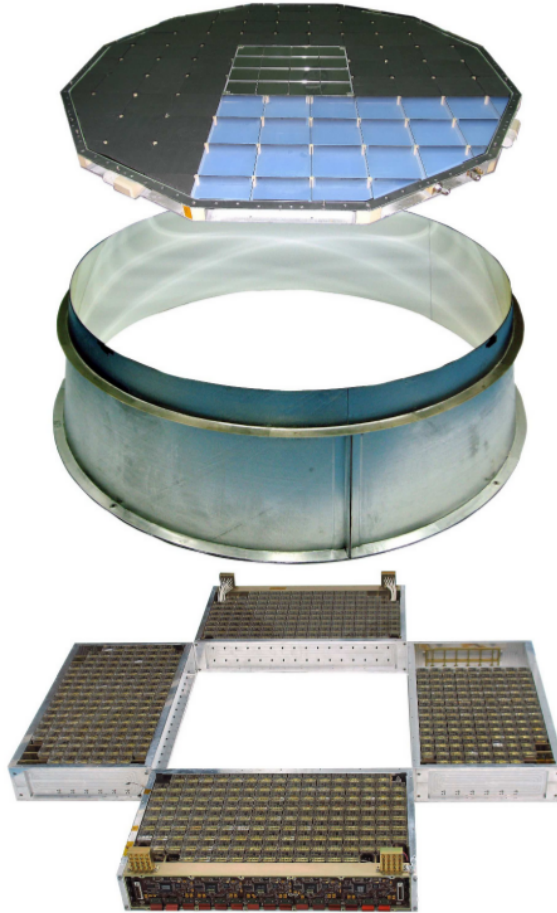


Figure 2.13: RICH exploded view. From top to bottom, the radiator plane, the conical mirror and the detection plane are shown [169].

The radiator consists of an array of 2.5 cm thick aerogel tiles with refractive index $n \sim 1.05$, which surrounds a central $34 \times 34 \text{ cm}^2$ region equipped with 5 mm thick sodium fluoride (NaF) radiator, with refractive index $n \sim 1.33$. The dual radiator configuration optimizes the overall counter acceptance, since the Cherenkov photons radiated with higher angular aperture inside the NaF radiator can cross the detection area.

The detector plane at the bottom of the detector has an empty $64 \times 64 \text{ cm}^2$ area in its center, matching the active area of the electromagnetic calorimeter located below. Outside the central hole, 680 4×4 multi-anode PMTs are arranged to cover the circular 134 cm diameter surface at the basis of the conical mirror. The total number of readout channels is 10880 with a spatial granularity of $8.5 \times 8.5 \text{ cm}^2$.

The radiator and the detection plane are enclosed in the volume of a conical reflecting mirror of height 47 cm. The distance between the radiation and the detection planes optimizes the photon drift to maximize the measurement sensitivity. The mirror increases the RICH acceptance reflecting high inclination photons that would have crossed outside the detection plane.

The collected Cherenkov light geometry allows, together with the particle incoming direction provided by the Tracker system, to estimate the aperture angle θ_c . The precision knowledge of the radiator refractive indices [197] allows to achieve a velocity resolution $\sigma(\beta)/\beta \sim 10^{-3}$ for $Z = 1$ particles and improving for higher charges. Moreover, the RICH can measure the particle charge through photon counting, providing a measurement of the nuclei charges up to iron ($Z = 26$), with a charge resolution below 0.5 charge units for light nuclei (see Figure 2.14) [198].

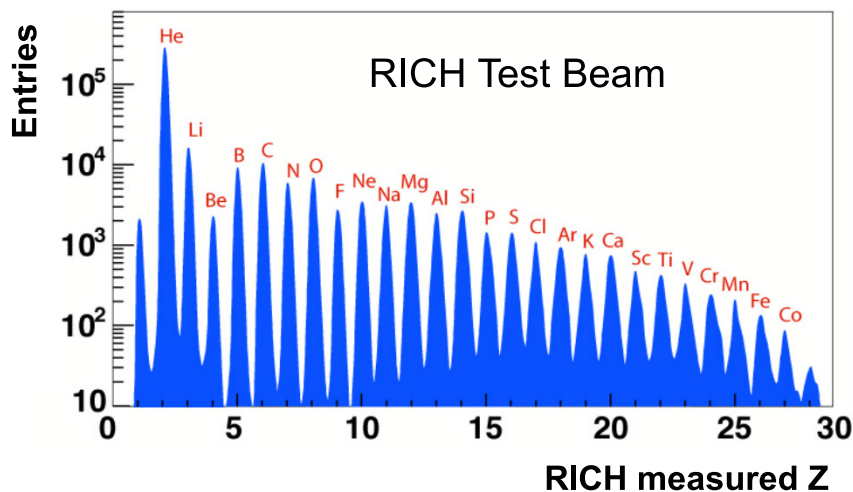


Figure 2.14: Measurement of nuclei charges from a RICH test beam. The RICH provides the charge measurement up to iron ($Z = 26$), with a resolution better than 0.5 charge units for light nuclei.

2.7 Electromagnetic Calorimeter ECAL

The AMS ECAL is a lead-scintillating fiber sampling calorimeter [199]. Particles crossing the active volume release their energy and produce light collected by photomultipliers (PMTs) at the fiber end. The structure [200, 201] is developed to maximize the X_0/λ ratio (X_0 is the electromagnetic interaction length and λ the nuclear interaction length). It consists in a lead-fiber-glass volume ratio of 1:0.57:0.15, an average density of $\sim 6.8 \text{ g/cm}^3$ and a radiation length X_0 of about 1 cm. The ECAL length corresponds to $\sim 17X_0$ and to only $\lambda \sim 0.6$. The active volume (*pancake*) is built up by a pile of 9 *superlayers* (SL) consisting of 11 grooved 1 mm lead foils interleaved by 1 mm plastic scintillating fibers. The fibers are glued by means of optical cement and they run, in each superlayer, in one direction only. Each superlayer is designed as a square parallelepiped with 68.5 cm side and 1.85 cm height, for a total active dimension of $68.5 \times 68.5 \times 16.7 \text{ cm}^3$, corresponding to $\sim 17X_0$ for perpendicular incident particles (Figure 2.15). The pancake has a weight of 496 kg, for a total weight of the calorimeter of 638 kg (including mechanical structures and readout cables).

Each superlayer is read out on one end only by 36 PMTs, alternately arranged on the two opposite sides to avoid mechanical interference. The PMTs are shielded from magnetic field by a 1 mm thick soft iron square parallelepiped tube, which also acts as mechanical support for the light collection system.



Figure 2.15: ECAL active volume (*pancake*). 9 superlayers are piled-up for a total of 50,000 1 mm \varnothing scintillating fibers running in opposite directions. The total $68.5 \times 68.5 \times 16.7$ cm³ pancake volume consists of a lead-fiber-glue volume ratio of 1:0.57:0.15, for an average density of ~ 6.8 g/cm³ [202].

Each PMT accommodates four 8.9×8.9 mm² anodes. The anodes define the ECAL granularity, for a total of $18 \times 72 = 1296$ readout *cells*. The 3D imaging of shower development is achieved by alternating 5 SLs with fibers along the x axis and 4 SLs with fibers along the y axis. The ECAL Molière radius, measured to be ~ 2 cm, corresponds approximately to 1 PMT width.

In order to obtain the necessary sensitivity on minimum ionizing particles (~ 7 MeV/cell) and to measure energies up to 1 TeV (~ 60 GeV/cell) using standard 12-bit ADCs, the digitization is performed by the front-end readout system at two different gains, with a gain ratio of about 33. Besides the eight signal from anodes, each PMT's last dynode signal is also read out and its information used to have a redundant signal in case of anode breakdowns and also to build up the ECAL standalone trigger (see Section 2.8).

Each ECAL PMT response is equalized by setting the PMT gain to a common value and correcting the residual response of each cell to hadronic MIP particles offline [203].

Electrons, positrons and photons reaching ECAL interact starting an electromagnetic shower. The mean longitudinal profile of the energy deposit by an electromagnetic shower is usually described by a gamma distribution [204]:

$$\left\langle \frac{1}{E} \frac{dE(t)}{dt} \right\rangle = \frac{(\beta t)^{\alpha-1} e^{-\beta t}}{\Gamma(\alpha)} \quad (2.2)$$

where $t = x/X_0$ is the shower depth in units of radiation length, $\beta \sim 0.5$ is the scaling parameter and α the shape parameter. The total thickness of the ECAL ($\sim 17 X_0$) allows the containment of 75% of the shower energy deposit for 1 TeV e^\pm .

The energy of the incoming particle is measured applying corrections for the rear and lateral energy leakage, and for the anode efficiency, to the deposited energy. These corrections ensure the energy linearity to be under control to better than 1% up to 300 GeV. The calorimeter energy resolution $\sigma(E)/E$ has been measured during the test beams [205] (see Figure 2.16) and can be parametrized as a function of the particle energy E by:

$$\frac{\sigma(E)}{E} = \frac{10.4 \pm 0.2}{\sqrt{E(\text{GeV})}} \% \oplus (1.4 \pm 0.1) \% \quad (2.3)$$

The fine ECAL 3D readout granularity allows to reconstruct the shower axis and direction with high precision. The ECAL pointing accuracy is an extremely important parameter for gamma ray

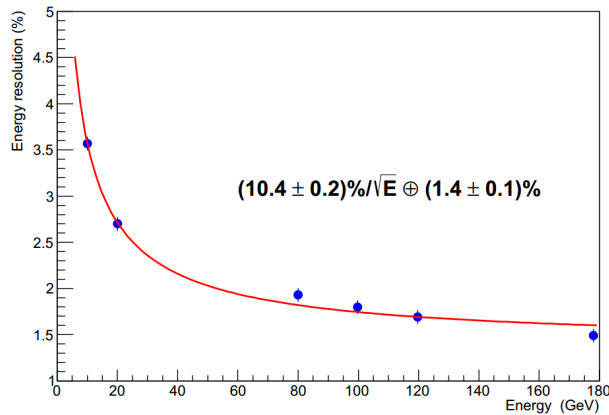


Figure 2.16: ECAL energy resolution measured using e^\pm test beams for perpendicularly incident particles [205].

astrophysics. The ECAL angular resolution has been measured to be better than 1° for energies above 50 GeV [206]. The ECAL standalone trigger, whose efficiency for non-interacting photons is better than 99% at energies above 5 GeV, allows to measure photons inside the AMS field of view and which did not interact before the calorimeter. Given the amount of radiation length X_0 in front of the calorimeter, more than 60% of photons crossing the detector from the top reach directly the calorimeter without interactions. Photons that interact in the material before the ECAL are instead measured by the detection of $e^- - e^+$ pairs in the Silicon Tracker.

One of the main purposes of the ECAL is the identification of electrons and protons. The electromagnetic shower starting point, its shape and the matching between the deposited energy in the ECAL and the rigidity measured by the Tracker are used to identify e^\pm while rejecting the hadronic background. The ECAL proton rejection capabilities, measured directly from data, are shown in Figure 2.17. More details about these tools will be given in Section 4.2.1.

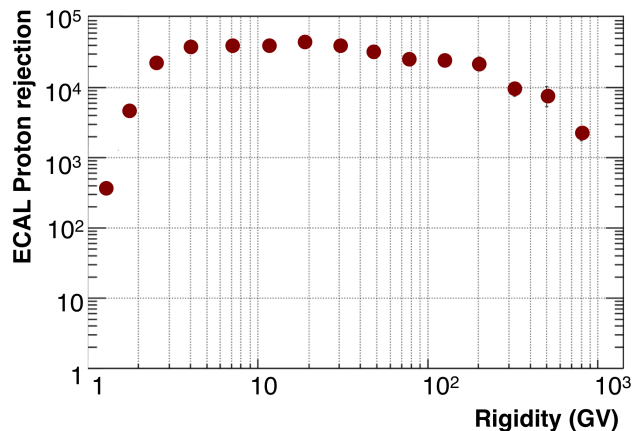


Figure 2.17: Electron/proton rejection measured from data collected in space using the ECAL shower topology analysis and the matching between the deposited energy in the ECAL and the rigidity measured by the Silicon Tracker [176]. The efficiency of the selection for e^\pm is 90%. The proton rejection is above 10^4 in almost the whole energy range.

2.8 Data Acquisition DAQ and Trigger

The AMS Data Acquisition System (DAQ) [207] has been designed to collect and process the signal coming from $\sim 300,000$ analog channels. The system is based on a *Master-Slave* communication principle: data transactions are started from each slave only on request from its master, and the reply is directly given after the master's request. A total of circa 300 Digital Signal Processors (DSP) based computing nodes are arranged in a tree-like structure (see Figure 2.18), which culminates to the main DAQ Computer JMDC [208]. 264 Data Reduction nodes (xDR, where x specifies a subdetector) collect data from the analog front-end electronics and apply a fast-online data reduction algorithm (“*zero suppression*”) to reduce the amount of data sent to ground. Eight SDR nodes collect data from TOF/ACC and produce the trigger signals. Fourteen JINF nodes with double redundancy collect data from xDRs belonging to the same event from the same subdetector, send them to the master interface JINJ (4 times redundant) and finally to the main computer JMDC, also 4 times redundant. The trigger board JLV1, double redundant, coordinates the processing of trigger signals produced by TOF, ACC and ECAL boards and send the data to JMDC through JINJs. A dedicated protocol (*AMSwire*) has been developed to manage the inter-node communication.

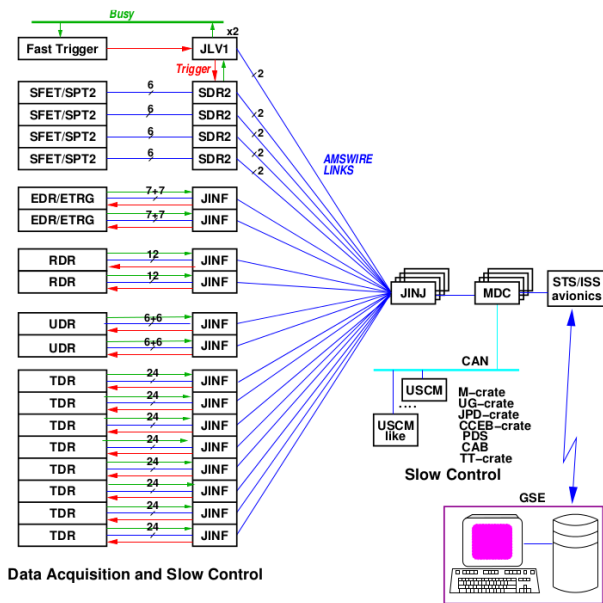


Figure 2.18: AMS data acquisition system. About 300,000 analog channels are processed by about 300 DSP computers in a *Master-Slave* based architecture. Due to the impossibility of any repair, the system has been designed allowing maximal redundancy of boards and cable connections: in case of any failure, the detector performance is not degraded [208].

All electronic boards are hosted in dedicated external radiators to favor the heat exchange to the external environment. Two data streams are sent from the ISS to the ground, with an average downlink rate of 17 Mbps: a *science* stream, containing subdetector processed data from triggering particles, and a *housekeeping* stream, containing information about each subdetector status and its working parameters (temperatures, voltages, etc...) mainly for online monitoring purposes (see Section 2.9). Finally, all the nodes are regularly tested for accidental *bit-flips* caused by heavy ions crossings and, in case of positive outcome, the node is reset to normal status⁴.

The AMS Trigger signal is built in the JLV1 board using the signal measured in TOF, ACC and ECAL [209]. The trigger decision is taken from JLV1 if two trigger conditions are satisfied: the *Fast Trigger* (FT) first, followed by the *Level 1* (LVL1) signal. The signal from TOF and ECAL is sampled with

⁴On average, one unit per day fails the test and is restored

25 MHz rate and analysed to check simple conditions. During this phase, no dead time is introduced to the DAQ. If such signals fulfill minimal conditions in TOF or ECAL, the FT signal is produced⁵ and the JLV1 starts the evaluation of LVL1. The system is set to *busy* status for 1 μ s while the signals in TOF, ACC and ECAL are evaluated to produce seven more complex sub-trigger signals [210]:

- Unbiased charged: 3/4 (HT⁶) TOF planes. A prescale factor of 100 is applied to reduce the trigger rate.
- Single charge: 4/4 (HT) TOF planes, no ACC fired.
- Normal ions: 4/4 (SHT) TOF planes above a higher threshold.
- Slow ions: 4/4 (SHT) TOF planes above a higher threshold, delayed gate width.
- Electrons: 4/4 (HT) TOF planes, ECAL energy deposit above threshold in both projections.
- Photons: ECAL energy deposit above threshold in both projections, ECAL axis inside AMS field of view.
- Unbiased EM: ECAL energy deposit above threshold in any projection. A prescale factor of 1000 is applied to reduce the trigger rate.

If one or more sub-trigger signal is produced, the signal is distributed to all xDR nodes and the event is recorded. The system is set in *busy* status while each subdetector front-end reads and digitizes the signal. This operation takes $\sim 220 \mu$ s⁷. After this, the DAQ system is set ready to trigger another event while the signal reduction in xDRs continues in parallel on buffered data, to reduce the dead time.

In order to evaluate the detector livetime \mathcal{L} , defined as the fraction of time in which the detector was ready to measure a new event⁸, a fine scaler is used to sample the status of the DAQ every 20 ns: \mathcal{L} is defined for each second as the ratio of samples which found the detector not *busy* with respect to the total number of samples.

2.9 AMS operations

AMS has been successfully installed on the ISS on 19th May 2011, and since that day it is continuously recording cosmic particles without any major interruption to the DAQ (see Appendix A for a graphical illustration).

The ISS orbits around the Earth at an altitude between 330 km and 410 km completing 15.7 orbits per day. The orbit plane is inclined by 51.6° with respect to the Earth equator. Maps of geodetic coverage of ISS are shown in Figure 2.19. The DAQ livetime depends on the particle rate. The rate of low energy (< 30 GV) particles is highly influenced by the Earth magnetic field. It increases in polar regions and in the South Atlantic Anomaly (SAA). In the polar regions, the detector livetime is decreased from the optimal operating value. In the SAA region [56] (see Section 1.1.3), the low energetic trapped particle rate saturates the DAQ and the livetime goes to zero.

Data are recorded in *runs* lasting ~ 23 minutes each. Four runs are recorded for each ISS orbit. At equator crossing (every other run), a calibration of the electronics is performed: using random triggers (in order to avoid energy deposit by CRs in the detectors), the electronic readout is sampled and the pedestal and the noise of each channel are measured. These parameters are then used by xDRs during the event data reduction procedure. At the beginning and end of every run, specific read-out commands

⁵FT is the logical “OR” of 3 Fast Triggers: FTE (electromagnetic shower deposit in ECAL), FTC (single charge signal in TOF) and FTZ (heavy nuclei and strangelets in TOF).

⁶The meaning of the HT and the SHT thresholds is described in Section 2.2.

⁷During the *busy* time window, $\sim 90 \mu$ s are effectively used for the digitization. The rest of the window is set as redundant recovery time.

⁸ livetime fraction = 1 – deadtime fraction

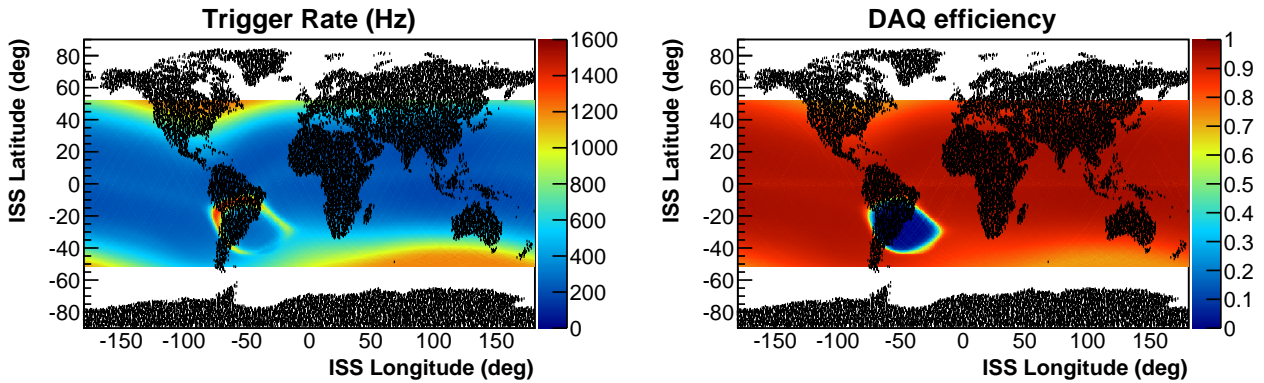


Figure 2.19: ISS orbit in geodetic coordinates. **Left:** the AMS trigger rate is superimposed. The trigger rate spans from ~ 200 Hz in the equator up to ~ 1500 Hz near the Earth magnetic poles, where the lower Earth magnetic field allows low energetic cosmic particles to reach the detector. **Right:** AMS DAQ efficiency. The average efficiency is 88%, where the inefficiencies are dominated by the highest trigger rate regions. In the South Atlantic Anomaly region the DAQ efficiency goes to zero due to the high flux of low energetic trapped particles.

are sent to check the status of the detector electronics and temperature sensors. These data, with all other housekeeping parameters, are continuously monitored around-the-clock on ground in the Payload and Operations Control Center (POCC) sited in the European Laboratory for Particle Physics (CERN) in Genève, Switzerland, and in Chungshan Institute of Science and Technology (CSIST) in Taiwan.

2.10 AMS physics

AMS is the most accurate particle experiment in space for detection of charged CRs. The physics spectrum of AMS is wide and involves many important fundamental physics topics.

AMS has already measured the e^\pm fluxes, as well as the positron fraction, reaching an energy range never explored so far and improving the precision of the measurements up to the % level. As discussed in Section 1.2, the impact of these results on the understanding of the e^+ and e^- production mechanisms and diffusion in the Galaxy has been huge. The increase in the size of the e^\pm dataset in the coming years will allow AMS to extend these measurements up to TeV energies. This is one of the main goals of AMS, as it will help to disclose the presence of indirect DM signatures in the e^\pm channels. The increase in the e^\pm dataset size will also improve the constraints on the e^\pm arrival direction anisotropy, fundamental to determine the presence of point-like sources of e^\pm in the nearby galactic environment.

The measurement of the \bar{p} component provides complementary information for the search of DM. The charge sign separation power of the magnet allows to identify and to remove the proton background. The measurement of the \bar{p} flux and its ratio to the standard proton component is another primary goal of the AMS spectrometer.

AMS is able to complete the DM indirect search measurements via the detection of other rare components in the cosmic radiation, like γ rays and anti-deuterium (\bar{D}). Any detection of \bar{D} by AMS at energies below 1 GeV possible for a set of models [156], would be a smoking gun to claim indirect evidence of DM signature in CRs.

AMS has already released preliminary results on nuclei CRs. The proton flux has been measured up to 1.8 TV and the Helium spectrum has been measured up to 3.0 TV [193, 211]. These are the highest energies ever reached by balloon or space experiments. The B/C ratio has also been measured

up to 500 GV/nucleon improving the accuracy of the data by an order of magnitude in the whole energy range with respect to previous measurements [212]. In the incoming years, AMS will provide accurate measurements of cosmic nuclei up to iron. This will have a substantial role in the understanding of standard propagation mechanisms in the Galaxy, whose uncertainty is one of the most limiting factors for model interpretation of CR data.

The other primary role of AMS is the measurement of primordial anti-matter in the cosmic radiation. Large anti-matter domains and even anti-matter clusters could be present in the Universe since the Big Bang. As of today, no experimental support from CP-violation and proton decay measurements could rule out this hypothesis. Production of $\bar{\text{He}}$ or heavier anti-nuclei in the interaction of ordinary matter in space is out of the sensitivity of current space and balloon experiments. The observation of $\bar{\text{He}}$ in the cosmic radiation would constitute a strong argument in favor of the anti-matter domain hypothesis. The AMS sensitivity in the search for $\bar{\text{He}}$ is shown in Figure 2.20. Compared to current results, the expected improvement in sensitivity is more than three orders of magnitude.

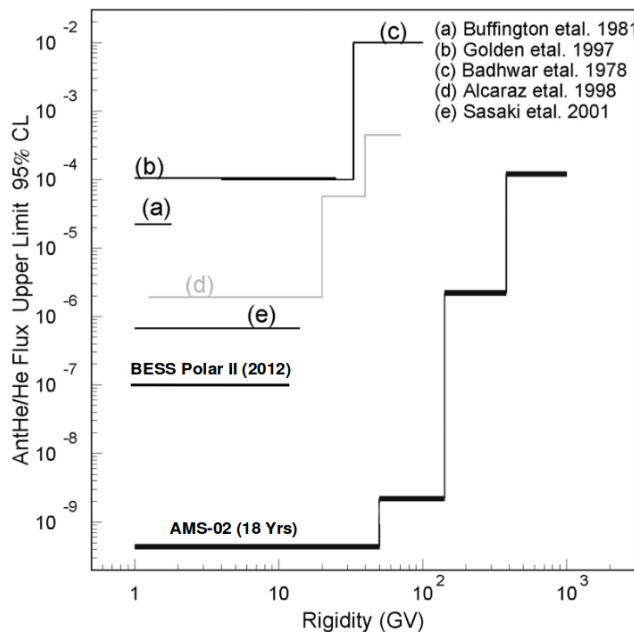


Figure 2.20: Expected sensitivity in the search for $\bar{\text{He}}$ for 18 years of data taking for AMS compared with the available measurements [213].

The length of the AMS mission over more than 1 solar cycle opens the possibility to investigate transient solar phenomena and the adiabatic solar activity. The time dependent measurement of low energetic CR fluxes will help to improve the current knowledge of solar physics and low energy CR propagation in the long term.

Finally, AMS will use its precise particle measurements to search for exotic physics in the cosmic radiation. Strangelets, hypothetical particles composed of the (u,s,d) quark triplet – which are predicted to be stable by QCD calculations – have not been found at accelerator collisions so far. Neutron stars could be however a strangelet source. Strangelets have a typical signature $Z/A \sim 0.1$ much smaller than standard nuclei for which $Z/A \sim 0.5$. AMS could therefore be able to detect such new form of matter.

Chapter 3

Introduction to the flux measurement

In this chapter, the concept of *flux* is introduced. The experimental process and the observables needed to measure cosmic particle fluxes are subsequently discussed. Furthermore, the dataset used in this analysis, the treatment of the AMS data and of the Monte Carlo (MC) simulation data are discussed.

3.1 The flux measurement

The direct measurement of the intensity of the flux of a certain cosmic species is achieved by the collection and the analysis of cosmic rays with a detector. The properties of the collected cosmic rays, such as their energy or their charge, are inferred through the analysis of their interactions and energy deposits in the detector material. The analysis of the interaction signatures in the detector allows to infer the properties of the primary cosmic ray before its detection (or “at the top of the instrument”). The measured intensity is however a physical quantity that depends on the detector and its properties. In order to retrieve the flux at the top of the instrument and to compare it with theoretical expectations, the measured intensity has to be corrected for the detector properties.

The term *flux* refers to the number of particles in a certain point of space per time, area, solid angle and energy, and it is measured in units of $[\text{GeV m}^2 \text{ sr s}]^{-1}$. The normalization corrects the total number of particles collected by the instrument by the measuring time, the effective area covered by the instrument and by the size of the energy bin width. A continuous energy measurement is not possible with a realistic detector, as a non-zero number of cosmic rays can only be collected in a finite size energy range.

In the most general case, the flux $\Phi_i(E, \Omega, t, \vec{x})$ for the i^{th} particle species is function of the energy E , the solid angle Ω , the measured time t and the spatial coordinates \vec{x} . Assuming for now no dependence on the spatial coordinates \vec{x} , and defining $N_i(E, \Omega, t)$ the number of particles identified by the detector in the energy range $[E, E + \Delta E]$, in the collection time $[t_0, t_0 + \Delta T]$ and with arrival direction in the solid angle $[\Omega, \Omega + \Delta\Omega]$, the flux $\Phi_i(E, \Omega, t)$ is implicitly defined by the following equation:

$$N_i(E, \Omega, t) = \int_{t_0}^{t_0 + \Delta T} \int_E^{E + \Delta E} \int_{\Omega}^{\Omega + \Delta\Omega} \int_S \Phi_i(E', \Omega', t') \xi_i(E', \Omega', t') \hat{r}' \cdot d\vec{S}' d\Omega' dE' dt' \quad (3.1)$$

where $\hat{r} \cdot d\vec{S}$ represents the differential area of the detector crossed by the particles in the direction of $d\Omega$, which is integrated over the full detector area S . The factor $\xi_i(E, \Omega, t)$ represents the impact of all the factors, including the instrument itself and external environment factors, which affect the detection of the particles of species i . In the general case, $\xi(E, \Omega, t)$ can be factorized in independent contributions:

$$\xi_i(E, \Omega, t) = \mathcal{L}(t) \varepsilon_{\Phi}(E, \Omega, t) \varepsilon_i(E, \Omega, t) \quad (3.2)$$

where

- $\mathcal{L}(t)$ represents the detector livetime, defined as the fraction of time the instrument was able to detect and record an event. More details are discussed in 2.8.
- $\varepsilon_{\Phi}(E, \Omega, t)$ represents the probability for a particle with energy E and coming from the direction Ω to reach the detector through the external environment. The geomagnetic field can prevent in fact a particle coming from outside the Earth magnetosphere to reach the instrument. The factor ε_{Φ} takes these effects into account.
- $\varepsilon_i(E, \Omega, t)$ represents the instrument detection efficiency for the i^{th} type of particle.

Assuming that the detector response does not depend on the time and combining all the time dependent effects:

$$\xi_i(E, \Omega, t) = \mathcal{T}(E, \Omega, t) \varepsilon_i(E, \Omega) \quad (3.3)$$

where $\mathcal{T}(E, \Omega, t) = \mathcal{L}(t) \varepsilon_{\Phi}(E, \Omega, t)$, and Equation 3.1 can be expressed as:

$$N_i(E, \Omega, t) = \int_{t_0}^{t_0+\Delta T} \int_E^{E+\Delta E} \int_{\Omega}^{\Omega+\Delta\Omega} \int_S \Phi_i(E', \Omega', t') \mathcal{T}(E', \Omega', t') \varepsilon_i(E', \Omega') \hat{r}' \cdot d\vec{S}' d\Omega' dE' dt' \quad (3.4)$$

which correctly accounts for any transient or adiabatic time dependences in the particle flux.

Assuming that the flux has no dependence on time or, equivalently, that the target measurement is the average effective flux in the measurement time ΔT , it is possible to define the *Exposure Time* of the instrument (ΔT_{exp}) as:

$$\Delta T_{\text{exp}}(E, \Omega) = \int_{t_0}^{t_0+\Delta T} \mathcal{T}(E', \Omega', t') dt' \quad (3.5)$$

which represents the total time the instrument was “ready” for the detection of a particle which could potentially reach the detector itself.

In the following it is assumed that exposure time $\Delta T_{\text{exp}}(E, \Omega)$ does not depend on the energy in the energy range $[E, E + \Delta E]$ and that any dependence of ΔT_{exp} on the particle incoming direction Ω can be safely neglected¹. The term $N_i(E, \Omega, t)$ can be further simplified:

$$N_i(E, \Omega, t) = \Delta T_{\text{exp}} \int_E^{E+\Delta E} \int_{\Omega}^{\Omega+\Delta\Omega} \int_S \Phi_i(E', \Omega') \varepsilon_i(E', \Omega') \hat{r}' \cdot d\vec{S}' d\Omega' dE' \quad (3.6)$$

The measured number of particles depends, under these assumptions, on the response of the detector to the incoming flux only. The response includes both geometrical and inefficiency effects.

The *differential effective acceptance* of the detector is defined as:

$$A(E, \Omega)^{(\Omega)} = \int_S \varepsilon_i(E, \Omega) \hat{r}' \cdot d\vec{S}' \quad (3.7)$$

while the *effective acceptance* $A(E)$ is the result of the integration of the differential acceptance over the whole solid angle

$$A(E) = \int_{\Omega} \int_S \varepsilon_i(E, \Omega') \hat{r}' \cdot d\vec{S}' d\Omega' \quad (3.8)$$

Both the effective acceptance and its differential form collapse to the so called (*differential*) *geometrical factor* in the ideal case $\varepsilon_i(E, \Omega) = 1$.

¹This strong assumptions will be justified later in this analysis. See Section 4.1.4 and Section 5.1 for the details on the rejection of secondary particles trapped in the geomagnetic field.

Equation 3.6 simplifies further to:

$$N_i(E, \Omega) = \Delta T_{\text{exp}} \int_E^{E+\Delta E} \int_{\Omega}^{\Omega+\Delta\Omega} \Phi_i(E', \Omega') A(E', \Omega')^{(\Omega')} d\Omega' dE' \quad (3.9)$$

or to:

$$N_i(E) = \Delta T_{\text{exp}} \int_E^{E+\Delta E} \Phi_i(E') A(E') dE' \quad (3.10)$$

if the measured flux is integrated over the full solid angle.

In Equation 3.9 and 3.10 the main experimental observables used to measure the particle flux are now explicit.

A realistic experiment can only provide a binned analysis, as events are integrated in separate and finite energy ranges to collect enough counts. In the binned case, in Equation 3.10 the explicit flux term can be expressed as:

$$\Phi_i(\tilde{E}) = \frac{N_i(E)}{\Delta T_{\text{exp}} \Delta E A_i(\tilde{E})}, \quad (3.11)$$

where $N_i(E)$ is the number of events collected in the energy range $[E, E + \Delta E]$ and identified as i^{th} particle species by the detector. $A_i(\tilde{E})$ is the most representative value for the acceptance of the instrument in the same energy range for the i^{th} particle species. The quantity $\Phi_i(\tilde{E})$ is the measurement of the best estimation of the flux of cosmic rays detected by the instrument in the energy range $[E, E + \Delta E]$. The energy value \tilde{E} denotes the most representative energy of the bin for the measured flux. More details about the properties of the \tilde{E} energy value and of the procedure to its evaluation will be discussed in Section 6.1.2.

Equation 3.11 describes a common way to measure fluxes using any realistic detector. The measurement of the $(e^+ + e^-)$ flux presented in this thesis is driven by Equation 3.11.

In order to evaluate the cosmic ray e^+ and e^- flux, several experimental challenges have to be solved. First, the number of collected e^\pm events (N_{e^\pm}) has been extracted from the overwhelming background of protons and nuclei. The exposure time of the experiment (ΔT_{exp}) has to be evaluated taking into account possible effects introduced by the geomagnetic field and its energy dependence. Finally, the acceptance of the detector has to be computed for e^\pm . In the rest of this thesis, all the processes and techniques used for the evaluation of the above contributions and of the systematic uncertainties are discussed.

3.2 Data sample

In this analysis, a total of 41×10^9 events, corresponding to the total data triggered in the first 30 months of AMS data-taking (May 20, 2011 – Nov 29, 2013), have been analyzed.

The “raw” digital data collected by the electronics for each triggered event are sent to ground and processed. Calibrations, clustering algorithms and corrections are applied to the raw electronics data in order to obtain higher level reconstructed (or “physics”) objects. This procedure is applied by the *gBatch* framework, developed and continuously maintained by the AMS collaboration. The increasing understanding of the detector details and response allows to constantly improve the calibration and reconstruction algorithms with a positive impact on the quality and accuracy of the reconstructed data. Therefore, the complete AMS raw data are regularly reprocessed to provide the best precision for data analysis. In this thesis, the latest available reprocessing of AMS data has been analyzed.

Moreover, in order to investigate certain features of the analysis and to assess systematic uncertainties, the official AMS Monte Carlo simulation (MC) data has been used. A dedicated, full MC simulation

of the response of the AMS detector based on the GEANT-4.9.4 package [214] has been developed by the AMS collaboration. The software simulates the interactions of particles in the active and passive materials of AMS. The analog signals in the detection volumes are converted to the equivalent experimental signals through the simulation of the signal digitization processes. The digitized “raw” signals are finally reconstructed using the same algorithms and calibration constants used for the data reconstruction.

The simulated e^- sample is generated isotropically from a square plane at $z = 1.95$ m with side length 3.9 m and centered in the AMS z axis (see Section 2.4 for the description of the AMS reference frame). The data are generated in three intervals with a generated energy E_{gen} spectrum $dN/dE_{\text{gen}} \propto E_{\text{gen}}^{-1}$. The total number of events in the MC simulation dataset in three generation intervals amounts to:

- [0.5 - 5] GeV, $\sim 43.9 \times 10^9$ simulated events
- [5.0 - 100.0] GeV, $\sim 269.2 \times 10^9$ simulated events
- [100.0 - 2000.0] GeV, $\sim 0.23 \times 10^9$ simulated events

The generated MC data size has been set in order to provide a negligible statistical error with respect to the collected e^\pm counts, as qualitatively shown in Figure 3.1. From the picture it is also evident that the MC simulation spectra do not represent the spectral shape of e^\pm collected by the instrument. Therefore, unless differently specified, in this analysis the MC events are re-weighted in order to best represent the spectral features of the e^\pm data collected by AMS. The reweighting procedure will be explained in the next section.

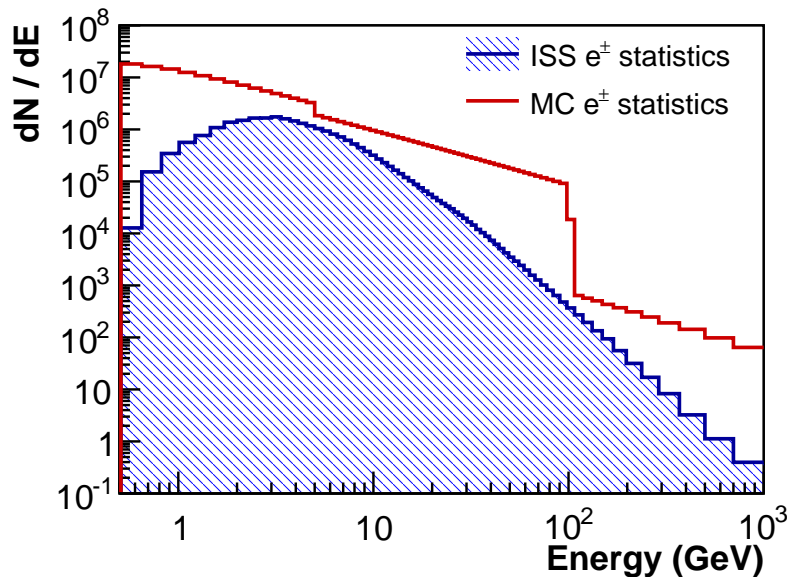


Figure 3.1: Comparison between the AMS e^\pm collected number of events (in blue) and the MC e^\pm dataset generated in the MC simulation (in red). For ISS data, the energy at the top of the instrument is measured using the ECAL, while for MC data the events are binned according to the generated energy. The MC events are generated in 3 contiguous energy ranges according to a generation spectrum $\propto E_{\text{gen}}^{-1}$, with a total statistics much higher than the number of collected e^\pm . From the picture, it is clear that the MC events have to be re-weighted to best represent the spectral shape of the data. The re-weighting procedure is described in Section 3.3.

3.3 The Monte Carlo simulation spectral shape and normalization

The MC simulated events are generated in three energy intervals j . In each energy interval events are generated with a spectral shape $dN/dE_{\text{gen}} = k^{(j)}E_{\text{gen}}^{-1}$ as function of the generated particle energy E_{gen} . The resulting raw MC spectrum does not therefore represent the spectral shape and the sample size of the ($e^+ + e^-$) events collected by AMS. The characteristics of the generated sample should be taken into account explicitly:

- when different samples of MC events are combined to study the properties of the reconstructed events over the full energy range accessible to AMS;
- when the MC simulation and the collected data samples are compared as a function of reconstructed energy or rigidity.

In this section, the procedure used to correctly process the MC sample is explained.

First of all, the MC events have been renormalized to a continuous spectrum in the whole energy range. In each of the 3 generation intervals, the normalization $k^{(j)}$ is constrained by the total number of events $N_{\text{gen}}^{(j)}$ generated in the interval:

$$N_{\text{gen}}^{(j)} = \int_{E_{\text{min}}^{(j)}}^{E_{\text{max}}^{(j)}} k^{(j)} E^{-1} dE \implies k^{(j)} = \frac{N_{\text{gen}}^{(j)}}{\ln(E_{\text{max}}^{(j)}) - \ln(E_{\text{min}}^{(j)})} \quad (3.12)$$

The cross-normalization of the MC statistics generated in the different energy ranges is achieved by the assignment of a weight $w_{\text{norm}}^{(j)}$ to each event defined as:

$$w_{\text{norm}}^{(j)} = \frac{k^{\text{ref}}}{k^{(j)}} \quad (3.13)$$

To define the reference normalization (k^{ref}), the energy interval with the smallest generated dataset has been used.

As second step the spectral shape of the incident flux, $f(E)$, has to be simulated. Therefore, the analytical shape of $f(E)$ has been parametrized from a fit to the preliminary release of the ($e^+ + e^-$) flux [215]. The MC events have been consequently reweighted according to the generated energy as following:

$$w_{\text{flux}}(E) = \frac{f(E_{\text{gen}})}{E_{\text{gen}}^{-1}} \quad (3.14)$$

where the E_{gen}^{-1} factor at the denominator removes the unphysical energy dependence of the generated spectrum $\propto E_{\text{gen}}^{-1}$.

The exposure time of the experiment ΔT_{exp} shows an energy dependence below ~ 30 GeV, as explained in detail in Section 5.1. Therefore, the preliminary $e^+ + e^-$ spectrum, whose spectral shape $f(E)$ is used in the renormalization procedure, does not represent the flux detected by the experiment correctly (as it is corrected by the energy dependent exposure time factor).

A more realistic model of the incident particle spectrum detected by AMS ($f_T(E)$) can be obtained by an additional reweighting of the events using the exposure factor $w_{\Delta T}(E)$. The exposure factor $w_{\Delta T}(E)$ depends on the exposure time ΔT_{exp} and it is defined as:

$$f_T(E) = f(E) \frac{\Delta T_{\text{exp}}(E)}{\Delta T_{\text{exp}}(E = \infty)} \implies w_{\Delta T}(E) = \frac{\Delta T_{\text{exp}}(E)}{\Delta T_{\text{exp}}(E = \infty)} \quad (3.15)$$

Table 3.1: Energy intervals which define the measurement bins above ~ 150 GeV. The complete list of 74 bin is reported, together with the flux measurement, in Table F.2

E_{\min}	148.81	169.86	197.69	237.16	290.0	370.0	500.0	700.0
E_{\max}	169.86	197.69	237.16	290.0	370.0	500.0	700.0	1000.0

The total re-weighting factor can be finally expressed as product of the previous contributions:

$$w(E)^{(j)} = w_{\text{norm}}^{(j)} w_{\text{flux}}(E) w_{\Delta T}(E) \quad (3.16)$$

In this analysis the MC events are re-weighted according to Equation 3.16².

3.4 Energy intervals for the flux measurement

The $e^+ + e^-$ flux over the [0.5 - 1000.0] GeV energy range has been measured independently in 74 separated energy intervals, or energy bins. In this analysis, the e^\pm energy is estimated using the energy measurement of the ECAL, which provides better accuracy than the Tracker rigidity measurement, especially at high energies. From now on, if not differently specified, the term E will refer to the ECAL energy estimation.

The energy bins have been chosen to have a width that corresponds to 2σ ECAL energy resolution, as parametrized in Equation 2.3. With this choice, the migration of e^\pm events to neighboring bins due to the finite ECAL resolution has a negligible contribution to the systematic uncertainties above 2 GeV. The resulting systematic uncertainties on the flux measurement due to the bin-to-bin migration of e^\pm events will be discussed in Section 6.1.1.

A minimum number of expected events (N_{exp}) is however required to populate the bin. If this requirement is not fulfilled, the bin width is increased. The parameter N_{exp} is varied dynamically with increasing energy. This algorithm provides a smooth binning up to 290 GeV. Above this energy, the bins have been arbitrarily set to integer bounds. The energy intervals are reported in Table F.2 together with the result of the ($e^+ + e^-$) flux measurement. Table 3.1 reports the energy intervals for the bins above ~ 150 GeV.

² A possible alternative to take the energy effect of the exposure time correctly into account is to simulate, on an event basis, the effect of the geomagnetic cutoff as it is in ISS data. For each MC event a value of geomagnetic rigidity cutoff R_{co} is randomly chosen from the distribution of R_{co} of the whole flight dataset. The MC events is assigned a weight of 0 or 1 depending on whether it satisfies the requirement to be a primary particle above R_{co} and not a secondary particle trapped in the geomagnetic field according to its measured energy E (the procedure is described in Section 4.1.4). The available MC simulation sample size is, however, reduced by the rejection of MC events that do not pass the selection. The impact of the choice between the two different procedures used to renormalize the MC events has been tested and proven to be negligible for this analysis.

Chapter 4

Electron and positron identification with the AMS experiment

The main challenge of the $(e^+ + e^-)$ flux measurement is to identify and efficiently select e^\pm within the overwhelming background of protons (p) and nuclei in a wide energy range. The TRD and ECAL detectors, developed in order to maximize to electron/proton (e/p) separation capabilities, are the key instruments used to achieve this task.

In this work, the analysis of the shower shape topology in the ECAL is used to reject most of the proton background. The energy deposit in the TRD is used to statistically separate the e^\pm signal from the proton background through a template fit to the distributions of e^\pm and protons.

Figure 4.1 shows the signature of a 600 GeV e^- collected by the AMS detector. Highlighted in the picture are the energy deposits in the AMS subdetectors. In order to identify e^\pm among all the triggered cosmic rays, the measurements of all the subdetectors have been consistently combined to provide a reliable estimation of the cosmic ray nature, energy, mass and charge.

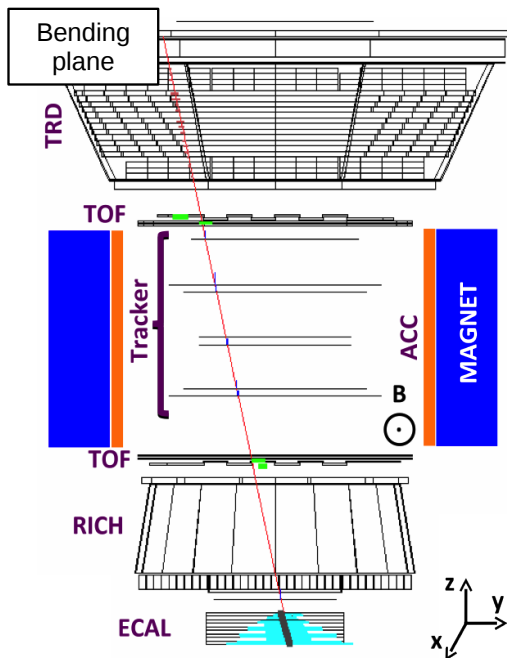


Figure 4.1: Event display of a 600 GeV e^- collected by the AMS detector. For each subdetector the energy deposit clusters are highlighted. The reconstructed track is shown in red. The event readout is triggered by the energy deposit in the TOF and in the ECAL subdetectors. The TOF measures the velocity v/c and the flight direction. The Tracker reconstructs the particle incoming direction and the curvature inside the magnetic field, providing a measurement of the particle rigidity R and charge-sign. The energy deposit in the Tracker layers is also used to measure the charge Z and to reject nuclei. The energy of the incoming e^- is measured with high precision by the ECAL. The shower shape topology in the ECAL, together with the analysis of the energy deposit in the TRD layers, finally confirms that the track is a genuine electron and not a misidentified proton.

An event pre-selection has been first applied to the whole data sample in order to select clean events

with a relativistic, downward-going, $Z=1$ particle reconstructed in the TRD, TOF, Tracker and ECAL detectors and to remove secondary particles from local interactions trapped in the geomagnetic field¹. In this chapter, the pre-selection cuts are introduced and discussed. The selection acceptance and the efficiency corrections are discussed in Chapter 5.

The pre-selected sample is mostly constituted by e^\pm and protons, with an e^\pm signal to proton background ratio (S/B) varying from $O(10\%)$ at 10 GeV down to $<O(\%)$ at energies above few hundred GeVs. A selection based on the shower shape development in the first $5 X_0$ of the ECAL – with high efficiency on the e^\pm events – has been applied to achieve a first suppression of the background. This allows to minimize the uncertainties in the final steps of the analysis.

The number of e^\pm events is then evaluated by means of a data-driven template fit to the TRD signal after a further suppression of the background component with a selection based on the full shower shape topology in the ECAL. In this chapter, the techniques developed to extract the $(e^+ + e^-)$ events are presented and the relative systematic uncertainties are discussed. The ECAL selection efficiency is discussed separately from all the other preselection cuts in this chapter.

4.1 Sample definition

In order to measure the $(e^+ + e^-)$ flux, a clean sample of e^+ and e^- has been extracted from the triggered data. In this section, the cuts used to define the sample of relativistic and downward-going $Z=1$ particles are discussed. The preselected sample is mostly constituted by e^\pm and protons. Later, in this chapter, the techniques used to identify the $(e^+ + e^-)$ events are discussed.

Differently from the separate flux analyses, the $(e^+ + e^-)$ flux measurement does not distinguish between the charge sign of the e^\pm . This constitutes one of the biggest advantages of this analysis. In order to have a reliable estimation of the e^\pm charge sign and of the charge confusion² systematic uncertainty, the separate flux analyses apply much more stringent cuts, especially on the Tracker reconstruction, to select a higher quality sample of e^\pm . In this analysis, instead, a much looser selection has been applied to select the $(e^+ + e^-)$ events. The selection relies on a small set of minimal but relevant cuts. The advantage is that the systematic error introduced by the uncertainty of each selection cut efficiencies is minimized. Statistical fluctuations are also diminished by the increase in the final sample size.

The pre-selection criteria can be separated according to the intent as following:

- (a) **Good data taking and ISS attitude³ conditions:** at first, a selection on the instrument data taking and environment parameters and on the availability of calibrated data has been applied in order to guarantee the correctness of the raw and reconstructed data.
- (b) **Geometrical selection and clean event reconstruction:** secondly, the quality of the triggered event has been checked by requiring a clean, full and self-consistent reconstruction in the whole detector.
- (c) **Charge-one particle:** subsequently, the sample has been further cleaned selecting $Z=1$ particles using the energy deposit in the TRD and in the Tracker. Events with production of energetic secondary particles due to interactions with the detector materials have also been identified and removed.

¹For the sake of brevity, secondary particles produced from the interactions of cosmic rays with the local medium and trapped in the geomagnetic field are also named *trapped secondaries* or *under-cutoff secondaries*.

²The term “charge confusion” refers to the migration of e^+ in the e^- sample (and viceversa) due to the misidentified charge sign by the Tracker.

³The term attitude refers to the orientation of a spacecraft (in this case, the ISS) in relation to its direction of motion.

- (d) **Geomagnetic cutoff selection:** finally, only particles with energy high enough to reach the detector through the geomagnetic field are selected. This allows to remove secondary particles eventually trapped in the magnetic field.

The selection has been optimized to be efficient on high energy e^\pm . Therefore, some inefficiency arises at low energy. This will be, however, correctly covered in the flux analysis by the correction for the acceptance. The selection has been applied to the whole AMS statistics collected in the first 30 months of data taking, and corresponding to $\sim 41 \times 10^9$ trigger events.

The details of each selection category are addressed in the following sections.

4.1.1 (a) Good data taking and attitude conditions

The orbital and the relevant instrument DAQ parameters are stored for each second of AMS data taking period in the Real Time Information (RTI) database. The information contained in the database is used to perform a selection on the quality of the collected raw data. This selection is based purely on time information and does not depend on the single reconstructed event properties. All the events collected during seconds of data taking that do not fulfill the DAQ quality requirements have been rejected.

First of all, any time period with hardware failures or errors affecting the top level electronic boards or, in general, with any failure in the DAQ process have been rejected. In addition to this, any period with missing raw data blocks due to unpredicted data transmission losses⁴ has also been removed from the analysis. Time periods that considerably differ from nominal operations have been identified by anomalous trigger rates (above 1800 Hz) and anomalous event size per triggered events. These events have not been analyzed. A cut on the detector livetime \mathcal{L} (evaluated on a second basis as explained in Section 2.8) has been applied to remove seconds when the DAQ was close to saturation. These cuts remove completely the SAA region (see Figure 4.2).

The AMS event quality is also affected by ISS operations. Apart from the rare periods in which the detector has to be powered down or operated in limited performances to give priority to extraordinary ISS operations, care has to be taken in order to avoid that the AMS field of view could intercept the ISS structure or even pointing to the Earth. AMS is, in fact, fixed to the ISS with a tilted angle to the zenith of $\sim 12^\circ$ with no possibility of self-orientation. The distribution of the AMS pointing angle is shown in Figure 4.2. Taking into account the $\sim 40^\circ$ field of view of AMS, a maximum deviation of 40° from the zenith angle is allowed. If this condition is not fulfilled the period has not been analyzed.

Finally, all the runs that were not dedicated to science data acquisition (this includes calibration runs, test runs, TRD refill runs, ...) have been removed.

The total impact of the selection on the DAQ conditions discussed so far is shown in Figure 4.3 as function of time. AMS has been effectively operated for 96% of the time since the first day of data taking on the ISS. 92% of the DAQ time has been selected for this analysis.

4.1.2 (b) Geometric selection and clean event reconstruction

Not every triggered event contains the minimum information needed to identify e^\pm . In particular, some of the triggered events could be outside the geometrical acceptance of the detector. Some triggers may contain more than one detected particles due to interactions in the detector or due to the simultaneous⁵ detection of two or more primary cosmic rays (*pileup* effect). Finally, some recorded events could have been triggered just by stochastic or induced noise in the detector. Therefore, a basic selection on reconstructed objects, as well as geometrical requirements, has been applied to select only events for which

⁴In the case of unpredicted data losses data have not been buffered in the AMS on-board laptop.

⁵Here, “simultaneous” is referred to more than one primary particle crossing the detector and recorded by the same trigger.

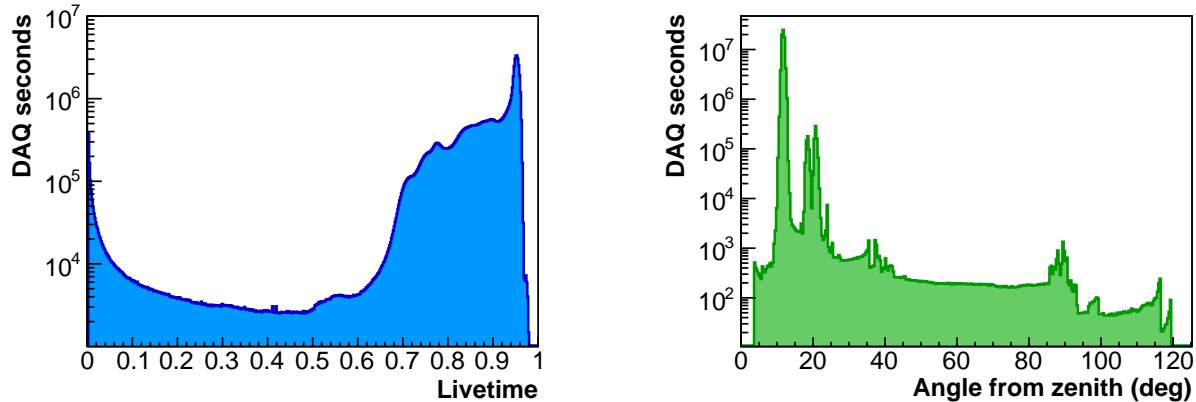


Figure 4.2: **Left:** Distribution of AMS livetime \mathcal{L} for all seconds of data taking included in the analysis. For most of the data taking period, the detector livetime is above 94%, with tails up to low values due to saturation effects that dominates in the SAA region. A cut on $\mathcal{L} > 50\%$ removes most of the SAA region and periods during which the DAQ was saturated. **Right:** Distribution of the AMS angle with respect to the zenith for all seconds of data taking included in the analysis. A maximum deviation of 40° from the zenith angle is allowed in this analysis. This removes periods when AMS was pointing towards a not nominal direction, mostly due to extraordinary ISS operations.

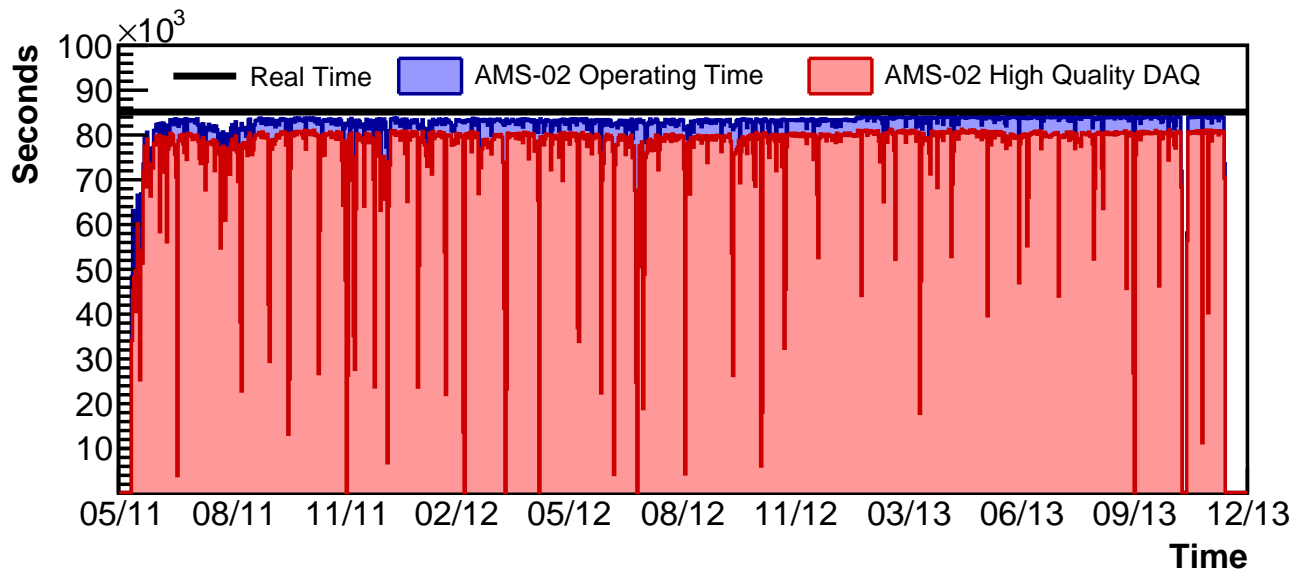


Figure 4.3: AMS DAQ quality as a function of time. Each bin corresponds to ~ 1 day. The black line represents the real time. The blue histogram corresponds to the periods in which the AMS DAQ was active and the detector was successfully taking data. AMS has been operated successfully for $\sim 96\%$ of the time since the beginning of its operations. This inefficiency is partly dominated by the first period of detector commissioning. The red histogram represents the seconds of data taking which are selected for the analysis. This corresponds to $\sim 92\%$ of the total DAQ time.

additional physical constraints could be meaningfully applied at a later stage.

First of all, any purely *unbiased* trigger event (see Section 2.8 and 5.2 for the definition) has been

removed from the analysis, as they do not fulfill any of the minimum requirements of the AMS physics trigger. Furthermore, all the events reporting any offline reconstruction software error have been also removed. Only less than 0.1% triggered events shows, however, reconstruction errors.

The event reconstruction software builds high-level objects from the raw ADC data. Raw data are clustered together for each sub-detector to build dedicated high-level physics object (like `TRD Track` objects in the TRD detector or `ECAL Shower` objects in the ECAL). Some objects, like the `ECAL Shower`, are clustered using standalone algorithms. Others, like the `Tracker Track` and the `TOF Track` objects, use information from other sub-detectors to improve the reconstruction quality⁶.

High level objects are further combined together to define the top-most level object `Particle`, that provides the most relevant properties of the detected particles combining efficiently the information gathered and reconstructed by several sub-detectors. In this analysis, the `Particle` object has been used to define the event selection. In particular, the presence of at least one basic `Particle` defined by one `Tracker Track` and one `TOF Track` with good angular and geometrical matching in the event has been required⁷. This defines the “seed” of the clustering which, from this point on, has been tuned to be optimal and efficient for high energy e^\pm .

It is worth mentioning that other approaches can be explored at this level of the analysis in order to measure the $(e^+ + e^-)$ flux. Since, in principle, the charge sign is not used to distinguish e^+ and e^- separately in this analysis, a possible alternative approach could allow also events with no clustered `Tracker Track` in the analysis. The `Tracker Track` reconstruction for e^\pm events can fail due to inefficiencies in the tracking detector itself, in the clustering algorithm or in presence of high activity in the Tracker due to interactions in the detector. Since this analysis relies on the possibility to extract a pure sample of e^- from data (using the charge sign measured by the Tracker and the matching between the energy measured by the `ECAL Shower` E and the rigidity measured by the `Tracker Track` R) to determine systematic uncertainties in various phases of the analysis, this approach has not been explored here. Parallel studies are however studying the feasibility of this approach, that would provide a gain of $\sim 10\%$ in e^\pm statistics at high energy and more at low energies.

The energy deposit timing information, provided by the TOF paddles clustered in the `TOF Track`, has been used to define the velocity $\beta = v/c$ and the direction of the incoming particle. Upward-going particles (i.e. particles crossing the AMS detector from the bottom) have been efficiently identified and removed. Moreover, only highly relativistic tracks have been selected. Figure 4.4 shows the distribution of $1/\beta$ for MC electrons. The distribution is Gaussian, as expected from the TOF velocity measurement technique. The symmetric cut $0.8 < 1/\beta < 1.2$ has been applied to every particle candidate. This selection also partially removes secondary pion, proton and nuclei contamination at energies below a few GeV, for which these particles are not yet relativistic.

The e^\pm analysis relies substantially on the ECAL measurement, in particular for the estimation of the particle energy and for the separation of e^\pm and hadrons. First of all, the extrapolation of the `Tracker Track` has been checked to pass through the ECAL volume. Particles that do not cross the calorimeter volume have been rejected. Moreover, special care has to be taken in order to define

⁶The interplay between different sub-detectors during the reconstruction phase may induce unwanted correlations between high-level objects. This has to be correctly taken into account during the evaluation of the detector acceptance and its systematic uncertainty, as discussed in detail in Section 5.4.1.1 for the case of the TOF reconstruction.

⁷The AMS official software matching algorithm for these two objects, well tested within the collaboration, has been used in this analysis.

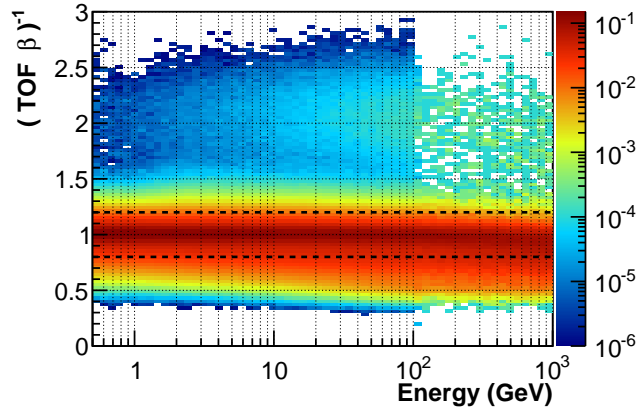


Figure 4.4: Energy dependence of $1/\beta$ for MC downward-going electrons. For each bin on the x axis, the entire slice in y is normalized to 1. The bulk of the distribution is Gaussian around the peak value $\beta \approx 1$, as expected from the TOF velocity measurement. The populations outside the bulk indicate a wrong TOF reconstruction. The black dashed lines represent the cut applied to select relativistic e^\pm .

the ECAL fiducial volume. For particles crossing the calorimeter too close to the border the energy resolution could be severely affected by lateral energy leakages in the broader region of the shower. On the other hand, a strict requirements on the fiducial volume would reduce the detector selection acceptance significantly. First of all, the extrapolated **Tracker Track** at the top and at the bottom of the ECAL is required to be contained inside the calorimeter volume (maximum distance of 32.4 cm in both x and y directions). This selection removes particles that crossed the border of the calorimeter, where the readout PMTs and the electronic boards are connected. Moreover, particles crossing vertically all the border cells of the calorimeter have been also rejected, as they suffer critical energy leakages from the side. Any other configuration, which implies that the particle crossed the calorimeter with enough inclination to be far enough away from the border, is accepted. Figure 4.5 shows the impact on the reconstructed energy resolution for MC electrons in the energy range [200.0 - 350.0] GeV. Figure 4.5 also shows the efficiency of the selection as a function of the ECAL reconstructed energy E . The blue points describe the fiducial volume used in this analysis, which represents a good compromise between high acceptance and good energy resolution even at the borders.

An additional requirement has been tested in order to check the consistency between the ECAL **Shower** and the **Tracker Track** reconstructions. The ECAL **Shower Center Of Gravity** (CoG_{ECAL}) is defined as the barycenter of the ECAL energy deposit in the whole 3D shower development. In this point the fluctuations of the energy deposit in the ECAL are minimum. At this coordinate, the geometrical distance $\Delta_{X,Y}$ between the **Tracker Track** and the ECAL **Shower** axis has been checked. In particular, on the x projection, the distance has been required to be less than 2 PMT lengths, corresponding to $\Delta_X < 3.6$ cm. On the y bending projection instead, where the effect of Bremsstrahlung emission for e^\pm inside the magnetic field affects the **Tracker** reconstruction and extrapolation, the requirement has been enlarged to $\Delta_Y < 7.2$ cm, corresponding to 4 PMT length. The distribution of $\Delta_{X,Y}$ as function of the ECAL reconstructed energy E , as well as the cut applied, is shown in Figure 4.6. The efficiency is better than 98% at energies higher than 2 GeV. At lower energies, where the growing effect of multiple scattering in the detector material worsens the accuracy of the **Tracker Track** extrapolation and the lower energy deposit in the ECAL worsens the accuracy of the ECAL **Shower** axis reconstruction, the cut efficiency is of the order of 90% at 1 GeV.

The other sub-detector that plays a primary role in the identification of e^\pm for the AMS detector is the TRD. The TRD e/p separation power relies on the different energy deposits per unit length

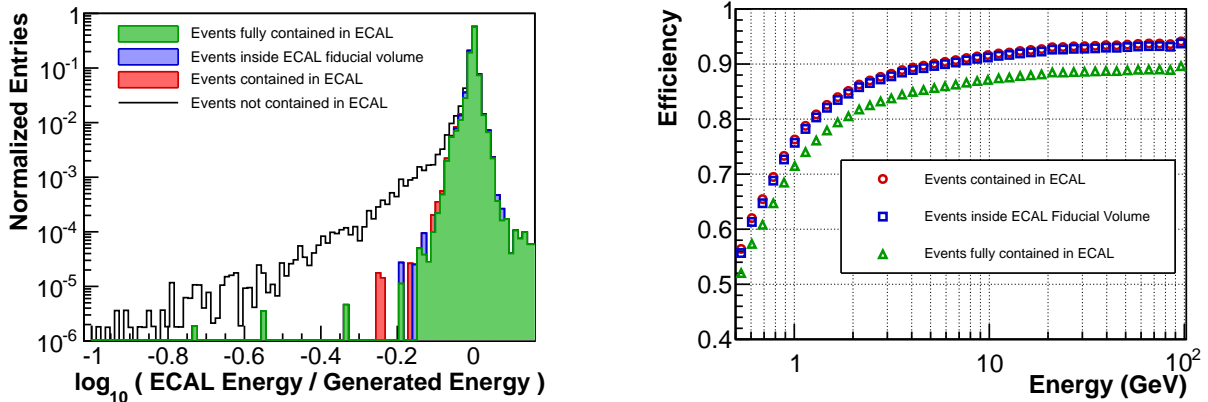


Figure 4.5: **Left:** Energy measurement resolution in the energy range [200.0 - 350.0] GeV for MC simulation electrons for different definitions of the ECAL fiducial volume. **Right:** Efficiency of the selection as function of the ECAL reconstructed energy E for different configurations. The normalization is set by events with a reconstructed ECAL shower.

Electrons which are “fully” contained in the ECAL (Tracker Track crossing the top and bottom of the ECAL within 31.5 cm from the border) have the lowest impact due to lateral leakages (here, in green). However, the efficiency of the selection is rather low. Allowing the Tracker Track to cross the top OR the bottom of the ECAL also in the last cell enhances the efficiency by $\sim 5\%$ without any worsening of the energy resolution. This is therefore used as the definition of ECAL fiducial volume in this analysis (here, in blue). Other configurations, which imply particles crossing vertically the border of the calorimeter (here, in red) or even crossing the calorimeter from the sides (here, in black), are rejected.

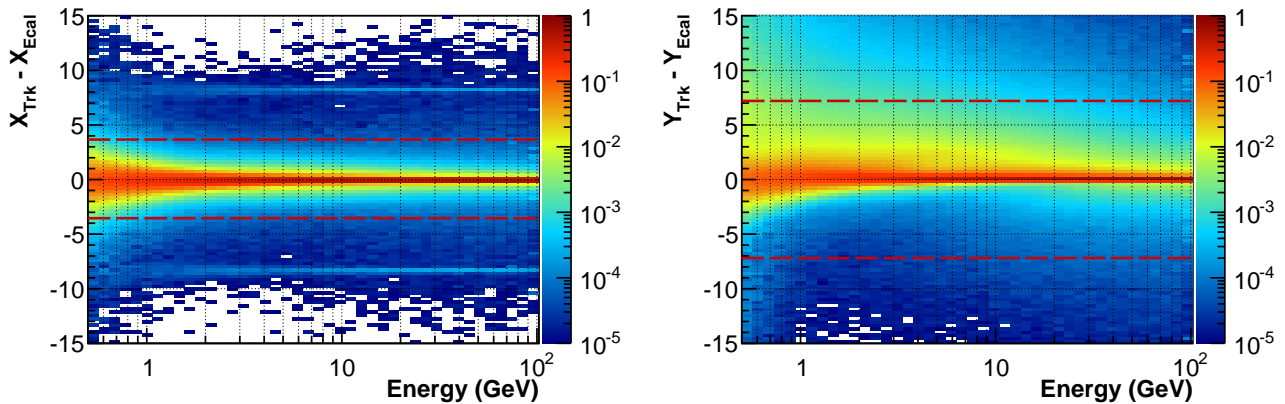


Figure 4.6: Distribution of the distance between the Tracker Track extrapolation and the ECAL Shower reconstructed axis in the x view (Δ_X , **Left**) and in the y bending view (Δ_Y , **Right**) as function of the ECAL reconstructed energy E for MC electrons. Distances are evaluate at the ECAL shower energy deposit barycenter. For each bin on the x axis, the entire slice in y is normalized to 1. The cut used to define the geometrical matching is superimposed. While in the x view the matching is symmetric, in the bending y view the accuracy of the Tracker extrapolation is worsened by Bremsstrahlung events, which also induces an asymmetry in the distribution. The same distribution, for positrons, shows in the y view similar tails in the opposite direction. The symmetric cut avoids the introduction of biases between the e^+ and the e^- selection.

(dE/dX^{tube}) for electrons and protons. The energy deposit in the straw tubes (Δ_E^{tube}) depends on the path length inside the tube. This last factor is used to normalize Δ_E^{tube} to the energy deposit per unit length dE/dX^{tube} . In this analysis the **Tracker Track** has been extrapolated in the TRD volume. Only the TRD hits crossed by the **Tracker Track** are clustered and used to retrieve the TRD information. Events with a low number of TRD hits matching with the **Tracker Track** ($N_{\text{hit}}^{\text{TRD}}$) have been rejected. This ensured a enough sampling of the energy deposit in the TRD to provide a reliable estimation of the TRD classification tools. It also guarantees that the primary particle crossed through the geometrical volume of the TRD. Finally, it contributes to the rejection of events with particularly wrong **Tracker Track** reconstruction or highly affected by multiple scattering in the detector. Figure 4.7 shows the distribution of $N_{\text{hit}}^{\text{TRD}}$. The events having $N_{\text{hit}}^{\text{TRD}} < 9$ have been removed from the analysis. The efficiency at high energies is of the order of 99.2% with a decreasing trend at low energies.

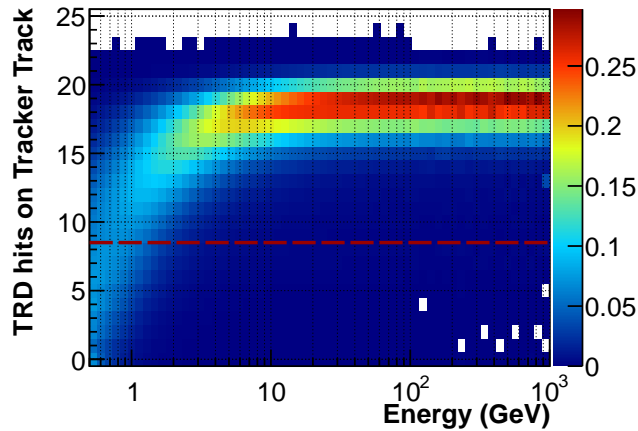


Figure 4.7: Number of TRD hits crossed by the Tracker Track extrapolation for MC electrons as function of the ECAL reconstructed energy. For each bin on the x axis, the entire slice in y is normalized to 1. Only events having at least 9 (out of 20) TRD layers with a hit in the layer matched with the Tracker Track are accepted for the e^\pm analysis. The cut is shown in red. The efficiency of the selection is better than 99% at high energies. At low energies, it decreases mainly because of the effect of multiple scattering which limits the accuracy of the Tracker Track extrapolation.

4.1.3 (c) Charge-one particle

After the selection described previously in Section 4.1.2, the sample consists of events with relativistic, down-going particles crossing the TRD, TOF, Tracker and ECAL sub-detectors. Further requirements are applied in order to ensure that the sample is clean and suitable for the e^\pm analysis by removing nuclei and interaction events. In the context of this analysis, the term “interaction events” refers to the production of secondary e^\pm by interactions of primary cosmic rays (including protons and nuclei) with the detector material. Secondary e^\pm can cross the calorimeter and can be reconstructed as primary particles in the AMS instead of the triggering particle, and could constitute a source of irreducible background for this analysis.

The energy deposit in the strips of the inner Tracker layers (2 - 8) is used to estimate the charge of the particle (Z^{TRK}) through the analysis of the ionization yield. Other sub-detectors of AMS can be used to infer the charge of the particle. Figure 4.8 shows, as an example, the correlation of the charge measured by Tracker and by the TOF for events in the energy range [50.0 - 80.0] GeV collected in space. Despite the use of the TOF charge measurement could increase the accuracy of the charge separation

also for e^\pm , its resolution is worse compared to the Tracker measurement. In order to reduce systematic effects and to maximize the data sample, only a selection on the Inner Tracker charge ($0 < Z^{\text{TRK}} < 1.5$) has been applied in this analysis.

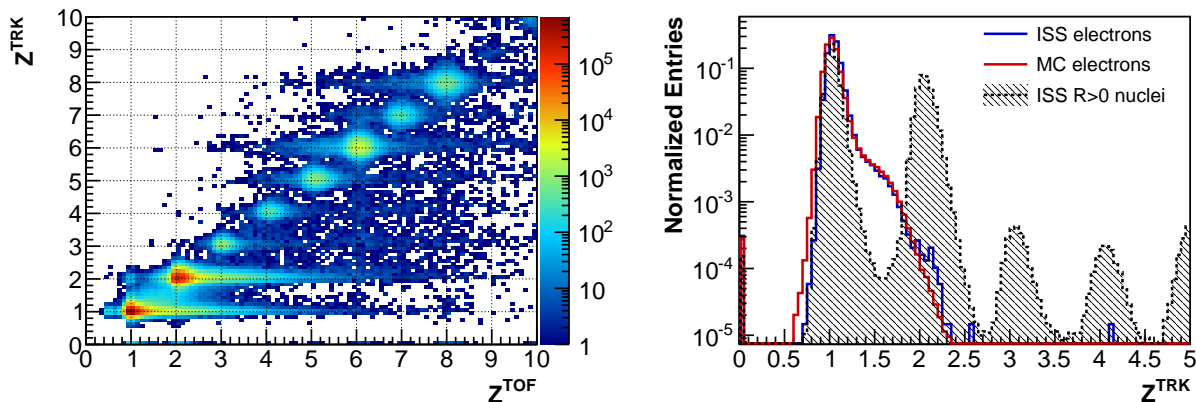


Figure 4.8: **Left:** Distribution of the charge estimation inferred by the ionization measurement in the TOF paddles (Z^{TOF}) and in the Tracker silicon strips (Z^{TRK}) for events collected in space in the energy range [50.0 - 80.0] GeV. The AMS charge separation capabilities, fundamental for the analysis of nuclei, can be appreciated. In this analysis however, in order to maximize the statistics and to reduce systematic uncertainties of the selection efficiencies, only a cut on the Tracker charge Z^{TRK} is applied. **Right:** distribution of the charge measured by the Inner Tracker Z^{TRK} for positively charged nuclei in data (black) and for electrons selected in data (blue) and in the MC simulation (red) in the energy range [50.0 - 80.0] GeV. The structures of the distribution in data, induced by interactions of e^\pm , are well confirmed by the MC simulation.

Figure 4.8 shows the distribution of the Tracker measured charge Z^{TRK} for e^\pm and all nuclei in the [50.0 - 80.0] GeV energy range. The separation power of Z^{TRK} is enough to remove most of the $Z \geq 2$ nuclear background. The tail of e^\pm for $Z^{\text{TRK}} > 1.5$ arising in the data, which is a clear indication of interactions before the Inner Tracker or Bremsstrahlung events with collinear conversion in e^\pm pairs, is confirmed by the MC simulation. The cut $0 < Z^{\text{TRK}} < 1.5$ removes this contributions, which is negligible up to medium energies and becomes a source of inefficiency at higher energies as shown in detail in Section 5.4.1.6. The same section shows that the MC/data agreement is, however, good and the systematic uncertainties associated to this selection has a negligible impact on the total error.

The energy deposit in the TRD can also be used to build a classifier dedicated to the separation between e^\pm and He nuclei. Following the same approach that will be described in detail for the e/p separation in Section 4.2.2, the energy deposit in the 20 TRD layers is combined to build a likelihood ratio classifier $\text{TRD}_{\text{thr}}^{e/\text{He}}$ which maximizes the separation between e^\pm and He nuclei [216]. A selection on $\text{TRD}_{\text{thr}}^{e/\text{He}}$ has been therefore used to efficiently remove any residual contamination of $Z=2$ nuclei. The separation power of this classifier allows to reduce the contamination of He nuclei efficiently. Figure 4.9 shows the distribution of $\text{TRD}_{\text{thr}}^{e/\text{He}}$ for e^\pm and He nuclei in the energy range [50.0 - 80.0] GeV. In this analysis, the cut $\text{TRD}_{\text{thr}}^{e/\text{He}} < 0.8$ enhances the purity of the e^\pm sample with a negligible inefficiency on the signal and, therefore, with a negligible impact on the measurement systematic.

An additional requirement applied on the e^\pm sample is needed to suppress, as much as possible, the number of interaction events in the detector. Given the amount of material in the detector a non-negligible fraction of e^\pm or proton and nuclei events can interact in the detector and produce spurious signals. The reasons to suppress this kind of events are many. First of all, interaction events produce a high level of activity and noise in the detector, afflicting the quality of the clustering and of the re-

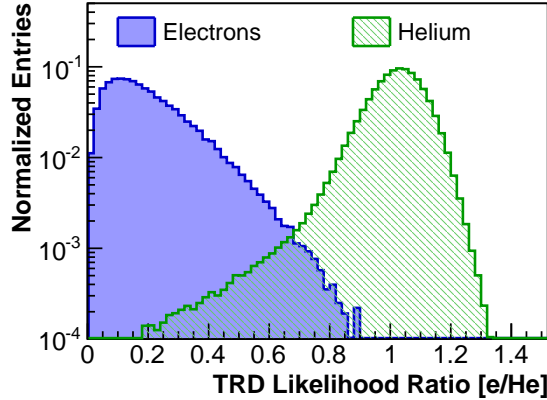


Figure 4.9: TRD e/He likelihood ratio ($TRD_{lhr}^{e/He}$) distribution for electrons and Helium nuclei, selected from data in the energy range [50.0 - 80.0] using a selection based on the charge sign and on the calorimeter. The cut $TRD_{lhr}^{e/He} < 0.8$ assures the rejection of any Helium contamination left after the selection on the Tracker charge estimation with a negligible inefficiency on the e^\pm signal in the whole energy range.

construction algorithms and resulting in a worsening of the measured particle quantities. Moreover, interaction events may introduce unwanted correlations between different sub-detectors, especially between the TRD and the ECAL. High energetic secondaries produced in the TRD can indeed pass through the magnet without suffering enough deflection and can be clustered together with the primary particle in the ECAL.

In addition, proton or nuclei events interacting in the detector can be a source of e^\pm . This is not a problem for hadrons interacting after the upper TOF, as the magnet sweeps out low energy secondaries and the combined measurement of the TRD and ECAL sub-detectors is used to resolve the nature of the primary particle. For events interacting inside or even before TRD, however, there is a non-negligible probability that the secondary e^\pm have enough energy to be reconstructed as primary particles in the detector. This kind of events is a source of irreducible background in the analysis, with increasing impact at high energies. Dedicated studies [217] have shown that the amount of this irreducible background is non-negligible for energies higher than 300 GeV, and it has an impact on the measurement systematic even at lower energies. For these reasons, an effort has been done to reduce the number of interaction events in this analysis.

Interaction events can be identified in several ways. Naively, a dedicated selection on the energy deposits in the TOF paddles can be used to locate energy deposit over the average expectations for single particles. This selection is, however, not fully efficient and its MC description is not satisfactory to justify its use.

On the other hand interaction events in the TRD and above may result in the reconstruction of more than one **Tracker Track** object. The number of reconstructed **Tracker Track** (N^{TRK}) can be used to identify interaction events. This requirement also increases the robustness of the matching algorithms. Systematic uncertainties introduced by the wrong matching between different sub-detector objects may, in fact, arise for multi-track events.

The requirement of having single track events ($N^{TRK} = 1$) is effective enough to reduce the systematic uncertainties due to irreducible background in the ($e^+ + e^-$) flux analysis to a negligible value with respect to other sources of errors. Therefore, the $N^{TRK} = 1$ selection has been applied to select clean e^\pm sample. The uncertainty on the efficiency of this selection is, however, non-negligible and it constitutes one of the largest measurement systematic uncertainties at medium energies. The effect on the measurement

systematic uncertainties of this requirement will be discussed in Section 5.4.1.7.

The energy dependence of the number of reconstructed Tracker Track (N^{TRK}) and the efficiency of the single track requirement is shown in Figure 4.10 for MC electrons after the Z^{TRK} and $\text{TRD}_{\text{thr}}^{e/\text{He}}$ selection. The number of multi-track events is below 10% in the whole energy range, and does not depend significantly on the e^\pm energy.

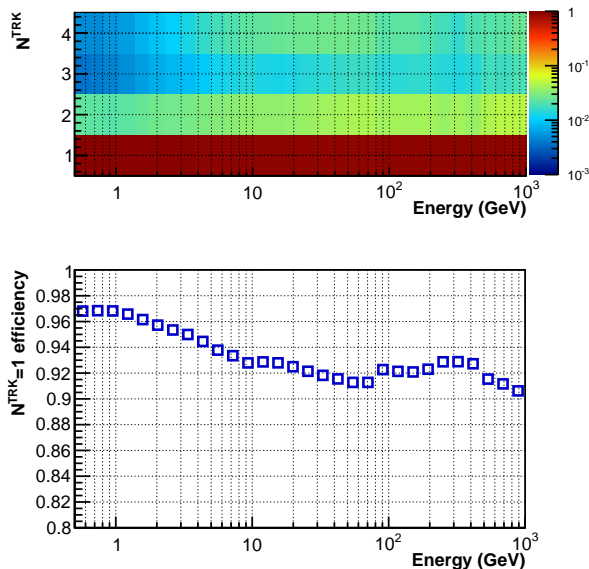


Figure 4.10: **Top:** Distribution of the number of reconstructed Tracker track N^{TRK} as a function of energy for MC electrons. For each bin on the x axis, the entire slice in y is normalized to 1. **Bottom:** Efficiency of the single track requirement for MC electrons. The amount of multi-track events, correlated to the activity in the detector and to the interactions in the detector, is below 10% in the whole energy range. However, as discussed in Section 5.4.1.7, the efficiency of the single track selection depends on the additional cuts on the event quality applied to define the e^- sample.

In principle, interaction events can also be tagged and evaluated using the timing information stored in the ACC hits. Interaction events are usually correlated with high activity in the ACC paddles. The timing correlation between ACC and TOF hits can be used to distinguish between ECAL back-splash and interaction events⁸. Figure 4.11 shows the clear correlation between N^{TRK} and the number of interactions identified in the event N^{int} using this technique. The requirement of single shower reconstruction, $N^{\text{TRK}} = 1$, allows to reduce interaction effects in the event as expected. Any further requirement on N^{int} could improve the quality of the events. The MC simulation description for N^{int} is, however, not satisfactory enough and the systematic uncertainty introduced by this additional requirement would worsen the accuracy of the measurement. Therefore, N^{int} has been used only as an auxiliary variable to support the calculation of the acceptance systematic error, as discussed in detail in Section 5.4.2.

4.1.4 (d) Geomagnetic cutoff selection

After the selection described in Section 4.1.1, 4.1.2 and 4.1.3 the event collected and reconstructed by the detector is in principle a good $Z = 1$ candidate for the $(e^+ + e^-)$ analysis. Part of the collected

⁸If $\Delta t_{\text{bks,int}}$ is defined as the time difference between the TOF hit and the ACC hit for respectively ECAL back-splash and interaction events, on average $\Delta t_{\text{bks}} > \Delta t_{\text{int}}$. The time needed by secondary particles produced before the calorimeter to reach the ACC counter is in fact smaller than the time needed for the primary particle to reach the calorimeter and produce back-splash particles with enough energy to reach and produce a signal in the ACC paddles.

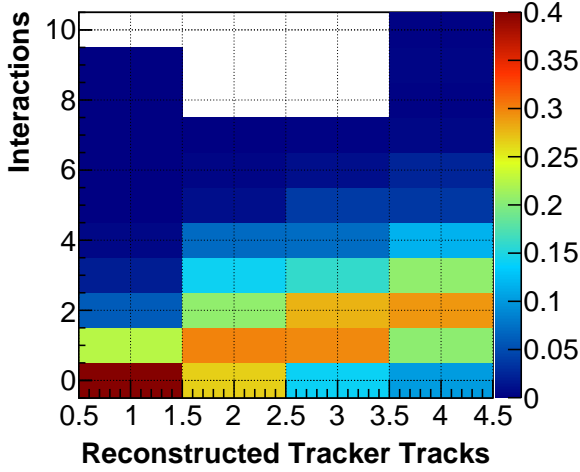


Figure 4.11: Correlation between interaction events identified in the detector using the timing information from ACC and TOF hits (N^{int}) as function of the number of reconstructed Tracker tracks (N^{TRK}) for MC electrons in the energy range [350.0 - 500.0] GeV. For each bin on the x axis, the entire slice in y is normalized to 1. The requirement of single track reconstruction reduces the number of interactions in the events. This is used to reduce the amount of irreducible background from e^{\pm} secondaries produced by interactions of hadrons at the top of the detector. The cut also reduces the correlations between subdetectors induced by high activity in the detector.

particles could be, however, not representative of the cosmic e^{\pm} flux⁹.

A fraction of particles crossing the AMS detector are, indeed, low energy secondary particles produced by the interaction of primaries with the local medium and trapped in the geomagnetic field. These secondaries have to be rejected from the analysis sample.

For each second of data taking the ISS geomagnetic coordinates are calculated assuming a simple shifted tilted dipole model [218]. The Størmer Rigidity Cutoff $R_{co}^{\pm}(\theta, \phi)$ is calculated assuming positive and negative charged particle using Equation 1.5 as function of the geomagnetic galactic altitude and azimuthal angles $\theta^{(gal)}$, $\phi^{(gal)}$ and then transformed in the AMS reference frame directions θ, ϕ . Finally, the Maximum Rigidity cutoff $R_{max}^{40^{\circ}}$ is calculated as the maximum value of $R_{co}^{\pm}(\theta, \phi)$ for positive and negative particle in the whole AMS field of view, here conservatively assumed to be 40° :

$$R_{max}^{40^{\circ}} = \max \{ R_{co}^{+}(\theta, \phi), R_{co}^{-}(\theta, \phi) \}, \quad \theta, \phi \in \Omega_{40^{\circ}}^{FOV} \quad (4.1)$$

$\Omega_{40^{\circ}}^{FOV}$ being the domain of θ and ϕ for the AMS field of view. Figure 4.12 shows the average value of $R_{max}^{40^{\circ}}$ as function of the ISS orbit. The strength of the geomagnetic field varies with the geographic latitude. It is minimum at the polar regions and gets the maximum value at the equator. The $R_{max}^{40^{\circ}}$ varies, accordingly, from few GV to ~ 30 GV.

Only particles with rigidity above $R_{max}^{40^{\circ}}$, independently from the charge sign or from the arrival direction, are purely primaries with no trapped secondaries contamination. However, the evaluation of $R_{max}^{40^{\circ}}$ is subject to uncertainties due to the validity of the geomagnetic model. Different models, including data driven approaches, have been tested and compared [219]. A safety factor of 1.2 has been used to completely cover all the uncertainties and to guarantee a selection with no residual contamination of trapped secondaries. For each particle with energy E belonging to the energy bin $[E_{min}, E_{max}]$, the particle has been selected for the flux analysis only if $E_{min} > 1.2 \times R_{max}^{40^{\circ}}$. Since $E > E_{min}$, this requirement is more conservative but it is completely consistent with the evaluation of the exposure

⁹ A minor fraction of incoming particles could be secondaries produced by the interaction of cosmic rays with the local ISS environment. The AMS field of view is not shaded by any obstacle during nominal ISS operations and no secondaries produced according to this mechanism are expected to be collected. ISS solar arrays could, however, “shade” the AMS field of view for a limited period of time. Therefore, all the particles with reconstructed trajectory traversing the solar array panels have been rejected from the analysis. The periods in which the solar arrays were however shading the AMS field of view is limited, and this cut removes $\ll \%$ of the events. Most of the particles which do not originate from outside the magnetosphere are however secondary particle trapped in the geomagnetic field. The rejection of these secondaries is discussed in the text.

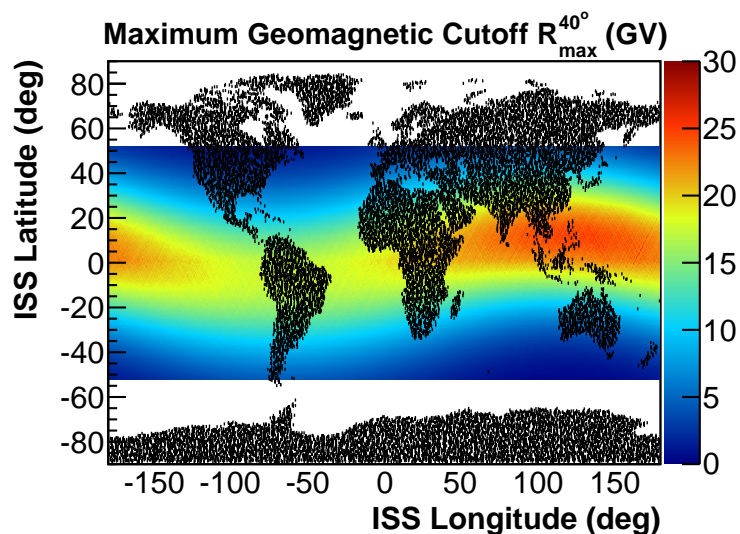


Figure 4.12: Maximum geomagnetic cutoff R_{\max}^{40} as a function of the ISS orbit position in geographical coordinates. The cutoff value varies from ~ 1 GV in the polar regions to ~ 30 GV in the equatorial regions. Particles with rigidity below this value could be secondaries trapped in closed geomagnetic field trajectories. Higher energy particles reaching the detector are primaries coming from outside the Earth’s magnetosphere.

time, as discussed in detail in Section 5.1. The efficiency of this selection amounts to $\sim 20\%$ on the total sample. The inefficiency is dominated mostly by the proton component. For protons the energy measured by the ECAL E is much smaller than the true proton energy, and most of protons above the cutoff are rejected with this cut. For e^{\pm} the efficiency of this cut is approximately 100%.

4.1.5 Selection summary

At the end of the selection described in Section [4.1.1 – 4.1.4], the selected sample consists of $Z=1$ primary particles containing a high statistics sample of the $(e^+ + e^-)$ events. The final selected dataset available corresponds to $\sim 125 \times 10^6$ events with energies above 0.5 GeV, mostly dominated by protons. Figure 4.13 shows the efficiency of the selection on the events triggered by AMS. The e^{\pm} signal in the selected sample is identified and extracted from the overwhelming proton background as explained in Section 4.2.

4.2 ECAL and TRD and their role in the e^{\pm} identification

The sample selected using the criteria described in Section 4.1 consists of the e^{\pm} component and, mostly, of protons (p) and a small, negligible fraction of antiprotons (\bar{p}). From now on, the term “signal” will refer to e^{\pm} or to $(e^+ + e^-)$, while the term “background” will refer to p.

In order to extract the number of e^{\pm} from the overwhelming proton background, the ECAL and TRD separation capabilities have been exploited. The response of the ECAL and TRD detectors is the same for e^- and e^+ . The magnetic field between the two sub-detector (that minimizes the inter-correlations) and the detector measurement redundancy allow to select a pure sample of e^- from data with one sub-detector to tune and develop the separation tools of the other sub-detector, and vice versa. The proton background is suppressed in the negative charge sign sample and the purity of the e^- sample is consequently enhanced. The use of e^- control samples selected from data to calibrate and study the ECAL and TRD detectors allows to minimize the dependence of the analysis on the MC simulation and

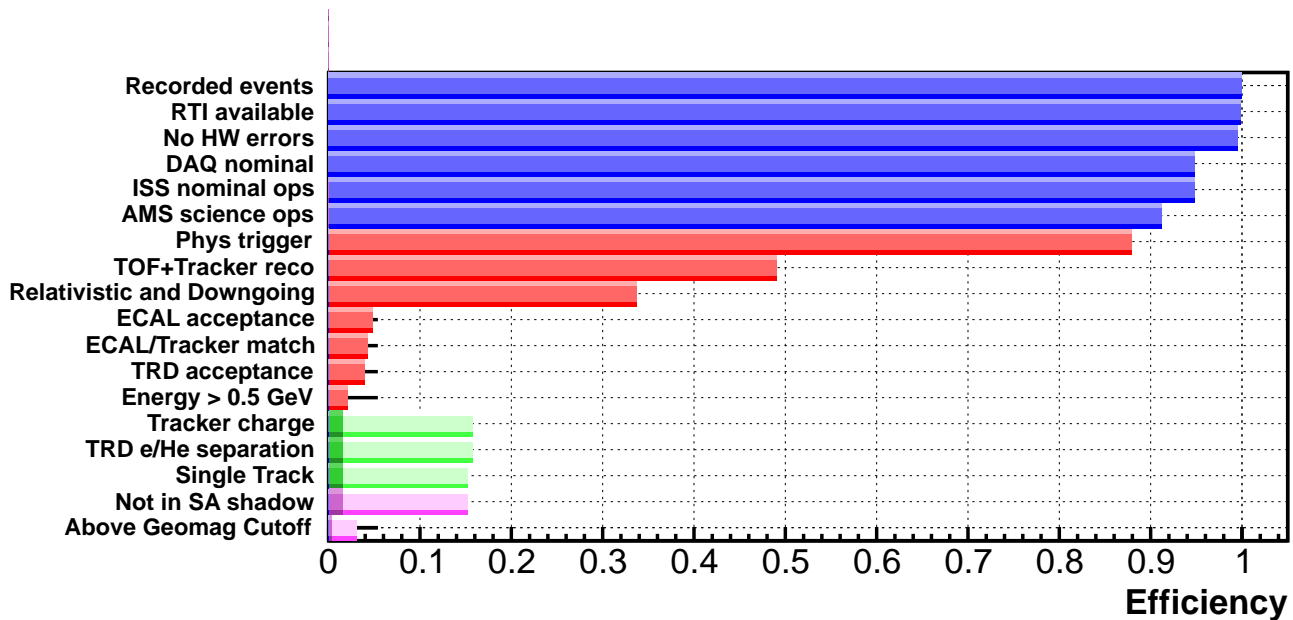


Figure 4.13: Efficiency of the selection on the total AMS triggered data for: **a)** Good data taking and ISS attitude conditions (blue) **b)** Geometrical selection and clean event reconstruction (red) **c)** Charge-one particle (green) **d)** Primary particle selection (violet). The lighter contributions for **c)** and **d)** are multiplied by 10 in order to appreciate the effect of the selection. Among 41×10^9 triggered events, $\sim 125 \times 10^6$ events ($\sim 3\%$ of the total dataset collected by AMS) are selected for the analysis. The selected sample consists of e^\pm and mostly protons, which have been identified and separated by means of the ECAL and TRD detectors as explained in the next section.

to reduce the systematic uncertainties of the measurement. In this section, the basic properties of the detectors, as well as the tools that have been used to extract the e^\pm signal, are introduced and discussed.

4.2.1 ECAL electron/proton separation

Electrons impinging the ECAL calorimeter start electromagnetic showers which have a different topology from hadronic showers. Electromagnetic (em) showers are mostly only a combination of Bremsstrahlung and pair production effects. The physics of em shower development and its parametrization is, in general, well known [204]. Hadronic showering processes are, instead, a succession of inelastic hadronic interactions and hadron decays. Hadronic showers are characterized by a broader lateral and longitudinal distribution with respect to the em showers, with an em core due to the decay of neutral pions $\pi^0 \rightarrow \gamma\gamma$. Moreover, since the ECAL material corresponds to only $\sim 0.6\lambda$ (nuclear interaction lengths) for perpendicular crossing particle, only $\sim 50\%$ of the protons start nuclear interactions in the calorimeter. The remaining half behave as Minimum Ionizing Particles (MIPs) and they only ionize, leaving on average < 250 MeV in the detector. The identification MIP protons is, therefore, trivial.

The 3D ECAL shower reconstruction allows to sample the transverse and longitudinal shower shape using the measurement of the of energy deposit in individual cells. In principle, a cut based approach could be used to explore the shower topology properties by a selection on each variable. However, the efficiency of each cut would have to be evaluated separately, and the correlations between different variables would not be explored. In order to maximize the rejection power of the calorimeter, a MultiVariate Approach (MVA) has been adopted. In particular, a Boosted Decision Tree (BDT) [220] technique has been developed to implement the e/p separation. The algorithm has been developed on test beam events

[202] and then applied on data collected in space [221]. The BDT has been trained¹⁰ on e^- and protons selected from ISS data, with no input from MC. A strong selection on the TRD energy deposit, using the tools which will be introduced in Section 4.2.2, and on the charge sign, allows to extract a pure sample of protons and e^- that have been used to train the BDT. The classification tool used in this analysis, ECAL_{BDT} , relies on a total of 22 variables describing the *longitudinal* shower development and 39 variables describing the *lateral* shower development. The variables have been renormalized to remove their energy dependence, as described in [222]. The ECAL_{BDT} has been trained in 14 separate energy bins, the last one starting at ~ 250 GeV, in order to locally maximize the e/p separation. Figure 4.14 shows the distribution of ECAL_{BDT} for electrons and protons from ISS data in the energy range [100.0 - 200.0] GeV. The distribution of ECAL_{BDT} for electrons is composed of one only population with tails coming from lower quality events. For protons it is possible to distinguish several populations, which are correlated to the interaction depth in the calorimeter. Protons interacting early in the calorimeter represent the most difficult background to separate for the ECAL, as the energy deposit and the electromagnetic component of the shower are most similar to e^\pm em showers.

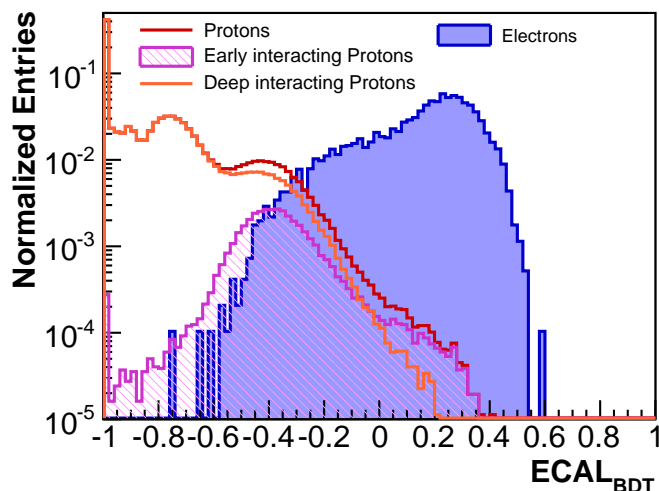


Figure 4.14: ECAL_{BDT} distribution for electrons and protons selected from data using the TRD and the charge sign in the energy range [100.0 - 200.0] GeV. The distributions are normalized to the number of entries. Electrons (in blue) are characterized by high values of ECAL_{BDT} . Protons (in red) have lower values of ECAL_{BDT} . Values toward -1 indicate protons interacting deeply in the calorimeter (in orange) which can be easily distinguished from e^\pm em showers. Proton interacting in the first layers of the calorimeter (in violet) have a shower topology more comparable to e^\pm , that renders the discrimination less effective.

Figure 4.15 shows the energy dependence of ECAL_{BDT} for e^- selected from data. The borders of the energy training intervals show up as discontinuities in the classifier energy distribution. At high energies even a strong selection on TRD and Tracker is not sufficient to select a pure control sample of e^- and the distribution is contaminated by a non-negligible proton contribution. An important step of this analysis is the calculation of the ECAL_{BDT} efficiency for the selections used to suppress the proton background at high energies. The contamination of protons in the e^- control sample prevents to calculate

¹⁰The *training* procedure is the phase in which a pure sample of signal and background events are used by the MVA algorithm to “learn” the differences in the variable distributions and their correlations. The algorithm can therefore construct a set of criteria that will be used to define the nature of unknown events during the *application* phase.

the ECAL_{BDT} efficiency directly from data using a simple *Tag&Probe*¹¹ method. The unphysical nature of the classifier and the choice to train the classifier in separate energy bins do not allow to extrapolate the results obtained at low energies (for which the *Tag&Probe* approach is still feasible) to the high energy range.

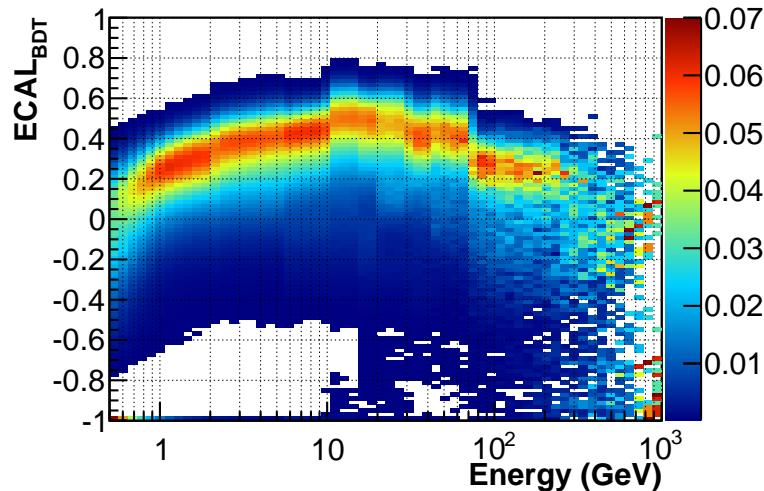


Figure 4.15: Energy dependence of ECAL_{BDT} for e^- selected from data using the TRD and the charge sign. For each bin on the x axis, the entire slice in y is normalized to 1. The discontinuities are a consequence of the definition of training energy ranges to locally maximize the e/p separation power. At high energies, the proton contamination that survives after the strong TRD and Tracker cuts is clearly visible at $\text{ECAL}_{\text{BDT}} \sim -1$.

The use of the MC simulation represents an alternative method to get a description of the properties of the classifier at high energies. The distribution of ECAL_{BDT} for data and MC e^- in the energy range [100.0 - 200.0] GeV is shown in Figure 4.16. The description of the shower development in the MC simulation is not accurate enough to provide a satisfactory agreement. The agreement improves at low energies, but the unphysical nature of the ECAL_{BDT} classifier and the split in energy ranges prevent any safe extrapolation at high energies. The data/MC disagreement is dominated by the description of the lateral development of the shower. As shown in Figure 4.17 for a sample of topology variables for e^- in the [80.0 - 100.0] GeV range, the description of the longitudinal shower development is well represented in the MC simulation. The lateral development simulation shows strong deviations from data. The MC simulation lateral shape is, in fact, “narrower” than the shape of the e^\pm showers measured in data.

As described later in Section 4.3, the selection of e^\pm for the measurement of the $(e^+ + e^-)$ flux relies on the fit of the TRD energy deposit shape to the data. The same technique allows also to calculate the ECAL_{BDT} efficiency from data in the whole energy range with limited systematic impact on the measurement uncertainty. In order to correctly exploit this technique up to the TeV energy, a preliminary selection based on ECAL is necessary to remove the bulk of the proton background. In Section 4.2.1.2, the development of a dedicated ECAL MC tool, whose efficiency on data can be evaluated with negligible systematic uncertainties up to the TeV energies, will be presented.

¹¹The term *Tag&Probe* refers to a method used to identify a certain population in presence of two (or more) discriminating variables. In this case, electrons from data can be *tagged* using a selection on TRD and Tracker. Assuming that any correlation between the variables is negligible, the tagged sample is representative of the whole population, and can be used to *probe* (or test) several properties of the population directly from data.

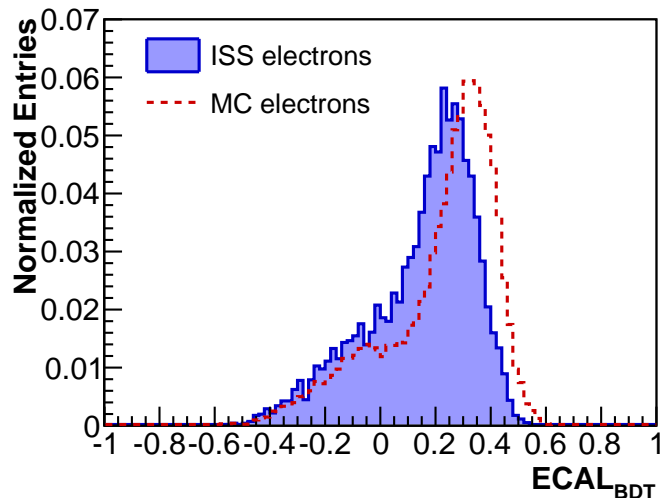


Figure 4.16: $ECAL_{BDT}$ distribution for data (blue) and MC simulation (red) e^- in the energy range [100.0 - 200.0] GeV. Data e^- are selected using the TRD and Tracker information. The same selection is applied on MC e^- . The discrepancy in the MC simulation is mostly due to the shower lateral energy distribution description, which does not fully agree with data.

4.2.1.1 Tracker role in electron/proton separation

The measurement of the particle rigidity R and momentum p using the AMS Tracker can substantially increase the e/p separation capabilities, when combined with the energy measurement by ECAL E .

For e^\pm the momentum measurement is expected to be compatible with the energy measurement inside the Tracker resolution. For Bremsstrahlung events in the Tracker, however, part of the energy is carried away by the radiated photon and the curvature measurement is overestimated. The photon is however mostly collinear with the primary e^\pm and its energy deposit in the ECAL is clustered together with the primary shower. For Bremsstrahlung events, therefore, $E > p$.

For protons, instead, the energy deposit in ECAL is on average much smaller than the incoming particle energy. Protons interact deep in the calorimeter and suffer usually energy leakages, or they do not interact at all and only leave an ionization track. Therefore, for protons, $E < p$. The ECAL response to protons is shown in Figure 4.18 for 400 GV protons collected during the test beam at ground and for MC simulation protons in the [2,4000] GeV energy range. The ECAL energy measurement for protons is always smaller than the proton energy. For $\sim 50\%$ of the protons that only leave an ionization track the ECAL energy measurement is below 0.5 GeV. These protons are easily identified and do not concur as background for the $(e^+ + e^-)$ flux analysis. For interacting protons of a given true energy E_{true} , the energy measurement E has a wide distribution peaking around $E \sim 1/2 E_{true}$. This has a relevant impact on the e^\pm analysis, as the background protons in each energy bin are typically much more energetic than the e^\pm signal events, with an energy spectrum starting roughly from the bin energy up to well above the TeV. Although the flux of high energy proton is suppressed by the flux factor, this feature of the proton background has a visible systematic effect in the signal measurement procedure, as discussed later in Section 4.4.

The ratio between the ECAL energy deposit E_{dep} and the momentum measurement by the Tracker p is thus a powerful discriminating variable, that can be used to increase the e/p separation capabilities of AMS. Figure 4.19 shows, on the left, the distribution of E_{dep}/p for electrons and protons in the [80.0 - 100.0] GeV energy range. The discrimination is clear. The separation power decreases, however, with

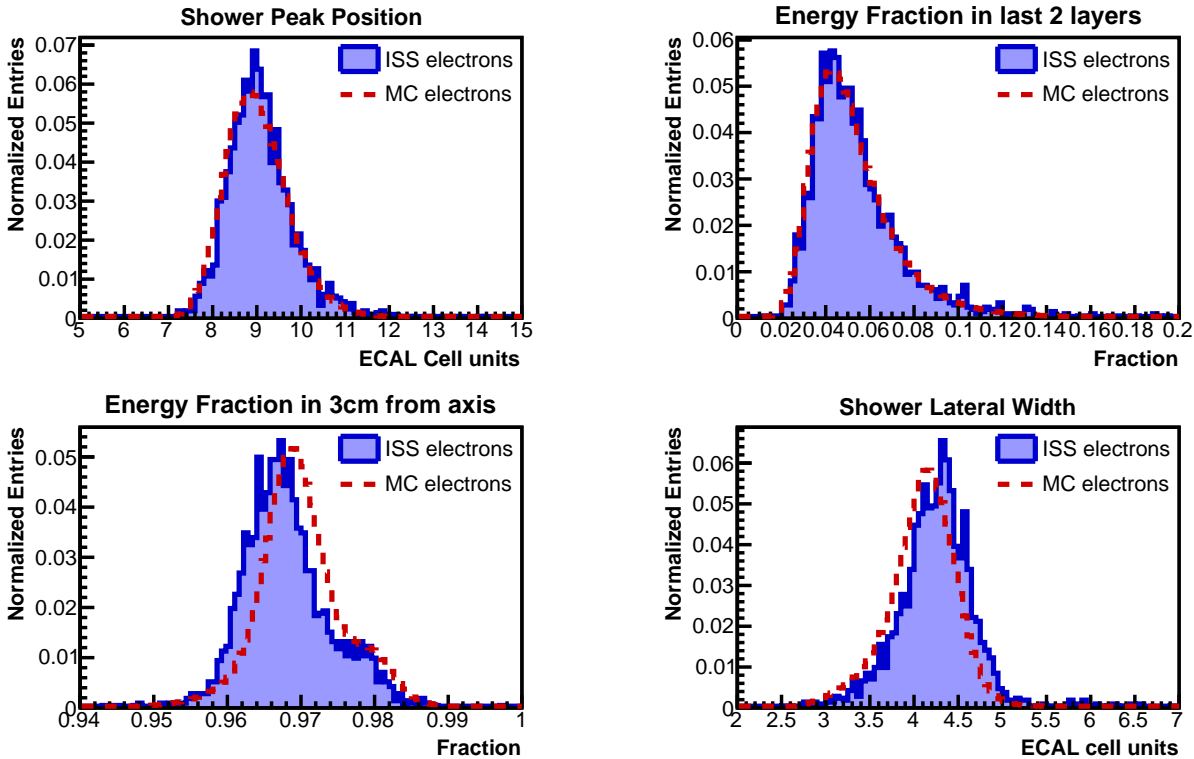


Figure 4.17: Selection of topology variables for data (blue) and MC simulation (red) e^- in the [80.0 - 100.0] GeV energy range. The longitudinal development of the shower, described by the two top variables, is well represented in the MC simulation. The lateral development, here represented by the bottom plots, shows a non-negligible deviations from the data. The MC simulated shower is, on average, narrower than real e^\pm showers. This is due to known limitations of the AMS MC simulation in the description of the low energy components of the em showers which define the energy deposit in the most lateral borders of the shower.

increasing energy. For higher ECAL measured energy, in fact, the energy deposit of protons tends to agree more and more with the primary energy.

The E_{dep}/p rejection capabilities can be increased requiring more stringent cuts on the Tracker reconstruction quality. This has not been done, however, in this analysis. The $(e^+ + e^-)$ flux measurement does not rely on the track curvature reconstruction quality, since no selection on the charge sign is applied to identify the $(e^+ + e^-)$ signal. The e^\pm dataset has been therefore maximized by a loose selection on the Tracker track, as discussed in Section 4.1. Because of this, the E_{dep}/p ratio has been used only as a crosscheck tool to investigate systematic uncertainties, and it has not been applied directly to select the e^\pm sample for the flux measurement. This also removes the contribution given by the uncertainty on the E_{dep}/p efficiency in the measurement uncertainty, providing a more accurate measurement¹².

Another additional feature of the E_{dep}/p ratio is its sensitivity to wrongly reconstructed e^\pm tracks, which can lead to the measurement of the wrong charge sign. This phenomenon, also known as *charge confusion*, is a major systematic uncertainty in the separate e^- and e^+ analyses, as well in the positron fraction measurement [83, 176]. Figure 4.19 shows, on the right, the distribution of E_{dep}/p for MC electrons with correct and with wrong reconstructed charge sign. The distribution of E_{dep}/p for charge

¹²For the E_{dep}/p selection, which involves electron/proton separation, the assessment of the efficiency uncertainty is even more difficult than for the other selection cuts due to the difficulty to select control samples of e^- from data independently from the E_{dep}/p selection.

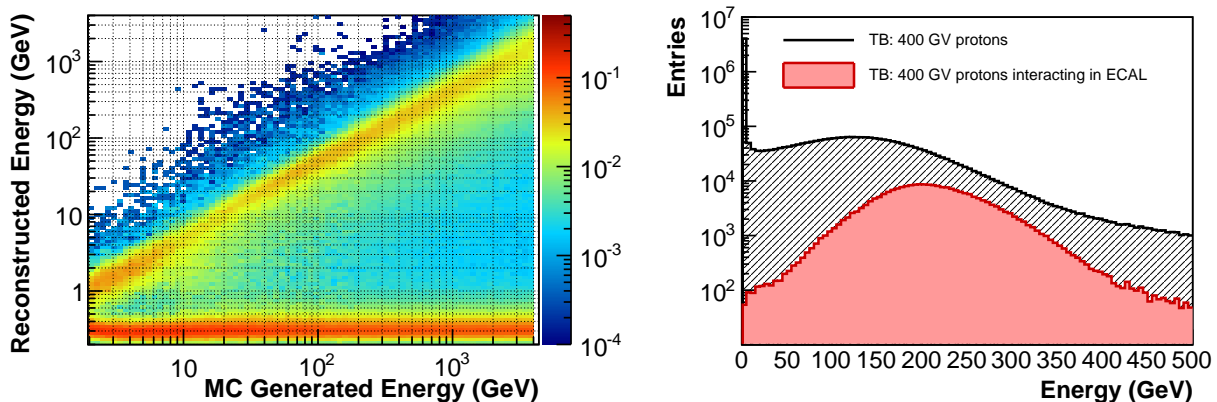


Figure 4.18: **Left:** Distribution of ECAL energy measurement as function of the generated energy for MC simulation protons. For each bin on the x axis, the entire slice in y is normalized to 1. MIP protons populate the bottom part of the distribution. Interacting protons populate the upper rising band. The average energy measured by the ECAL for interacting protons is typically smaller than the real proton energy by a factor of ~ 2 . **Right:** ECAL energy measurement for 400 GV protons collected during the test beam on ground. The spectrum of 400 GV protons covers the whole energy range from well below 1 GeV, where the peak of MIP protons is dominating, up to above 400 GeV for ill-reconstructed events. Interacting protons have instead a narrower distribution peaking at ~ 200 GeV. This confirms, together with the MC simulation, that in each energy bin the background protons have a distribution of true energy value peaking at much higher values than the bin energy range itself.

confused electrons has a much broader shape. It is possible also to distinguish two populations. The population at low values of E_{dep}/p is a statistical effect due to the finite resolution of the Tracker. The population at high values is due to the overestimation of the trajectory curvature. This happens when wrong hits are clustered to the Tracker Track due to interactions above the Tracker or inefficiencies in the clustering algorithms. More details can be found in [216]. This property of the E_{dep}/p ratio is, however, not exploited in this analysis.

4.2.1.2 ECAL Longitudinal shower development BDT

As discussed previously, the procedure to evaluate the e^\pm yield in the selected sample with limited systematic uncertainty needs a first reduction of the proton contamination. This can be achieved using the ECAL detector. The efficiency of the selection has to be, however, known at a precise level in the whole energy range. In order to achieve this task, an additional ECAL selection tool has been developed in the framework of this analysis.

A BDT classifier has been built using only a subset of the shower properties with the best agreement between data and MC. The energy deposit fractions in the first five layers of the calorimeter, which correspond to approximately $5 X_0$, have been used. The longitudinal shower development in the first X_0 s in fact well represented by the MC simulation and shows a minor dependence on the primary particle energy with respect to other shower topology variables. The classifier has been therefore named *ECAL longitudinal BDT* ($\text{ECAL}_{\text{BDT}}^{\text{long}}$). The good data/MC agreement allows to calculate the $\text{ECAL}_{\text{BDT}}^{\text{long}}$ efficiency from the MC simulation with limited uncertainty, as described later.

In order to be able to extract the properties of the classifier up to the TeV energies, the e^\pm input variable energy dependence has been removed. Each variable x has been transformed to a normally distributed and energy independent variable ($x \rightarrow x_N$). The transformation procedure is discussed in

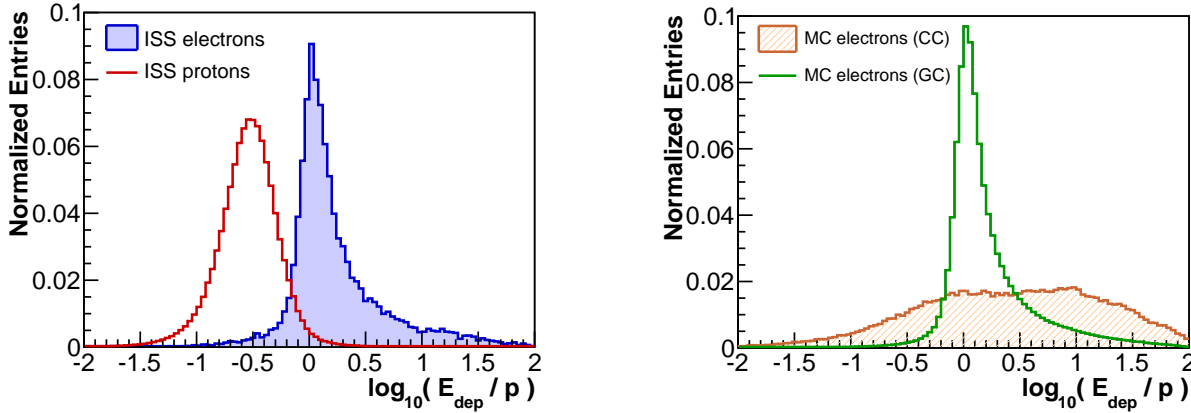


Figure 4.19: **Left:** distribution of the E_{dep}/p ratio for ISS electrons (blue) and protons (red) in the energy range [80.0 - 100.0] GeV. For electrons, the distribution peaks at a value slightly larger than 1 with long tails for $E > p$, as expected from Bremsstrahlung events, up to values of $E_{\text{dep}}/p \sim 100$. For protons, instead, $E_{\text{dep}}/p < 1$ as expected for hadronic shower energy deposit in the ECAL. **Right:** distribution of the E_{dep}/p ratio for MC electrons in the energy range [80.0 - 100.0] GeV. The distribution for electrons with correct charge sign reconstructed (in green) differs from that of charge confused electrons (in orange). For this last category, two populations are visible, one at low values of E_{dep}/p , which is given by statistical effects induced by the finite resolution of the Tracker, and one at high values of E_{dep}/p , which is a consequence of curvature overestimation due to interaction or noisy events.

Appendix B. Figure 4.20 shows the resulting energy dependence for the energy deposit fraction in the 2nd ECAL layer after the transformation and the comparison with the MC simulation. The comparison has been performed in the energy interval [35, 80] GeV, where it is possible to define a pure e^- sample by a TRD and Tracker selection. As expected, the transformed x_N variables are energy independent in terms of shape, mean and width. The MC description of the transformed variable agrees reasonably well with data.

The training procedure has been performed using MC e^- and with no discontinuities in energy. Only MC electrons with energies above 350 GeV have been used for the training to improve the BDT performance at high energies. More details on $\text{ECAL}_{\text{BDT}}^{\text{long}}$ training are discussed in Appendix B. The resulting $\text{ECAL}_{\text{BDT}}^{\text{long}}$ distribution for MC e^- , ISS e^- and ISS protons is shown in Figure 4.21. The $\text{ECAL}_{\text{BDT}}^{\text{long}}$ provides a lower separation power than the complete ECAL_{BDT} classifier. The agreement between data and MC is however substantially improved.

The $\text{ECAL}_{\text{BDT}}^{\text{long}}$ classifier does not exhibit a rejection power as high as the ECAL_{BDT} , since it exploits only the longitudinal development of the shower in the first $5 X_0$ of the ECAL. However – due to the good data/MC agreement of its input variables – its efficiency can be reliably evaluated on MC.

A clean control sample of e^- has been identified using TRD and Tracker on ISS data in the energy interval [1, 100] GeV. Above this energy, the unavoidable proton contamination prevents any safe data/MC comparison. A consistency check has been performed applying the same $\text{ECAL}_{\text{BDT}}^{\text{long}}$ cut on the ISS e^- control sample on the MC e^- control sample and the resulting efficiencies in the two samples have been compared. The result is shown in Figure 4.22. The ratio between the selection efficiency measured on MC and ISS data for a target 90% efficiency cut is presented. The good data-MC agreement is clear over the whole energy range. Any deviation from unity has to be considered in the total systematic uncertainty of the measurement.

The ratio exhibits a small dependence with energy, which has been parametrized using a log-linear

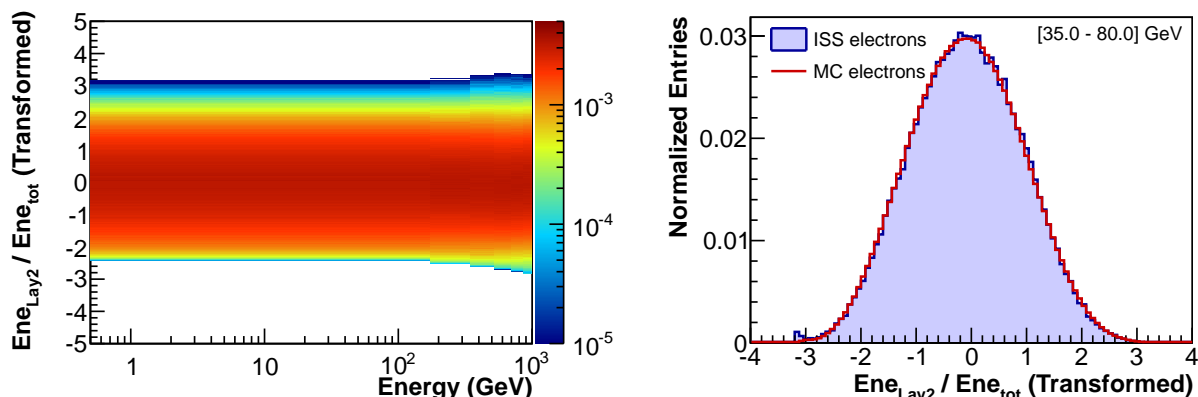


Figure 4.20: **Left:** Energy dependence of the energy deposit fraction in the 2nd ECAL layer after the transformation procedure described in Appendix B. The same distribution for the variable before the transformation is shown in the Appendix in Figure B.1. The transformed variable is energy independent in terms of shape, mean and width. **Right:** Data/MC comparison of the same variable for a control sample of e^- selected in the energy range [35.0 - 80.0] GeV. The MC description of the selected variables is sufficiently accurate to guarantee a good MC description of the resulting classifier after its training.

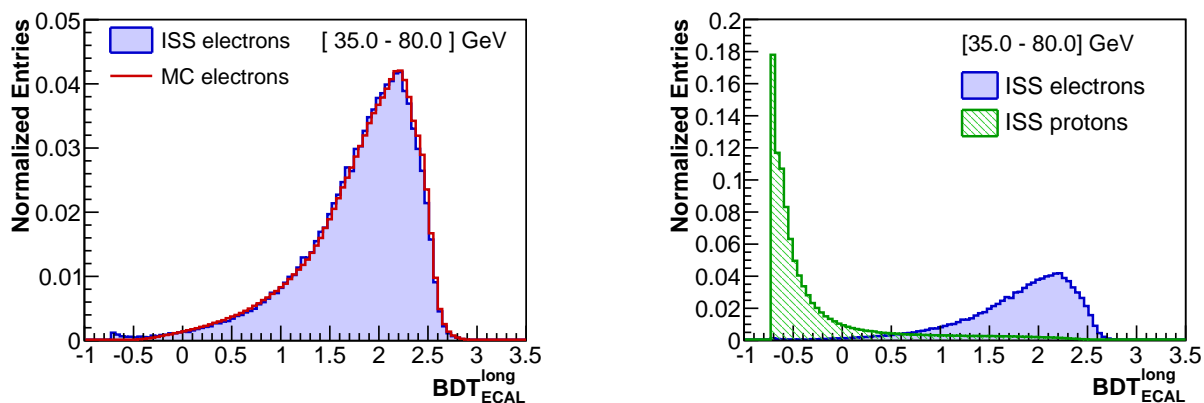


Figure 4.21: Distribution of ECAL_{BDT}^{long} for **Left:** ISS data e^- (blue), MC simulation e^- (red); **Right:** ISS data e^- (blue) and ISS data protons (green). Data and MC are selected in the energy range [35.0 - 80.0] GeV. Although this classifier has a lower e/p rejection power than the ECAL_{BDT}, the agreement between data and MC distributions for e^\pm events is substantially improved.

function. The discrepancy between data and MC, extrapolated continuously up to 1 TeV, contributes no more than 1% to the acceptance uncertainty in the flux normalization. The systematic difference between the data and MC is however added as a contribution to the final measurement systematic uncertainty as part of the acceptance normalization uncertainty, with a minor contribution in the whole energy range (see Section 5.4 for an exhaustive discussion on the definition of the total acceptance error). In addition to this, in most of the analysis energy range below 100 GeV the ECAL_{BDT}^{long} cut has been applied with an efficiency on the signal of 99%, and the strength of the selection smoothly decreases down to 91% at 1 TeV. The estimation of the systematic uncertainty on a target 90% ECAL_{BDT}^{long} efficiency is therefore

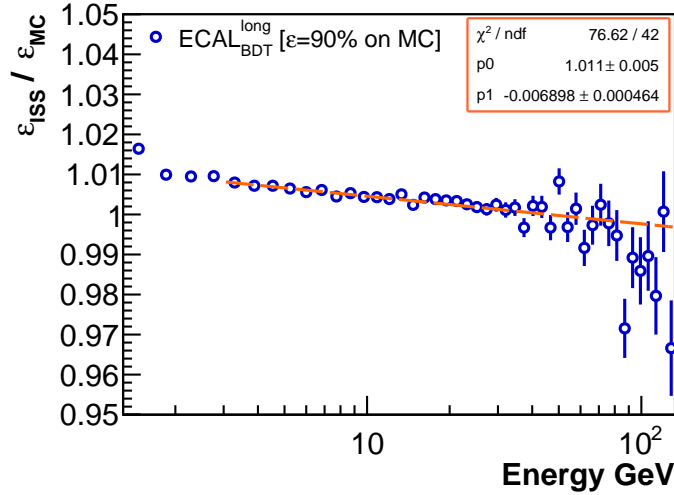


Figure 4.22: Energy dependence for the comparison between the efficiency of the $\text{ECAL}_{\text{BDT}}^{\text{long}}$ selection calculated on a sample of e^- for ISS data and for the MC simulation. The cut has an efficiency of 90% defined on MC. The good agreement between the data and the MC suggests a systematic uncertainty on the final measurement normalization not greater than 1%. The energy trend has been parametrized using a log-linear fit and extrapolated at high energies. The removal of the energy dependence of the input variables and the continuous application of the classifier with no discontinuities in energy guarantee a safe extrapolation to high energies.

conservative¹³. At higher energies, other systematic sources dominate over the normalization, and the uncertainty on the $\text{ECAL}_{\text{BDT}}^{\text{long}}$ cut is still negligible. An additional a-posteriori check has been performed in order to confirm the validity of the $\text{ECAL}_{\text{BDT}}^{\text{long}}$ efficiency calculation. A preliminary analysis of the $(e^+ + e^-)$ flux measurement has been run with different strengths of the $\text{ECAL}_{\text{BDT}}^{\text{long}}$ classifier and the results have been compared. As discussed in Appendix B, the systematic effects observed are covered by the uncertainty on the $\text{ECAL}_{\text{BDT}}^{\text{long}}$ efficiency.

4.2.2 TRD electron/proton separation

The particle identification concept of the TRD detector relies on the dependence for the probability of the transition radiation (TR) emission on the Lorentz factor $\gamma = E/m$. The difference between the detector response to e^\pm and protons provides e/p separation power up to the TeV region.

Particles traversing the TRD pass through 20 layers each composed of a radiator and of a layer of proportional tubes. In the radiator fleece particle undergo $\sim O(100)$ crossing of different dielectric materials. TR photons of typically ~ 10 keV energy can be produced at each crossing with a probability $P \propto \gamma$. The particles cross further through the proportional tube where the ionization energy is detected. In case a TR photon has been produced, it typically crosses the same tube as the primary particle and its energy is collected in the proportional tube together with the primary ionization. The probability to undergo TR energy losses for ultra relativistic e^\pm is much higher than protons with the same energy. The ADC signal in each layer, proportional to the energy deposit in the tube, is used for the TRD e/p discrimination.

¹³For any cut, the uncertainty introduced by the evaluation of the efficiency grow as the cut strength increases. Therefore, the systematic uncertainty evaluated using the target 90% $\text{ECAL}_{\text{BDT}}^{\text{long}}$ efficiency overestimate the real uncertainty introduced in the final analysis, in which the $\text{ECAL}_{\text{BDT}}^{\text{long}}$ is always applied with higher efficiency.

As described in Section 2.1, the response of the TRD detector depends substantially on the environment conditions. The CO₂ and Xe partial pressures, which define the separation properties of the TRD, have a strong time dependence induced by CO₂ diffusion through the tube walls and routine detector operations. In addition, the gain of each tube is different due to different HV feeds and other intrinsic properties. The response of the 5248 tubes has therefore been in the first step equalized and intercalibrated as function of time using CR protons.

The TRD event reconstruction involves the identification of tubes with charge deposit from the triggering particle among the background noise hits due to electronic noise or due to particles that crossed the TRD outside the AMS field of view. In addition, the path-length of the particle inside the tube has to be precisely known in order to correct the energy deposit signals to the energy deposit per unit length. The changes in the thermal environment induce however thermal expansions and contractions of the tubes. A dynamic alignment procedure using CR protons is therefore applied. This ensures to accurately determine the position of the TRD tubes using several techniques based on the extrapolation of the Tracker Track in the TRD or using TRD standalone algorithms [223, 175].

In this analysis, the TrdK TRD reconstruction package [216], which provides calibration, alignment and particle identification tools, has been used. Independent analyses based on the use of different TRD reconstruction packages obtained similar results for the ($e^+ + e^-$) flux measurement with negligible differences with respect to the final measurement systematics.

The ADC spectrum released by electrons and protons inside one TRD tube is shown in Figure 4.23. For protons, only the ionization spectrum is visible. For electrons, instead, the TR spectrum corresponding to higher energy release is superimposed on top of the ionization spectrum.

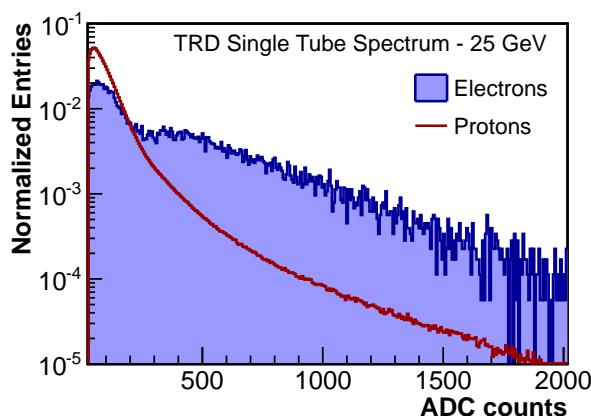


Figure 4.23: TRD single tube ADC spectra for 25 GeV electrons (blue) and protons (red) selected from ISS data. Protons only lose ionization energy in the tubes. Electrons, instead, can produce TR X-rays with consequent higher energy release, visible in the right tail of the distribution.

The information on the energy release from all the 20 tubes can be combined in a discriminating classifier. Differently from the ECAL, the correlation between the energy deposit in the TRD tubes is negligible. In this case a standard statistical classification tool applied on an event-by-event basis can be used to obtain the optimal separation capabilities from the TRD. Electrons and protons selected with the ECAL and Tracker from ISS data have been used to define a parametrization of the Probability Density Function (PDF) $P_i^{e,p}(x|p, l, f_{Xe})$ for the ADC deposit x in the i^{th} layer, as function of the particle momentum p , of the path-length in the tube l and of the Xe partial pressure f_{Xe} , and for the

electron e and proton p hypothesis. For each event the set of signals measured in the n TRD layers with energy deposit above threshold, x_1, \dots, x_n , is used to define the event *likelihood* for the electron or proton hypothesis $\mathcal{L}^{e,p}$ as following:

$$\mathcal{L}^{e,p} = \sqrt[n]{\prod_{i=1}^n P_i^{e,p}(x_i | p, l, f_{Xe})} \quad (4.2)$$

The value of $\mathcal{L}^{e,p}$ is not a likelihood value in the strict statistical sense. Instead, it has to be interpreted as the probability to release the x_1, \dots, x_n set of signal values normalized to the number of TRD layers that enter in the definition of $\mathcal{L}^{e,p}$, which depends on the event. In order to set the likelihood value range in a reasonable interval for comparisons, the $\mathcal{L}^{e,p}$ will be redefined from now as *TRD classifier* $\text{TRD}_{\text{class}}$, without any loss of physical information, as following:

$$\text{TRD}_{\text{class}}^{e/p} = -(\log_{10}(\mathcal{L}^{e,p}) + 2) \quad (4.3)$$

The likelihood information, which already summarizes the TRD identification potential for one hypothesis, can be combined in a test statistic dedicated to the e/p separation. The *likelihood ratio* can be finally defined as:

$$\text{TRD}_{\text{hr}}^{e/p} = -\log\left(\frac{\mathcal{L}^e}{\mathcal{L}^e + \mathcal{L}^p}\right) \quad (4.4)$$

Since the correlation between the energy deposit of different TRD layers is minor, the $\text{TRD}_{\text{hr}}^{e/p}$ represents the statistical combination of the 20 TRD measurements that maximizes the e/p separation.

The evaluation of the momentum p of the incoming particle is critical for the definition of the correct PDF to evaluate. This is true especially for high energy protons, whose PDFs change drastically as function of energy above ~ 300 GeV. The evaluation of p using the rigidity measurement of the **Tracker Track** reconstruction introduces, however, unwanted correlations between the value of the TRD classifier and the rigidity (and charge sign) measurement. For example, when the measured rigidity is exceptionally higher than the true value, the rapid development of the TR component in the proton PDF significantly bias the value of the TRD classifier. This happens especially for events with high activity in the Tracker. These correlations limit the accuracy of this analysis drastically. In order to avoid this, the best value of the rigidity has been evaluated using the **ECAL Shower** energy estimation E . For the electron PDF it is assumed $p = E$. For the proton PDF instead, according to what has been discussed in Section 4.2.1.1, the guess $p = 2 \times E$ has been adopted. Using this definition, the TRD classifiers show a negligible dependence on the **Tracker Track** rigidity. Moreover, the use of the same measured quantity to define the energy in both the electron and proton hypotheses assures the self-consistency of the method. Below 2 GeV the **ECAL Shower** energy resolution for e^\pm drastically worsens and the **Tracker Track** momentum measurement is instead used as best estimator for p . All the discontinuities in the TRD classifier distributions at 2 GeV are due to this definition.

Figure 4.24 shows the distribution of $\text{TRD}_{\text{hr}}^{e/p}$ and $\text{TRD}_{\text{class}}^e$ for ISS electrons, MC electrons and ISS protons in the energy range [100.0 - 200.0] GeV. For both classifiers, the MC simulation does not reproduce the data at a reasonable level¹⁴. This fact, similarly for the case of the ECAL_{BDT} classifier, prevents the use of the MC simulation to define the properties of the classifiers for high energy data.

As expected from its statistical definition, the $\text{TRD}_{\text{hr}}^{e/p}$ classifier exhibits a higher discrimination power, and it has therefore been chosen for the AMS positron fraction analysis [176, 83]. In this

¹⁴The discrepancy between the ISS data and the MC simulation for the TRD detector has been partially recovered in the most recent release of the AMS software. The improvement procedure is, however, not yet concluded. Future corrections to the software will improve the simulation up to an agreement at the level of % needed for this analysis.

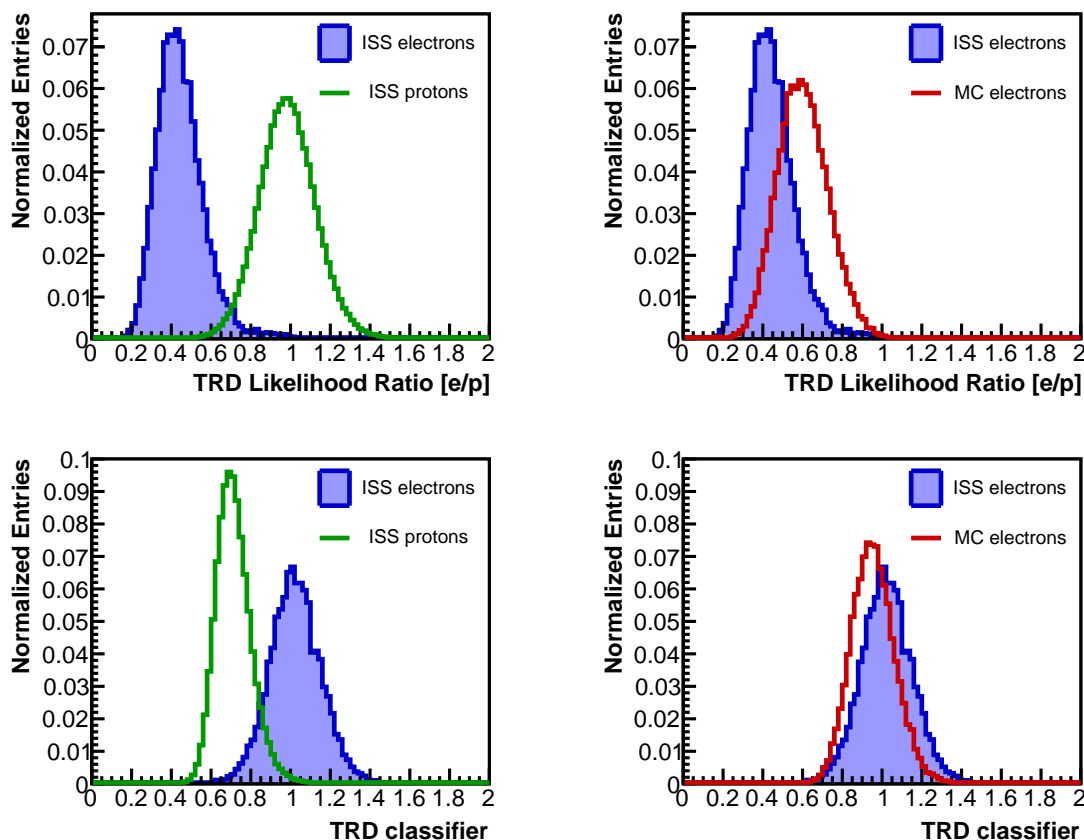


Figure 4.24: TRD electron/proton discriminator for ISS electrons (blue), MC electrons (red) and ISS protons (green) in the energy range [100.0 - 200.0] GeV. **Top:** $\text{TRD}_{\text{thr}}^{e/p}$ e/p likelihood ratio. **Bottom:** $\text{TRD}_{\text{class}}^e$ electron likelihood. The $\text{TRD}_{\text{thr}}^{e/p}$ variable shows higher discrimination power, as expected from its statistical definition. For both variables, however, the comparison with MC does not exhibit a good agreement. This prevents the use of the TRD MC simulation to define the classifier properties.

analysis, however, the stability of the classification tool and the accuracy level to which the distribution features are known are more important than the its e/p separation capabilities. This is true especially at high energies: it is in fact impossible to select a sample of high energy e^\pm from data, using a selection based on the ECAL only, and pure enough to extract the shapes of the TRD classifiers. The energy dependence of the two TRD discrimination tools is shown in Figure 4.25 for ISS data electrons selected using the ECAL and Tracker selection. It is clear that above ~ 400 GeV the purity of the selection is not high enough to guarantee a description of the shape at the desired percent level. Moreover, the stringent selection on ECAL and Tracker reduces the e^- control sample to a subset of the same e^\pm sample that has to be analyzed for the flux measurement. The main difference is however visible in the energy dependence of the classifiers. The $\text{TRD}_{\text{thr}}^{e/p}$ has a strong energy dependence, induced by the input of the energy dependent \mathcal{L}^p in its definition (Equation 4.4). The $\text{TRD}_{\text{class}}^e$, instead, does not show any energy dependence above ~ 10 GeV on data. This is due to the fact that the TR emission for highly energetic electrons saturates above this energy. This last property is confirmed by the MC simulation (see Figure 4.26) which, ignoring the fact that the absolute value of the classifier is not well described, also shows no energy dependence above ~ 10 GeV. The MC analysis shows a minimum residual energy

trend in the $\text{TRD}_{\text{class}}^e$ mean, due to the relativistic rise in the ionization yield for e^\pm . The impact of the minor energy trend on the final measurement has been tested a posteriori running the analysis with and without this correction. The difference in the results has been found to be negligible with respect to other sources of systematic uncertainties. The same reasoning applies for the trend in the $\text{TRD}_{\text{class}}^e$ RMS distribution.

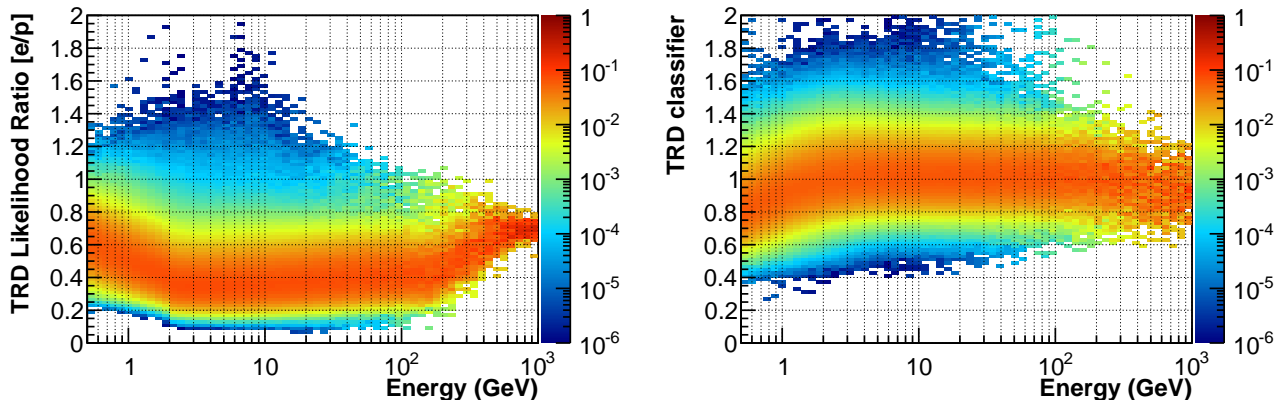


Figure 4.25: Energy dependence of the TRD e/p discriminators for a control sample of e^- selected from ISS data with the ECAL and the Tracker. **Left:** $\text{TRD}_{\text{lhr}}^{e/p}$ e/p likelihood ratio. **Right:** $\text{TRD}_{\text{class}}^e$ electron likelihood. For both classifiers the purity of the selection at high energies is not high enough to guarantee a description of the shape at the desired percent level. The proton contamination is in fact well visible. The $\text{TRD}_{\text{lhr}}^{e/p}$ distribution shows an energy dependence. The $\text{TRD}_{\text{class}}^e$, instead, shows hardly an energy dependence above ~ 10 GeV on data. This last tool is, therefore, more suitable for high energy e^\pm analysis.

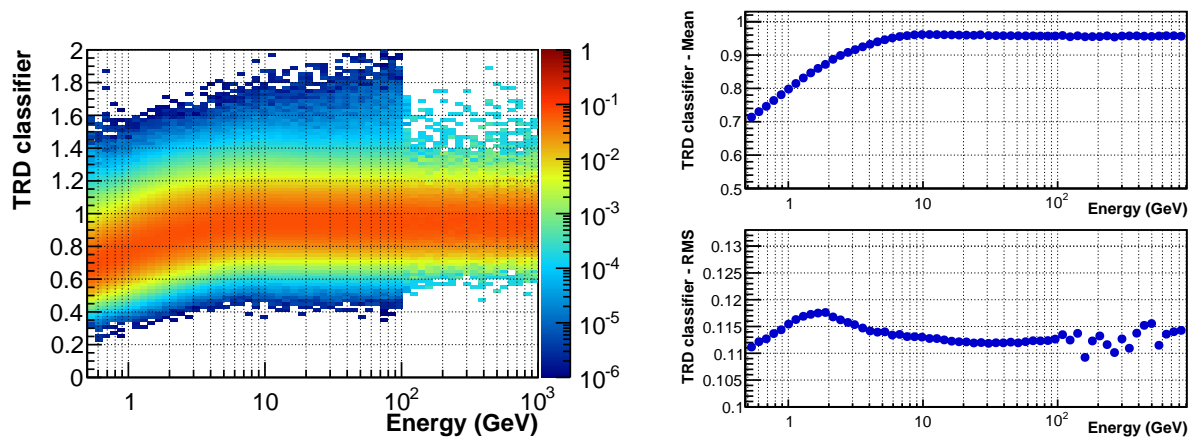


Figure 4.26: **Left:** $\text{TRD}_{\text{class}}^e$ as a function of energy for MC electrons. **Right:** $\text{TRD}_{\text{class}}^e$ mean and width as function of energy for MC electrons. Above ~ 10 GeV, the classifier shape does not show any relevant energy dependence. The minor energy trend of its mean and of its RMS has been proven to be negligible in this analysis.

The properties of the $\text{TRD}_{\text{class}}^e$ mentioned so far make it a safe and stable tool up to the TeV range. Its properties at low energies, derived from data, can be safely extrapolated up to the highest energies. For this reason, it has been chosen to be used for the signal extrapolation procedure described in the next section. From now on, the term $\text{TRD}_{\text{class}}$ will refer indirectly to $\text{TRD}_{\text{class}}^e$. The $\text{TRD}_{\text{lhr}}^{e/p}$ classifier

has been however used in this analysis as a support tool to investigate systematic uncertainties.

4.3 Electron and positron signal extraction

The ECAL and TRD detectors provide several tools with different properties that can be combined to extract the e^\pm component in the preselected sample:

- ECAL_{BDT} , based on the analysis of the complete shower topology in ECAL, trained on data to locally maximize the e/p separation but with poor MC/data agreement.
- $\text{ECAL}_{\text{BDT}}^{\text{long}}$, based on the analysis of the longitudinal shower development in the first $5 X_0$ of ECAL, trained on MC to maximize the e/p separation at high energies, with good MC/data agreement.
- $\text{TRD}_{\text{class}}$, based on the analysis of the energy deposit in the TRD tubes, with lower e/p separation capabilities if compared to the $\text{TRD}_{\text{thr}}^{e/p}$ classifier but with negligible energy dependence for the e^\pm shape.

The strategy used in this work to evaluate the number of e^\pm , applied separately to each energy bin, is the following:

1. An efficient cut on $\text{ECAL}_{\text{BDT}}^{\text{long}}$ is applied on the preselected sample. This allows to remove the bulk of proton contamination with efficiency on signal known better than percent level. This preliminary ECAL selection allows to reduce the systematic uncertainty in the evaluation of the e^\pm component, as discussed later.
2. A strong calorimetric selection based on ECAL_{BDT} is applied on the remaining sample, in order to achieve an advantageous signal/background (S/B) ratio. The efficiency of the ECAL_{BDT} cut can be measured directly from data, as discussed in this section, taking advantage of the preliminary $\text{ECAL}_{\text{BDT}}^{\text{long}}$ cut to reduce the uncertainties in the procedure.
3. The reference spectra (or *templates*) of the $\text{TRD}_{\text{class}}$ – known with high accuracy for e^\pm and p – are fitted to the data by varying the normalizations of the signal (e^\pm) and the background (p) components to extract the signal yield.

Figure 4.27 shows a chart flow scheme of the procedure for illustration purpose. The whole procedure is described in detail in this section. The assessment of systematic uncertainties will be addressed in the next section.

4.3.1 TRD classifier templates

The reference spectra of the $\text{TRD}_{\text{class}}$ variable has to be retrieved in each energy bin directly from data due to the poor MC/data agreement.

The properties of the $\text{TRD}_{\text{class}}$ variable and its energy independence for e^\pm provide several advantages for the definition of the signal template shape. A *universal* $\text{TRD}_{\text{class}}$ shape for all energies above 15 GeV can in fact be defined using low energetic e^- events, for which the proton contamination can be safely set to a negligible value using a selection based on the ECAL shower shape. This minimizes possible uncertainties coming from the inclusion of any background contamination in the reference template distribution. Moreover, the data sample size available to define the e^\pm reference distribution up to the highest energies is enhanced. Finally, in each energy bin the template is defined using an independent set of events, avoiding statistical correlations between the fitted signal and the reference distributions.

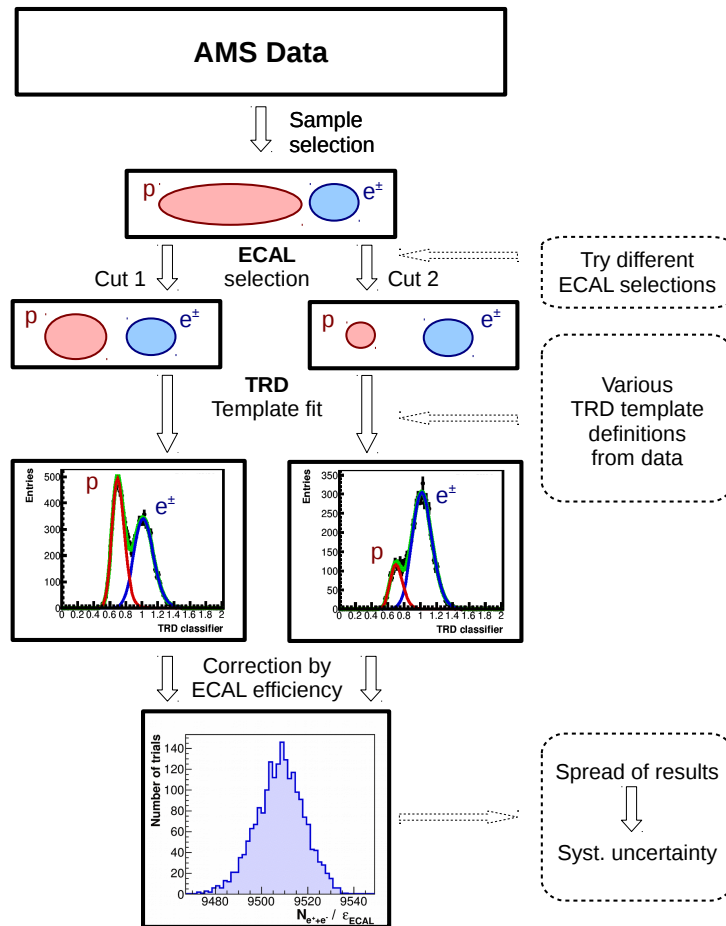


Figure 4.27: Signal identification flowchart. A sample of relativistic, downward-going $|Z|=1$ particles is selected from the total AMS dataset. The selected sample consists mostly of protons (background) and e^\pm (signal). The majority of protons are rejected using an ECAL based selection, with cuts on the $\text{ECAL}_{\text{BDT}}^{\text{long}}$ and on the ECAL_{BDT} classifiers. Different selections, leading to different amounts of protons and e^\pm , are tested. The e^\pm component in the sample is identified using the TRD information. Reference spectra – or *templates* – of the $\text{TRD}_{\text{class}}$ variable for e^\pm and protons are fitted to the data varying their normalizations. The templates are defined from the data using pure samples of protons and e^- . The template fit yields the number of e^\pm ($N_{(e^+ + e^-)}$) and its statistical uncertainty. The template fit is performed for various efficiencies of the ECAL selection (ϵ_E) and various definitions of the $\text{TRD}_{\text{class}}$ template shapes. The spread of the results for $N_{(e^+ + e^-)}/\epsilon_E$ for the various ECAL selections and template definitions provides the systematic uncertainty of the signal identification procedure. The whole procedure is described in detail in the text in Sections 4.3 and 4.4.

The *universal* $\text{TRD}_{\text{class}}$ reference distribution for signal has been determined using a pure sample of e^- in the energy interval [15.4 - 84.1] GeV, where the proton contamination can be set to a negligible contribution using the calorimetric selection. A representative e^- sample has been extracted from the preselected sample with a selection on the charge sign, $\text{ECAL}_{\text{BDT}} > 0$ and $E_{\text{dep}}/p > 0.5$. The resulting *universal* $\text{TRD}_{\text{class}}$ template is shown in Figure 4.28. Below 15.4 GeV, the $\text{TRD}_{\text{class}}$ templates for the

signal are determined separately for each energy bin¹⁵.

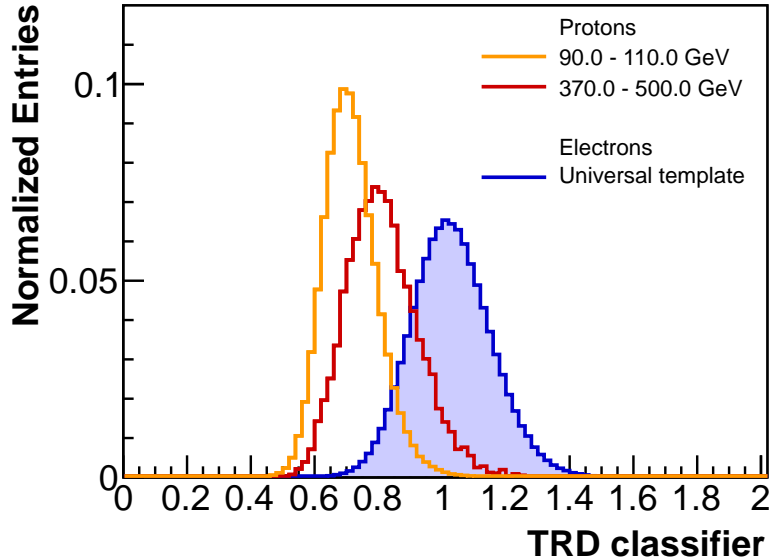


Figure 4.28: The universal $\text{TRD}_{\text{class}}$ template for e^{\pm} , defined with high statistics from data and energy independent above ~ 15 GeV, is shown in blue together with the $\text{TRD}_{\text{class}}$ templates for low energy (orange) and high energy (red) protons. As the proton energy increases, the proton ionization increases and protons eventually also start to produce TR photons. As a consequence of this, the TRD separation power decreases. The proton $\text{TRD}_{\text{class}}$ distribution moves consequently towards the electron range and the overlap area increases.

The same approach for the proton templates is not possible, since the shape of $\text{TRD}_{\text{class}}$ for protons depends on the energy. Therefore, proton templates are defined separately for each energy bin. However, since protons are the dominant cosmic ray species, the impact on the analysis is smaller than for the case of e^{\pm} .

Several proton templates definitions have been tested. Unlike for the universal e^{\pm} template, and especially at high energies, the proton template shape depends on the particular selection applied to select the representative proton sample from data. The uncertainty on the proton template shape, which constitutes one of the major systematic uncertainty of the analysis, will be discussed in Section 4.4. More details about the proton template definition will be also given in the same section. An example of proton templates for different energy ranges, after a standard selection, is shown together with the universal e^{\pm} template in Figure 4.28. The energy dependence of the TRD classifier distribution is clear: as the proton energy increases, the TRD separation power decreases (due to the increase of ionization energy deposit for protons and eventually TR emission for the highest energies) and the classifier distribution moves towards the signal range. The increase of overlap area enhance the background fluctuations in the signal region and limits the accuracy to which the e^{\pm} yield can be separated from the background.

The energy dependence of the signal and background templates is sketched in Figure 4.29. It is clear, qualitatively, that above 10 GeV the TRD proton template does not exhibit any strong energy dependence until ~ 200 GeV. At this ECAL energy, which corresponds roughly to a spectrum of protons peaking at 400 GV, protons start to emit TR X rays and the separation power decreases. The distribution

¹⁵Different cut combinations, used to select the representative e^- sample for the signal template definition, have been tested. The shape of the resulting distributions shows no dependence for any reasonable choice of cuts. The systematic uncertainty of this selection is therefore neglected in the final uncertainty.

overlap coefficient K_{OVL} , which measures the amount of overlap area between two statistical distributions $f(x)$ and $g(x)$ [224]:

$$K_{OVL} = \int_{-\infty}^{+\infty} \min\{f(x), g(x)\} dx \quad (4.5)$$

also shows that the overlap between the signal and background increases with increasing energy above ~ 200 GeV.

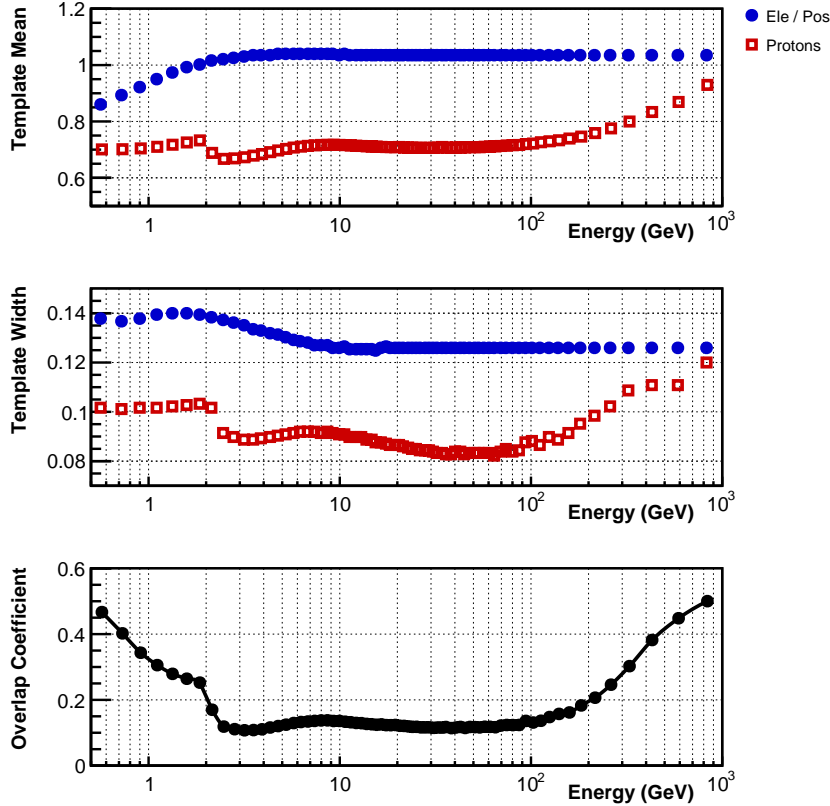


Figure 4.29: Distribution of the mean (**Top**) and width (**Middle**) for the signal (blue) and background (red) $\text{TRD}_{\text{class}}$ templates as function of the energy. The overlap coefficient between the two distributions (**Bottom**) clearly shows that the separation power of the TRD starts to decrease above ~ 200 GeV measured energy, corresponding to an average value of 400 GeV for the proton real energy.

The standard approach used to evaluate the e^\pm yield in the AMS experiment [176, 83] makes use of the $\text{TRD}_{\text{hr}}^{e/p}$ classifier. This implies however to build - separately for each energy bin - the templates for both signal and background. Especially at the highest energies, where the e^- data sample is small and a residual proton contamination in the signal template is unavoidable, larger systematic uncertainties in the template definition and a strong statistical correlation between the fitted signal and its reference template arise. The use of the $\text{TRD}_{\text{class}}$ as discriminating variable in this analysis has the advantage to remove this source of systematic effects at high energies.

4.3.2 Signal yield extraction

The $\text{TRD}_{\text{class}}$ reference spectra are used to statistically separate the signal (e^\pm) contribution from the p background. For each energy bin, the $\text{TRD}_{\text{class}}$ distribution of data is fitted as a sum of a signal and background contributions using the template shapes defined in Section 4.3.1. The fitting procedure has

been performed using an Extended Maximum Likelihood fit with the RooFit package [225]. The fit procedure provides the yield of ($e^+ + e^-$) events ($N_{(e^++e^-)}$) in the selected sample.

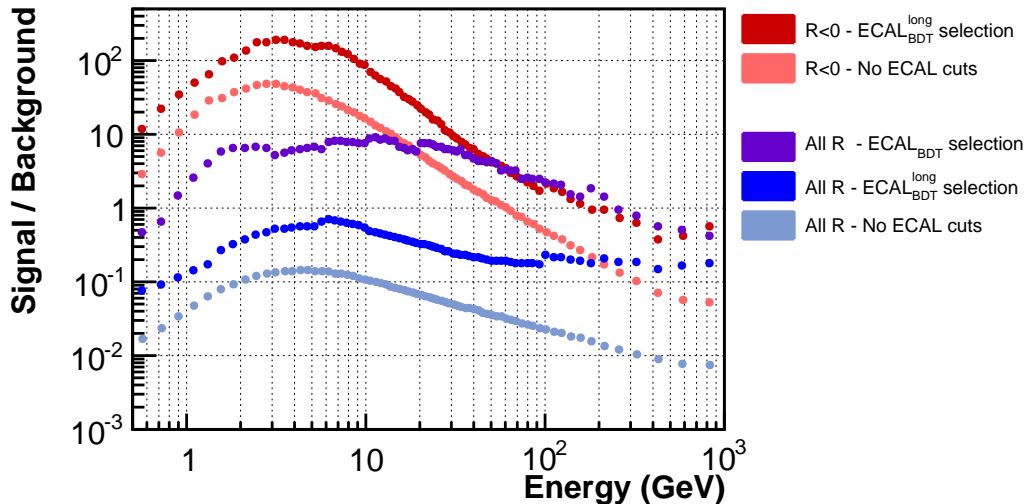


Figure 4.30: S/B ratio for different data samples of the analysis. The yield of signal (S) and proton background (B) is estimated from data using the template fit technique described in the text. In the $R < 0$ sample the signal to proton ratio when no ECAL selection is applied (salmon circles) is enhanced by the selection on the $\text{ECAL}_{\text{BDT}}^{\text{long}}$ classifier. The resulting S/B (red circles), higher than ~ 0.5 even at the highest energies and $\gg 1$ below ~ 100 GeV, allows to have a reliable estimation of the $R < 0$ yield with no further ECAL selection. For the total sample, where no selection on the charge sign is applied, the starting S/B (light blue) is first increased by the $\text{ECAL}_{\text{BDT}}^{\text{long}}$ cut (blue circles) and by the additional selection on ECAL_{BDT} used to explore the full shower development in the ECAL (violet circles). The ECAL_{BDT} selection is chosen in order to maximize the sensitivity of the measurement. The resulting S/B yield allows in fact to extract the ($e^+ + e^-$) counts with a good compromise between high efficiency and contained systematics.

As seen in Figure 4.30 the signal/background ratio (S/B) at the end of the sample pre-selection – before the application of any ECAL based cut – is just of the order of few % at energies around 100 GeV, and it decreases even below at the highest energies of the analysis. After the selection of the negative charge sign to enhance the e^- sample signal purity the proton background is at least 10 times higher than the signal level above 300 GeV. Under these overwhelming background conditions, any result from a template fit would be dominated by the uncertainties in the description of the proton $\text{TRD}_{\text{class}}$ shape and would severely depend on possible fluctuation of its tails in the region where it overlaps to the e^\pm template, leading to unstable results in the measurement.

Before the fitting procedure, a further selection to the data sample based on the $\text{ECAL}_{\text{BDT}}^{\text{long}}$ discriminator has been applied. Its efficiency is well known from MC and correctly reproduced in data as discussed in Section 4.2.1.2. The $\text{ECAL}_{\text{BDT}}^{\text{long}}$ selection has an efficiency of $\sim 99\%$ on the signal up to 100 GeV. Above this energy, the strength of the cut increases with energy up to $\sim 91\%$ in the [700.0 - 1000.0] GeV energy bin. This choice maximizes the available data sample size while enhancing the S/B ratio at high energies by a factor of ~ 10 in the $R < 0$ sample and even more in the full sample¹⁶.

In Figure 4.31 an example of the fitting procedure used to evaluate the signal is shown for the whole sample and for the $R < 0$ in the energy range [148.8 - 168.9] GeV at different stages of the calorimetric

¹⁶The $R < 0$ is defined by a selection on the charge sign measured by the Tracker. This sample is mostly constituted by e^- and a contamination of charge confused protons.

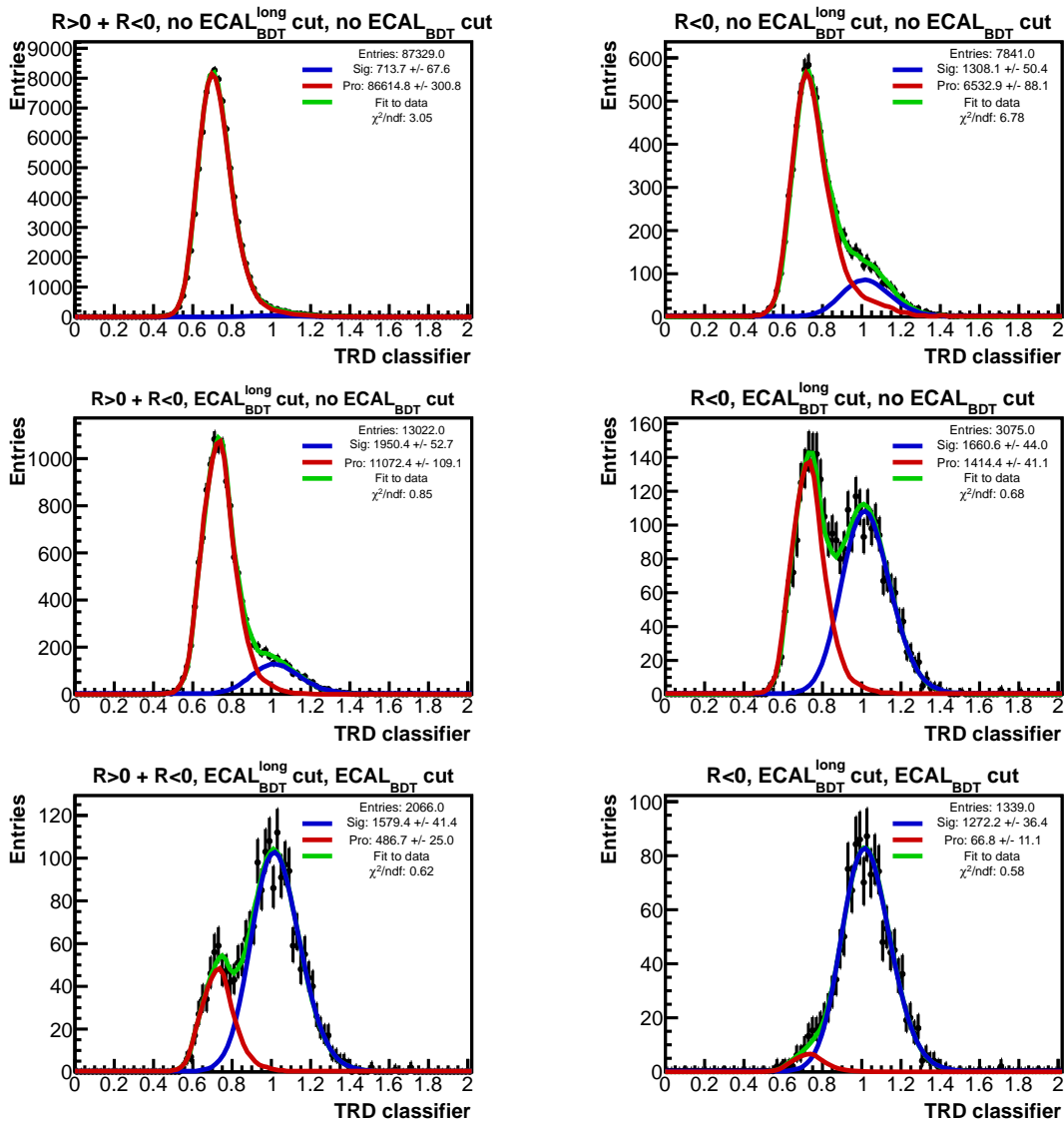


Figure 4.31: Template fit to the TRD_{class} distribution in the energy range [148.8 - 168.9] GeV. The fitted signal and background components are represented by the blue and red curves respectively. The green line represents the overall fit superimposed on the black data points. On the left, the distribution for all the events used to evaluate the $(e^+ + e^-)$ signal. On the right, the distribution for $R < 0$ only events, used to evaluate the $ECAL_{BDT}$ cut efficiency. On the top row, no calorimetric cut is applied. The background contribution dominates over the signal and prevents the estimation of the signal yield with reasonable accuracy. In the middle row, a cut on $ECAL_{BDT}^{long}$ with 97% efficiency on e^\pm is applied in order to remove the bulk of the background and the S/B has improved. On the bottom row, the full calorimetric selection using the $ECAL_{BDT}$ classifier has been applied. In this case, the signal component dominates and the accuracy of its estimation is enhanced.

selection. With no ECAL selection at all, the e^\pm estimation is not reliable. The background component dominates the sample and any pollution in the definition of the template tails would severely bias the signal yield estimation. The application of the $ECAL_{BDT}^{long}$ cut allows to achieve a reasonable S/B ~ 1 ratio in the $R < 0$ sample and thus a reliable estimate of the e^- content. Conversely, the background still dominates in the full data sample where the $(e^+ + e^-)$ component is completely superimposed to the tails of the proton distribution. To evaluate the $(e^+ + e^-)$ signal in the cleanest S/B condition, a

further selection on the full shower development based on the ECAL_{BDT} classifier has been applied. The ECAL_{BDT} cut has been chosen in order to minimize the overall uncertainty (statistical + systematic) in the analysis. An overview of the fit results for a selection of energies and of ECAL selection is presented in Appendix C.

The resulting S/B ratio for the $R < 0$ and for the total sample after the ECAL selection is shown in Figure 4.30. The ECAL selection improves the purity of the sample better than $S/B=1$ up to 200 GeV. Above this energy, the S/B decreases up to $S/B \sim 0.5$ at 1 TeV. The systematics on the result induced by the proton template shape uncertainty are therefore reduced.

Details on the assessment of the systematic uncertainties and its dependence on the ECAL_{BDT} cut will be discussed in Section 4.4. In Section 4.3.2.1 the method used to evaluate the ECAL_{BDT} efficiency cut from data is presented.

The energy spectrum of events identified as $(e^+ + e^-)$ ($dN_{(e^++e^-)}/dE$), together with the $\text{ECAL}_{\text{BDT}}^{\text{long}}$ and ECAL_{BDT} selection efficiency, is shown in Figure 4.32. In principle, this spectrum could be used to determine the $(e^+ + e^-)$ flux according to Equation 3.11. The resulting spectra are however affected by systematic uncertainties, which are dominated by the choice of a particular calorimetric selection, by the ECAL_{BDT} efficiency knowledge and by the $\text{TRD}_{\text{class}}$ template definition. In the next section, the procedure to obtain the best estimate of the measured $N_{(e^++e^-)}$ yield and its systematic uncertainty will be discussed.

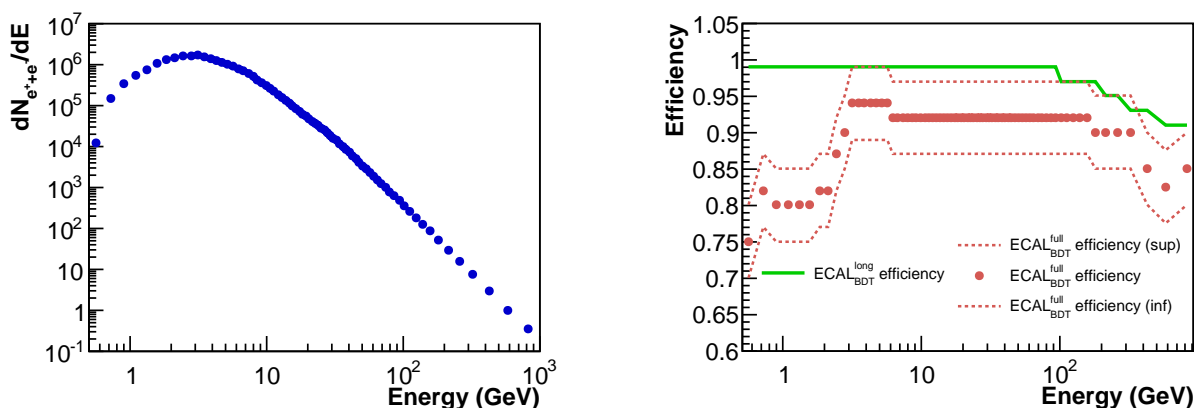


Figure 4.32: **Left:** Energy spectra of the events identified as $(e^+ + e^-)$ ($N_{(e^++e^-)}$) identified in data using the $\text{TRD}_{\text{class}}$ template fit procedure. **Right:** Energy dependence of the efficiency for the $\text{ECAL}_{\text{BDT}}^{\text{long}}$ selection (green) and for the ECAL_{BDT} selection applied in order to enhance the S/B ratio. For the ECAL_{BDT} , the band represents the interval of selections explored to assess the systematic uncertainties, as described in Section 4.4.

4.3.2.1 Data driven estimation of ECAL selection efficiency

As discussed in Section 4.2.1, the efficiency of the ECAL_{BDT} selection cannot be safely estimated from the MC simulation. The agreement between data and MC is not accurate enough. In addition to this, the comparison between the data and the MC simulation cannot be tested at the highest energies due to lack of statistics and purity of the e^- control sample. In this work a data driven method has been used to estimate the ECAL_{BDT} selection efficiency up to the TeV range. The key point for the efficiency evaluation is the correct estimate of the number of signal events in the sample before any ECAL_{BDT} cut is applied ($N^{(\text{tot})}$). Any background contamination would in fact spoil the accuracy of the normalization in the efficiency curve, leading to a systematic underestimation of the efficiency value. A *Tag&Probe* approach based on a tight TRD and Tracker selection is not powerful enough to select a pure e^- control

sample and fails to provide a correct estimation of the efficiency¹⁷. In this analysis the efficiency has been evaluated on the $R < 0$ sample – where the S/B ratio is enhanced – and the number of signal events has been estimated using the TRD template fitting procedure, similarly as done for the $(e^+ + e^-)$ signal yield identification. This is illustrated in the right column of Figure 4.31. The use of the template fit technique allows, differently from the *Tag&Probe* method, to correctly identify and remove all the proton contamination in the e^- control sample. The ECAL_{BDT} selection efficiency ε_E for the cut $\text{ECAL}_{\text{BDT}} > x$ is calculated in this analysis as:

$$\varepsilon_E = N_{R<0}^{(x)} / N_{R<0}^{(\text{tot})} \quad (4.6)$$

where $N_{R<0}^{(\text{tot})}$ is the number of signal events fitted in the $R < 0$ sample without any ECAL_{BDT} selection and $N_{R<0}^{(x)}$ is the number of signal events fitted in the same sample after the selection $\text{ECAL}_{\text{BDT}} > x$. An example of the efficiency scan result on the e^- sample, obtained varying the ECAL_{BDT} cut in its whole range, is presented in Figure 4.33 for the [148.8 - 169.9] GeV energy interval. The efficiency profile has been parametrized in order to smoothen out statistical fluctuations. In the rightmost plot, the efficiency correction is applied to the number of fitted $(e^+ + e^-)$ signal events of the full sample as a function of the ECAL_{BDT} cut. As expected, despite the much higher level of background contamination than that in the $R < 0$ sample, the number of fitted $(e^+ + e^-)$ events is stable after being corrected for the ECAL_{BDT} efficiency. This holds only in the region where the S/B ratio is $\sim O(1)$. For lower values of ECAL_{BDT} cut, the background yield dominates and any bias in the proton template shape affects the estimation of the signal component. Any instability of such a profile is a hint of a systematic effect in the procedure, as discussed in the next section.

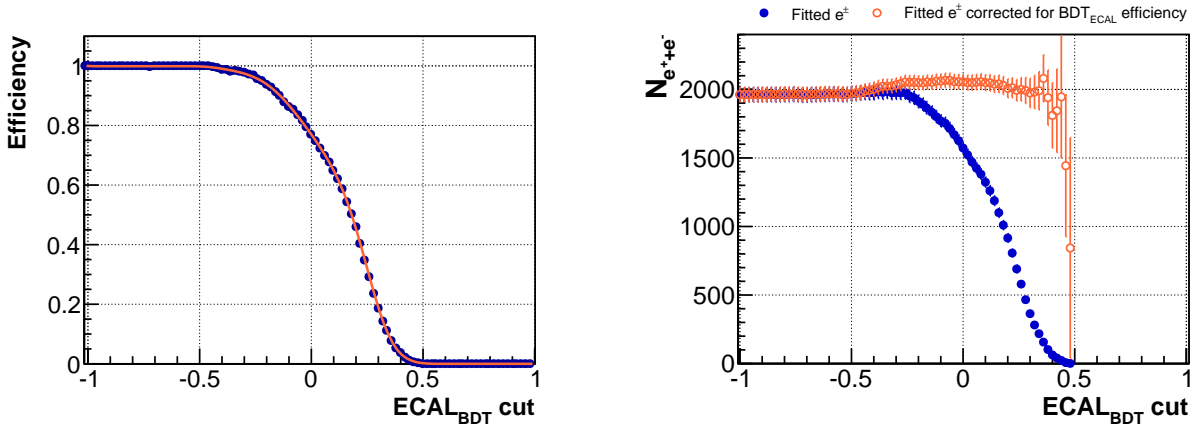


Figure 4.33: **Left:** ECAL_{BDT} efficiency profile in the energy range [148.8 - 168.9] GeV. For each point, the number of fitted signal in the $R < 0$ sample after the ECAL_{BDT} selection has been normalized to the number of events fitted with no ECAL_{BDT} selection. An analytical parametrization of the profile has been performed in order to smoothen out statistical fluctuations. **Right:** Fitted $(e^+ + e^-)$ events for different ECAL_{BDT} cut, with and without corrections for the cut efficiency. The number of corrected counts is stable within the error after the S/B ratio has been enhanced. At low values of ECAL_{BDT} cut, the proton background dominates the data sample and the signal yield evaluation is affected by any bias in the proton template tails.

¹⁷The *Tag&Probe* approach is also sensitive to any correlation between ECAL and TRD which may be present, as example, in interacting events.

4.4 Electron and positron identification uncertainties

In addition to purely statistical fluctuations, several uncertainties affect the evaluation of the $(e^+ + e^-)$ yield by means of the template fit to the $\text{TRD}_{\text{class}}$ distribution. In particular, the total uncertainty can be classified into two main categories:

1. uncertainty due to the **finite separation capabilities of the TRD classifier**. This will be referred as *separation* systematic uncertainty, or δ_{sep} .
2. systematic uncertainties related to the **selection procedure**. This will be referred as *selection* systematic uncertainty, or δ_{sel} .

The *separation* systematic uncertainties are related to the finite separation power of the TRD and to the background fluctuations during the template fit procedure. The *separation* systematics have been defined from the total statistical error provided by the fit routine on the signal component (σ_{stat}) according to the following formula:

$$\sigma_{\text{stat}} = \delta_{\text{poiss}} \oplus \delta_{\text{sep}} \quad (4.7)$$

where $\delta_{\text{poiss}} = \sqrt{N_{(e^+ + e^-)}}$ denotes the purely statistical signal fluctuations of the fitted events $N_{(e^+ + e^-)}$. Such decomposition of the statistical uncertainty σ_{stat} is useful to investigate the details of the single contributions δ_{poiss} and δ_{sep} and to optimize the sensitivity of the analysis.

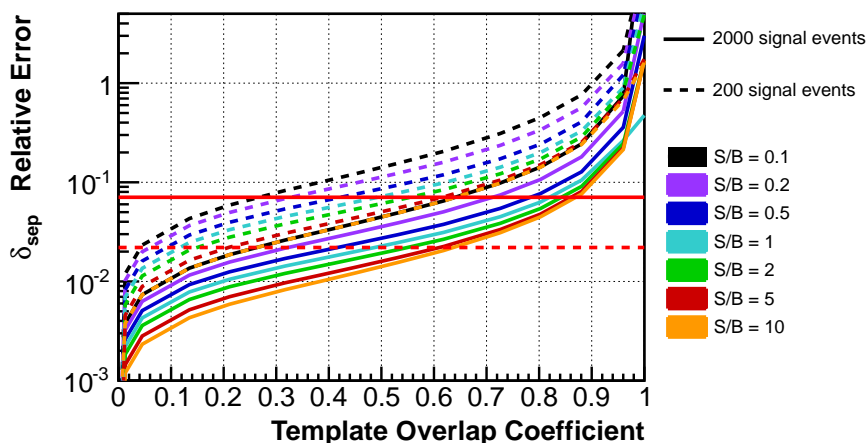


Figure 4.34: Relative δ_{sep} error on the fitted signal yield evaluated using a statistical simulation approach. A fixed number of 2000 and 200 signal events has been generated according to the $\text{TRD}_{\text{class}}$ distribution. This corresponds approximately to the $(e^+ + e^-)$ statistic available in the ~ 180 GeV energy bin and in the ~ 600 GeV energy bin. The number of background events, distributed according to the $\text{TRD}_{\text{class}}$ distribution, has been defined according to different S/B ratios. The $\text{TRD}_{\text{class}}$ distribution for signal and background has been assumed to be Gaussian, and the separation between the signal and background components has been varied from a situation of complete overlap (OVL=1) to complete separation (OVL=0). The same fit procedure applied to extract the $(e^+ + e^-)$ component from data has been applied on the total distribution of simulated events. The red lines represent the value of the poissonian fluctuations (δ_{poiss}) for the simulated statistics. The relative systematic uncertainty increases as the distributions overlap more and more. The dependence on the S/B ratio confirms that this is due to statistical fluctuation of signal and background in the template overlap area. As the number of signal events decreases, the goal to keep the *separation* systematics well below the purely Poisson fluctuation errors become more and more challenging.

The additional uncertainty δ_{sep} to the $(e^+ + e^-)$ fitted component is given by statistical fluctuations of both the signal and the background components in the region where their $\text{TRD}_{\text{class}}$ distributions

overlap. This is confirmed by a statistical simulation. Figure 4.34 shows the dependence of the δ_{sep} component for a simulation using templates with known shape, as a function of the S/B ratio and the overlap between the $\text{TRD}_{\text{class}}$ templates. The δ_{sep} uncertainty is indeed directly correlated to the TRD discrimination power: it increases with energy as the TRD separation power weakens. The fluctuations of the background and therefore the uncertainty on the fitted number of $(e^+ + e^-)$ can be however mitigated by a reduction of the background component in the sample. In this analysis, this is achieved through the calorimetric selection.

The total uncertainty on the signal events (σ_{stat}) is quoted as statistical error for the $(e^+ + e^-)$ flux. The values of σ_{stat} for each energy bin are reported in Table F.1 together with other sources of uncertainty that will be discussed later. The value of σ_{stat} is also reported in Table F.2 together with the measurement of the $(e^+ + e^-)$ flux, that will be discussed in Section 6.2.

The *selection* systematics is, on the other hand, uncorrelated to the fitting technique itself. It describes the uncertainty on the measured $(e^+ + e^-)$ events due to the limited knowledge of the template shapes and of the efficiency of the calorimetric selection.

In this analysis the signal and background template shapes are not evaluated using the MC simulation but they have been extracted from ISS data using a selection on the ECAL and on the Tracker. However, the template shape could have been biased by the selection and would therefore not be representative of the sample to fit.

The *signal* reference template has been determined using the procedure explained in Section 4.3.1. Different selections in a wide range of ECAL_{BDT} and E_{dep}/p have been explored and the impact on the e^\pm template shape has been proven to be negligible in the fit result. A unique definition (introduced in Section 4.3.1) has been therefore applied and the same template shape has been used for the fitting procedure up to the highest energy.

The *background* reference templates depend on the energy and they must be evaluated separately in different energy intervals. The background templates are defined using proton candidates selected by means of the estimated charge sign, the ECAL_{BDT} and E_{dep}/p values¹⁸. Any cut on these variables effectively introduces a bias on the proton template shape, especially at the highest energies. In fact, the proton selection efficiency of any of these cuts has an unavoidable energy dependence: the energy spectrum of the reference protons used to define the template is therefore different with respect to the spectrum of the proton background in the measurement sample. Therefore, the template shape may not be fully representative of the background to fit. The effect is more relevant at high energies for which the template shape rapidly changes with energy and the measurement is performed in wider energy bins. In addition to this, care has to be taken to remove any e^\pm contamination in the reference proton sample. e^\pm events would in fact enrich the tail of the template shape in the signal region. This would result in an overestimation of the background yield and a consequent underestimation of the signal yield.

Different proton template definitions have been explored in this analysis. Each template definition has been used to select reference protons from data and to construct the corresponding background $\text{TRD}_{\text{class}}$ template. For every proton template definition, a corresponding fit to the selected data has been applied (as discussed in Section 4.3) to extract the $(e^+ + e^-)$ signal contribution. The different

¹⁸For the proton template selection a cut on the $\text{ECAL}_{\text{BDT}}^{\text{long}}$ classifier has also been applied. The strength of the cut has been set looser than the cut used to define the sample to fit containing the $(e^+ + e^-)$ signal. The choice of the cut is a compromise between two conflicting requirements. The same $\text{ECAL}_{\text{BDT}}^{\text{long}}$ selection used to define the final measurement sample should be applied. Different values could bias the proton energy spectrum distribution. Conversely, the proton template should be defined using a data sample larger than the measurement sample, not only to minimize the statistical uncertainty of the template but also to minimize the statistical correlation between the two sets of events. The value of the cut on $\text{ECAL}_{\text{BDT}}^{\text{long}}$ has therefore been determined to give a good compromise between high proton efficiency and limited spectrum modification effect.

background templates show slightly different shapes and consequently yield different numbers of fitted ($e^+ + e^-$) signal. The choice of the background template definition is arbitrary. The uncertainty on the ($e^+ + e^-$) flux measurement due to the arbitrary choice in the definition of the proton template will be discussed in Section 4.4.1.

A total of five proton template categories have been defined depending on the selection applied¹⁹:

1. $R > 0$, no cut on ECAL_{BDT}
2. $R > 0$, $\text{ECAL}_{\text{BDT}} < 0$
3. no cut on R , no cut on ECAL_{BDT}
4. no cut on R , $\text{ECAL}_{\text{BDT}} < 0$
5. $R < 0$, $\text{ECAL}_{\text{BDT}} < 0$

and for each category, 6 different requirements on the E_{dep}/p have been explored²⁰. In total 36 proton template definitions have been investigated²¹.

The impact of the proton template selection is almost negligible at low energies, but become a major uncertainty at high energies, as is visible in the template shapes shown in Figure 4.35. This is confirmed by the spread in the ECAL_{BDT} efficiency shapes, shown in the same picture. The measured efficiency depends indeed on the proton template definition used to estimate the background in the $R < 0$ sample. In fact, fluctuations are dominated by the uncertainty on the fitted e^- when no ECAL_{BDT} cut is applied, which defines the efficiency normalization. Clearly, the same effect is present (and enhanced by the lower S/B ratio) for the fit of the ($e^+ + e^-$) signal yield in the total sample.

The effect of the systematic uncertainty on the final measurement due to the background template definition can be mitigated only by reducing the background level as much as possible. The higher the S/B ratio in the sample the lower will be the systematic uncertainty on the signal yield evaluation. For this reason the key point is the application of a calorimetric selection to enhance the S/B ratio prior to the template fitting and a good estimate of its efficiency.

This is achieved in this analysis by:

- 1) the calorimetric selection performed with the $\text{ECAL}_{\text{BDT}}^{\text{long}}$ which minimizes the proton content in the $R < 0$ sample, thus allowing a reliable estimate of the ECAL_{BDT} efficiency in the full energy range of the measurement
- 2) the $\text{ECAL}_{\text{BDT}}^{\text{long}} + \text{ECAL}_{\text{BDT}}$ selection on the full sample, which allows to reach the target S/B and to limit the systematics associated to the signal extraction.

Figure 4.30 summarizes the S/B level at different stages of this analysis, both in the $R < 0$ sample and in the total sample used to evaluate the ($e^+ + e^-$) counts.

Although the calorimetric cut has been applied to reduce the *separation* and *selection* systematics, a leftover contribution to the final uncertainty remains. In the next section, the method used to estimate the level of systematic uncertainty in the estimation of the ($e^+ + e^-$) events is presented.

¹⁹the sample with ($R < 0$, no cut on ECAL_{BDT}) has not been investigated due to the large contamination of e^- events that would introduce a severe bias in the proton template

²⁰ $E_{\text{dep}}/p < 0.9/0.8/0.7/0.6/0.5$ and no cut on E_{dep}/p

²¹ Category 1) is well suited to extract the signal from the total sample, because the cut on $R > 0$ assures a minimal contribution of signal events in the background templates. However, it may still contain a fraction of e^\pm whose net effect is an underestimation of the signal counts in the fit procedure. A cut on $\text{ECAL}_{\text{BDT}} < 0$ is therefore applied in the category 2) to further reject the e^\pm signal. The cut may, however, alter the template shape due to the bias on the proton spectrum discussed beforehand. In order to also take into account the bias introduced by the cut on the charge sign, category 3) 4) and 5) are also investigated. Those templates contain also $R < 0$ proton candidates. The rigidity distribution of charge-confused proton, which anyhow constitutes part of the background to be fitted in the measurement, is well different from the distribution of correct-charge protons. Charge confused protons have therefore a different distribution of the TRD classifier.

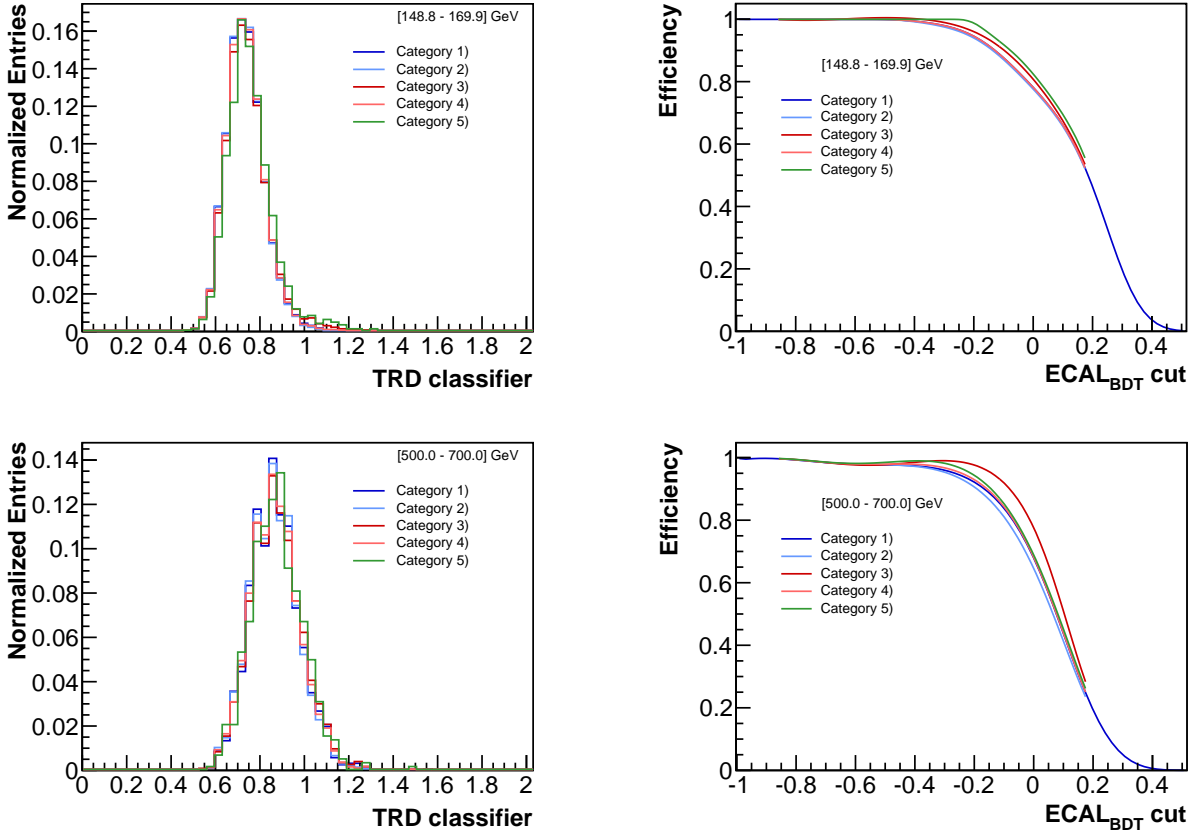


Figure 4.35: On the left, TRD classifier distribution in the energy range [148.8 - 169.9] GeV (**Top**) and [500.0 - 700.0] GeV (**Bottom**) for protons. The selection used to define each category is specified in the text. The same E_{dep}/p selection is applied for each definition. The different selections have visible impact on the template shapes due to: a) leftover e^{\pm} signal contamination after the proton selection b) modification of the proton spectrum induced by the energy dependent efficiency of the cuts applied. On the right the ECAL_{BDT} efficiency shape calculated using e^{-} data are shown. The spread in the curves is defined by the uncertainty to which the efficiency normalization is known. Some categories give slightly different shapes depending on the energy. The assessment of the systematic uncertainty associated to the choice of the proton template is addressed in Section 4.4.1.

4.4.1 Data driven estimation of signal identification systematic uncertainties

As stated in the previous section, one of the dominant systematic uncertainty in the signal extraction procedure is the uncertainty on the knowledge of the background template shapes. The same uncertainty could bias both the signal yield evaluation and the ECAL_{BDT} efficiency shape determination. The impact depends also on the S/B ratio set by the ECAL_{BDT} cut.

If such effects were to be treated separately, the same systematic uncertainty would be counted twice in the final uncertainty. Let's assume a simple case in which the analysis has been carried out with only one proton template definition and where a given ECAL_{BDT} cut, with efficiency ε_E , has been applied in order to select the signal. If any bias was introduced in the proton template distribution, the same kind of systematics would then propagate both on the estimate of the signal ($N_{(e^+ + e^-)}$) and indirectly on the ECAL_{BDT} efficiency estimation. Since the number of ($e^+ + e^-$) events is corrected by the selection efficiency in the flux measurement, namely $N^{(E)} = N_{(e^+ + e^-)}/\varepsilon_E$, the bias coming from the selection of a specific proton template would enter twice on this last quantity and its effect could be enhanced. Different net effects could arise depending on the ECAL_{BDT} cut applied to select the signal. In order to

correctly evaluate the systematic uncertainty, a “mashup” approach has been applied.

The idea of the “mashup” approach is to investigate all possible combinations of:

- ECAL_{BDT} selection used to enhance the sample purity;
- definition of the background template used in the estimation of the signal yield in the analysis sample. This yields the number of $(e^+ + e^-)$ events $N_{(e^++e^-)}$;
- definition of the background template used in the estimation of the signal yield in the $R < 0$ sample. This yields the ECAL_{BDT} efficiency which is used together with $N_{(e^++e^-)}$ to define $N^{(E)}$.

The investigation of all the possible combinations of the parameters allows to smear out correlations between different proton template definitions and to find the set of analysis parameters to apply in order to increase the sensitivity of the method.

The complete analysis has been repeated for 100 different cuts in ECAL_{BDT}, each defined for constant efficiency $\varepsilon_E^{(i)}$ steps²². The range $\varepsilon_E \in [0.55, 0.95]$ has been explored. For each $\varepsilon_E^{(i)}$ cut applied ($i = 0, \dots, 99$), the corrected $(e^+ + e^-)$ counts $N_{(e^++e^-)}^{(E)(ijk)}$ have been evaluated using the following definition:

$$N_{(e^++e^-)}^{(E)(ijk)} = N_{(e^++e^-)}^{(ij)} / \varepsilon_E^{(ik)} \quad (4.8)$$

where $N_{(e^++e^-)}^{(ij)}$ denotes the fitted signal yield evaluated using the j^{th} proton template definition and $\varepsilon_E^{(ik)}$ denotes the ECAL_{BDT} efficiency value estimated using the k^{th} proton template definition. Both j and k index runs on the proton template definitions described in Section 4.4. This allows to mix the different proton template categories in the $(e^+ + e^-)$ identification procedure.

The resulting $N_{(e^++e^-)}^{(E)(ijk)}$ populate therefore a hyper-cube with all the possible measurements as function of $\varepsilon_E^{(i)}$ and of the j^{th} and k^{th} proton template definitions. An example of a slice at fixed $\varepsilon_E^{(i)}$ of the different measurements obtained using the various proton template definitions is shown in Figure 4.36 for two energy bins. The spread of the counts has to be taken into account in the *selection* systematics, as shown later in this section.

In the same picture, Figure 4.36, the dependence of the result as function of the i^{th} ECAL_{BDT} cut, after averaging over all the j^{th} and k^{th} proton template definitions, is also shown. If no systematic uncertainty were present, and if the ECAL_{BDT} efficiency shape were completely correct, this profile has to be flat. Any trend in the profile is a hint of a systematic effect.

It is clearly visible from the picture that not all the proton template definition are suitable for the measurement. In fact, different template definitions are more suitable for the fit of the $R < 0$ sample, used to evaluate ε_E , or for the fit of the total sample. An algorithm based on the fit quality has been applied to dynamically select the best ten proton templates for each energy bin²³.

In order to quote the *selection* systematics for each given $\varepsilon_E^{(i)}$ cut, all the $N_{(e^++e^-)}^{(E)(jk)}, \forall j, k$ in an efficiency window of 10% around $\varepsilon_E^{(i)}$ have been considered. The spread of the distribution of the results around its mean value σ_{mash} is used as an estimation of the *selection* systematics. A graphical example

²²The choice to investigate the result in ε_E steps and not in ECAL_{BDT} steps allows to explore the signal selection parameters space uniformly.

²³All the proton template definitions have been tested for a fit with no ECAL_{BDT} cut and with a typical ECAL_{BDT} cut applied later in the analysis to extract the signal. The templates which best describe the background shape in the case when no ECAL_{BDT} cut is applied have been chosen to determine signal yield in the $R < 0$ sample. On the other hand, the templates which best describe the background shape in the case when the ECAL_{BDT} cut is applied (as explained before) have been chosen to determine the signal yield in the total sample. The proton templates that provide the best fit χ^2 has been used. In most cases, categories 1) and 4) resulted to be appropriate in both cases.

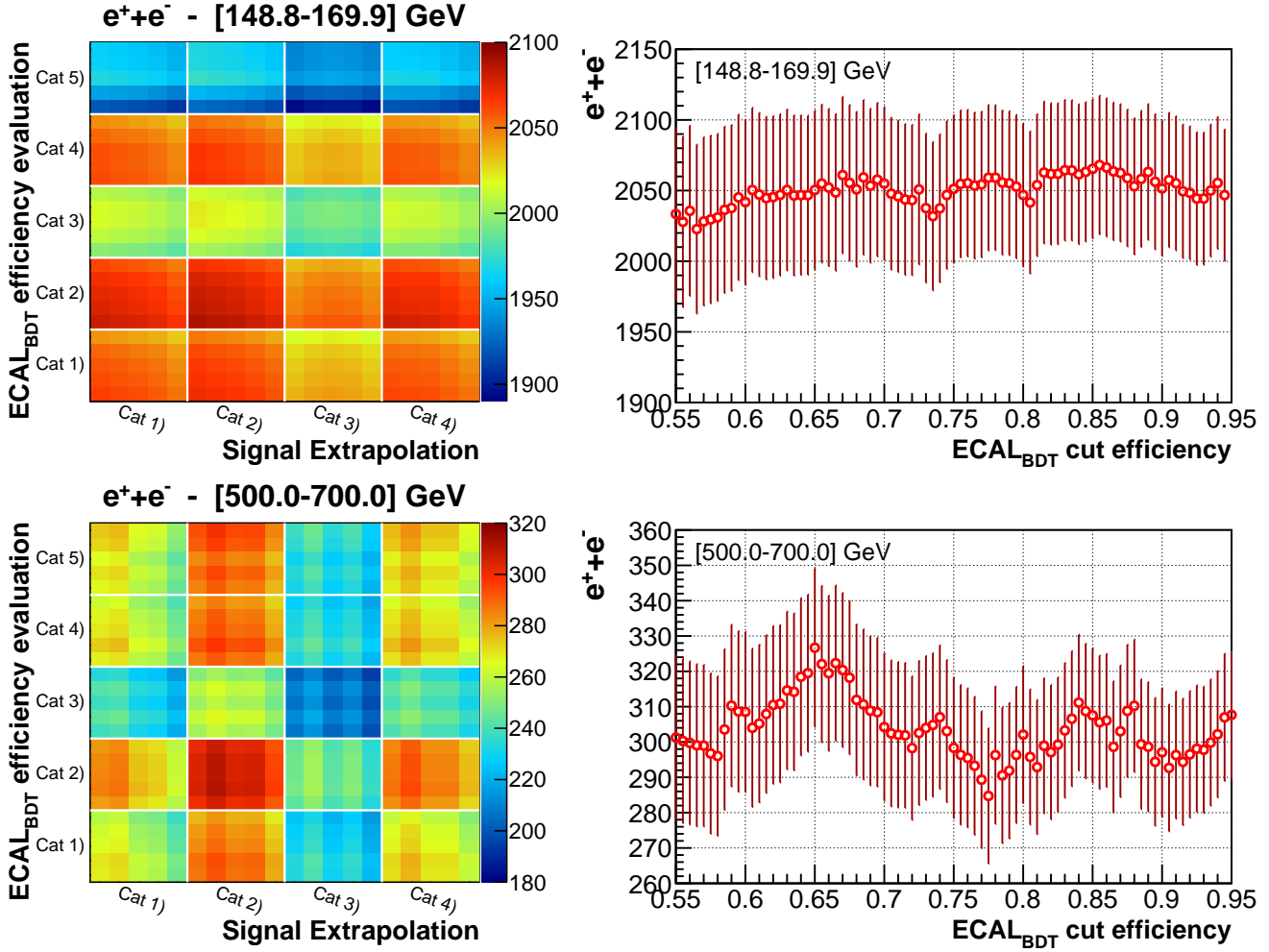


Figure 4.36: On the **Left**, the number of fitted ($e^+ + e^-$) counts corrected by the efficiency $N_{(e^+e^-)}^{(E)(jk)} = N_{(e^+e^-)}^{(j)} / \varepsilon_E^{(k)}$ for a fixed ECAL_{BDT} efficiency. The outcome is plotted as function of the proton template definition used to estimate the signal yield and of the proton template definition used to define the efficiency shape. Shown are the energy range [148.8 - 169.9] GeV on **Top** and [500.0 - 700.0] GeV on the **Bottom**. Within each category, the E_{dep}/p cut has also been varied. The result depends on the combination of the proton template categories. At low and medium energies up to ~ 250 GeV, Cat 5) is not suited to define the efficiency shape. It is worth noticing that, especially at high energies, the combination of the same proton template category typically enhances the bias on the final measurement. The idea of the “mashup” approach is to smoothen this effect out exploring all the possible proton template category combinations. On the **Right**, the result $N_{(e^+e^-)}^{(E)}$ for a wide region of ECAL_{BDT} efficiency in the same energy ranges is shown. Each point represent the median of the distribution of all the possible trials for a fixed ε_E (see the picture on the left). Error bars are statistical only. Any trend in the ECAL_{BDT} efficiency scan is taken into account in the final systematics.

is given in Figure 4.37, where the red distribution is built using all the results in the 10% efficiency window around the selected ECAL_{BDT} cut. The spread of the distribution around the mean is therefore a good estimation of the systematic associated to this selection. The median of the distribution is used as best estimation of the number of measured ($e^+ + e^-$) in the energy bin corrected by the ECAL_{BDT} efficiency.

The width of the distribution contains a purely statistical contribution, shown in blue in the same picture. The number of signal events for each $\varepsilon_E^{(i)}$ point sampled in this procedure changes inside the 10%

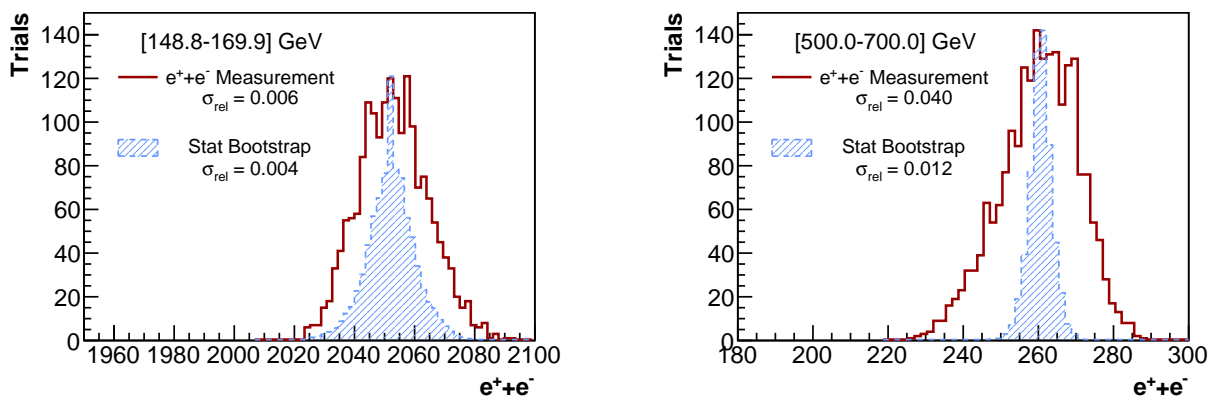


Figure 4.37: In red, the distribution of the fitted signal yield corrected by the ECAL_{BDT} efficiency ($N_{(e^+e^-)}^{(E)}$) in a 10% efficiency window around the chosen ECAL_{BDT} cut for the [148.8 - 169.9] GeV and the [500.0 - 700.0] GeV energy intervals. The distribution also includes the impact of the definition of the proton templates using ECAL and Tracker selections. The spread of the distribution is used to define the *selection* systematic error. The median of the distribution is used as the best estimation of $N_{(e^+e^-)}$ corrected by the ECAL_{BDT} efficiency in Equation 3.11 for the measurement of the $(e^+ + e^-)$ flux. In blue, the distribution of the result according to statistical fluctuations only, evaluated through a statistical bootstrap procedure. Its contribution to the total error is subtracted as described in the text.

efficiency window: this effect induces a purely statistical contribution to the distribution width. This effect has been evaluated and removed through a statistical bootstrap simulation. For each energy bin, the purely statistical width σ_{bstr} has been evaluated in a statistical simulation. The number of signal events fitted from data has been varied within the efficiency window according to statistical fluctuations and taking into account the correlations between different efficiency values. The scan of the resulting fitted signal component has been treated using the same procedure as in data. This procedure has been repeated several times to evaluate the uncertainty on the statistical simulation, $\Delta(\sigma_{\text{bstr}})$. The mashup distribution width σ_{mash} has been finally compared to the outcome of this procedure. If σ_{mash} has been found to be compatible within the $\Delta(\sigma_{\text{bstr}})$ error with σ_{bstr} , the *selection* systematics has been set to 0 because completely compatible with statistical fluctuations. Otherwise, the statistical contribution has been subtracted and the *selection* systematics evaluated according to the following formula:

$$\delta_{\text{sel}} = \sqrt{\sigma_{\text{mash}}^2 - \sigma_{\text{bstr}}^2} \quad (4.9)$$

Figure 4.38 shows the distribution of σ_{mash} and σ_{bstr} as function of the energy. In a wide energy range ([20-150] GeV) the *selection* systematics is compatible with statistical effects. Therefore a negligible *selection* systematic uncertainty is associated to the measurement in this energy range.

In order to quote the final result, for each energy bin the result has been evaluated through the described processes using a sliding ECAL_{BDT} window with a 10% width, in the range $\varepsilon_E \in [55\%-95\%]$. For each i^{th} iteration with the symmetric ECAL_{BDT} centered in $\varepsilon_E^{(i)}$, the total uncertainty associated to the signal extraction $\delta N^{(i)}$ has been evaluated taking into account:

- *selection* systematic uncertainty $\delta_{\text{sel}}^{(i)}$, evaluated using the “mashup” approach in the i^{th} window
- *separation* systematic uncertainty $\delta_{\text{sep}}^{(i)}$, evaluated as already discussed and averaged over the whole i^{th} window and over all the template definitions used to extract the signal

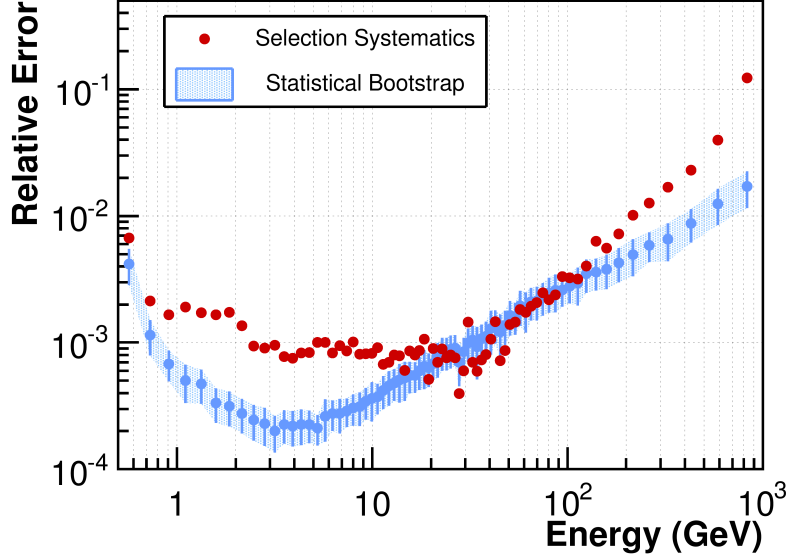


Figure 4.38: Mashup distribution width σ_{mash} (red) and statistical bootstrap σ_{bstr} (azure) evaluated in each energy bin. The azure error band represents the width of the statistical distribution defined by the limited statistic sampled for each iteration. In the region [20-150] GeV the *selection* systematic uncertainty is negligible, any fluctuations in the signal extrapolation procedure can be explained as effects of statistical fluctuations.

- *Poissonian* uncertainty $\delta_{\text{poiss}}^{(i)}$, evaluated as the purely statistical uncertainty due to fitted signal events fluctuations.

and calculated as the quadratic sum of all contributions.

$$\delta N_i = \delta_{\text{sel}}^{(i)} \oplus \delta_{\text{sep}}^{(i)} \oplus \delta_{\text{poiss}}^{(i)} \quad (4.10)$$

In general, a stronger cut on ECAL_{BDT} allows to reduce δ_{sel} and δ_{sep} but increases the pure statistical uncertainty. On the other hand, a loose cut on ECAL_{BDT} maximizes the statistics, but would suffer from higher systematics due to the disadvantageous S/B. Therefore for each energy bin the choice of the calorimetric selection using the ECAL_{BDT} cut has been optimized to minimize the total uncertainty $\delta N^{(i)}$. The efficiency on the ECAL_{BDT} cut, together with its 10% window, is shown in Figure 4.32. An example of the procedure used to determine the most sensitive ECAL_{BDT} cut is sketched in Figure 4.39. The total uncertainty δN is however stable for a wide range of ε_E choices: this confirms a-posteriori the stability and the correctness of the signal extraction procedure applied in this analysis.

Figure 4.40 shows the evolution of statistical and selection uncertainties as a function of the energy bin. Above 15 GeV, where the TRD signal universal template has been applied, and up to 150 GeV, the *selection* systematics is negligible. Its contribution to the total error remains however minor in the whole energy range from 0.5 GeV to 1 TeV. The statistical error²⁴ dominates instead always over the signal selection systematics. In particular, the statistical error is dominated by pure signal statistical fluctuation up to ~ 500 GeV. Above this energy, the fluctuations of the fitted signal and background yield in their template overlap region induced by the decrease of the TRD separation power takes over and dominate the statistical uncertainty. A summary of the sources of error discussed in this section and the values of $N_{(e^+e^-)}^{(E)}$ for each energy bin are reported in Table F.1 together with other sources of uncertainty discussed in the next chapters.

²⁴As a reminder, in this work the statistical error σ_{stat} is defined as in Equation 4.7.

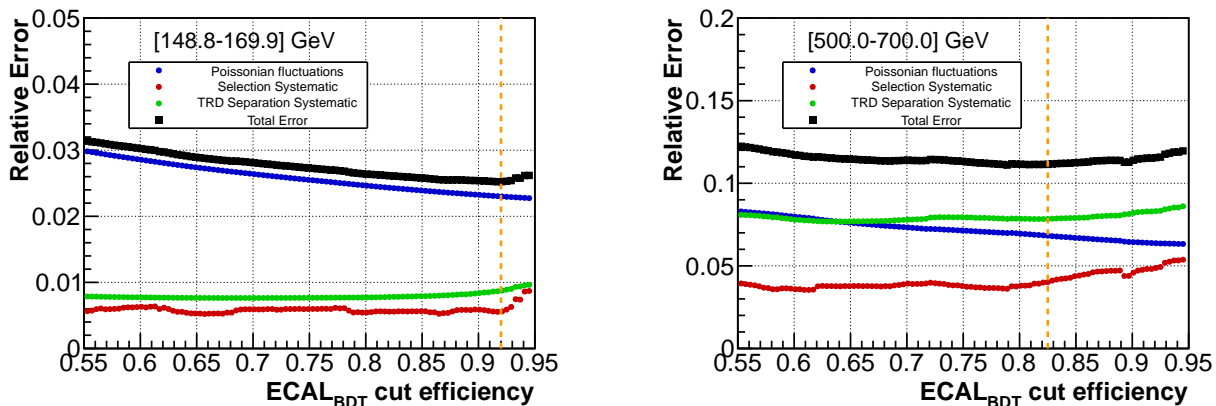


Figure 4.39: Relative uncertainty on signal extraction from different sources. Shown are the energy range [148.8 - 169.9] GeV on the **Left** and the energy range [500.0 - 700.0] GeV on the **Right**. For each ECAL_{BDT} efficiency value, a sliding 10% region around the mean ε_E is considered to evaluate the uncertainty. **Blue**: δ_{poiss} Poissonian statistical fluctuations in the region. **Red**: δ_{sel} : *selection* systematic uncertainties in the region (takes into account instability of the result by any change of a wide range of the analysis parameters). **Green**: δ_{sep} TRD *separation* systematics in the region (template separation and background fluctuations). **Black**: total uncertainty in the region, calculated as quadratic sum of the previous contributions. The final result in each energy bin is selected at the point where the total uncertainty is minimum, here represented by the vertical orange line.

4.5 Summary

In this chapter, the electron and positron identification capabilities of AMS have been discussed.

The identification of e^\pm in the cosmic radiation is not trivial. The overwhelming proton component in the cosmic radiation, which is $\sim 10^2$ (10^3) times more abundant than e^- (e^+), represents an unavoidable source of background especially for the e^+ and for the ($e^+ + e^-$) identification.

AMS is the first spectrometer in space with complete redundancy for the e^\pm identification. The Transition Radiation Detector (TRD), on top of the spectrometer, can distinguish between e^\pm and protons through the measurement of TR X-rays produced with higher probability by e^\pm . The Electromagnetic Calorimeter (ECAL), located at the bottom of the spectrometer, separates e^\pm and protons by the topological analysis of the electromagnetic and hadronic showers started by the primary particles. The Tracker rigidity measurement can finally be combined to the energy measurement of the ECAL to increase the separation capabilities by a comparison of the two measurements.

The redundant capabilities of the detector allow to select a pure control sample of e^- from data through a *Tag&Probe* approach using the measurement of the charge sign from the Tracker and the ECAL (or TRD) detector, and that sample can be used to calibrate the other subdetector TRD (or ECAL). The ECAL and TRD e/p separation algorithms have been therefore tuned on data to maximize the proton rejection.

In this analysis, the redundancy has been exploited to identify e^\pm in the data using a data-driven method which does not rely on any statistical subtraction of the expected background from data based on the MC simulation (as typically done by previous experiments).

The steps of the method are the following:

1. A high quality sample of relativistic, downward-going charge 1 particles has been selected from the total 41×10^9 events triggered by the AMS detector. The selection is based on the analysis of the energy deposit in all the subdetectors of AMS. Secondary particles trapped inside the geomagnetic

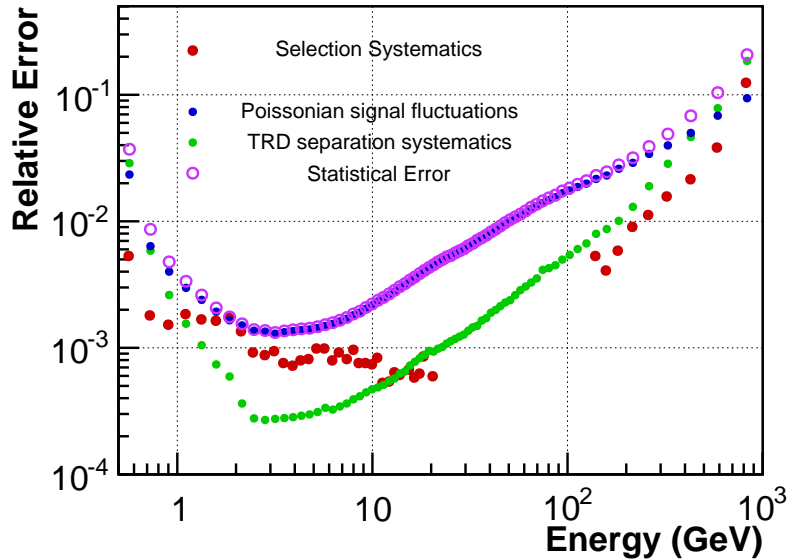


Figure 4.40: Contribution to the measurement uncertainty from the signal extraction procedure and statistical fluctuations as a function of the $(e^+ + e^-)$ energy. In every energy bin, the selection parameters have been defined such that the total signal estimation uncertainty is minimum (see Figure 4.39). The selection systematic error (in red) has a negligible contribution between 20 and 150 GeV, and it is not reported in this picture. Outside this energy range, its contribution to the total error remains minor. The purely statistical fluctuations of the fitted $(e^+ + e^-)$ yield (in blue) dominate the uncertainty up to ~ 500 GeV. Above this energy, the fluctuations of signal and background in the overlapping TRD template region (in green) take over and dominate up to 1 TeV. The total statistical uncertainty (in violet) always dominates over the selection systematics.

field have been removed using a selection on the geomagnetic rigidity cutoff.

2. The bulk of the proton background distribution has been removed from the selected sample using a selection based on the longitudinal shower development in the first five X_0 of the calorimeter. A multivariate separation tool based on a Boosted Decision Tree algorithm has been developed in order to achieve a compromise between good e/p separation and high level of agreement with the MC simulation. The agreement with the MC simulation is better than 1% in the whole energy range. The efficiency of the selection can therefore be estimated from the MC simulation with a minor impact in the final measurement uncertainty.
3. The remaining proton contamination in the sample is identified by a template fit procedure. A TRD based variable for the electron/proton separation has been defined with lower separation power with respect to standard statistical tools but with a negligible energy dependence for e^\pm . The TRD template shapes can be therefore inferred from low energetic e^\pm and applied up to TeV energies. The TRD shape normalization has been varied to fit the data in each energy bin and the signal and background yields have been extracted. In total, ~ 10.6 million $(e^+ + e^-)$ have been identified between 0.5 GeV and 1 TeV.
4. Before the fitting procedure an additional reduction of the proton background is needed, especially at high energies when protons start to become highly relativistic and emit transition radiation in the TRD. This results in closer peaks in the TRD classifier distribution for e^\pm and protons, and a larger overlap in their distribution tails. The net effect is an increased uncertainty on the estimated number of $(e^+ + e^-)$ due to statistical fluctuations of both the signal and background components

where their TRD classifier distributions overlap. The proton reduction has been achieved through a selection on the full analysis of the electromagnetic shower in ECAL. The cut that minimizes the total measurement uncertainty has been used to define the measured number of $(e^+ + e^-)$. The ECAL selection efficiencies has been retrieved with a data-driven method without any use of the MC simulation.

5. Systematic effects affect the event selection uncertainty and are mainly related to the knowledge of the TRD classifier reference templates, which enter both in the $(e^+ + e^-)$ yield evaluation and in the ECAL cut efficiency assessment. The template fit analysis has therefore been repeated ~ 2000 times in each energy bin to explore a wide range of combinations of the ECAL selection cut and of the selection criteria used to build the reference templates. The spread of the results has been used to estimate the systematic uncertainty affecting the evaluation of the $(e^+ + e^-)$ events.

The robustness of the method and the high e/p separation capabilities of ECAL and TRD allow to measure the number of $(e^+ + e^-)$ events in the data with an uncertainty which is always dominated by statistical fluctuations in the whole energy range. The impact of the ECAL and Tracker selection in the method does introduce only a minor systematic uncertainty, and the result is well stable inside statistical fluctuations. At high energies, where the TRD separation power starts to decrease, background fluctuations enhance the statistical uncertainties, and dominate the measurement statistical error starting at ~ 500 GeV.

In the next chapter, the normalization of the measured $(e^+ + e^-)$ counts to the flux on top of the detector and the relative systematic uncertainties will be discussed in detail.

Chapter 5

Normalization to the $(e^+ + e^-)$ flux on top of the detector

In the previous chapter, the procedure used to evaluate the number of $(e^+ + e^-)$ events collected by the AMS detector has been reviewed. The proportionality between the collected $(e^+ + e^-)$ events ($N_{(e^+ + e^-)}$) and the flux on top of the detector ($\Phi_{e^+ + e^-}$) is described by Equation 3.11. In addition to the trivial ΔE factor, the collected counts have to be renormalized to the experiment exposure time ΔT_{exp} and to the effective acceptance A .

In this section, the procedure used to evaluate the two correction factors is described. A separate session is dedicated to the study of the e^\pm trigger efficiency. The assessment of the systematic uncertainties due to the accuracy to which the detector acceptance and the selection efficiencies are known will be discussed in detail.

5.1 Exposure time

The number of cosmic rays detected by AMS in a time interval in which the incoming flux can be considered constant is proportional to the time the experiment was not busy with the electronics readout and was ready to start the DAQ for cosmic rays that triggered the experiment¹. The total time interval ΔT_{exp} has to be measured to normalize the collected $(e^+ + e^-)$ events to the experiment detection time.

For the calculation of the $(e^+ + e^-)$ flux the events collected during seconds of not nominal data taking have been removed from the analysis sample. The second-based selection has been already discussed in Section 4.1.1.

For all the ~ 30 months of data taking, livetime (\mathcal{L}) weighted seconds passing the selection described in Section 4.1.1 have been summed up. The livetime factor takes into account the fraction of time in which the detector was not busy and consequently ready to start the DAQ.

The exposure time does not coincide for all incoming particles in the same real time interval. At a certain geomagnetic coordinate, only the flux of particles with rigidities above a certain threshold is not contaminated with secondaries trapped in the geomagnetic field. Seconds of data taking are integrated to the total exposure time only in the energy bins fulfilling the selection on the geomagnetic rigidity cutoff. The selection applied to remove secondaries trapped in the geomagnetic field, described in Section 4.1.4, introduces consequently an energy dependence in the exposure time.

Since the measurement of the $(e^+ + e^-)$ flux is binned, the exposure time has been set constant in each energy bin. For each second of DAQ the requirement on $R_{\text{max}}^{40^\circ}$ has been tested using the lower

¹This statement is not true for a wide time window because the incoming flux, and consequently the number of particles crossing the detector, changes as function of the geomagnetic coordinates. In this analysis the exposure time is evaluated on a second by second basis, and this assumption holds.

energy border of the bin. In the analysis, therefore, self-consistency has been achieved by selecting particles above $R_{\max}^{40^\circ}$ not according to their rigidity, but according to the lower energy border of the bin they belong², as explained in detail in Section 4.1.4

The formula for the calculation of the exposure time $\Delta T_{\text{exp}}(E_{\min}, E_{\max})$ for the energy E belonging to the bin $[E_{\min}, E_{\max}]$ reads therefore:

$$\Delta T_{\text{exp}}(E \in [E_{\min}, E_{\max}]) = \sum_{t=t_{\min}}^{t=t_{\max}} \mathcal{L}(t) \theta(t, E_{\min}) \quad (5.1)$$

where the sum runs over all the seconds of data taking and $\theta(t, E_{\min})$ is a time dependent function that takes the value 1 if E_{\min} is above the geomagnetic cutoff according to the procedure described before and takes the value 0 otherwise.

Figure 5.1 shows the energy dependence of $\Delta T_{\text{exp}}(E)$ for the whole data taking period used in this analysis. The values reported in the picture are used in Equation 3.11 for the measurement of the ($e^+ + e^-$) flux. The ‘‘plateau’’ value of the exposure time above ~ 30 GeV, where the effect of the geomagnetic field starts to be negligible, is $\sim 6.2 \cdot 10^7$ seconds. This corresponds to an overall detector time efficiency of $\sim 78\%$.

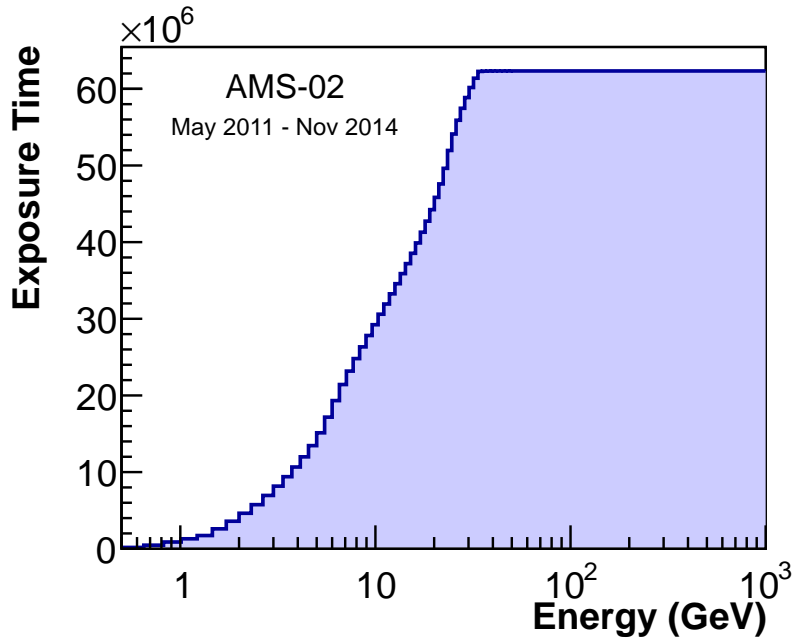


Figure 5.1: Exposure time corresponding to ~ 30 months of AMS operations, after requirements on the DAQ quality. At low energies the decrease is due to the energy dependent selection to remove secondaries trapped in the geomagnetic field. Above ~ 30 GeV, the plateau value of $\sim 6.2 \cdot 10^7$ s corresponds to $\sim 78\%$ of the total time from the detector activation in May 2011.

5.2 Trigger

Particles crossing AMS are detected only if they satisfy the online trigger conditions. If the trigger fails, the DAQ boards do not store the electronic information and the cosmic ray is not recorded.

²For relativistic e^\pm , the value of the energy coincides numerically with the value of the rigidity (if expressed in natural units). No bias is introduced in checking the requirement on the particle rigidity using the ECAL energy measurement.

The DAQ settings of the AMS experiment allow to measure the trigger efficiency ($\varepsilon_{\text{trig}}$) directly from the data collected in space. As already introduced in Section 2.8, seven trigger signals can be produced by the LVL1 board. If any LVL1 trigger signal is produced, the event is recorded. The seven trigger signals can be divided in two big categories according to their purpose:

1. *Physics Trigger* (PHYS), with no prescale factor:

- Single charge (SC) trigger
- Normal ion (NI) trigger
- Slow ion (SI) trigger
- Electron (EL) trigger
- Photon (PH) trigger

2. *Unbiased Trigger* (UNB):

- Single charge unbiased (SCunb) trigger, with a prescale factor $w_{(\text{SC})} = 100$
- Electromagnetic unbiased (EMunb) trigger, with a prescale factor $w_{(\text{EM})} = 1000$

The prescale factors $w_{(\text{SC,EM})}$ have been introduced to reduce the busy time of the detector: the trigger board sets the UNB trigger bit and the event is recorded only once every $w_{(\text{SC,EM})}$ events that fulfilled the UNB requirements. The bit is otherwise not set and the event is recorded only if one of the PHYS trigger conditions are fulfilled. PHYS triggers are meant to record cosmic ray events for physics analyses. Only PHYS events have been selected for the ($e^+ + e^-$) flux measurement, with no distinction on the subtrigger channels. The purpose of the UNB triggers is, instead, to start the acquisition of events dedicated to the calculation of the PHYS trigger efficiency. UNB triggers are defined by much looser trigger conditions than the PHYS triggers, and they are consequently used to estimate the PHYS trigger efficiencies.

For each PHYS trigger channel, the trigger efficiency ($\varepsilon_{\text{trig}}^i$) for e^\pm can be calculated directly from the flight data according to the following formula:

$$\varepsilon_{\text{trig}}^i = \frac{N_{e^\pm}^i}{N_{e^\pm}^i + w_{(\text{SC})}N_{e^\pm}^{\text{SCunb}} + w_{(\text{EM})}N_{e^\pm}^{\text{EMunb}} + w_{(\text{SC+EM})}N_{e^\pm}^{\text{SCunb+EMunb}}} \quad (5.2)$$

where $N_{e^\pm}^i$ is the number of e^\pm which have been triggered (not exclusively) by the i^{th} trigger channel, $N_{e^\pm}^{\text{SCunb}}$ and $N_{e^\pm}^{\text{EMunb}}$ are the number of e^\pm triggered only by the SCunb or by the EMunb trigger and $N_{e^\pm}^{\text{SCunb+EMunb}}$ is the number of e^\pm triggered only by both unbiased triggers.

Equation 5.2 has been used to calculate the trigger efficiency on a control sample of e^- selected from data using strict requirements on the Tracker (including the charge sign) and on the TRD. Electrons are triggered by the SC, EL and PH triggers. Other trigger channels, which require a high energy deposit in the TOF paddles, have an efficiency on e^\pm lower than 1%. At low energies, most of the e^\pm are triggered by the SC trigger. Below 2 GeV the ECAL trigger energy deposit threshold is in fact not reached by e^\pm em showers. However the SC trigger contains a veto on the number of fired ACC. For e^\pm events the backscattering of secondaries from the ECAL limits the SC efficiency, which decreases as the e^\pm energy (and consequently the probability of high activity on the ACC paddles) increases. The EL trigger has been introduced in AMS in order to recover the inefficiency induced by the ACC veto. The EL trigger uses the ECAL and the TOF energy deposit to produce the trigger signal with no requirements on the ACC. When the energy of e^\pm is high enough to deposit energy in the ECAL above the threshold, the EL trigger efficiency rapidly rises above 95%. The PH trigger, which relies on the ECAL energy deposit and angular reconstruction only, reaches the maximum plateau for electrons above 99% from 10 GeV

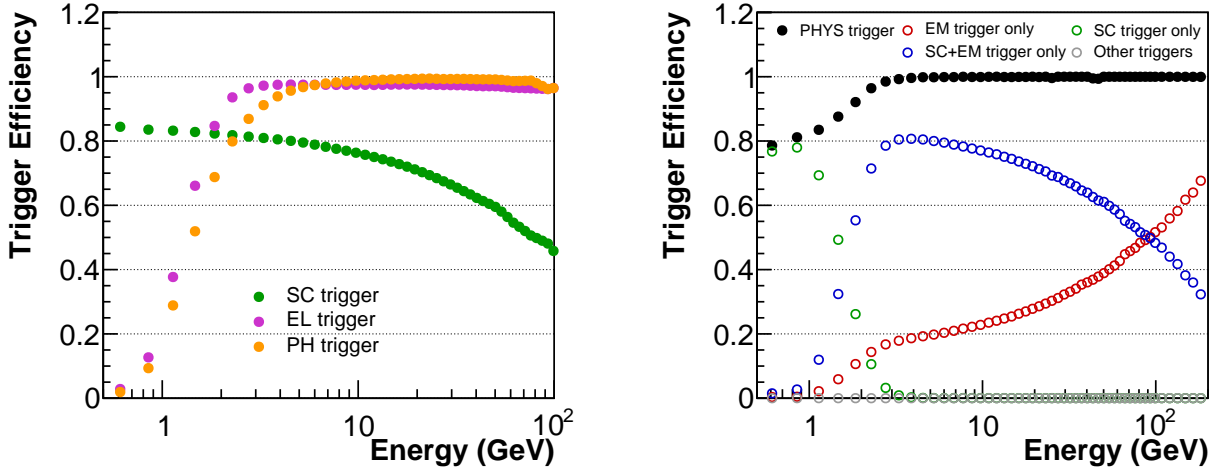


Figure 5.2: On the **Left**, the inclusive^a e^\pm trigger efficiencies for the Single Charge (SC), the Electron (EL) and the Photon (PH) trigger channels are shown. The efficiencies are calculated on an e^- control sample selected from flight data using the Tracker and the TRD subdetectors. The value of the trigger efficiency is inferred using the unbiased triggers recorded during data taking. Above ~ 3 GeV, the EL and PH triggers have efficiencies well above 95%. Below 2 GeV e^\pm are triggered mostly only by the SC trigger, whose efficiency on e^\pm decreases at high energies due to backscattering hits in the ACC paddles. On the **Right**, the total e^\pm trigger efficiency (in black) is shown. The efficiency starts from a value of $\sim 80\%$ at 0.5 GeV and reaches the plateau value of $\sim 100\%$ from 3 GeV on. In the same picture, the trigger composition as sum of SC exclusive triggers (green), electromagnetic (EL, PH) exclusive triggers (red) and SC+electromagnetic (blue) exclusive triggers is shown. Above 3 GeV, most of the events are triggered by the three channels together. At high energies, the fraction of exclusive electromagnetic triggers dominates the sample. Other trigger channels contribute to the total collected sample by less than 1%.

^aTwo or more PHYS trigger can be set for each event. The “inclusive” efficiency is calculate considering all events with the selected trigger bit on, disregarding the rest of the bit word. On the contrary, the “exclusive” efficiency considers events with only the selected bit word set.

on. The energy dependence of the e^\pm trigger efficiency for the SC, EL and PH triggers is shown in Figure 5.2. In the same picture, the total e^\pm PHYS trigger efficiency is shown. The e^\pm total trigger efficiency rises from a value of $\sim 80\%$ at 0.5 GeV up to $\sim 100\%$ at energies above 3 GeV. All e^\pm events above 3 GeV are correctly recorded by the AMS detector. The composition of the efficiency itself is also reported. While at low energies e^\pm are triggered only by the SC trigger, starting from ~ 2 GeV more than 50% of events are triggered by the SC, EL and PH trigger together. As the energy increases, the fraction of events triggered only by the electromagnetic triggers only increases due to the inefficiency in the SC trigger. The ECAL triggers (EL and PH) play a fundamental role in the detection of e^\pm , as they guarantee a $\sim 100\%$ trigger efficiency for e^\pm above 3 GeV. The number of e^\pm triggered by other channels is always below 1% in the whole energy range.

The $\sim 100\%$ trigger efficiency for e^\pm events assures that no systematic uncertainty are introduced by the trigger selection on the ($e^+ + e^-$) sample and on its acceptance above ~ 3 GeV. The impact of the trigger efficiency uncertainty at low energies on the ($e^+ + e^-$) flux measurement will be covered in the next section together with all other selection cuts used to define the acceptance for ($e^+ + e^-$).

5.3 AMS acceptance for e^\pm

The detector geometry and the interactions experienced by the incoming particles within the detector material have to be correctly taken into account to evaluate the incident flux. The normalization of the measured number of ($e^+ + e^-$) to the flux impinging on top of the detector is determined by the acceptance factor A already defined in Section 3.1:

$$\mathcal{A}(E, \Omega) = \int_{\Omega} \int_S \varepsilon_i(E, \Omega) \hat{r} \cdot d\vec{S} d\Omega \quad (5.3)$$

In this chapter, the acceptance formulation procedure and its application to the ($e^+ + e^-$) flux measurement are reviewed. The assessment of systematic uncertainties for the acceptance evaluation is discussed in the next section.

5.3.1 Acceptance formulation

Equation 5.3 can be solved analytically only for simple regular geometries. In the case of an ideal planar detector with dimensions σ_x , σ_y and σ_z , $\sigma_z \ll \sigma_{x,y}$, $S = \sigma_x \sigma_y$ and with detection efficiency $\varepsilon(E, \Omega) = 1 \forall (E, \Omega)$ the integral can be solved analytically as follows:

$$A = \int_{\Omega} \int_S \hat{r} \cdot d\vec{S} d\Omega = \int_{-1}^0 \int_{2\pi} \int_S \cos\theta d\cos\theta d\phi dS = \pi S \quad [\text{m}^2\text{sr}] \quad (5.4)$$

where the assumption of an only downward-going flux ($\cos\theta \in [-1, 0]$) and no dependence of the selection efficiency on the incoming direction (θ, ϕ) has been applied.

In case of more complex geometries, and in general if the interactions of particles with the detector materials have to be taken into account, Equation 5.3 cannot be solved analytically. As originally discussed in [226] a MC simulation approach can be adopted. A total number of particles N_{gen} are generated with a known energy spectrum and known directional dependence from an opening aperture with known acceptance A_{gen} . The particles are then propagated inside the detector volume, simulating the detector geometry, the interactions in the materials and the selection algorithms applied in the analysis. Using the MC simulation method, the detector acceptance can be evaluated only in energy intervals, or bins. The value of the acceptance is representative only for a particular energy value $\tilde{E} \in [E, E + \Delta E]$ of the energy bin. The value \tilde{E} depends on the energy spectrum of particles injected in the detector, as will be discussed in detail in Section 6.1.2. The detector acceptance is inferred from the number of simulated particles detected in the energy bin according to the following scaling law:

$$A(\tilde{E}) = A_{\text{gen}} \frac{N_{\text{sel}}(E)}{N_{\text{gen}}(E)} \quad (5.5)$$

or, using Equation 5.4,

$$A(\tilde{E}) = \pi S \frac{N_{\text{sel}}(E)}{N_{\text{gen}}(E)} \quad (5.6)$$

in case of a planar generation plane. In Equation 5.5, $N_{\text{sel}}(E)$ and $N_{\text{gen}}(E)$ indicate the number of particles generated and detected in the energy range $[E, E + \Delta E]$.

5.3.2 Acceptance calculation for the ($e^+ + e^-$) flux measurement

For the calculation of the acceptance used for the flux measurement, the MC approach has been used. As already described in Section 3.2, the simulated e^- sample is generated isotropically³

$$dN/d\cos\theta \propto \cos\theta \quad dN/d\phi = \text{const}$$

and with a generated energy E_{gen} spectrum

$$dN/dE_{\text{gen}} \propto E_{\text{gen}}^{-1}$$

in each of the three generation intervals. Particles are generated from a square plane at $z = 1.95$ m with side length 3.9 m and centered in the AMS z axis. Using the result obtained in Equation 5.4 for a planar detector, the generation plane has an acceptance of $\pi S \simeq 47.78$ m²sr.

The acceptance for the ($e^+ + e^-$) flux measurement is calculated in various forms according to Equation 5.6 for the requirements

- Geometrical selection and clean event reconstruction
- Charge-one particle

introduced in Section 4.1. The normalization to the additional requirements on (i) good data taking and ISS attitude conditions and on (ii) rejection of trapped secondaries, is covered by the calculation of the exposure time ΔT_{exp} as described in Section 5.1.

The efficiency and the systematic uncertainties of the proton rejection cuts, namely the selection on ECAL_{BDT} and $\text{ECAL}_{\text{BDT}}^{\text{long}}$, have also been evaluated with a dedicated procedure as described in Chapter 4.

The total acceptance term $A^{e^\pm}(E)$ can be therefore factorized as follows:

$$A^{e^\pm}(E) = \mathcal{A}_{\text{MC}}^{e^\pm}(E) (1 + \delta(E)) \varepsilon_{\text{ECAL}}^{e^\pm}(E) \quad (5.7)$$

where the term $\varepsilon_{\text{ECAL}}^{e^\pm}(E)$ indicates the ECAL selection efficiency and $\mathcal{A}_{\text{MC}}^{e^\pm}(E)$ the effective acceptance retrieved from the MC simulation without any ECAL proton rejection selection. The factor δ covers any correction to the MC acceptance due to inconsistencies between the MC simulation and the data. The estimation of the correction factor δ will be discussed in the next section. In this section, the acceptance term $\mathcal{A}_{\text{MC}}^{e^\pm}(E)$ will be studied in detail and will be named \mathcal{A}_{MC} in the following.

The energy dependence of the acceptance \mathcal{A}_{MC} is shown in Figure 5.3 at different steps of the particle selection.

The purely geometrical acceptance, defined by the detector structure only, has been first calculated removing any effect of interactions with the detector material and with the magnetic field. A cosmic ray originated from the generation surface has been considered inside the geometrical acceptance of AMS if it crossed the TRD from top to bottom, the 4 TOF layers, at least one layer for each layer pair of the inner Tracker⁴ and finally ECAL from top to bottom (see the green aperture in Figure 5.4 for a graphical

³The acceptance calculation in the MC approach depends on the angular distribution of the generated spectrum. The acceptance is therefore not a property of the detector alone, but describes the response of the detector to a particular directional distribution of the incoming flux. In this analysis, the acceptance always refers to an isotropic incoming flux. Deviations from the isotropy assumptions of the incoming flux (inside the limits of the measured ($e^+ + e^-$) isotropy level) have been tested in parallel studies and found to be negligible with respect to the other systematic uncertainties affecting the acceptance calculation.

⁴The minimum requirement to have a fit to the Tracker track is to have hits in at least one Tracker plane for each inner Tracker plane pair (L3-4, L5-6, L7-8).

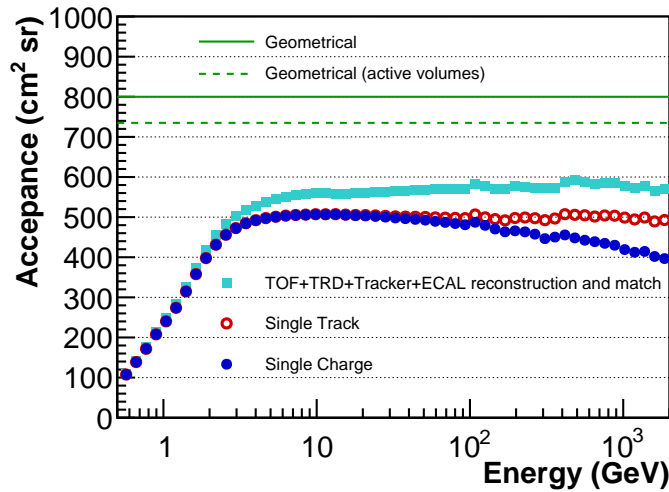


Figure 5.3: Energy dependence of the $(e^+ + e^-)$ acceptance for different steps of the selection. The green line shows the purely geometrical acceptance for particle crossing the TRD, TOF, Tracker and ECAL volumes ($\sim 800 \text{ cm}^2\text{sr}$). The dashed line represents the acceptance if the requirement of crossing through active volumes of the detector is added. The light blue points show the acceptance after all the requirements on each subdetector reconstruction and matching. At low energies, the acceptance drastically drops due to inefficiencies in the reconstruction algorithms, interactions and multiple scattering with the detector materials. The effect becomes smaller above 10 GeV, where the acceptance reaches a plateau value of $\sim 550 \text{ cm}^2\text{sr}$. The further requirements on the event quality applied to remove interaction events set the maximum value of the acceptance at $\sim 500 \text{ cm}^2\text{sr}$ at 10 GeV, with a trend to slightly decrease for higher energies up to $\sim 400 \text{ cm}^2\text{sr}$ at 1 TeV.

illustration). These requirements correspond to a purely geometrical acceptance of $\sim 800 \text{ cm}^2\text{sr}$. In order to produce a detectable signal, the particle has to cross the active materials of the detector. Including this additional requirement, the acceptance decreases to $\sim 735 \text{ cm}^2\text{sr}$. The inefficiency is mainly dominated by the crossing of inactive areas of the inner Tracker silicon layers.

The requirements on each subdetector reconstruction and on the geometrical compatibility between different subdetectors reduce the acceptance to $\sim 550 \text{ cm}^2\text{sr}$ above 10 GeV. Below this energy, the increase of the trajectory bending in the magnetic field and the increase of the energy losses and multiple scattering during interactions with the detector materials induce inefficiencies in the reconstruction algorithms. The acceptance is consequently reduced to its minimum value of $\sim 100 \text{ cm}^2\text{sr}$ at 0.5 GeV. The additional requirements on the event quality to remove interactions in the detector further decrease the acceptance by a factor $\sim 15\%$ at medium energies. The effect grows as the energy increases, and the acceptance assumes a mild energy trend varying from $\sim 500 \text{ cm}^2\text{sr}$ at 10 GeV to $\sim 400 \text{ cm}^2\text{sr}$ at 1 TeV. The acceptance shown in the picture does not include the ECAL selection used to reduce the proton background, whose efficiency has been evaluated using an independent data-driven method as explained in Section 4.3.2.1.

In order to correctly normalize the measured number of $(e^+ + e^-)$ events, the resulting acceptance – here evaluated separately in each energy bin – has been parametrized using an analytic function to smoothen out statistical fluctuations. The resulting parametrization $\mathcal{A}_{\text{MC}}^f(E)$ is shown superimposed to the binned acceptance in Figure 5.5. It is worth to mention, though, that the application of the acceptance factor from the parametrization $\mathcal{A}_{\text{MC}}^f(E)$ to the measured number of $(e^+ + e^-)$ in each energy bin is not trivial. The flux measured from the collection of $(e^+ + e^-)$ events in a discrete energy interval $[E_{\text{min}}, E_{\text{max}}]$ is, in fact, representative only of a certain energy inside the bin (\tilde{E}). For a steeply falling power law spectrum, like the e^\pm spectra, the value of the representative energy \tilde{E} tends to assume values smaller

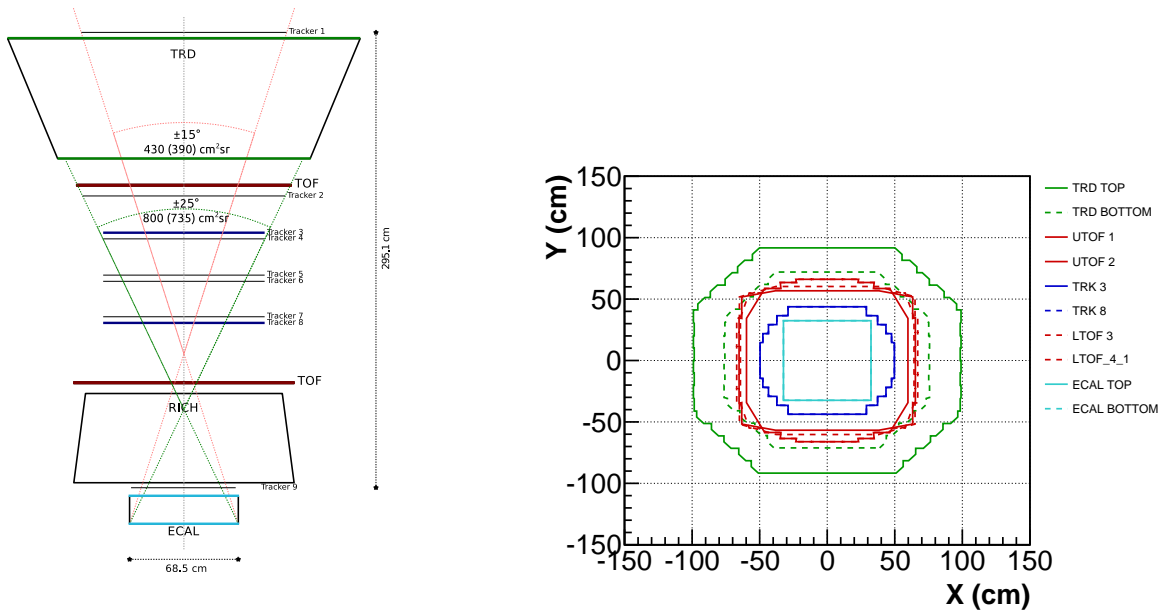


Figure 5.4: On the **Left**, schematics of the AMS detector^a. The planes that are used to define the geometrical acceptance are highlighted. The planes are shown also on the **Right** side in the XY projection. A particle is considered in the AMS geometrical acceptance for the $(e^+ + e^-)$ analysis when the TRD, TOF and ECAL are fully crossed and when all pair of layers inside the inner Tracker are intercepted (green aperture). The corresponding acceptance amounts to $\sim 800 \text{ cm}^2\text{sr}$. As a reference, the value of the acceptance if the presence of the Tracker first layer is included (pink aperture) is shown. The presence of the first Tracker layer enhances the quality of the Tracker reconstruction, but it reduces the acceptance by almost a factor of two. In this analysis, in order to maximize the e^\pm statistics, no requirement on the external Tracker layers is applied. In parenthesis, the value of the acceptance obtained if the particle is required to cross the active areas of the subdetectors is reported. The inefficiency is dominated by the inactive areas in the Tracker planes.

^aadapted from [27]

than the mean energy of the bin, and the effect is enhanced as the energy bin width increases. The acceptance correction has been therefore evaluated in \tilde{E} to correctly normalize the number of counts. The evaluation of \tilde{E} is discussed in detail in Section 6.1.2. The expected impact on the flux measurement due to the uncertainty on \tilde{E} and, consequently, on $\mathcal{A}_{\text{MC}}(\tilde{E})$ is however mitigated by the weak energy dependence of the acceptance at high energies (where the effect is enhanced by the increase of the bin size). Therefore the systematic effects introduced by the uncertainty of \tilde{E} in the evaluation of $\mathcal{A}_{\text{MC}}(\tilde{E})$ for the flux measurement are negligible.

In this analysis only the integrated $(e^+ + e^-)$ flux has been measured. For its measurement, the detailed study of the angular dependence of the detector acceptance is not critical. The understanding of the detector angular differential acceptances represents however a key point for the study of differential fluxes and consequently for the search of anisotropies in the e^\pm arrival directions. Detailed studies has been performed in this context, and found that the differential acceptance features are well represented by the MC simulation at the percent level [227]. The formalism used for the definition of the angular differential acceptance and the calculation of differential acceptances for the selection used in this analysis are discussed and shown in Appendix D.

For the $(e^+ + e^-)$ flux measurement the description of the energy dependence of the acceptance $\mathcal{A}_{\text{MC}}(E)$ has a major impact in the final result. The acceptance evaluation relies completely on the MC simulation. This is indeed the only possible method to assess the absolute normalization of the detector

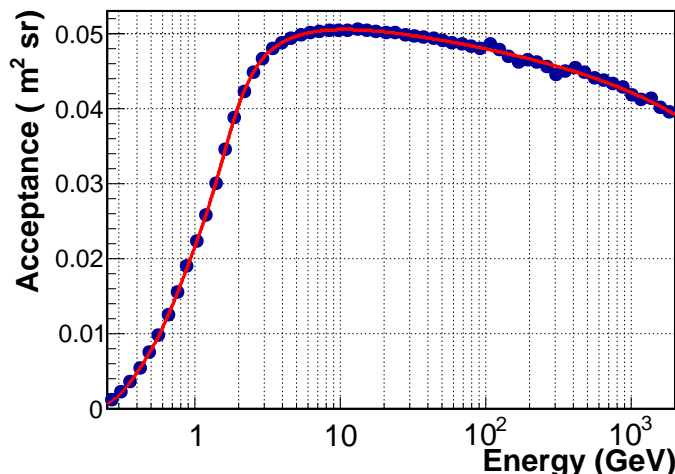


Figure 5.5: Binned acceptance evaluated using the MC simulation according to Equation 5.5 for the ($e^+ + e^-$) flux measurement. The acceptance shown here does not include any ECAL e/p separation selection. The analytically fit used to smooth out statistical fluctuations at high energies is superimposed in orange.

acceptance. The MC simulation, however, cannot be fully representative of the detector response. Therefore, a detailed comparison between the flight data and the MC simulation has been performed in order to assess the correctness of the MC simulation and correct for possible discrepancies. The following section covers the description of the procedure used to estimate the accuracy to which the MC simulation acceptance describes the real detector acceptance. The estimation of the uncertainty of the acceptance absolute scale is also discussed.

5.4 Assessment of the acceptance systematic uncertainties

The evaluation of the detector acceptance \mathcal{A}_{MC} is completely based on the MC information. Only the MC simulation, in fact, can be used to assess the absolute acceptance normalization. As already shown in the previous sections, however, the MC simulation may not perfectly describe the detector geometry and the interactions undergone by the particles within the detector materials. Any discrepancy between the MC simulation and the data has to be taken into account and \mathcal{A}_{MC} has to be consequently corrected. Following the notation in [26, 1], the additive correction to the MC acceptance is denoted as $\delta(E)$. Neglecting any dependence on the incoming angle (θ, ϕ) and taking out the ECAL selection efficiency $\varepsilon_{ECAL}^{e^\pm}(E)$ from Equation 5.7, the best estimate for the real detector acceptance $A^{e^\pm}(E)$ (shortened as $A(E)$ from now on) can be evaluated as

$$A(E) = (1 + \delta(E))\mathcal{A}_{MC}(E)$$

or, equivalently, as:

$$A(E) = \eta(E) \times \mathcal{A}_{MC}(E), \quad (5.8)$$

where $\eta(E) = 1 + \delta(E)$ represents the multiplicative correction factor used to scale any discrepancy between the MC simulation and the reality. The factor $A(E)$ defined in Equation 5.8 has been used to measure the ($e^+ + e^-$) flux according to Equation 3.11.

The correction factor $\eta(E)$ has to take into account of all the discrepancies between the flight data and the MC simulation. The uncertainty on the correction factor ($\Delta\eta(E)$) induces a systematic uncertainty on the flux measurement. In this section, the strategy used to evaluate $\eta(E)$ and $\Delta\eta(E)$ is

reviewed. Any dependence on (θ, ϕ) of the correction factor can be safely neglected for the evaluation of the absolute flux, and will not be covered in this study.

The basic idea of the strategy is to infer the correction factor $\eta(E)$ directly from e^- flight data. In principle, the correct way to measure $\eta(E)$ would be to compare the distributions of all the variables involved in the MC acceptance determination with the same distributions of an e^- control data sample. Correlations between different cuts should also be taken into account. This is, however, clearly unfeasible: e^- are a rare species in the cosmic radiation. A strong selection, stronger than that applied during the analysis, is needed to select a pure sample of e^- .

The data/MC comparison is therefore affected by several difficulties. First, any unavoidable proton background will contaminate the data e^- control sample, and could potentially spoil the comparison between the data and the MC detector response. Moreover, any additional (but indispensable) selection applied to enhance the purity of the e^- control sample could introduce unwanted biases in the data or in the MC control samples that may suppress discrepancies (which could in turn not be spotted and therefore neglected). Finally, correlations between the different cuts in the acceptance evaluation cannot be completely taken into account without applying all single cuts “in cascade”. This procedure is not possible on e^- data since they are not the most abundant species in the cosmic radiation.

In the following sections, the data/MC comparison for the most representative selections will be reviewed in order to highlight the main features that concur to the definition of $\eta(E)$ and $\Delta\eta(E)$. Consequently, the complete procedure developed to estimate the correction factor $\eta(E)$ and the assessment of its systematic uncertainties is reviewed.

5.4.1 Comparison between data and MonteCarlo simulation

In this section, the comparison between the efficiencies evaluated on data and on MC e^- control samples for a representative set of selections is reviewed. All the cuts refer to the e^\pm selection routine presented in Section 4.1.2 and 4.1.3. For each selection cut, the ratio between the efficiency obtained for the data control sample $\varepsilon_{\text{Data}}^i(E)$ and for the MC control sample $\varepsilon_{\text{MC}}^i(E)$ is a good estimator for the accuracy to which the MC simulation can describe the flight data. Any discrepancy from unity is a hint of systematic effects. The goal of this section is to highlight the main features that concur to the definition of the acceptance correction uncertainty. The correction factor $\eta(E)$ and its uncertainty will be evaluated in the next section.

It is important to stress that the efficiencies calculated in this section are determined on a biased sample of e^- . The efficiencies have been calculated using a *Tag&Probe* approach, where the e^- control sample has been selected from data and from MC using requirements which do not use the measurements of the sub-detector under study. The selection of the control sample is however always tighter than the selection used to define the $(e^+ + e^-)$ sample for the flux measurement. Different definitions of the control samples may result in a different level of data/MC agreement. The impact of the control sample definition on the correction factor uncertainty will be addressed in the next section.

For all the checks, the data/MC comparison has been done up to 200 GeV. Above this energy the irreducible proton contamination in the e^- flight data control samples and the decrease of the sample size prevent any reasonable approach to the comparison. The intrinsic discrepancy between data and MC for the $(e^+ + e^-)$ selection is however not expected to diverge at high energies. Therefore, the result

of the comparison can be safely extrapolated continuously up to TeV energies⁵. In addition to this, above 200 GeV the flux measurement uncertainty is dominated by the selection systematic uncertainties and by the statistical fluctuations. The uncertainty introduced by the extrapolation of the correction factor above 200 GeV is negligible with respect to the other error sources.

5.4.1.1 TOF reconstruction

The TOF reconstruction - which results in the assembly of a `Tof Track` object - has to be carefully investigated since, together with the `Tracker Track` reconstruction, it represents the “seed” for the selection of e^\pm candidate events. The Tracker and TOF reconstructions are, moreover, very correlated: their reconstruction is not a standalone algorithm (like, for example, for the ECAL) but they rely on the measurements from the other subdetector at different steps of the event reconstruction.

Naively, a good Tracker reconstruction selection could be required before the check of the TOF reconstruction, and vice versa. This would allow to use the Tracker rigidity measurement to identify $R < 0$ particles and therefore enhance the purity of the e^- control sample. As shown later, subtle discrepancies between data and MC are screened in this case. In order to perform a fair data/MC comparison and to spot any feature or discrepancy, the TOF reconstruction has been checked using an *unbiased* procedure leaving out also any requirement on the Tracker.

An unbiased e^\pm control sample⁶ definition has been achieved with a dedicated selection of the control sample based on the ECAL and TRD subdetectors only. Events with a geometrical and angular matching between the `Ecal Shower` axis and the `Trd Track` have been selected. In order to remove upward-going particles, that are usually removed with a selection using the TOF, the `Ecal Shower` profile has been used to obtain the directional information⁷. Finally, the `ECALBDT` and the `TRDhre/p` tools have been used to select e^\pm .

The resulting `Tof Track` reconstruction efficiency $\varepsilon_{\text{MC,Data}}^{(\text{TOF})}$ is shown in Figure 5.6 with a comparison between a Tracker biased selection and the unbiased approach. On the right, Figure 5.6 reports instead the ratio $\eta^{(\text{TOF})} = \varepsilon_{\text{Data}}^{(\text{TOF})} / \varepsilon_{\text{MC}}^{(\text{TOF})}$ in the two hypotheses. For a perfect data/MC agreement, a value of $\eta = 1$ is expected. Any deviation from 1 is a sign of systematic effects due to the finite accuracy of the MC simulation.

The impact of the Tracker selection in the definition of the control samples is evident. In particular, the resulting bias is clear in the $\eta^{(\text{TOF})}$ ratio. When no selection on the Tracker track is required at all, a discontinuity only in the MC simulation efficiency at ~ 13 GeV is observed. This step does not have any physical origin, and it is caused by a change of interaction models in the MC simulation which modifies the agreement with the data. Due to the interplay between the Tracker and the TOF during the event reconstruction, the additional requirement on the Tracker track for the definition of the e^- control sample remove the feature in the data/MC discrepancy⁸. In order to include this discrepancy in the acceptance systematic uncertainty, only the *unbiased* comparison for the `Tof Track` reconstruction

⁵This is true only if the ECAL particle identification selection is not considered. For the `ECALBDT` selection, which has been trained locally in different energy ranges to maximize the e/p separation capabilities, any extrapolation above 200 GeV is not safe. The behavior of this classification tool – which does not have an energy dependence that could be justified by physics like, for example, the length at which the energy deposit of an electromagnetic shower is maximum – is indeed not predictable. The data driven approach for the determination of the `ECALBDT` efficiency, already discussed in Section 4.3.2.1, allows however to avoid the use of the MC simulation for the evaluation of the efficiency uncertainty of this variable.

⁶In this case the control sample is composed of e^- and e^+ since no selection on the charge sign is possible without using the rigidity measurement of the Tracker.

⁷The typical Γ function profile of an electromagnetic shower can be used to infer the flight direction, with a resolution worse than the analysis of the timing information in the TOF paddles.

⁸The same discontinuity is observed also in the Tracker reconstruction data/MC efficiency ratio when no selection on the TOF is applied to define the e^- control sample.

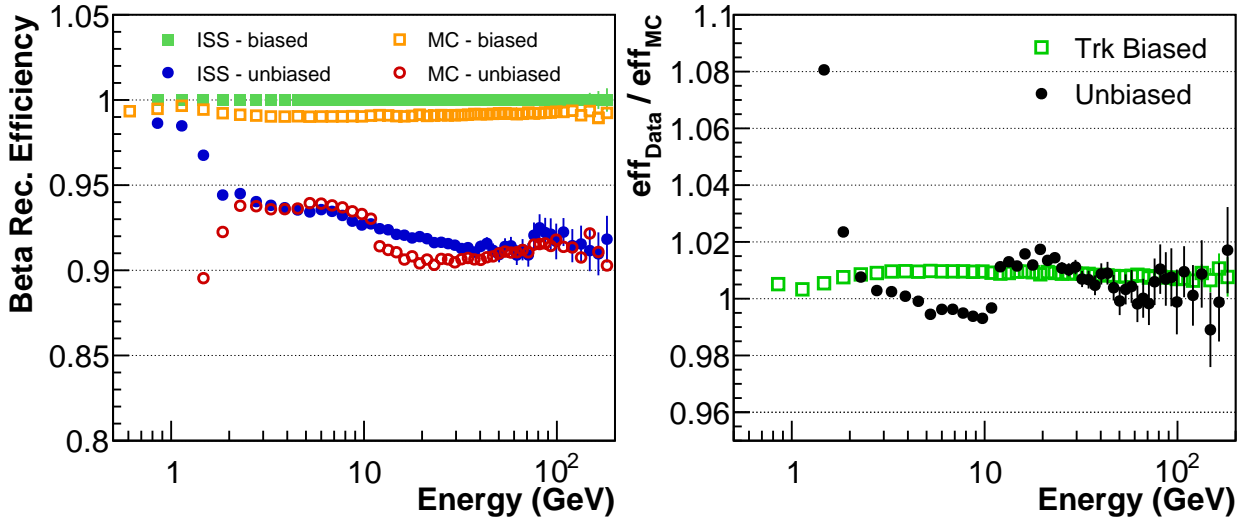


Figure 5.6: Efficiency for the TOF Track reconstruction. On the **Left**, the efficiency for ISS data (blue, green) and for MC (red, orange) for a control sample of e^\pm selected by means of the TRD and ECAL only (circles) and with additional requirements on the Tracker (squares). On the **Right**, the ratio between the data and MC efficiencies depending on the Tracker requirement is shown. In order to correctly estimate any discrepancy between data and MC, which are removed by the selection on the Tracker, the TOF reconstruction systematics are evaluated using e^\pm control samples defined by ECAL and TRD only.

is used in this analysis. The *Tof Track* efficiency reconstruction study further confirms that a naive “last cut” *Tag&Probe* approach, where the efficiency of a selection cut is evaluated after applying all other cuts but the cut itself, is not satisfactory enough to provide a correct estimation of the systematic effects in the MC simulation.

The discrepancy at low energies, observed only for the unbiased check, is probably induced by irreducible proton background which could not be rejected by the ECAL and TRD only e^\pm selection.

Figure 5.7 shows the efficiency for the relativistic and downward-going particle selection using the $\beta = v/c$ measurement of the TOF. The disagreement with data is not worse than 0.5% in most of the energy range. At high energies, the contamination of secondaries produced by interactions in the detector contaminate the e^- control sample and the agreement tends to worsen.

5.4.1.2 Tracker reconstruction

The *Tracker Track* reconstruction represents, together with that of the *Tof Track*, the core of the AMS event reconstruction. The efficiency of the reconstruction has been evaluated on a control sample of e^\pm identified with a ECAL and TRD selection. The ECAL and TRD axes have been required to cross the inner Tracker layers. Since the TOF reconstruction efficiency has been estimated independently of the Tracker, additional requirements on the TOF can be included for the Tracker reconstruction check. In this way, the common systematic features shared with the TOF are removed and do not have a double impact on the final acceptance systematics. The e^- control sample candidates are therefore selected with requirements on the TOF β direction and on the TOF charge measurement.

The efficiency for data and for MC and the data/MC agreement for the *Tracker Track* reconstruction is shown in Figure 5.8. An energy independent discrepancy at the level of $\sim 1\%$ in the Tracker

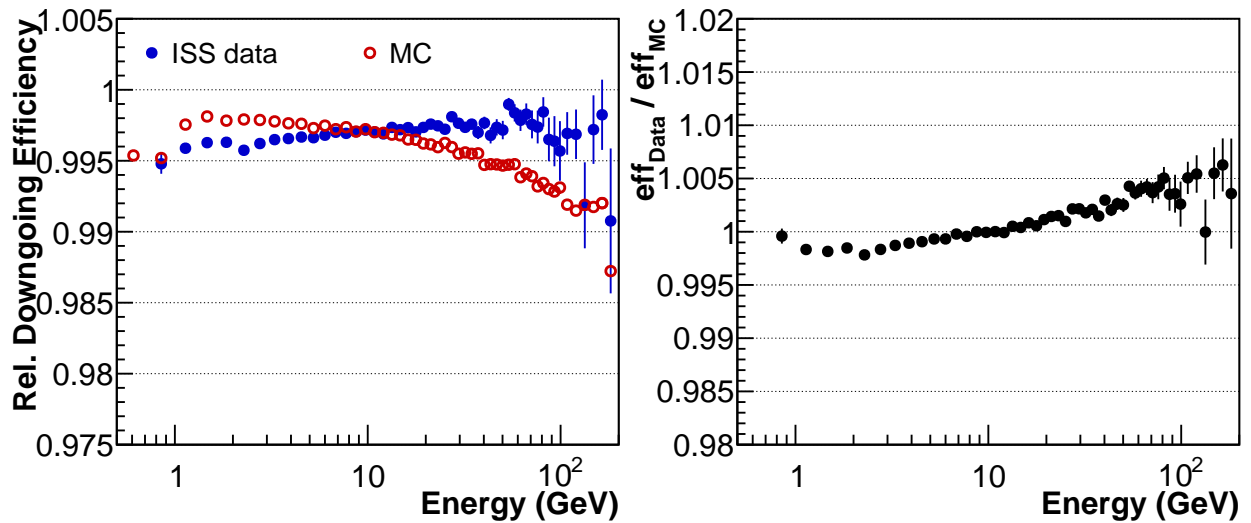


Figure 5.7: Efficiency for the relativistic and downward-going particle selection, based on the β measurement provided by the TOF. On the **Left**, the efficiency for ISS data (blue) and for MC (red) for a control sample of e^- selected by means of the Tracker, TRD and ECAL. On the **Right**, the ratio between the data and the MC efficiency is shown.

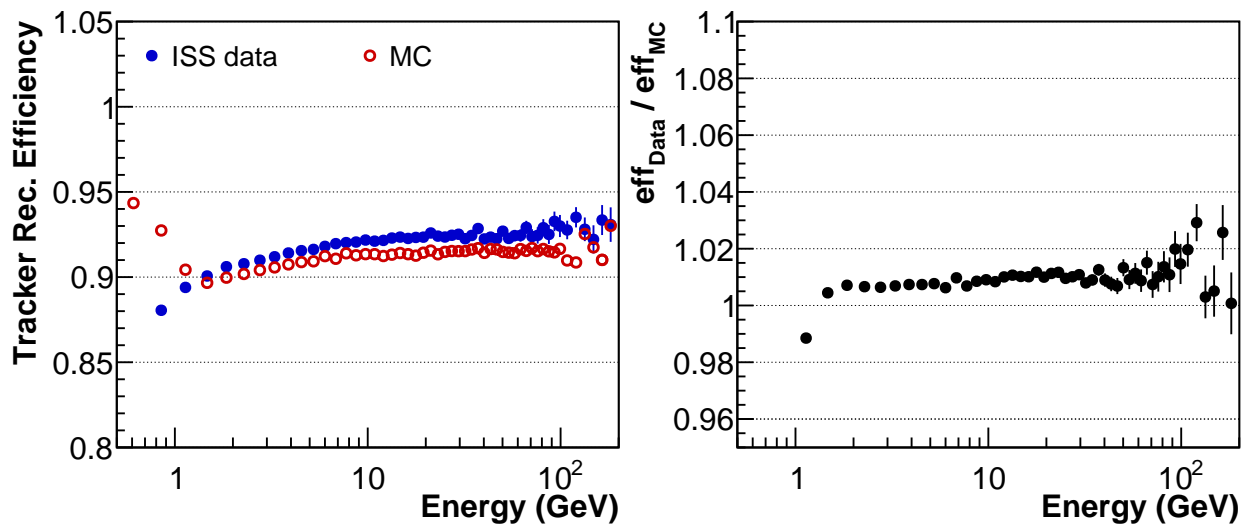


Figure 5.8: Efficiency for the Tracker Track reconstruction. On the **Left**, the efficiency for ISS data (blue) and MC (red) for a control sample of e^- selected by means of the TRD, ECAL and TOF. On the **Right**, the ratio between the data and the MC efficiency is shown. Above 2 GeV, an energy independent 1% discrepancy between the data and MC efficiency is observed.

reconstruction efficiency is observed for energies above 2 GeV.

5.4.1.3 TRD acceptance and quality

The quality of the TRD e/p separation algorithms depends on by the number of TRD hits used for its calculation. As described in Section 4.1.2, in this analysis the **Tracker Track** has to interpolate at least eight TRD tubes to fulfill the $e^+ + e^-$ sample selection. This does not only guarantee high performances for the TRD identification tools, but it also defines the TRD geometrical acceptance.

The efficiency of the selection for the TRD quality and acceptance has been evaluated on a control sample of e^- identified with the Tracker, TOF and ECAL subdetectors. The rejection of protons has been achieved by a selection on the $ECAL_{BDT}$ and on the E_{dep}/p ratio, in addition to the requirement on the negative charge sign measured by the Tracker.

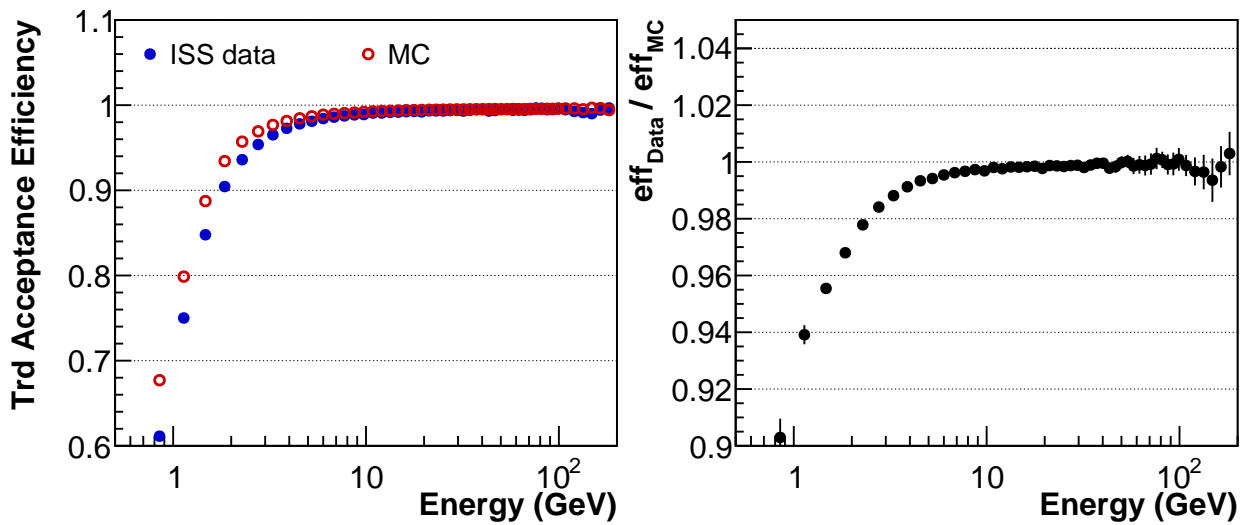


Figure 5.9: Efficiency for the TRD quality and acceptance selection. On the **Left**, the efficiency for ISS data (blue) and MC (red) for a control sample of e^- selected by means of the TOF, Tracker and ECAL. On the **Right**, the ratio between data and MC efficiency is shown. The efficiency of the selection is better than 99% above 10 GeV, with negligible discrepancy between data and MC. At lower energies, the efficiency decreases and the systematic difference in the MC simulation increases due to effects of multiple scattering with the detector material which worsen the accuracy of the Tracker track extrapolation in the TRD.

The resulting efficiency and the comparison between data and MC are presented in Figure 5.9. The efficiency of the selection is better than 99% at energies above 10 GeV, since the TRD acceptance is constrained by the geometrical requirement on the Tracker planes and on the ECAL volume. The discrepancy between data and MC is negligible. At lower energy, the efficiency decreases due to multiple scattering of e^- with the detector material which worsen the accuracy of the **Tracker Track** extrapolation in the TRD. The agreement between the data and the MC is consequently reduced. The increase of the data/MC discrepancy at low energies is a common feature of any selection that involves the geometric extrapolation of the Tracker, and limits the accuracy of this measurement at low energies⁹.

⁹ A dedicated study for the low energy e^\pm flux measurement can be developed with a dedicated selection to improve the data/MC agreement at low energies. The TRD standalone reconstruction algorithm could be in fact used to drop the necessity of the extrapolation of the Tracker track in the TRD volume. The resulting e/p separation power would be however decreased, and it would result in an increase of the systematic uncertainty due to proton contamination in the e^\pm sample. Feasibility studies about the possibility to improve the measurement accuracy at low energies using this approach are under investigation.

5.4.1.4 ECAL fiducial volume

The requirement on the ECAL fiducial volume, defined by the geometric extrapolation of the **Tracker Track**, is crucial to reduce the effect of energy lateral leakages that could spoil the resolution of the ECAL energy measurement. The efficiency of the requirement is checked on a e^- control sample defined by the TOF, Tracker and TRD. Moreover, since this selection is based only on the Tracker extrapolation and not on the ECAL reconstruction itself, the requirement of activity in the ECAL is added.

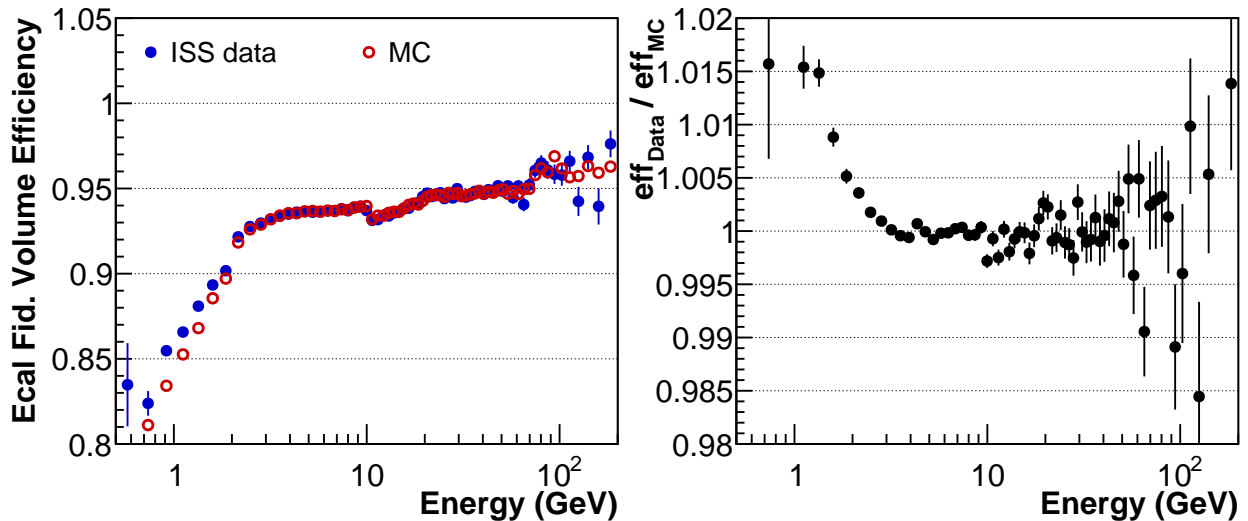


Figure 5.10: Efficiency for the ECAL fiducial volume definition. On the **Left**, the efficiency for ISS data (blue) and MC (red) for a control sample of e^- selected by means of the TOF, Tracker and TRD. On the **Right**, the ratio between data and MC efficiency is shown. The efficiency, at the level of $\sim 95\%$, drastically decreases below 2 GeV due to the impact of the accuracy of the Tracker Track extrapolation. The MC simulation agrees with data within fluctuations above 2 GeV. Below this energy, the maximum deviation is at the level of 1.5%, safely negligible with respect to other sources of systematic uncertainties.

The efficiency for the ECAL fiducial volume selection is shown in Figure 5.10. The efficiency at intermediate and high energies, at the level of $\sim 95\%$, drastically decreases below 2 GeV. This is due to the impact of multiple scattering for the geometrical **Tracker Track** extrapolation. The disagreement between data and MC is negligible, even below 2 GeV where other systematic effects due to data/MC differences for other selections dominate.

5.4.1.5 ECAL reconstruction and Tracker matching

The **Ecal Shower** reconstruction has been checked using a control sample of e^- selected by means of TOF, Tracker and TRD subdetector, with the additional requirement on the extrapolation of the **Tracker Track** inside the ECAL fiducial volume. The reconstruction efficiency is shown, as function of the Tracker rigidity R , in Figure 5.11. Above 2 GeV the ECAL reconstruction is 100% efficient when the particle crosses the ECAL fiducial volume both in data and MC. Below 2 GeV, the efficiency decreases, with a maximum systematic deviation of 4% at 0.5 GeV.

The geometrical matching between the **Ecal Shower** and the **Tracker Track** has been checked on the same e^- sample for events with a successful ECAL reconstruction. The resulting efficiencies on data

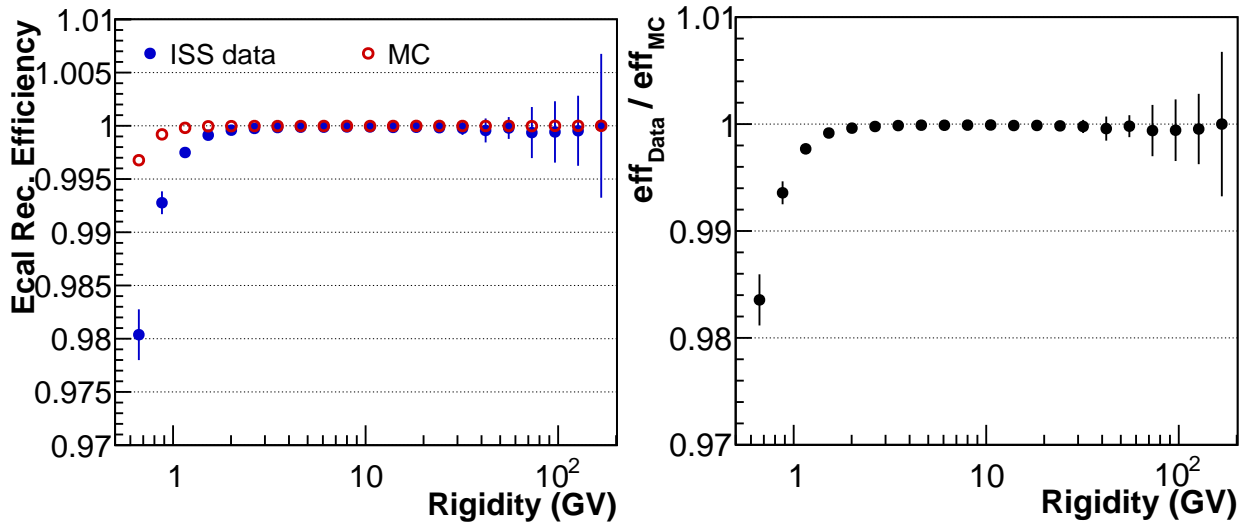


Figure 5.11: Efficiency for the ECAL Shower reconstruction. On the **Left**, the efficiency for ISS data (blue) and MC (red) for a control sample of e^- selected by means of the TOF, TRD and Tracker track crossing the ECAL fiducial volume. On the **Right**, the ratio between data and MC efficiency is shown. Above 2 GeV, the ECAL reconstruction efficiency is 100% and no systematic difference between data and MC is observed.

and MC as function of the ECAL energy E and the relative comparison is shown in Figure 5.12. The disagreement is smaller than $\sim 1\%$ in the whole energy range even at the lowest energies.

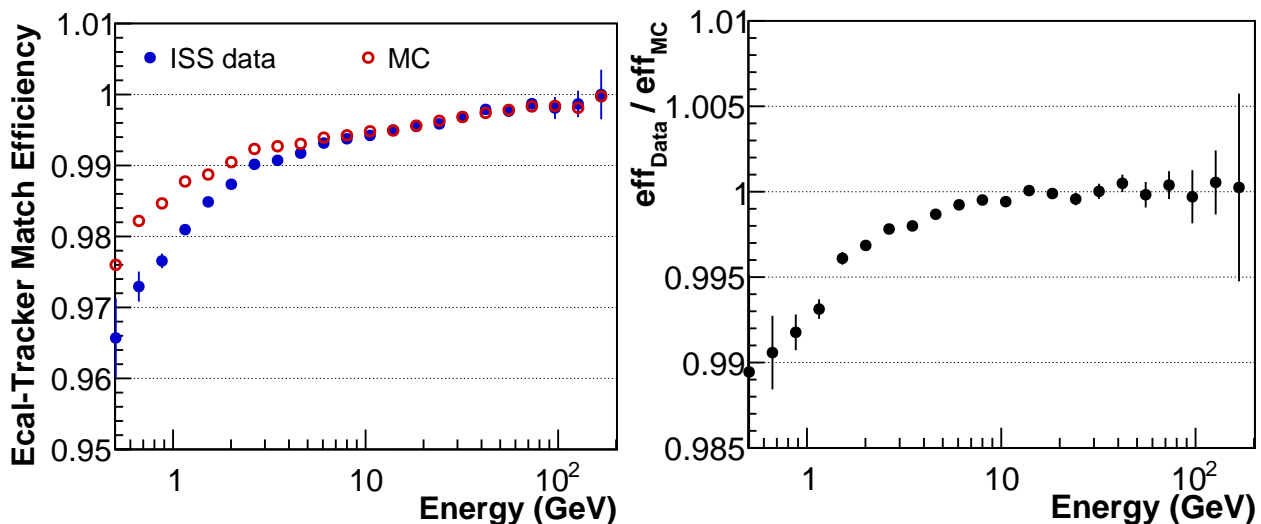


Figure 5.12: Efficiency for the ECAL-Tracker geometrical matching. On the **Left**, the efficiency for ISS data (blue) and for MC (red) for a control sample of e^- selected by means of the TOF, TRD and Tracker. On the **Right**, the ratio between data and MC efficiency is shown. The agreement is better than 99% in the entire energy range.

5.4.1.6 Rejection of nuclei above Helium

The selection to reject nuclei with $Z \geq 2$ using the charge estimator from the Tracker is checked on a control sample of e^- selected with TOF, TRD, Tracker and ECAL. The small contamination of remaining spillover nuclei in the $R < 0$ sample is rejected by an additional selection on the TOF energy deposit. The result is shown in Figure 5.13.

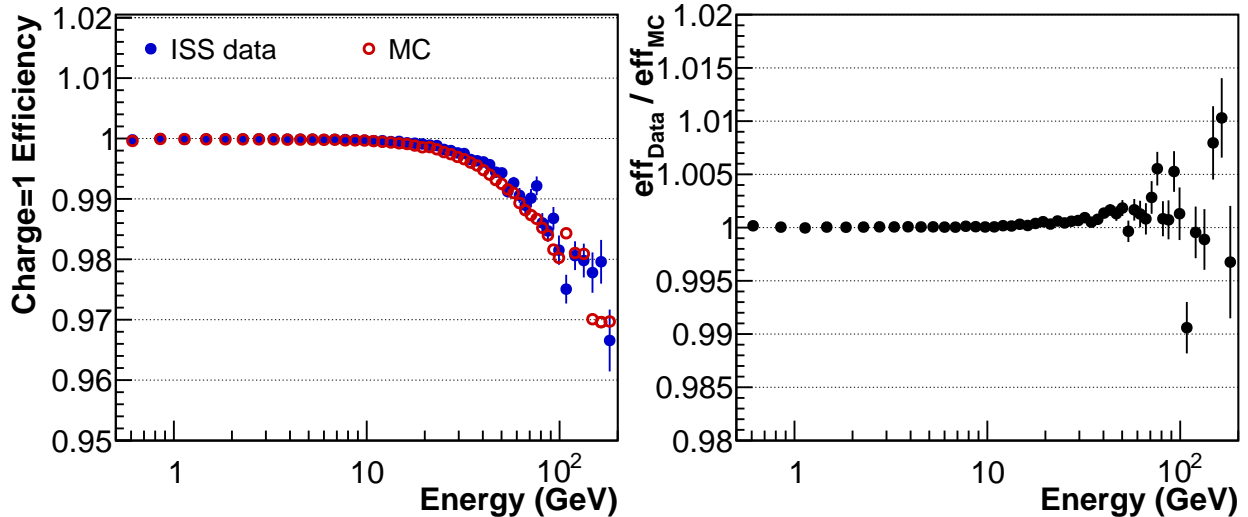


Figure 5.13: Efficiency for the selection of $Z=1$ particles using the energy deposit in the inner Tracker layers. The efficiency is measured on a control sample of e^- selected using TOF, Tracker, ECAL and TRD. On the **Left**, the efficiency for ISS data (blue) and for MC (red) is shown, together with the ratio between data and MC efficiency on the **Right**. The efficiency of the selection, which is 100% at low energies, decreases at high energy due to interactions of e^- before reaching the calorimeter. The MC simulation agrees with data at a level better than 99% in the whole energy range.

The efficiency of the selection on the control sample is 100% both for data and MC up to 10 GeV. Above this energy, it starts to slightly decrease up to a value of $\sim 97\%$ at 150 GeV. The loss in efficiency is due to e^- events that start to interact above the calorimeter and produce secondaries whose energy deposit in the Tracker layers is clustered together with the primary e^- deposit. The MC simulation describes the flight data at a level better than 99% in the whole energy range.

5.4.1.7 Single Track

The efficiency for the single track ($N^{\text{TRK}} = 1$) requirement has been checked on a control sample of e^- selected with TOF, Tracker, ECAL and TRD. The resulting efficiencies and the data/MC comparisons are shown in Figure 5.14. In the same picture, the variation of the result as function of the number of ACC interaction hits detected in the event is also shown.

The ACC paddles usually gets fired by particles crossing the detector from outside its field of view, by particles backscattered from the calorimeter or by spurious secondaries produced by interactions of the primary particle with the detector material. Using the correlation between the timing information of the ACC hits and the TOF paddles, it is possible to disentangle the nature of the ACC hit and to identify the presence of secondaries produced by interactions with the detector.

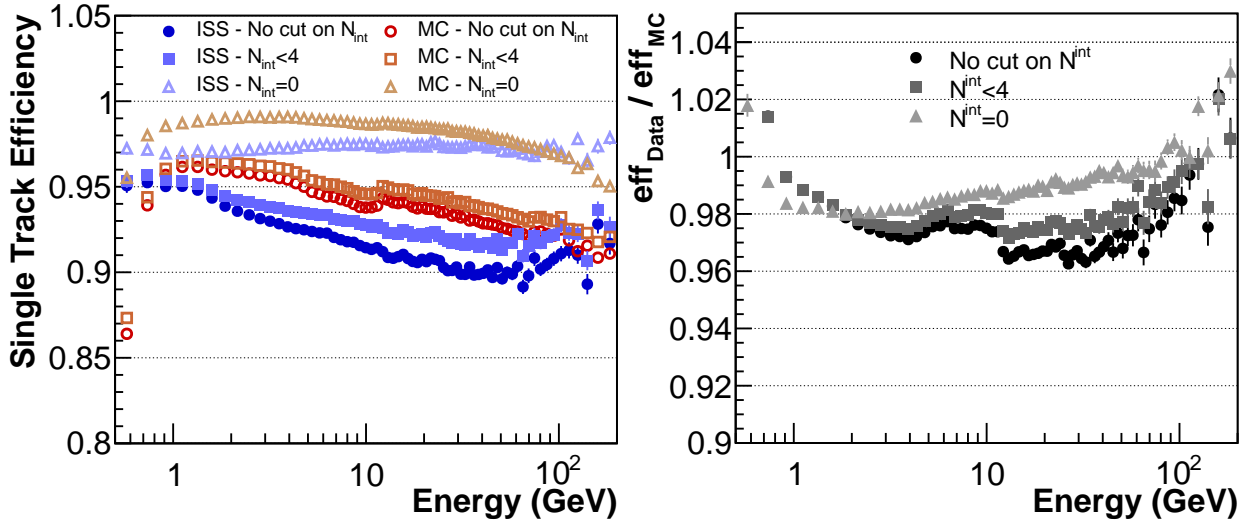


Figure 5.14: Efficiency for the single track ($N^{\text{TRK}} = 1$) selection measured in a control sample of e^- selected using TOF, Tracker, ECAL and TRD. On the **Left**, the efficiency for ISS data and for MC is shown as function of the selection of the number of ACC hits from interactions identified in the event. On the **Right**, the ratio between the data and the MC efficiency is shown. The absolute value of the efficiencies and the ratio depends strongly on the purity of the e^- control sample. When no selection on the ACC activity is required, the control sample is more representative of the $(e^+ + e^-)$ sample selected for the flux measurement. Discrepancies between data and MC arise, however, due to interactions of primary protons in data which are not simulated in the MC. If the yield of interacting protons is reduced through a cut on the number of ACC interaction hits, the data/MC agreement improves as expected. The data e^- control sample is however less representative of the analysis $(e^+ + e^-)$ sample in this case. Even with a strong selection, the discrepancy between data and MC is at the level of 1% \sim 2% depending on the energy, partially induced by pile-up events in data (not simulated in the MC) and partially due to intrinsic limitations of the MC simulation.

Without any requirement on the ACC activity, the data/MC disagreement depends strongly on energy and it is usually worse than 2%. The e^- control sample is however contaminated not only by genuine protons, but it also contains events for which the ECAL shower belongs to a secondary e^- produced by the interaction of the primary (mainly protons) with the detector. This events are present in data but not in the e^- MC simulation (only primary e^- are in fact generated in the MC sample¹⁰). The data/MC efficiency comparison is therefore not completely consistent. A further selection on the number of ACC interaction hits (N^{int}) is used to reduce the fraction of interacting proton events. The same selection applied both on data and MC improves the level of agreement. A small fraction of the remaining discrepancy after the $N^{\text{int}} = 0$ selection can be ascribed to pile-up events in data, which are also not reproduced in the MC simulation. The rest is an evident hint of an intrinsic systematic deficit in the MC simulation for multi-track events, that has to be taken into account in the corrections for

¹⁰ Independent analyses based on the study of dedicated proton MC simulations have shown that the contamination of protons that remains in the e^- control sample after a typical selection is below the percent level up to 200 GeV [217]. The uncertainty on this estimation is however compatible with the estimation itself, due to the limitations in the MC simulation to describe the interactions of protons with the detector materials at the precision needed for this analysis. Therefore in this analysis the proton MC simulation has not been used to assess the systematic uncertainty on the data/MC comparisons. The procedure used to assess the uncertainty on the data/MC comparisons and to evaluate the impact of the proton contamination in the e^- control samples is discussed in Section 5.4.2.

\mathcal{A}_{MC} .

The single track efficiency is a clear example of the intrinsic problems of the *Tag&Probe* approach used to determine the correction $\eta(E)$ for \mathcal{A}_{MC} . As it is impossible to select a pure sample of e^- from data with a looser selection than the selection used to define the acceptance itself, the resulting data/MC comparison is biased and it is not fully representative of the ($e^+ + e^-$) sample selected in the main analysis. For the single track efficiency, as an example, the outcome on the comparison depends drastically on the purity of the e^- control sample. If the e^- control sample purity is enhanced by a selection on N^{int} , the data sample becomes more compatible with the MC sample but less representative of the ($e^+ + e^-$) sample identified in the main analysis. Vice versa, if all interaction events are kept in the control sample, the data control sample is more representative of the selected ($e^+ + e^-$) sample but the comparison with the MC sample, where primary protons are not simulated, is not consistent.

5.4.1.8 Trigger

The evaluation of the trigger efficiency, as explained already in Section 5.2, relies on the collection of cosmic rays recorded using an unbiased sample of triggers. The e^- control sample has been defined using a selection on TOF, Tracker, TRD and ECAL without any selection on the trigger pattern. For the trigger efficiency evaluation, the number of events with at least one PHYS trigger bit set is compared to the total sample. The trigger algorithms - including the digitization of the signal and the prescaling factor for unbiased events - have been reproduced in the MC simulation. Although the trigger efficiency could be in principle calculated directly on data, the support from the MC simulation is needed to confirm the result.

The comparison between the trigger efficiencies obtained in data and in MC are shown in Figure 5.15. The efficiency for both data and MC e^- is $\sim 100\%$ above 5 GeV. Below 5 GeV, the efficiency decreases up to $\sim 80\%$ for flight data and $\sim 65\%$ for the MC simulation, with a maximum discrepancy of $\sim 25\%$ at 0.5 GeV. The discrepancy is mainly due to two factors. First, the energy deposit in the detector active material used for the trigger algorithms is not fully described. Next to the trigger threshold, in fact, any small discrepancy between data and MC induce a not negligible discrepancy in the trigger efficiency of the control sample. Secondly, the e^- control sample is contaminated by interaction events and protons that can spoil the evaluation of the trigger efficiency for flight data especially at low energies. The trigger efficiency study provides further confirmation that, despite all the efforts, an accurate comparison between the data and the MC simulation for the e^- sample below 2 GeV is not feasible at the percent level of accuracy.

5.4.2 Acceptance corrections and systematic uncertainties

The MC acceptance $\mathcal{A}_{MC}(E)$, evaluated as described in Section 5.3.2, has to be corrected using the input from flight data in order to take into account any discrepancy or inaccuracy in the MC simulation. For each i^{th} cut used in the definition of the acceptance, the data/MC efficiency comparison reviewed in Section 5.4.1 could in principle be used to infer the single cut correction as:

$$\eta^i(E) = \varepsilon_{\text{Data}}^i(E)/\varepsilon_{\text{MC}}^i(E) \quad (5.9)$$

and the total correction to \mathcal{A}_{MC} could be estimated as:

$$\eta(E) = \prod_i \eta^i(E) \quad (5.10)$$

As discussed in the previous section, the evaluation of the data/MC correction factor η^i is however not straightforward. The outcome of the comparisons shows in fact many features which depend on the

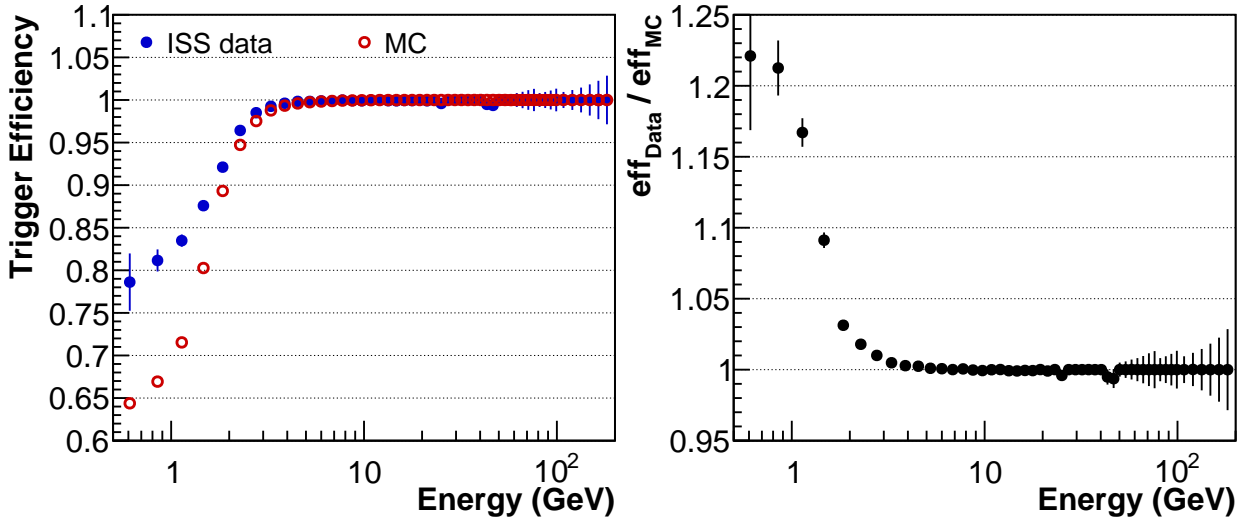


Figure 5.15: Trigger efficiency evaluated on a control sample of e^- selected with TOF, Tracker, TRD and ECAL and without any requirement on the trigger. The trigger efficiency is calculated using a sample of unbiased triggers with looser requirements than the standard physics triggers (see Section 5.2 for the definition of the unbiased trigger sample). The same algorithms and prescaling factor defined in the data trigger boards are simulated also in the MC. On the **Left**, the trigger efficiency for ISS data (blue) and MC (red). The efficiency is $\sim 100\%$ above 5 GeV. At lower energies it decreases up to $\sim 80\%$ for flight data and $\sim 65\%$ for the MC simulation. The ratio between the data and the MC simulation efficiencies is shown on the **Right** plot. The discrepancy, which reaches 25% at 0.5 GeV, is due to the limits in the MC to reproduce the interactions of the particles in the detector active materials and to the contamination in the data sample that bias the result.

various selections analyzed. The following features are common to many of them and they have to be taken into account to define the procedure used to evaluate the correction factor:

- **All the data/MC comparisons have been evaluated on a biased e^- control sample.** What has been compared is therefore not an absolute efficiency on a representative sample of e^\pm used for the flux measurement, but it is the efficiency defined on a particular sample of e^- which does not fully represent the $(e^+ + e^-)$ sample used for the flux measurement.
- **The outcome of the comparison depends strongly on the definition of the e^- control sample.** This has been pointed out already for the $N^{\text{TRK}} = 1$ selection in Section 5.4.1.7, but the effect holds for every selection cut. Since this is a consequence of intrinsic systematic uncertainties in the procedure, the effect has to be quantified and included in the total correction uncertainty.
- **The differences between the flight data and the MC simulation tend to diverge at energies below 2 GeV** especially for selections involving the Tracker Track. This is due to multiple scattering phenomena and interactions in the detector materials. Care has to be taken in order to avoid the overestimation of the correction factor (and its uncertainty) if this effect is counted multiple times.

The first, unavoidable, point is also strictly connected to the second point. In what follows, the procedure developed to limit the impact of the e^- control sample definition used for the $\eta(E)$ calculation will be presented. The estimation of the uncertainty induced by the e^- control sample definition will be

also discussed. The procedure used to correctly define the acceptance error for the very low energies, strictly connected to the last point, will be covered afterward.

For each check i , the data/MC comparison for a certain definition of the e^- control sample can be treated as a particular *measurement/realization* given a certain control sample selection, or *tag*, j . For each check, the “phase-space” of all the possible realizations $\eta^{ij}(E)$ has been investigated by the variation of the tag definition. The distribution of the realizations can be therefore used to evaluate the best estimate of the correction factor $\bar{\eta}^i$. The spread of the outcomes for η^{ij} can be used to infer the intrinsic systematic on the correction factor introduced by definition of the e^- control sample. The following requirements for the definition of the control samples have been explored:

- $\text{ECAL}_{\text{BDT}} > x$, $x \in \{-0.2, -0.1, 0.0, +0.1, +0.2\}$
- $\text{TRD}_{\text{thr}}^{e/p} < x$, $\varepsilon \in \{97\%, 95\%, 91\%, 87\%, 83\%\}$, ε being the efficiency of the $\text{TRD}_{\text{thr}}^{e/p}$ for e^\pm .
- $Z^{\text{TRK}} < x$, $x \in \{1.3, 1.4, 1.5, 1.6, 1.7\}$
- $\chi_{\text{xy}}^{\text{TRK}} < x$, $x \in \{10, 20, \infty\}$, $\chi_{\text{xy}}^{\text{TRK}}$ being the track reconstruction χ^2 for both X,Y projections normalized to the number of degrees of freedom of the fit.
- $E_{\text{dep}}/p > x$, $x \in \{0.0, 0.4, 0.5, 0.6, 0.75\}$
- $N^{\text{int}} < x$, $x \in \{4, 6, 11, \infty\}$

For each check i , all the possible combinations of cuts (on top of a fixed selection which depends on the check itself) have been explored to define the e^- control sample¹¹. Every tag j refers to a combination of cuts according to the available possibilities. The cuts used in this approach have been proposed with the aim of exploring the measurement phase-space as much as possible and to keep the background contamination of the flight data e^- control sample under control. Different combination of cuts will provide however different purities of the e^- control samples and will bias the result differently.

As a graphical example for the outcome of this approach, Figure 5.16 shows the distribution of the data/MC comparisons for the energy ~ 40 GeV for the $N^{\text{TRK}} = 1$ requirement. The figure shows how the outcome of the comparison depends on the definition of the e^- control sample set by the j^{th} tag. The effect has been investigated and quantified for every check.

As for all the other checks, the distribution of the measurements groups together around a certain value. However, some measurements tend to aggregate away from the bulk. This is caused by particular tag selections for which a certain cut could have introduced a strong bias or a not negligible proton contamination in the data e^- control sample. Such results should not be taken into account in the evaluation of the MC acceptance corrections. Therefore, $\bar{\eta}^i$ has been estimated as the median¹² of the total distribution ($\hat{\eta}^i$), which is an estimator more resilient to outliers in the distribution than the standard mean. The width of the distribution around the median, instead, represents a good estimator of the intrinsic systematic uncertainty for $\bar{\eta}^i$ due to the arbitrariness of the e^- control sample definition. The width $\Delta\hat{\eta}^i$ is estimated via the Median Absolute Deviation (MAD)¹³ of the distribution which, as

¹¹For each check i is not always possible to completely explore the proposed cuts. For example, during the analyses of the Tracker efficiency, it is not possible to cut on Z^{TRK} or on $\chi_{\text{xy}}^{\text{TRK}}$. Therefore, such cuts are not included in the tag collection for this particular check.

¹² 50-th percentile of the total distribution.

¹³The Median Absolute Deviation (MAD) is defined as the median of the absolute deviations from the data median \hat{X} as follows:

$$\text{MAD} = \sqrt{\text{median}_j((X_j - \hat{X})^2)}$$

For normally distributed variables, the standard deviation σ is related to the MAD by $\sigma \simeq 1.48 \times \text{MAD}$. In this analysis, the term $\Delta\hat{\eta}^i$ will improperly refer to $1.48 \times \text{MAD}$

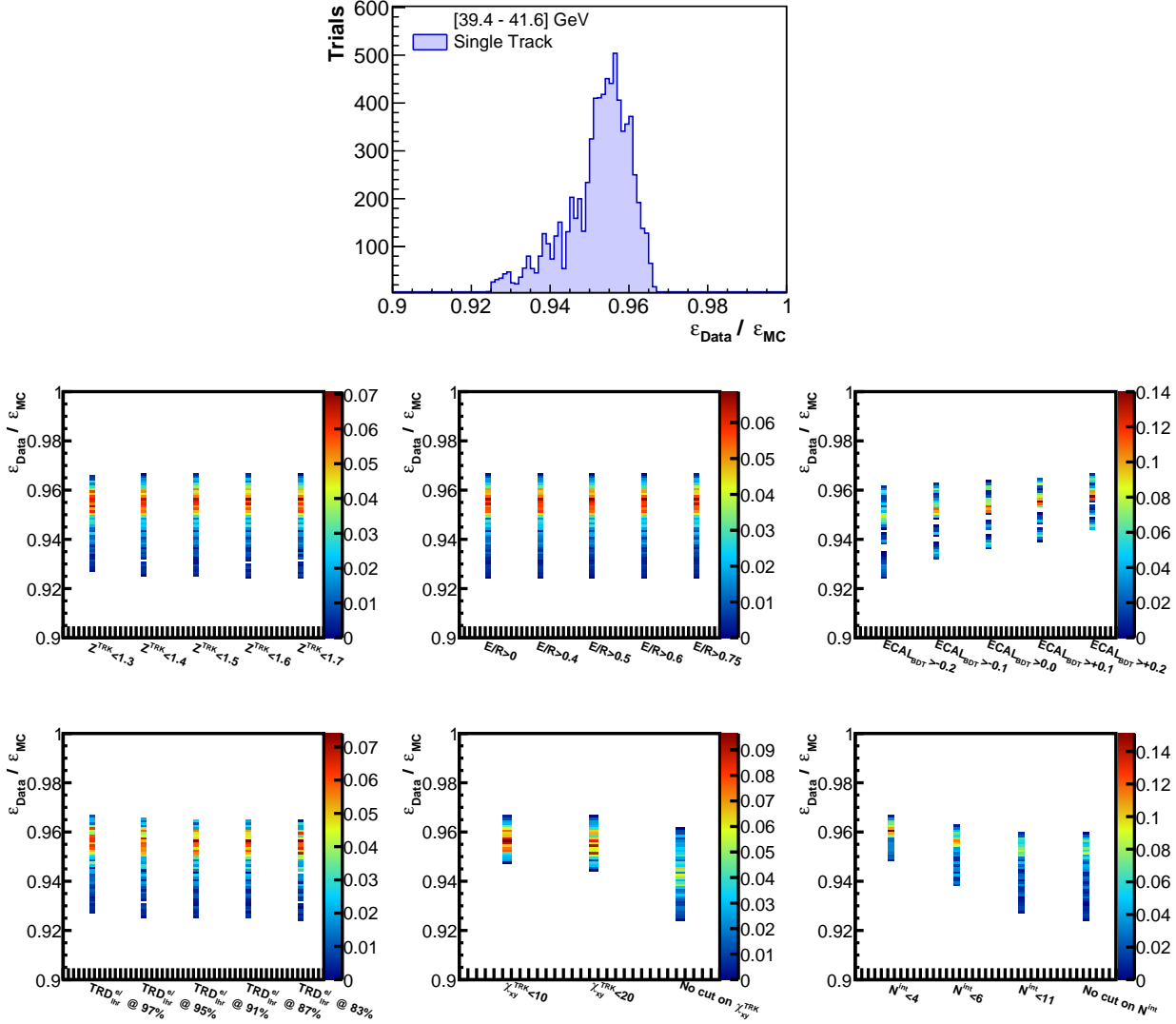


Figure 5.16: On **Top**, the distribution of all possible realizations for the $\eta = \epsilon_{\text{Data}}/\epsilon_{\text{MC}}$ data/MC comparison for the single track $N^{\text{TRK}} = 1$ requirement. Each entry of the histogram represents the η^j outcome for a single j tagging of the control sample. Most of the results tend to cluster together. The tails on the left are given by particular combinations of cuts that most probably enhance the bias in the final result or that allow for a non-negligible contribution of background events in the e^- control sample. On **Bottom**, the marginal distribution for η as function of the e^- control sample tag selection are shown. Each entry of the histogram represents the η^j outcome for a single j tagging of the control sample. For each bin on the x axis, the entire slice in y is normalized to 1. Only a subset of variables induce a spread in the final result. In this case, the major impact is given by the arbitrary choice of the selection in ECAL_{BDT} , χ_{xy}^{TRK} and N^{int} .

the median, is less sensitive to the distribution outliers.

Figure 5.17 shows the energy dependence of $\bar{\eta}^i$ for all the cuts applied to define the MC acceptance.

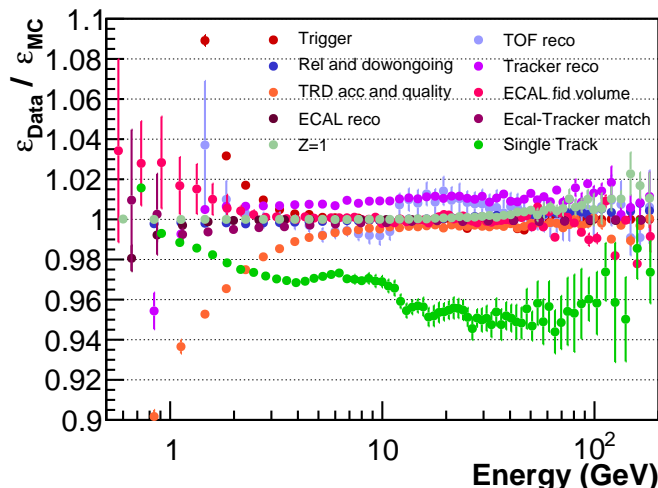


Figure 5.17: Energy dependence of the data/MC efficiency ratio η for all the MC acceptance selections. For each energy bin, the best estimation of the correction for the i^{th} check ($\bar{\eta}^i$) is evaluated by the median of all the possible realizations as function of the tagging selection. The error bar represents the spread $\Delta\hat{\eta}^i \simeq 1.48 \times \text{MAD}$ around the median value of the same distribution. It describes the intrinsic systematic uncertainty of the data/MC comparison induced by the arbitrariness of the e^- control sample selection. The deviation of the point from 1 hints to an unavoidable difference between the flight data and the MC simulation, which is also taken into account in the final acceptance systematic.

For all the checks shown in Figure 5.17, the spread $\Delta\hat{\eta}^i$ has been taken into account in the acceptance systematics. Figure 5.18 shows the evolution of the single check *tagging* uncertainty as a function of the energy. Below 3 GeV, the TOF reconstruction and the definition of the ECAL fiducial volume dominate the error. Above 3 GeV instead the single track requirement error prevails together with the TOF reconstruction. The reason for which the uncertainty on the TOF reconstruction dominates the *tagging* error is explained by the fact that the data/MC comparison has been evaluated using the unbiased procedure (see Section 5.4.1.1 and Figure 5.6). An enhanced contamination of background protons and interaction in the e^- control sample is expected and the η^{TOF} distribution results consequently broader.

For each cut, the error steadily increases as a function of the energy. Since there is no physical motivation for this behavior, the effect has to be related to statistical effects introduced by the decrease of statistic in the high energy e^- control sample.

For each energy bin, the **tagging** systematic uncertainty σ^{tag} has been defined as the quadratic sum of the error $\Delta\hat{\eta}^i$ for each cut:

$$\sigma^{\text{tag}} = \sqrt{\sum_i (\Delta\hat{\eta}^i)^2} \quad (5.11)$$

The impact of σ^{tag} in the total acceptance error will be discussed later in this section.

In Figure 5.17 some checks show a negligible or even null deviation from 1 within the error bars, pointing to an optimal agreement between the data and the MC. Other checks, however, show an appreciable deviation from 1. In this case an intrinsic difference between the data and the MC simulation, hence some lack of knowledge in the detector response or geometry simulated in the MC, is present. This

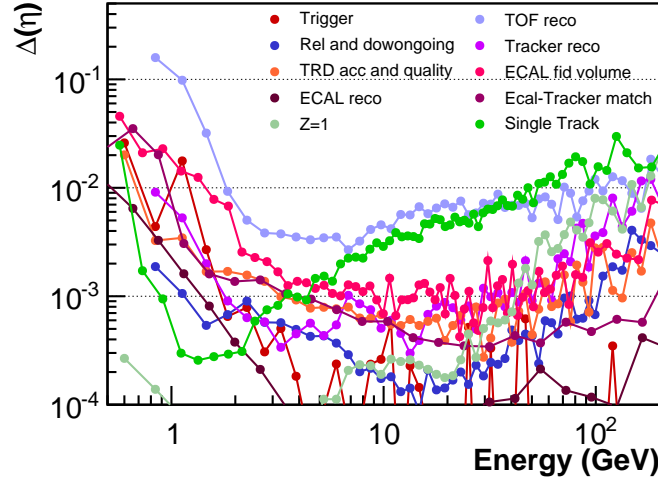


Figure 5.18: Energy dependence of the tagging error $\Delta\widehat{\eta}^i$ for each check i . For each energy bin, the total tagging error σ^{tag} is defined as the quadratic sum of each contribution. Below 3 GeV, the TOF reconstruction and the definition of the ECAL fiducial volume dominate the error. Above 3 GeV the single track efficiency prevails together with the TOF reconstruction. The steady rise at high energies, common to all checks, is explained by statistical effects due to the decrease of events in the data sample.

has to be reflected in the uncertainty to which the acceptance scale is known. In this analysis, the systematic effect due to the data/MC discrepancy is described by the **absolute** systematic uncertainty σ^{abs} . For each check, half of the difference of the point from the unity ($\delta_{1/2}^i$) is used as estimation of such uncertainty¹⁴ and the quadratic sum of every contribution defines the yield of the total absolute systematics:

$$\sigma^{\text{abs}} = \sqrt{\sum_i (\delta_{1/2}^i)^2} \quad (5.12)$$

The single contributions $\delta_{1/2}^i$ are assumed to be uncorrelated for the definition of σ^{abs} . The impact of this assumption is discussed later in this section. The energy dependence of $\delta_{1/2}^i$ for every cut is shown in Figure 5.19. At low energies the MC discrepancies for the trigger efficiency, for the TRD requirements and for the TOF reconstruction are severe and absolutely not compatible with a selection effect. At higher energies the $N^{\text{TRK}} = 1$ requirement dominate the systematics. The discontinuity observed at ~ 13 GeV for the $N^{\text{TRK}} = 1$ requirement is due to a change of interaction models in the MC simulation which modifies the agreement with the data. This has already been discussed in Section 5.4.1.1.

The total data/MC correction factor $\eta(E)$ is estimated via the product of the single $\overline{\eta}^i$, corresponding to the points in Figure 5.17, as follows:

$$\eta(E) = \prod_i \overline{\eta}^i \quad (5.13)$$

The energy dependence of $\eta(E)$ is shown on the left in Figure 5.20. Above 3 GeV the value of $\eta(E)$ has been used to define the correction for the acceptance. This choice is based on the assumption that at these energies the discrepancies between the flight data and the MC simulations are mainly due

¹⁴A symmetric error with half-difference defined in this way covers the complete uncertainty interval given by the distance to the expected “1” value.

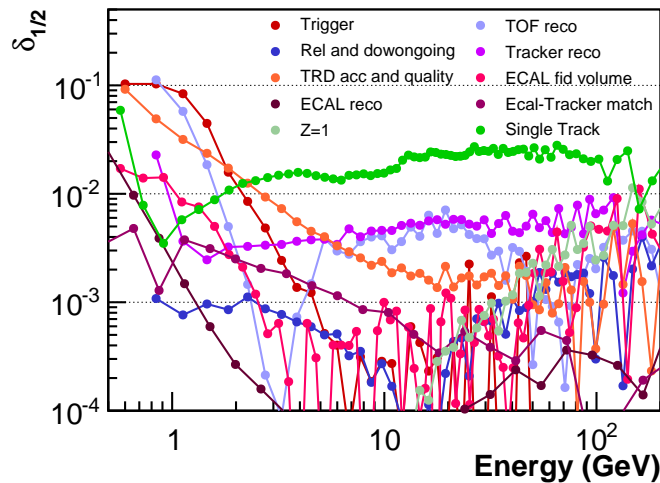


Figure 5.19: Energy dependence of the absolute error $\delta_{1/2}^i$ for every check i . The total absolute error σ^{abs} is defined as the quadratic sum of each contribution. The discrepancies between the flight data and the MC simulation for the TRD requirements, for the trigger efficiency and for the TOF reconstruction dominate the acceptance normalization uncertainty below 2 GeV. At higher energies the $N^{\text{TRK}} = 1$ requirement set the uncertainty on the acceptance normalization.

to limitations in the MC simulation. In order to smooth out statistical fluctuations, the acceptance has been parametrized using a log-linear analytical description. Below 3 GeV the assumption that the discrepancies are due only to the MC simulation limitations is not safe. As discussed previously, the definition of the e^- control sample at low energies is not straightforward and the resulting discrepancy observed between the flight data and the MC simulation cannot be attributed to the simulation only. Therefore, below 1 GeV, only half of the correction defined from the value of $\eta(E)$ is used to correct the MC acceptance. This choice corresponds to the assumption that both the impurities and the bias in the data control sample and the limitations in the MC simulation concur with equal weights ($1/2$) to the observed discrepancy. Between 1 and 3 GeV, the weight ($1/2$) is varied smoothly up to 1 to obtain a continuous parametrization of the acceptance correction.

The difference between the correction applied in this analysis and the correction that would have been obtained with different assumptions is well contained in the systematics itself. Therefore it has no impact on the final result inside the measurement error.

The parametrization of the correction above 3 GeV may introduce additional systematics. The effect induced by the uncertainty on the fitted parameters describes in particular the uncertainty encountered when the correction is extrapolated up the highest energies. It is included, therefore, in the total systematic as **parametrization** systematics σ^{par} .

Figure 5.21 shows the energy dependence of various contributions to the total acceptance systematics. The parametrization uncertainty has a negligible impact in the total error. Above 3 GeV, the tagging systematics σ^{tag} , steadily increases as function of the energy. However, the increase is due to the finite statistics of the control samples that induced intrinsic statistical fluctuation in the data/MC comparisons. This effect should not be included in the definition of the acceptance error. The tagging systematic uncertainty turns out to be negligible with respect to other sources of uncertainty. The absolute systematics, which describes the discrepancies between the MC simulation and the data, shows a constant behavior above 3 GeV with a discontinuity at ~ 13 GeV. The origin of this discontinuity, as already discussed before, is due to a change of interaction models in the MC simulation. The step is

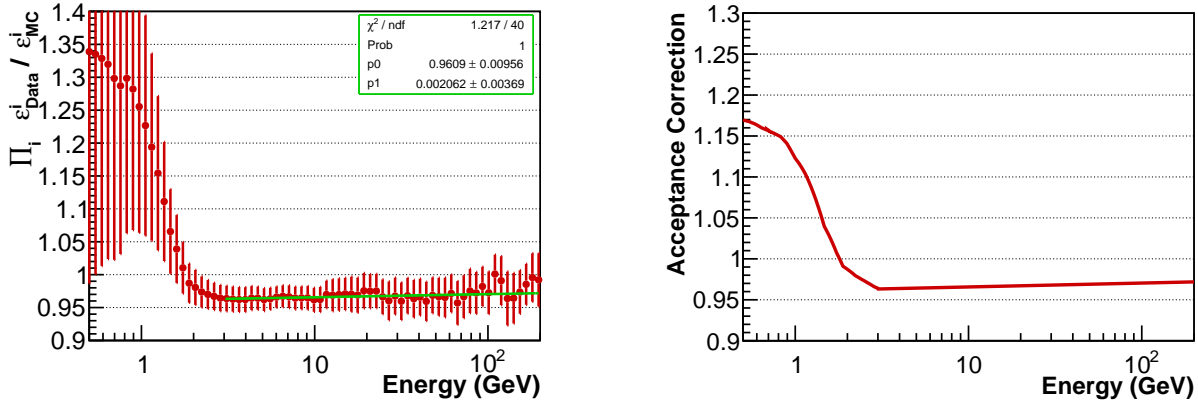


Figure 5.20: On the **Left**, the energy dependence of the $\eta(E)$ parameter which defines the correction to apply to the MC acceptance to cover the discrepancies observed between the flight data and the MC simulation. The energy dependence is parametrized with a log-linear function at high energies in order to smooth out statistical fluctuations. The energy dependence of the resulting correction factor, defined using the algorithm discussed in the text, is shown on the **Right** picture.

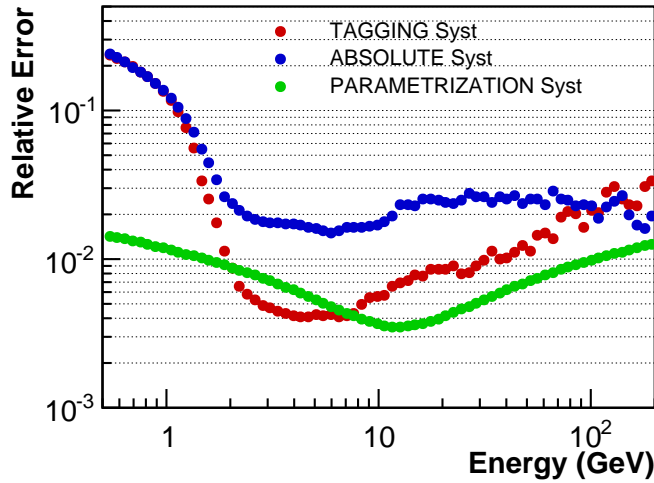


Figure 5.21: Contributions to the definition of the acceptance correction uncertainty. The parametrization systematics (green), which is defined by the uncertainty on the fit result for the $\eta(E)$ energy dependence parametrization, has a minor contribution to the total error. The tagging systematics (red), which defines the intrinsic error due to the definition of a biased e^- control sample for the data/MC comparison, increases with energy and starts to be comparable to the dominating contribution above ~ 100 GeV. The increase with energy is a statistical effect due to the decreasing size of the control samples used for the data/MC comparisons. The absolute systematics (blue), which defines the uncertainty induced by the difference observed in the efficiency calculation between the flight data and the MC simulations, dominates the systematic uncertainties above 2 GeV. It amounts to $\sim 2\%$ below ~ 13 GeV. Above this energy, a discontinuity is observed and the discrepancy increases up to $\sim 2.5\%$.

therefore not physical. The discontinuity is observed in the data/MC comparison for the TOF reconstruction and for the $N^{\text{TRK}} = 1$ requirement (see Figure 5.17 and it biases the two results in different directions and its effect cancels out in the acceptance correction factor. Because of this, this step in σ^{abs} can be safely disregarded above 13 GeV and the result below 13 GeV can be extrapolated to be \sim

2% above this energy. This assumption is also confirmed by the energy dependence of the acceptance correction factor ($\eta(E)$) shown in Figure 5.20. While σ^{abs} is in fact assuming no correlation between the different contributions, the half distance from 1 of $\eta(E)$ represents on the contrary an “effective” estimation of σ^{abs} which partially takes into account for the correlations between the single contributions. Above 3 GeV the half difference from 1 of the acceptance correction is always below 2 %. In conclusion, above 3 GeV the contribution of σ^{abs} to the acceptance systematics (σ_{acc}) has been estimated to be 2%.

The acceptance error contains also the systematic uncertainty on the ECAL_{BDT}^{long} selection. This selection is different from all the cuts that enter the \mathcal{A}_{MC} definition studied in this chapter, because it involves e/p separation. The procedure used so far cannot be applied for such a cut, since any minimal proton contamination in the e^\pm sample would bias the result more than the real systematics. The efficiency of the ECAL_{BDT}^{long} cut is however high, and the good data/MC comparison assures a systematic effect well below 1% (as discussed already in Section 4.2.1.2). The impact of this additional systematic, added in quadrature to σ_{acc} , is indeed negligible.

At low energies the systematic uncertainty increases up to more than 20%. Additional checks have been performed in order to test the stability of this result.

First of all, the impact of the requirement on the number of interactions N^{int} in the definition of the e^- control sample selection has been tested. The requirement on N^{int} introduces the highest bias in the control sample definitions, and could push the result at low energies to wrong values.

Moreover, all the MC/data comparisons so far have been evaluated using only $R < 0$ electron candidates. This selection assures to reduce at maximum the remaining background yield in the e^- control sample data. It could, however, introduce a non-negligible bias to the resulting correction for the ($e^+ + e^-$) measurement, which does not require any cut on the e^\pm signal charge sign.

In order to test the impact of the N^{int} selection and the $R < 0$ requirement, the systematic evaluation procedure has been applied both on e^- and e^\pm control samples, with and without the check on N^{int} . The total 4 outcomes for the total error $\Delta\eta^{(\text{tot})}$, here calculated as

$$\Delta\eta^{(\text{tot})} = \sigma^{\text{abs}} \oplus \sigma^{\text{par}} \oplus \sigma^{\text{tag}}$$

are shown in Figure 5.22.

The scenario in Figure 5.22 confirms that the impact of the charge sign selection to define the control sample is negligible. The results for the e^- and for the e^\pm control sample are in fact compatible.

Above 2 GeV, all methods provides compatible results, confirming the validity of the estimation of the acceptance scale uncertainty.

Below 2 GeV the selection on the number of interactions N^{int} changes drastically the result. The check on N^{int} confirms that the method used to evaluate $\Delta\eta$ is not robust under 2 GeV. At low energies in fact the contribution of events with substantial energy losses from interactions with the detector material is considerable, and most of the protons collected by AMS migrate to low energies due to the energy measurement of the ECAL. The definition of the e^- control sample in the lowest energy range is therefore more difficult. The systematic uncertainty σ_{acc} is consequently overestimated by the additional biases added to the procedure.

In order to estimate the systematics at low energies the resulting flux measurement (described in the next chapter) has been compared with the results provided by other analysis groups within the AMS collaboration. The same dataset of events collected by AMS has been analyzed with independent procedures to extract the signal contribution and, most importantly, to estimate the acceptance and its systematic uncertainties. Since at low energies the dominating contribution to the measurement uncertainty is covered by the acceptance systematic effects, the maximum half difference $\Delta_{1/2} = 1/2 (\Phi_{\text{max}} - \Phi_{\text{min}})$ between the results of all other analyses has been used to set the systematic of the acceptance. The results are

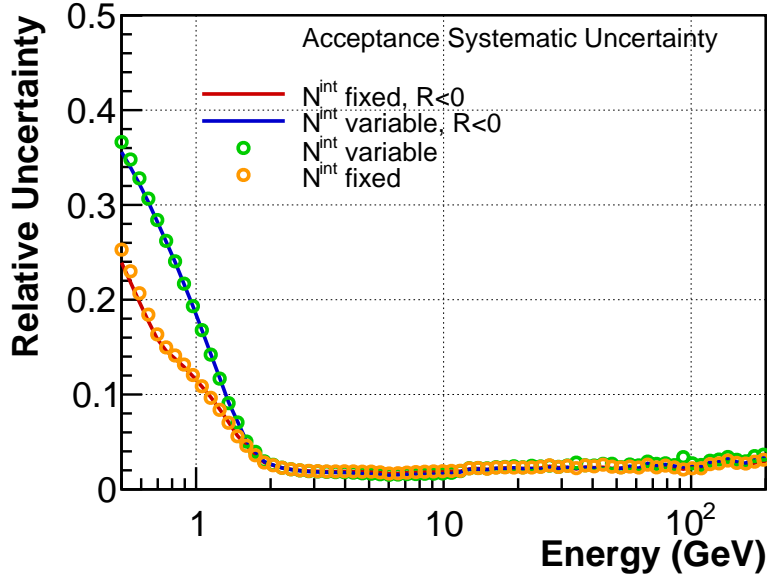


Figure 5.22: Comparison of $\Delta\eta^{(\text{tot})}$ evaluated using different methods. In blue, the procedure discussed so far – for which the e^- control sample is defined with different selections on the number on interactions N^{int} – is shown. The red line refers to the same procedure if no selection on N^{int} is applied at all. The green and orange circles describe the same two procedures applied on a e^\pm control sample, where no selection on the charge sign has been applied. The requirement on the charge sign has a negligible impact on the definition of the systematic error. The choice to define the e^- (or e^\pm) control sample using a selection on the activity in the detector changes drastically the result at low energies. Above 2 GeV all the procedures provide compatible results.

all compatible within the systematic error of 2% already assigned for energies above 3 GeV. Above this energy the acceptance uncertainty is consequently not modified. Below this energy, the discrepancy between the different analyses rises up to $\sim 6\%$ at 1 GeV and $\sim 20\%$ at 0.5 GeV. The value of $\Delta_{1/2}$ has been parametrized below 3 GeV and it has been used as best estimation for σ_{acc} below 3 GeV.

The resulting uncertainty on the flux measurement due to the acceptance systematic σ_{acc} is finally shown in Figure 5.23. The uncertainty on the acceptance scale is $\sim 2\%$ above 3 GeV and increases strongly at low energies up to a level of $\sim 20\%$ at 0.5 GeV. It therefore dominates the measurement uncertainty over the statistical error and the selection systematic uncertainties up to ~ 100 GeV. Above this energy, the other two sources take over and set the scale of the measurement error.

Part of the flux measurement uncertainty introduced by the acceptance correction is correlated between neighboring energy bins. A fraction of the uncertainty covers, in fact, a possible shift of the flux normalization highly correlated as function of the energy. Such contribution to the error has to be explicitly provided since it can affect the phenomenological interpretation, such as discussed in Section 6.3. On the other hand, in other applications the normalization of the flux has to be taken into account in the data interpretation.

An estimation of the bin-to-bin correlated contribution to the flux error can be deduced from the discrepancies between the flight data and the MC simulation. As shown already in Figure 5.18 and in Figure 5.19, some selections exhibit a substantial difference from the perfect agreement. The correlated contribution to the error is dominated by the single cut which shows the maximum deviation. Above 3 GeV, the $N^{\text{TRK}} = 1$ selection shows the maximum disagreement. The correction to the acceptance from this single cut above 3 GeV amounts to $1.4\% \pm 0.2\%$, where the error describes the tolerance due the minor energy dependence of the data/MC comparison. The discontinuity observed at ~ 13 GeV

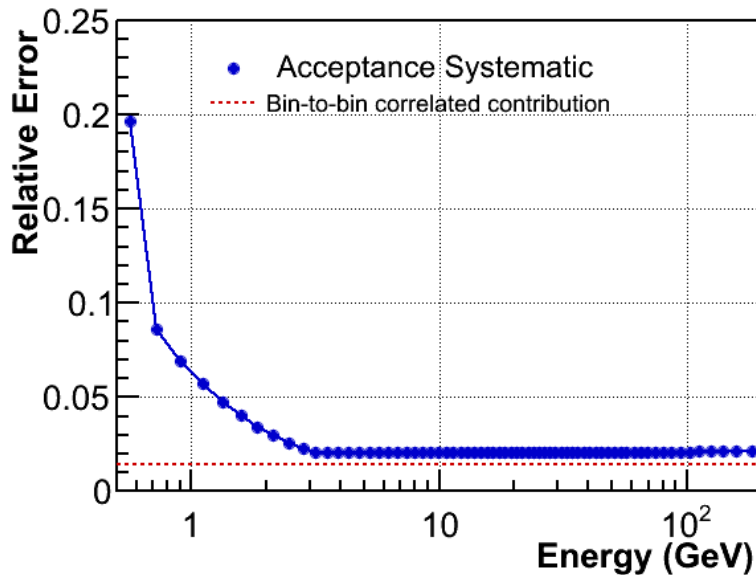


Figure 5.23: Systematic uncertainty on the knowledge of the absolute scale of the $e^+ + e^-$ acceptance. Above 3 GeV, the uncertainty is nearly flat at a value of $\sim 2\%$. Below 3 GeV the uncertainty increases up to a maximum value $\sim 20\%$ at 0.5 GeV. The red dashed line represents the bin-to-bin correlated contribution to the measurement uncertainty.

has been neglected. This is a good estimation of the bin-to-bin correlated contribution to σ_{acc} . The same amount of correlated contribution to the uncertainty has been evaluated by analyses from other working groups, and they agree to $\sim 1.4\%$. Therefore, this estimate is provided as bin-to-bin correlated contribution to the flux measurement error. Below 3 GeV, instead, the difficulties encountered to measure the acceptance corrections prevent to calculate a reliable estimate of such contribution. The estimate of $\sim 1.4\%$ for the correlated error can be however considered with good confidence a lower limit and it has been therefore extrapolated as constant below 3 GeV to provide a conservative estimate. Further studies of the low energy e^\pm fluxes will provide in future a more reliable estimate for such contribution. The bin-to-bin correlated contribution to the acceptance error is shown, for reference, with the red dashed line in Figure 5.23.

5.5 Summary

In this chapter, the normalization of the number of ($e^+ + e^-$) events to the flux entering at the top of the detector has been discussed. The number of events collected by the detector depends on the properties and on the operations of the detector itself. The $e^+ + e^-$ counts have therefore been corrected for the detector exposure time and the detector acceptance.

The exposure time has been calculated for the whole data taking period, removing intervals when the detector was operated in not-nominal conditions. The time has been reweighted by the livetime in order to correctly take into account of the detector *busy* periods. In total, 6.2×10^7 s of data has been effectively used for the flux measurement above 30 GeV. This corresponds to $\sim 78\%$ of the real time from the detector deployment on the ISS. Below 30 GeV, instead, geomagnetic field effects decrease the effective exposure time down to 2.0×10^7 s at ~ 5 GeV and to less than 5.0×10^6 s below 2 GeV.

The trigger properties and performance for e^\pm have been studied using a dedicated stream of events

recorded by the detector with looser trigger conditions. Electrons and positrons are triggered using the ECAL trigger with $\sim 100\%$ efficiency above 3 GeV. No data have been lost due to trigger inefficiencies above this energy. At lower energies, the use of the TOF trigger recovers the inefficiency of the ECAL standalone triggers, which amount to less than 20% below 1 GeV. The e^\pm trigger efficiency decreases down to a value of $\sim 80\%$ at 0.5 GeV, which is still remarkable for a detector designed for the measurement of high energy cosmic rays.

The detector acceptance, which describes the geometry of the detector convoluted with the efficiency of the e^\pm selection, amounts to a maximum value of $\sim 500 \text{ cm}^2\text{sr}$ at medium energies and it decreases down to $\sim 400 \text{ cm}^2\text{sr}$ at 1 TeV. Below 3 GeV, the acceptance drastically decreases down to a minimum value of $\sim 100 \text{ cm}^2\text{sr}$ at 0.5 GeV. The decrease of acceptance at very low energies is induced by a loss of efficiency in the e^\pm selection due to interactions of low energetic particles in the detector, by the increased bending effect of the magnetic field and by multiple scattering phenomena.

The absolute normalization of the e^\pm acceptance for this analysis has been set using the MC simulation. The uncertainty of the detector acceptance is defined by the accuracy to which the MC simulation is able to reproduce the detector geometry and, most importantly, the interactions of incoming e^\pm with the detector material. In order to assess to quality of the MC simulation, the efficiency of each selection cut used to define the $(e^+ + e^-)$ sample for the flux measurement has been evaluated on flight data and on the MC simulation and compared.

The data/MC comparisons are first used to assess a correction factor to apply to the MC acceptance in order to correctly represent the flight data cut efficiencies. Above 2 GeV the correction is a smooth function of the energy and it is smaller than 4%. Below 2 GeV the correction shows a strong energy dependence. It amounts to $\sim 5\%$ at 1.5 GeV and $\sim 15\%$ at 0.5 GeV.

Since e^\pm are a minor component of the cosmic radiation, a strong selection has been applied on data (and correspondingly also on the MC simulation) to select a pure sample of e^- . For each subdetector selection cut, a control sample of e^- has been selected using all the other subdetectors and the efficiency of the selection has been tested using a *Tag&Probe* approach. The results represent the efficiency of the selection on a biased sample of electrons, which is not fully representative of the $e^+ + e^-$ sample used for the flux measurement. Moreover the data/MC agreement depends on the particular choice of the definition of the e^- control sample.

In order to evaluate the impact of the control sample definition on the data/MC comparison outcome, multiple definitions of the e^- control sample have been tested, and the spread of the resulting comparisons has been considered in the assessment of the acceptance uncertainty. In addition to this, the deviation from perfect agreement between the flight data and the MC simulation efficiencies contributes to the acceptance systematic uncertainties.

The acceptance error σ_{acc} is dominated by the differences between the data and the MC simulation above 2 GeV. Above this energy, it amounts to $\sim 2\%$. Below 2 GeV, instead, it increases up to $\sim 6\%$ at 1 GeV and $\sim 20\%$ at 0.5 GeV.

The acceptance uncertainty σ_{acc} contains a contribution that introduces a correlation between neighboring energy bins. The bin-to-bin correlated contribution to σ_{acc} has been estimated to be at the level of 1.4%.

The uncertainty on the detector acceptance dominates the flux measurement uncertainty up to 100 GeV. Above 200 GeV the statistical fluctuations associated to the $(e^+ + e^-)$ signal extraction procedure take over and set the total measurement uncertainty.

In the next chapter, the results discussed in this chapter and in the previous chapters are combined to retrieve the measurement of the $(e^+ + e^-)$ flux.

Chapter 6

The ($e^+ + e^-$) flux measurement

In the previous chapters, the data collected by the AMS detector in the first 30 months of data taking have been analyzed to measure the ($e^+ + e^-$) flux ($\Phi_{e^+e^-}$). Among 41×10^9 collected events, 10.6×10^6 events have been identified as ($e^+ + e^-$). The analysis of the shower development in the ECAL has been used to remove most of the proton background and the information provided by the TRD has been used to extract the remaining ($e^+ + e^-$) signal yield using a template fit procedure. The redundant TRD and ECAL e/p discrimination capabilities allow the separation of the proton background and the identification of the number of ($e^+ + e^-$) events in each energy bin with systematic uncertainties below the statistical fluctuations.

The AMS detector acceptance for the $\Phi_{e^+e^-}$ measurement has been calculated using the MC simulation. Above 10 GeV, it amounts to $500 \text{ cm}^2\text{sr}$ and decreases down to $400 \text{ cm}^2\text{sr}$ at 1 TeV. The uncertainty to which the acceptance is known has been evaluated by a detailed comparison of the ($e^+ + e^-$) selection efficiencies between the MC simulation and control samples of e^- from the flight data. The level of accuracy to which the acceptance is known, which amounts to $\sim 2\%$ above 3 GeV, dominates the systematic uncertainty of the flux measurement below ~ 150 GeV. Above this energy, the statistical fluctuations dominate the measurement uncertainty.

In this chapter, first the impact of the ECAL energy measurement for the $\Phi_{e^+e^-}$ evaluation is described. In particular, the ECAL energy resolution and the accuracy to which the absolute scale of the ECAL energy measurement is known are discussed. Subsequently, the previous results are combined to provide the measurement of $\Phi_{e^+e^-}$ using the AMS data. The result is compared with previous experiments and the consistency with other independent AMS measurements is checked. Finally, the phenomenological implications of the result are discussed. The spectral shape of the $\Phi_{e^+e^-}$ flux is analyzed independently from any physical model to retrieve information about its spectral index. Afterward, the $\Phi_{e^+e^-}$ measurement is used together with the positron fraction measurement to infer basic implications on cosmic ray e^\pm production and propagation models.

6.1 The ECAL energy measurement

The best estimate for the energy of e^\pm cosmic rays at the top of the AMS detector is provided by the measurement of the electromagnetic calorimeter ECAL.

The ECAL energy reconstruction algorithms have been tuned during test beams on ground in order to correctly measure the energy of e^\pm entering the AMS detector. They include corrections for energy losses in the materials before the calorimeter, lateral and rear leakage corrections in the ECAL itself, temperature dependent corrections and detector inefficiency corrections.

During the test beams, the absolute scale of the energy measurement has been tuned to best reproduce

the e^\pm beam momentum. The deviation from linearity measured using e^\pm beams between 10 GeV and 290 GeV is below the 1% level [199]. The energy measurement resolution, measured by the spread of the energy measurement around the beam energy, is parametrized¹ as already reported in Equation 2.3:

$$\sigma^{\text{res}}(E)/E = \frac{(10.4 \pm 0.2)\%}{\sqrt{E(\text{GeV})}} \oplus (1.4 \pm 0.1)\% \quad (6.1)$$

The ECAL energy measurement properties on ground are known to the 1% level.

After the deployment in space the ECAL calibration has to be checked and monitored. During space operations the ECAL cannot be calibrated using beams with known rigidity. Moreover, differently from collider experiments, there is no sharp feature at known energy in cosmic rays that could be used to calibrate the energy measurements of the detector in flight.

As discussed later in Section 6.1.1, any miscalibration of the absolute energy measurement will be reflected in a systematic uncertainty on the final flux measurement. Such uncertainty is enhanced by the power law energy dependence of the flux. This can be shown analytically for a power law flux:

$$\Phi(E) \propto E^{-\gamma} \implies \left| \frac{d\Phi}{\Phi} \right| = \gamma \frac{dE}{E} \quad (6.2)$$

Since the measured flux (Φ_{rec}) is calculated after the collection of $N \propto \int_{\Delta E} \Phi(E) dE$ cosmic rays in an energy interval of width ΔE , Equation 6.2 has to be modified to take into account the energy integration factor:

$$\left| \frac{d\Phi_{\text{rec}}}{\Phi_{\text{rec}}} \right| = (\gamma - 1) \frac{dE}{E} \quad (6.3)$$

The last relation holds only if a power law flux is assumed and if the energy dependencies introduced by the detector measurements are neglected. For a spectral index $\gamma = 3$, the relative uncertainty on the flux amounts to 2 times the uncertainty on the energy measurement.

In the following sections, the uncertainty to which the ECAL energy scale is known and the impact on the flux measurement are discussed.

6.1.1 ECAL resolution and absolute scale

The ECAL energy calibration has been tuned using test beam data and using the MC simulation in the energy range not covered by the test beams. The time dependence of the energy scale is continuously monitored and crosschecked using flight data. In particular, the stability of the most probable value for the energy deposit of Minimum Ionizing Particle (MIP) protons and He nuclei is used to determine a time dependent correction to the energy measurement. The correction factor applied is below 2% for the whole data taking period.

The residual uncertainty is evaluated using the redundant momentum measurement (p) provided by the Tracker. The E/p distribution has been compared between test beam data and flight data, both for e^\pm and MIP protons. The agreement between the E/p peak position between ground and flight data confirms that the ECAL calibration and the energy scale defined on ground can be safely applied on flight data². A maximum residual disagreement at the level of 1% for e^\pm and 2% for protons has been found [229].

¹The parametrization is only valid for particles impinging the calorimeter vertically, and it tends to improve for inclined particles, as they cross more material in the ECAL.

²It is assumed that any difference in the observed E/p ratio could be introduced only by a miscalibration of the ECAL. The absolute scale of the spectrometer is defined by the accuracy to which the magnetic field map and the alignment of the silicon sensors, that are monitored with high precision using cosmic ray protons, are known. Given the accuracy to which the AMS spectrometer parameters are monitored [228], the rigidity measurement scale can be assumed to be known with higher precision than the energy measurement scale.

On top of this, the stability of the ECAL response in flight has been confirmed by the stability of the E/p dependence for e^\pm as function of time. Figure 6.1 shows that the observed fluctuations are at the maximum level of 1%.

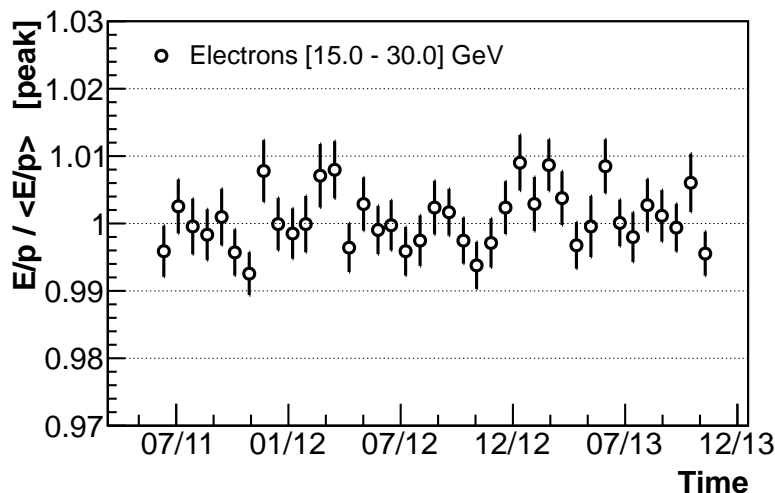


Figure 6.1: Time dependence of the ratio between the ECAL energy measurement E and the Tracker momentum measurement p for e^- data collected in space by AMS in the energy range [15.0 - 30.0] GeV. The figure reports the value of the E/p distribution peak. The error represents the uncertainty on the E/p peak value, which is estimated via the fit of its analytic parametrization to the distribution. The values are normalized to their average in the whole data taking period. The stability of the ratio within 1% confirms that the ECAL energy measurement does not show any trend above the systematic uncertainty of the scale itself.

The residual uncertainty on the ECAL energy scale $\sigma(E)/E$ after all the corrections and checks discussed so far is estimated to be 2% between 10 GeV and 290 GeV. Outside the test beam energy range $\sigma(E)/E$ rises up to 5% at 0.5 GeV and at 1 TeV. This conservative estimation covers further discrepancies with the MC simulation at very low and very high energies. The energy dependence of the ECAL scale uncertainty is sketched for reference in Figure 6.2 together with the parametrization of the ECAL energy resolution.

For the e^\pm flux measurements, the uncertainty on the ECAL energy scale is treated as uncertainty on the energy bin borders [83, 26, 1]. However, this uncertainty translates indirectly into a systematic effect on the flux measurement. This has to be carefully taken into account when the flux measurement is used to infer physics information through the comparison of physics models to the data points.

The finite ECAL energy resolution and the energy absolute scale uncertainties induce different effects on the flux measurement. The energy resolution describes the intrinsic spread of the measurement around the average value due to the migration of events to neighboring energy bins, and the effect on the flux measurement is therefore mitigated by its statistical symmetric nature. It contributes, however, to the error on the flux measurement. The uncertainty on the absolute scale covers a possible bias in the energy measurement which is applied coherently to all the events, and whose effect is enhanced by the steeply falling power-law behavior of the flux itself. In addition to this, a possible deviation from the linearity as function of the energy is also considered in the energy scale uncertainty.

A dedicated study has been performed to assess the impact of these effects on the measurement of $\Phi_{e^+e^-}$. The procedure and results are described in the following section.

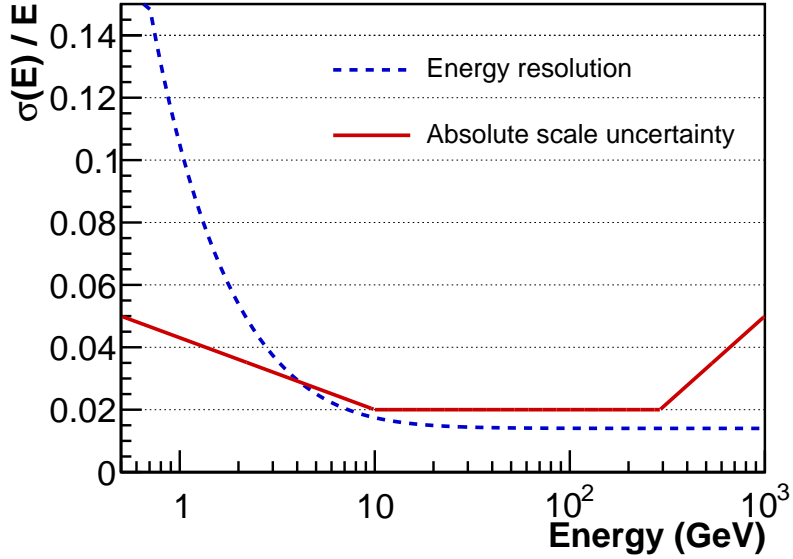


Figure 6.2: Parametrization of the ECAL energy resolution (in blue) and of the energy measurement absolute scale uncertainty (in red). Both curves have been parametrized between 10 GeV and 290 GeV using test beam e^\pm . The ECAL resolution energy dependence has been extrapolated continuously outside this range. The uncertainty on the absolute scale grows towards low and high energies in order to cover further discrepancies with the MC simulation.

6.1.1.1 ECAL energy measurement uncertainty

As discussed previously, the uncertainty on the ECAL energy measurement translates into an indirect systematic uncertainty for the flux measurement. In particular, the symmetric effect of the event bin-to-bin migration due to the finite energy resolution results in a different impact than a rigid shift given by a miscalibration at the percent level of the ECAL energy scale.

Figure 6.3 shows the ECAL resolution matrix for MC simulation e^\pm . For a fixed generated energy E_{gen} , the width of the distribution of the reconstructed energy E_{rec} represents the effect of the finite ECAL measurement intrinsic resolution. Any large deviation from $E_{\text{rec}}/E_{\text{gen}} = 1$ points to the existence of a systematic shift effect. This is particularly evident for values of $E_{\text{rec}} < 5$ GeV and it is probably generated by inefficiencies in the shower clustering or in the leakage corrections for events interacting before the calorimeter. Disregarding these events, the MC simulation shows a maximum deviation from the linearity at the percent level above 2 GeV.

Equation 6.3 cannot be used directly to infer the impact of the energy measurement resolution on the flux measurement. The bin-to-bin migration affects, in fact, only the events which are collected by the detector and selected during the analysis. The energy dependence of the incoming flux in Equation 6.3 has to be hence corrected by the energy dependent acceptance and exposure time. This ensures that the correct energy spectrum of detected events is used for the evaluation of the bin-to-bin migration effects.

Therefore the MC simulation events have been correctly reweighted according to the procedure explained in Section 3.3 assuming an injection flux $\Phi_{\text{gen}}^*(E_{\text{gen}})$ representative of the incoming ($e^+ + e^-$) flux. The analysis selection chain has been applied on MC simulation e^- events. The bias introduced in the energy measurement by every cut of the analysis is in this way taken into account. The selected e^- events are then accumulated in histograms according to the reconstructed energy value E_{rec} and the re-

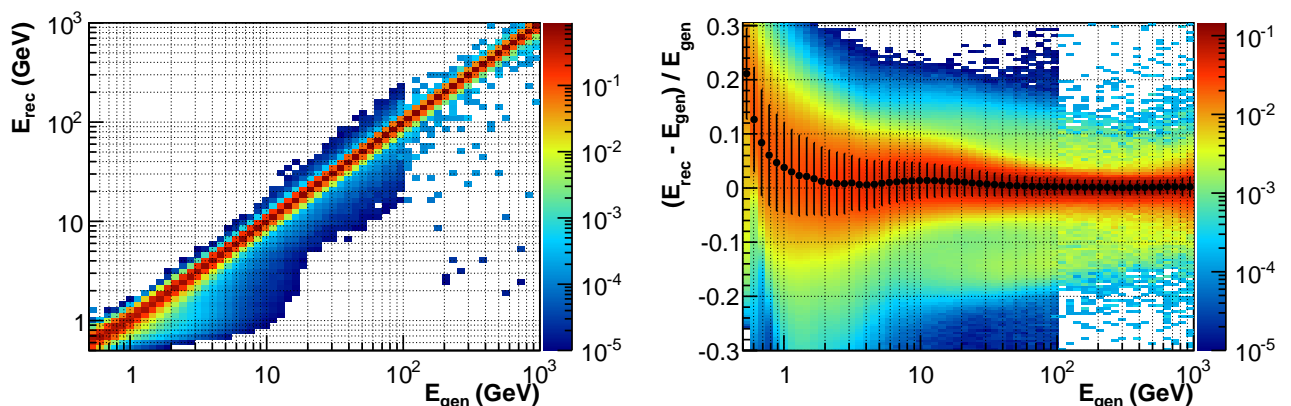


Figure 6.3: **Left:** ECAL energy resolution matrix for MC simulation e^- . The energy measured by the ECAL (E_{rec}) is compared to energy generated at the top of the detector (E_{gen}). For each bin on the x axis, the entire slice in y is normalized to 1. At low energy, in a minority of events $\ll 1\%$, E_{rec} is much smaller than the generated energy. This is mostly due to inefficiencies in the shower clustering algorithms and in leakages corrections for events interacting above the calorimeter. **Right:** Relative uncertainty on the measured energy. For each bin on the x axis, the entire slice in y is normalized to 1. Superimposed for each generated energy slice is the mean of a Gaussian fit to the resolution profile. The error represents the width of the gaussian parametrization. For energies above 2 GeV, the maximum deviation from the agreement is at the level of 1%. The disagreement increases for energies below 2 GeV.

constructed flux $\Phi_{\text{rec}}^*(E_{\text{rec}})$ is computed, as done for data, according to the prescription of Equation 3.11. Finally $\Phi_{\text{rec}}^*(E_{\text{rec}})$ is compared to the known input flux $\Phi_{\text{gen}}^*(E_{\text{gen}})$. Any discrepancy between the two values has to be considered a consequence of bin-to-bin event migrations due to the finite ECAL energy measurement resolution and to any non-linearity in the energy scale.

The uncertainty of the flux measurement due to the bin-to-bin event migration induced by the finite ECAL energy measurement resolution has been studied using this approach. For each MC simulation event, the value of E_{rec} has been determined by applying a smearing to the value of E_{gen} according to the energy resolution observed in the ECAL migration matrix. Any deviation from the linearity, observed in Figure 6.3, has been neglected in this approach to disentangle the bin-to-bin event migrations from the event migrations due to a miscalibration of the energy scale. The result of the comparison of $\Phi_{\text{rec}}^*(E_{\text{rec}})$ with the known input flux $\Phi_{\text{gen}}^*(E_{\text{gen}})$ is shown in Figure 6.4. The red points quantify the amount of systematic uncertainty for the flux measurement due to the discrepancy between $\Phi_{\text{rec}}^*(E_{\text{rec}})$ and $\Phi_{\text{gen}}^*(E_{\text{gen}})$. This effect has been studied independently also by other analysis groups within the AMS collaboration. The parametrization that has been chosen by the collaboration to describe the bin-to-bin migration effect on the measured flux is shown in green in Figure 6.4. This contribution has been included in the definition of the $\Phi_{e^+e^-}$ systematic uncertainty as discussed in Section 6.2. The $\Phi_{e^+e^-}$ bin-to-bin migration systematic uncertainty (σ_{migr}) is shown, together with other sources of systematics uncertainties, in Table F.1. Its contribution to the total $\Phi_{e^+e^-}$ measurement systematic uncertainty is negligible with respect to other sources of systematic effects in the whole energy range.

The additional effect of a possible systematic shift in the ECAL absolute scale, covered by the uncertainty to which the scale itself is known, has been investigated using the same MC simulation approach. Figure 6.5 shows the effect of a simulated $\pm 2\%$ miscalibration on the measured flux. A fixed shift of $\pm 2\%$ has been applied to E_{gen} to retrieve E_{rec} . The net systematic effect on the flux measurement is of the order of $\sim 4\%$ above 2 GeV, as expected from Equation 6.3 for a power law flux with spectral index $|\gamma| = 3$. The minor deviation from this result is induced by the real shape of the generated

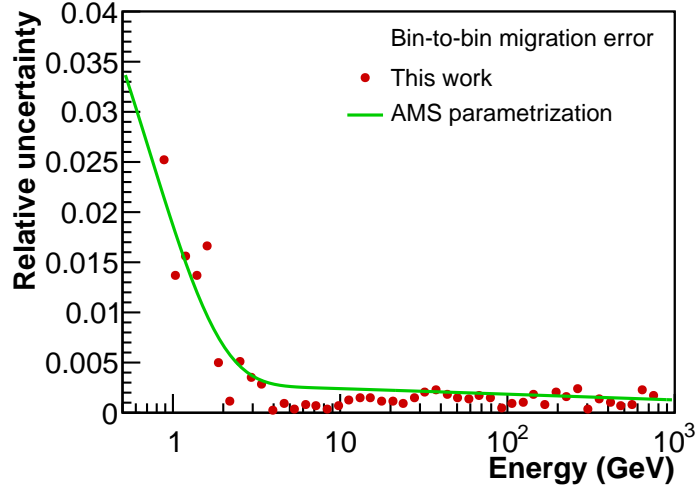


Figure 6.4: Contribution of the bin-to-bin event migration due to the finite ECAL energy resolution for the flux systematic uncertainty. The red points represent the result obtained in this analysis using the MC simulation approach. The green line represents the parametrization chosen by the AMS collaboration to quantify this effect. The parametrization agrees with the result of this analysis and it is slightly more conservative between 3 and 30 GeV. The bin-to-bin migration uncertainty for the flux measurement is smaller than 0.5% above 3 GeV and it slightly increases below 3 GeV. As shown in Table F.1, its contribution to the total $\Phi_{e^+e^-}$ measurement systematic uncertainty is minor and negligible with respect to other sources of systematic effects in the whole energy range.

spectrum and the energy dependence of $A(E)$ and $\Delta T_{\text{exp}}(E)$ taken into account in the procedure. The deviation increases drastically below 2 GeV, where the energy dependence of the acceptance significantly modifies the spectrum of the collected e^\pm events.

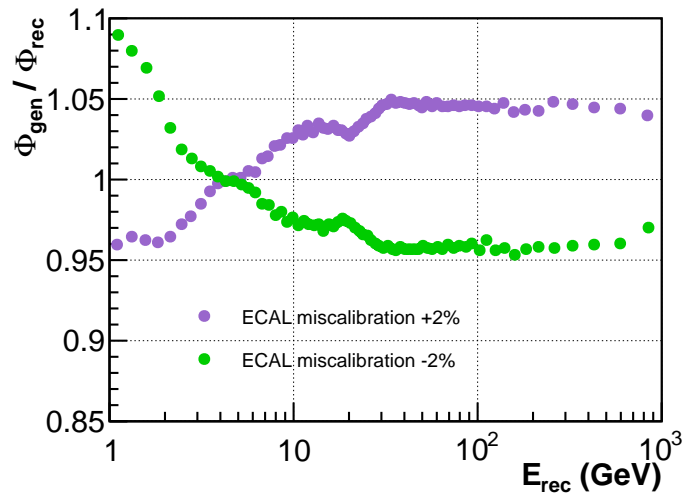


Figure 6.5: Comparison of $\Phi_{\text{gen}}^*(E_{\text{gen}})$ and $\Phi_{\text{rec}}^*(E_{\text{rec}})$ in case of a systematic shift of +2% (violet) and -2% (green) applied to the generated energy E_{gen} to calculate the reconstructed energy E_{rec} . This simulates a fixed miscalibration of $\pm 2\%$ of the energy measurement scale. The maximum deviation from the unity observed above 2 GeV is of the order of 4%, as expected from Equation 6.3 for a $\gamma \sim -3$ generated spectral index and for a mild energy dependence of the detector acceptance.

Following the custom approach adopted from previous measurements of the e^\pm fluxes, the systematic effect on the final flux measurement is not quoted in the final result as uncertainty on the flux itself. The uncertainty on the ECAL energy scale is rather considered as an uncertainty on the bin border energy and it is reported in Table F.2 together with the best estimation for the energy value in each bin (discussed in the next section).

Any phenomenological interpretation of the ($e^+ + e^-$) flux has therefore to take into account independently of this additional effect introduced by energy measurement scale uncertainty. More details are discussed in the next section.

6.1.2 Where to stick the data points

Experimental data are used to constrain the parameters that define models for diffusion of cosmic rays in the galactic environment (see Section 1.1.2). The solution of the transport equation according to a propagation model³, $\Phi_{\text{mod}}(E)$, is compared to the experimental data for a selected number of particle species. The goodness of the model is then evaluated, for example, through a χ^2 test⁴. The experimental result provides redundant information about the energy range in which the flux is measured:

- (a) the minimum and maximum energy of the bin, E_{min} and E_{max} are provided. In this form, the propagation solution can be compared to the measured flux simulating the measurement itself: the flux $\Phi_{\text{mod}}(E)$ is first integrated between E_{min} and E_{max} and then divided by the energy interval width. The uncertainty on the ECAL energy measurement has to be considered in the definition of the measurement bin borders and consequently propagated for the comparison during the integration procedure.
- (b) the most representative energy point in the energy bin $\tilde{E} \in [E_{\text{min}}, E_{\text{max}}]$, in which the propagation solution $\Phi_{\text{mod}}(E)$ has to be locally evaluated, is provided. The uncertainty on the ECAL energy measurement is propagated to the uncertainty $\Delta(\tilde{E})$ on the point itself.

The second case is also particularly interesting for the experimental measurement itself. Several quantities, like for instance the parametrization of the acceptance, have to be evaluated for each energy bin during the flux measurement procedure. The natural choice is to evaluate those quantities at the point that is the most representative of the ($e^+ + e^-$) energy distribution collected in the energy bin.

In the case of a steeply falling power spectrum, as discussed originally in [230], the point has to be chosen carefully in order to avoid the introduction of unwanted biases, especially if the energy bin is wide. It can be shown that both the arithmetic mean

$$\langle E \rangle_{\text{AM}} = \frac{E_{\text{min}} + E_{\text{max}}}{2}$$

and the geometric mean, widely used in the literature

$$\langle E \rangle_{\text{GM}} = \sqrt{E_{\text{min}} \times E_{\text{max}}}$$

do not represent the average value of the energy distribution of ($e^+ + e^-$) events inside the energy bin.

³In this context, the term “model” usually refers to a set of free parameters of the transport equation.

⁴The numerical solution of the transport equation (Equation 1.2) is available only for a set of energy intervals, constrained by the resolution to which certain energy losses (or gain) processes have to be resolved during the solution of the equation. The model energy grid typically does not coincide with the experimental energy bins. This introduces some further difficulty to define the value of the model flux at the experimental bin borders. In this discussion, this complication will be neglected.

Following the prescription suggested in [230], the point \tilde{E} which should be used is the point at which the value $\Psi(\tilde{E}) = \Phi(\tilde{E}) \times A(\tilde{E})$ (to which the number of collected events is proportional) is equal to its average value in the bin itself:

$$\Psi(\tilde{E}) = \frac{1}{E_{\max} - E_{\min}} \int_{E_{\min}}^{E_{\max}} \Psi(t) dt \quad (6.4)$$

Equation 6.4 correctly contains the energy dependence of the flux $\Phi(E)$ itself and the additional energy dependence of the acceptance $A(E)$ inside the energy bin. The energy dependence of the exposure time, constant inside the energy bin, is here neglected.

This implicit equation can be solved analytically after an assumption on the flux and on the acceptance energy dependence. Assuming a power law input spectrum $\Phi \propto E^{-\gamma}$ and neglecting the energy dependence of the acceptance, the solution for $\langle E \rangle_{-\gamma}$ can be easily calculated as:

$$\langle E \rangle_{-\gamma} = \left(\frac{E_{\max}^{1-\gamma} - E_{\min}^{1-\gamma}}{(1-\gamma)(E_{\max} - E_{\min})} \right)^{-\frac{1}{\gamma}} \quad (6.5)$$

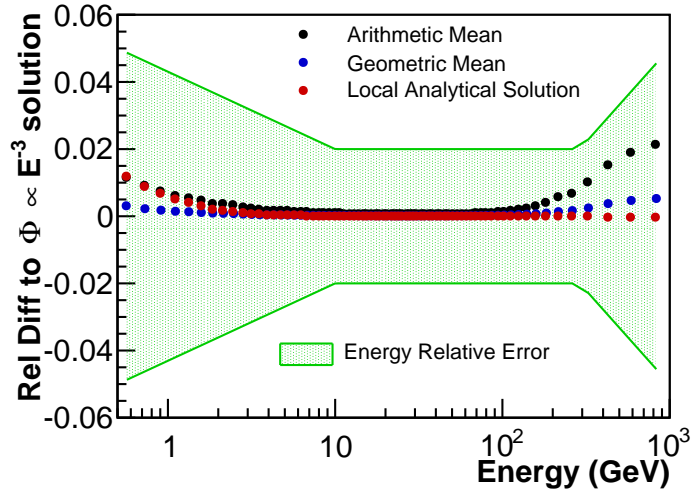


Figure 6.6: Relative difference of the value for the most representative energy \tilde{E} calculated according to several algorithms with respect to the reference value provided in the measurement table. The arithmetic mean (in black), the geometric mean (in blue) and the local numerical solution of Equation 6.4 (in red), which is assumed to be the best estimator for \tilde{E} , have been compared to the value $\langle E \rangle_{-3}$ obtained assuming a power law flux with spectral index $\gamma = -3$ and neglecting any energy dependence of the acceptance. The disagreement between $\langle E \rangle_{-3}$ and the numerical solution for \tilde{E} is at the level of 0.1% above 2 GeV. This holds even at high energies where the width of the bin boosts the effect of the steeply falling shape of the incoming spectrum. At low energies the wrong assumptions on the spectral index and on the energy dependence of the acceptance induce a deviation of 1% maximum at 0.5 GeV. This deviation is however well contained inside the systematic uncertainty on the value of the energy itself. The value of $\langle E \rangle_{-3}$, together with the uncertainty on the energy measurement, can be therefore safely provided to ensure the reproducibility of the result with no major impact on the phenomenological analysis of the experimental data.

In order to provide an easily reproducible value, in this analysis the quantity $\tilde{E} = \langle E \rangle_{-3}$ has been provided as most representative point in the energy bin. The value of \tilde{E} and its uncertainty $\Delta(\tilde{E})$ –

defined by the ECAL absolute scale uncertainty – is provided together with the flux measurement in Table F.2.

The dependence of the value \tilde{E} on the assumptions on the spectral index ($\gamma = -3$) for the incoming spectrum and on the assumption of an energy independent acceptance has been tested. Figure 6.6 shows the relative difference between $\langle E \rangle_{-3}$ and the value \tilde{E} obtained using a numerical solution of Equation 6.4 in a local range around the energy bin. For this calculation, the energy dependent acceptance and a preliminary measurement of $\Phi_{e^+e^-}$ have been used to obtain the best estimate of \tilde{E} . It is clear from Figure 6.6 that the assumptions introduced to calculate $\langle E \rangle_{-3}$ do not introduce any significant difference with respect to the best estimate of \tilde{E} – calculated using the numerical local solution of Equation 6.4 – above 2 GeV. At energies below 2 GeV, however, the assumptions on the spectral index and on the acceptance introduce a deviation of $\sim 1\%$ at 0.5 GeV. The impact of the wrong assumption is mitigated by the small width of the bin itself. The discrepancies are contained within the uncertainty on the ECAL energy measurement itself.

6.2 The measurement of the cosmic ray ($e^+ + e^-$) flux from 0.5 GeV to 1 TeV

In the previous Chapters 4 and 5, the measurements of the ($e^+ + e^-$) events collected by AMS ($N_{(e^+e^-)}$), the exposure time (ΔT_{exp}) and the acceptance (A), together with their relative uncertainties, have been evaluated. By means of Equation 3.11, they have been used to calculate the flux of ($e^+ + e^-$) ($\Phi_{e^+e^-}$) measured by AMS according to the procedure described in chapter 3.

Figure 6.7 reports the amount of the main contributions to the definition of the $\Phi_{e^+e^-}$ uncertainty. Up to ~ 300 GeV, the measurement systematic uncertainty is dominated by the uncertainty on the acceptance normalization (σ_{acc}) which describes the limit to which the MC simulation reproduces the flight data. The acceptance is known to an accuracy of $\sim 2\%$ above 3 GeV. The uncertainty increases at low energies up to $\sim 20\%$ at 0.5 GeV. The uncertainty on the acceptance covers a 1.4% contribution that introduces a bin-to-bin correlation between the $\Phi_{e^+e^-}$ data points. Above ~ 500 GeV the systematic uncertainty for the procedure used to identify the ($e^+ + e^-$) signal (σ_{sel}) takes over and dominates the systematic uncertainty. In the whole energy range, the minor systematic uncertainty introduced by the bin-to-bin migration of e^\pm events due to the finite ECAL energy measurement resolution (σ_{migr}) is always negligible with respect to the other sources of systematic uncertainties. The total systematic uncertainty, calculated as the quadratic sum of all the contributions, dominates the total uncertainty up to ~ 100 GeV. Above ~ 150 GeV the statistical fluctuations dominate the measurement total uncertainty. The statistical uncertainties are induced not only by the finite ($e^+ + e^-$) detected statistics, but also by the fluctuations of the signal and of the background during the fitting procedure, especially in the area where the TRD template shapes overlap. The total systematic uncertainty, calculated as the quadratic sum of each contribution, amounts to $\sim 2\%$ at energies above 20 GeV, and smoothly increases as function of energy up to a value of $\sim 4\%$ at ~ 200 GeV and $\sim 20\%$ at 1 TeV. At energies below 3 GeV, it rapidly increases up to $\sim 20\%$ at 0.5 GeV. The separate contributions to the $\Phi_{e^+e^-}$ measurement uncertainty are reported in Table F.1.

The measurement of $\Phi_{e^+e^-}$, which is the main result of this thesis, is reported together with its statistical (σ_{stat}) and total systematic uncertainty (σ_{syst}) in Table F.2 and in [1]. The total systematic uncertainty is calculated as the quadratic sum of (i) σ_{acc} (ii) σ_{sel} and (iii) σ_{migr} .

In the table, the value of the most representative energy in the bin (\tilde{E}) for the $\Phi_{e^+e^-}$ measurement, calculated as described in 6.1.2, is also reported. The uncertainty on \tilde{E} is set by the accuracy to which the absolute scale of the ECAL is known, discussed already in 6.1.1.

The resulting flux is shown, together with other previous experimental measurements of $\Phi_{e^+e^-}$, in

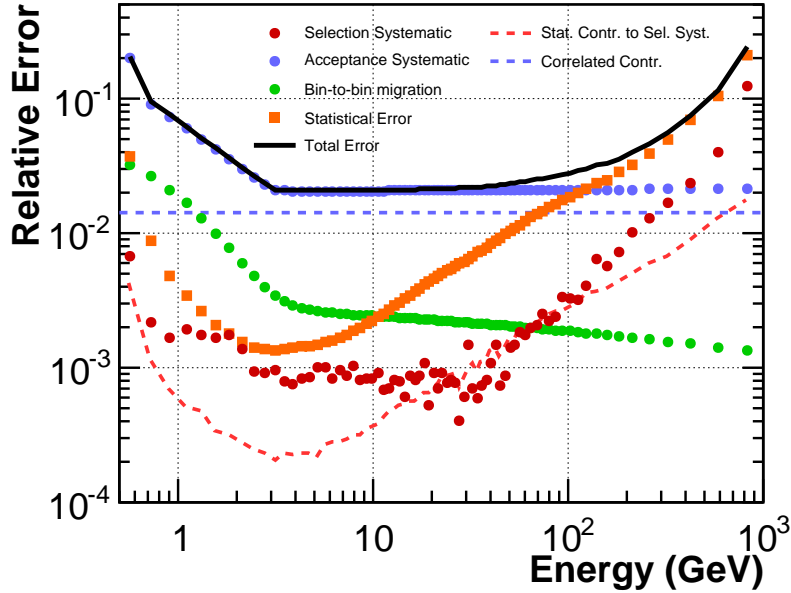


Figure 6.7: Energy dependence of the main uncertainty contributions to the $\Phi_{e^+e^-}$ measurement. The uncertainty on the acceptance scale (σ_{acc} , in blue), defined by the level of agreement between the data and the MC simulation, amounts to $\sim 2\%$ above 3 GeV and increases up to $\sim 20\%$ at 0.5 GeV. The acceptance uncertainty dominates the measurement systematic uncertainty up to 300 GeV. The acceptance uncertainty covers a 1.4% contribution that introduces a bin-to-bin correlation between the data points. This contribution is here shown with the blue dashed line. In red the systematic uncertainty due to the ($e^+ + e^-$) signal identification procedure (σ_{sel}) is shown. It dominates the measurement systematic uncertainty above ~ 500 GeV. The red dashed line represent the purely statistical contribution to this uncertainty source. This contribution has been removed from σ_{sel} . The uncertainty introduced by the minor bin-to-bin event migration due to the finite ECAL energy measurement resolution (σ_{migr}) is shown with the green points. Its contribution to the measurement uncertainty is negligible in the whole energy range. The statistical uncertainty (σ_{stat} , in orange), is below the percent level at low energies, and it increases for higher energies due to the fluctuations of the signal and of the background in the fitting procedure used to identify the number of ($e^+ + e^-$) among the proton background. The statistical uncertainties exceed over the acceptance systematics at ~ 150 GeV and start to dominate the measurement uncertainty up to 1 TeV. The total uncertainty (σ_{tot}), calculated as the quadratic sum of the systematic and statistical uncertainties, is here represented by the black line.

Figure 6.8. Figure 6.9 shows the same result multiplied by E^3 to highlight possible spectral features. AMS is the first experiment that measured the flux of ($e^+ + e^-$) from 0.5 GeV to 1 TeV. The measurement accuracy has been improved in the whole energy range with respect to previous experiments. The flux measured by AMS does not show any prominent feature in the whole spectrum and it excludes the claim of a structure above 300 GeV observed by the ATIC and PPB-BETS experiments [7, 9]. The discrepancies between the experimental results at energies below ~ 30 GeV are due to the different solar activity which influenced the low energy fluxes in different data acquisition periods.

Figure 6.10 shows a comparison of the measurement of $\Phi_{e^+e^-}$ for space experiments only, including the combinations of the latest data for the separate Φ_{e^-} and Φ_{e^+} measurements of the Fermi-LAT and PAMELA satellite experiments.

Figure 6.11 shows the impact of the precise ECAL energy measurement on the $\Phi_{e^+e^-}$ measurement with respect to other experiments.

The $\Phi_{e^+e^-}$ flux has been determined independently by several analyses within the AMS collabora-

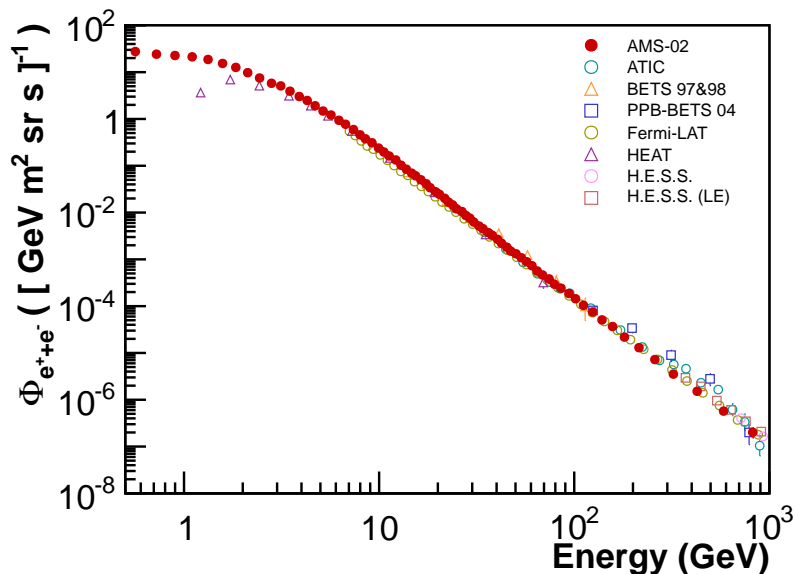


Figure 6.8: The $\Phi_{e^+e^-}$ measurement by the AMS detector between 0.5 GeV and 1 TeV is shown in red. The flux measured by AMS is compared with previous recent space experiments [18], balloon-borne experiments [8, 9, 7, 10, 11] and ground experiments [20, 21]

tion using the same set of data. The correctness of the analysis presented in this work has been verified a-posteriori by the comparison with the other results, which are all compatible within the uncertainties [231].

The ($e^+ + e^-$) flux can be also compared to the flux estimation derived from the combination of the e^- and e^+ separate fluxes. The $\Phi_{e^+e^-}$ flux measured by AMS and presented in this thesis has been compared to the flux obtained by the combination of the independent measurements of Φ_{e^-} , Φ_{e^+} and of the positron fraction (PF) by AMS [83, 26]. The comparison is shown in Figure 6.12. The measurement of the PF is interpolated to the energy value of the $\Phi_{e^+e^-}$ measurement. The separate fluxes share the same energy binning with the $\Phi_{e^+e^-}$ measurement, and no interpolation is needed. The uncertainties of the combined measurements are propagated assuming uncorrelated statistical errors and completely correlated systematic errors⁵. The results are compatible within the uncertainties in the whole energy range, with a deviation below 1 GeV and, in a smaller extent, at ~ 250 GeV induced by a fluctuation in the Φ_{e^-} measurement. The same figure shows, on the right, the comparison between the uncertainties associated to the $\Phi_{e^+e^-}$ results. As expected, the direct measurement of $\Phi_{e^+e^-}$ presented in this thesis provides a more accurate measurement than the combination of the Φ_{e^-} , Φ_{e^+} and PF measurements. It also allows to increase the maximum energy by a factor of 2.

The separate Φ_{e^\pm} measurements are characterized by much stronger requirements on the Tracker reconstruction quality. The Tracker charge sign estimation is in fact a fundamental parameter that enters into the e^+ and e^- separation. The selected e^\pm sample is therefore smaller than what obtained in this analysis. For the analysis of the separate e^\pm fluxes, which use the same dataset as in this analysis, a total of 9.8 million of e^\pm have been identified after the selection cuts, to be compared to 10.6 million of ($e^+ + e^-$) selected for this analysis. With respect to the $\Phi_{e^+e^-}$ measurement, the systematic uncertainty for the separate fluxes measurement is partially increased by the additional uncertainty introduced by

⁵Most of the same systematic effects are in fact shared between the different measurements and the assumption of linearly correlated systematic uncertainties is, in this case, a good estimation for the correlation between two measurements performed using the same detector and the same datasets.

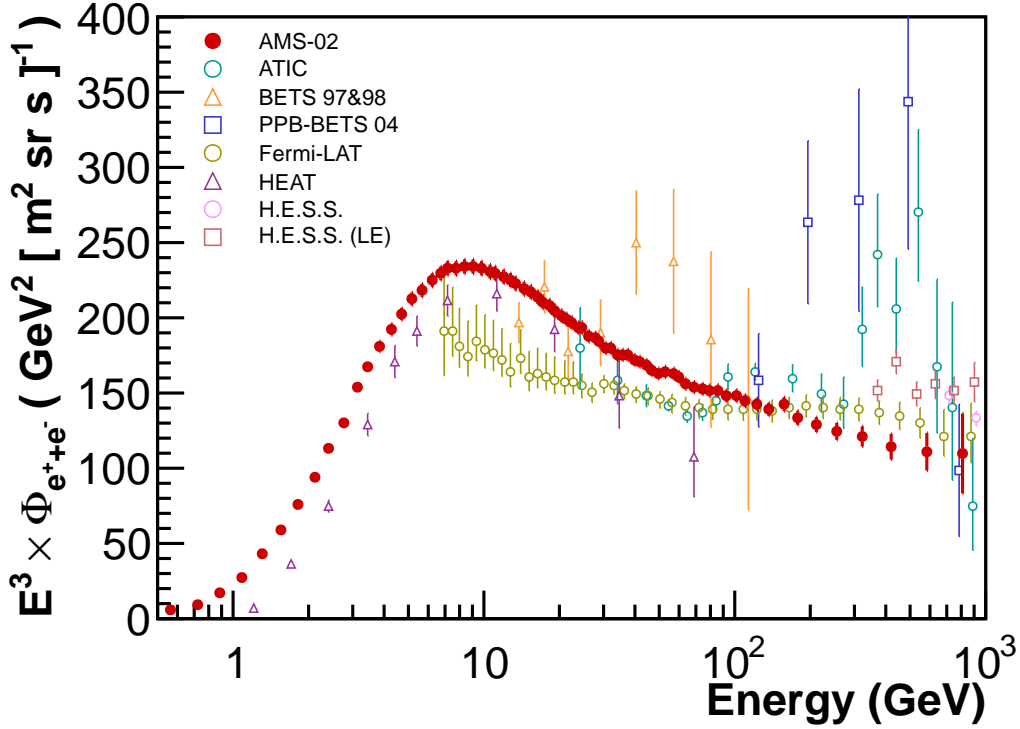


Figure 6.9: The $\Phi_{e^+e^-}$ measurement by the AMS detector between 0.5 GeV and 1 TeV is shown in red. The flux is multiplied by E^3 to highlight any spectral feature. The flux measured by AMS is compared with previous recent space experiments [18], balloon-borne experiments [8, 9, 7, 10, 11] and ground experiments [20, 21]

the charge confusion. The strongest increase to the systematic uncertainty is however mostly due to the much stronger selection that results in a higher uncertainty on the knowledge of the acceptance. As a consequence of this, the accurate positron fraction (PF) measurement can therefore be combined with the $\Phi_{e^+e^-}$ measurement to derive the separate Φ_{e^\pm} measurements with competing uncertainty. Figure 6.13 shows the comparison between the native Φ_{e^\pm} AMS measurements and the same quantities derived from the combination of the $\Phi_{e^+e^-}$ and the PF measurements by AMS. The combination of the $\Phi_{e^+e^-}$ and the PF measurements provides an estimation of Φ_{e^\pm} which is in agreement with the direct measurements and which shows a slight improvement in the accuracy of the measurement.

In the next section, the basic implications of the precise $\Phi_{e^+e^-}$ measurement for the phenomenological interpretation of the e^\pm fluxes will be discussed.

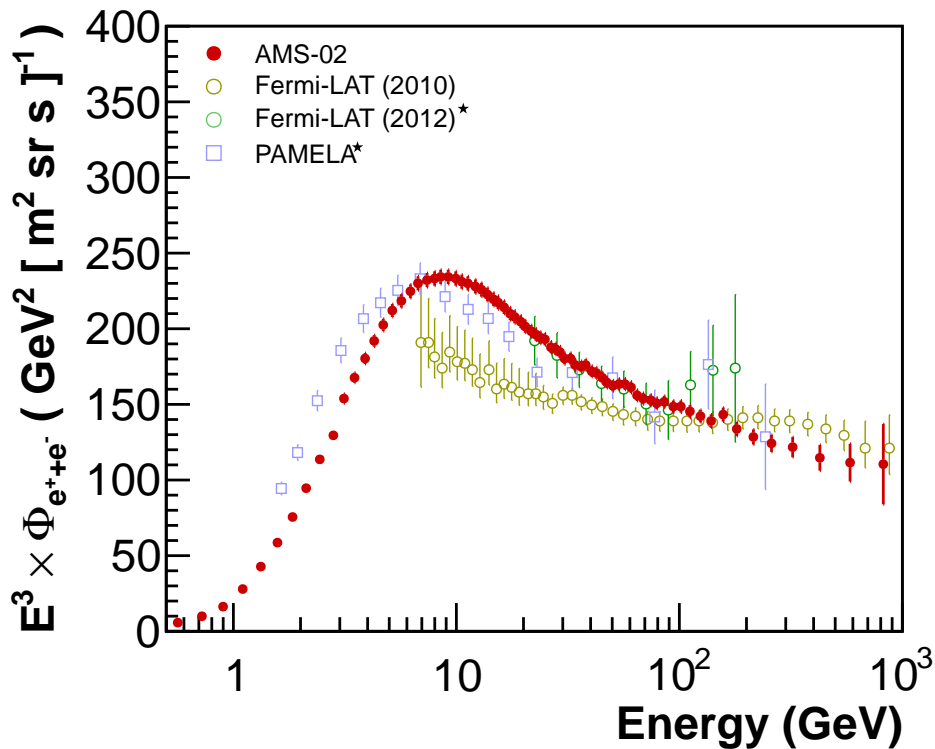


Figure 6.10: The AMS $\Phi_{e^+e^-}$ measurement between 0.5 GeV and 1 TeV, shown in red, together with the most recent measurements of the Fermi-LAT and PAMELA space experiments. The measurement of PAMELA and the last measurement from Fermi-LAT are a combination of the published separate Φ_{e^-} and Φ_{e^+} measurements [16, 19]. The Fermi-LAT $\Phi_{e^+e^-}$ measurement [18], here shown in gold, is in tension with the AMS measurement in the whole energy range. The $\Phi_{e^+e^-}$ measurement derived from the latest PAMELA and Fermi-LAT Φ_{e^-} and Φ_{e^+} data agree significantly better with the AMS measurement. The internal tension between the Fermi-LAT data is briefly discussed in Section 6.3.1.

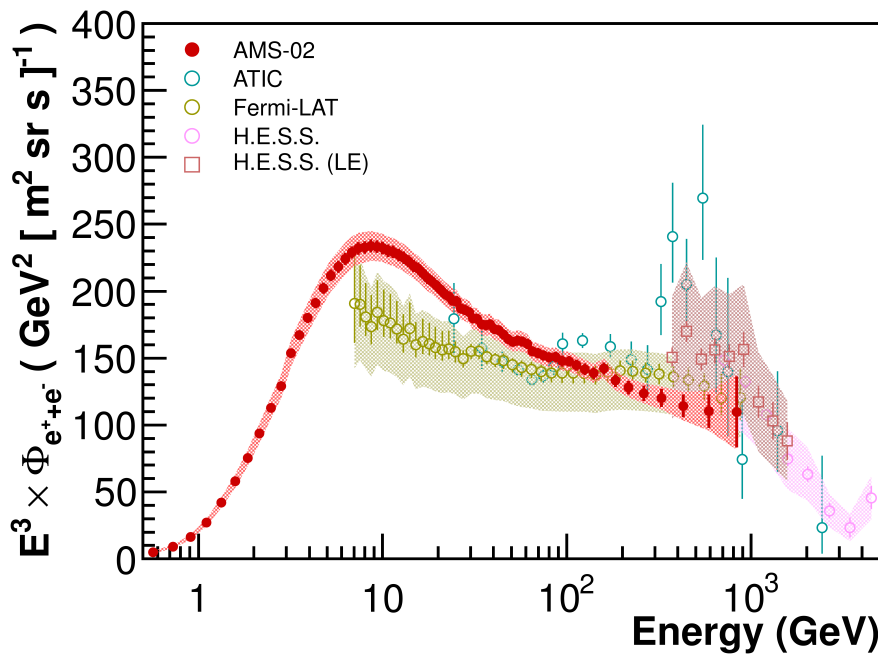


Figure 6.11: $\Phi_{e^+e^-}$ measurement for a selection of experiments. The dashed area covers the additional uncertainty introduced by the finite knowledge on the energy measurement scale. The uncertainty to which the AMS energy scale is known amounts to $\pm 2\%$ between 10 GeV and 290 GeV. It rises up to 5% at 0.5 GeV and 1 TeV. For the Fermi-LAT, it amounts to $^{+5\%}_{-10\%}$ in the whole energy range [18]. For the H.E.S.S. ground detector, it amounts to $\pm 15\%$ in the whole energy range [20, 21]. The shaded areas represent the uncertainty on the $\Phi_{e^+e^-}$ flux in the assumption that the energy scale uncertainty covers an energy independent miscalibration of the energy scale. For the sake of comparison, the uncertainty on the measurement is assumed to be two times the uncertainty on the energy scale, as expected for a flux $\propto E^{-3}$. A more precise study for the AMS measurement is discussed in Section 6.1.1.1. The increase of accuracy with respect to previous experiments provided by the precise energy measurement of the AMS ECAL is significant. The tension between the AMS and the Fermi-LAT $\Phi_{e^+e^-}$ measurements above 100 GeV could be explained by a possible unaccounted shift in the calibration of the energy measurement absolute scale.

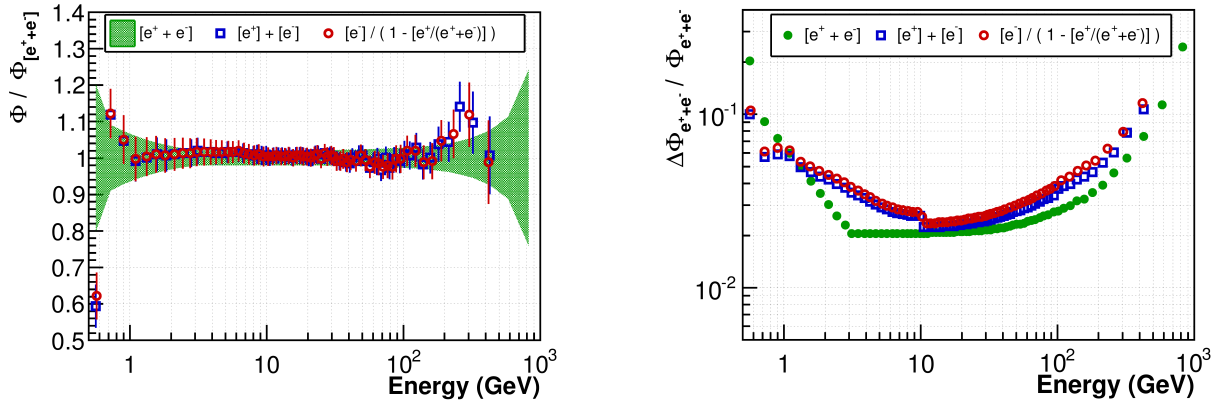


Figure 6.12: **Left:** Comparison between the $\Phi_{e^+e^-}$ flux inferred from the combination of the Φ_{e^-} , Φ_{e^+} and of the positron fraction (PF) measurements by AMS and the $\Phi_{e^+e^-}$ flux measured by AMS and presented in this thesis. The separate fluxes Φ_{e^-} and Φ_{e^+} and the positron fraction (PF) measured by AMS have been used to calculate $\Phi_{e^+e^-}$ as sum of the separate fluxes ($[e^+] + [e^-]$, here shown in blue) or as a combination of Φ_{e^-} and the PF measurements ($[e^-] / (1 - [e^+ / (e^+ + e^-)])$), here shown in red). The agreement is compatible within the uncertainties in the whole energy range. A discrepancy is observed at ~ 0.5 GeV and, in smaller amount, at ~ 250 GeV. **Right:** Comparison of the total uncertainties $\Delta\Phi_{e^+e^-}$ for the $\Phi_{e^+e^-}$ results. The direct measurement of $\Phi_{e^+e^-}$ described in this thesis provides, as expected, a more precise measurement than the combination of the other e^\pm measurements by AMS. The measurement accuracy is improved, as described in the text, especially at high energies.

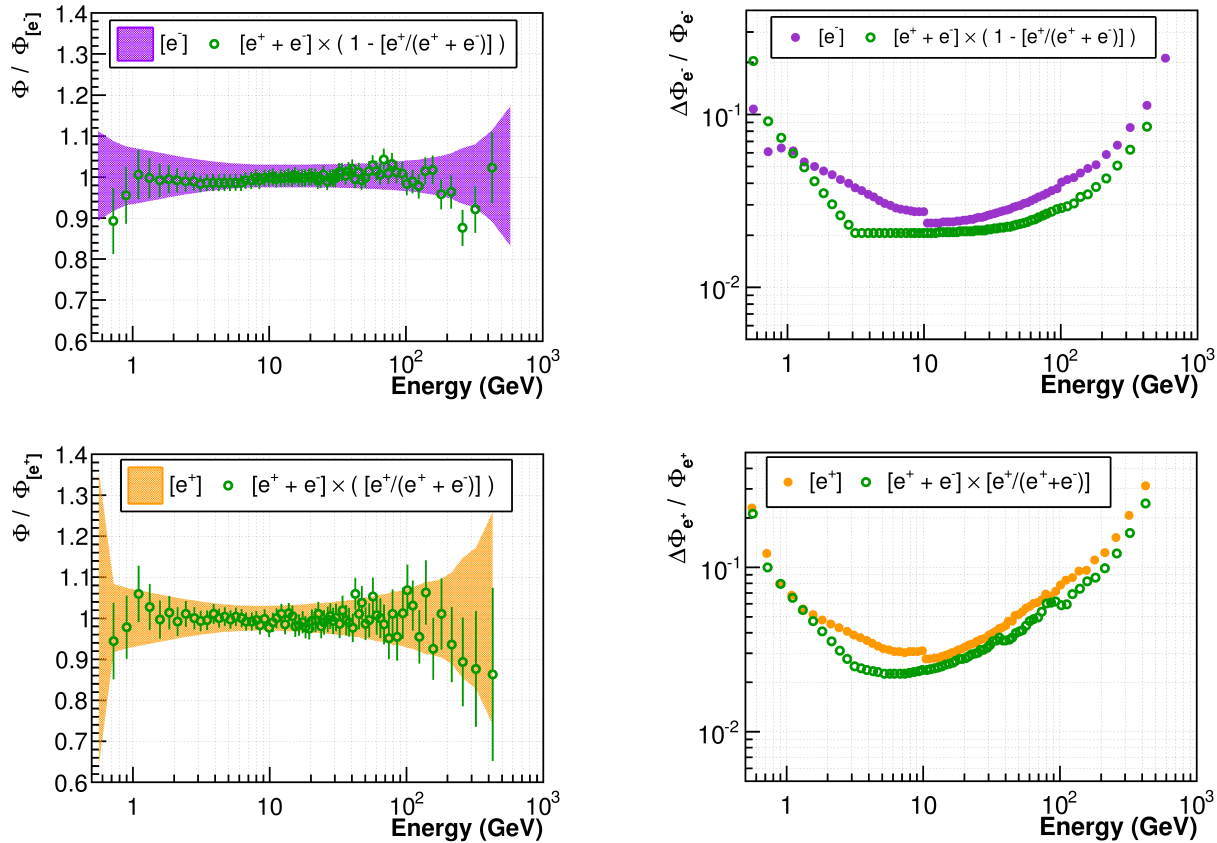


Figure 6.13: Comparison between the AMS Φ_{e^-} (**Top**) and the Φ_{e^+} (**Bottom**) flux measurements according to independent results. The direct Φ_{e^-} (in violet) and Φ_{e^+} (in orange) flux measurements are compared to the result obtained by the combination (in green) of the AMS $\Phi_{e^+e^-}$ flux measured in this analysis and the positron fraction (PF) measurement. The agreement between the results (shown in the left plots) is compatible within the uncertainty in the whole energy range. A discrepancy is observed at ~ 0.5 GeV and, in smaller extent, at ~ 250 GeV for the Φ_{e^-} flux. The uncertainty on the e^\pm fluxes provided by the combination of the accurate PF measurement with the $\Phi_{e^+e^-}$ flux measured in this analysis is comparable and slightly improved with respect to the direct Φ_{e^-} and Φ_{e^+} measurements in the whole energy range.

6.3 Phenomenological interpretation of the measurement

As already discussed in Chapter 1, the antimatter component in the cosmic radiation can be used as a probe to search for an indirect DM annihilation or decay signature. The study of the spectral shape of the e^- and e^+ fluxes in particular improves the knowledge of their production and propagation mechanisms and of the details of the neighboring galactic environment. In the next years the measurements by AMS of the e^- , e^+ and ($e^+ + e^-$) fluxes, together with other observables like the positron fraction, the time dependence of their low energy fluxes and the level of anisotropy in their arrival directions, will represent the most accurate data that will be used to investigate the properties of the cosmic e^\pm radiation.

The detailed analysis of the e^\pm spectra involves the numerical solution of the transport equation (Equation 1.2) using the knowledge of the galactic environment parameters (magnetic fields, ISM density and distribution, astrophysical source distribution....) simultaneously for nuclei and for e^\pm . This approach, explored in detail in the literature, is beyond the scope of this work. Basic physics conclusions can be however derived using simple approaches to the data analysis. In the following sections two different approaches to the analysis of the ($e^+ + e^-$) flux, with different levels of physics assumptions, are discussed.

6.3.1 Model independent ($e^+ + e^-$) flux spectral analysis

As discussed in Chapter 1, the fluxes of cosmic rays measured at Earth can be described, at first approximation and in certain energy ranges, by a power law spectrum $\Phi(E) \propto E^{-\gamma}$. This is a rough approximation, since there is no specific reason to expect a power law behavior for all cosmic ray species. In addition, for the ($e^+ + e^-$) flux this assumption is even stronger since the sum of two power laws is not expected to be a power law itself. The smoothness of the spectrum encourages, however, to test if it can be parametrized by a single power law starting from a certain energy.

The measured $\Phi_{e^++e^-}$ flux has been analyzed in order to check if a local power law parametrization is compatible with the data. A single power law parametrization of the flux:

$$\Phi(E) = A E^\gamma \quad (6.6)$$

has been fit to the data between a minimum energy E_{\min} and a maximum energy E_{\max} . A wide energy range from 5 GeV to 500 GeV has been analyzed using a sliding fit window technique. The width of the window has been chosen according to two different algorithms: (i) a window containing 16 data points (and a decreasing number of data points when moving towards high energies); (ii) a window with constant logarithmic width $\Delta_{\log}(E) = \log_{10}(E_{\max}) - \log_{10}(E_{\min})$ that moves towards higher energies with steps constant in $\log(E)$. The bin-to-bin correlated systematic uncertainty has been removed from the data points used for the fit procedure, since it provides no additional information for the fit of the spectral index.

The result of the scan for the two sliding window techniques is shown in Figure 6.14. For each energy window, the value of the fitted γ is shown, together with its resulting fit uncertainty, at the energy $\tilde{E} = \langle E \rangle_{-3}$ calculated according to the procedure discussed in Section 6.1.2. The results are compatible for both procedures (i) and (ii), and the difference in the parameter uncertainties is due to the different widths of the sliding windows.

The local spectral index softens from $\gamma \sim -2.7$ at 5 GeV to a minimum of $\gamma = -3.26$ at ~ 20 GeV. This is indeed expected at low energies, where the Local Interstellar Spectrum (LIS) flux is modified by the effects of solar modulation. Above this energy, the spectrum tends to locally harden up to a value of $\gamma \sim -3.17$ at ~ 80 GeV. The value of γ remains constant within its uncertainties for higher energies.

The result for the local power law parametrization shown in Figure 6.14 suggests the possibility to parametrize the ($e^+ + e^-$) flux with a single power law from a certain minimum energy E_{\min} up to

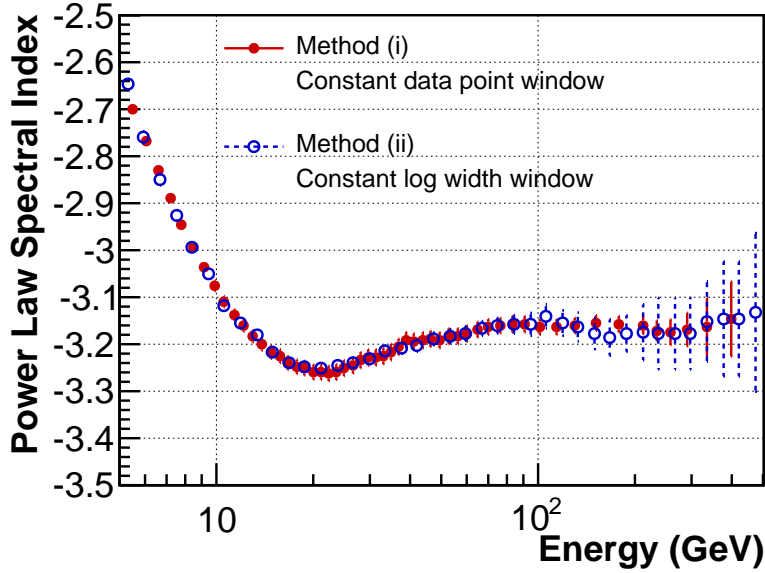


Figure 6.14: Local power law fit to the $\Phi_{e^+e^-}$ measurement. The data points have been fitted using a parametrization $\Phi(E) \propto E^\gamma$. The bin-to-bin correlated systematic uncertainty has been removed from the measurement error. The energy range used to fit the local spectral index has been chosen according to two different methods, explained in the text. Both methods provide compatible results. The fitted spectral index γ is shown, together with its fit uncertainty, in the energy point $\tilde{E} = \langle E \rangle_{-3}$, calculated as discussed in Section 6.1.2. The local spectral index softens from $\gamma \sim -2.7$ at 5 GeV to a minimum of $\gamma = -3.26$ at ~ 20 GeV. Above this energy, the spectral index hardens up to ~ -3.17 at ~ 80 GeV. From this energy on, it remains constant within its uncertainties.

$E_{\max} = 1$ TeV. A scan on E_{\min} has been performed in order to test this hypothesis and to find the minimum energy from which this parametrization is compatible with the data.

For each value of E_{\min} , the energy range $[E_{\min}, E_{\max}]$ has been divided in two continuous intervals, $[E_{\min}, E_{\text{mid}}]$ and $[E_{\text{mid}}, E_{\max}]$. A single power law fit has been performed in both intervals to provide the value of the spectral indices $\gamma_l \pm \Delta\gamma_l$ and $\gamma_h \pm \Delta\gamma_h$ respectively in the lower and higher energy window. If the single power law parametrization correctly fits to the data above E_{\min} , then the values of γ_l and γ_h are expected to be compatible within their uncertainties. The significance parameter σ_{lh} calculated as

$$\sigma_{\text{lh}} = \frac{\gamma_h - \gamma_l}{\sqrt{(\Delta\gamma_h)^2 + (\Delta\gamma_l)^2}} \quad (6.7)$$

has been used as estimator for the compatibility between γ_l and γ_h .

Figure 6.15 shows, on the left, an example of the procedure and the resulting γ_l and γ_h for $E_{\min} = 29$ GeV and $E_{\text{mid}} = 72$ GeV. The choice of E_{mid} is arbitrary. For each value of E_{\min} , the value of E_{mid} has been varied inside the energy range. Only the values of E_{mid} that provide enough degrees of freedom to perform the fit in the lower and higher ranges have been considered. The significance σ_{lh} has been calculated for each value of E_{mid} . The resulting σ_{lh} as function of E_{\min} is shown in the right plot of Figure 6.15. For a given value of E_{\min} , the values of σ_{lh} shown correspond to different choices of $E_{\text{mid}} \in [E_{\min}, E_{\max}]$. The horizontal lines correspond to the maximum value of σ_{lh} for which the spectral indices γ_l and γ_r are compatible with a confidence level (CL) of 90% and 95% according to a single-sided statistical test. The values of the spectral indices γ_l and γ_r are compatible for any choice of E_{mid} for all energies starting from $E_{\min}^{95\%} = 27.2$ GeV and from $E_{\min}^{90\%} = 30.2$ GeV with a CL of, respectively, 95% and

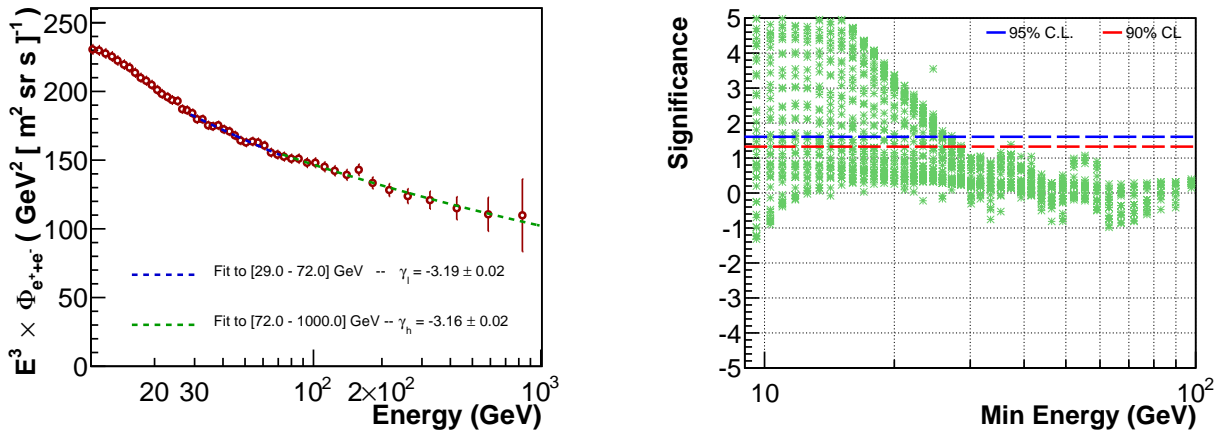


Figure 6.15: Procedure used to test the possibility to parametrize the ($e^+ + e^-$) flux with a single power law for energies above E_{\min} . For each value of E_{\min} , the interval up to 1 TeV has been divided in two continuous ranges at the value E_{mid} and a power law fit has been performed in both ranges. On the **Left**, an example of the two fits for $E_{\min} = 29$ GeV and $E_{\text{mid}} = 72$ GeV. The resulting spectral indices, γ_l and γ_h , are reported with their fit uncertainties. For each value of E_{\min} , the spectral index compatibility significance σ_{1h} , calculated according to Equation 6.7, is shown in the **Right** plot. Each entry represents the value of σ_{1h} for a certain choice of $E_{\text{mid}} \in [E_{\min}, E_{\text{max}}]$. The horizontal lines represent the maximum value of σ_{1h} for which the fitted spectral indices are compatible at 90% and 95% CL. Above 27.2 GeV and 30.2 GeV, at a CL of 95% and 90% respectively, γ_l and γ_h are compatible for any choice of separation energy E_{mid} and the ($e^+ + e^-$) flux can be consistently parametrized with a single power law up to 1 TeV.

90%. According to the current experimental accuracy the ($e^+ + e^-$) flux can be therefore parametrized above ~ 30 GeV by a single power law spectrum up to 1 TeV.

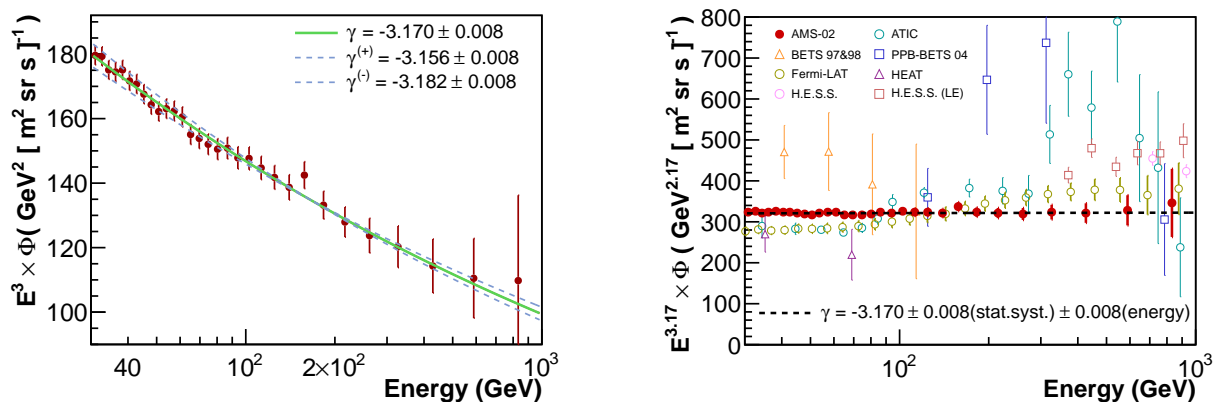


Figure 6.16: **Left**: in green, single power law parametrization of the ($e^+ + e^-$) flux above 30 GeV. The dashed blue lines represent the fit to the data that have been modified to simulate an extreme bias due to the uncertainty on the ECAL energy measurement linearity as described in the text. The resulting spectral indices represent a conservative estimation of this bias. The resulting spectral index of the single power law fit from 30 GeV to 1 TeV amounts to $\gamma = -3.170 \pm 0.008(\text{stat.}+\text{syst.}) \pm 0.008(\text{energy})$. **Right**: single power law fit to the AMS data compared with other experiments. The data points are multiplied by $E^{+|\gamma|}$ to appreciate the single power law behavior of the $\Phi_{e^+e^-}$ flux. The accuracy of the AMS data allows to measure the spectral index with an accuracy of 0.4%. This represents a major improvement with respect to previous measurements.

The result of the single power law fit to the ($e^+ + e^-$) flux measurement from 30 GeV to 1 TeV is shown in green in Figure 6.16. The fit results in the value $\gamma = -3.170$. The statistical and systematic uncertainty from the fit amounts to $\sigma(\text{stat.}+\text{syst.}) = 0.008$.

The additional bias for the evaluation of the spectral index introduced by any non-linearity in the ECAL energy measurement has been investigated. The systematic uncertainty on the ECAL energy scale, discussed in Section 6.1, covers the uncertainty on the ECAL linearity and on the absolute energy scale. The ECAL scale normalization does not affect the evaluation of γ . Any non-linearity, instead, could modify the measurement of the flux differently in each point, hence modifying its spectral shape. The most extreme case that could bias the determination of the spectral index happens if the non-linearity monotonously increases or decreases as function of the energy. For the sake of illustration, the measured flux would appear in this case as if a “torque” would have been applied to the incoming flux.

The ECAL linearity has been measured to be better than $\sim 0.5\%$ in the test beam energy range [199]. This corresponds, in that energy range, to a contribution of ~ 0.25 of total ECAL energy uncertainty $\sigma(E)/E$. In order to maintain a conservative estimation of the effect, a maximum non-linearity of $\pm 0.5\sigma(E)/E$ has been assumed and applied to the data. Since the non-linearity value is not known, it has been assumed to have a flat distribution between the extremes. A statistical simulation has been performed to assess the systematic uncertainties on the fit: random values of non-linearity have been chosen in the interval and each data point has been shifted to simulate an extreme bias introduced by the chosen level of non-linearity. The data have been shifted in the opposite directions at the extremes values (30 GeV and 1 TeV). This represents the worst case scenario for the determination of the spectral index given a certain value of non-linearity. The single power law fit has then been performed on the modified data. The procedure has been repeated for many choices of the non-linearity level. The resulting fit to the modified data for the maximum level of non-linearity allowed ($\pm 0.5\%$) is shown in light blue in Figure 6.16. It yields a value of $\gamma^{(+)} = -3.156$ and $\gamma^{(-)} = -3.182$. The spread (standard deviation) of the distribution of the fitted spectral indices for all the possible trials is a good estimator of the uncertainty on γ introduced by the unknown level of energy measurement non-linearity. The resulting standard deviation⁶ amounts to $\Delta\gamma = 0.008$.

In conclusion, the ($e^+ + e^-$) flux can be parametrized by a single power law with spectral index $\gamma = -3.170 \pm 0.008(\text{stat.}+\text{syst.}) \pm 0.008(\text{energy})$ above 30 GeV. The resulting fit to the AMS data above 30 GeV is shown in the right plot of Figure 6.16.

The precise energy measurement and the large dataset of the AMS experiments provide a measurement of the ($e^+ + e^-$) spectral index with a precision of 0.4%. This represents a major improvement with respect to the results from previous experiments. The spectral index measured by AMS is not compatible with the results of the Fermi-LAT satellite that measured a much harder spectrum ($\gamma = -3.08 \pm 0.05$) [18] and that represented, so far, the most accurate result on the ($e^+ + e^-$) spectral shape before the measurement of AMS. The result of the Fermi-LAT experiment is however highly influenced by the uncertainty on the energy scale, which is quoted to be $^{+5\%}_{-10\%}$ in the whole energy range. As for AMS, this uncertainty may also cover a level of non-linearity in the energy measurement, especially for high energies (the Fermi-LAT calorimeter has a depth of 8.6 X_0 for perpendicular incident particles, much smaller than the 17 X_0 AMS ECAL. An higher level of energy rear leakages for high energy events in Fermi-LAT is consequently expected). The systematic effect on the $\Phi_{e^+e^-}$ spectral index measurement by Fermi-LAT could be partially increased and the level of agreement with the AMS result would consistently improve. In addition to this, it is observed in Figure 6.10 that the separate Φ_{e^-} and Φ_{e^+} flux measurements by Fermi-LAT show an internal tension with the preceding Fermi-LAT $\Phi_{e^+e^-}$ mea-

⁶It is worth to note that, since the fitted spectral index is highly correlated to the non-linearity, the standard deviation of the distribution of all the trials is similar to the standard deviation of a flat distribution between $\gamma^{(+)}$ and $\gamma^{(-)}$, namely $(\gamma^{(+)} - \gamma^{(-)})/\sqrt{12} = 0.008$.

surement. The combination of the separate Φ_{e^-} and Φ_{e^+} agrees much better with the AMS $\Phi_{e^++e^-}$ measurement between 20 and 100 GeV than the previous direct $\Phi_{e^++e^-}$ measurement by Fermi-LAT⁷. It is possible that the spectral shape of the $\Phi_{e^++e^-}$ measured by Fermi-LAT could slightly change when the analysis will be updated using the updated detector calibration. A future release of the updated Fermi-LAT $\Phi_{e^++e^-}$ measurement will confirm or disprove this hypothesis.

Independent measurements of the Φ_{e^-} flux up to 700 GeV and of the Φ_{e^+} flux up to 500 GeV by AMS have also shown, similarly as done in this analysis, that a single power law parametrization can describe the e^- and e^+ fluxes starting from 52.3 GeV for electrons and 27.2 GeV for positrons [26]. The simultaneous single power law behavior for the e^- , the e^+ and the ($e^+ + e^-$) fluxes is an unexpected feature⁸. The analysis of the e^\pm data collected by AMS in the coming years will provide an improvement in the flux measurement precision that could allow to resolve their spectral shapes with higher accuracy and eventually solve the origin of this unexpected behaviour.

6.3.2 Model dependent parametrization of the e^- and e^+ fluxes

Basic physics information can be inferred from the cosmic ray e^- and e^+ measurements using the data to constrain the parameters of physics models. In this section a simple model for the e^- and e^+ fluxes at Earth is assumed and conclusions are deduced from a fit of the model to the data.

The combination of the $\Phi_{e^++e^-}$ and the PF measurements provide comprehensive information about the separate e^- and e^+ fluxes. In the following data analysis, the Φ_{e^-} and Φ_{e^+} parametrization are simultaneously fit to the $\Phi_{e^++e^-}$ and to the PF measurements by AMS, while the Φ_{e^-} and Φ_{e^+} flux measurements are used for a consistency check of the AMS measurements.

In what follows, the analysis will be first performed using only the high energy data, for which the effect of the solar modulation can be safely neglected. The analysis is then extended to the low energies including a parametrization of the solar modulation.

High energy data parametrization

A simple power law description can be used to parametrize the flux of primary e^- produced and accelerated by SNR [89, 176, 83]. The same approximation holds for the description of the flux of secondary e^+ produced by the interactions of nuclei with the ISM. The assumptions behind the choice of the single power law parametrization for the primary e^- and secondary e^+ contributions are discussed in Appendix E.

In order to correctly describe the rise in the PF, a common primary source for e^\pm has to be assumed. Following the procedure commonly adapted in the literature [89], the common, primary contribution to the e^- and e^+ fluxes is parametrized by a power law spectrum with a cutoff energy E_{co} . The cutoff energy parameter defines the energy at which the common source contribution to the e^\pm fluxes starts to drop. This shape is a first order approximation of the spectral shape expected for e^\pm produced by pulsars or DM annihilation. According to these assumptions the flux of e^\pm at Earth is parametrized, neglecting solar modulation effects, as:

$$\begin{aligned}\Phi_{e^-}(E) &= A_{e^-} E^{-\gamma_-} + A_c E^{-\gamma_c} e^{-\xi E} \\ \Phi_{e^+}(E) &= A_{e^+} E^{-\gamma_+} + A_c E^{-\gamma_c} e^{-\xi E}\end{aligned}\tag{6.8}$$

where A_{e^-} , A_{e^+} and A_c represent the normalization for the single e^\pm power laws and for the common source, and γ_- , γ_+ and γ_c are the spectral indices for the single e^\pm power laws and for the common source.

⁷Above 100 GeV, the discrepancy could be induced by an underestimation of the background in the Fermi-LAT sample.

⁸Even if the separate e^- and e^+ are single power law fluxes above a certain energy, their sum is not expected to be parametrized by a single power law.

The parameter ξ corresponds to the inverse of E_{co} ⁹. The energy E is the energy measured at Earth. In this parametrization the contribution of secondary e^- produced by the interaction of nucleons with the ISM, much smaller than the secondary production of e^+ , has been neglected. The parametrization of Equation 6.8 is valid only in the assumption that solar modulation effects can be neglected. In this analysis this is assumed to be the case for energies above 30 GeV.

In order to determine the set of free parameters $\vec{\theta}$ of Equation 6.8, a simultaneous fit of the Φ_{e^-} and Φ_{e^+} parametrizations to the two datasets, with N_{Φ} data points for the $\Phi_{e^+e^-}$ measurement and N_{PF} data points for the PF measurement, has been performed using a combined χ^2 minimization procedure. The function to be minimized has been defined as:

$$\chi^2(\vec{\theta}) = \vec{\Delta}^T \mathbf{V}^{-1} \vec{\Delta} \quad (6.9)$$

where $\vec{\Delta} = (\vec{y} - \vec{y}(\vec{\theta})^{(*)})$ is the vector containing the $N = N_{\Phi} + N_{\text{PF}}$ differences between the data measurements y_i and the data parametrizations $y(\vec{\theta})_i^{(*)}$ and \mathbf{V} is the $N \times N$ covariance matrix between the data points. In the definition of the χ^2 to minimize, the sum run over all the N data points of the $\Phi_{e^+e^-}$ and of the PF measurements. This allows to find the best set of parameters that best fits simultaneously to both datasets. The uncertainty of each data point, that contributes to the diagonal terms of \mathbf{V} , is calculated as the quadratic sum of the statistical and uncorrelated systematic uncertainties. The bin-to-bin correlated systematic uncertainty for the $\Phi_{e^+e^-}$ measurement is taken into account by non-zero off-diagonal terms in \mathbf{V} , evaluated following the procedure introduced in [232]. Bin-to-bin correlations for the PF measurement are neglected. Correlations between the $\Phi_{e^+e^-}$ and the PF measurements are also negligible, as discussed in Appendix E.

The systematic uncertainty on the fit result due to the uncertainty of the energy absolute scale and the level of possible non-linearity in the energy measurement has been evaluated using the procedure discussed in Appendix E. The resulting uncertainty is quoted for each parameter, together with the fit result, later in this section.

The result of the fit to $\Phi_{e^+e^-}$ in the energy range [30.0-1000.0] and to the PF in the energy range [30.0-500.0] GeV is shown in Figure 6.17. The numerical fit results are reported in Table 6.1. The value of $\chi^2/ndf = 25.6/45$ is biased by the $\Phi_{e^+e^-}$ contribution, as reported in the same Figure. More details will be discussed later in next section.

In this scenario the common source production of e^+ dominates over the e^+ single power law contribution and represents 1/3 of the total ($e^+ + e^-$) flux at 500 GeV. The common source spectrum is much harder than those of e^{\pm} . Its cutoff parameter $\xi = 1/E_{\text{co}} = 1.0 \pm 0.8 \text{ TeV}^{-1}$, which corresponds to a cutoff energy of $\sim 1 \text{ TeV}$, is constrained by the flattening of the PF above $\sim 250 \text{ GeV}$ and by the conflicting absence of a significant drop in the $\Phi_{e^+e^-}$ flux. The accuracy to which the energy cutoff parameter is known is of the order of $\sim 75\%$ and it is dominated by the experimental accuracy of the measurements at high energies. The fit to the PF clearly shows that the additional primary e^+ source is required to describe the rise in the data. At 100 GeV, as example, the simple e^+ power law contributes only $\sim 1\%$ to the PF and its contribution decreases as function of the energy. Although the parametrization is very basic, it describes the data correctly. The high energy range of the fit does not follow the decreasing trend in the PF data. This is due to the high uncertainty in the last points of the PF measurement and to the fact that the $\Phi_{e^+e^-}$ measurement, which has smaller relative errors and extends to higher energies, does not show any drop within the current experimental uncertainties. The fit result is therefore constrained by the smooth behaviour of the $\Phi_{e^+e^-}$ data. A single fit to

⁹In the minimization procedure the inverse of the cutoff energy, $\xi = 1/E_{\text{co}}$, is used as free parameter. The profile of the χ^2 distribution around the best fit value for ξ is, in fact, well described by a 2^{nd} order polynomial. This assures that the uncertainty on the parameter can be correctly propagated maintaining its statistical properties. This property does not hold for its inverse E_{co} .

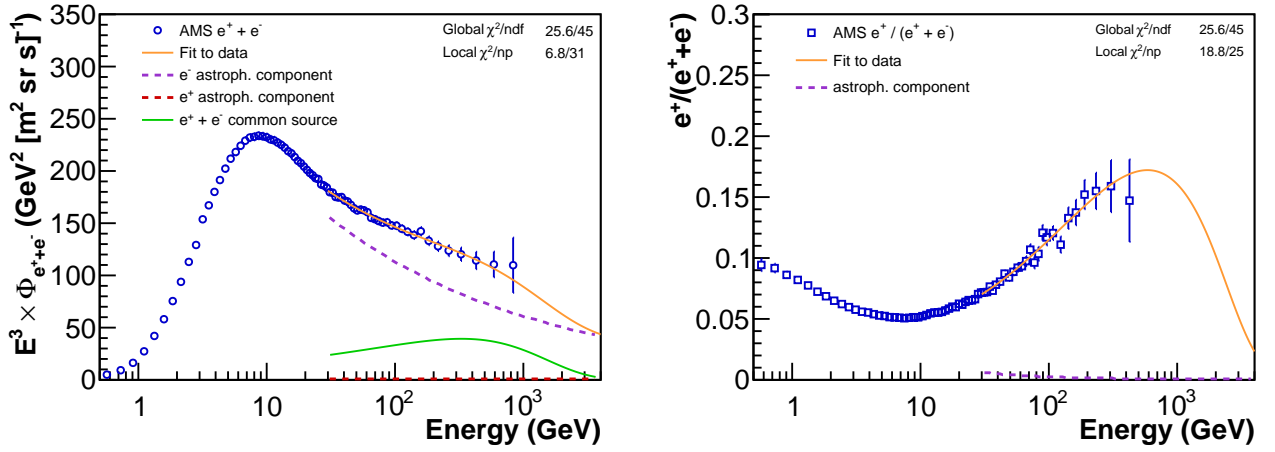


Figure 6.17: Result of the combined fit to the $\Phi_{e^+e^-}$ and PF measurements, in orange, superimposed to the $\Phi_{e^+e^-}$ measurement (on the left) and to the PF measurement (on the right). The description of the free parameters and the numerical fit results are reported in Table 6.1. For both measurements, the value of the global χ^2/ndf and the local χ^2 relative to that dataset and normalized to the number of data points (χ^2/np) are reported. The $\Phi_{e^+e^-}$ and the PF data have been fitted starting from 30 GeV. The dashed azure and red line represent the single power law parametrization of the SNR contribution to the e^- flux (e^- astroph. component) and the secondary e^+ flux (e^+ astroph. component) respectively. The green line represents the common source contribution to the e^- and e^+ fluxes parametrized as single power law with energy cutoff. The data favor a common source contribution that dominates over the standard astrophysical e^+ flux. The common source contribution, that represents 1/3 of the total ($e^+ + e^-$) flux at 500 GeV, has a cutoff energy parameter $\xi = 1/E_{co} = 1.0 \pm 0.8 \text{ TeV}^{-1}$ in this scenario.

the PF only would describe better the decrease in the slope observed in the high energy range for the PF.

Parametrization of the whole energy range

The result obtained in the previous scenario is mostly constrained by the high energy data. The sensitivity to the power law e^+ contribution is, in this case, low. The secondary e^+ contribution can be set with much higher reliability including the low energy data, where the common source contribution is expected to be negligible. In order to extend the fit to energies below 30 GeV, the parametrization of Φ_{e^-} and Φ_{e^+} has to be modified to include the effects of the solar modulation. Using the *Force Field Approximation* discussed in Section 1.1.3 to describe the propagation in the heliosphere, Equation 6.8 is modified into:

$$\begin{aligned}\Phi_{e^-}(E) &= A_{e^-} f_{\odot} \tilde{E}^{-\gamma_-} + A_c f_{\odot} \tilde{E}^{-\gamma_c} e^{-\xi \tilde{E}} \\ \Phi_{e^+}(E) &= A_{e^+} f_{\odot} \tilde{E}^{-\gamma_+} + A_c f_{\odot} \tilde{E}^{-\gamma_c} e^{-\xi \tilde{E}}\end{aligned}\quad (6.10)$$

using:

$$\begin{aligned}f_{\odot}(\phi, E) &= \frac{E^2 - m_e^2}{(E + \phi)^2 - m_e^2} \\ \tilde{E} &= E + Ze\phi = E + \phi \text{ (MV)}\end{aligned}\quad (6.11)$$

where ϕ is the effective solar modulation potential, m_e is the electron mass, \tilde{E} is the energy of the cosmic ray in the local interstellar space before it enters the heliosphere and f_{\odot} is the attenuation of the flux

introduced by the interaction with the heliosphere. Both \tilde{E} and f_\odot depend on the solar modulation potential ϕ and on the energy measured at Earth E . The solar modulation potential is assumed to be charge dependent and consequently different for e^- and e^+ . For a given measured energy E , f_\odot and \tilde{E} are also different for e^- and e^+ .

Finally, the current data can be described if the parametrization allows for a broken spectral index of the SNR e^- contribution, namely:

$$\Phi_{e^-}^{(\text{SNR})}(E) = \begin{cases} A_{e^-}^{(a)} f_\odot \tilde{E}^{-\gamma_-^{(a)}} & E < E_b \\ A_{e^-}^{(b)} f_\odot \tilde{E}^{-\gamma_-^{(b)}} & E \geq E_b \end{cases} \quad (6.12)$$

where E_b represents the energy at which the break is observed. This assumption introduces only two additional degrees of freedom to the fit, since one degree of freedom is fixed by the continuity of the flux at E_b . A break in the energy spectrum for e^- can be introduced by the existence of two injection processes at the source or by two different propagation mechanisms that dominate in different energy ranges. With the current data accuracy, no break in the e^+ spectrum parametrization is required.

The result of the combined fit to the $\Phi_{e^+e^-}$ and to the PF measurements in the energy range starting from 0.5 GeV is shown in Figure 6.18 and it is reported in the right column of Table 6.1.

The constraints introduced do not change the outcome of the best fit common source parameters significantly. In this scenario the common source contribution, which represents $\sim 40\%$ of the total ($e^+ + e^-$) flux at 500 GeV, has an inverse cutoff energy $\xi = 0.8 \pm 0.6 \text{ TeV}^{-1}$ corresponding to $\sim 1.3 \text{ TeV}$, in agreement with the previous estimation within the errors. The SNR e^- spectrum is well described by a break in the spectral index at $29 \pm 1 \text{ GeV}$. It is also remarkable that the common source starts to dominate over the SNR e^+ contribution already at $\sim 20 \text{ GeV}$. Finally, the solar modulation potentials required by the low energy data amounts to $\phi_{e^-} = 1.29 \pm 0.02 \text{ GV}$ and $\phi_{e^+} = 1.00 \pm 0.04 \text{ GV}$. The two effective potentials are therefore significantly different for e^- and e^+ . The best fit value is however high if compared from the results provided by the numerical solution of the transport equation¹⁰, which typically fits lower values of $\phi_{e^-} \sim 0.8 \text{ GV}$ and $\phi_{e^+} \sim 0.7 \text{ GV}$ [47]. The steadily decreasing contribution of the single power law e^+ only to the PF (dashed-azure line) clearly shows that the rise of the PF is not compatible with a pure power law component of e^+ . Similarly as the previous result, the model fails to describe the decrease in slope observed in the PF fraction due to the constraints introduced by the high energy data points of the $\Phi_{e^+e^-}$ measurement. The value of $\chi^2/ndf = 89.8/129$ is biased by the $\Phi_{e^+e^-}$ contribution, as reported in the same Figure. The PF contribution to χ^2/ndf is compatible with expected statistical fluctuations. Figure 6.19 shows the local fit agreement with the two datasets.

The distribution of the local fit agreement shows that the simple parametrization used in this approach does not fully represent the experimental data. A discussion on the possible improvements is provided at the end of this section.

The correlation between the fit parameters is shown in Figure 6.20. The parameters that describe the same contribution terms, like A_{e^-} and γ_{e^-} , are highly correlated, as expected. The solar modulation parameters ϕ_\pm also show a high correlation with all other parameters. This indicates that the description of the solar modulation, which sets the normalization of the contributions at low energies, also affects the yield of all the contributions at high energies. The dependence of the results on the solar modulation parameters will be further discussed below. The common source parameters are uncorrelated from the e^- yield but they are highly correlated with the single power law e^+ parameters. This confirms that the description of the low energy data, where the e^+ common contribution is negligible compared with

¹⁰The solution of the transport equation shows, in fact, that the low energy flux of secondary e^+ is suppressed below 1 GeV and it cannot be described by a single power law parametrization. Therefore, the solar modulation potential expected to describe the data using a single power law parametrization is higher than what needed to describe the data according to the solution of the transport equation.

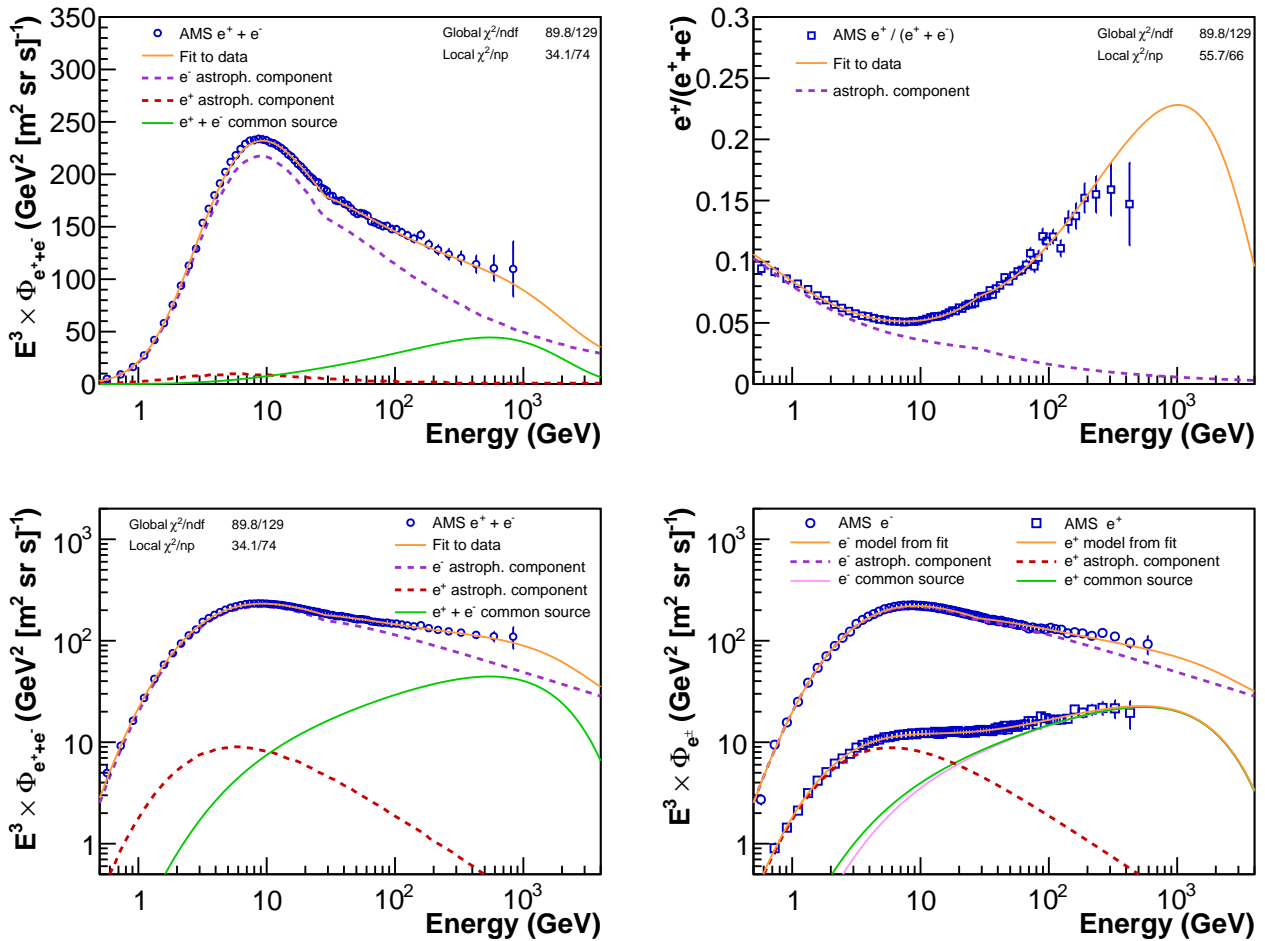


Figure 6.18: Result of the combined fit to the $\Phi_{e^+e^-}$ and to the PF measurement, in orange, superimposed to the $\Phi_{e^+e^-}$ measurement (on the top left) and to the PF measurement (on the top right) in the energy range [0.5-1000.0] GeV. The model allows for solar modulation modification of the spectra in the Force Field Approximation parametrization. The description of the fit parameters and the numerical fit results are reported in Table 6.1. For both measurements, the value of the global χ^2/ndf and the local χ^2 relative to that dataset and normalized to the number of data points (χ^2/np) are reported. The correlations between the fitted parameters is reported and discussed in Figure 6.20. The bottom left figure represents the fit to $\Phi_{e^+e^-}$ in logarithmic scale to appreciate the contributions at low energies. In the bottom right plot the resulting parametrization for the Φ_{e^-} and Φ_{e^+} fluxes are superimposed to the AMS data. The e^- and e^+ data shown in this figure do not enter the χ^2 minimization and are used only to show the compatibility between the different measurements of AMS. The dashed azure and red line represents the single power law parametrization of the SNR contribution to the e^- flux (e^- astroph. component) and to the e^+ flux (e^+ astroph. component) respectively. The green line represents the common source contribution to the e^- and e^+ fluxes, parametrized as single power law with energy cutoff. In the bottom right figure, instead, the common source contributions are separately shown by the green and pink lines. The relative difference between the two contributions is introduced by the difference in the solar modulation potentials ϕ_+ and ϕ_- . The data favour a common source contribution that dominates over the standard astrophysical e^+ flux. The common source contribution, which represents $\sim 40\%$ of the total ($e^+ + e^-$) flux at 500 GeV, has a cutoff energy parameter $\xi = 1/E_{co} = 0.8 \pm 0.6$ TeV⁻¹ in this scenario. The fit to the $\Phi_{e^+e^-}$ and to the PF measurements describes correctly also the separate Φ_{e^-} and Φ_{e^+} AMS measurements. The steadily decreasing contribution of the single power law e^+ to the PF (dashed-azure line) clearly shows that the rise of the PF is not compatible with a single power law e^+ contribution.

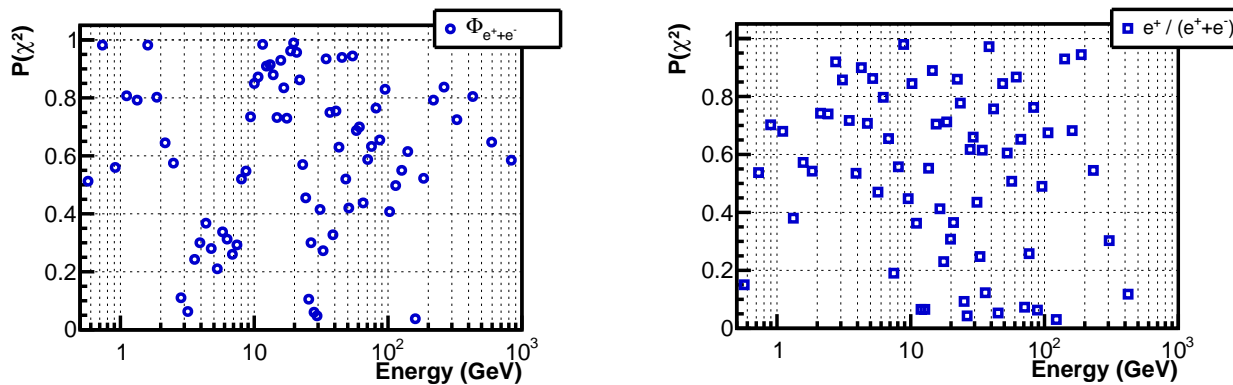


Figure 6.19: Local probability for the χ^2 distribution ($P(\chi^2)$) for each data point of the $\Phi_{e^+e^-}$ (left) and PF (right) datasets. The pattern observed below 30 GeV for the $\Phi_{e^+e^-}$ dataset and the tendency to observe high values for $P(\chi^2)$ hints that the parametrization used in this section is not fully adequate to describe the measurement and that the uncorrelated contribution to the $\Phi_{e^+e^-}$ uncertainty may have been overestimated. The uniform distribution of $P(\chi^2)$ for the PF dataset shows that the parametrization consistently describes the measurement between 3 and 200 GeV, with a slightly tendency to deviate outside this energy range.

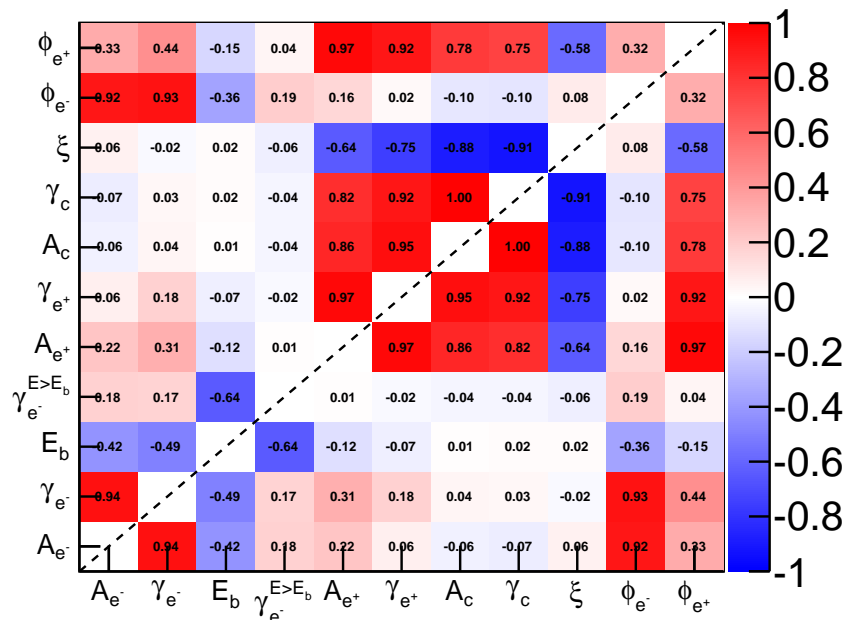


Figure 6.20: Correlation matrix for the result of the combined fit to the $\Phi_{e^+e^-}$ measurement and to the PF measurement in the energy range [0.5-1000.0] GeV. The result of the fit is shown in Figure 6.18. The color scale indicates the correlation between two parameters. The correlation ranges from -1 to +1. Red colors indicate a positive correlation. Blue colors indicate a negative correlation.

the e^+ single power law term, strongly constrains the description of the high energy data, where the e^+ common source term dominates the e^+ yield. The correlation matrix shown in Figure 6.20 confirms that the level of degeneracy between the fit parameters is substantial and it prevents to derive solid physics

Table 6.1: Result of the combined fits of the power law models described in the text to the AMS $\Phi_{e^+e^-}$ and PF measurements. The fit has been performed from 30 GeV, neglecting any effect of solar modulation, and starting from 0.5 GeV. In the second case, the solar modulation has been parametrized using the *Force Field Approximation* approach. A broken power law index for the e^- power law has been introduced to obtain a better description of the experimental data. The physical interpretation of the parameters and the result are discussed in the text. The first error represents the statistical uncertainty provided by the fit procedure. The second error represents the uncertainty ($\sigma^{(\text{energy})}$) due to a possible correlation between data points introduced by the uncertainty on the energy scale. More details about the procedure used to infer $\sigma^{(\text{energy})}$ are provided in Appendix E.

Parameter name [units]	Parameter definition	Fit from 30 GeV	Fit from 0.5 GeV
A_{e^-} [$\text{GeV}^{-1} \text{ m}^{-2} \text{ sr}^{-1} \text{ s}^{-1}$]	e^- norm.	$394 \pm 20 \pm 3$	$2250 \pm 102 \pm 45$
γ_{e^-}	e^- spec. index	$3.27 \pm 0.01 \pm 0.01$	$3.71 \pm 0.01 \pm 0.01$
E_b (e^-) [GeV]	e^- break energy	—	$28.6 \pm 0.8 \pm 0.4$
$\gamma_{e^-} (E > E_b)$	e^- spec. index above E_b	—	$3.395 \pm 0.009 \pm 0.002$
A_{e^+} [$\text{GeV}^{-1} \text{ m}^{-2} \text{ sr}^{-1} \text{ s}^{-1}$]	e^+ norm.	$41 \pm 89 \pm 35$	$100 \pm 16 \pm 1$
γ_{e^+}	e^+ spec. index	$4.1 \pm 0.05 \pm 0.2$	$3.85 \pm 0.10 \pm 0.01$
A_C [$\text{GeV}^{-1} \text{ m}^{-2} \text{ sr}^{-1} \text{ s}^{-1}$]	Com. source norm	$3.80 \pm 2.35 \pm 0.15$	$2.29 \pm 0.98 \pm 0.06$
γ_C	Com. source spec. index	$2.66 \pm 0.15 \pm 0.01$	$2.57 \pm 0.10 \pm 0.01$
$\xi = 1/E_{co}$ [TeV^{-1}]	Inv. com. source cutoff	$1.0 \pm 0.8 \pm 0.1$	$0.8 \pm 0.6 \pm 0.1$
ϕ_{e^-} [GV]	e^- solar mod. pot.	—	$1.29 \pm 0.02 \pm 0.03$
ϕ_{e^+} [GV]	e^+ solar mod. pot.	—	$1.00 \pm 0.04 \pm 0.02$

conclusions from the data parametrization shown in this Section. Additional independent constraints to Φ_{e^-} and Φ_{e^+} , set by the analysis of the hadron component of cosmic rays, improve the significance of the fit to the e^\pm data. This approach involves the parametrization of the propagation of cosmic rays in the Galaxy according to Equation 1.2 which is beyond the scope of this thesis. Further related prospects are discussed at the end of this Section.

The result from the fit to the $\Phi_{e^+e^-}$ and to the PF measurements has been compared to the separate Φ_{e^\pm} measurement of AMS. This is shown in the bottom right plot in Figure 6.18. The χ^2 hypothesis test for the agreement between the flux parametrization and the measured data results $\chi^2/ndf = 80.2/73$ and $\chi^2/ndf = 43.6/72$ for the e^- and e^+ flux respectively. The χ^2 value has been evaluated according to Equation 6.9 taking into account the 2% bin-to-bin correlated scaling uncertainty quoted in [26] as done previously in this section. The a posteriori agreement between the Φ_{e^\pm} parametrization (based on the fit to the $\Phi_{e^+e^-}$ and PF measurements) and the AMS e^\pm flux measurement confirms the possibility to have a coherent description of the $\Phi_{e^+e^-}$, Φ_{e^-} , Φ_{e^+} and PF measured by AMS.

The previous result provide more accurate and distinct information with respect to the first approach, where only the data above the solar modulation range are used to infer the properties of the common source at high energies. The low energy data are crucial to constrain the secondary e^+ and the SNR e^- contribution. Figure 6.21 shows, for example, the two contributions to the e^+ flux and the resulting contribution to the PF in the two approaches discussed so far. Both the single power law and the common source contributions to the e^+ flux depend on the minimum energy of the fit and, therefore, on the assumptions used in the flux parametrization.

A comparison of the fit result for the two procedures is shown in Table 6.1.

The effective parametrization of the solar modulation at low energies used in this approach is however not fully adequate. As shown in Figure 6.22, in fact, the best fit ϕ parameters show a strong dependence on the minimum energy used to fit the data. Due to the level of correlation in the fit result, other fit parameters show a dependence on the fit minimum energy which is not comprised within their statistical

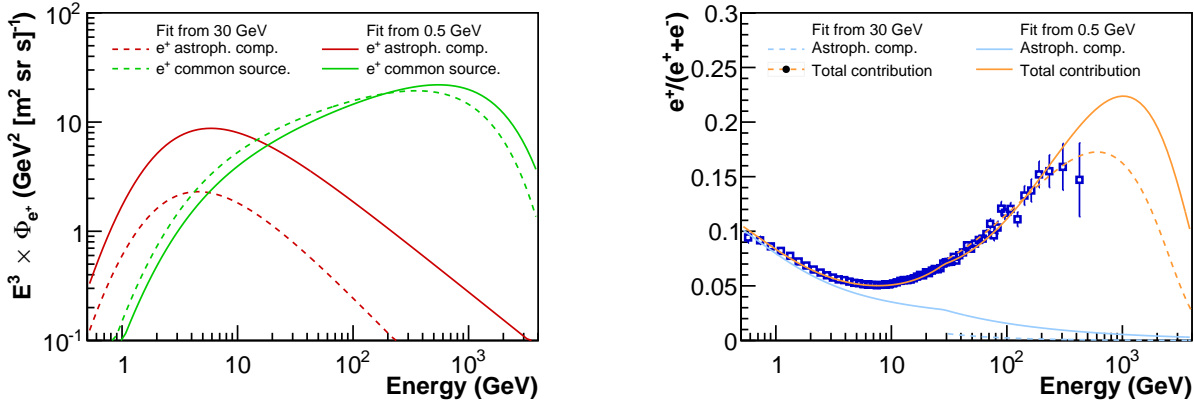


Figure 6.21: **Left**: Contributions to the e^+ flux described by astrophysical secondary production component (in red) and by the common e^\pm source (in green). The dashed lines represent the result from the fit to high energies only which does not include any solar modulation parametrization. The contribution from secondary e^+ at low energies depends drastically whether the solar modulation effects are taken into account or not. The shape of the common e^\pm contribution (here shown for e^+ only) depends consequently on the secondary e^+ yield extrapolated at high energies. **Right**: Contribution of single power law e^+ to the PF (azure line) and total e^+ contribution to the PF (orange line) depending on the flux parametrization and on the minimum energy of the fit. The contributions of the single power law e^+ and of the common source are different at high energies in the two models.

uncertainties. In the same figure, the dependence for the ξ parameter is shown for example. The same representation for all the fit parameters is shown in Appendix E. This confirms that the power law

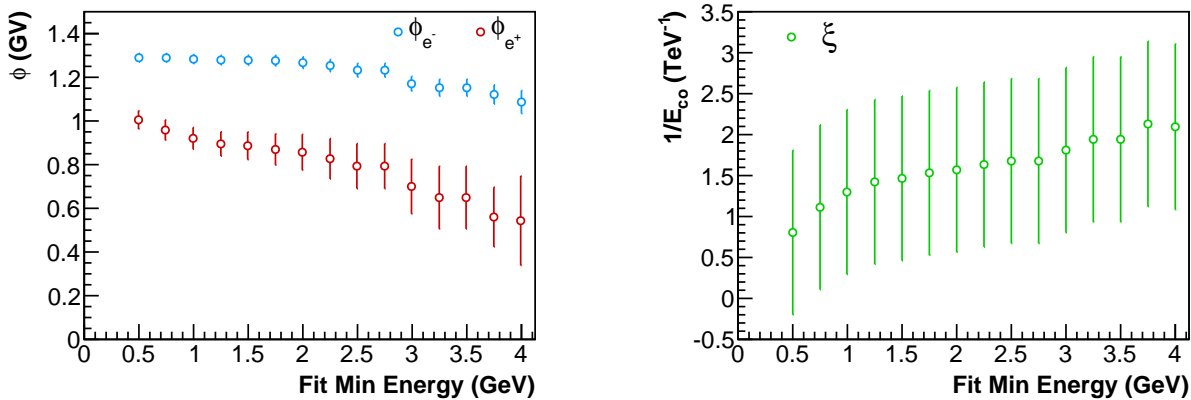


Figure 6.22: Best fit value for the effective solar modulation parameters ϕ_{e^-} and ϕ_{e^+} (**Left**) and for the inverse of the common e^\pm source energy cutoff, $\xi = 1/E_{co}$ (**Right**), as function of the minimum energy used for the fit to the $\Phi_{e^+e^-}$ and to the PF measurements. The uncertainties represent the standard deviations of the parameter evaluated during the fit procedure. The energy dependence, not consistent with the statistical uncertainties of the fit, hints that the solar modulation model used to parametrize the low energy data is not adequate to describe the e^+ and e^- data with the current experimental accuracy. This consequently introduces a dependence for all other fit parameters, which are shown in Appendix E.

parametrization used in this section, together with the parametrization of the solar modulation, does not adequately represent the e^\pm fluxes in the GeV to TeV energy range. More sophisticated conclusions can be achieved by the fit of the numerical solution of the transport equation to the data. This is

heavily discussed in the literature and an overview has already been given in Section 1.2.3. The basic parametrization proposed in this section highlights, however, crucial points which are in common with the conclusions obtained with more complicated approaches. First of all, it confirms that a coherent description of the ($e^+ + e^-$) flux measurement and the separate e^- and e^+ flux measurements from AMS is possible. Moreover, it asserts that a parametrization of the data as single power laws for e^- and e^+ does not describe the data. In particular, a common source of e^\pm is needed to explain the rise in the PF and it dominates over the astrophysical SNR e^+ component starting already from ~ 20 GeV. It also confirms that the major contribution of e^- at low energies shows a break in the power law index around ~ 30 GeV. Finally, it shows that the low energy data play a major role in defining the secondary e^+ and e^- SNR contributions and consequently set the properties of the common source at high energies.

The data collected by AMS in the coming years will be used to improve the experimental measurements. The improvement in the measurement accuracy at high energies will be useful to set stronger constraints on the common source properties. At low energies the measurement of the time dependent e^\pm fluxes will provide an useful tool to improve the knowledge of the solar physics and its effect on the cosmic ray spectra. Whether the nature of the common source is dominated by DM annihilation or by additional astrophysical sources will not be, however, disclosed by the analysis of the spectral shape. As already discussed in Section 1.2.3, only the accurate study of the incoming e^\pm arrival directions and, eventually, the detection of a level of anisotropy in the e^\pm fluxes will be useful to disentangle between the two hypotheses.

6.4 Summary

The precise e^\pm energy measurement provided by the ECAL allows to search for features in the energy spectrum with high sensitivity. The 17 X_0 calorimeter has been calibrated and tested during test beams on ground. The ECAL energy resolution has been measured to be $\sim 1.5\%$ above 20 GeV. The uncertainty for the $\Phi_{e^++e^-}$ measurement introduced by the minor bin-to-bin migration of events due to the finite energy resolution has been found to be negligible in comparison to other sources of systematic uncertainties.

The ECAL absolute energy scale has been also tuned during test beams on ground using beams of e^- and e^+ of known momentum from 10 GV to 290 GV. Differently from collider experiments, in space there is no sharp feature at known energy that could be used to calibrate the energy scale. This renders the calibration of the energy scale measured using calorimetric techniques a major problem for space experiments. The redundant measurement of the e^\pm momentum using the AMS spectrometer provides a powerful tool to crosscheck the ECAL energy measurement. The ratio between the ECAL energy measurement E and the Tracker momentum measurement p for e^\pm and MIP nuclei has been exploited. The comparison of the E/p ratio between the test beam and the data collected during operations in space and the stability of the E/p ratio as function of time confirm that the ECAL absolute scale is known with an uncertainty of 2% between 10 GeV and 290 GeV. Below and above the test beam energy range the uncertainty increases to 5% at 0.5 GeV and at 1 TeV. The effect of a 2% energy independent shift in the ECAL energy measurement results into a correlated and simultaneous systematic shift of the overall spectrum by $\sim 4\%$ at high energies. The uncertainty on the ECAL energy scale is quoted in this analysis as an uncertainty on the energy bin borders.

In this analysis, the $\Phi_{e^++e^-}$ flux has been measured from 0.5 GeV to 1 TeV using the data collected by AMS during the first 30 months of data taking [1]. Below 300 GeV the measurement systematic uncertainty is dominated by the systematic uncertainties on the detector acceptance. Above this energy, the systematic uncertainties on the ($e^+ + e^-$) signal extracted from the data take over and dominate

over other sources of systematic uncertainties. The measurement total uncertainty is dominated by systematic effects below 100 GeV. Above 150 GeV, instead, the statistical uncertainties on the ($e^+ + e^-$) signal dominate the total uncertainty. The total uncertainty amounts to $\sim 2\%$ between 3 GeV and 200 GeV. Below 3 GeV, it increases up to $\sim 20\%$ at 0.5 GeV. Above 200 GeV, it also rises up to a value of $\sim 11\%$ at 700 GeV and $\sim 20\%$ at 1 TeV. The measurement of $\Phi_{e^+e^-}$ has been performed on the same data by independent analysis groups within the AMS collaboration. All the results agree in the whole energy range within the uncertainties.

Differently from the separate Φ_{e^-} and Φ_{e^+} flux measurements [26], the $\Phi_{e^+e^-}$ measurement does not distinguish the e^\pm charge sign. This allowed to apply a less stringent selection to identify the e^\pm sample used for the analysis. The result is an increase in the e^\pm data sample used for the $\Phi_{e^+e^-}$ measurement and a decrease of the systematic uncertainty which limits the level of accuracy to which the detector acceptance is known. In addition to this the charge confusion uncertainty does not contribute at all to the systematic uncertainty of the measurement. The $\Phi_{e^+e^-}$ flux measurement is therefore more accurate and reaches higher energies than the separate Φ_{e^\pm} flux measurements. If combined with the accurate measurement of the positron fraction (PF) by AMS up to 500 GeV [83], the $\Phi_{e^+e^-}$ measurement can be used to provide an estimation of the separate Φ_{e^-} and Φ_{e^+} fluxes. The results are compatible within the uncertainties, and the precision of the data obtained by the combination of the $\Phi_{e^+e^-}$ and of the PF measurements provides a competing accuracy with respect to the direct Φ_{e^-} and Φ_{e^+} measurements.

In comparison to ($e^+ + e^-$) flux measurements provided by previous experiments, the accuracy of the AMS measurement is outstanding. AMS is the first experiment that measured the flux of ($e^+ + e^-$) in a wide energy range from 0.5 GeV to 1 TeV. The precise energy measurement of the ECAL allows to finally reject the claim of a feature in the spectrum observed by previous balloon experiment above ~ 300 GeV. No evident spectral features are observed in the ($e^+ + e^-$) flux in the whole energy range. The $\Phi_{e^+e^-}$ flux measured by AMS can be described by a single power law parametrization from 30 GeV to 1 TeV with 90% CL. The fitted spectral index results $\gamma = -3.170 \pm 0.008(\text{stat.} + \text{syst.}) \pm 0.008(\text{energy})$, where the last contribution to the error is given by the uncertainty of the ECAL energy measurement linearity. The AMS measurement improves the level of accuracy to which the spectral shape of the ($e^+ + e^-$) flux is known up to 1 TeV. This is mostly due to the precision of the calorimetric e^\pm energy measurement. Moreover, the flux measured by AMS results to be softer than previous experimental measurements.

The precise measurement of the ($e^+ + e^-$) flux above 700 GeV provides additional remarkable information to the experimental scenario. The highest AMS energy range overlaps in fact with the lowest energy boundary of ground based detector measurements, that measured the ($e^+ + e^-$) flux using completely different techniques. Taking into account the uncertainty introduced by the finite accuracy to which the detector energy scales are known, the measurement of the AMS space detector is compatible with that of ground detectors.

The $\Phi_{e^+e^-}$ measurement can be used together with the PF measurement to extract basic information about the origin and the propagation of cosmic e^\pm . An accurate description of the data involves the solution of the transport equation in the galactic environment and in the heliosphere for e^\pm and for other hadronic observables used to constrain the production and propagation parameters. In this analysis, a more basic hypothesis has been tested. The flux of e^- and e^+ have been parametrized using separate simple power laws. A common additional contribution of e^\pm has been introduced to model the shape of the e^\pm flux expected from a pulsar acceleration or from DM annihilation production. The solar modulation effect at energies below 30 GeV have been parametrized according to the *Force Field Approximation* introducing additional degrees of freedom to the model. This parametrization of the Φ_{e^\pm} fluxes has been fitted to the $\Phi_{e^+e^-}$ and to the PF measurements from 0.5 GeV to 1 TeV. The data are described with a good χ^2/ndf . The best fit parametrization at high energies does not describe

accurately the drop of the PF because it is constrained by the more accurate $\Phi_{e^+e^-}$ flux data which extend smoothly up to 1 TeV. A χ^2 test of the resulting model to the Φ_{e^-} and Φ_{e^+} measurements by AMS confirms that a coherent description of the e^- , e^+ and $(e^+ + e^-)$ measurements by AMS is possible. The result of the fit depends strongly on the minimum energy used in the χ^2 minimization procedure. This fact, together with the difficulty to describe the drop of the PF at high energies, confirms that the parametrization of the e^\pm fluxes using simple power laws and the parametrization of the effects of solar modulation at energies below 30 GeV do not adequately describe the data. The result of this procedure furnishes therefore only a qualitative interpretation of the data. More complicated and comprehensive approaches, as discussed before, have to be used to infer quantitative physics results from the accurate AMS data.

Conclusions

Summary

The measurement of the e^\pm cosmic ray component provides fundamental insights into the physics of production and propagation of cosmic rays in the Galaxy. The e^\pm spectrum measured at Earth can potentially show indirect signatures of Dark Matter phenomenology. These prospects motivated an exceptional interest in the astroparticle physics community in the last decades, driving a huge experimental effort to measure these low abundant components of cosmic rays.

The latest, state-of-the-art experiment for the measurement of cosmic ray e^\pm is the Alpha Magnetic Spectrometer (AMS-02) detector, which has been operating and collecting cosmic rays on the International Space Station since 19th May 2011. The AMS collaboration recently released the measurements of the e^+ flux (Φ_{e^+}) up to 500 GeV, of the e^- flux (Φ_{e^-}) up to 700 GeV and of the positron fraction $e^+/(e^+ + e^-)$ up to 500 GeV [83, 26]. The high accuracy of the AMS subdetectors provided precision measurements that substantially improved the previous experimental scenario. For the first time, a change of slope has been observed in the e^+ flux at ~ 35 GeV and at ~ 200 GeV, while no feature has been observed in the smooth e^- flux. As confirmed by the rise observed in the positron fraction, these features point to the existence of an additional component in the e^+ flux that dominates over the standard secondary e^+ component at high energies. The additional primary e^\pm component can be a consequence of e^\pm pair production by nearby pulsars, of Dark Matter annihilation or decay or a combination of both processes. AMS also provided the first experimental evidence of a flattening of the positron fraction starting at ~ 200 GeV [83]. This remarkable result has fundamental consequences in the interpretation of the e^\pm spectral features in terms of additional primary e^\pm sources.

The body of experimental knowledge of the e^\pm cosmic ray component is enriched by the most recent AMS measurement of the $(e^+ + e^-)$ flux ($\Phi_{e^++e^-}$) from 0.5 GeV to 1 TeV [1], which is the result of this Ph.D. thesis. The $\Phi_{e^++e^-}$ measurement extends with reduced systematics to the highest energy range ever reached by AMS and provides more precise information on the flux in the whole energy range with respect to the separate Φ_{e^+} and Φ_{e^-} measurements. More stringent constraints can be set on e^\pm cosmic ray physics using the additional information provided by this measurement.

In this thesis, the AMS detector capabilities have been exploited to provide a high precision measurement of the $(e^+ + e^-)$ flux. The most challenging issue for the measurement of the $(e^+ + e^-)$ flux at high energies is the separation of the e^\pm signal from the overwhelming proton background. The combined information provided by the analysis of the energy deposit in the Transition Radiation Detector (TRD) and of the shower topology in the Electromagnetic Calorimeter (ECAL) allows for identification of the $(e^+ + e^-)$ signal with high accuracy.

The measurement of the ECAL shower development has been used in different steps of the analysis to enhance the purity of the $(e^+ + e^-)$ sample. The high electron/proton separation capabilities of the ECAL allow for removal of most of the proton background up to the TeV energy range. The remaining

proton background has been identified and subtracted using a data driven approach. A template fit of the energy deposit distributions in the TRD, which are known with high accuracy in the whole energy range, has been applied to the data and to identify the $(e^+ + e^-)$ signal. An example of the template fit is shown in Figure 4.31 for different ECAL selections. The combined approach to the signal identification using the ECAL and TRD detectors allows for the identification of the $(e^+ + e^-)$ component with limited systematic effects. At high energies the uncertainty on the $(e^+ + e^-)$ signal estimation increases due to the decrease in the electron/proton separation power of the TRD. Nevertheless the statistical fluctuations dominate over the signal identification systematic uncertainty in the whole energy range.

The acceptance of the detector has been estimated using a MonteCarlo (MC) simulation of the interactions of e^\pm with the AMS detector. The differences between the data and the MC simulation have been quantified by a comparison of the efficiencies for all the cuts of the analysis using control samples of e^- selected from the data. The charge sign measurement has been provided by the Tracker. The agreement between the data and the MC simulation defines the systematic uncertainty on the acceptance scale, which is known at the level of $\sim 2\%$ above 3 GeV. The uncertainty increases at lower energies.

The bin-to-bin event migration induced by the finite ECAL energy resolution has been investigated. The precise energy measurement guarantees a minor contribution from this source to the measurement uncertainty in the whole energy range. The impact of the ECAL energy scale uncertainty on the $\Phi_{e^+ + e^-}$ measurement has also been studied. The ECAL energy scale is known at the 2% level in the test beam energy range between 10 GeV and 290 GeV, and increases up to 5% at 0.5 GeV and at 1 TeV. This uncertainty has been assigned as uncertainty to the energy for the $\Phi_{e^+ + e^-}$ measurement result.

The total systematic uncertainty of the $\Phi_{e^+ + e^-}$ measurement is dominated by the acceptance uncertainty below 300 GeV. Above this energy, the systematic uncertainties introduced by the $(e^+ + e^-)$ signal identification procedure dominate the systematic uncertainty. The total uncertainty is dominated by systematic effects below 100 GeV. Above this energy statistical fluctuations take over and start to dominate the total uncertainty at 150 GeV. Figure 6.7 shows the energy dependence of the statistical and systematic contributions to the measurement uncertainty.

The $(e^+ + e^-)$ flux has been measured using the first 30 months of data collected by AMS. Among the data, 10.6 million of e^\pm events have been identified. The precision of the AMS data provides new and distinct information to the body of experimental knowledge. The measurement of the $\Phi_{e^+ + e^-}$ is shown in Figure 6.9. The spectral shape of $\Phi_{e^+ + e^-}$ is smooth and does not show any prominent feature. The flux measurement extends up to 1 TeV, which is the highest e^\pm energy ever measured by space detectors, and it overlaps with the minimum energy domain of ground based experiments. Above ~ 30 GeV, the flux can be described by a single power law parametrization at 90% CL. The spectral index of the flux is measured to be $\gamma = -3.170 \pm 0.008(\text{stat.} + \text{syst.}) \pm 0.008(\text{energy})$. The flux is softer than what measured by previous experiments, and the feature above 300 GeV claimed by previous balloon experiments has been excluded.

Outlook

Together with the positron fraction measurement, the precision of the $\Phi_{e^+ + e^-}$ result constraints the properties of the additional primary e^\pm cosmic ray component. Future measurements by AMS of Φ_{e^+} , Φ_{e^-} and $\Phi_{e^+ + e^-}$ will increase the accuracy of the current data and will explore higher energy ranges. The accurate measurements of the high energy flux spectral shape is not, however, sufficient to constrain the nature of the positron fraction rise at high energies.

Dark Matter signatures can show up also in different cosmic ray species. The search for signatures in the hadronic channels of cosmic rays provides complementary information to the Dark Matter search.

The flux of \bar{p} and its ratio to the standard proton component is one of the most sensitive observables. No excess of \bar{p} with respect to the astrophysical background has been observed in cosmic rays up to 200 GeV [154]. The AMS collaboration is currently analyzing the data collected so far to spot any feature in the \bar{p} component at higher energies and to improve the sensitivity of this measurement at low energies. In case of agreement with standard astrophysical \bar{p} production models, this measurement will set strong constraints on the phenomenology of Dark Matter. In addition to the \bar{p} channel, the flux of low energy \bar{D} in cosmic rays may disclose evidence for Dark Matter activity. The detection of any \bar{D} below 1 GV in the data collected by AMS would strongly point to production of \bar{D} from Dark Matter annihilation, as the expected flux of \bar{D} from standard astrophysical processes is below the AMS sensitivity.

Besides the spectral shape of the cosmic ray fluxes, the analysis of the arrival directions of high energy e^\pm represents a powerful tool to disentangle whether the additional primary e^\pm source is dominated by astrophysical pulsar production or by Dark Matter annihilation or decay. Pulsars are e^\pm point sources. A preferred arrival direction is therefore expected for primary e^\pm accelerated by pulsars. On the contrary, Dark Matter annihilation or decay are instead expected to occur isotropically, with a minor directionality induced by the gradient of the galactic Dark Matter density. The directional information carried by e^\pm is reduced by the diffusive motion in the turbulent galactic magnetic fields. The level of expected anisotropy for e^\pm produced by point sources is therefore below the percent level, but it is typically above the expected anisotropy for standard e^\pm accelerated in supernova remnants. The detection of an anisotropy in the arrival direction of high energy e^\pm would point to the existence of nearby point sources, which could not be attributed to Dark Matter e^\pm production. The data collected by AMS will be used to search for anisotropies in the incoming e^\pm direction and to test and provide limits on many e^\pm production and galactic propagation models.

The lowest energy range of the spectrum is interesting because, as shown in this thesis, the details of the e^\pm flux at low energies set stringent constraints on the yield of the additional primary sources at high energies. The physics of the heliosphere and its effect on the low energy e^\pm is still not known with sufficient accuracy. This limits the confidence in the extrapolation of the fluxes measured at Earth to the fluxes of primary cosmic rays in the Local Interstellar Medium, before they enter the heliosphere. Detailed studies of the low energy e^\pm flux will be provided by AMS to study the time dependent and charge dependent effects of the solar wind on e^\pm . The data will not only improve the understanding of solar physics, but they will also set further constraints on the lowest energy products of the primary e^\pm sources and, therefore, on the nature of the source itself.

AMS will improve the knowledge on the nuclei spectra and abundances significantly. The measurement of the standard nuclear component of the cosmic radiation (proton and nuclear fluxes, secondary to primary ratios, unstable isotopes ratios) will serve to constrain and define the propagation models in the Galaxy. More stringent limits on the propagation models will reduce the systematic uncertainty on the expected e^\pm fluxes at Earth. This will improve the sensitivity in the comparisons between the experimental measurements and the model prediction for all the phenomenological interpretations of the e^\pm data, including the indirect searches for Dark Matter signatures.

The data collected by AMS have confirmed the scientific potential of the cosmic radiation. The hope to find Dark Matter signatures in cosmic rays, and especially in the e^\pm component, has driven a race to develop particle physics experiments to be operated in space.

The DArk Matter Particle Explorer (DAMPE) [65] is a scientific satellite mission scheduled to be launched in late 2015. The DAMPE detector is equipped with a silicon-tungsten tracker-converter, a plastic scintillator strips detector (PSD) that serves as anti-coincidence detector, a 31 X_0 BGO imaging calorimeter and a neutron detector to improve the electron/proton separation. Its total acceptance amounts to 0.3 m^2sr . The detector aims to measure the $(e^+ + e^-)$ and γ flux in the energy range between 5 GeV and 10 TeV, with an energy resolution better than 1.5% and an angular resolution of

$\sim 0.1^\circ$ at high energies. It will also use the BGO calorimeter to measure, with lower resolution, the flux of nuclei up to above the TeV energies.

The CALorimetric Electron Telescope (CALET) [233] is a $0.12 \text{ m}^2\text{sr}$ detector that will be operated on the ISS for a total of 5 years starting from 2015. It consists of two layers of 14 plastic scintillators on top of the detector, a $\sim 3 X_0$ scintillating fiber sampling calorimeter for precise reconstruction of the initial development of the electromagnetic showers and a $\sim 27 X_0$ homogeneous PbWO_4 scintillating bar calorimeter. The main scientific target of CALET is the extension of the $(e^+ + e^-)$ flux measurement above 10 TeV with a $\sim 2\%$ energy resolution. The gamma ray flux will be also measured. Finally, it will measure the flux of protons and nuclei up to Iron in the high TeV energy range with an energy resolution between 30% and 40% depending on the nuclear species above the TeV. In addition to this, CALET also aims to extend the measurement of ultra heavy nuclei above Iron with competing statistics compared to the latest balloon missions [234].

The Gamma Astronomical Multifunctional Modular Apparatus (GAMMA-400) [143] is the next generation high acceptance $\sim 3 \text{ m}^2\text{sr}$ satellite observatory optimized for the detection of gamma rays, which is planned to begin operations in 2018. The detector consists of a silicon strip detector interleaved with tungsten conversion foils that act as a converter-tracker system, a time of flight system, a $25X_0$ CsI (Tl) crystal calorimeter and a neutron detector at the bottom to maximize the electron/proton separation. The subdetectors are surrounded by a scintillator veto system. The detector has been conceived for the precise measurement of gamma rays at 100 GeV, where the excellent 1% energy resolution maximizes the potential of discovering a line in the gamma spectrum and the $\sim 0.01^\circ$ angular resolution could allow to precisely locate the source of the γ line. Despite the gamma ray based concept, GAMMA-400 has also the potential to measure the flux of $(e^+ + e^-)$ from 100 MeV to 10 TeV.

Besides electromagnetic calorimeter based experiments, the space detector scenario is enriched by experiments dedicated to the measurements of the nuclear component at the knee in the cosmic ray spectrum between 10^{15} and 10^{16} eV. The balloon-borne Cosmic Ray Energetics And Mass (CREAM) experiment concept has been adopted to be operated on the ISS starting in 2015. The ISS-CREAM detector [235] is composed of an ionization calorimeter to measure the charge of cosmic rays and to provide tracking, a silicon detector to measure the charge, and additional scintillator and neutron detector systems to improve the electron/hadron separation. The total acceptance of the detector amounts to $\sim 4 \text{ m}^2\text{sr}$. ISS-CREAM will measure the flux of protons and heavy nuclei beyond PeV energies to investigate the composition of cosmic rays in an energy range never analyzed with direct detection space experiments so far.

Figure 6.23 shows an overview of past, of operating and of future balloon and space missions for direct detection of charged cosmic rays and gamma rays. Despite the progress in space detector technology and the improvement in the energy resolution and range for the next generation experiments, AMS will keep a fundamental role among cosmic rays space detectors. None of the new generation experiments features, in fact, a magnet. AMS is the only space detector that will be able to identify the rare antimatter components in the cosmic rays and to search for Dark Matter signatures in specific channels like e^+ , \bar{p} and \bar{D} for the next years.

The measurements of the e^\pm fluxes represent only the first results obtained by the accurate analysis of the precise data collected by AMS. The broad spectrum of many more future AMS results will serve as a powerful tool to broaden our knowledge on the origin and propagation of cosmic rays and to test particle physics and astrophysics at energy scales never achieved before.

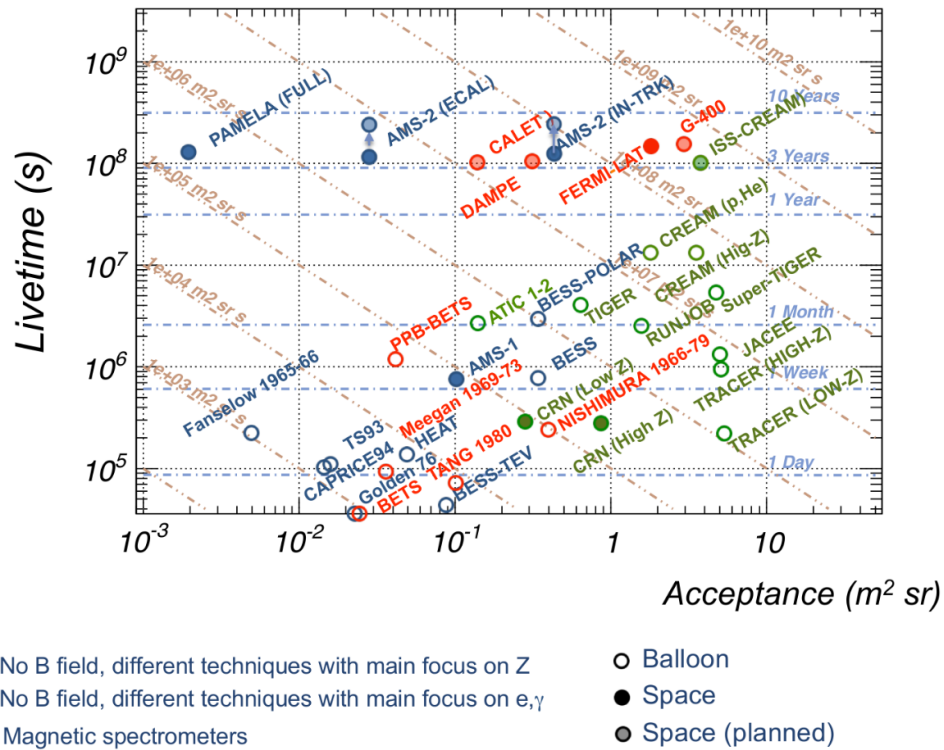


Figure 6.23: Overview of balloon and space borne experiments aimed to the direct detection of charged cosmic rays and gamma rays [236]. The blue circles represent spectrometer detectors that feature a magnet. Green and red circles represent detectors that do not feature any magnet and that are optimized for the detection of nuclei and e^\pm, γ respectively. CALET, DAMPE, GAMMA-400 and ISS-CREAM are the current approved mission that will be operated in space starting from 2015. The detector concepts are reviewed in the text. The total collected exposure (in $m^2 sr s$) will be improved by at least an order of magnitude in comparison to the expectations for the ECAL-based measurements of AMS. However, none of the next generation space detectors has the capability to measure the charge sign of cosmic rays. In the future years, AMS will be the only detector able to identify the rare antimatter components in the cosmic rays and to search for Dark Matter signatures in specific channels like e^+ , \bar{p} and \bar{D} .

Appendix A

Cosmic ray events collected by AMS

AMS has been successfully installed on ISS on 19th May 2011, and since that day it continuously recorded cosmic particles without any major interruption to the DAQ. Figure [A.1](#) shows the total statistics accumulated over more than 3 years of AMS operations.

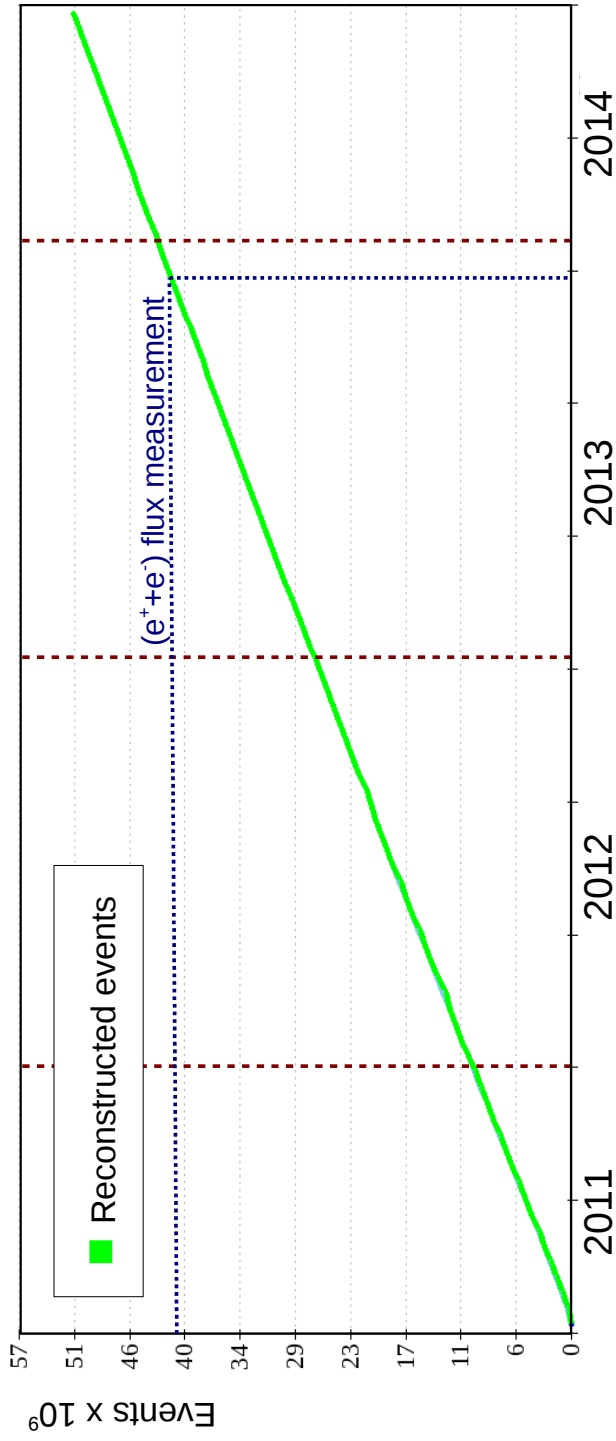


Figure A.1: Number of cosmic ray events collected by the AMS experiment from the start of operations in May 19, 2011. AMS collected ~ 50 billion events during the first 3 years of data taking, with no major interruptions. The blue lines define the $\sim 41 \times 10^9$ triggers collected in the first 30 months of data taking used to measure the $(e^+ + e^-)$ flux. Data are transferred on the ground and efficiently reconstructed on the fly. This allows a prompt calibration of freshly delivered data and continuous monitoring of the detector performances.

Appendix B

ECAL Longitudinal BDT

Transformation of training variables

The energy deposit fraction in the first 5 ECAL layers, which correspond to approximately 5 X_0 are used to build the $\text{ECAL}_{\text{BDT}}^{\text{long}}$ classifier. The fractions depend however on the shower energy. In order to minimize the $\text{ECAL}_{\text{BDT}}^{\text{long}}$ energy dependence, the variables are first “normalized”¹ with a multi-step procedure defined on a sample of MC e^- :

1. The shape of each input variable $x^{(i)}$ has been transformed using Box-Cox transformations $x^{(i)} \rightarrow \chi^{(i)}$ (see later for the details). The Box-Cox transformation provides a gaussian distribution of the variable $\chi^{(i)}$.
2. The mean ($\mu^{(i)}$) and the width ($\sigma^{(i)}$) of the resulting symmetric distributions for $\chi^{(i)}$ have been determined as a function of the reconstructed energy for each layer i . The $\mu^{(i)}(E)$ and $\sigma^{(i)}(E)$ energy dependence has been parametrized with an analytical fit.
3. The normalized variables $x_N^{(i)} = (\chi^{(i)} - \mu^{(i)})/\sigma^{(i)}$ have been defined. By construction, they have null mean and unitary width.

The Box-Cox [237] transformations belong to the family of *power transformations*. In statistics, this term denotes a family of functions that are applied to create a rank-preserving transformation of data using power functions. Box-Cox transformations are used to enhance the normal-regularity of data distributions, and in general to improve the validity of statistical tests. Box-Cox transformations $\chi(x, \lambda)$ are completely defined by the regularization parameter λ and are defined by the following rule:

$$\chi = \begin{cases} (x^\lambda - 1)/\lambda & , \lambda \neq 0 \\ \log(x) & , \lambda = 0 \end{cases} \quad (\text{B.1})$$

A modified version of the Box-Cox transformations, the Manly [238] exponential transformations, have been adopted in this analysis:

$$\chi = \begin{cases} (\exp(\lambda x) - 1)/\lambda & , \lambda \neq 0 \\ x & , \lambda = 0 \end{cases}. \quad (\text{B.2})$$

Manly transformations preserve all the properties associated to Box-Cox transformations. They have, however, some additional interesting features:

¹In this context, the concept of normalization is used to indicate the correction applied to render ECAL variables energy independent.

- $\lambda = 0$ is the unitary transformation.
- It can be applied also to negative variables.
- $x = 0 \rightarrow \chi = 0 \quad \forall \lambda$. This implies that the distribution of χ will be similar to the distribution of X around 0: the physical meaning of the variable is therefore not strongly modified.
- The dependence of the transformation $\chi(x, \lambda)$ on the regularization parameter λ is less strong than for plain Box-Cox transformations. This implies that even if the estimation of λ is slightly wrong or biased the result does not deviate much from the expectation.

It is always possible to define a λ which maximizes the regularity for X distribution. Different values of the λ parameter has been tested and finally the value that maximizes the gaussian likeness of the distribution has been chosen. In this analysis, the value of λ that minimizes the skewness for the transformed distribution has been used as regularization parameter.

An example of the result of the transformation is shown in Figure B.1. The distribution of the y axis, as a function of an indexing x variable, is shown on the top left plot. The value of λ is shown on the top right plot. A smooth parametrization has been fitted to the dependence of $\lambda(x)$ to smooth out statistical fluctuation and to regularize the transformation. The resulting distribution for χ is shown the second row, on the left. The result of the complete transformation (x_N) is shown in Figure 4.20. After the transformation, each ECAL variable used for the ECAL_{BDT}^{long} training is energy independent in terms of mean, width and shape. This allows the optimum control in terms of energy dependence for any multi-variate discriminator built from this set of normalized inputs.

Classifier training

After the energy normalization of the input variables, a discriminant classifier has been built. Different approaches have been tested, using both custom algorithms and multivariate classifiers.

- (i) Average, or mean
- (ii) Likelihood
- (iii) TMVA Likelihood
- (iv) TMVA Decorrelated Likelihood (LikelihoodD)
- (v) TMVA BDT AdaBoost (BDT)
- (vi) TMVA BDT GradientBoost (BDTG)

For the multivariate classifiers (iii) to (vi), the TMVA [239] package has been used². The Mean is the classifier which, by construction, would have had the best statistical properties, preserving the gaussian behavior of the input variables and a complete independence from energy. An a-posteriori check has shown however that its e/p discrimination power is not effective enough at the highest energies of the analysis. The likelihood and the BDT approaches provide a higher separation power with respect to the simple mean showing similar mild dependencies with energy. The comparison between different discriminators in terms of rejection of the background is shown in Figure B.2. The GradientBoost BDT has been selected to be used as ECAL longitudinal discriminator, namely ECAL_{BDT}^{long}. Its normalized distribution, for MC and ISS electrons and for ISS protons, is shown in Figure 4.21 in the energy range [35.0 – 80.0] GeV. The gain the MC-data agreement with respect to the ECAL_{BDT} classifier is substantial.

The training process for the ECAL_{BDT}^{long} needs a set of signal (electron) events and a set of background (proton) events. Given the good data/MC agreement for the signal input variables distributions, MC

²See [239] for the definition of each classifier properties

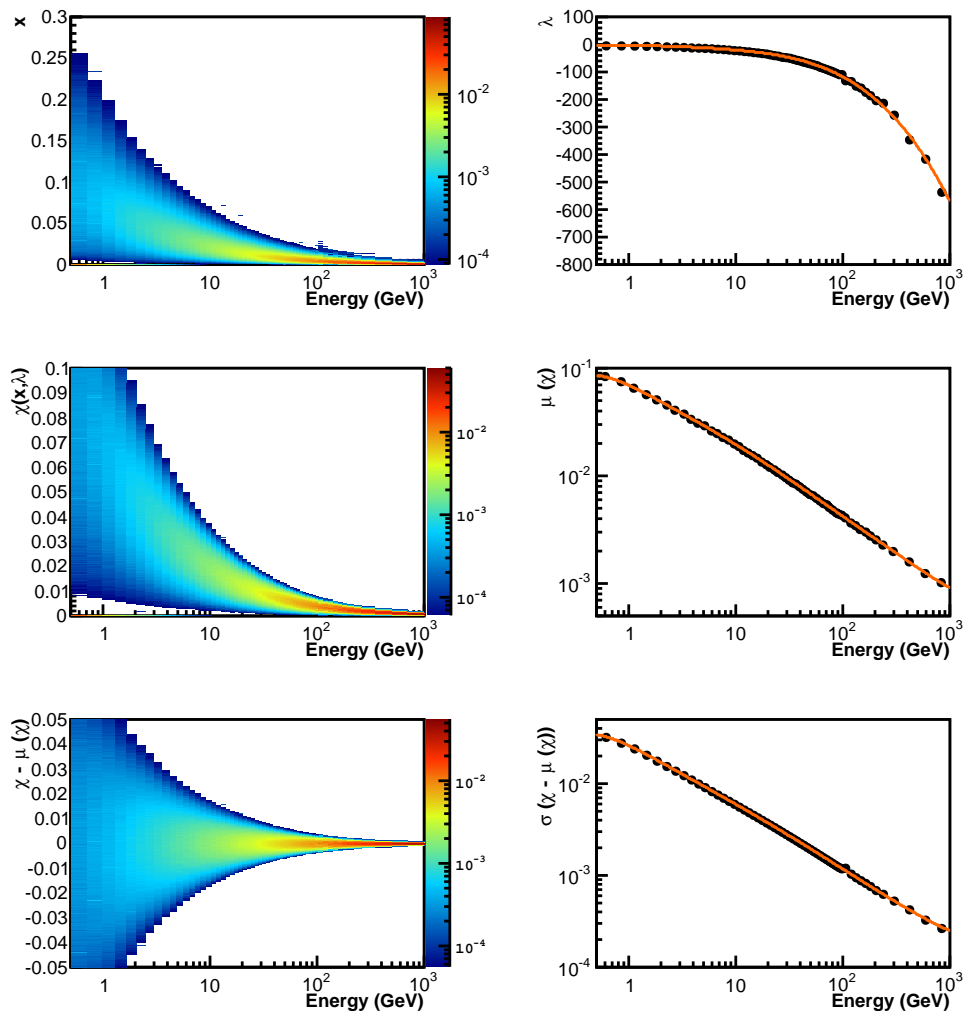


Figure B.1: Example of the procedure for the renormalization of the energy deposit fraction in the second ECAL layer. In the first row the raw variable x (left), as a function of energy, and the λ parameter that minimizes, bin by bin, the skewness of the distribution (right) are shown. In the second row the distribution after the Box-Cox transformation χ (left) and its mean, $\mu(\chi)$, (right) are presented. At this step, the resulting distribution is symmetric in each energy bin. In the third row the distribution after the mean correction (left) and its RMS, $\sigma(\chi)$, (right) are shown. The result of the normalization procedure, $x_N = (x - \mu)/\sigma$, is shown in Figure 4.20

e^- have been used to avoid the limitation in statistics and purity of the high energies ISS e^- sample. Conversely, hadronic cascades are not well reproduced in MC and, given their abundance in the cosmic ray flux, it is relatively easy to define a clean sample of protons using the TRD and the Tracker even at high energies: the background sample has been therefore selected directly from ISS data. The training has been performed on the highest energies only ($E > 350$ GeV) where the classifier has to be as much discriminant as possible. To guarantee a smooth $\text{ECAL}_{\text{BDT}}^{\text{long}}$ energy dependence and to safely extrapolate the validation from the low energies up to the TeV energy, only one $\text{ECAL}_{\text{BDT}}^{\text{long}}$ training has been performed and applied to the whole energy range. No splitting in energy bins has been applied for the training as done for the ECAL_{BDT} classifier.

It is worth to stress that the proton sample used for the training procedure and used to evaluate the rejection power shown in Figure B.2, chosen with a TRD selection on $R > 0$ protons, constitutes

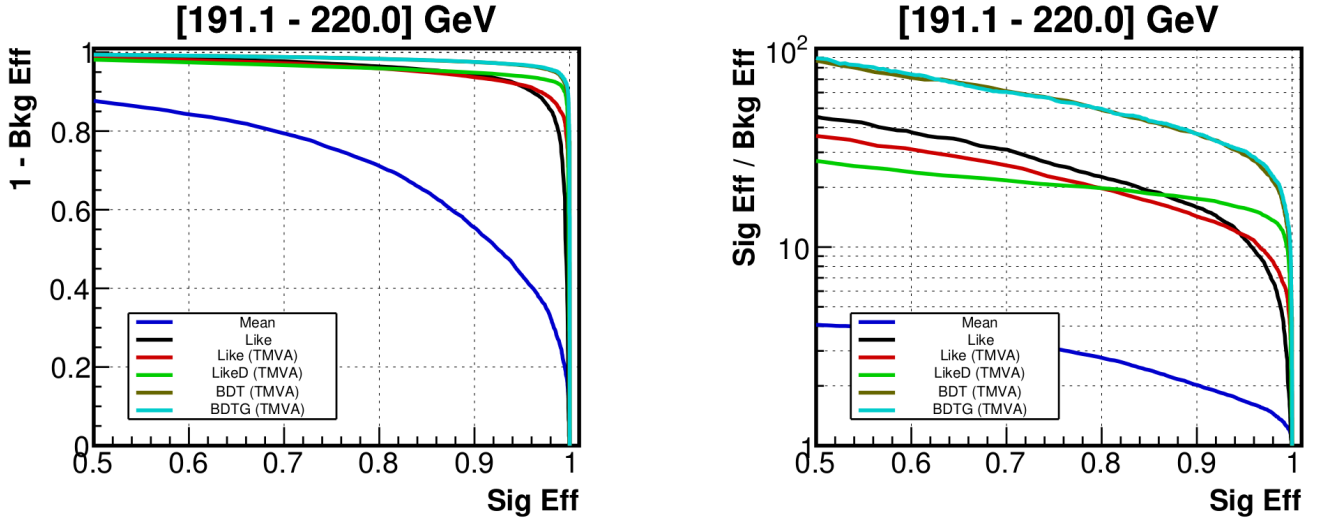


Figure B.2: **(Left)** Receiver operating characteristic (ROC) curve and **(Right)** Rejection curve for the different multivariate approaches tested in the [190.0, 220.0] GeV energy range. The ‘Mean’ is clearly not enough discriminant, the BDTG is the most effective and has been chosen to define the $\text{ECAL}_{\text{BDT}}^{\text{long}}$ classifier.

a subsample of the total background of the $(e^+ + e^-)$ flux analysis. The presence of spillover protons ($R < 0$ protons) or interaction events in the e^\pm data sample is not contained in the training sample. Therefore, a smaller discrimination power of the $\text{ECAL}_{\text{BDT}}^{\text{long}}$ classifier is expected when applied on the total sample.

Longitudinal BDT a-posteriori efficiency check

In addition to the data/MC comparison discussed in Section 4.2.1.2, an additional a-posteriori check has been done in order to confirm the validity of the $\text{ECAL}_{\text{BDT}}^{\text{long}}$ efficiency calculation. A preliminary analysis of the $(e^+ + e^-)$ flux measurement has been run with different strengths of the $\text{ECAL}_{\text{BDT}}^{\text{long}}$ classifier and the results have been compared. This is shown in Figure B.3. The agreement at the $\sim 1\%$ level between different results even up to $\text{ECAL}_{\text{BDT}}^{\text{long}}$ efficiencies of 60% confirms the validity of the procedure used to calculate the classifier efficiency using the data/MC comparison and that the systematic uncertainty on the $\text{ECAL}_{\text{BDT}}^{\text{long}}$ efficiency is negligible if compared with other systematic sources in the whole energy range.

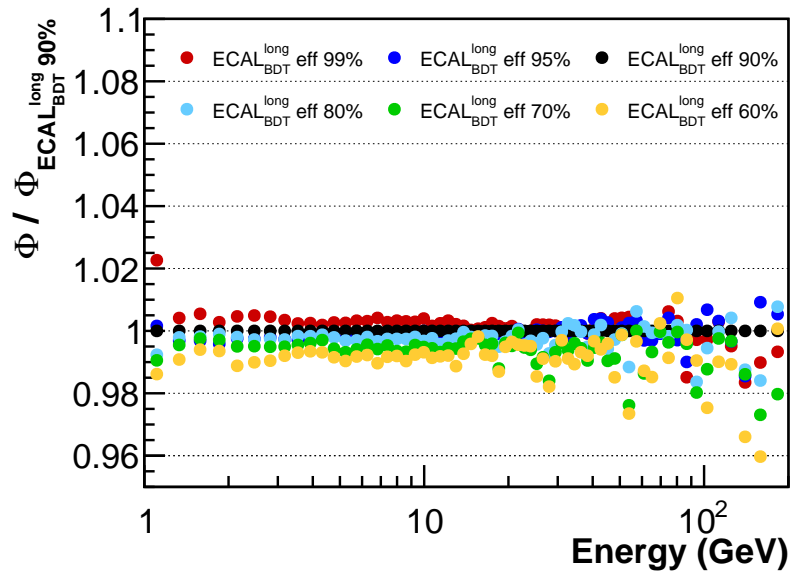


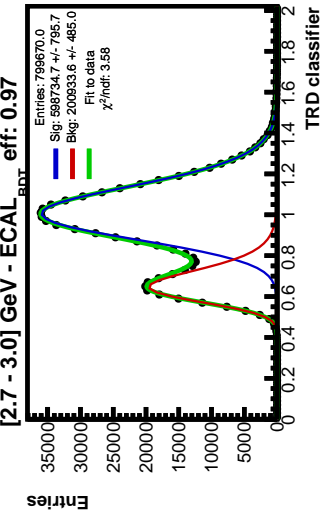
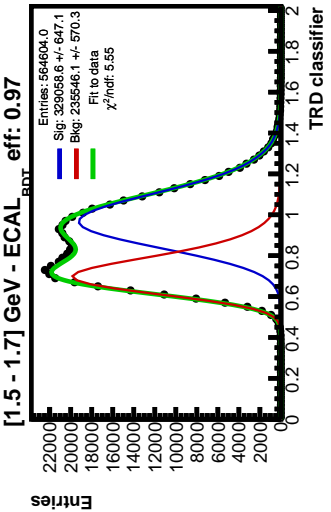
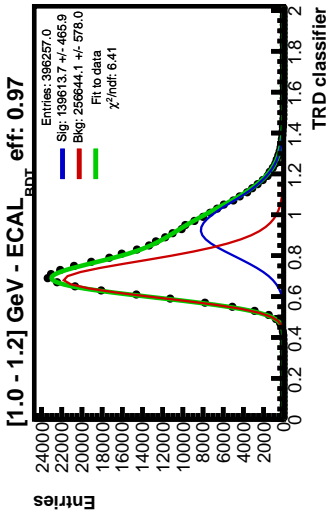
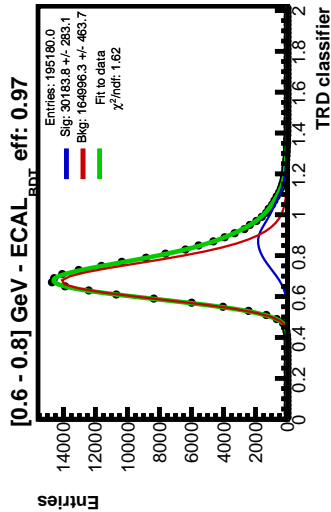
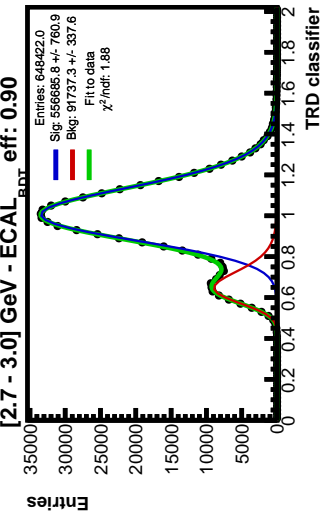
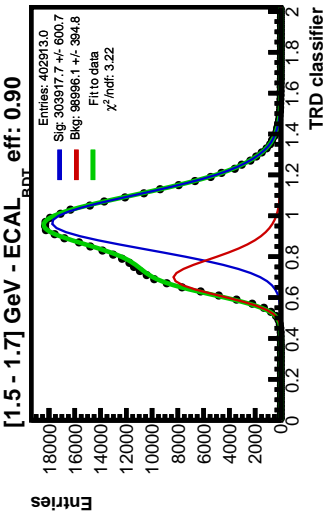
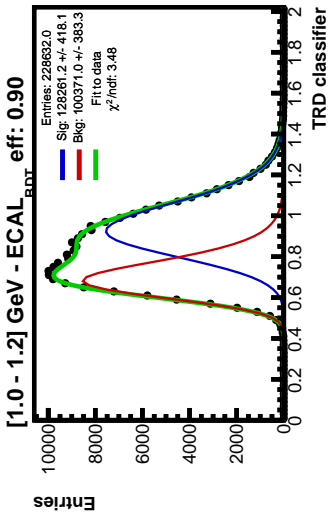
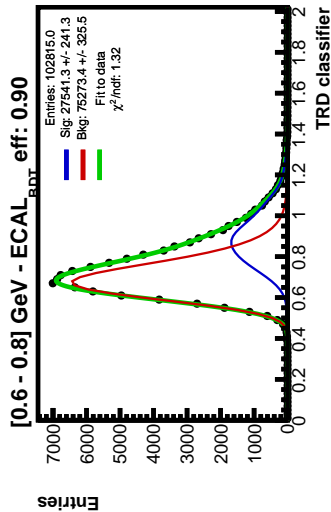
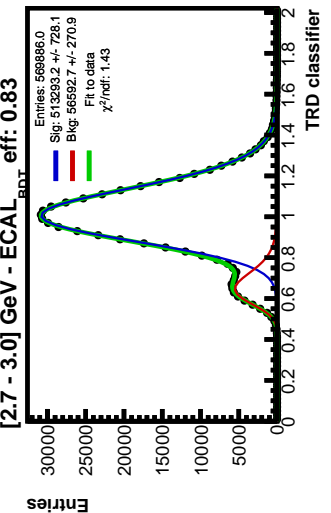
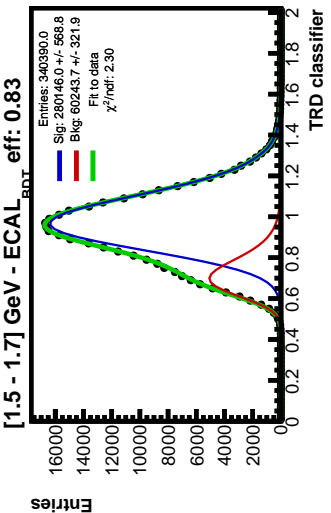
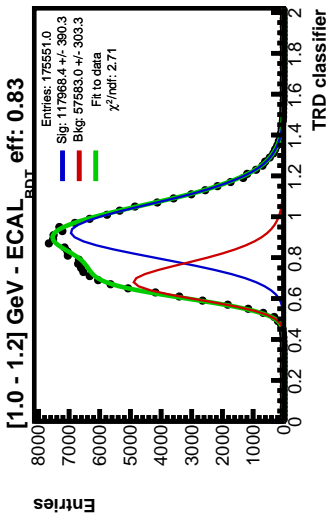
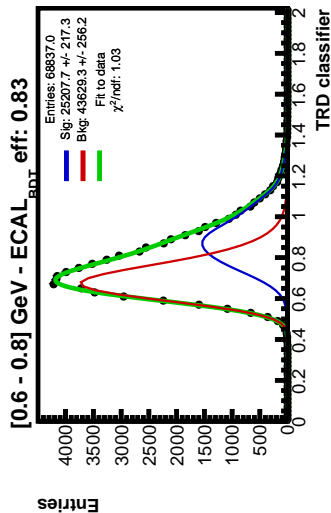
Figure B.3: Comparison between the $(e^+ + e^-)$ flux measurement performed with different $\text{ECAL}_{\text{BDT}}^{\text{long}}$ cuts. For the measurement, the $\text{ECAL}_{\text{BDT}}^{\text{long}}$ cut efficiency depends on energy and it is never stronger than 91%. The normalization has been set here to $\text{ECAL}_{\text{BDT}}^{\text{long}} = 90\%$. For a wide range of cuts, even much stronger than the final cuts applied in the final analysis, the different results agree better than 1%: this is a further confirmation that the $\text{ECAL}_{\text{BDT}}^{\text{long}}$ efficiency estimated from MC has been correctly evaluated.

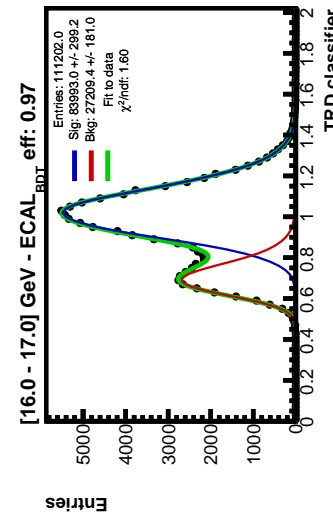
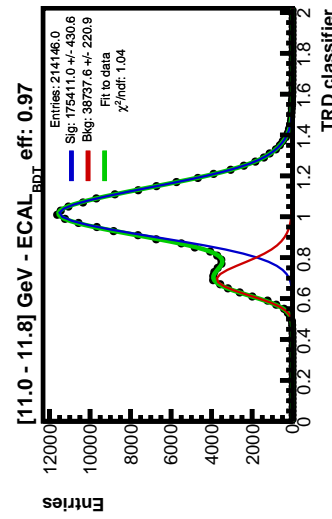
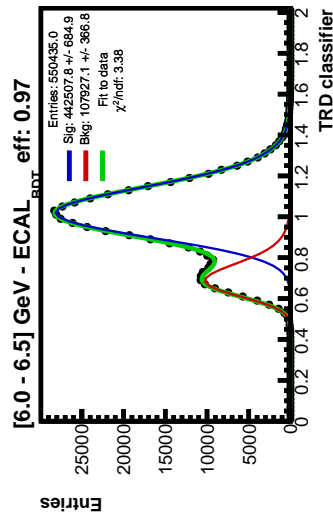
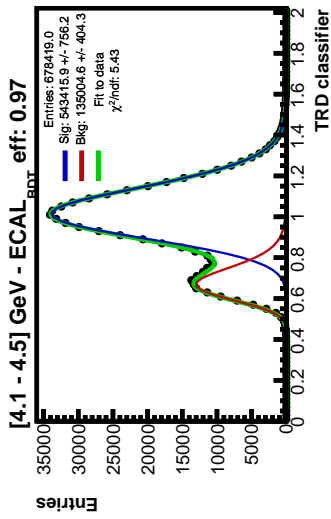
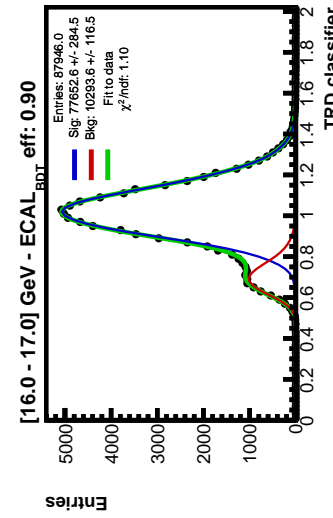
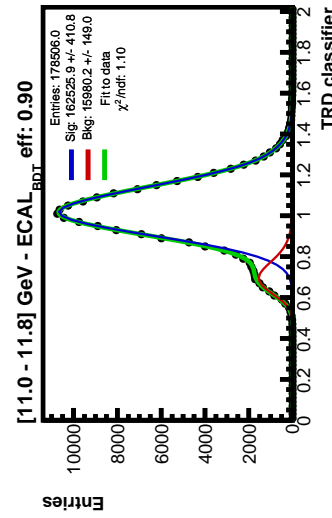
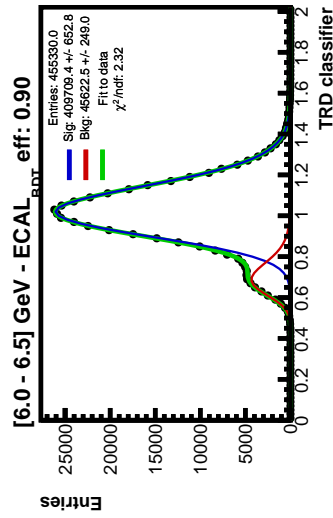
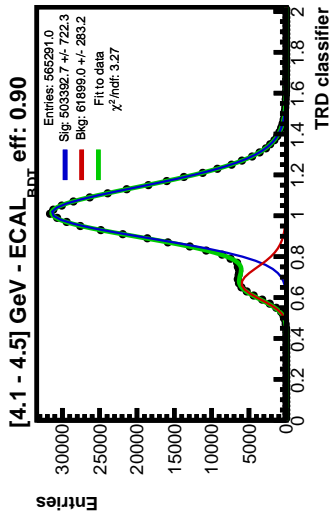
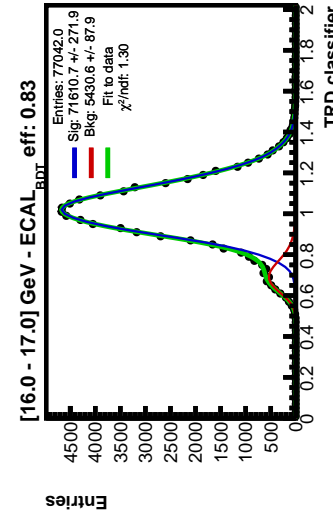
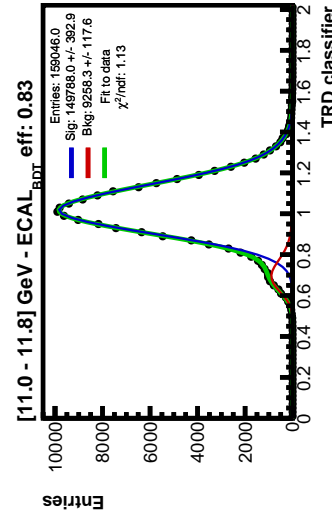
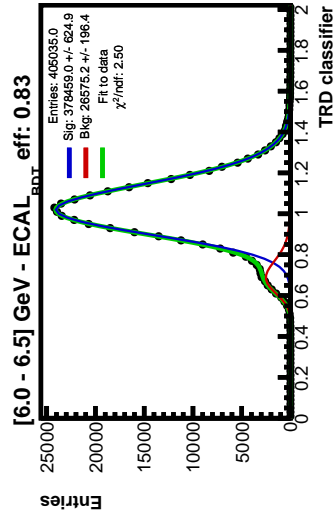
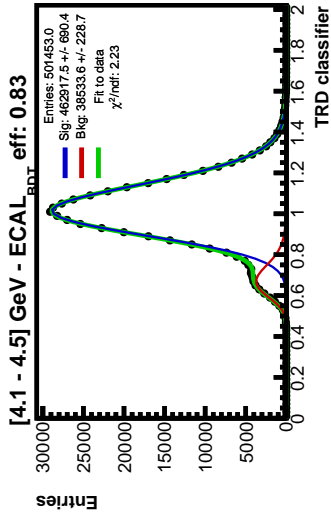
Appendix C

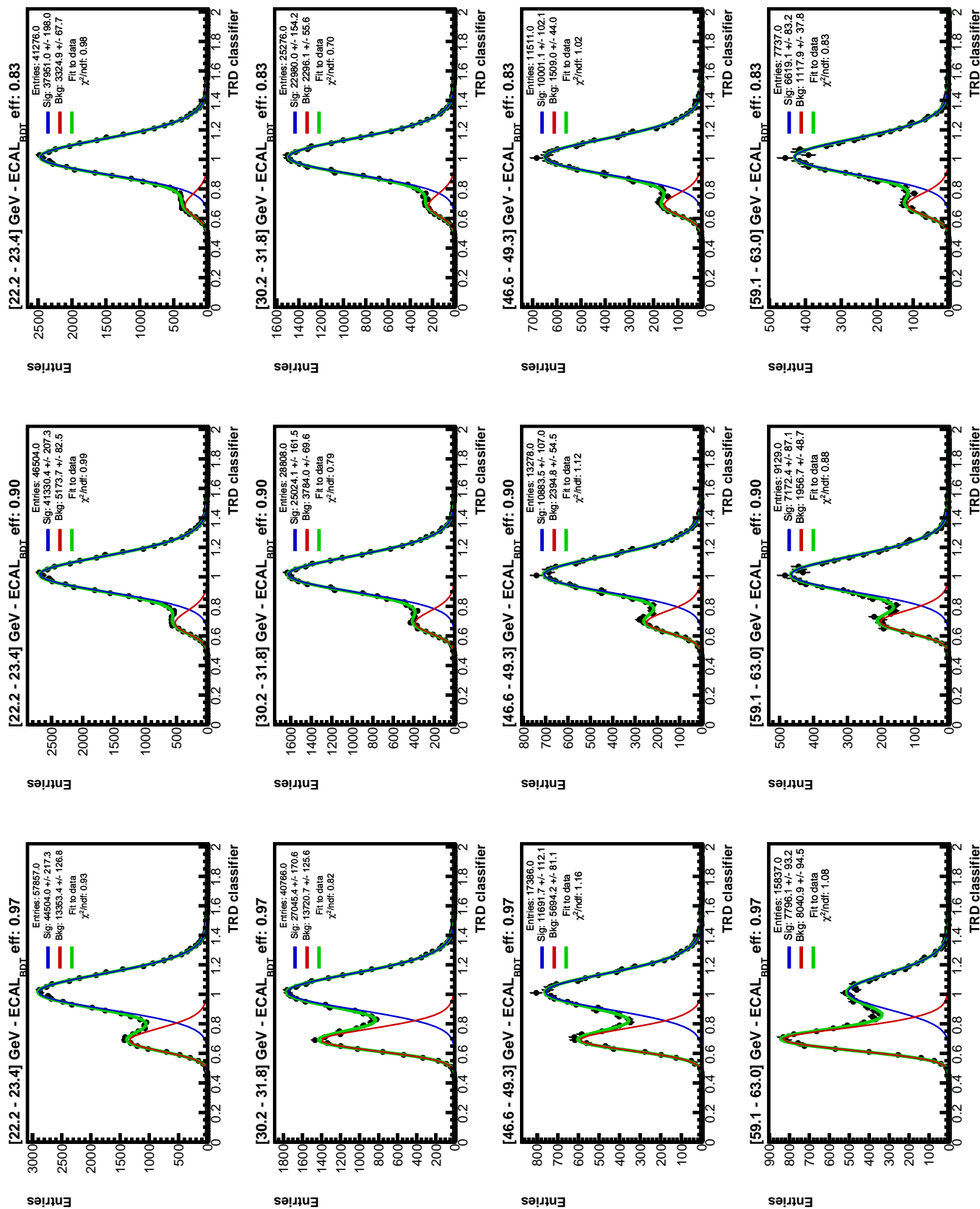
TRD template fit examples

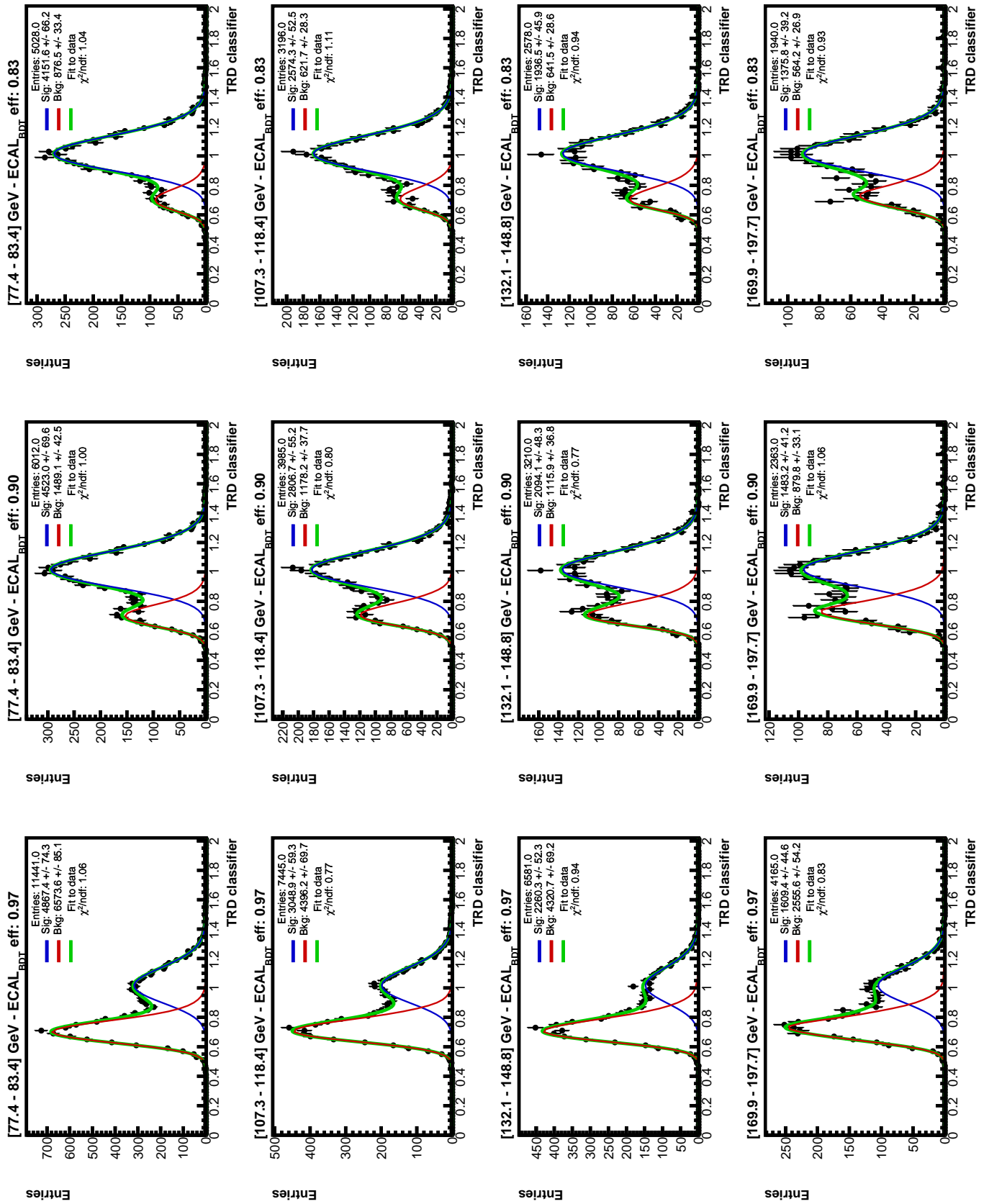
In this section, the result of the template fits for a choice of energy bins and ECAL_{BDT} selections is shown. For each energy, a preliminary cut on the $\text{ECAL}_{\text{BDT}}^{\text{long}}$ classifier is applied to remove the bulk of the proton background. The efficiency of the $\text{ECAL}_{\text{BDT}}^{\text{long}}$ cut depends on the energy and its energy dependence is shown in Figure 4.32. The strenght of the ECAL selection defines the purity of the fitted sample, the statistical fluctuations of the signal and of the background and the systematic uncertainty to which the $(e^+ + e^-)$ yield is known. This is discussed in Section 4.4. The ECAL_{BDT} cut value that minimizes the total uncertainty on the $(e^+ + e^-)$ yield is shown in Figure 4.32.

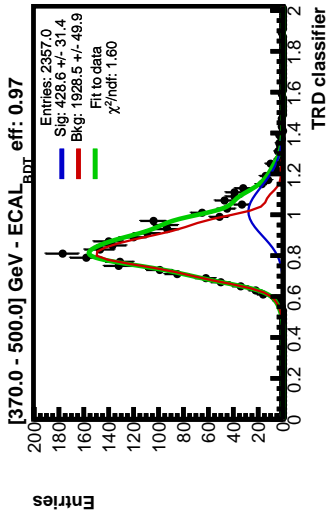
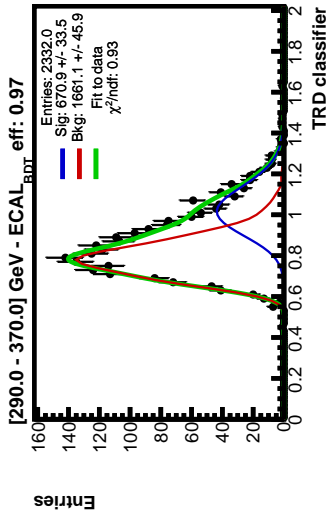
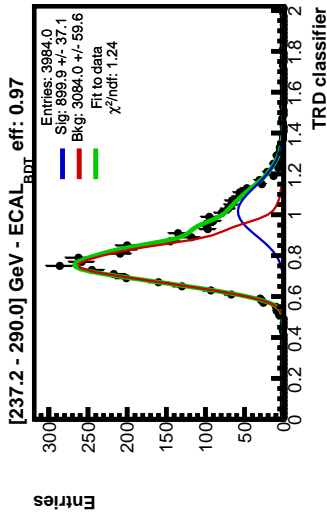
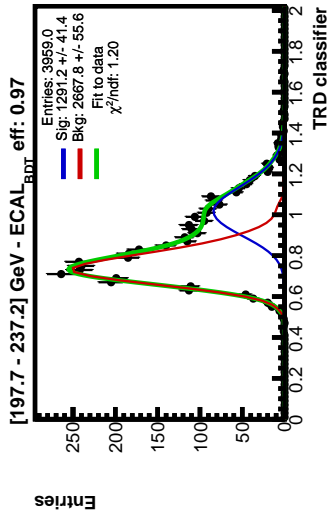
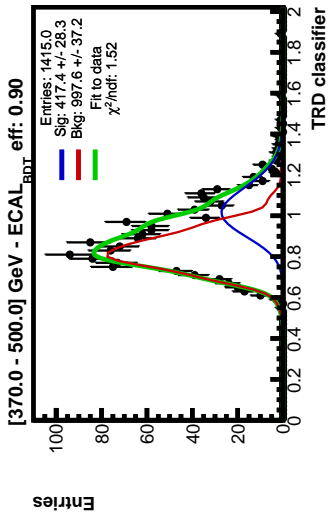
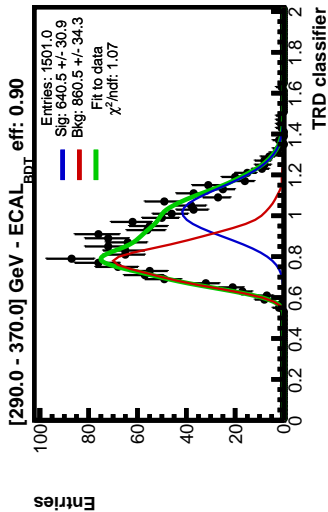
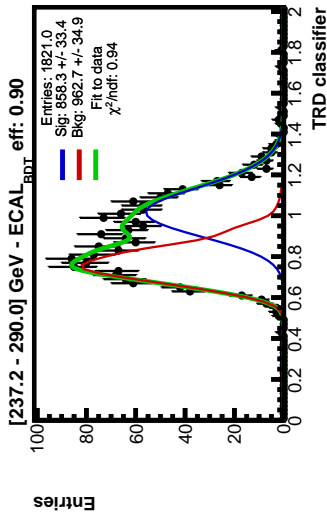
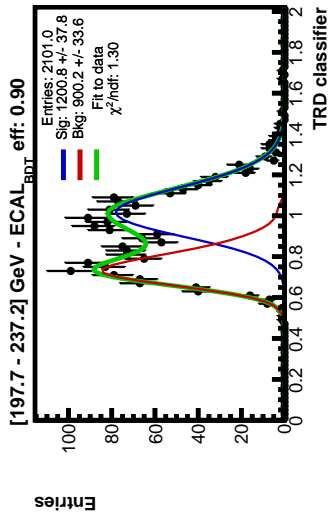
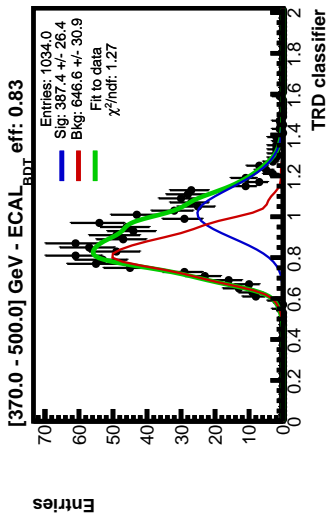
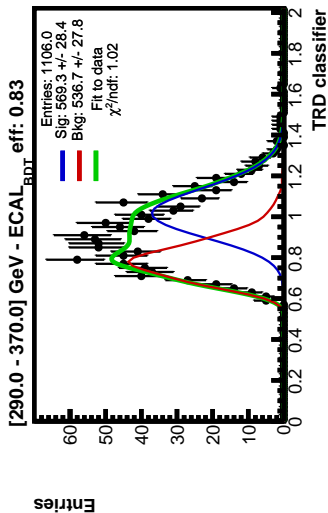
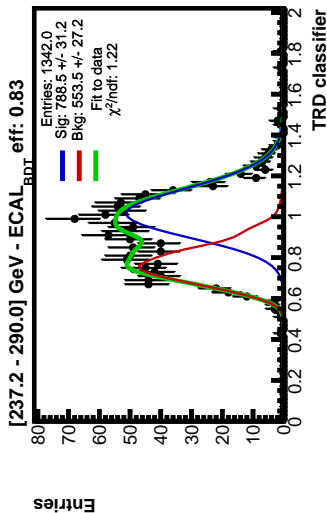
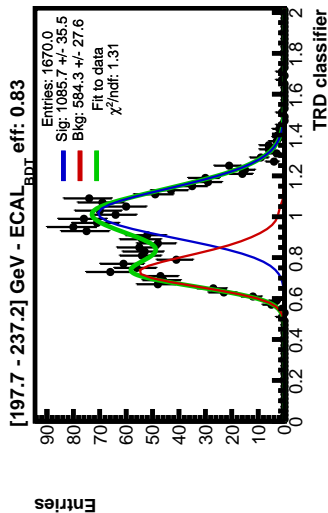
For each energy, the fit results for values of the ECAL_{BDT} efficiency ($\varepsilon_{\text{ECAL}}$) of 97%, 90%, and 83% is shown. The green line shows the sum of the signal template (in blue) and of the background template (in red) fitted to the data points (in black).

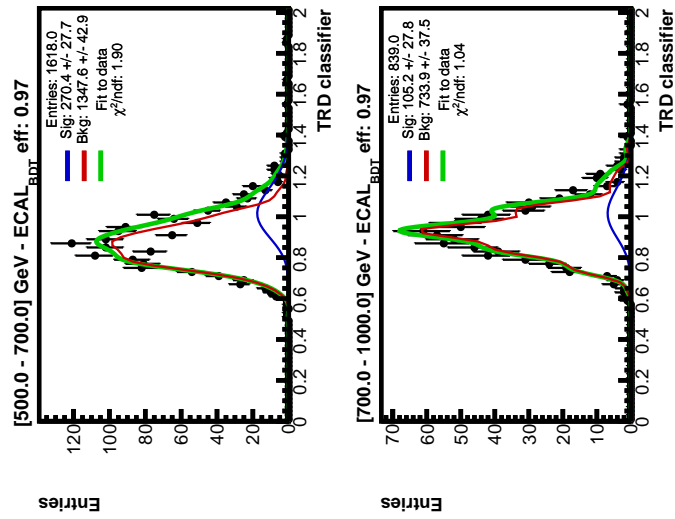
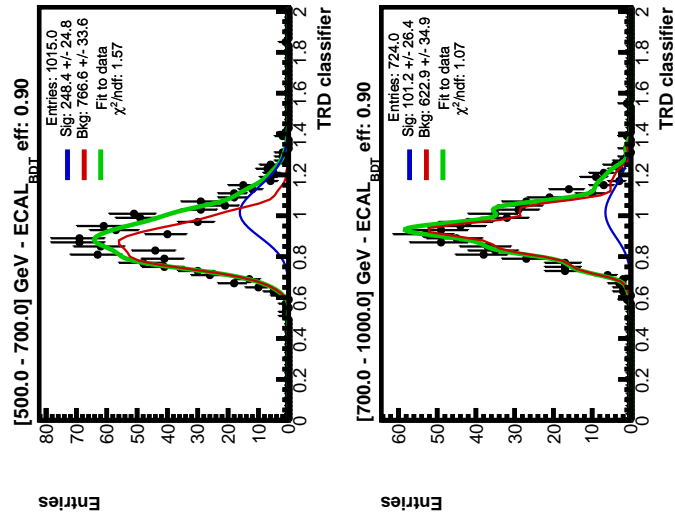
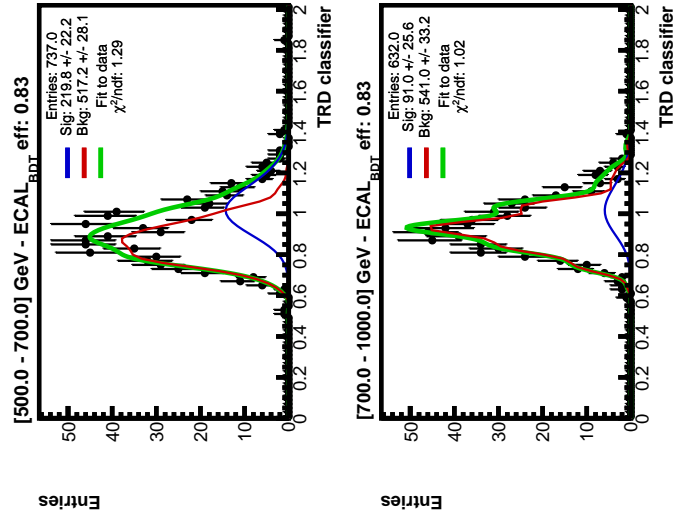












Appendix D

Differential acceptances for the $e^+ + e^-$ flux measurement

The results on the acceptance formulation discussed in Section 5.3.1 can be naturally extended for the calculation of the differential acceptances.

In case any dependence on the polar direction θ only has to be taken into account, Equation 5.4 used for the calculation of the differential acceptance for a planar detector with dimension σ_x , σ_y and σ_z , $\sigma_z \ll \sigma_{x,y}$, $S = \sigma_x \sigma_y$ and with detection efficiency $\varepsilon(E, \Omega) = 1 \forall (E, \Omega)$ reads instead:

$$A^{(\theta)}(\cos\theta) = \int_{2\pi} \int_S \cos\theta \, d\cos\theta \, d\phi \, dS = 2\pi S \cos\theta \quad [\text{m}^2 \text{rad}] \quad (\text{D.1})$$

Allowing also for dependencies in the azimuthal direction ϕ :

$$A^{(\theta, \phi)}(\cos\theta, \phi) = \int_S \cos\theta \, d\cos\theta \, dS = S \cos\theta \quad [\text{m}^2] \quad (\text{D.2})$$

The superscripts $^{(\theta)}$, $^{(\theta, \phi)}$ are used to indicate the differential nature of $A^{(\theta)}(\cos\theta)$ and $A^{(\theta, \phi)}(\cos\theta, \phi)$.

The result of Equation 5.5 for the calculation of acceptances using a MC simulation based approach can also be naturally extended to the calculation of differential acceptances. Assuming no dependence on ϕ , the differential acceptance $A^{(\theta)}(\widetilde{E}, \widetilde{\cos\theta})$ is calculated as:

$$A^{(\theta)}(\widetilde{E}, \widetilde{\cos\theta}) = A_{\text{gen}}^{(\theta)} \frac{N_{\text{sel}}^{(\theta)}(E, \cos\theta)}{N_{\text{gen}}^{(\theta)}(E, \cos\theta)} \quad (\text{D.3})$$

where $N_{\text{gen}}^{(\theta)}(E, \cos\theta)$ and $N_{\text{sel}}^{(\theta)}(E, \cos\theta)$ represent the number of particles generated and detected in the energy range $[E, E + \Delta E]$ and in the angular range $[\cos\theta, \cos\theta + \Delta \cos\theta]$. As discussed already in Section 5.3.1, the value of the acceptance determined using the binned MC simulation method is representative only for a certain value of energy (\widetilde{E}) and angle ($\widetilde{\cos\theta}, \widetilde{\phi}$) inside the energy and angular range in consideration, and they depend on the energy and angular spectrum of particle that crossed the detector. For an isotropic generated flux, $N_{\text{gen}}^{(\theta)}(E, \cos\theta)$ is easily related to the total number of generated particle $N_{\text{gen}}(E)$ by

$$N_{\text{gen}}^{(\theta)}(E, \cos\theta) = 2\cos\theta \, \Delta \cos\theta \, N_{\text{gen}}(E)$$

and can be used together with Equation D.1 to obtain the formula to determine $A^{(\theta)}(E, \cos\theta)$

$$A^{(\theta)}(\widetilde{E}, \widetilde{\cos\theta}) = A_{\text{gen}}^{(\theta)} \frac{N_{\text{sel}}^{(\theta)}}{2\cos\theta \, \Delta \cos\theta \, N_{\text{gen}}(E)} \quad (\text{D.4})$$

Introducing also the ϕ angular dependence, and considering the relation between the total number of generated particles $N_{\text{gen}}(E)$ and the number of particles $N_{\text{gen}}^{(\theta,\phi)}(E)$ generated in the angular interval $[\cos\theta, \Delta\cos\theta][\phi, \phi + \Delta\phi]$

$$N_{\text{gen}}^{(\theta,\phi)}(E) = \frac{\widetilde{\cos\theta} \Delta\cos\theta \Delta\phi}{\pi} N_{\text{gen}}(E)$$

the formula for the differential acceptance $A^{(\theta,\phi)}(\widetilde{E}, \widetilde{\cos\theta}, \widetilde{\phi})$ is similarly deduced as:

$$A^{(\theta,\phi)}(\widetilde{E}, \widetilde{\cos\theta}, \widetilde{\phi}) = A_{\text{gen}}^{(\theta,\phi)} \frac{\pi N_{\text{sel}}^{(\theta,\phi)}(E)}{N_{\text{gen}}(E) \widetilde{\cos\theta} \Delta\cos\theta \Delta\phi} \quad (\text{D.5})$$

where $N_{\text{sel}}^{(\theta,\phi)}$ represents the number of particle detected in the energy range $[E, E + \Delta E]$ and in the angular range $[\cos\theta, \cos\theta + \Delta\cos\theta], [\phi, \phi + \Delta\phi]$.

Similarly as before, Equation D.1 and D.2 can be substituted in the previous results to obtain the differential acceptances in the case of a planar generation surface:

$$A^{(\theta)}(\widetilde{E}, \widetilde{\cos\theta}) = \frac{\pi S N_{\text{sel}}^{(\theta)}}{N_{\text{gen}} \Delta\cos\theta} \quad (\text{D.6})$$

$$A^{(\theta,\phi)}(\widetilde{E}, \widetilde{\cos\theta}, \widetilde{\phi}) = \frac{\pi S N_{\text{sel}}^{(\theta,\phi)}}{N_{\text{gen}} \Delta\cos\theta \Delta\phi} \quad (\text{D.7})$$

The result on the differential acceptances $\mathcal{A}_{\text{MC}}^{(\theta,\phi)}$ and $\mathcal{A}_{\text{MC}}^{(\theta)}$ calculated according to Equation D.6 and Equation D.7 are shown in Figure D.1 and D.2. The acceptance correspond to the same selection used to evaluate the energy dependence of \mathcal{A}_{MC} already shown in Figure 5.3. The pattern in the azimuthal direction is given by the detector geometry, which is not cylindrical (due to, for example, to the square shape of the calorimeter). In the polar direction, the acceptance steeply decreases as the particle incoming direction gets more inclined. At $\theta \sim 20^\circ$ the acceptance is already decreased to less than 10% of its maximum value.

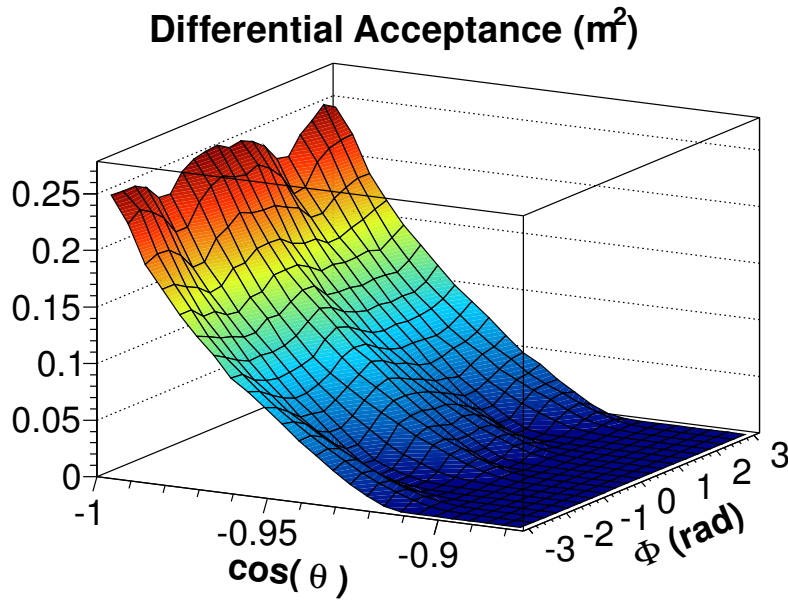


Figure D.1: Differential acceptance for the $(e^+ + e^-)$ selection described in Section 4.1 for 20 GeV electrons. The pattern in the azimuthal coordinate ϕ is caused by the detector geometry which does not have cylindrical symmetry.

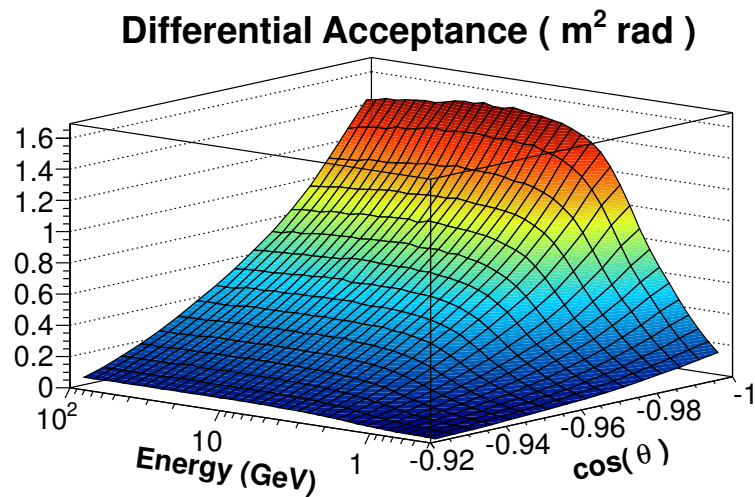


Figure D.2: Differential acceptance for the $(e^+ + e^-)$ selection described in Section 4.1. The acceptance has been integrated over the azimuthal angle ϕ . The differential acceptance decreases as a function of $\cos\theta$, vanishing at $\cos\theta \sim 0.92$, which represents the maximum aperture angle of the electromagnetic calorimeter.

Appendix E

Further aspects of the e^+ and e^- flux parametrization

In Section 6.3.2, the e^+ and e^- flux parametrization described by Equation 6.8 and by Equation 6.10 has been fit to the $\Phi_{e^+e^-}$ flux and to the positron fraction (PF) measurements.

The $\Phi_{e^+e^-}$ measurement alone does not provide enough information to test the hypotheses for the e^\pm production and propagation mechanisms. As discussed in Section 6.2, cosmic ray e^+ have different origins than cosmic ray e^- . Therefore, the data used to constrain the model parameters must distinguish between e^- and e^+ . The PF is sensitive to the different amounts of e^- and e^+ in cosmic rays. However a fit to the PF alone cannot resolve the normalization of the e^\pm fluxes, because it provides information only on relative differences between the e^- and e^+ fluxes and not on absolute quantities (see [176, 83] for an example of fit to the PF with the same data parametrization used in Section 6.3.2). Since the PF measurement carries a complementary information than that provided by the $\Phi_{e^+e^-}$ measurement, a combined fit to both the observables can be used to extract the full information from the experimental data. In this Appendix, technical aspects related to the combined fit to the $\Phi_{e^+e^-}$ and to the PF measurements are discussed.

Correlation between the datasets

In the combined fit to the $\Phi_{e^+e^-}$ and to the PF measurements, the correlations between the two datasets and between the systematic errors of the measurements have to be taken into account. Statistical fluctuations dominate the $\Phi_{e^+e^-}$ measurement uncertainty above 200 GeV and the PF measurement uncertainty above 10 GeV. The correlations between statistical fluctuations do not have any effect in the data interpretation below 10 GeV. Between 10 GeV and 200 GeV, the statistical fluctuations define the uncertainty for the PF measurement only, while the $\Phi_{e^+e^-}$ uncertainty is still dominated by the systematic uncertainty on the detector acceptance. Correlated statistical fluctuations may arise above 200 GeV where both the $\Phi_{e^+e^-}$ and the PF measurements are dominated by statistical uncertainties. The statistical fluctuations in the PF measurement above 200 GeV are dominated by the finite e^+ data sample and by the fluctuations of the background identified using a data-driven method similar to that used in this analysis (see Section 4.3). The $\Phi_{e^+e^-}$ measurement uncertainty above 200 GeV is instead defined by the statistical fluctuations of the $(e^+ + e^-)$ sample, mostly composed of e^- , and by the statistical fluctuations of the proton background which does not coincide with that of the PF measurement. The correlation between the statistical fluctuations is therefore expected to be unimportant¹. Below 10

¹The correlation between the statistical fluctuations between the two measurements could be qualitatively estimated by the comparison of the overlap between the two datasets *before* the signal identification procedure with the template fit approach.

GeV, where correlation between systematic uncertainties could bias the fit result, the $\Phi_{e^+e^-}$ systematic uncertainty is defined by the uncertainty to which the detector acceptance is known. This uncertainty does not affect the PF measurement. Below 10 GeV, the PF measurement systematic uncertainty is dominated by selection effects and by the bin-to-bin migration effects. For these reasons, in the analysis presented in Section 6.3.2 the correlations between the $\Phi_{e^+e^-}$ and the PF measurement uncertainties have been neglected.

An alternative approach is the use of the separate Φ_{e^-} and Φ_{e^+} measurements to extract the information from the data. The two measurements each provide complementary information about the e^- and e^+ fluxes. In addition to this, they are almost statistically uncorrelated by construction. A small statistical correlation is introduced by the migration of events with wrong measured charge sign (charge confusion effect). The systematic uncertainties are instead almost completely correlated between the Φ_{e^-} and the Φ_{e^+} measurements. On the other hand, as discussed already in Section 6.2, additional systematic effects increase the uncertainty of the separate flux measurements above the uncertainty of the $\Phi_{e^+e^-}$ measurement, and the combination of the Φ_{e^-} and Φ_{e^+} has less constraining power on the fit parameters than the combination of the PF and $\Phi_{e^+e^-}$ measurement. Moreover the $\Phi_{e^+e^-}$ measurement extend up to 1 TeV and it increases the maximum energy to which the data parametrizations can be tested. For these reasons, in the analysis presented in Section 6.3.2 the Φ_{e^-} and Φ_{e^+} parametrizations have been simultaneously fit to the $\Phi_{e^+e^-}$ and to the PF measurements, while the Φ_{e^-} and Φ_{e^+} flux measurements have been used for a consistency check of the AMS measurements.

Single power law parametrization assumptions

As discussed in Chapter 1, the spectra of particles produced and accelerated by SNR are expected to have a power law energy spectrum $\Phi(E) \propto E^{-\gamma}$ after their injection in the ISM. The diffusive propagation in the turbulent magnetic fields maintains, in first approximation, the spectral functional shape possibly with a different spectral index. A simple power law description can be therefore used to parametrize the flux of primary e^- produced and accelerated by SNR [89, 176, 83]. The same approximation holds for the description of the flux of secondary e^+ produced by the interactions of nuclei with the ISM. The secondary e^+ spectrum has roughly the same functional shape of the simple power law spectrum of the primary nuclei. Deviations from the power law energy dependence for secondary e^+ are observed at energies below 1 GeV using the solution of the transport equation, Equation 1.2 [47]. This effect is neglected in this analysis. At high energies, deviations from the power law spectrum are expected due to Synchrotron losses and to partial escape from the Galaxy. At low energies ionization and Coulomb interaction losses also modify the spectral shape. In the minimal approach used in Section 6.3.2 these effects are assumed to be negligible.

Energy scale systematic uncertainty

The systematic effect on the $\Phi_{e^+e^-}$ measurement due the minor uncertainty on the energy scale has been taken into account by introducing the uncertainty provided in Table F.2 for \tilde{E} in each energy point for the minimization procedure. The correlation between data points introduced by the energy scale uncertainty has not been introduced directly in the minimization routines. This source of correlation can change the result of the fit. In order to correctly take this into account in the definition of the parameter uncertainty, various possibilities have been explored.

The uncertainty on the energy scale ($\sigma(E)/E$) covers a possible energy independent miscalibration of the absolute energy scale and a possible energy dependent non-linearity of the energy scale. The real relative amount of these effects is not known.

As discussed in Section 6.3.1, the effect of the non-linearity can be conservatively assumed to be at most $0.5 \times \sigma(E)/E$, while the energy independent miscalibration can be conservatively assumed to be at most equal to $\sigma(E)/E$. In order to assess the systematic impact on the fit parameters due to the uncertainty of the energy measurement, the fit routine has been repeated on modified sets of data. The energy value of the data have been modified according to a constant, rigid shift of $\pm\sigma(E)/E$. The data have been also modified by applying an extreme non-linearity factor of $\pm 0.5 \times \sigma(E)/E$ covering the whole energy range, using a similar procedure to that used to assess the systematic uncertainty on the single power law spectral index discussed in Section 6.3.1. Since these possibilities represent the extreme cases covered by the uncertainty on the energy scale, the dispersion of the result fit parameters is a good estimator of the systematic effect of possible correlations between bins. In order to obtain a conservative estimation of this effect, for each parameter x the systematic uncertainty $\sigma^{(\text{energy})}$ is defined by the half difference between the maximum (x_{max}) and minimum (x_{min}) values obtained in the various trials:

$$\sigma^{(\text{energy})} = \frac{x_{\text{max}} - x_{\text{min}}}{2}$$

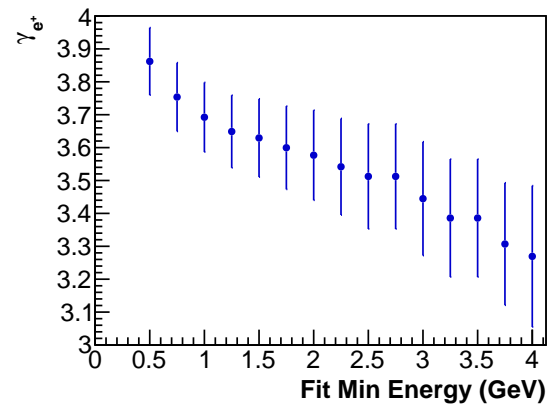
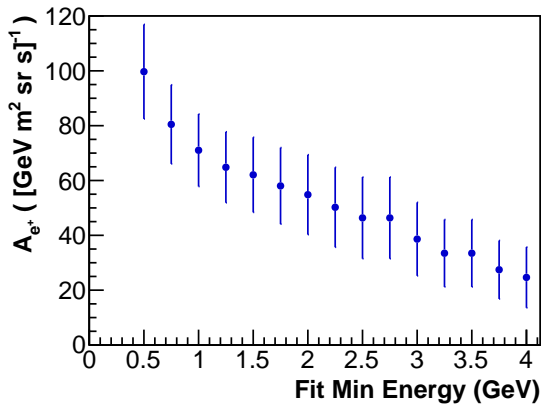
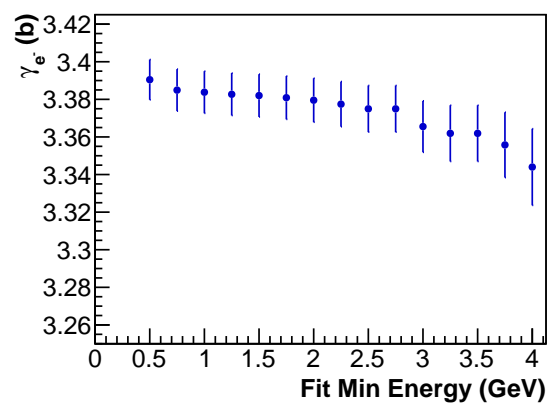
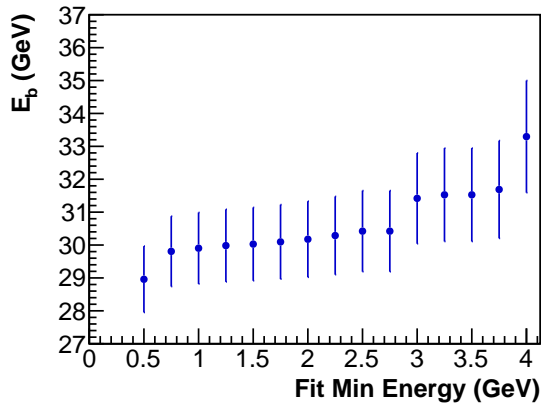
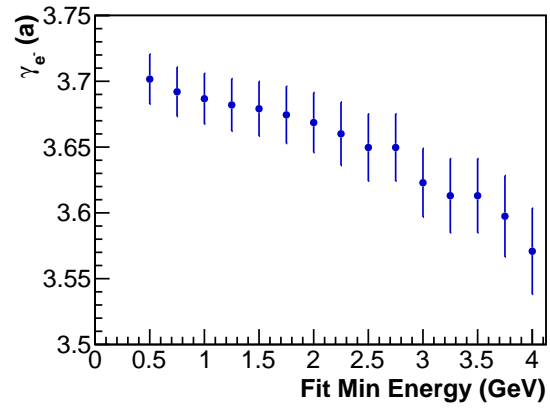
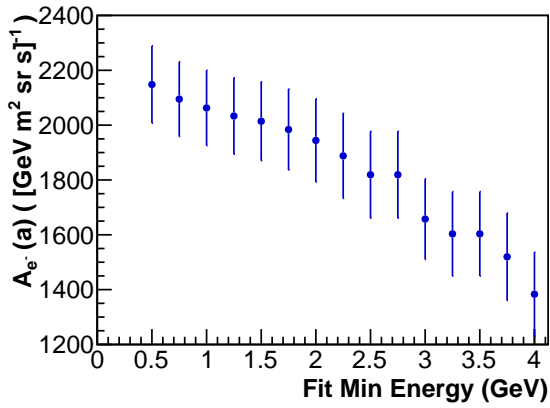
The systematic uncertainty derived using this approach is quoted, together with the parameter error provided by the minimization procedure, in Table 6.1. For most of the parameters, this uncertainty is negligible with respect to the error provided by the minimization routine. For some parameters it is comparable with the minimization routine uncertainty but it never dominates. The level of correlation between the parameters, shown in Figure 6.20, is not affected. Because of the precise energy measurement of the ECAL, the energy scale uncertainty does not affect significantly the result for the approach discussed in this section.

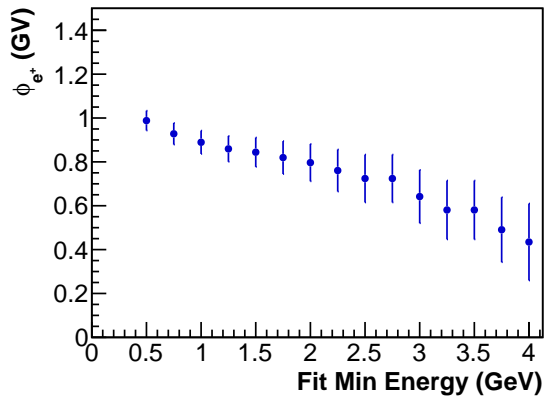
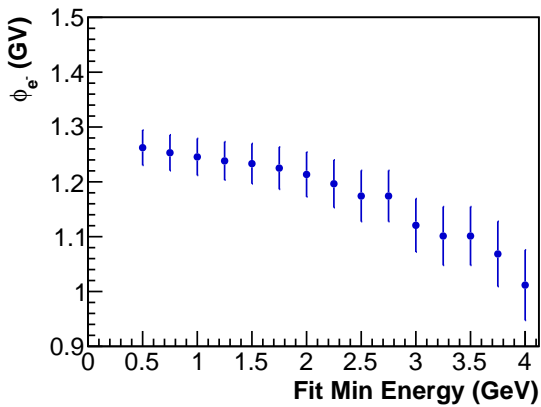
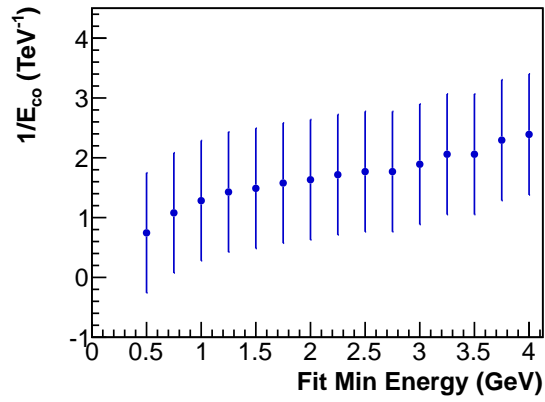
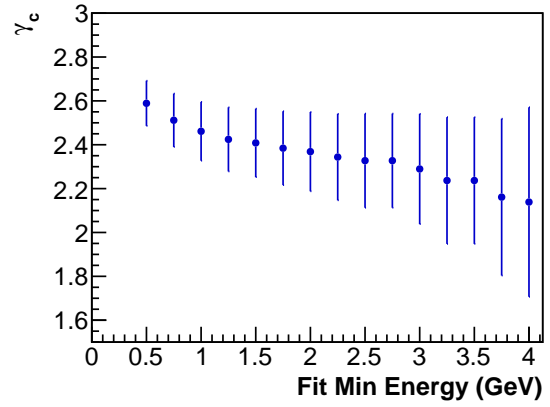
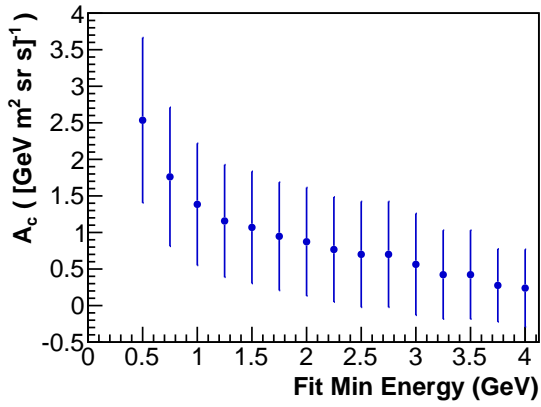
Stability study

The parameters that enter the definition of the Φ_{e^-} and Φ_{e^+} show a dependence on the fit minimum energy. This has been already shown in Figure 6.22 for a selection of parameters. This hints to the fact that the basic analytical model that been used, together with the parametrization of the solar modulation described by the *Force Field Approximation*, is not adequate to describe the current data.

In the following, the dependence of the fit parameters as function of the fit minimum energy is shown. The error bars represent the standard deviation of the parameter returned from the χ^2 minimization. In order of appearance:

1. A_{e^-} (a): single power law e^- flux normalization below the break energy;
2. γ_{e^-} (a): single power law e^- flux spectral index below the break energy;
3. E_b : single power law e^- spectral index energy break;
4. γ_{e^-} (b): single power law e^- flux spectral index above the break energy;
5. A_{e^+} : single power law e^+ flux normalization;
6. γ_{e^+} : single power law e^+ flux spectral index;
7. A_c : common e^\pm source flux normalization;
8. γ_c : common e^\pm source flux spectral index;
9. $\xi = 1/E_{co}$: inverse common e^\pm source cutoff energy;
10. ϕ_{e^-} : e^- solar modulation effective potential;
11. ϕ_{e^+} : e^+ solar modulation effective potential;





Appendix F

Tables

Table F.1: Contributions to the $\Phi_{e^+e^-}$ measurement uncertainty. $N_{(e^+e^-)}^{(E)}$ represents the number of $e^+ + e^-$ events identified in the data. The apex $^{(E)}$ indicates that $N_{(e^+e^-)}$ is reported here after the correction for the ECAL selection efficiency. The systematic uncertainty σ_{syst} is calculated as the quadratic sum of the systematic uncertainties from the event selection σ_{sel} , the acceptance σ_{acc} and the bin-to-bin migration σ_{migr} . Between 19 GeV and 132 GeV, σ_{sel} is compatible with purely statistical effects and does not contribute to the definition of σ_{syst} . The total uncertainty σ_{tot} is calculated as quadratic sum of σ_{syst} and of the statistical uncertainty σ_{stat} . The uncertainties quoted in the table are relative uncertainties. A bin-to-bin correlated uncertainty of 1.4% contributes to σ_{syst} . The bin boundaries and are the energies at the top of AMS.

Energy [GeV]	$N_{(e^+e^-)}^{(E)}$	σ_{sel}	σ_{acc}	σ_{migr}	σ_{syst}	σ_{stat}	σ_{tot}
0.50 – 0.65	2436	5.26×10^{-3}	1.96×10^{-1}	3.17×10^{-2}	1.99×10^{-1}	3.71×10^{-2}	2.02×10^{-1}
0.65 – 0.82	30304	1.79×10^{-3}	8.62×10^{-2}	2.59×10^{-2}	9.00×10^{-2}	8.64×10^{-3}	9.04×10^{-2}
0.82 – 1.01	78450	1.52×10^{-3}	6.93×10^{-2}	2.08×10^{-2}	7.24×10^{-2}	4.78×10^{-3}	7.25×10^{-2}
1.01 – 1.22	141590	1.84×10^{-3}	5.68×10^{-2}	1.65×10^{-2}	5.92×10^{-2}	3.36×10^{-3}	5.93×10^{-2}
1.22 – 1.46	219223	1.66×10^{-3}	4.72×10^{-2}	1.28×10^{-2}	4.90×10^{-2}	2.61×10^{-3}	4.90×10^{-2}
1.46 – 1.72	337091	1.62×10^{-3}	3.98×10^{-2}	9.85×10^{-3}	4.10×10^{-2}	2.07×10^{-3}	4.11×10^{-2}
1.72 – 2.00	449457	1.71×10^{-3}	3.40×10^{-2}	7.62×10^{-3}	3.48×10^{-2}	1.75×10^{-3}	3.49×10^{-2}
2.00 – 2.31	542028	1.33×10^{-3}	2.93×10^{-2}	5.96×10^{-3}	2.99×10^{-2}	1.55×10^{-3}	3.00×10^{-2}
2.31 – 2.65	618593	9.04×10^{-4}	2.55×10^{-2}	4.76×10^{-3}	2.59×10^{-2}	1.39×10^{-3}	2.60×10^{-2}
2.65 – 3.00	618284	8.75×10^{-4}	2.23×10^{-2}	3.95×10^{-3}	2.27×10^{-2}	1.37×10^{-3}	2.27×10^{-2}
3.00 – 3.36	638614	9.33×10^{-4}	2.02×10^{-2}	3.43×10^{-3}	2.05×10^{-2}	1.32×10^{-3}	2.05×10^{-2}
3.36 – 3.73	602344	7.43×10^{-4}	2.02×10^{-2}	3.10×10^{-3}	2.04×10^{-2}	1.36×10^{-3}	2.05×10^{-2}
3.73 – 4.12	578011	7.21×10^{-4}	2.02×10^{-2}	2.88×10^{-3}	2.04×10^{-2}	1.39×10^{-3}	2.04×10^{-2}
4.12 – 4.54	559104	7.96×10^{-4}	2.05×10^{-2}	2.74×10^{-3}	2.07×10^{-2}	1.41×10^{-3}	2.08×10^{-2}
4.54 – 5.00	546982	8.03×10^{-4}	2.05×10^{-2}	2.65×10^{-3}	2.07×10^{-2}	1.43×10^{-3}	2.07×10^{-2}
5.00 – 5.49	518522	9.85×10^{-4}	2.05×10^{-2}	2.59×10^{-3}	2.07×10^{-2}	1.47×10^{-3}	2.07×10^{-2}
5.49 – 6.00	481952	9.70×10^{-4}	2.05×10^{-2}	2.55×10^{-3}	2.07×10^{-2}	1.52×10^{-3}	2.07×10^{-2}
6.00 – 6.54	455373	7.82×10^{-4}	2.05×10^{-2}	2.52×10^{-3}	2.07×10^{-2}	1.58×10^{-3}	2.07×10^{-2}
6.54 – 7.10	416426	9.06×10^{-4}	2.05×10^{-2}	2.49×10^{-3}	2.07×10^{-2}	1.65×10^{-3}	2.07×10^{-2}
7.10 – 7.69	377746	8.09×10^{-4}	2.05×10^{-2}	2.47×10^{-3}	2.07×10^{-2}	1.74×10^{-3}	2.07×10^{-2}
7.69 – 8.30	332232	9.61×10^{-4}	2.05×10^{-2}	2.45×10^{-3}	2.07×10^{-2}	1.85×10^{-3}	2.07×10^{-2}
8.30 – 8.95	301029	7.48×10^{-4}	2.05×10^{-2}	2.43×10^{-3}	2.07×10^{-2}	1.95×10^{-3}	2.07×10^{-2}
8.95 – 9.62	262260	7.42×10^{-4}	2.05×10^{-2}	2.42×10^{-3}	2.07×10^{-2}	2.09×10^{-3}	2.08×10^{-2}
9.62 – 10.32	231756	7.40×10^{-4}	2.05×10^{-2}	2.40×10^{-3}	2.07×10^{-2}	2.22×10^{-3}	2.08×10^{-2}
10.3 – 11.0	201201	8.35×10^{-4}	2.05×10^{-2}	2.39×10^{-3}	2.07×10^{-2}	2.38×10^{-3}	2.08×10^{-2}
11.0 – 11.8	180547	5.27×10^{-4}	2.05×10^{-2}	2.37×10^{-3}	2.07×10^{-2}	2.51×10^{-3}	2.08×10^{-2}
11.8 – 12.6	158995	5.29×10^{-4}	2.05×10^{-2}	2.36×10^{-3}	2.07×10^{-2}	2.67×10^{-3}	2.08×10^{-2}

Energy [GeV]	$N_{e^+e^-}^{(E)}$	σ_{sel}	σ_{acc}	σ_{migr}	σ_{syst}	σ_{stat}	σ_{tot}
12.6 – 13.4	140240	6.39×10^{-4}	2.05×10^{-2}	2.34×10^{-3}	2.07×10^{-2}	2.85×10^{-3}	2.09×10^{-2}
13.4 – 14.2	122359	6.03×10^{-4}	2.05×10^{-2}	2.33×10^{-3}	2.07×10^{-2}	3.05×10^{-3}	2.09×10^{-2}
14.2 – 15.1	110264	$0.00 \times 10^{+00}$	2.05×10^{-2}	2.31×10^{-3}	2.07×10^{-2}	3.21×10^{-3}	2.09×10^{-2}
15.1 – 16.1	96749	6.62×10^{-4}	2.05×10^{-2}	2.30×10^{-3}	2.07×10^{-2}	3.43×10^{-3}	2.10×10^{-2}
16.1 – 17.0	86416	5.75×10^{-4}	2.05×10^{-2}	2.28×10^{-3}	2.07×10^{-2}	3.63×10^{-3}	2.10×10^{-2}
17.0 – 18.0	76445	6.23×10^{-4}	2.05×10^{-2}	2.27×10^{-3}	2.07×10^{-2}	3.86×10^{-3}	2.10×10^{-2}
18.0 – 19.0	68256	8.44×10^{-4}	2.05×10^{-2}	2.26×10^{-3}	2.07×10^{-2}	4.09×10^{-3}	2.11×10^{-2}
19.0 – 20.0	61412	5.14×10^{-4}	2.06×10^{-2}	2.24×10^{-3}	2.07×10^{-2}	4.31×10^{-3}	2.11×10^{-2}
20.0 – 21.1	55365	9.01×10^{-4}	2.06×10^{-2}	2.23×10^{-3}	2.07×10^{-2}	4.53×10^{-3}	2.12×10^{-2}
21.1 – 22.2	49690	7.01×10^{-4}	2.06×10^{-2}	2.22×10^{-3}	2.07×10^{-2}	4.79×10^{-3}	2.12×10^{-2}
22.2 – 23.4	45833	8.94×10^{-4}	2.06×10^{-2}	2.21×10^{-3}	2.07×10^{-2}	4.98×10^{-3}	2.13×10^{-2}
23.4 – 24.6	41633	7.58×10^{-4}	2.06×10^{-2}	2.20×10^{-3}	2.07×10^{-2}	5.23×10^{-3}	2.13×10^{-2}
24.6 – 25.9	39570	8.00×10^{-4}	2.06×10^{-2}	2.18×10^{-3}	2.07×10^{-2}	5.37×10^{-3}	2.14×10^{-2}
25.9 – 27.2	35977	7.57×10^{-4}	2.06×10^{-2}	2.17×10^{-3}	2.07×10^{-2}	5.63×10^{-3}	2.14×10^{-2}
27.2 – 28.7	33402	3.95×10^{-4}	2.06×10^{-2}	2.16×10^{-3}	2.07×10^{-2}	5.84×10^{-3}	2.15×10^{-2}
28.7 – 30.2	31006	5.97×10^{-4}	2.06×10^{-2}	2.15×10^{-3}	2.07×10^{-2}	6.06×10^{-3}	2.16×10^{-2}
30.2 – 31.8	27805	1.45×10^{-3}	2.06×10^{-2}	2.13×10^{-3}	2.07×10^{-2}	6.41×10^{-3}	2.17×10^{-2}
31.8 – 33.5	25688	7.00×10^{-4}	2.06×10^{-2}	2.12×10^{-3}	2.07×10^{-2}	6.68×10^{-3}	2.18×10^{-2}
33.5 – 35.4	23218	5.93×10^{-4}	2.06×10^{-2}	2.11×10^{-3}	2.07×10^{-2}	7.09×10^{-3}	2.19×10^{-2}
35.4 – 37.3	20988	7.30×10^{-4}	2.06×10^{-2}	2.10×10^{-3}	2.07×10^{-2}	7.40×10^{-3}	2.20×10^{-2}
37.3 – 39.4	19084	8.03×10^{-4}	2.06×10^{-2}	2.08×10^{-3}	2.07×10^{-2}	7.76×10^{-3}	2.21×10^{-2}
39.4 – 41.6	16936	1.06×10^{-3}	2.06×10^{-2}	2.07×10^{-3}	2.07×10^{-2}	8.23×10^{-3}	2.23×10^{-2}
41.6 – 44.0	15333	1.46×10^{-3}	2.06×10^{-2}	2.06×10^{-3}	2.07×10^{-2}	8.65×10^{-3}	2.25×10^{-2}
44.0 – 46.6	13645	7.22×10^{-4}	2.06×10^{-2}	2.04×10^{-3}	2.07×10^{-2}	9.18×10^{-3}	2.27×10^{-2}
46.6 – 49.3	12083	8.67×10^{-4}	2.07×10^{-2}	2.03×10^{-3}	2.08×10^{-2}	9.76×10^{-3}	2.29×10^{-2}
49.3 – 52.3	10865	1.39×10^{-3}	2.07×10^{-2}	2.01×10^{-3}	2.08×10^{-2}	1.03×10^{-2}	2.32×10^{-2}
52.3 – 55.6	9878	1.45×10^{-3}	2.07×10^{-2}	2.00×10^{-3}	2.08×10^{-2}	1.08×10^{-2}	2.34×10^{-2}
55.6 – 59.1	8926	1.83×10^{-3}	2.07×10^{-2}	1.98×10^{-3}	2.08×10^{-2}	1.14×10^{-2}	2.37×10^{-2}
59.1 – 63.0	7992	1.73×10^{-3}	2.07×10^{-2}	1.97×10^{-3}	2.08×10^{-2}	1.21×10^{-2}	2.40×10^{-2}
63.0 – 67.3	6981	1.93×10^{-3}	2.07×10^{-2}	1.95×10^{-3}	2.08×10^{-2}	1.29×10^{-2}	2.45×10^{-2}
67.3 – 72.0	6274	2.06×10^{-3}	2.07×10^{-2}	1.94×10^{-3}	2.08×10^{-2}	1.37×10^{-2}	2.49×10^{-2}
72.0 – 77.4	5620	2.47×10^{-3}	2.07×10^{-2}	1.92×10^{-3}	2.08×10^{-2}	1.45×10^{-2}	2.54×10^{-2}
77.4 – 83.4	5021	2.19×10^{-3}	2.07×10^{-2}	1.90×10^{-3}	2.08×10^{-2}	1.53×10^{-2}	2.58×10^{-2}
83.4 – 90.2	4546	2.38×10^{-3}	2.07×10^{-2}	1.88×10^{-3}	2.08×10^{-2}	1.61×10^{-2}	2.63×10^{-2}

Energy [GeV]	$N_{e^+e^-}^{(E)}$	σ_{sel}	σ_{acc}	σ_{migr}	σ_{syst}	σ_{stat}	σ_{tot}
90.2 – 98.1	4021	3.33×10^{-3}	2.08×10^{-2}	1.86×10^{-3}	2.09×10^{-2}	1.74×10^{-2}	2.72×10^{-2}
98 – 107	3546	3.25×10^{-3}	2.08×10^{-2}	1.84×10^{-3}	2.08×10^{-2}	1.83×10^{-2}	2.78×10^{-2}
107 – 118	3123	3.17×10^{-3}	2.08×10^{-2}	1.82×10^{-3}	2.09×10^{-2}	1.96×10^{-2}	2.87×10^{-2}
118 – 132	2758	4.01×10^{-3}	2.08×10^{-2}	1.79×10^{-3}	2.09×10^{-2}	2.10×10^{-2}	2.96×10^{-2}
132 – 149	2326	5.20×10^{-3}	2.08×10^{-2}	1.76×10^{-3}	2.15×10^{-2}	2.31×10^{-2}	3.15×10^{-2}
149 – 170	2053	4.08×10^{-3}	2.08×10^{-2}	1.73×10^{-3}	2.13×10^{-2}	2.46×10^{-2}	3.26×10^{-2}
170 – 198	1650	5.80×10^{-3}	2.09×10^{-2}	1.70×10^{-3}	2.17×10^{-2}	2.79×10^{-2}	3.54×10^{-2}
198 – 237	1326	8.82×10^{-3}	2.09×10^{-2}	1.65×10^{-3}	2.28×10^{-2}	3.18×10^{-2}	3.91×10^{-2}
237 – 290	958	1.11×10^{-2}	2.09×10^{-2}	1.61×10^{-3}	2.38×10^{-2}	3.90×10^{-2}	4.57×10^{-2}
290 – 370	702	1.55×10^{-2}	2.10×10^{-2}	1.55×10^{-3}	2.61×10^{-2}	4.90×10^{-2}	5.55×10^{-2}
370 – 500	474	2.13×10^{-2}	2.11×10^{-2}	1.48×10^{-3}	3.00×10^{-2}	6.82×10^{-2}	7.45×10^{-2}
500 – 700	261	3.76×10^{-2}	2.11×10^{-2}	1.41×10^{-3}	4.32×10^{-2}	1.04×10^{-1}	1.13×10^{-1}
700 – 1000	135	1.22×10^{-1}	2.12×10^{-2}	1.32×10^{-3}	1.23×10^{-1}	2.08×10^{-1}	2.42×10^{-1}

Table F.2: The electron plus positron flux, $\Phi_{e^+e^-}$, measured by AMS with its statistical and systematic uncertainties. The representative energy of the bin, \tilde{E} , is defined as described in the text with its systematic uncertainty derived from the energy scale uncertainty. The bin boundaries and \tilde{E} are the energies at the top of AMS.

Energy [GeV]	\tilde{E} [GeV]	$\Phi_{e^+e^-} \pm \sigma_{\text{stat}} \pm \sigma_{\text{syst}} [(\text{GeV} \cdot \text{m}^2 \cdot \text{sr} \cdot \text{s})^{-1}]$
0.50 – 0.65	0.57 ± 0.03	(2.71 ± 0.10 ± 0.54) × 10 ⁺¹
0.65 – 0.82	0.73 ± 0.03	(2.38 ± 0.02 ± 0.21) × 10 ⁺¹
0.82 – 1.01	0.91 ± 0.04	(2.17 ± 0.01 ± 0.16) × 10 ⁺¹
1.01 – 1.22	1.11 ± 0.05	(2.01 ± 0.01 ± 0.12) × 10 ⁺¹
1.22 – 1.46	1.33 ± 0.05	(1.78 ± 0.01 ± 0.09) × 10 ⁺¹
1.46 – 1.72	1.58 ± 0.06	(1.46 ± 0.00 ± 0.06) × 10 ⁺¹
1.72 – 2.00	1.85 ± 0.07	(1.19 ± 0.00 ± 0.04) × 10 ⁺¹
2.00 – 2.31	2.15 ± 0.08	(9.47 ± 0.01 ± 0.28) × 10 ⁰
2.31 – 2.65	2.47 ± 0.08	(7.48 ± 0.01 ± 0.19) × 10 ⁰
2.65 – 3.00	2.82 ± 0.09	(5.77 ± 0.01 ± 0.13) × 10 ⁰
3.00 – 3.36	3.17 ± 0.10	(4.81 ± 0.01 ± 0.10) × 10 ⁰
3.36 – 3.73	3.54 ± 0.11	(3.77 ± 0.01 ± 0.08) × 10 ⁰
3.73 – 4.12	3.92 ± 0.12	(2.99 ± 0.00 ± 0.06) × 10 ⁰
4.12 – 4.54	4.32 ± 0.12	(2.37 ± 0.00 ± 0.05) × 10 ⁰
4.54 – 5.00	4.76 ± 0.13	(1.87 ± 0.00 ± 0.04) × 10 ⁰
5.00 – 5.49	5.24 ± 0.14	(1.47 ± 0.00 ± 0.03) × 10 ⁰
5.49 – 6.00	5.74 ± 0.15	(1.16 ± 0.00 ± 0.02) × 10 ⁰
6.00 – 6.54	6.26 ± 0.15	(9.13 ± 0.01 ± 0.19) × 10 ⁻¹
6.54 – 7.10	6.81 ± 0.16	(7.24 ± 0.01 ± 0.15) × 10 ⁻¹
7.10 – 7.69	7.39 ± 0.17	(5.76 ± 0.01 ± 0.12) × 10 ⁻¹
7.69 – 8.30	7.99 ± 0.18	(4.57 ± 0.01 ± 0.09) × 10 ⁻¹
8.30 – 8.95	8.62 ± 0.19	(3.65 ± 0.01 ± 0.07) × 10 ⁻¹
8.95 – 9.62	9.28 ± 0.19	(2.92 ± 0.01 ± 0.06) × 10 ⁻¹
9.62 – 10.32	9.96 ± 0.20	(2.35 ± 0.01 ± 0.05) × 10 ⁻¹
10.3 – 11.0	10.7 ± 0.2	(1.89 ± 0.00 ± 0.04) × 10 ⁻¹
11.0 – 11.8	11.4 ± 0.2	(1.54 ± 0.00 ± 0.03) × 10 ⁻¹
11.8 – 12.6	12.2 ± 0.2	(1.26 ± 0.00 ± 0.03) × 10 ⁻¹
12.6 – 13.4	13.0 ± 0.3	(1.03 ± 0.00 ± 0.02) × 10 ⁻¹
13.4 – 14.2	13.8 ± 0.3	(8.42 ± 0.03 ± 0.17) × 10 ⁻²
14.2 – 15.1	14.7 ± 0.3	(6.91 ± 0.02 ± 0.14) × 10 ⁻²

Energy [GeV]	\tilde{E} [GeV]	$\Phi_{e^+e^-} \pm \sigma_{\text{stat}} \pm \sigma_{\text{syst}} [(\text{GeV} \cdot \text{m}^2 \cdot \text{sr} \cdot \text{s})^{-1}]$
15.1 – 16.1	15.6 ± 0.3	(5.73 ± 0.02 ± 0.12) × 10 ⁻²
16.1 – 17.0	16.5 ± 0.3	(4.74 ± 0.02 ± 0.10) × 10 ⁻²
17.0 – 18.0	17.5 ± 0.3	(3.93 ± 0.02 ± 0.08) × 10 ⁻²
18.0 – 19.0	18.5 ± 0.4	(3.29 ± 0.01 ± 0.07) × 10 ⁻²
19.0 – 20.0	19.5 ± 0.4	(2.75 ± 0.01 ± 0.06) × 10 ⁻²
20.0 – 21.1	20.6 ± 0.4	(2.31 ± 0.01 ± 0.05) × 10 ⁻²
21.1 – 22.2	21.7 ± 0.4	(1.94 ± 0.01 ± 0.04) × 10 ⁻²
22.2 – 23.4	22.8 ± 0.5	(1.65 ± 0.01 ± 0.03) × 10 ⁻²
23.4 – 24.6	24.0 ± 0.5	(1.39 ± 0.01 ± 0.03) × 10 ⁻²
24.6 – 25.9	25.2 ± 0.5	(1.19 ± 0.01 ± 0.02) × 10 ⁻²
25.9 – 27.2	26.6 ± 0.5	(9.98 ± 0.06 ± 0.20) × 10 ⁻³
27.2 – 28.7	28.0 ± 0.6	(8.52 ± 0.05 ± 0.17) × 10 ⁻³
28.7 – 30.2	29.4 ± 0.6	(7.22 ± 0.04 ± 0.15) × 10 ⁻³
30.2 – 31.8	31.0 ± 0.6	(6.03 ± 0.04 ± 0.12) × 10 ⁻³
31.8 – 33.5	32.7 ± 0.7	(5.15 ± 0.03 ± 0.11) × 10 ⁻³
33.5 – 35.4	34.4 ± 0.7	(4.29 ± 0.03 ± 0.09) × 10 ⁻³
35.4 – 37.3	36.3 ± 0.7	(3.64 ± 0.03 ± 0.08) × 10 ⁻³
37.3 – 39.4	38.3 ± 0.8	(3.11 ± 0.02 ± 0.06) × 10 ⁻³
39.4 – 41.6	40.5 ± 0.8	(2.59 ± 0.02 ± 0.05) × 10 ⁻³
41.6 – 44.0	42.8 ± 0.9	(2.18 ± 0.02 ± 0.04) × 10 ⁻³
44.0 – 46.6	45.3 ± 0.9	(1.81 ± 0.02 ± 0.04) × 10 ⁻³
46.6 – 49.3	47.9 ± 1.0	(1.49 ± 0.01 ± 0.03) × 10 ⁻³
49.3 – 52.3	50.8 ± 1.0	(1.24 ± 0.01 ± 0.03) × 10 ⁻³
52.3 – 55.6	53.9 ± 1.1	(1.04 ± 0.01 ± 0.02) × 10 ⁻³
55.6 – 59.1	57.3 ± 1.1	(8.62 ± 0.10 ± 0.18) × 10 ⁻⁴
59.1 – 63.0	61.0 ± 1.2	(7.06 ± 0.09 ± 0.15) × 10 ⁻⁴
63.0 – 67.3	65.1 ± 1.3	(5.62 ± 0.07 ± 0.12) × 10 ⁻⁴
67.3 – 72.0	69.6 ± 1.4	(4.56 ± 0.06 ± 0.09) × 10 ⁻⁴
72.0 – 77.4	74.6 ± 1.5	(3.66 ± 0.05 ± 0.08) × 10 ⁻⁴
77.4 – 83.4	80.3 ± 1.6	(2.91 ± 0.04 ± 0.06) × 10 ⁻⁴
83.4 – 90.2	86.7 ± 1.7	(2.32 ± 0.04 ± 0.05) × 10 ⁻⁴
90.2 – 98.1	94.0 ± 1.9	(1.78 ± 0.03 ± 0.04) × 10 ⁻⁴
98 – 107	103 ± 2	(1.37 ± 0.03 ± 0.03) × 10 ⁻⁴
107 – 118	113 ± 2	(1.01 ± 0.02 ± 0.02) × 10 ⁻⁴

Energy [GeV]	\tilde{E} [GeV]	$\Phi_{e^+e^-} \pm \sigma_{\text{stat}} \pm \sigma_{\text{syst}}$ [(GeV · m ² · sr · s) ⁻¹]
118 – 132	125 ± 3	(7.26 ± 0.15 ± 0.15) × 10 ⁻⁵
132 – 149	140 ± 3	(5.04 ± 0.12 ± 0.11) × 10 ⁻⁵
149 – 170	159 ± 3	(3.55 ± 0.09 ± 0.08) × 10 ⁻⁵
170 – 198	183 ± 4	(2.17 ± 0.06 ± 0.05) × 10 ⁻⁵
198 – 237	216 ± 4	(1.27 ± 0.04 ± 0.03) × 10 ⁻⁵
237 – 290	262 ± 5	(6.89 ± 0.27 ± 0.16) × 10 ⁻⁶
290 – 370	327 ± 7	(3.45 ± 0.17 ± 0.09) × 10 ⁻⁶
370 – 500	429 ± 13	(1.45 ± 0.10 ± 0.04) × 10 ⁻⁶
500 – 700	589 ± 22	(5.41 ± 0.56 ± 0.23) × 10 ⁻⁷
700 – 1000	832 ± 38	(1.90 ± 0.40 ± 0.23) × 10 ⁻⁷

List of Figures

1.1	All-particle cosmic ray differential energy spectrum	6
1.2	Galactic cosmic rays solar system abundances	7
1.3	B/C and $^{10}\text{Be}/^9\text{Be}$ measurements	11
1.4	Solar wind modulation effect on the proton flux	12
1.5	Geomagnetic field configuration	13
1.6	Geomagnetic field intensity	14
1.7	Geometric visualization of Geomagnetic Cutoff	15
1.8	The PAMELA satellite detector	16
1.9	The ATIC balloon borne detector	17
1.10	The Pierre Auger Observatory ground detector	18
1.11	Energy losses for electron and nucleon cosmic rays during propagation	20
1.12	The Φ_{e^-} , Φ_{e^+} , $\Phi_{e^+e^-}$ and $e^+/(e^+ + e^-)$ measurements	22
1.13	Acceleration of e^\pm in pulsar wind nebulae	23
1.14	Pulsar contribution to the e^\pm flux	24
1.15	Nearby pulsar fit to the positron fraction	25
1.16	Galaxy rotational curves	27
1.17	The <i>Bullet Cluster</i>	28
1.18	The Cosmic Microwave Background power spectrum	30
1.19	WIMP number density evolution in the early Universe	32
1.20	Dark Matter experimental searches	34
1.21	Dark Matter direct search constraints	36
1.22	Higgs-portal model for Dark Matter search constraints	37
1.23	Examples of Dark Matter searches using γ rays	39
1.24	The antiproton flux measurements	40
1.25	Dark Matter contributions to the positron fraction	42
1.26	Dark Matter annihilation cross section boost factor	42
1.27	Dark Matter annihilation fit example to the positron fraction	43
1.28	Dark Matter constraints set by the AMS positron fraction measurement	44
2.1	The AMS detector	48
2.2	The Transition Radiation Detector (TRD) subdetector	49
2.3	The TRD module	50
2.4	TRD electron/proton rejection	50
2.5	The TRD gas system	51
2.6	The Time Of Flight (TOF) subdetector	52
2.7	TOF velocity resolution and charge measurement	52
2.8	AMS permanent magnet	53
2.9	AMS magnet field configuration	54

2.10	The Silicon Tracker subdetector	55
2.11	Silicon Tracker nuclei charge measurement	55
2.12	Silicon Tracker rigidity measurement resolution	56
2.13	The Ring Imaging Cherenkov (RICH) subdetector	57
2.14	RICH charge spectrum	58
2.15	The Electromagnetic Calorimeter (ECAL) subdetector	59
2.16	ECAL energy resolution	60
2.17	ECAL energy resolution	60
2.18	DAQ block diagram	61
2.19	ISS orbit and DAQ parameters	63
2.20	AMS sensitivity for primordial antimatter search	64
3.1	MC generated statistics. Comparison with ISS data	68
4.1	Event display of a 600 GeV electron	71
4.2	AMS data taking parameters	74
4.3	AMS DAQ quality time dependence	74
4.4	The TOF velocity measurement	76
4.5	Definition of ECAL fiducial volume	77
4.6	ECAL-Tracker geometrical matching	77
4.7	TRD hits matching with Tracker Track	78
4.8	The Tracker charge measurement	79
4.9	TRD electron/Helium likelihood ratio	80
4.10	Reconstructed Tracker tracks energy dependence	81
4.11	Correlation between reconstructed Tracker tracks and interaction events	82
4.12	ISS position dependent geomagnetic rigidity cutoff	83
4.13	Efficiency of selection to define the data sample	84
4.14	ECAL BDT distribution for electrons and protons	85
4.15	ECAL BDT energy dependence for electrons	86
4.16	ECAL BDT distribution for data and MC electrons	87
4.17	ECAL longitudinal and lateral distributions for data and MC electrons	88
4.18	ECAL energy measurement for test beam and MC simulation protons	89
4.19	Energy/Momentum matching	90
4.20	ECAL longitudinal BDT input variables	91
4.21	ECAL longitudinal BDT distribution for electrons and protons	91
4.22	ECAL longitudinal BDT data/MC comparison	92
4.23	TRD single tube ADC spectra	93
4.24	TRD discriminator comparison	95
4.25	TRD discriminator energy dependence	96
4.26	TRD classifier energy dependence for MC electrons	96
4.27	Signal identification procedure scheme	98
4.28	TRD classifier templates for electrons and protons	99
4.29	TRD classifier template energy dependence	100
4.30	Signal/Background ratio in the ($e^+ + e^-$) fitted sample	101
4.31	TRD classifier fit example	102
4.32	($e^+ + e^-$) energy spectrum identified in data and ECAL selection efficiency	103
4.33	ECAL BDT efficiency	104
4.34	Characterization of the template fit error	105

4.35	TRD classifier proton template categories	108
4.36	Impact of the selection on the measured signal yield	110
4.37	Selection systematic uncertainty definition	111
4.38	Selection systematic uncertainty energy dependence	112
4.39	Choice of the most sensitive ECAL selection	113
4.40	Energy dependence of the statistical and selection systematic uncertainty	114
5.1	Exposure time	118
5.2	Electron trigger efficiency	120
5.3	Acceptance for different steps of ($e^+ + e^-$) selection	123
5.4	Definition of the geometric acceptance	124
5.5	AMS acceptance analytic parametrization	125
5.6	TOF reconstruction data/MC comparison	128
5.7	Relativistic and downward-going particle data/MC comparison	129
5.8	Tracker reconstruction data/MC comparison	129
5.9	TRD acceptance and quality data/MC comparison	130
5.10	ECAL fiducial volume data/MC comparison	131
5.11	ECAL reconstruction data/MC comparison	132
5.12	ECAL-Tracker matching data/MC comparison	132
5.13	Unitary charge selection data/MC comparison	133
5.14	Single track selection data/MC comparison	134
5.15	Trigger data/MC comparison	136
5.16	Electron control sample systematic uncertainty	138
5.17	Energy dependence for the single cut data/MC correction	139
5.18	Acceptance correction tagging error energy dependence	140
5.19	Acceptance correction absolute error energy dependence	141
5.20	Acceptance correction	142
5.21	Contributions to the acceptance correction systematic uncertainty	142
5.22	Comparison of different methods to evaluate the acceptance systematic uncertainty	144
5.23	Acceptance correction systematic uncertainty	145
6.1	ECAL energy scale time stability	149
6.2	ECAL energy resolution and absolute scale uncertainty	150
6.3	ECAL resolution matrix	151
6.4	Contribution of the bin-to-bin migration to the flux uncertainty	152
6.5	Systematic effect induced by a miscalibration of the ECAL energy measurement	152
6.6	Definition of the most representative energy value in a bin	154
6.7	Summary of contributions to the $\Phi_{e^+e^-}$ measurement uncertainty	156
6.8	The AMS $\Phi_{e^+e^-}$ measurement from 0.5 GeV to 1 TeV	157
6.9	The AMS $\Phi_{e^+e^-}$ measurement from 0.5 GeV to 1 TeV	158
6.10	The $\Phi_{e^+e^-}$ measurement by recent space experiments	159
6.11	Energy scale systematic impact on the $\Phi_{e^+e^-}$ flux measurement	160
6.12	The $\Phi_{e^+e^-}$ measurement compared with non-native data	161
6.13	The Φ_{e^-} and Φ_{e^+} flux measurements compared with non-native data	162
6.14	$\Phi_{e^+e^-}$ Single power law fit scan	164
6.15	Minimum energy determination for a single power law data parametrization	165
6.16	$\Phi_{e^+e^-}$ single power law parametrization	165
6.17	$\Phi_{e^+e^-}$ and positron fraction combined fit with simple model from 30 GeV	169

6.18	$\Phi_{e^+e^-}$ and positron fraction combined fit with simple model from 0.5 GeV	171
6.19	$\Phi_{e^+e^-}$ and positron fraction combined fit local agreement	172
6.20	Correlation matrix for the $\Phi_{e^+e^-}$ and positron fraction combined fit	172
6.21	Power law contributions to Φ_{pos}	174
6.22	Dependence of selected fit parameters on the minimum fit energy	174
6.23	Balloon and space detector overview and outlook	183
A.1	AMS collected events	186
B.1	ECAL longitudinal energy deposit renormalization procedure	189
B.2	ECAL longitudinal classifier performance comparison	190
B.3	Comparison between the $(e^+ + e^-)$ flux measurement performed with different ECAL longitudinal BDT cuts	191
D.1	AMS angular differential acceptance	203
D.2	AMS angular differential acceptance	203

Bibliography

- [1] M. Aguilar et al. “Precision Measurement of the ($e^+ + e$) Flux in Primary Cosmic Rays from 0.5 GeV to 1 TeV with the Alpha Magnetic Spectrometer on the International Space Station”. In: *Phys. Rev. Lett.* 113 (2014), p. 221102.
- [2] A. A. Abdo et al. “Observation of supernova remnant IC 443 with the FERMI Large Area Telescope”. In: *The Astrophysical Journal* 712 (2010), p. 459.
- [3] The CMS collaboration. “Observation of a new boson at a mass of 125 GeV with the CMS experiment at the LHC”. In: *Physics Letters B* 716 (2012), p. 30.
- [4] The ATLAS collaboration. “Observation of a new particle in the search for the Standard Model Higgs boson with the ATLAS detector at the LHC”. In: *Physics Letters B* 716 (2012), p. 1.
- [5] R. L. Golden et al. “Measurement of the positron to electron ratio in the cosmic rays above 5-GeV”. In: *The Astrophysical Journal* 457 (1996), p. 103.
- [6] M. Boezio et al. “The Cosmic-Ray Electron and Positron Spectra Measured at 1 AU during Solar Minimum Activity”. In: *The Astrophysical Journal* 532 (2000), p. 653.
- [7] J. Chang et al. “An excess of cosmic ray electrons at energies of 300-800 GeV”. In: *Nature* 456 (2008), p. 362.
- [8] S. Torii et al. “The Energy Spectrum of Cosmic-Ray Electrons from 10 to 100 GeV Observed with a Highly Granulated Imaging Calorimeter”. In: *The Astrophysical Journal* 559 (2001), p. 973.
- [9] K. Yoshida et al. “Cosmic-ray electron spectrum above 100 GeV from PPB-BETS experiment in Antarctica”. In: *Advances in Space Research* 42 (2008), p. 1670.
- [10] S. W. Barwick et al. “The Energy Spectra and Relative Abundances of Electrons and Positrons in the Galactic Cosmic Radiation”. In: *The Astrophysical Journal* 498 (1998), p. 779.
- [11] M. A. DuVernois et al. “Cosmic-Ray Electrons and Positrons from 1 to 100 GeV: Measurements with HEAT and Their Interpretation”. In: *The Astrophysical Journal* 559 (2001), p. 296.
- [12] C. Grimani et al. “Measurements of the absolute energy spectra of cosmic-ray positrons and electrons above 7-GeV”. In: *Astron. Astrophys.* 392 (2002), p. 287.
- [13] R. L. Golden et al. “Observations of cosmic ray electrons and positrons using an imaging calorimeter”. In: *The Astrophysical Journal* 436 (1994), p. 769.
- [14] J. Alcaraz et al. “Leptons in near earth orbit”. In: *Physics Letters B* 484 (2000), p. 10.
- [15] M. Aguilar et al. “Cosmic-ray positron fraction measurement from 1 to 30-GeV with AMS-01”. In: *Physics Letter B* 646 (2007), p. 145.
- [16] O. Adriani et al. “Cosmic-Ray Electron Flux Measured by the PAMELA Experiment between 1 and 625 GeV”. In: *Phys. Rev. Lett.* 106 (2011), p. 201101.

- [17] O. Adriani et al. “An anomalous positron abundance in cosmic rays with energies 1.5-100 GeV”. In: *Nature* 458 (2009), p. 607.
- [18] M. Ackermann et al. “Fermi LAT observations of cosmic-ray electrons from 7 GeV to 1 TeV”. In: *Phys. Rev. D* 82 (2010), p. 092004.
- [19] M. Ackermann et al. “Measurement of Separate Cosmic-Ray Electron and Positron Spectra with the Fermi Large Area Telescope”. In: *Phys. Rev. Lett.* 108 (2012), p. 011103.
- [20] F. Aharonian et al. “Energy Spectrum of Cosmic-Ray Electrons at TeV Energies”. In: *Phys. Rev. Lett.* 101 (2008), p. 261104.
- [21] F. Aharonian et al. “Probing the ATIC peak in the cosmic-ray electron spectrum with H.E.S.S.” In: *Astron. Astrophys.* 508 (2009), p. 561.
- [22] C. D. Anderson. “The Positive Electron”. In: *Phys. Rev.* 43 (1933), p. 491.
- [23] S. H. Neddermeyer and C. D. Anderson. “Note on the Nature of Cosmic-Ray Particles”. In: *Phys. Rev.* 51 (1937), p. 884.
- [24] C. M. G. Lattes, G. P. S. Occhialini, and C. F. Powell. “Observation of the tracks of slow mesons in photographic emulsions”. In: *Nature* 160 (1947), p. 453.
- [25] G. D. Rochester and C. C. Butler. “Evidence for the Existence of New Unstable Elementary Particles”. In: *Nature* 160 (1947), p. 855.
- [26] M. Aguilar et al. “Electron and Positron Fluxes in Primary Cosmic Rays Measured with the Alpha Magnetic Spectrometer on the International Space Station”. In: *Phys. Rev. Lett.* 113 (2014), p. 121102.
- [27] L. Baldini. “Space-Based Cosmic-Ray and Gamma-Ray Detectors: a Review”. In: *ArXiv e-prints* (2014). eprint: 1407.7631.
- [28] J. S. George et al. “Elemental composition and energy spectra of galactic cosmic rays during solar cycle 23”. In: *The Astrophysical Journal* 698 (2009), p. 1666.
- [29] E. Fermi. “On the Origin of the Cosmic Radiation”. In: *Phys. Rev.* 75 (1949), p. 1169.
- [30] M. S. Longair. *High energy astrophysics*. Vol. 2. Cambridge University Press, 2002.
- [31] F. A. Aharonian et al. “High-energy particle acceleration in the shell of a supernova remnant”. In: *Nature* 432 (2004), p. 75.
- [32] J. R. Hoerandel. “A review of experimental results at the knee”. In: *Journal of Physics: Conference Series* 47 (2006), p. 41.
- [33] K. Greisen. “End to the Cosmic-Ray Spectrum?” In: *Phys. Rev. Lett.* 16 (1966), p. 748.
- [34] J. Abraham et al. “Measurement of the energy spectrum of cosmic rays above 1018 eV using the Pierre Auger Observatory”. In: *Physics Letters B* 685 (2010), p. 239.
- [35] A. W. Strong, I. V. Moskalenko, and V. S. Ptuskin. “Cosmic-Ray Propagation and Interactions in the Galaxy”. In: *Annual Review of Nuclear and Particle Science* 57 (2007), p. 285.
- [36] R. Beck. “Galactic and extragalactic magnetic fields a concise review”. In: *Astrophys. Space Sci. Trans.* 5 (2009), p. 43.
- [37] G. Brunetti et al. “Alfvénic reacceleration of relativistic particles in galaxy clusters: MHD waves, leptons and hadrons”. In: *Monthly Notices of the Royal Astronomical Society* 350 (2004), p. 1174.
- [38] D. Breitschwerdt and T. Schmutzler. “The dynamical signature of the ISM in soft X-rays. I. Diffuse soft X-rays from galaxies”. In: *Astron. Astrophys.* 347 (1999), p. 650.

- [39] A. W. Strong and I. V. Moskalenko. “Propagation of Cosmic-Ray Nucleons in the Galaxy”. In: *The Astrophysical Journal* 509 (1998), p. 212.
- [40] V. S. Ptuskin et al. “Transport of relativistic nucleons in a galactic wind driven by cosmic rays”. In: *Astron. Astrophys.* 321 (1997), p. 434.
- [41] I. Gebauer and W. de Boer. “An Anisotropic Propagation Model for Galactic Cosmic Rays”. In: *ArXiv e-prints* (2009). eprint: 0910.2027 (astro-ph.GA).
- [42] A. Putze, L. Derome, and D. Maurin. “A Markov Chain Monte Carlo technique to sample transport and source parameters of Galactic cosmic rays. II. Results for the diffusion model combining B/C and radioactive nuclei”. In: *Astron. Astrophys.* 516 (2010).
- [43] *GALPROP code*. URL: <http://galprop.stanford.edu/>.
- [44] *DRAGON code*. URL: <http://dragon.hepforge.org/DRAGON/Home.html>.
- [45] V. L. Ginzburg and V. S. Ptuskin. “On the origin of cosmic rays: Some problems in high-energy astrophysics”. In: *Rev. Mod. Phys.* 48 (1976), p. 161.
- [46] G. Di Bernardo et al. “Cosmic ray electrons, positrons and the synchrotron emission of the Galaxy: consistent analysis and implications”. In: *Journal of Cosmology and Astroparticle Physics* 3 (2013), p. 36.
- [47] S. Kunz. “Constraints on Transport Models for Galactic Cosmic Rays and their Implications for the Anomalous Positron Abundance”. PhD thesis. Karlsruhe Institute of Technology, 2014.
- [48] T. Hams et al. “Measurement of the Abundance of Radioactive ^{10}Be and Other Light Isotopes in Cosmic Radiation up to 2 GeV Nucleon $^{-1}$ with the Balloon-borne Instrument ISOMAX”. In: *The Astrophysical Journal* 611 (2004), p. 892.
- [49] E. N. Parker. “Dynamics of the Interplanetary Gas and Magnetic Fields.” In: *The Astrophysical Journal* 128 (1958), p. 664.
- [50] L. J. Gleeson and W. I. Axford. “Solar Modulation of Galactic Cosmic Rays”. In: *The Astrophysical Journal* 154 (1968), p. 1011.
- [51] H. Gast and S. Schael. “Charge-dependent solar modulation in light of the recent PAMELA data”. In: *International Cosmic Ray Conference*. 2009.
- [52] M. S. Potgieter. “The charge-sign dependent effect in the solar modulation of cosmic rays”. In: *Advances in Space Research* 53 (2014), p. 1415.
- [53] L. Maccione. “Low Energy Cosmic Ray Positron Fraction Explained by Charge-Sign Dependent Solar Modulation”. In: *Phys. Rev. Lett.* 110 (2013), p. 081101.
- [54] F. J. Lowes. “Introduction to Geomagnetism”. In: *Physics of the Earth and Planetary Interiors* 33 (1983), p. 336.
- [55] J. De Keyser et al. “Magnetopause and Boundary Layer”. In: *Space Science Reviews* 118 (2005), p. 231.
- [56] J. A. Van Allen. “The geomagnetically trapped corpuscular radiation”. In: *Journal of Geophysical Research* 64 (1959), p. 1683.
- [57] *School of Geology and Geophysics, University of Oklahoma*. URL: http://geophysics.ou.edu/solid_earth/notes/mag_earth/earth.htm.
- [58] D. F. Smart and M. A. Shea. “A review of geomagnetic cutoff rigidities for earth-orbiting spacecraft”. In: *Advances in Space Research* 36 (2005), p. 2012.

- [59] O. Adriani et al. “Measurement of the isotopic composition of hydrogen and helium nuclei in cosmic rays with the PAMELA experiment”. In: *The Astrophysical Journal* 770 (2013), p. 2.
- [60] M. Garcia-Munoz, G. M. Mason, and J. A. Simpson. “The cosmic-ray age deduced from the Be-10 abundance”. In: *The Astrophysical Journal* 201 (1975), p. 141.
- [61] W. B. Atwood et al. “The Large Area Telescope on the Fermi Gamma-Ray Space Telescope Mission”. In: *The Astrophysical Journal* 697 (2009), p. 1071.
- [62] W. Menn et al. “The PAMELA space experiment”. In: *Advances in Space Research* 51 (2013), p. 209.
- [63] A. Kounine. “Status of the AMS Experiment”. In: *ArXiv e-prints* (2010). arXiv: 1009.5349v1 [astro-ph].
- [64] M. Casolino et al. “Detecting ultra-high energy cosmic rays from space with unprecedented acceptance: objectives and design of the JEM-EUSO mission”. In: *Astrophysics and Space Sciences Transactions* 7 (2011), p. 477.
- [65] J. Wu. “Progress of DAMPE: Chinese high energy cosmic particle detector to be in space”. In: *ICRC 2013, proceeding ID 868*. 2013.
- [66] E. S. Seo et al. “CREAM: 70 days of flight from 2 launches in Antarctica”. In: *Advances in Space Research* 42 (2008), p. 1656.
- [67] E. S. Seo. “Direct measurements of cosmic rays using balloon borne experiments”. In: *Astroparticle Physics* 3940 (2012). Cosmic Rays Topical Issue, p. 76.
- [68] A. Yamamoto et al. “The BESS Program”. In: *Nuclear Physics B - Proceedings Supplements* 166 (2007), p. 62.
- [69] *The ATIC Balloon Payload*. URL: <http://atic.phys.lsu.edu/Instrument.html>.
- [70] H. S. Ahn et al. “Energy Spectra of Cosmic-ray Nuclei at High Energies”. In: *The Astrophysical Journal* 707 (2009), p. 593.
- [71] P. J. Boyle et al. “Cosmic ray composition at high energies: The TRACER project”. In: *Advances in Space Research* 42 (2008), p. 409.
- [72] S. A. I. Mognet et al. “The prototype GAPS (pGAPS) experiment”. In: *Nuclear Instruments and Methods in Physics Research A* 735 (2014), p. 24.
- [73] W. R. Binns et al. “The SUPERTIGER Instrument: Measurement of Elemental Abundances of Ultra-Heavy Galactic Cosmic Rays”. In: *The Astrophysical Journal* 788 (2014), p. 18.
- [74] D. Heck and T. Pierog. *Extensive Air Shower Simulations with CORSIKA: A User’s Guide*. URL: https://web.ikp.kit.edu/corsika/usersguide/corsika_tech.html.
- [75] R. Ulrich, R. Engel, and M. Unger. “Hadronic multiparticle production at ultrahigh energies and extensive air showers”. In: *Phys. Rev. D* 83 (2011), p. 054026.
- [76] T. Abu-Zayyad et al. “The Cosmic Ray Energy Spectrum Observed with the Surface Detector of the Telescope Array Experiment”. In: *The Astrophysical Journal* 768 (2013), p. L1. eprint: 1205.5067.
- [77] *Detection des RCUHE : l’Observatoire Pierre Auger*. URL: <http://cdfbb.in2p3.fr/Public/Activites/Presentations/JJC/node3.html>.
- [78] A. Aab et al. “Depth of Maximum of Air-Shower Profiles at the Pierre Auger Observatory: Measurements at Energies above $10^{17.8}$ eV”. In: *arXiv e-prints* (2014). Submitted to Phys. Rev. D. arXiv: 1409.4809 [astro-ph.HE].

- [79] A. Aab et al. “Searches for Large-Scale Anisotropy in the Arrival Directions of Cosmic Rays Detected above Energy of 10^{19} eV at the Pierre Auger Observatory and the Telescope Array”. In: *The Astrophysical Journal* 794 (2014), p. 172.
- [80] M. Kachelriess, S. Ostapchenko, and R. Tomas. “Antimatter production in supernova remnants”. In: *The Astrophysical Journal* 733 (2011), p. 119.
- [81] M. S. Longair. *High energy astrophysics*. Vol. 1. Cambridge University Press, 2002.
- [82] I. Gebauer. “An Anisotropic Model for Galactic Cosmic Ray Transport and its Implications for Indirect Dark Matter Searches”. PhD thesis. Karlsruhe Institute of Technology, 2010.
- [83] L. Accardo et al. “High Statistics Measurement of the Positron Fraction in Primary Cosmic Rays of 0.5–500 GeV with the Alpha Magnetic Spectrometer on the International Space Station”. In: *Phys. Rev. Lett.* 113 (2014), p. 121101.
- [84] B. Ishak. “Pulsar Astronomy, 4th edn., by A. Lyne and F. Graham-Smith”. In: *Contemporary Physics* 54 (2013), p. 107.
- [85] A. Capriola. *The History of Joy Division’s “Unknown Pleasures” Album Art*. Web blog. 2014.
- [86] F.A. Aharonian, S.V. Bogovalov, and D. Khangulyan. “Abrupt acceleration of a ‘cold’ ultrarelativistic wind from the Crab pulsar”. In: *Nature* 482 (2012), p. 507.
- [87] D. Malyshev, I. Cholis, and J. Gelfand. “Pulsars versus dark matter interpretation of ATIC/PAMELA”. In: *Phys. Rev. D* 80 (2009), p. 063005.
- [88] S. Profumo. “Dissecting cosmic-ray electron-positron data with Occam’s razor: the role of known pulsars”. In: *Central European Journal of Physics* 10 (2012), p. 1.
- [89] D. Gaggero and L. Maccione. “Model independent interpretation of recent CR lepton data after AMS-02”. In: *Journal of Cosmology and Astroparticle Physics* 1312 (2013), p. 11.
- [90] M. Di Mauro et al. “Interpretation of AMS-02 electrons and positrons data”. In: *Journal of Cosmology and Astroparticle Physics* 2014 (2014), p. 6.
- [91] M. Ackermann et al. “Searches for cosmic-ray electron anisotropies with the Fermi Large Area Telescope”. In: *Phys. Rev. D* 82 (2010), p. 092003.
- [92] D. Campana et al. “Search for cosmic ray electron-positron anisotropies with the Pamela data”. In: *Journal of Physics: Conference Series* 409 (2013), p. 012055.
- [93] F. Zwicky. “Die Rotverschiebung von extragalaktischen Nebeln”. In: *Helvetica Physica Acta* 6 (1933), p. 110.
- [94] V. C. Rubin and W. K. Ford Jr. “Rotation of the Andromeda Nebula from a Spectroscopic Survey of Emission Regions”. In: *The Astrophysical Journal* 159 (1970), p. 379.
- [95] T. S. van Albada et al. “Distribution of dark matter in the spiral galaxy NGC 3198”. In: *The Astrophysical Journal* 295 (1985), p. 305.
- [96] M. Persic, P. Salucci, and F. Stel. “The universal rotation curve of spiral galaxies: I. The dark matter connection”. In: *Monthly Notices of the Royal Astronomical Society* 281 (1996), p. 27.
- [97] A. Einstein. “Lens-like action of a star by the deviation of light in the gravitational field”. In: *Science* (1936), p. 506.
- [98] R. J. Weymann, D. Walsh, R. F. Carswell. “0957 + 561 A, B: twin quasistellar objects or gravitational lens?” In: *Nature* (1979), p. 381.
- [99] D. Clowe et al. “A Direct Empirical Proof of the Existence of Dark Matter”. In: *The Astrophysical Journal* 648 (2006), p. 109.

- [100] M. Milgrom. “A modification of the Newtonian dynamics as a possible alternative to the hidden mass hypothesis”. In: *The Astrophysical Journal* 270 (1983), p. 365.
- [101] A. G. Riess et al. “A 3% Solution: Determination of the Hubble Constant with the Hubble Space Telescope and Wide Field Camera 3”. In: *The Astrophysical Journal* 730 (2011), p. 119. arXiv: 1103.2976 [astro-ph.CO].
- [102] Planck Collaboration et al. “Planck 2013 results. I. Overview of products and scientific results”. In: *ArXiv e-prints* (2013). arXiv: 1303.5062 [astro-ph.CO].
- [103] A. G. Riess et al. “Observational Evidence from Supernovae for an Accelerating Universe and a Cosmological Constant”. In: *The Astronomical Journal* 116 (1998), p. 1009.
- [104] Planck Collaboration et al. “Planck 2013 results. I. Overview of products and scientific results”. In: *ArXiv e-prints* (2013). arXiv: 1303.5062 [astro-ph.CO].
- [105] D. J. Fixsen. “The Temperature of the Cosmic Microwave Background”. In: *The Astrophysical Journal* 707 (2009), p. 916.
- [106] Planck Collaboration et al. “Planck 2013 results. XVI. Cosmological parameters”. In: *ArXiv e-prints* (2013). arXiv: 1303.5076 [astro-ph.CO].
- [107] Planck collaboration et al. “Planck 2013 results. XV. CMB power spectra and likelihood”. In: *ArXiv e-prints* (2013). arXiv: 1303.5075 [astro-ph.CO].
- [108] C. M. Bender and S. Sarkar. “Asymptotic analysis of the Boltzmann equation for dark matter relics”. In: *Journal of Mathematical Physics* 53, 103509 (2012), p. 103509.
- [109] K. A. Olive et al. “Review of Particle Physics”. In: *Chin. Phys.* C38 (2014), p. 090001.
- [110] P. Gondolo. “Non-baryonic dark matter”. In: *NATO Sci. Ser. II* 187 (2005), p. 279.
- [111] S. P. Martin. “A Supersymmetry primer”. In: *Adv. Ser. Direct. High Energy Phys.* 21 (2010), pp. 1–153.
- [112] P. Fayet. “Spontaneously broken supersymmetric theories of weak, electromagnetic and strong interactions”. In: *Physics Letters B* 69 (1977), p. 489.
- [113] U. Amaldi, W. de Boer, and H. Furstenuau. “Comparison of grand unified theories with electroweak and strong coupling constants measured at LEP”. In: *Physics Letter B* 260 (1991), pp. 447–455.
- [114] M. W. Goodman and E. Witten. “Detectability of certain dark-matter candidates”. In: *Phys. Rev. D* 31 (1985), p. 3059.
- [115] S. Scorza. “EDELWEISS-II, direct Dark Matter search experiment: first data analysis and results”. PhD thesis. Université Claude Bernard Lyon-I, 2009.
- [116] G. Bertone, D. Hooper, and J. Silk. “Particle dark matter: evidence, candidates and constraints”. In: *Physics Reports* 405 (2005), p. 279.
- [117] M. Vogelsberger et al. “Phase-space structure in the local dark matter distribution and its signature in direct detection experiments”. In: *Monthly Notices of the Royal Astronomical Society* 395 (2009), p. 797.
- [118] E. Armengaud et al. “Final results of the EDELWEISS-II WIMP search using a 4-kg array of cryogenic germanium detectors with interleaved electrodes”. In: *Physics Letters B* 702 (2011), p. 329.
- [119] R. Agnese et al. “Silicon Detector Dark Matter Results from the Final Exposure of CDMS II”. In: *Phys. Rev. Lett.* 111 (2013), p. 251301.

- [120] R. Agnese et al. “Search for Low-Mass Weakly Interacting Massive Particles Using Voltage-Assisted Calorimetric Ionization Detection in the SuperCDMS Experiment”. In: *Phys. Rev. Lett.* 112 (2014), p. 041302.
- [121] G. Angloher et al. “Results from 730 kg days of the CRESST-II Dark Matter search”. In: *European Physical Journal C* 72 (2012), p. 1971.
- [122] E. Aprile et al. “Dark Matter Results from 225 Live Days of XENON100 Data”. In: *Phys. Rev. Lett.* 109, 181301 (2012), p. 181301.
- [123] D.S. Akerib et al. “First results from the LUX dark matter experiment at the Sanford Underground Research Facility”. In: *Phys. Rev. Lett.* 112 (2014), p. 091303.
- [124] R. Bernabei et al. “New results from DAMA/LIBRA”. In: *The European Physical Journal C* 67 (2010), p. 39.
- [125] C. E. Aalseth et al. “Search for an Annual Modulation in a p-Type Point Contact Germanium Dark Matter Detector”. In: *Phys. Rev. Lett.* 107 (14 2011), p. 141301.
- [126] G. Angloher et al. “Results on low mass WIMPs using an upgraded CRESST-II detector”. In: *ArXiv e-prints* (2014). arXiv: 1407.3146 [astro-ph.CO].
- [127] H. Kraus et al. “EURECA - the European Future of Dark Matter Searches with Cryogenic Detectors”. In: *Nuclear Physics B - Proceedings Supplements* 173 (2007), p. 168.
- [128] E. Aprile and XENON1T collaboration. “The XENON1T Dark Matter Search Experiment”. In: *ArXiv e-prints* (2012). arXiv: 1206.6288 [astro-ph.IM].
- [129] D.C. Mallin et al. “After LUX: The LZ Program”. In: *ArXiv e-prints* (2011). arXiv: 1110.0103 [astro-ph.IM].
- [130] Private discussion with S. Scorza, October 2014.
- [131] L. Evans and P. Bryant. “LHC Machine”. In: *Journal of Instrumentation* 3 (2008), S08001.
- [132] The ATLAS Collaboration. “The ATLAS Experiment at the CERN Large Hadron Collider”. In: *Journal of Instrumentation* 3 (2008), S08003.
- [133] The CMS Collaboration. “The CMS experiment at the CERN LHC”. In: *Journal of Instrumentation* 3 (2008), S08004.
- [134] V. Kachatryan et al. “Search for dark matter, extra dimensions, and unparticles in monojet events in proton-proton collisions at $\sqrt{s} = 8$ TeV”. In: *ArXiv e-prints* (2014). arXiv: 1408.3583 [hep-ex].
- [135] G. Aad et al. “Search for Dark Matter Candidates and Large Extra Dimensions in Events with a Photon and Missing Transverse Momentum in pp Collision Data at $\sqrt{s}=7$ TeV with the ATLAS Detector”. In: *Phys. Rev. Lett.* 110 (2013), p. 011802.
- [136] S. Chatrchyan et al. “Search for invisible decays of Higgs bosons in the vector boson fusion and associated ZH production modes”. In: *European Physical Journal C* 74 (2014), p. 2980.
- [137] G. Aad et al. “Search for Invisible Decays of a Higgs Boson Produced in Association with a Z Boson in ATLAS”. In: *Phys. Rev. Lett.* 112 (2014), p. 201802.
- [138] G. Aad et al. “Search for direct production of charginos, neutralinos and sleptons in final states with two leptons and missing transverse momentum in pp collisions at $\sqrt{s} = 8$ TeV with the ATLAS detector”. In: *JHEP* 1405 (2014), p. 071.
- [139] G. Aad et al. “Search for direct production of charginos and neutralinos in events with three leptons and missing transverse momentum in $\sqrt{s} = 8$ TeV pp collisions with the ATLAS detector”. In: *JHEP* 1404 (2014), p. 169.

- [140] T. Bringmann and C. Weniger. “Gamma ray signals from dark matter: Concepts, status and prospects”. In: *Physics of the Dark Universe* 1 (2012), p. 194.
- [141] W. Weniger. “A tentative gamma-ray line from Dark Matter annihilation at the Fermi Large Area Telescope”. In: *Journal of Cosmology and Astroparticle Physics* 2012 (2012), p. 007.
- [142] M. Ackermann et al. “Search for gamma-ray spectral lines with the Fermi Large Area Telescope and dark matter implications”. In: *Phys. Rev. D* 88 (8 2013), p. 082002.
- [143] A. M. Galper et al. “Design and performance of the GAMMA-400 gamma-ray telescope for dark matter searches”. In: *AIP Conference Proceedings* 1516 (2013), p. 288.
- [144] L. Goodenough and D. Hooper. “Possible Evidence For Dark Matter Annihilation In The Inner Milky Way From The Fermi Gamma Ray Space Telescope”. In: *ArXiv e-prints* (2009). arXiv: 0910.2998 [hep-ph].
- [145] T. Daylan et al. “The Characterization of the Gamma-Ray Signal from the Central Milky Way: A Compelling Case for Annihilating Dark Matter”. In: *ArXiv e-prints* (2014). arXiv: 1402.6703 [astro-ph.HE].
- [146] T. Lacroix, C. Boehm, and J. Silk. “Fitting the Fermi-LAT GeV excess: On the importance of including the propagation of electrons from dark matter”. In: *Phys. Rev. D* 90 (2014), p. 043508.
- [147] A. Abramowski et al. “Search for Photon-Linelike Signatures from Dark Matter Annihilations with H.E.S.S.” In: *Phys. Rev. Lett.* 110 (2013), p. 041301.
- [148] M. G. Aartsen et al. “IceCube search for dark matter annihilation in nearby galaxies and galaxy clusters”. In: *Phys. Rev. D* 88 (2013), p. 122001.
- [149] M. G. Aartsen et al. “Search for Dark Matter Annihilations in the Sun with the 79-String IceCube Detector”. In: *Phys. Rev. Lett.* 110 (2013), p. 131302.
- [150] M. Cirelli. “Indirect searches for dark matter”. In: *Pramana* 79 (2012), p. 1021.
- [151] N. Fornengo, L. Maccione, and A. Vittino. “Constraints on particle dark matter from cosmic-ray antiprotons”. In: *Journal of Cosmology and Astroparticle Physics* 1404 (2014), p. 003.
- [152] M. Cirelli and G. Giesen. “Antiprotons from Dark Matter: current constraints and future sensitivities”. In: *Journal of Cosmology and Astroparticle Physics* 2013 (2013), p. 15.
- [153] M. Cirelli et al. “Antiproton constraints on the GeV gamma-ray excess: a comprehensive analysis”. In: (2014). arXiv: 1407.2173 [hep-ph].
- [154] O. Adriani et al. “PAMELA Results on the Cosmic-Ray Antiproton Flux from 60 MeV to 180 GeV in Kinetic Energy”. In: *Phys. Rev. Lett.* 105 (2010), p. 121101.
- [155] F. Donato, N. Fornengo, and P. Salati. “Antideuterons as a signature of supersymmetric dark matter”. In: *Phys. Rev. D* 62 (4 2000), p. 043003.
- [156] N. Fornengo, L. Maccione, and A. Vittino. “Dark matter searches with cosmic antideuterons: status and perspectives”. In: *Journal of Cosmology and Astroparticle Physics* 2013 (2013), p. 031.
- [157] H. Fuke et al. “Search for Cosmic-Ray Antideuterons”. In: *Phys. Rev. Lett.* 95 (2005), p. 081101.
- [158] M. Cirelli et al. “Anti-helium from dark matter annihilations”. In: *Journal of High Energy Physics* 2014, 9 (2014), p. 6.
- [159] E. Carlson et al. “Antihelium from dark matter”. In: *Phys. Rev. D* 89 (7 2014), p. 076005.
- [160] M. Cirelli et al. “Model-independent implications of the , cosmic ray spectra on properties of Dark Matter”. In: *Nuclear Physics B* 813 (2009), p. 1.

- [161] L. Pieri et al. “Implications of high-resolution simulations on indirect dark matter searches”. In: *Phys. Rev. D* 83 (2 2011), p. 023518.
- [162] I. Cholis and D. Hooper. “Dark matter and pulsar origins of the rising cosmic ray positron fraction in light of new data from the AMS”. In: *Phys. Rev. D* 88 (2 2013), p. 023013.
- [163] A. Sommerfeld. “Ueber die Beugung und Bremsung der Elektronen”. In: *Annalen der Physik* 403 (1931), p. 257.
- [164] M. Lattanzi and J. Silk. “Can the WIMP annihilation boost factor be boosted by the Sommerfeld enhancement?” In: *Phys. Rev. D* 79 (8 2009), p. 083523.
- [165] M. Cirelli et al. “Addendum including AMS 2013 data to Model-independent implications of the , cosmic ray spectra on properties of Dark Matter [Nucl. Phys. B 813 (12) (2009) 121]”. In: *Nuclear Physics B* 873 (2013), p. 530.
- [166] L. Bergström et al. “New Limits on Dark Matter Annihilation from Alpha Magnetic Spectrometer Cosmic Ray Positron Data”. In: *Phys. Rev. Lett.* 111 (17 2013), p. 171101.
- [167] Ki-Young Choi, Bumseok Kyae, and Chang Sub Shin. “Decaying WIMP dark matter for AMS-02 cosmic positron excess”. In: *Phys.Rev.* D89 (2014), p. 055002. eprint: 1307.6568.
- [168] S. Profumo. “The detection of a cosmic-ray electron-positron anisotropy is a sufficient (but not necessary) condition to discard a Dark Matter origin for the anomalous positron fraction”. In: *ArXiv e-prints* (2014). arXiv: 1405.4884 [astro-ph.HE].
- [169] AMS-02 collaboration. *AMS-02 website*. <http://www.ams02.org>.
- [170] M. L. Cherry and D. Müller. “Measurements of the Frequency Spectrum of Transition Radiation”. In: *Phys. Rev. Lett.* 38 (1977), p. 5.
- [171] M. L. Cherry et al. “Transition radiation from relativistic electrons in periodic radiators”. In: *Phys. Rev. D* 10 (1974), p. 3594.
- [172] A. Andronic and J. P. Wessels. “Transition radiation detectors”. In: *Nuclear Instruments and Methods in Physics Research A* 666 (2012), p. 130.
- [173] P. von Doetinchem et al. “Performance of the AMS-02 transition radiation detector”. In: *Nuclear Instruments and Methods in Physics Research A* 558 (2006), p. 526.
- [174] T. Kirn. “Threshold transition radiation detectors in astroparticle physics”. In: *Nuclear Instruments and Methods in Physics Research A* 563 (2006), p. 338.
- [175] K. Andeen, M. Heil, and F. Spada. “Operations and Alignment of the AMS-02 Transition Radiation Detector”. In: *ICRC 2013 proceedings* (2013). To be published.
- [176] M. Aguilar et al. “First Result from the Alpha Magnetic Spectrometer on the International Space Station: Precision Measurement of the Positron Fraction in Primary Cosmic Rays of 0.5-350 GeV”. In: *Phys. Rev. Lett.* 110 (2013), p. 141102.
- [177] W. Sun and Z. Weng. “Measurement of the absolute charge of cosmic ray nuclei with the AMS Transition Radiation Detector”. In: *ICRC 2013 proceedings* (2013). To be published.
- [178] V. Bindi et al. “The scintillator detector for the fast trigger and time-of-flight (TOF) measurement of the space experiment AMS-02”. In: *Nuclear Instruments and Methods in Physics Research A* 623 (2010), p. 968.
- [179] A. Basili et al. “The TOF-ACC flight electronics for the fast trigger and time of flight of the AMS-02 cosmic ray spectrometer”. In: *Nuclear Instruments and Methods in Physics Research A* 707 (2013), p. 99.

- [180] L. Quadrani. “The AMS-02 time of flight (TOF) system: construction and overall performances in space”. In: *ICRC 2013 proceedings* (2013). To be published.
- [181] Q. Yan. “Calibration of the AMS-02 Time of Flight detector”. In: *ICRC 2013 proceedings* (2013). To be published.
- [182] T. Bruch and W. Wallraff. “The Anti-Coincidence Counter shield of the AMS tracker”. In: *Nuclear Instruments and Methods in Physics Research A* 572 (2007), p. 505.
- [183] P. von Doetinchem et al. “The AMS-02 Anticoincidence Counter”. In: *Nuclear Physics B - Proceedings Supplements* 197 (2009), p. 15.
- [184] K. Luebelmeyer et al. “Upgrade of the Alpha Magnetic Spectrometer (AMS-02) for long term operation on the International Space Station (ISS)”. In: *Nuclear Instruments and Methods in Physics Research A* 654 (2011), p. 639.
- [185] M. Aguilar et al. “The Alpha Magnetic Spectrometer (AMS) on the International Space Station: Part I results from the test flight on the space shuttle”. In: *Physics Reports* 366 (2002), p. 331.
- [186] S. Ahlen et al. “An antimatter spectrometer in space”. In: *Nuclear Instruments and Methods in Physics Research A* 350 (1994), p. 351.
- [187] M. Duranti. “Measurement of the Atmospheric Muon Flux on Ground with the AMS-02 Detector”. PhD thesis. Università degli studi di Perugia, 2011.
- [188] P. Zuccon. “The AMS silicon tracker: Construction and performance”. In: *Nuclear Instruments and Methods in Physics Research A* 596 (2008), p. 74.
- [189] D. Hass. “The Silicon Tracker of AMS-02”. In: *Nuclear Instruments and Methods in Physics Research A* 530 (2004), p. 173.
- [190] P. Zuccon. “AMS-02 Track reconstruction and rigidity measurement”. In: *ICRC 2013 proceedings* (2013). To be published.
- [191] Z. Zhang et al. “Stable and self-adaptive performance of mechanically pumped CO₂ two-phase loops for AMS-02 tracker thermal control in vacuum”. In: *Applied Thermal Engineering* 31 (2011), p. 3783.
- [192] P. Saouter. “Nuclear charge measurement with the AMS-02 Silicon Tracker”. In: *ICRC 2013 proceedings* (2013). To be published.
- [193] H. Sadakazu. “Precision measurement of the proton flux with AMS”. In: *ICRC 2013 proceedings* (2013). To be published.
- [194] S. Schael S. Natale. “The AMS-02 Tracker Alignment System: design and performances”. In: *ICRC 2009 proceedings* (2009).
- [195] M. Aguilar-Benitez et al. “In-beam aerogel light yield characterization for the AMS RICH detector”. In: *Nuclear Instruments and Methods in Physics Research A* 614 (2010), p. 237.
- [196] R. Pereira. “The AMS-02 RICH detector: Performance during ground-based data taking at CERN”. In: *Nuclear Instruments and Methods in Physics Research A* 639 (2011), p. 37.
- [197] W. Gillard. “High precision measurement of the AMS-RICH aerogel refractive index with cosmic-ray”. In: *ICRC 2013 proceedings* (2013). To be published.
- [198] F. Giovacchini and I. Rodriguez. “In-flight determination of the AMS-RICH photon yield”. In: *ICRC 2013 proceedings* (2013). To be published.
- [199] C. Adloff et al. “The AMS-02 lead-scintillating fibres Electromagnetic Calorimeter”. In: *Nuclear Instruments and Methods in Physics Research A* 714 (2013), p. 147.

- [200] F. Cervelli et al. “A reduced scale e.m. calorimeter prototype for the AMS-02 experiment”. In: *Nuclear Instruments and Methods in Physics Research A* 490 (2002), p. 132.
- [201] F. Cadoux et al. “The AMS-02 electromagnetic calorimeter”. In: *Nuclear Physics B - Proceedings Supplements* 113 (2002), p. 159.
- [202] V. Vagelli. “Identification of positrons and electrons in the cosmic radiation with the electromagnetic calorimeter ECAL for the AMS-02 experiment”. MA thesis. Università degli studi di Pisa, 2011.
- [203] L. Basara. “Energy Calibration with MIP in space and charge measurement with AMS-02 Electromagnetic Calorimeter”. In: *ICRC 2013 proceedings* (2013). To be published.
- [204] G. Grindhammer and S. Peters. “The Parameterized simulation of electromagnetic showers in homogeneous and sampling calorimeters”. In: (1993). arXiv: hep-ex/0001020 [hep-ex].
- [205] S. Di Falco. “Performance of the AMS-02 Electromagnetic Calorimeter in Space”. In: *ICRC 2013 proceedings* (2013). To be published.
- [206] M. Vecchi. “A 3-dimensional electromagnetic shower characterization and its application to AMS-02 pointing capability”. In: *ICRC 2013 proceedings* (2013). To be published.
- [207] A. Sabellek. “The Space Qualified Data Acquisition for the Transition Radiation Detector of the AMS-02 Experiment on the International Space Station”. PhD thesis. Karlsruhe Institute of Technology, 2009.
- [208] A. Kounine and V. Koutsenko. *Flight Software for xDR and JINx nodes in AMS-02*. AMS internal notes. 2011.
- [209] C. Lin. *Trigger Logic Design Specification*. AMS internal notes. 2005.
- [210] F. Barao and L. Derome. *AMS rate evaluation from new physical triggers: acceptances, rates and livetime*. Report to AMS-02 collaboration. 2011.
- [211] V. Choutko. “Precision measurement of the helium flux with AMS”. In: *ICRC 2013 proceedings* (2013). To be published.
- [212] A. Oliva. “Precision measurement of the boron to carbon ratio and nuclei with AMS”. In: *ICRC 2013 proceedings* (2013). To be published.
- [213] A. Kounine. “The Alpha Magnetic Spectrometer on the International Space Station”. In: *International Journal of Modern Physics E* 21 (2012), p. 1230005.
- [214] S. Agostinelli et al. “Geant4: a simulation toolkit”. In: *Nuclear Instruments and Methods in Physics Research A* 506 (2003), p. 250.
- [215] B. Bertucci. “Precision measurement of the electron plus positron spectrum with AMS”. In: *ICRC 2013 proceedings* (2013). To be published.
- [216] Z. Weng. “Particle Identification Using Transition Radiation Detector and Precision Measurement of Cosmic Ray Positron Fraction with the AMS-02 Experiment”. PhD thesis. Sun Yat-Sen University, 2013.
- [217] M. Graziani. *Irreducible background from interacting protons*. Presented at the AMS e^\pm analysis meeting, Jun 2014, Aachen.
- [218] NOAA National Geophysical Data Center. *GMPOLE*. 1987. URL: http://www.ngdc.noaa.gov/geomag/geom_util/gmpole.shtml.
- [219] J. Bazo. *AMS data-driven cutoff estimation*. Presented at the AMS collaboration general analysis meeting, Dec 2013, Geneva.

- [220] B. P. Roe et al. “Boosted decision trees, an alternative to artificial neural networks”. In: *Nuclear Instruments and Methods A*543 (2005), p. 577. eprint: physics/0408124.
- [221] C. Corti. “Measure of the positrons fraction in cosmic rays with AMS-02”. MA thesis. Università degli studi di Pisa, 2012.
- [222] C. Corti, M. Incagli, and V. Vagelli. *A study for an ECAL standalone classification algorithm using the Boosted Decision Tree (BDT) technique*. AMS internal notes. 2014.
- [223] M. Heil. “Measurement of the positron fraction in cosmic rays from 0.5 - 350 GeV with the AMS-02 detector on the International Space Station”. PhD thesis. Karlsruhe Institute of Technology, 2013.
- [224] F. Schmid and A. Schmidt. “Nonparametric Estimation of the Coefficient of Overlapping-theory and Empirical Application”. In: *Comput. Stat. Data Anal.* 50 (2006), p. 1583.
- [225] W. Verkerke and D. Kirkby. “The RooFit toolkit for data modeling”. In: *ArXiv Physics e-prints* (2003). eprint: physics/0306116.
- [226] J. D. Sullivan. “Geometric factor and directional response of single and multi-element particle telescopes”. In: *Nuclear Instruments and Methods* 95 (1971), p. 5.
- [227] M. Crispoltoni. “Measure of the positrons fraction in cosmic rays with AMS-02”. MA thesis. Università degli studi di Perugia, 2014.
- [228] C. Delgado. “Alignment of the AMS-02 silicon Tracker”. In: *ICRC 2013 proceedings* (2013). To be published.
- [229] M. Incagli. *ECAL energy scale for e^\pm measurements*. Presented at the AMS e^\pm analysis meeting, May 2014, Perugia.
- [230] G. D. Lafferty and T. R. Wyatt. “Where to stick your data points: The treatment of measurements within wide bins”. In: *Nucl. Instrum. Meth.* A355 (1995), p. 541.
- [231] M. Duranti. *Electron and positron measurement consistency checks*. Presented at the AMS collaboration general analysis meeting, July 2014, Geneva.
- [232] G. D’Agostini, W. de Boer, and G. Grindhammer. “Determination of α_s and the Z^0 Mass From Measurements of the Total Hadronic Cross-section in e^+e^- Annihilation”. In: *Phys. Lett.* B229 (1989), p. 160.
- [233] N. Mori. “CALET: a calorimeter for cosmic-ray measurements in space”. In: *Nuclear Physics B - Proceedings Supplements* 239240 (2013), pp. 199–203.
- [234] B.F. Rauch. “Predicted CALET measurements of ultra-heavy cosmic ray relative abundances”. In: *Advances in Space Research* 53 (2014), pp. 1444–1450.
- [235] E.S. Seo et al. “Cosmic Ray Energetics And Mass for the International Space Station (ISS-CREAM)”. In: *Advances in Space Research* 53 (2014), pp. 1451–1455.
- [236] B. Bertucci. *Overview of direct Cosmic Rays measurements*. International Symposium on Very High Energy Cosmic Ray Interactions (ISVHECRI, August 2014).
- [237] G. E. P. Box and D. R. Cox. “An Analysis of Transformations”. In: *Journal of the Royal Statistical Society. Series B (Methodological)* 26 (1964), p. 211.
- [238] B. F. J. Manly. “Exponential Data Transformations”. In: *Journal of the Royal Statistical Society. Series D (The Statistician)* 25 (1976), p. 37.
- [239] A. Hoecker et al. “TMVA: Toolkit for Multivariate Data Analysis”. In: *PoS ACAT* (2007), p. 40.

Acknowledgements

The development and the completion of this thesis has been possible due to the support, help and presence of many persons that I would like here to acknowledge.

I express my gratitude to Prof. Wim de Boer for accepting me to work with his group and for always being available to share his astonishing knowledge with me (and by “always”, I really mean that!). His role in the development of this work has been essential from the very beginning. Similarly, I’d like to acknowledge all the colleagues and professors of the IEKP that have always been very supportive and friendly (especially when I wandered around the institute corridors asking for help for my analysis). In particular, I’m very grateful to Prof. Ulrich Husemann for the patience he had to read this work, for his useful suggestions and for the enjoyable discussions we had.

I also thank Dr. Iris Gebauer for gathering together our group and for the amazing coordination of all the projects we joined and faced. I’ve been really lucky in having her as supervisor. Working with the group has always been stimulating and fun. For this, I also have to thank all my colleagues that are working and worked with me in the AMS group and in the theory group. Stefan, for always being willing to help and for being a good friend of mine. Karen, you really had an infinite patience with me and my stupid requests (and sorry for all the english horrors you had to correct... I hope I improved a bit after your suggestions). Simon and Conny, with whom I shared our common final suffering and pain. Daniele, even you are just an impostor in the group, thank you for being a great friend of mine, and for all the great time, beers and discussions we had together. And all the other friends and colleagues in the group, you all contributed in different and positive manners to help me in these last years.

Another special gratitude goes to Prof. Bruna Bertucci and her AMS group in Perugia. She always supported me and my work and contributed with amazing ideas. The same gratitude goes to Prof. Marco Incagli, for introducing me to the AMS collaboration since the old good times of my bachelor internship and for the help and suggestions he gave to improve and develop the analysis. I also thank all my friends in the AMS group in Perugia. Maura, Mimmo, Marta, Federico, Giovanni, Pepe, Cecilia, Francesco. Thanks for all the dinners and the beautiful times we spent together in Perugia and at CERN. A (really) special thanks goes of course to my friend Matteo, that shared with me the pain and suffering that is hidden behind the beautiful results of this work. I will miss all the blood we spit on the plots and on the numbers of this analysis, the neverending nights before the general meetings and all the interesting discussions we had about physics and (un)related stuff . And thank you for showing me the meaning of playing and having fun with physics. I owe you a lot. Daje!

I want to thank also all my colleagues in the AMS collaboration. Working with the group has always been motivating, gratifying and funny. And special thanks to all the AMS friends I met in this last years for making the hard working times way more enjoyable, and for all the nice time spent together in Houston, in Cape Canveral and in Geneva.

Similar gratitude goes to all my friends in Karlsruhe which covered a major role in these last days of panic, crisis and emotional breakdowns. Thanks a lot to Silvia, Fabio, Matteo, Francesca, Alice, Lorenzo, Denis and all my other friends for always being there to listen to my complains and whinings and for keeping myself together in the last days of rush (also, thanks for offering me soups to eat and

wine to drink at non human hours. I really appreciated that!).

Finally, there are no words to express the primary role that my family played in these last years. Despite all my questionable choices, they always supported me in every decision and in every difficult situation I had to face. They have always been to my side, no matter what I did, no matter what I had to do. I would never have reached this and many other goals without them. All the efforts I put in this work are dedicated to my family. To my mother, my father, my little brother, my grandpas and grandmas.